

A minimal synthetic  
genome pp. 1380 & 1414

Unearthing an epic battle in  
Bronze Age Germany p. 1384

Ad hoc international  
ethics review p. 1399

# Science

\$15  
25 MARCH 2016  
sciencemag.org

AAAS

## *Recycling light*

Perovskite solar cells reuse emitted photons

pp. 1401 & 1430

# CONTENTS



1384

Bronze Age bling decorated warriors' hair and clothing

25 MARCH 2016 • VOLUME 351 • ISSUE 6280

## NEWS

### IN BRIEF

**1372** News at a glance

### IN DEPTH

#### **1376 CRUNCH TIME FOR DARK MATTER HUNT**

Little confidence that biggest WIMP detector ever will find hypothesized particles *By A. Cho*

#### **1377 DON'T BLAME SPORTS FOR ZIKA'S SPREAD**

Viral genomes suggest ordinary travel brought the disease to Brazil in late 2013 *By G. Vogel*

► N. R. FARIA ET AL. 10.1126/SCIENCE.AAF5036

#### **1378 COMB JELLY 'ANUS' GUTS IDEAS ON ORIGIN OF THROUGH-GUT**

Videos of captive marine creatures unexpectedly show jellies defecate from pores, not via their mouths *By A. Maarmen*

#### **1380 SYNTHETIC MICROBE HAS FEWEST GENES, BUT MANY MYSTERIES**

One-third of 473 genes in microbes have unknown functions *By R. F. Service*

► RESEARCH ARTICLE P. 1414

#### **1381 TURKISH SCHOLAR WHO ELUDED ARREST DESCRIBES 'WITCH HUNT'**

Three of Meral Camcı's fellow academics are imprisoned for criticizing the government; more arrests may follow *By J. Bohannon*

#### **1382 CHINA'S FIVE-YEAR PLAN BOOSTS BASIC RESEARCH FUNDING**

Blueprint gives few details, but scientists foresee more generous grants and new facilities *By H. Xin*

### FEATURE

#### **1384 SLAUGHTER AT THE BRIDGE**

Grisly find suggests Bronze Age northern Europe was more organized—and violent—than thought *By A. Curry*

► PODCAST

## INSIGHTS

### PERSPECTIVES

#### **1390 A BIG BANG IN SPLICEOSOME STRUCTURAL BIOLOGY**

3D snapshots reveal dynamics of the spliceosome on the mRNA splicing pathway *By J. H. D. Cate*

► RESEARCH ARTICLE P. 1416

#### **1392 THERMAL TROUBLE IN THE TROPICS**

Tropical species may be highly vulnerable to climate change

*By T. M. Perez et al.*

► REPORT P. 1437

#### **1394 A BENCHMARK FOR MATERIALS SIMULATION**

Material properties can now be predicted reliably from first-principles calculations *By C.-K. Skylaris*

► RESEARCH ARTICLE P. 1415

#### **1395 TWO-DIMENSIONAL NANOFUIDICS**

Restacked exfoliated sheets create interconnected nanofluidic channels for ion transport *By A. R. Koltonow and J. Huang*

#### **1396 DON'T FORGET THE SURFACE**

Surface effects play a key role in cloud droplet formation *By B. Noziere*

► REPORT P. 1447

#### **1398 THE ONCOGENE MAKES ITS ESCAPE**

Disruptions in 3D genomic architecture allow cancer genes to evade transcriptional silencing *By J. Wala and R. Beroukheim*

► REPORT P. 1454

#### **1399 ETHICS REVIEW FOR INTERNATIONAL DATA-INTENSIVE RESEARCH**

Ad hoc approaches mix and match existing components

*By E. S. Dove et al.*

#### **1401 LEAD HALIDES JOIN THE TOP OPTOELECTRONIC LEAGUE**

Lead halide materials have the properties needed to reach the highest photovoltaic efficiencies *By E. Yablonovitch*

► REPORT P. 1430

### BOOKS ET AL.

#### **1403 THE SOCIETY OF GENES**

*By I. Yanai and M. Lercher, reviewed by J. Swift*

#### **1404 KUHN'S STRUCTURE OF SCIENTIFIC REVOLUTIONS AT FIFTY**

*R. J. Richards and L. Daston, Eds., reviewed by S. D. Mitchell*

### LETTERS

#### **1405 BASIC SCIENCE: BEDROCK OF PROGRESS**

*By F. S. Collins et al.*

#### **1405 A RESEARCH SYMBIONT**

*By B. Fecher and G. G. Wagner*

#### **1406 PSEUDONYMOUS FAME**

*By M. C. Wendl*

#### **1406 TECHNICAL COMMENT ABSTRACTS**

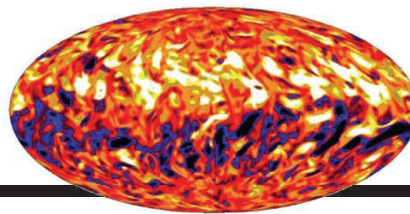
Science Staff .....	1368
AAAS News & Notes .....	1408
New Products .....	1479
Science Careers .....	1480



PHOTO: STEVEN HADDOCK/JELLYWATCH.ORG



# CONTENTS



1427

Simulating solar magnetism

25 MARCH 2016 • VOLUME 351 • ISSUE 6280

## RESEARCH

### IN BRIEF

**1411** From *Science* and other journals

### RESEARCH ARTICLES

#### 1414 SYNTHETIC BIOLOGY

Design and synthesis of a minimal bacterial genome  
*C. A. Hutchison III* et al.

RESEARCH ARTICLE SUMMARY; FOR FULL TEXT:

[dx.doi.org/10.1126/science.aad6253](http://dx.doi.org/10.1126/science.aad6253)

► NEWS STORY P. 1380

#### 1415 DFT METHODS

Reproducibility in density functional theory calculations of solids  
*K. Lejaeghere* et al.

RESEARCH ARTICLE SUMMARY; FOR FULL TEXT:

[dx.doi.org/10.1126/science.aad3000](http://dx.doi.org/10.1126/science.aad3000)

► PERSPECTIVE P. 1394

#### 1416 STRUCTURAL BIOLOGY

Molecular architecture of the human U4/U6.U5 tri-snRNP  
*D. E. Agafonov* et al.

► PERSPECTIVE P. 1390

### REPORTS

#### C-H BOND ACTIVATION

**1421** Catalyst-controlled selectivity in the C-H borylation of methane and ethane  
*A. K. Cook* et al.

**1424** Catalytic borylation of methane  
*K. T. Smith* et al.

#### 1427 MAGNETOHYDRODYNAMICS

Large-scale magnetic fields at high Reynolds numbers in magnetohydrodynamic simulations  
*H. Hotta* et al.

#### 1430 SOLAR CELLS

Photon recycling in lead iodide perovskite solar cells  
*L. M. Pazos-Outón* et al.

► PERSPECTIVE P. 1401



1392  
& 1437

#### 1433 ECONOMICS

Evaluating replicability of laboratory experiments in economics  
*C. F. Camerer* et al.

#### 1437 PHYSIOLOGICAL ECOLOGY

Seasonal and daily climate variation have opposite effects on species elevational range size  
*W.-P. Chan* et al.

► PERSPECTIVE P. 1392

#### 1440 MEMORY FORMATION

Diversity in neural firing dynamics supports both rigid and learned hippocampal sequences  
*A. D. Groszmark* and *G. Buzsáki*

#### 1443 NEURODEVELOPMENT

Sequential transcriptional waves direct the differentiation of newborn neurons in the mouse neocortex  
*L. Telley* et al.

#### 1447 CLOUD FORMATION

An interfacial mechanism for cloud droplet formation on organic aerosols  
*C. R. Ruehl* et al.

► PERSPECTIVE P. 1396

#### 1450 PROTEIN EVOLUTION

Survey of variation in human transcription factors reveals prevalent DNA binding changes  
*L. A. Barrera* et al.

#### 1454 CANCER

Activation of proto-oncogenes by disruption of chromosome neighborhoods  
*D. Hnisz* et al.

► PERSPECTIVE P. 1398

#### 1458 HIV-1 VACCINES

HIV-1 broadly neutralizing antibody precursor B cells revealed by germline-targeting immunogen  
*J. G. Jardine* et al.

#### 1463 TUMOR IMMUNOLOGY

Clonal neoantigens elicit T cell immunoreactivity and sensitivity to immune checkpoint blockade  
*N. McGranahan* et al.

#### 1469 TRANSPORTER FUNCTION

Direct observation of proton pumping by a eukaryotic P-type ATPase  
*S. Veshaguri* et al.

### DEPARTMENTS

#### 1371 EDITORIAL

Einstein v. Roberts  
*By S. J. Gates Jr.*

#### 1494 WORKING LIFE

Lessons from a bridge generation  
*By Rosalind A. Segal*

### ON THE COVER

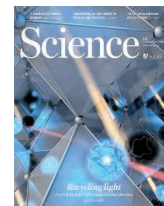


Illustration of the lead iodide perovskite crystal lattice with rays of sunlight falling onto the material, creating electron-hole pairs (electrons, blue; holes, black) as photons are absorbed. Upon later recombination of these charge pairs, photons are emitted and propagate within the crystal, regenerating charges when absorbed. This photon recycling process is crucial for obtaining high photovoltaic efficiencies and improving the performance of perovskite solar cells. See pages 1401 and 1430. *Illustration: C. Bickel/Science*

SCIENCE (ISSN 0036-8075) is published weekly on Friday, except the last week in December, by the American Association for the Advancement of Science, 1200 New York Avenue, NW, Washington, DC 20005. Periodicals mail postage (publication No. 484460) paid at Washington, DC, and additional mailing offices. Copyright © 2016 by the American Association for the Advancement of Science. The title SCIENCE is a registered trademark of the AAAS. Domestic individual membership and subscription (51 issues): \$165 (\$74 allocated to subscription). Domestic institutional subscription (51 issues): \$1522. Foreign postage extra: Mexico, Caribbean (surface mail) \$55; other countries (air assist delivery) \$89. First class, airmail, student, and emeritus rates on request. Canadian rates with GST available upon request. GST #R1254 88122. Publications Mail Agreement Number 1069624. Printed in the U.S.A. **Change of address:** Allow 4 weeks, giving old and new addresses and 8-digit account number. **Postmaster:** Send change of address to AAAS, P.O. Box 96178, Washington, DC 20090-6178. **Single-copy sales:** \$15.00 current issue, \$20.00 back issue prepaid includes surface postage; bulk rates on request. **Authorization to photocopy** material for internal or personal use under circumstances not falling within the fair use provisions of the Copyright Act is granted by AAAS to libraries and other users registered with the Copyright Clearance Center (CCC) Transactional Reporting Service, provided that \$35.00 per article is paid directly to CCC, 222 Rosewood Drive, Danvers, MA 01923. The identification code for Science is 0036-8075. Science is indexed in the Reader's Guide to Periodical Literature and in several specialized indexes.

**Editor-in-Chief** Marcia McNutt

**Executive Editor** Monica M. Bradford **News Editor** Tim Appenzeller

**Managing Editor, Research Journals** Katrina L. Kelner

**Deputy Editors** Barbara R. Jasny, Andrew M. Sugden(UK), Valda J. Vinson, Jake S. Yeston

## Research and Insights

**SR. EDITORS** Caroline Ash(UK), Gilbert J. Chin, Lisa D. Chong, Julia Fahrenkamp-Uppenbrink(UK), Pamela J. Hines, Stella M. Hurlley(UK), Paula A. Kiberstis, Marc S. Lavine(Canada), Kristen L. Mueller, Ian S. Osborne(UK), Beverly A. Purnell, L. Bryan Ray, Guy Riddihough, H. Jesse Smith, Jelena Stajic, Peter Stern(UK), Phillip D. Szurmi, Sacha Vignieri, Brad Wible, Nicholas S. Wigginton, Laura M. Zahn **ASSOCIATE EDITORS** Brent Grocholski, Keith T. Smith **ASSOCIATE BOOK REVIEW EDITOR** Valerie B. Thompson **ASSOCIATE LETTERS EDITOR** Jennifer Sills **CHIEF CONTENT PRODUCTION EDITOR** Cara Tate **SR. CONTENT PRODUCTION EDITORS** Harry Jach, Lauren Kmec **CONTENT PRODUCTION EDITORS** Jeffrey E. Cook, Chris Filatreau, Cynthia Howe, Barbara P. Ordway, Catherine Wolner **SR. EDITORIAL COORDINATORS** Carolyn Kyle, Beverly Shields **EDITORIAL COORDINATORS** Joi S. Granger, Lisa Johnson, Anita Wynn **PUBLICATIONS ASSISTANTS** Aneera Dobbins, Jeffrey Hearn, Dona Mathieu, Le-Toya Mayne Food, Shannon McMahon, Scott Miller, Caitlyn Phillips, Jerry Richardson, Rachel Roberts(UK), Alice Whaley(UK), Brian White **EXECUTIVE ASSISTANT** Anna Bashkistrova **ADMINISTRATIVE SUPPORT** Janet Clements(UK), Lizanne Newton(UK), Maryrose Madrid, John Wood(UK)

## News

**NEWS MANAGING EDITOR** John Travis **INTERNATIONAL EDITOR** Richard Stone **DEPUTY NEWS EDITORS** Daniel Clery(UK), Robert Coontz, Elizabeth Culotta, David Grimm, David Malakoff, Leslie Roberts **CONTRIBUTING EDITOR** Martin Enserink(Europe) **SR. CORRESPONDENTS** Jeffrey Mervis, Elizabeth Pennisi **NEWS WRITERS** Adrian Cho, Jon Cohen, Jennifer Couzin-Frankel, Carolyn Gramling, Eric Hand, Jocelyn Kaiser, Catherine Maticic, Kelly Servick, Robert F. Service, Erik Stokstad(Cambridge, UK), Emily Underwood **INTERNS** Hanae Armitage, Patrick Monahan, Nala Rogers **CONTRIBUTING CORRESPONDENTS** Michael Balter(Paris), John Bohannon, Warren Cornwall, Ann Gibbons, Mara Hvistendahl, Sam Kean, Eli Kintisch, Kai Kupferschmidt(Berlin), Andrew Lawler, Christina Larson(Beijing), Mitch Leslie, Charles C. Mann, Eliot Marshall, Virginia Morell, Dennis Normile(Shanghai), Heather Pringle, Tania Rabesandratana(London), Gretchen Vogel(Berlin), Lizzie Wade(Mexico City) **CAREERS** Donisha Adams, Rachel Bernstein(Editor) **COPY EDITORS** Julia Cole, Dorie Cheven, Jennifer Levin (Chief) **ADMINISTRATIVE SUPPORT** Jessica Adams

**Executive Publisher** Rush D. Holt

**Interim Publisher** Bill Moran **Chief Digital Media Officer** Rob Covey

**BUSINESS OPERATIONS AND PORTFOLIO MANAGEMENT DIRECTOR** Sarah Whalen **PRODUCT DEVELOPMENT DIRECTOR** Will Schweitzer **PRODUCT DEVELOPMENT ASSOCIATE** Hal Moore **BUSINESS SYSTEMS AND FINANCIAL ANALYSIS DIRECTOR** Randy Yi **MANAGER OF FULFILLMENT SYSTEMS** Neal Hawkins **SYSTEMS ANALYST** Nicole Mehmedovich **ASSISTANT DIRECTOR, BUSINESS OPERATIONS** Eric Knott **MANAGER, BUSINESS OPERATIONS** Jessica Tierney **SENIOR BUSINESS ANALYST** Cory Lipman **BUSINESS ANALYSTS** Sandy Kim, Meron Kebede **FINANCIAL ANALYST** Robert Clark **DIRECTOR, COPYRIGHTS LICENSING SPECIAL PROJECTS** Emilie David **PERMISSIONS ASSOCIATE** Elizabeth Sandler **RIGHTS, CONTRACTS, AND LICENSING ASSOCIATE** Lili Kiser

**MARKETING DIRECTOR** Elise Swinehart **ASSOCIATE DIRECTOR OF ACQUISITION AND RETENTION** Julianne Wielga **MARKETING ASSOCIATE** Elizabeth Sattler **SR. MARKETING EXECUTIVE** Jennifer Reeves **ASSOCIATE DIRECTOR, CREATIVE SERVICES** Tzeitel Sorrosa **ART ASSOCIATE** Seil Lee **JR. ART ASSOCIATE** Kim Huynh **ASSISTANT COMMERCIAL EDITOR** Selby Frame **MARKETING PROJECT MANAGER** Angelissa McArthur **PROGRAM DIRECTOR, AAAS MEMBER CENTRAL** Peggy Mihelich **FULFILLMENT SYSTEMS AND OPERATIONS** membership@aaas.org **MANAGER, MEMBER SERVICES** Pat Butler **SPECIALISTS** Terrance Morrison, Latasha Russell **MANAGER, DATA ENTRY** Mickie Napoleoni **DATA ENTRY SPECIALISTS** Brenden Aquilino, Fiona Giblin

**PUBLISHER RELATIONS MANAGER** Catherine Holland **PUBLISHER RELATIONS, EASTERN REGION** Keith Layson **PUBLISHER RELATIONS, WESTERN REGION** Ryan Rexroth **SALES RESEARCH COORDINATOR** Aiesha Marshall **MANAGER, SITE LICENSING OPERATIONS** Iqo Edim **SENIOR OPERATIONS ANALYST** Lana Guz **FULFILLMENT ANALYST** Judy Lillibridge **ASSOCIATE DIRECTOR, MARKETING** Christina Schlecht **MARKETING ASSOCIATE** Isa Sesay-Bah

**WEB TECHNOLOGIES SR. DEVELOPER** Chris Coleman **DEVELOPERS** Dan Berger, Jimmy Marks, Ryan Jensen **SR. PROJECT MANAGER** Trista Smith **PROJECT MANAGER** Nick Fletcher

**DIGITAL MEDIA DIRECTOR OF ANALYTICS** Enrique Gonzales **DIGITAL REPORTING ANALYST** Eric Hossinger **SR. WEB PRODUCER** Sarah Crespi **WEB PRODUCER** Alison Crawford **VIDEO PRODUCER** Nguyen Nguyen **SOCIAL MEDIA PRODUCER** Brice Russ

**DIRECTOR OF OPERATIONS PRINT AND ONLINE** Lizabeth Harman **DIGITAL/PRINT STRATEGY MANAGER** Jason Hillman **QUALITY TECHNICAL MANAGER** Marcus Spiegler **PROJECT ACCOUNT MANAGER** Tara Kelly **DIGITAL PRODUCTION MANAGER** Lisa Stanford **ASSISTANT MANAGER** DIGITAL/PRINT Rebecca Doshi **SENIOR CONTENT SPECIALISTS** Steve Forrester, Antoinette Hodal, Lori Murphy, Anthony Rosen **CONTENT SPECIALISTS** Jacob Hedrick, Kimberley Oster

**DESIGN DIRECTOR** Beth Rakouskas **DESIGN EDITOR** Marcy Atarod **SENIOR DESIGNER** Garvin Grullón **DESIGNER** Chrystal Smith **GRAPHICS MANAGING EDITOR** Alberto Cuadra **SENIOR SCIENTIFIC ILLUSTRATORS** Chris Bickel, Katharine Sutliff **SCIENTIFIC ILLUSTRATOR** Valerie Altounian **SENIOR ART ASSOCIATES** Holly Bishop, Nathalie Cary, Preston Huey **PHOTOGRAPHY MANAGING EDITOR** William Douthitt **PHOTO EDITORS** Leslie Blizard, Christy Steele

**DIRECTOR, GLOBAL COLLABORATION, CUSTOM PUBLICATIONS, ADVERTISING** Bill Moran **EDITOR, CUSTOM PUBLISHING** Sean Sanders: 202-326-6430 **ADVERTISING MARKETING MANAGER** Justin Sawyers: 202-326-7061 **science\_advertising@aaas.org** **ADVERTISING SUPPORT MANAGER** Karen Foote: 202-326-6740 **ADVERTISING PRODUCTION OPERATIONS MANAGER** Deborah Tompkins **SR. PRODUCTION SPECIALIST/GRAPHIC DESIGNER** Amy Hardcastle **SR. TRAFFIC ASSOCIATE** Christine Hall **SALES COORDINATOR** Shirley Young **ASSOCIATE DIRECTOR, COLLABORATION, CUSTOM PUBLICATIONS/CHINA/TAIWAN/KOREA/SINGAPORE** Ruolei Wu: +86-186 0082 9345, [rwu@aaas.org](mailto:rwu@aaas.org) **COLLABORATION/CUSTOM PUBLICATIONS/JAPAN** Adarsh Sandhu + 81-532-81-5142 [asandhu@aaas.org](mailto:asandhu@aaas.org) **EAST COAST/E. CANADA** Laurie Faraday: 508-747-9395, FAX 617-507-8189 **WEST COAST/W. CANADA** Lynne Stickrod: 415-931-9782, FAX 415-520-6940 **MIDWEST** Jeffrey Dembski: 847-498-4520 x3005, Steven Loerch: 847-498-4520 x3006 **UK EUROPE/ASIA** Roger Goncalves: TEL/FAX +41 43 243 1358 **JAPAN** Katsuyoshi Fukamizu(Tokyo): +81-3-3219-5777 [fukamizu@aaas.org](mailto:fukamizu@aaas.org) **CHINA/TAIWAN** Ruolei Wu: +86-186 0082 9345, [rwu@aaas.org](mailto:rwu@aaas.org)

**WORLDWIDE ASSOCIATE DIRECTOR OF SCIENCE CAREERS** Tracy Holmes: +44 (0) 1223 326525, FAX +44 (0) 1223 326532 [tholmes@science-int.co.uk](mailto:tholmes@science-int.co.uk) **CLASSIFIED** [advertise@sciencecareers.org](mailto:advertise@sciencecareers.org) **U.S. SALES** Tina Burks: 202-326-6577, Nancy Toema: 202-326-6578 **EUROPE/ROW SALES** Sarah Lelarge **SALES ASSISTANT** Kelly Grace **Japan** Hiroyuki Mashiki(Kyoto): +81-75-823-1109 [hsmashiki@aaas.org](mailto:hsmashiki@aaas.org) **CHINA/TAIWAN** Ruolei Wu: +86-186 0082 9345 [rwu@aaas.org](mailto:rwu@aaas.org) **MARKETING MANAGER** Allison Pritchard **MARKETING ASSOCIATE** Aimee Aponte

**AAAS BOARD OF DIRECTORS**, CHAIR Geraldine L. Richmond **PRESIDENT** Barbara A. Schaaf **PRESIDENT-ELECT** Susan Hockfield **TREASURER** David Evans **SHAW CHIEF EXECUTIVE OFFICER** Rush D. Holt **BOARD** Cynthia M. Beall, May R. Berenbaum, Carlos J. Bustamante, Stephen P.A. Fodor, Claire M. Fraser, Michael S. Gazzaniga, Laura H. Greene, Elizabeth Loftus, Mercedes Pascual

**SUBSCRIPTION SERVICES** For change of address, missing issues, new orders and renewals, and payment questions: 866-434-AAAS (2227) or 202-326-6417, FAX 202-842-1065. Mailing addresses: AAAS, P.O. Box 96178, Washington, DC 20090-6178 or AAAS Member Services, 1200 New York Avenue, NW, Washington, DC 20005

**INSTITUTIONAL SITE LICENSES** 202-326-6730 **REPRINTS:** Author Inquiries 800-635-7181 **COMMERCIAL INQUIRIES** 803-359-4578 **PERMISSIONS** 202-326-6765, [permissions@aaas.org](mailto:permissions@aaas.org) **AAAS Member Services** 202-326-6417 or <http://membercentral.aaas.org/discussions>

Science serves as a forum for discussion of important issues related to the advancement of science by publishing material on which a consensus has been reached as well as including the presentation of minority of conflicting points of view. Accordingly, all articles published in Science—including editorials, news and comment, and book reviews—are signed and reflect the individual views of the authors and not official points of view adopted by AAAS or the institutions with which the authors are affiliated.

**INFORMATION FOR AUTHORS** See pages 624 and 625 of the 5 February 2016 issue or access [www.sciencemag.org/authors/science-information-authors](http://www.sciencemag.org/authors/science-information-authors)

## SENIOR EDITORIAL BOARD

Gary King, Harvard University, Susan M. Rosenberg, Baylor College of Medicine, Ali Shilatifard, Northwestern University Feinberg School of Medicine

## BOARD OF REVIEWING EDITORS (Statistics board members indicated with \$)

Adriano Aguzzi, U. Hospital Zürich  
Takuzo Aida, U. of Tokyo  
Leslie Aiello, Wenner-Gren Foundation  
Judith Allen, U. of Edinburgh  
Sonia Altizer, U. of Georgia  
Sebastian Amigorena, Institut Curie  
Kathryn Anderson, Memorial Sloan-Kettering Cancer Center  
Meinrat O. Andreae, Max-Planck Inst. Mainz  
Paola Ariotta, Harvard U.  
Johan Auwerx, EPFL  
David Awechselom, U. of Chicago  
Clare Baker, University of Cambridge  
Nenad Ban, ETH Zurich  
Jordi Bascompte, University of Zurich  
Ray H. Baughman, U. of Texas, Dallas  
David Baum, U. of Wisconsin  
Carlo Beenakker, Leiden U.  
Kamran Behnia, ESPCI-ParisTech  
Yasmine Belkaid, NIAID, NIH  
Philip Benfey, Duke U.  
May Berenbaum, U. of Illinois  
Gabriele Bergers, U. of California, San Francisco  
Bradley Bernstein, Massachusetts General Hospital  
Peer Bork, EMBL  
Bernard Bourdon, Ecole Normale Supérieure de Lyon  
Chris Bowler, Ecole Normale Supérieure  
Ian Boyd, U. of St. Andrews  
Emily Brodsky, U. of California, Santa Cruz  
Ron Brookmeyer, U. of California Los Angeles (\$)  
Christian Büchel, U. Hamburg-Eppendorf  
Joseph A. Burns, Cornell U.  
Carter Tribble Butts, U. of California, Irvine  
Gyorgy Buzsaki, New York U. School of Medicine  
Blanche Capel, Duke U.  
Mats Carlsson, U. of Oslo  
Ib Chorkendorff, U. of Denmark  
David Clapham, Children's Hospital Boston  
Joel Cohen, Rockefeller U., Columbia U.  
James J. Collins, MIT  
Robert Cook-Deegan, Duke U.  
Lisa Coussens, Oregon Health & Science U.  
Alan Cowman, Walter & Eliza Hall Inst.  
Robert H. Crabtree, Yale U.  
Roberta Croce, Vrije Universiteit  
Janet Currie, Princeton U.  
Jeff L. Dangl, U. of North Carolina  
Tom Daniel, U. of Washington  
Frans de Waal, Emory U.  
Stanislas Dehaene, Collège de France  
Robert Desimone, MIT  
Claude Desplan, New York U.  
Dennis Discher, U. of Pennsylvania  
Gerald W. Dorn II, Washington U. School of Medicine  
Jennifer A. Doudna, U. of California, Berkeley  
Bruce Dunn, U. of California, Los Angeles  
William Dunphy, Caltech  
Christopher Dye, WHO  
Todd Ehlers, U. of Tübingen  
David Erhardt, Carnegie Inst. of Washington  
Tim Elston, U. of North Carolina at Chapel Hill  
Gerhard Ertl, Fritz-Haber-Institut, Berlin  
Barry Everitt, U. of Cambridge  
Ernst Fehr, U. of Zurich  
Anne C. Ferguson-Smith, U. of Cambridge  
Michael Feuer, The George Washington U.  
Toren Finkel, NHLBI, NIH  
Kate Fitzgerald, U. of Massachusetts  
Peter Fratzl, Max-Planck Inst.  
Elaine Fuchs, Rockefeller U.  
Daniel Geschwind, UCLA  
Karl-Heinz Glassmeier, TU Braunschweig  
Ramon Gonzalez, Rice U.  
Julia R. Greer, Caltech  
Elizabeth Grove, U. of Chicago  
Nicolas Gruber, ETH Zurich  
Kip Guy, St. Jude's Children's Research Hospital  
Taekjip Ha, U. of Illinois at Urbana-Champaign  
Wolf-Dietrich Hardt, ETH Zurich  
Christian Haass, Ludwig Maximilians U.  
Sharon Hammes-Schieff, U. of Illinois at Urbana-Champaign  
Michael Hasselmo, Boston U.  
Martin Heimann, Max-Planck Inst. Jena  
Yka Helariutta, U. of Cambridge  
James A. Hendler, Rensselaer Polytechnic Inst.  
Janet G. Hering, Swiss Fed. Inst. of Aquatic Science & Technology  
Kai-Uwe Hinrichs, U. of Bremen  
David Hodell, U. of Cambridge  
Lora Hooper, UT Southwestern Medical Ctr. at Dallas  
Tamas Horvath, Yale University  
Raymond Huey, U. of Washington  
Fred Hughson, Princeton U.  
Auke Ijspeert, EPFL Lausanne  
Stephen Jackson, USGS and U. of Arizona  
Steven Jacobsen, U. of California, Los Angeles  
Kai Johnsson, U. of Lausanne  
Peter Jonas, Inst. of Science & Technology (IST) Austria  
Matt Kaeblerlein, U. of Washington  
William Kaelin Jr., Dana-Farber Cancer Inst.  
Daniel Kahne, Harvard U.  
Daniel Kammen, U. of California, Berkeley  
Abby Kavner, U. of California, Los Angeles  
Masashi Kawasaki, U. of Tokyo  
V. Narry Kim, Seoul National U.

Joel Kingsolver, U. of North Carolina at Chapel Hill  
Robert Kingston, Harvard Medical School  
Etienne Koechlin, Ecole Normale Supérieure  
Alexander Kolodkin, Johns Hopkins U.  
Thomas Langer, U. of Cologne  
Mitchell A. Lazar, U. of Pennsylvania  
David Lazer, Harvard U.  
Thomas Lecuit, IBDM  
Virginia Lee, U. of Pennsylvania  
Stanley Lemon, U. of North Carolina at Chapel Hill  
Ottoline Leyser, Cambridge U.  
Wendell Lim, U.C. San Francisco  
Marcia C. Linn, U. of California, Berkeley  
Jianguo Liu, Michigan State U.  
Luis Liz-Marzan, CIC bioGUNE  
Jonathan Losos, Harvard U.  
Ke Lu, Chinese Acad. of Sciences  
Christian Lüscher, U. of Geneva  
Laura Machesky, CRUK Beatson Inst. for Cancer Research  
Anne Magurran, U. of St. Andrews  
Oscar Marin, CSIC & U. Miguel Hernández  
Charles Marshall, U. of California, Berkeley  
C. Robertson McClung, Dartmouth College  
Graham Medley, U. of Warwick  
Tom Misteli, NCI  
Yasushi Miyashita, U. of Tokyo  
Mary Ann Moran, U. of Georgia  
Richard Morris, U. of Edinburgh  
Alison Motsinger-Reif, NC State U. (\$)  
Thomas Murray, The Hastings Center  
Daniel Neumark, U. of California, Berkeley  
Kitty Nijmeijer, U. of Twente  
Pär Nordlund, Karolinska Inst.  
Helga Nowotny, European Research Advisory Board  
Ben Olken, MIT  
Joe Orenstein, U. of California  
Berkeley & Lawrence Berkeley National Lab  
Harry Orr, U. of Minnesota  
Pilar Ossorio, U. of Wisconsin  
Andrew Oswald, U. of Warwick  
Steve Palumbi, Stanford U.  
Jane Parker, Max-Planck Inst. of Plant Breeding Research  
Giovanni Parmigiani, Dana-Farber Cancer Inst. (\$)  
John H. J. Petrini, Memorial Sloan-Kettering Cancer Center  
Samuel Pfaff, Salk Institute for Biological Studies  
Joshua Plotkin, U. of Pennsylvania  
Albert Polman, FOM Institute AMOLF  
Philippe Pouchin, CNRS  
Jonathan Pritchard, Stanford U.  
David Randall, Colorado State U.  
Felix Rey, Institut Pasteur  
Trevor Robbins, U. of Cambridge  
Jim Roberts, Fred Hutchinson Cancer Research Ctr.  
Barbara A. Romanowicz, U. of California, Berkeley  
Amy Rosenzweig, Northwestern University  
Mike Ryan, U. of Texas, Austin  
Mitsunori Saitou, Kyoto U.  
Shimon Sakaguchi, Kyoto U.  
Miquel Salmeron, Lawrence Berkeley National Lab  
Jürgen Sandkühn, Medical U. of Vienna  
Alexander Schier, Harvard U.  
Vladimir Shalae, Purdue U.  
Robert Siliciano, Johns Hopkins School of Medicine  
Dennis Simon, Arizona State U.  
Uri Simonsohn, U. of Pennsylvania  
Alison Smith, John Innes Centre  
Richard Smith, U. of North Carolina (\$)  
John Speakman, U. of Aberdeen  
Allan C. Spradling, Carnegie Institution of Washington  
Jonathan Sprent, Garvan Inst. of Medical Research  
Eric Steig, U. of Washington  
Paula Stephan, Georgia State U. and National Bureau of Economic Research  
Molly Stevens, Imperial College London  
V. S. Subrahmanian, U. of Maryland  
Ira Tabas, Columbia U.  
Sarah Teichmann, Cambridge U.  
John Thomas, North Carolina State U.  
Joshua Tole, Tata Institute of Fundamental Research  
Christopher Tyler-Smith, The Wellcome Trust Sanger Inst.  
Herbert Virgin, Washington U.  
Bert Vogelstein, Johns Hopkins U.  
Cynthia Volkert, U. of Göttingen  
David Wallach, Weizmann Inst. of Science  
Ian Walsley, U. of Oxford  
Jane-Ling Wang, U. of California, Davis (\$)  
David A. Wardle, Swedish U. of Agric. Sciences  
David Waxman, Fudan U.  
Jonathan Weissman, U. of California, San Francisco  
Chris Wikle, U. of Missouri (\$)  
Ian A. Wilson, The Scripps Res. Inst. (\$)  
Timothy D. Wilson, U. of Virginia  
Rosemary Wyse, Johns Hopkins U.  
Jan Zaenen, Leiden U.  
Kenneth Zaret, U. of Pennsylvania School of Medicine  
Jonathan Zehr, U. of California, Santa Cruz  
Len Zon, Children's Hospital Boston  
Maria Zuber, MIT

## BOOK REVIEW BOARD

David Bloom, Harvard U. Samuel Bowring, MIT, Angela Creager, Princeton U., Richard Sweder, U. of Chicago, Ed Wasserman, DuPont



# Einstein v. Roberts

In the recent U.S. Supreme Court hearing on *A. Fisher v. the University of Texas* about university admission policies regarding minority students, Chief Justice John Roberts asked, “What unique perspective does a minority student bring to a physics class?” As an African-American physicist researching string theory, and a teacher of university students since 1972, I have a response.

Issues related to race in the United States have created barriers since the nation’s founding, determining which citizens experience benefits, and which deprivations. This problem is not new for physicists. Albert Einstein’s essay “The Negro Question” includes “What...can the man of good will do to combat this deeply rooted prejudice? He must have the courage to set an example by word and deed, and must watch lest his children become influenced by this racial bias.” Einstein described racism as a “disease,” and he recommended principles to end discrimination, aligning with the *O. Brown v. the Board of Education of Topeka, Kansas*, decision by the Supreme Court in 1954 to desegregate public schools.

Chief Justice Roberts’ question—premised on the idea that a person’s background, including race, is irrelevant in science—shows a fundamental misunderstanding of both science and human creativity. Science is a creative process, which is why the enterprise needs diverse thinking. The Chief Justice’s physics class may have consisted of plugging numbers into equations to find how long a dropped ball takes to reach the ground. But today’s science classes often strive for creative exploration and collaboration to foster innovation. This played out recently in my upper-level undergraduate class. Students worked in small groups to solve a problem involving vector calculus and group theory—mathematics related to the discovery of subatomic particles such as the Higgs boson. In one group, two European-American students led discussions into a mathematical dead end. An African-American group member eventually wrote something on the board, which, when finally noticed, unstuck the

group, and the problem was solved. Days afterward, the situation recurred, but this time, the group paid attention to the minority student, asking, “How did you come to that answer?” The students learned more than vector calculus that day. The majority students understood that a different perspective is an asset in science, while the minority student gained peer creditability and confidence. Together, the members became more efficient as problem solvers.

This is only an anecdote, but it shows what can happen in real-world classrooms. Several books have described the efficacy of diversity for the sake of innovation. For example, Scott E. Page explains that diversity’s

superiority emerges when a problem is difficult; that is, when no single individual always finds a solution, particularly in situations requiring creativity.

In 1969, I entered the Massachusetts Institute of Technology (MIT) expecting to be different from most of the other new undergraduate students. Although often challenging, I found that my difference could be an advantage: Distinctive backgrounds can lead to different approaches to framing problems. If MIT had been legally bound then to admissions based solely on test scores, I would never have been admitted. It would have been a personal

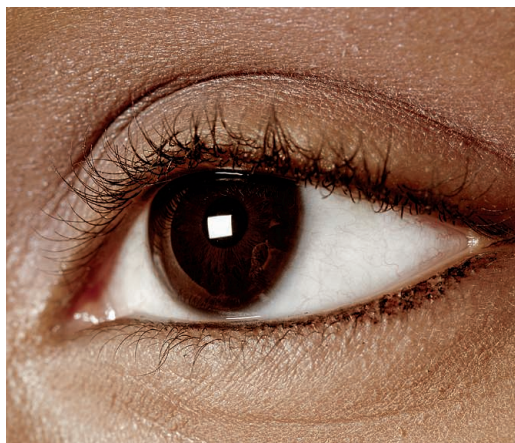
loss, but more importantly, unique mathematical and physics ideas created in my career, and tied to my idiosyncratic framing of problems, might never have seen the light of day.

Minorities have made progress in science, as my own life attests. People of color and women are the fastest-growing segments of the U.S. college population. But discrimination continues. Each individual brings unique experiences that influence the capacity to move science forward in creative ways. Colleges need ways to recognize this in admissions processes. In the meantime, the *Fisher v. Texas* decision is poised to shape how and whether people like me can emerge in future science at its highest levels.

— S. J. Gates, Jr.



*S. J. Gates, Jr. is a professor in the Department of Physics at the University of Maryland, College Park, MD, and a University System of Maryland Regents Professor. E-mail: gates@wam.umd.edu*



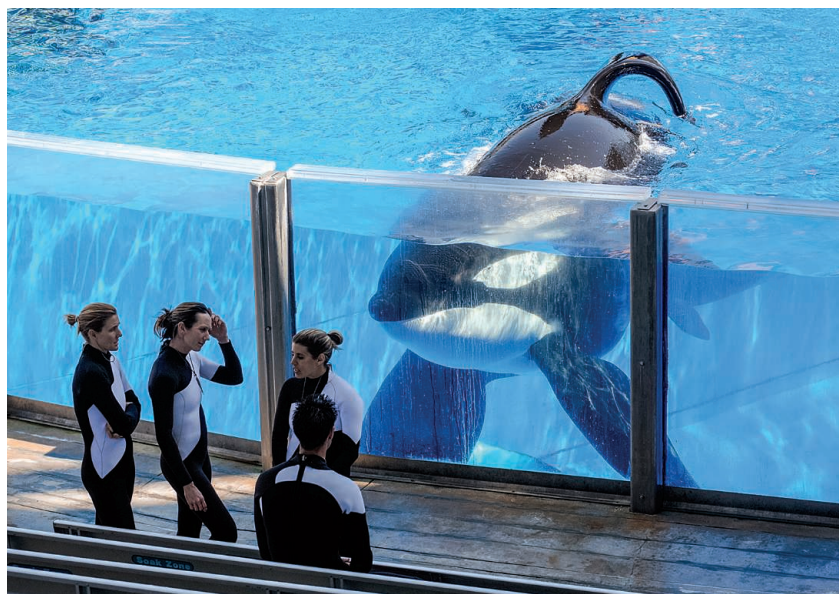
*“...a different perspective is an asset in science...”*

“I’m terribly sorry about all of this, @NERCscience.”

@JamesHand, a former BBC presenter, whose joking suggestion, *Boaty McBoatface*, now dominates an online contest to name the U.K. Natural Environment Research Council’s new £200 million ship. The winner will be chosen from the top nominees by a committee.

## IN BRIEF

### SeaWorld says it will stop breeding orcas



Killer whale Tilikum, subject of the 2013 documentary *Blackfish*, watches his trainers at SeaWorld.

SeaWorld announced last week that it will end orca breeding at its marine parks and will phase out killer whale shows, focusing instead on programs that emphasize “orca enrichment, exercise and overall health.” The move comes after years of pressure by animal rights and animal welfare advocates, as well as some scientists, who have argued that cetaceans (a group including whales and dolphins) shouldn’t be kept in captivity. Other researchers, however, express concern that removing all cetaceans from captivity could curtail important research that cannot be replicated in the wild. (There are currently about 600 cetaceans kept in 34 facilities in North America.) Studies of SeaWorld’s orcas have explored killer whale breeding and physiology, but how much research the park’s animals have been part of is unclear. As for its dolphins, SeaWorld has made no announcement. “I think the move is a good decision for killer whales, who can travel up to 160 kilometers in a day,” says animal behaviorist Richard Connor of the University of Massachusetts, Dartmouth. “But dolphins are more amenable to captivity, and we’ve just scratched the surface of what we can learn from them.” [http://scim.ag/\\_SeaWorld](http://scim.ag/_SeaWorld)

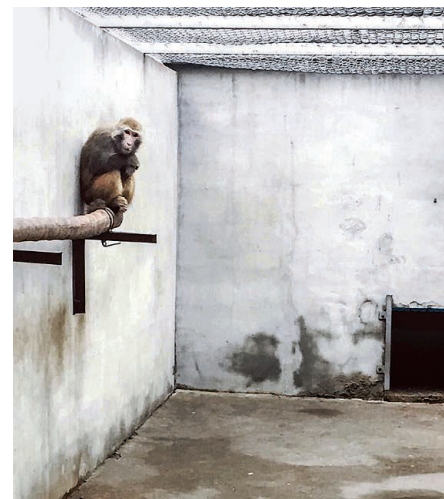
## AROUND THE WORLD

### Lassa fever case in Germany

FRANKFURT, GERMANY | A German mortician is being treated for Lassa fever at a hospital in Frankfurt after handling the body of a U.S. Agency for International Development worker who had apparently contracted the virus in Togo. It appears to be the first clear case of human-to-human transmission of the deadly virus outside of West Africa, where Lassa is endemic. (In 2000, a physician who treated a Lassa patient in Germany developed antibodies against the virus but did not fall ill.) The World Health Organization announced an outbreak of Lassa fever in Benin last month, and neighboring Nigeria and Togo have also reported cases. Nigeria alone has seen close to 400 cases and at least 63 deaths this year, according to the Nigeria Centre for Disease Control. Another U.S. citizen who worked in Togo is being treated for Lassa fever at Emory Hospital in Atlanta.

### China sets lab animal guidelines

BEIJING | China has released its first national standards governing the treatment of laboratory animals. The draft standards, which cover topics including euthanasia, pain management, transport, and housing, were posted last week for public comment and may be implemented



Rhesus macaques in a Beijing lab.



by the end of this year. Scientists hope the guidelines will not only improve conditions for animals, but also improve China's prospects for international research collaborations. Meanwhile, there is growing domestic concern about the mistreatment of lab animals because of recently documented incidents of abuse. According to the Chinese Academy of Medical Sciences's Institute of Laboratory Animal Sciences in Beijing, China uses roughly 20 million animals—mostly mice, but also large numbers of dogs, rabbits, and nonhuman primates—each year in research.  
<http://scim.ag/Chinalabanimal>

## Allen invests big in bioscience

WASHINGTON, D.C. | Philanthropist Paul G. Allen announced this week the creation of a new bioscience research initiative, which he is launching with \$100 million over the next 10 years. To determine which investigators would receive the first grants from the new Paul G. Allen Frontiers Group, “we asked everyone the same question: What is the dark matter of bioscience?” says the group’s executive director, biomedical engineer Tom Skalak in Seattle, Washington. Four researchers—Jennifer Doudna of the University of California (UC), Berkeley, Ethan Bier of UC San Diego, James Collins of the Massachusetts Institute of Technology in Cambridge, and Bassem Hassan of the Brain and Spine Institute in Paris—will receive \$1.5 million from the Frontiers Group to study topics ranging from novel techniques for gene editing, how shapes and forms arise over the course of evolution, and how synthetic biology can create microbes that can trap and kill dangerous bacteria. Allen will also fund two new research centers at Stanford University in Palo Alto, California, and Tufts University in Boston.

## NSF funding rules may ease

WASHINGTON, D.C. | U.S. Representative John Culberson (R-TX) says that he no longer favors specifying funding levels for individual research directorates at the National Science Foundation (NSF). If Culberson’s change of heart is real, it would be a significant victory for the U.S. research community, which has accused him and other congressional Republicans of imposing their own research priorities above those set by the agency and working scientists. Culberson, who chairs the spending subcommittee in the House of Representatives that controls NSF’s budget, pushed NSF last year to



## Hubble unveils monster stars

**T**he star cluster R136 is already home to the largest known star in the universe, a giant more than 250 times the mass of the sun. Now, astronomers using the Hubble Space Telescope to observe the cluster in ultraviolet light have found a total of nine stars with masses of more than 100 suns. The pack of heavyweights is located in the Tarantula Nebula (shown above, with R136 below center), some 170,000 light-years from Earth. How they form is a mystery; the current theory of star formation cannot explain how such behemoths could come together from the collapse of a cloud of gas and dust. One possible explanation was that giant stars could grow through the merger of binary star pairs, but that still wouldn’t explain this number of giants in close proximity, the team wrote last week in the *Monthly Notices of the Royal Astronomical Society*. They plan to continue observing R136 with Hubble in visible light, searching for binaries that could merge to produce such massive stars.

boost spending on four of its six research directorates—biology, computing, engineering, and mathematics and physical sciences—while trimming its investments in the social and geosciences. He noted his second thoughts last week after a hearing on NSF’s 2017 budget request, in which NSF Director France Córdova made a plea for creating a portfolio based on the

most exciting research across all fields.  
<http://scim.ag/NSFCulberson>

## Collections support suspended

ARLINGTON, VIRGINIA | The U.S. National Science Foundation (NSF) announced last week that it has indefinitely suspended its Collections in Support of Biological





Radar scans of the walls of Tutankhamun's tomb suggest concealed rooms.

## Tut's tomb may hide secret chambers

**K**ing Tutankhamun's famously rich tomb has been painstakingly scrutinized since its discovery by Western archaeologists in 1922. But it may still hide unexplored treasures—possibly even the tomb of the legendary Egyptian queen Nefertiti. On 17 March, Egypt's Antiquities Minister Mamdouh Eldamaty announced new finds from the tomb at a press conference held in Cairo. In November 2015, high-resolution radar scans of the tomb had suggested that additional chambers lay behind the walls of the pharaoh's burial chamber. Now, more detailed analyses of the data confirm the existence of two hidden chambers, with objects inside apparently made of metal and organic matter, Eldamaty said. No one knows yet what these objects are, but certain artifacts in King Tut's tomb—which some scholars suggest appear to have been made for someone else—offer the tantalizing prospect that the hidden chambers could contain Nefertiti's remains. Researchers will conduct more scans before making any plans to excavate the chambers.

Research (CSBR) program, one of the only public funding sources for basic museum infrastructure in the country. CSBR funded projects to maintain biological collections, such as upgrading freezers for tissue samples and building cabinets for plant collections. NSF will continue to fund existing grants, but won't accept new applications in 2016 while it assesses the future of the program. The move has sparked concern among members of the museum community, who worry that NSF is funding specific research projects while failing to support the infrastructure they rely on. Biological collections support a wide range of research projects, from describing new species to assessing the impacts of climate change on ecosystems.

## Backup plan for unfunded grants

**BETHESDA, MARYLAND** | Researchers whose grant proposals are rejected by the U.S. National Institutes of Health (NIH) may soon have a new way to find support

for their research. The Online Partnership to Accelerate Research (OnPAR), launched in pilot form this month, aims to play matchmaker between rejected NIH projects and second-chance funders, such as nonprofit disease research foundations or pharmaceutical companies. A collaboration between NIH and the defense, engineering, and health contractor Leidos, headquartered in Reston, Virginia, OnPAR lets researchers upload unfunded NIH proposals to an online portal where potential funders can review their scores and decide whether to put up cash. A similar project run by the National Health Council folded in 2012 after failing to secure any commitments from potential funders. The year-long OnPAR pilot, described in an editorial this week in *Science Translational Medicine*, has signed up seven potential funders—all nonprofit disease foundations, but its creators hope it will expand to include biotech companies and venture capital firms. <http://scim.ag/Allengrants>

## BY THE NUMBERS

# 24%

Share of grants funded by the National Science Foundation last year whose titles were changed to make them clearer to the public.

<http://scim.ag/NSFtitles>

# 18

The average life span reduction, in years, for people with autism spectrum disorder compared with the general population, according to a report by the philanthropic group Autistica.

<http://scim.ag/Autisticarep>

# 95%

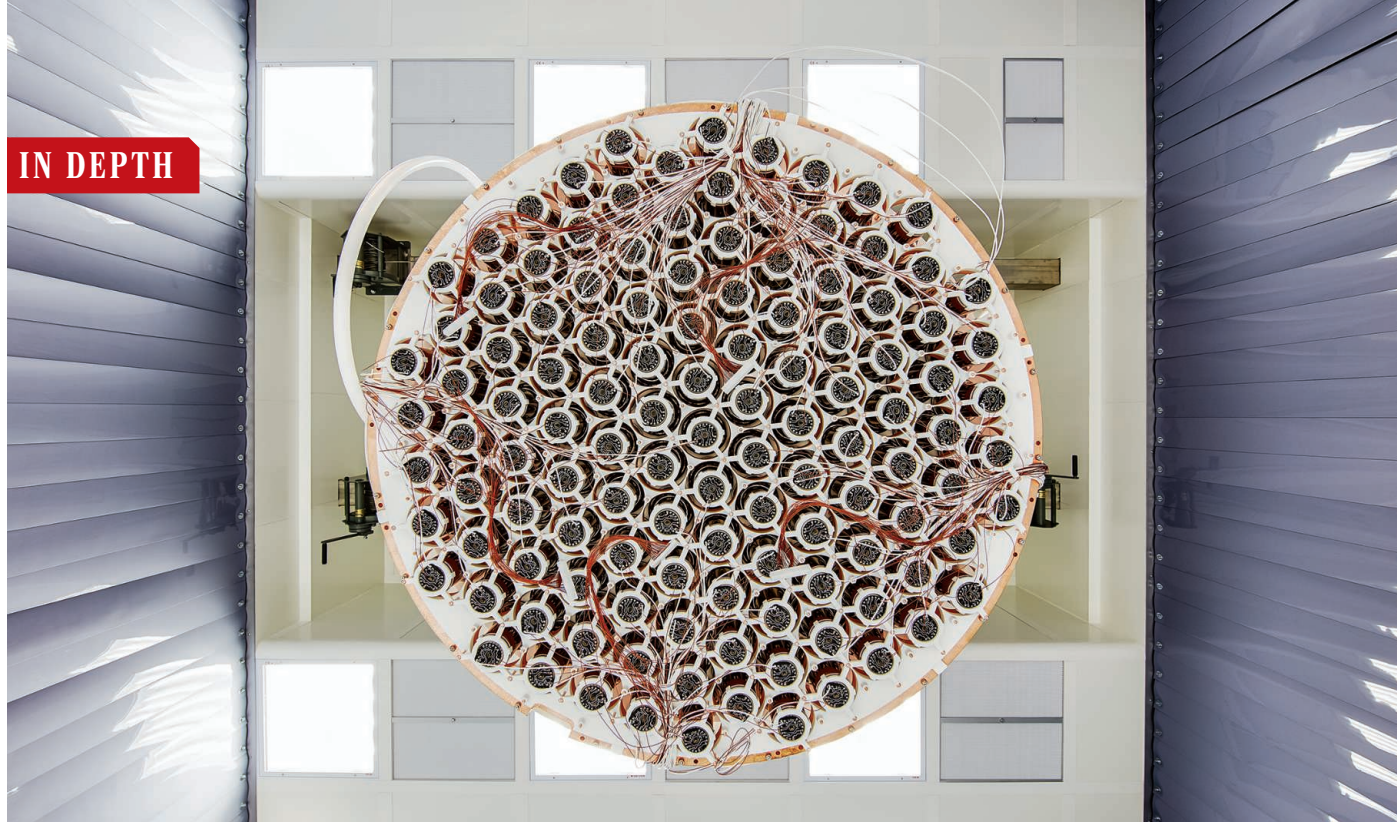
Fraction of some 1976 wild relatives of 81 crops that aren't adequately conserved in world gene banks, although they may have valuable traits, such as drought and pest resistance (*Nature Plants*). <http://scim.ag/wildcrops>

## NEWSMAKERS

### Simon to lead cancer moonshot

**Greg Simon**, a leukemia survivor, corporate executive, and veteran Washington, D.C., insider, has been tapped to head Vice President Joe Biden's \$1 billion "moonshot" to cure cancer. After working as a congressional aide and adviser to then-Vice President Al Gore, Simon joined with philanthropist Michael Milken to start FasterCures, a think tank aimed at speeding the development of cancer treatments. He moved on to Pfizer and is now CEO of Poliwogg, a life sciences investment company. The 64-year-old lawyer was diagnosed with chronic lymphocytic leukemia in 2014; after chemotherapy, he is now healthy. As executive director of the Cancer Moonshot Task Force, Simon will work with federal agencies to break down silos in cancer research ([http://scim.ag/\\_cancermoon](http://scim.ag/_cancermoon)). President Barack Obama is spending \$195 million on moonshot activities this year and has asked Congress for \$755 million in 2017.





## PARTICLE PHYSICS

# Crunch time for dark matter hunt

Little confidence that biggest WIMP detector ever will find hypothesized particles

By Adrian Cho

**T**his month, in a cavernous laboratory 1.4 kilometers below Gran Sasso d'Italia, the tallest peak in Italy's Apennine Mountains, physicists will begin filling a cylindrical tank with liquid xenon, a frigid substance three times as dense as water. About 1 meter tall and wide, the tank will form the heart of XENON1T, the biggest detector so far to hunt for weakly interacting massive particles (WIMPs), hypothetical particles that may make up the mysterious dark matter that pervades our galaxy and binds it with its gravity. But even as XENON1T crosses a key size threshold in physicists' 30-year search for WIMPs, researchers are starting to have doubts about the concept of WIMPs.

"It's crunch time," says Rocky Kolb, a theorist at the University of Chicago (UC) in Illinois, comparing the WIMP quest to a football game. "We're in the second half, maybe the fourth quarter. We haven't scored." Elena Aprile, an experimentalist at Columbia University and leader of the XENON team, says the new detector has a real shot at discovering WIMPs: "They could be right around the corner." But, she adds, "We're perhaps losing faith in the sense that we're not sure whether 1 ton or even 10 tons

will be enough to see anything."

Other dark matter researchers share her concerns. A few years ago, when the biggest WIMP detector weighed a few kilograms, most thought that a 1-ton experiment would either find WIMPs or stick a dagger in the idea. But generations of ever bigger detectors have come up empty, and physicists are rethinking the argument for WIMPs and what it might take to find them. They have bigger detectors in the works and are laying plans for the ultimate WIMP detector. But even avid dark matter hunters aren't sure that the giant detector is worth pursuing.

The concept of the WIMP dates back to the early 1980s. In 1983, experimenters at CERN, the European particle physics laboratory near Geneva, Switzerland, discovered the particles that convey the so-called weak nuclear force: the fleeting W boson and Z boson. At the time, theorists realized that if the bosons had a stable uncharged cousin of similar mass—say, a few hundred times that of a proton—then just enough of those heavy, aloof particles should linger from the big bang to provide the unseen mass whose gravity holds galaxies and other cosmic structures together. The WIMP was born.

Inspired by that "WIMP miracle," theorists realized that a concept called supersymmetry also predicts WIMPs. Supersymmetry posits

for every known particle a more massive partner with a different spin. In many versions of supersymmetry the lightest superpartner is stable, neutral, and interacts through only the weak force, just like a WIMP. That connection made the WIMP one of two leading candidates for dark matter particles. (The other is the axion, a hypothetical particle born of the theory of the strong nuclear force [*Science*, 1 November 2013, p. 552].)

Physicists envision detecting WIMPs in three ways (*Science*, 6 July 2007, p. 32). First, they hope to spot them directly as they crash into atomic nuclei in ultrasensitive detectors like XENON1T, placed deep underground where they're shielded from ordinary radiation. Second, they hope to produce them and other supersymmetric particles at the world's biggest atom-smasher, CERN's Large Hadron Collider (LHC). Third, they hope to spot telltale radiation from WIMPs colliding and annihilating one another in the center of our galaxy, as supersymmetry predicts they might.

When it comes to underground detectors, bigger is better, as a more massive experiment provides more nuclei for WIMPs to hit. Around the world, about a dozen teams are working on detectors of various types. The current sensitivity record belongs to the Large Underground Xenon (LUX) detector

This battery of photodetectors will look for flashes of light from WIMPs colliding with xenon nuclei.

at the Sanford Underground Research Facility in Lead, South Dakota, which contains 370 kilograms of liquid xenon. In 2014 LUX leapfrogged the previous, second version of XENON, which held 62 kilograms of liquid. XENON1T—which will actually contain 3.5 metric tons of liquid xenon—will vault into the lead when it starts taking data this spring, as it should be 100 times more sensitive than LUX.

But physicists are anxious about its prospects. Their main concern is that in 6 years of running, the LHC has found no evidence of supersymmetry—the foundation of the WIMP model. It's not too late, as until last year the LHC ran at only half energy. Still, “the 800-pound gorilla in the room is the lack of any sign of supersymmetry coming from the LHC,” says Juan Collar, an experimentalist at UC.

To hedge their bets, dark matter researchers are working on even bigger detectors. XENON1T is designed so that in 2 years it can be expanded to create XENONnT, which would hold 7.5 metric tons of xenon. And researchers with LUX are building a detector called LZ that should hold 10 metric tons of xenon and would come on line in 2019.

The drive for bigger WIMP detectors can't go on forever, physicists say. Detectors 100 times more sensitive than XENON1T would suffer from interference generated by neutrinos. Streaming from the sun and other sources, these particles will start to make confounding WIMP-like signals in the detectors. Hitting that neutrino background marks the end of the road, physicists say.

Physicists in Europe already are planning

to push to that limit. Laura Baudis, an experimentalist at the University of Zurich in Switzerland and a member of the XENON team, leads planning for DARWIN, a detector that also would sit in Gran Sasso and would contain 50 tons of liquid xenon. DARWIN would cost roughly \$60 million, and Baudis says the team hopes to get the go-ahead for construction in 2020.

Other physicists seem less than keen on the project. “What comes after [XENON1T] is when you take a broom and make sure you haven't missed anything in the corners,” says Rafael Lang, a XENON team member at Purdue University in West Lafayette, Indiana. UC's Collar says, “I don't know how many people would be interested in working on this. I know I certainly wouldn't be.”

But Baudis stresses that DARWIN would also pursue key experiments in neutrino physics. “I wouldn't do it only to close the gap on the WIMP,” she says. The detector could search for a hypothesized nuclear decay called neutrinoless double  $\beta$  decay that would prove that the neutrino is its own antiparticle. It could measure the spectrum of solar neutrinos to high precision.

Meanwhile, some experimenters think it's time to pursue other dark matter candidates. Collar is working on a small detector for more-speculative strongly interacting massive particles, which would interact with ordinary matter too strongly to reach underground detectors. But many other proposed dark matter particles lack a connection to known physics like the WIMP miracle. That makes it hard to know what sort of experiment to build, Aprile says. “There are too many ideas,” she says. If the WIMP doesn't show up soon, dark matter hunters may not know what to look for next. ■

## INFECTIOUS DISEASE

# Don't blame sports for Zika's spread

Viral genomes suggest ordinary travel brought the disease to Brazil in late 2013

By Gretchen Vogel

**W**orld Cup fans are probably not to blame for bringing Zika virus to Brazil in June and July 2014. And, contrary to other speculation, neither are the teams that attended a championship canoe race in September 2014. According to a new genome analysis, the virus, first detected in northeastern Brazil in March 2015, had likely been spreading there long before either event, having arrived sometime between May and December 2013. The researchers say it most likely slipped in on one of thousands of airline flights from French Polynesia or Southeast Asia.

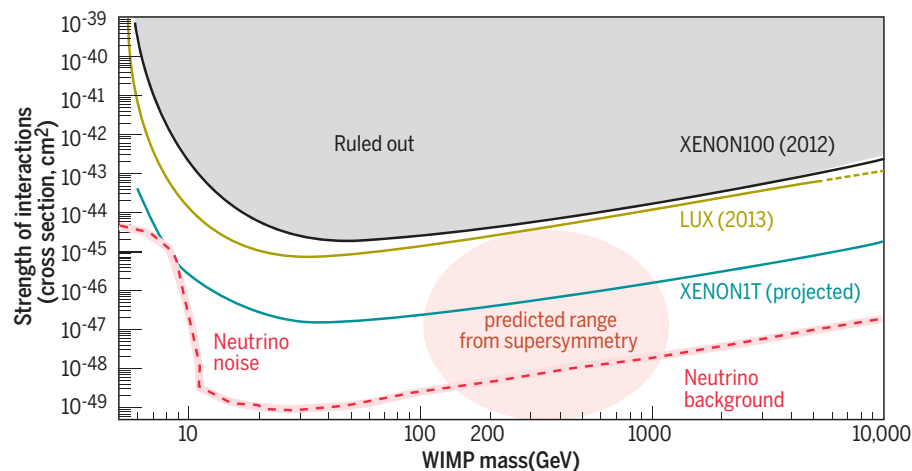
That is an important insight, says Matthew Ferrari, an epidemiologist and modeler at Pennsylvania State University, University Park, who wasn't involved in the study. “Starting with [one-time events] as hypotheses can be distracting,” he says. “The genome data suggest an entirely different timeline.”

More than 50 researchers from Brazil, the United Kingdom, Canada, and the United States collaborated on the study, published online today in *Science*. The scientists sequenced the full genome of virus samples taken from seven Brazilian patients who were infected with Zika between March and November 2015. The virus has now raced through the Americas, with local transmission reported in at least 33 countries. It usually causes only mild symptoms, but it has recently been linked to a striking increase in babies born with microcephaly, corresponding brain damage, and other neurological effects in adults.

Four of the virus samples came from patients with uncomplicated cases. One sample was from a baby born with microcephaly, who died shortly after birth. Another was taken from a 35-year-old man who died from complications of encephalitis after being infected with Zika. And the last came from a blood donor who developed a rash—a typi-

## End of the road for WIMP searches

The quest for weakly interacting massive particles (WIMPs) likely will end when increasingly sensitive detectors run into interference from neutrinos. They've already ruled out some of the range for supersymmetric WIMPs.





cal symptom of Zika—2 days after donating blood. The scientists looked for, but did not find, genetic signatures that would point to a mutation that might be fueling the virus's rapid spread or the serious complications.

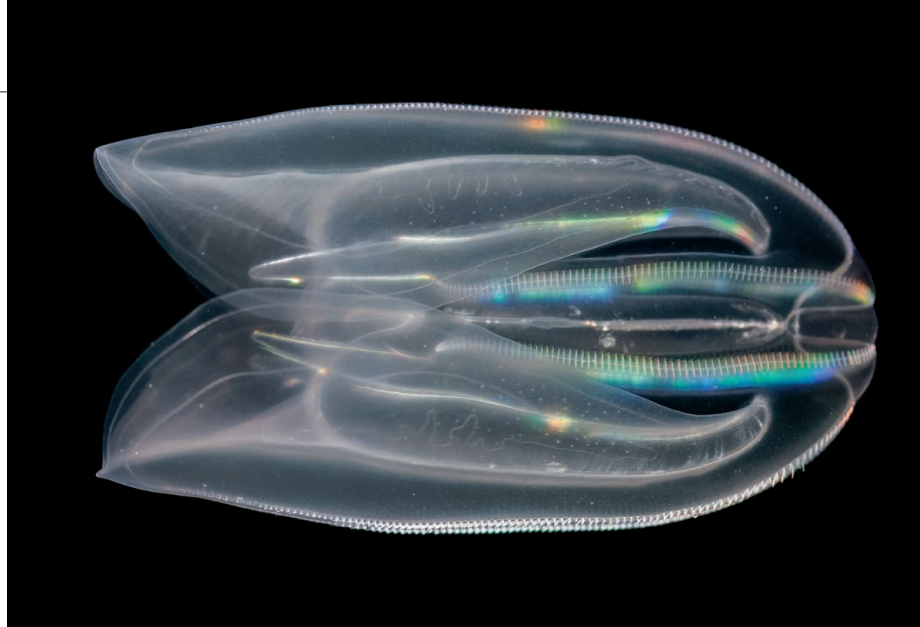
To try to retrace the virus's route, the scientists compared the genomes of the Brazilian samples to those from patients in nine other countries, six from the current outbreak in the Americas and one each from French Polynesia, the Cook Islands, and Thailand. The sequences from the Americas were the most closely related; the sequence from a patient in Thailand in 2013 was the most distant. That's consistent with the leading theory that the virus entered Brazil only once, from someone infected in the 2013 Zika epidemic in French Polynesia, and spread to the rest of the Americas from there, says Oliver Pybus, an evolutionary biologist at the University of Oxford in the United Kingdom, and a co-author on the paper.

It could have arrived, the authors say, during the Confederations Cup soccer tournament in late June 2013. That event brought the Tahitian national team to a stadium in Recife, near the epicenter of the Brazilian epidemic. (Tahiti lost to Uruguay, 8–0.) But that was several months before cases of Zika were reported in Tahiti, and Pybus thinks it's more fruitful to look at broader travel patterns rather than discrete events.

"If we can map flows of people and animals," researchers might be able to find patterns that could help forecast outbreaks, Pybus says. "No amount of looking at individual events is ever going to do that for us." He and his co-authors calculated that during 2013, air travel from Zika-endemic areas to Brazil increased by almost 50%, from roughly 3500 passengers arriving per month to nearly 5000.

Although researchers tend to focus on the well-studied outbreak in French Polynesia, other Zika-endemic countries have much larger populations and send more travelers to Brazil, Pybus notes. More than 1000 airline passengers arrived from the Philippines per month in 2013; Indonesia and Thailand sent similar numbers. It's plausible, he says, that travelers brought the virus directly from Southeast Asia to Brazil, and not from French Polynesia. Scott Weaver from the University of Texas Medical Branch in Galveston agrees. "The Philippines is a very likely source, it just hasn't been sampled," he says.

Scientists need more virus genomes from those countries to sort out the route Zika took to Brazil, Pybus says. "We have a bit of a black hole when it comes to understanding Zika transmission in Southeast Asia." The Tahitian team playing in Recife "is a great story," Pybus says, "but who knows if it's true." ■



Comb jellies such as *Mnemiopsis leidyi* have a through-gut, challenging when this evolutionary innovation arose.

## EVOLUTION

# Comb jelly 'anus' guts ideas on origin of through-gut

Videos of captive marine creatures unexpectedly show jellies defecate from pores, not via their mouth

By Amy Maxmen

**N**o butts about it, the butthole is one of the finest innovations in the past 540 million years of animal evolution. The first animals that arose seem to have literally had potty mouths: Their modern-day descendants, such as sea sponges, sea anemones, and jellyfish, all lack an anus and must eat and excrete through the same hole. Once an independent exit evolved, however, animals diversified into the majority of species alive today, ranging from earthworms to humans.

One apparent advantage of a second hole is that animals can eat while digesting a meal, whereas creatures with one hole must finish and defecate before eating again. Other possible benefits, say evolutionary biologists, include not polluting an animal's dining area and allowing an animal to evolve a longer body because it does not have to pump waste back up toward the head.

However, several unprecedented videos of gelatinous sea creatures called comb jel-

lies, or ctenophores, now threaten to upend the standard view of the evolution of the so-called through-gut. On 15 March, at the Ctenopolooza meeting in St. Augustine, Florida, evolutionary biologist William Browne of the University of Miami in Florida debuted films of comb jellies pooping—and it wasn't through their mouths.

Browne's videos elicited gasps from the audience because comb jellies, whose lineage evolved long before other animals with through-guts, had been thought to eat and excrete through a single hole leading to a saclike gut. In 1880, the German zoologist Carl Chun suggested a pair of tiny pores opposite the comb jelly mouth might secrete some substance, but he also confirmed that the animals defecate through their mouths. In 1997, biologists again observed indigestible matter exiting the comb jelly mouth—not the mysterious pores.

Browne, however, used a sophisticated video setup to continuously monitor two species that he keeps in captivity, *Mnemiopsis leidyi* and *Pleurobrachia bachei*. The movies he played at Ctenop-

**"Looks like I've been wrong for 30 years. ... If people don't see this video, they won't believe it."**

**George Matsumoto**, Monterey Bay Aquarium Research Institute

olooza capture the creatures as they ingest tiny crustaceans and zebrafish genetically engineered to glow red with fluorescent protein. Because comb jellies are translucent, the prey can be seen as it circulates through a network of canals lacing the jellies' bodies. Fast-forward, and 2 to 3 hours later, indigestible particles exit through the pores on the rear end. Browne also presented a close-up image of the pores, highlighting a ring of muscles surrounding each one. "This is a sphincterlike hole," he told the audience.

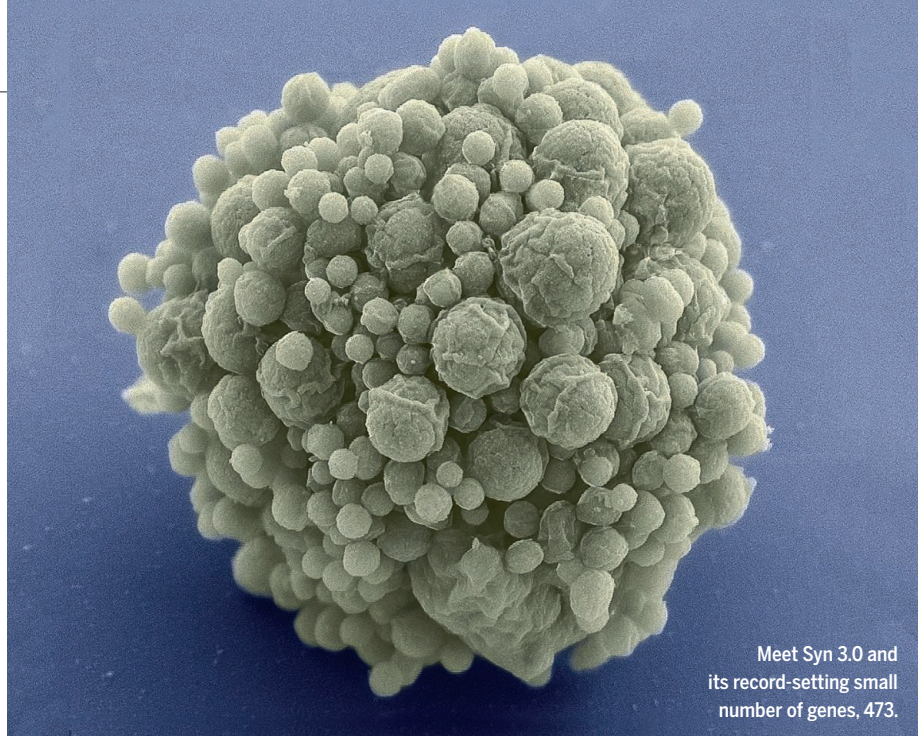
"Looks like I've been wrong for 30 years," said George Matsumoto, a marine biologist at Monterey Bay Aquarium Research Institute in Moss Landing, California, after he saw Browne's talk. "If people don't see this video, they won't believe it," he added. Matsumoto said he, as well as the biologists before him, likely missed the bowel movements because they did not observe their animals long enough after a meal. Jellies seen to expel waste from their mouths might have been, in effect, vomiting because they were fed too much, or the wrong thing.

According to recent DNA analyses, comb jellies evolved earlier than other animals considered to have one hole, including sea anemones, jellyfish, and possibly sea sponges. (Some studies suggest sponges arose first.) Consequently, Browne's as-yet unpublished findings disrupt the step-wise progression of digestive anatomy from one to two holes early in animal evolution.

One possibility is that the comb jellies evolved through-guts and anuslike pores on their own, independent of all other animals, over hundreds of millions of years. Alternatively, a through-gut and exit hole may have evolved once in an ancient animal ancestor, and subsequently became lost in anemones, jellyfish, and sponges. Perhaps if you're an anemone or a sponge stuck to a rock, suggests Matsumoto, it's better to push waste back into the current rather than below.

Browne is currently exploring the latter theory by seeing whether comb jellies activate the same genes when developing their pores that other animals do when growing an anus. If he finds that the genes are different, the evolution of our most unspeakable body part will no longer be considered the singular event zoologists long supposed. "We have all these traditional notions of a ladderlike view of evolution, and it keeps getting shaken," says Kevin Kocot, an evolutionary biologist at the University of Alabama, Tuscaloosa. ■

*Amy Maxmen is a writer based in Berkeley, California.*



## SYNTHETIC BIOLOGY

# Synthetic microbe has fewest genes, but many mysteries

One-third of 473 genes in microbe have unknown functions

By Robert F. Service

When it comes to genome size, a rare Japanese flower, called *Paris japonica*, is the current heavyweight champ, with 50 times more DNA than humans. At the other end of the scale, there's now a new lightweight record-holder growing in petri dishes in California. This week in *Science*, researchers led by genome sequencing pioneer Craig Venter report engineering a bacterium to have the smallest genome—and the fewest genes—of any freely living organism, smaller than the flower's by a factor of 282,000. Known as Syn 3.0, the new organism has a genome whittled down to the bare essentials needed to survive and reproduce, just 473 genes. "It's a tour de force," says George Church, a synthetic biologist at Harvard University.

The microbe's streamlined genetic structure excites evolutionary biologists and biotechnologists, who anticipate adding genes back to it one by one to study their effects. "It's an important step to creating a living cell where the genome is fully defined," says synthetic biologist Chris Voigt of the Massachusetts Institute of Technology in Cambridge. But Voigt and others note that this complete definition remains

a ways off, because the function of 149 of Syn 3.0's genes—roughly one-third—remains unknown. Investigators' first task is to probe the roles of those genes, which promise new insights into the basic biology of life.

As Syn 3.0's name suggests, it's not the first synthetic life made by Venter, who heads the J. Craig Venter Institute (JCVI) and is a founder of Synthetic Genomics, a biotech company, both in San Diego, California. In 2010, Venter's team reported that they had synthesized the sole chromosome of *Mycoplasma mycoides*—a bacterium with a relatively small genome—and transplanted it into a separate mycoplasma called *M. capricolum*, from which they had previously extracted the DNA. After several false starts, they showed that the synthetic microbe booted up and synthesized proteins normally made by *M. mycoides* rather than *M. capricolum* (*Science*, 21 May 2010, p. 958). Still, other than adding a bit of watermark DNA, the researchers left the genetic material in their initial synthetic organism, Syn 1.0, unchanged from the parent.

In their current work, Venter, along with project leader Clyde Hutchison at JCVI, set out to determine the minimal set of genes needed for life by stripping nonessential



genes from Syn 1.0. They initially formed two teams, each with the same task: using all available genomic knowledge to design a bacterial chromosome with the hypothetical minimum genome. Both proposals were then synthesized and transplanted into *M. capricolum* to see whether either would produce a viable organism.

"The big news is we failed," Venter says. "I was surprised." Neither chromosome produced a living microbe. It's clear, Venter says, that "our current knowledge of biology is not sufficient to sit down and design a living organism and build it."

Venter and his colleagues had better success with trial and error. They divided Syn 1.0's genome, with its 901 genes, into eight sections. To the beginning and end of each section they added identical DNA tags that made the pieces easy to reassemble. That allowed them to treat the sections as independent modules, removing each one in turn, deleting chunks of DNA, then reassembling the full genome and reinserting it into *M. capricolum* to see whether it produced a living cell. If the altered genome wasn't viable, they knew they had cut out an essential gene that had to be restored. The researchers also assessed the necessity of numerous genes in the microbe by inserting foreign genetic material, called transposons, to disrupt their function.

All this enabled them to systematically whittle away genes that either had non-essential functions or duplicated the function of another gene. In the end, Venter says, his team built, designed, and tested "multiple hundreds" of constructs before settling on Syn 3.0, with a genome about half the size of Syn 1.0's. (Syn 2.0 was an intermediate stage in this process, the first microbe with a genome smaller than that of *M. genitalium*, which with 525 genes has the fewest of any free-living natural organism.)

Once the whittling was complete, the researchers reordered the remaining genes, aligning ones that work in common pathways. The procedure tidied up the genome much as a computer compresses and reorganizes files on its hard drive to save disk space. This will likely make life much easier for synthetic biologists who will experiment with Syn 3.0 in the future, Voigt says.

With a total of 531,000 bases, the new organism's genome isn't much smaller than that of *M. genitalium*, with 600,000 bases. But *M. genitalium* grows so slowly that a population of cells can take weeks to double. Syn 3.0, by contrast, has a doubling time of 3 hours, suggesting that it thrives with its slimmed down genome. "We're not saying this is the ultimate minimum genome," Venter says. For now, however, Syn 3.0 reigns as the world's new lightweight champ. ■

## Q&A

# Turkish scholar who eluded arrest describes 'witch hunt'

Three of Meral Camcı's fellow academics are imprisoned for criticizing the government; more arrests may follow

By John Bohannon

**T**he simmering war between Turkish academics and their increasingly repressive government came to a boil last week with arrests and an escape. It began in January with the firing of dozens of academics, many of them scientists, from Turkey's universities. All had signed an online petition by a group calling itself Academics for Peace that is critical of the government's treatment of the Kurdish minority group. The firings sparked protests and statements from scientific organizations, including the U.S. National Academies of Science, Engineering, and Medicine, calling on the government to respect freedom of speech.

The standoff held until 13 March, when Kurdish separatists set off a car bomb in the capital, killing 37 people. The next day Turkey's president, Recep Tayyip Erdoğan, announced that the definition of "terrorism" should be expanded to include all who provide support in the form of "propaganda" and specifically called out academics.

Within hours of the president's speech, police arrived at the homes of four Turkish researchers. Three are now imprisoned; Turkish academics fear that many more arrests will follow. But Meral Camcı, a literary scholar who had been dismissed from her faculty position at Yeni Yüzyıl University in Istanbul, had gone to France on vacation just days before.

*Science* contacted Camcı through Turkish expat researchers. This interview has been edited for brevity and clarity.

**Q: More than 2000 scholars have signed the petition. What consequences have they suffered?**

**A:** At Turkey's 109 public universities, there have been at least 10 dismissals, five resignations, 471 disciplinary investigations, 27 suspensions, 156 criminal investigations, and 35 detentions. And at the 84 private

universities, at least 23 faculty members have been sacked, one was forced to retire, and 62 face investigations.

**Q: Why were you singled out for arrest?**

**A:** I was one of the four who read a press release on the 10th of March on behalf of Academics for Peace in Istanbul. This might have been the reason why they chose us first, but the criminal charges were based on the peace petition, which was titled "We will not be a party to this crime!"

***"I am not afraid of anyone or any institution to use my constitutionally guaranteed rights."***

Meral Camcı

**Q: What motivated you to take the risk?**

**A:** I wanted to make a contribution to the struggle for peace and democratic rights in my country, including the freedom of expression. What I could do was to sign a petition,

which spoke out against the "unacceptable deeds" of the state in the Kurdish regions of the country, and called for the state to take immediate steps toward peace. As for the [10 March] press release, what I can say is that after all the retaliations academics have faced, we wanted to emphasize that we are still standing for peace. [We also wanted] to make clear what we have been through at the universities—a kind of witch hunt carried out with dismissals, forced resignations, and disciplinary investigations. I am not afraid of anyone or any institution to use my constitutionally guaranteed human rights: freedom of speech and expression, freedom of thought, and my right to share and publish my peaceful demands.

**Q: When can you safely return home?**

**A:** I cannot say at the moment. But I am not seeking political asylum.

**Q: What is your next move?**

**A:** Our attorneys are trying to get the decision of the court canceled. There are no valid grounds under Turkish law. We have to denounce these unlawful and unjust arrests of our three colleagues. ■

## CHINA

# Five-year plan boosts basic research funding

Blueprint gives few details, but scientists foresee more generous grants and new facilities

By Hao Xin, in Beijing

China's economic slowdown could bring a windfall for basic science. Cosmic evolution, the structure of matter, the origins of life, and understanding how the brain works all deserve strengthened support, according to China's latest 5-year development plan, which could triple funding for basic research by 2020.

An outline of the plan, which covers 2016 through 2020, received pro forma approval by the National People's Congress (NPC) on 16 March at its closing session. The plan signals that top leaders are looking to researchers, even those doing fundamental work, for innovations that will drive the economy as it undergoes structural reforms. "Writing 'cosmic evolution' into the plan illustrates the importance the country places on science," Zheng Yong-Chun, a researcher at the National Astronomical Observatory (NAO) in Beijing, wrote in *People's Daily*, the official Communist Party newspaper.

Though details are still scarce, Chinese science leaders familiar with the plan expect that funding for basic research will rise to 10% of total R&D spending by 2020, up from less than 5% now. That falls short of a goal of devoting 15% of total R&D expenditures to fundamental science by 2020, set in a mid- to long-term science and technology plan adopted in 2005 (*Science*, 17 March 2006, p. 1548). But if the 10% goal is achieved, investment in basic research could hit 225 billion yuan, or about \$34.5 billion, in 2020, compared with last year's \$10 billion.

The National Natural Science Foundation of China (NSFC) in Beijing, which funds most peer-reviewed grants to individuals and small groups, expects its budget to increase an average of 10% annually, NSFC President Yang Wei told Chinese media. That would be half the 20%-plus average annual growth NSFC has enjoyed since it was established in 1986, but would still boost its appropriation from \$3.7 billion this year to about \$5.4 billion by 2020. Yang said the increase will, among other things, allow the foundation to double the size of grants awarded under its outstanding young scientist program.

The Chinese Academy of Sciences (CAS), a bastion of basic research, and the Ministry

of Science and Technology (MOST), which primarily supports applied research, can also expect hefty increases under the new 5-year plan. CAS is holding expert meetings to help it decide which programs to support, according to its website. MOST has already called for proposals in nine areas, including precision medicine, reproductive health, biomedical materials, global change, and cloud computing and big data mining.

New big science projects, too, are vying for a share of the increased funding. After the U.S.-based Advanced Laser Interferometer Gravitational-Wave Observatory an-

at the South Pole and made a premature detection claim 2 years ago. Some in the Chinese scientific community have suggested that the Ngari project should enlist international collaborators.

For one high-profile project the news is not as good. China plans to hold off on construction of the Circular Electron Positron Collider (CEPC), intended to generate large numbers of Higgs bosons to precisely measure the particle's mass. The project would cost somewhere between \$3.8 billion and \$5.4 billion, depending on its circumference.

Wang Yifang, director of CAS's Institute of High Energy Physics in Beijing, the chief sponsor of the CEPC, says the project continues to get R&D funding.

Some Chinese scientists say the country still has lessons to learn about how to support and run big science projects. A case in point is the Large Sky Area Multi-Object Fiber Spectroscopic Telescope (LAMOST) in Xinglong Station (*Science*, 4 April 2008, p. 34). Because of a design oversight, LAMOST's astronomical seeing—a measure of how blurred a point source appears—is not up to spec, says Lou Yu-Qing, an astrophysicist at Tsinghua University herein Beijing. Heat turbulence inside the telescope's white dome has degraded LAMOST's seeing from an expected

2 arcseconds to nearly 4 arcseconds or worse, Lou says. As a result, the telescope is limited to making observations within the Milky Way, although its original scientific goal was to reach beyond for extragalactic surveys. LAMOST does not have the budget or expertise to fix such problems.

As with most big science facilities, the central government footed the telescope's construction cost of about \$40 million. But it provided no funds for operations. CAS pays for utilities and maintenance but not personnel. According to Chinese media reports, LAMOST's chief scientist, Cui Xiangqun, lamented while attending the NPC that the facility has been borrowing money from the NAO to cover staff salaries.

A lack of support for ongoing research afflicts many of China's big science facilities. But the situation may soon change, now that "leaders want scientific results, too," says a scientist who requested anonymity, "and they want them fast." ■



China plans to search for primordial gravitational waves with a new microwave telescope, to be built at the 5100-meter-high Shiquanhe Observatory in Ngari, Tibet.

nounced last month that it had detected a gravitational wave from merging black holes, Chinese President Xi Jinping asked Chinese scientists what they could contribute to the field. Jumping at the chance, Zhongshan University in Guangzhou announced its Tianqin program to build a space-based gravitational-wave detector, which prompted a CAS group to announce its own competing Taiji Program in Space. Both projects call for multiple satellites and could cost billions of dollars.

Apparently neither has the inside track. Instead, CAS President Bai Chunli said at a news conference on the sidelines of the congress that the academy plans to build a microwave telescope at the Shiquanhe Observatory in Ngari, Tibet, which could detect the imprint of primordial gravitational waves on the cosmic microwave background. That is also the goal of Western projects such as Background Imaging of Cosmic Extragalactic Polarization 2, which uses a telescope



## FEATURES

# SLAUGHTER

## AT THE BRIDGE

Grisly find suggests Bronze Age northern Europe was more organized—and violent—than thought

By **Andrew Curry**, in Lübstorf, Germany



The flint arrowhead embedded in this upper arm bone first alerted archaeologists to the long-ago violence in the Tollense Valley.



About 3200 years ago, two armies clashed at a river crossing near the Baltic Sea. The confrontation can't be found in any history books—the written word didn't become common in these parts for another 2000 years—but this was no skirmish between local clans. Thousands of warriors came together in a brutal struggle, perhaps fought on a single day, using weapons crafted from wood, flint, and bronze, a metal that was then the height of military technology.

Struggling to find solid footing on the banks of the Tollense River, a narrow ribbon of water that flows through the marshes of northern Germany toward the Baltic Sea, the armies fought hand-to-hand, maiming and killing with war clubs, spears, swords, and knives. Bronze- and flint-tipped arrows

a single upper arm bone sticking out of the steep riverbank—the first clue that the Tollense Valley, about 120 kilometers north of Berlin, concealed a gruesome secret. A flint arrowhead was firmly embedded in one end of the bone, prompting archaeologists to dig a small test excavation that yielded more bones, a bashed-in skull, and a 73-centimeter club resembling a baseball bat. The artifacts all were radiocarbon-dated to about 1250 B.C.E., suggesting they stemmed from a single episode during Europe's Bronze Age.

Now, after a series of excavations between 2009 and 2015, researchers have begun to understand the battle and its startling implications for Bronze Age society. Along a 3-kilometer stretch of the Tollense River, archaeologists from the Mecklenburg-Vorpommern Department of Historic Pres-

Saxony State Service for Cultural Heritage in Hannover. "There's nothing to compare it to." It may even be the earliest direct evidence—with weapons and warriors together—of a battle this size anywhere in the ancient world.

Northern Europe in the Bronze Age was long dismissed as a backwater, overshadowed by more sophisticated civilizations in the Near East and Greece. Bronze itself, created in the Near East around 3200 B.C.E., took 1000 years to arrive here. But Tollense's scale suggests more organization—and more violence—than once thought. "We had considered scenarios of raids, with small groups of young men killing and stealing food, but to imagine such a big battle with thousands of people is very surprising," says Svend Hansen, head of the German Archaeological Insti-



Bones were closely packed in some parts of the excavation, as seen in this photo from 2013. One area of 12 square meters held 1478 bones, including 20 skulls.

were loosed at close range, piercing skulls and lodging deep into the bones of young men. Horses belonging to high-ranking warriors crumpled into the muck, fatally speared. Not everyone stood their ground in the melee: Some warriors broke and ran, and were struck down from behind.

When the fighting was through, hundreds lay dead, littering the swampy valley. Some bodies were stripped of their valuables and left bobbing in shallow ponds; others sank to the bottom, protected from plundering by a meter or two of water. Peat slowly settled over the bones. Within centuries, the entire battle was forgotten.

In 1996, an amateur archaeologist found

excavation (MVDHP) and the University of Greifswald (UG) have unearthed wooden clubs, bronze spearheads, and flint and bronze arrowheads. They have also found bones in extraordinary numbers: the remains of at least five horses and more than 100 men. Bones from hundreds more may remain unexcavated, and thousands of others may have fought but survived.

"If our hypothesis is correct that all of the finds belong to the same event, we're dealing with a conflict of a scale hitherto completely unknown north of the Alps," says dig co-director Thomas Terberger, an archaeologist at the Lower

tute's (DAI's) Eurasia Department in Berlin. The well-preserved bones and artifacts add detail to this picture of Bronze Age sophistication, pointing to the existence of a trained warrior class and suggesting that

people from across Europe joined the bloody fray.

There's little disagreement now that Tollense is something special. "When it comes to the Bronze Age, we've been missing a smoking gun, where we have a

battlefield and dead people and weapons all together," says University College Dublin (UCD) archaeologist Barry Molloy. "This is that smoking gun."

#### PODCAST

Hear a podcast with author Andrew Curry at [http://scim.ag/pod\\_6280](http://scim.ag/pod_6280).



**THE LAKESIDE HUNTING LODGE** called Schloss Wiligrad was built at the turn of the 19th century, deep in a forest 14 kilometers north of Schwerin, the capital of the northern German state of Mecklenburg-Vorpommern. Today, the drafty pile is home to both the state's department of historic preservation and a small local art museum.

In a high-ceilinged chamber on the castle's second floor, tall windows look out on a fog-shrouded lake. Inside, pale winter light illuminates dozens of skulls arranged on shelves and tables. In the center of the room, long leg bones and short ribs lie in serried ranks on tables; more remains are stored in cardboard boxes stacked on metal shelves reaching almost to the ceiling. The bones take up so much space there's barely room to walk.

When the first of these finds was excavated in 1996, it wasn't even clear that Tollense was a battlefield. Some archaeologists suggested the skeletons might be from a flooded cemetery, or that they had accumulated over centuries.

There was reason for skepticism. Before Tollense, direct evidence of large-scale violence in the Bronze Age was scanty, especially in this region. Historical accounts from the Near East and Greece described epic battles, but few artifacts remained to corroborate these boastful accounts. "Even in Egypt, despite hearing many tales of war, we never find such substantial archaeological evidence of its participants and victims," UCD's Molloy says.

In Bronze Age Europe, even the historical accounts of war were lacking, and all investigators had to go on were weapons in ceremonial burials and a handful of mass graves with unmistakable evidence of violence, such as decapitated bodies or arrowheads embedded in bones. Before the 1990s, "for a long time we didn't really believe in war in prehistory," DAI's Hansen says. The grave goods were explained as prestige objects or symbols of power rather than actual weapons. "Most people thought ancient society was peaceful, and that Bronze Age males were concerned with trading and so on," says Helle Vandkilde, an archaeologist at Aarhus University in Denmark. "Very few talked about warfare."

The 10,000 bones in this room—what's left of Tollense's losers—changed all that.

They were found in dense caches: In one spot, 1478 bones, among them 20 skulls, were packed into an area of just 12 square meters. Archaeologists think the bodies landed or were dumped in shallow ponds, where the motion of the water mixed up bones from different individuals. By counting specific, singular bones—skulls and femurs, for example—UG forensic anthropologists Ute Brinker and Annemarie Schramm identified a minimum of 130 individuals, almost all of them men, most between the ages of 20 and 30.

The number suggests the scale of the battle. "We have 130 people, minimum, and five horses. And we've only opened 450 square meters. That's 10% of the find layer, at most, maybe just 3% or 4%," says Detlef Jantzen, chief archaeologist at MVDHP. "If we excavated the whole area,

have a lot of them, often multiple marks on the same rib."

Scanning the bones using microscopic computer tomography at a materials science institute in Berlin and the University of Rosstock has yielded detailed, 3D images of these injuries. Now, archaeologists are identifying the weapons responsible by matching the images to scans of weapons found at Tollense or in contemporary graves elsewhere in Europe. Diamond-shaped holes in bones, for example, match the distinctive shape of bronze arrowheads found on the battlefield. (Bronze artifacts are found more often than flint at Tollense, perhaps because metal detectors were used to comb spoil piles for artifacts.)

The bone scans have also sharpened the picture of how the battle unfolded, Terberger says. In x-rays, the upper arm bone with an embedded arrowhead—the one that trig-

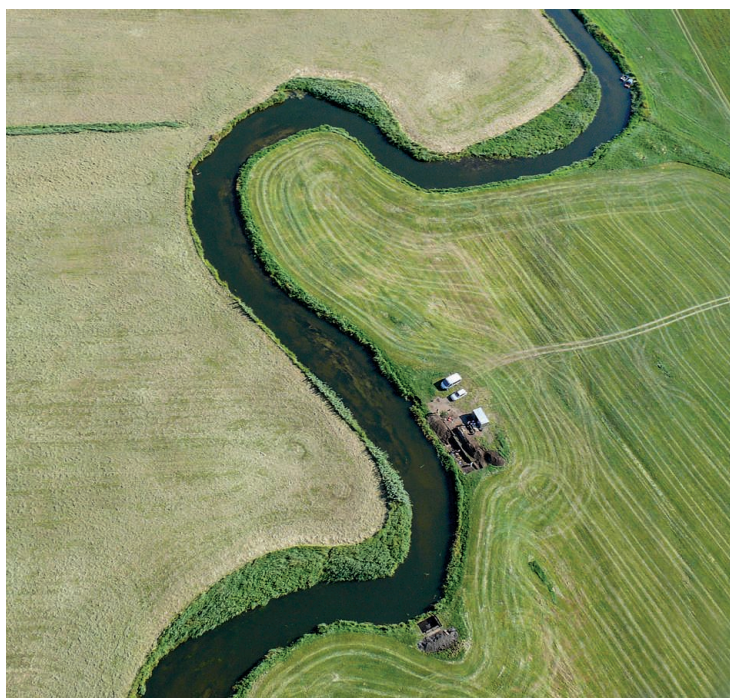
gered the discovery of the battlefield—seemed to show signs of healing. In a 2011 paper in *Antiquity*, the team suggested that the man sustained a wound early in the battle but was able to fight on for days or weeks before dying, which could mean that the conflict wasn't a single clash but a series of skirmishes that dragged out for several weeks.

Microscopic inspection of that wound told a different story: What initially looked like healing—an opaque lining around the arrowhead on an x-ray—was, in fact, a layer of shattered bone, compressed by a single impact that was probably fatal. "That let us revise the idea that this took place over weeks," Terberger says. So far no bodies show healed wounds, making it likely the battle happened in just a day,

or a few at most. "If we are dealing with a single event rather than skirmishes over several weeks, it has a great impact on our interpretation of the scale of the conflict."

In the last year, a team of engineers in Hamburg has used techniques developed to model stresses on aircraft parts to understand the kinds of blows the soldiers suffered. For example, archaeologists at first thought that a fighter whose femur had snapped close to the hip joint must have fallen from a horse. The injury resembled those that result today from a motorcycle crash or equestrian accident.

But the modeling told a different story. Melanie Schwinning and Hella Harten-Buga,



Today's peaceful meanders of the Tollense River once were the site of bitter fighting.

we might have 750 people. That's incredible for the Bronze Age." In what they admit are back-of-the-envelope estimates, he and Terberger argue that if one in five of the battle's participants was killed and left on the battlefield, that could mean almost 4000 warriors took part in the fighting.

Brinker, the forensic anthropologist in charge of analyzing the remains, says the wetness and chemical composition of the Tollense Valley's soil preserved the bones almost perfectly. "We can reconstruct exactly what happened," she says, picking up a rib with two tiny, V-shaped cuts on one edge. "These cut marks on the rib show he was stabbed twice in the same place. We



University of Hamburg archaeologists and engineers, took into account the physical properties of bone and Bronze Age weapons, along with examples of injuries from horse falls. An experimental archaeologist also plunged recreated flint and bronze points into dead pigs and recorded the damage.

Schwinning and Harten-Buga say a bronze spearhead hitting the bone at a sharp downward angle would have been able to wedge the femur apart, cracking it in half like a log. “When we modeled it, it looks a lot more like a handheld weapon than a horse fall,” Schwinning says. “We could even recreate the force it would have taken—it’s not actually that much.” They estimate that an average-sized man driving the spear with his body weight would have been enough.

Why the men gathered in this spot to fight and die is another mystery that archaeological evidence is helping unravel. The Tollense Valley here is narrow, just 50 meters wide in some spots. Parts are swampy, whereas others offer firm ground and solid footing. The spot may have been a sort of choke point for travelers journeying across the northern European plain.

In 2013, geomagnetic surveys revealed evidence of a 120-meter-long bridge or causeway stretching across the valley. Excavated over two dig seasons, the submerged structure turned out to be made of wooden posts and stone. Radiocarbon dating showed that although much of the structure predated the battle by more than 500 years, parts of it may have been built or restored around the time of the battle, suggesting the causeway might have been in continuous use for centuries—a well-known landmark.

“The crossing played an important role in the conflict. Maybe one group tried to cross and the other pushed them back,” Terberger says. “The conflict started there and turned into fighting along the river.”

In the aftermath, the victors may have stripped valuables from the bodies they could reach, then tossed the corpses into shallow water, which protected them from carnivores and birds. The bones lack the gnawing and dragging marks typically left by such scavengers.

Elsewhere, the team found human and horse remains buried a meter or two lower, about where the Bronze Age riverbed might have been. Mixed with these remains were gold rings likely worn on the hair, spiral rings of tin perhaps worn on the fingers, and tiny bronze spirals likely used as decorations. These dead must have fallen or been dumped into the deeper parts of the river, sinking quickly to the bottom, where their valuables were out of the grasp of looters.



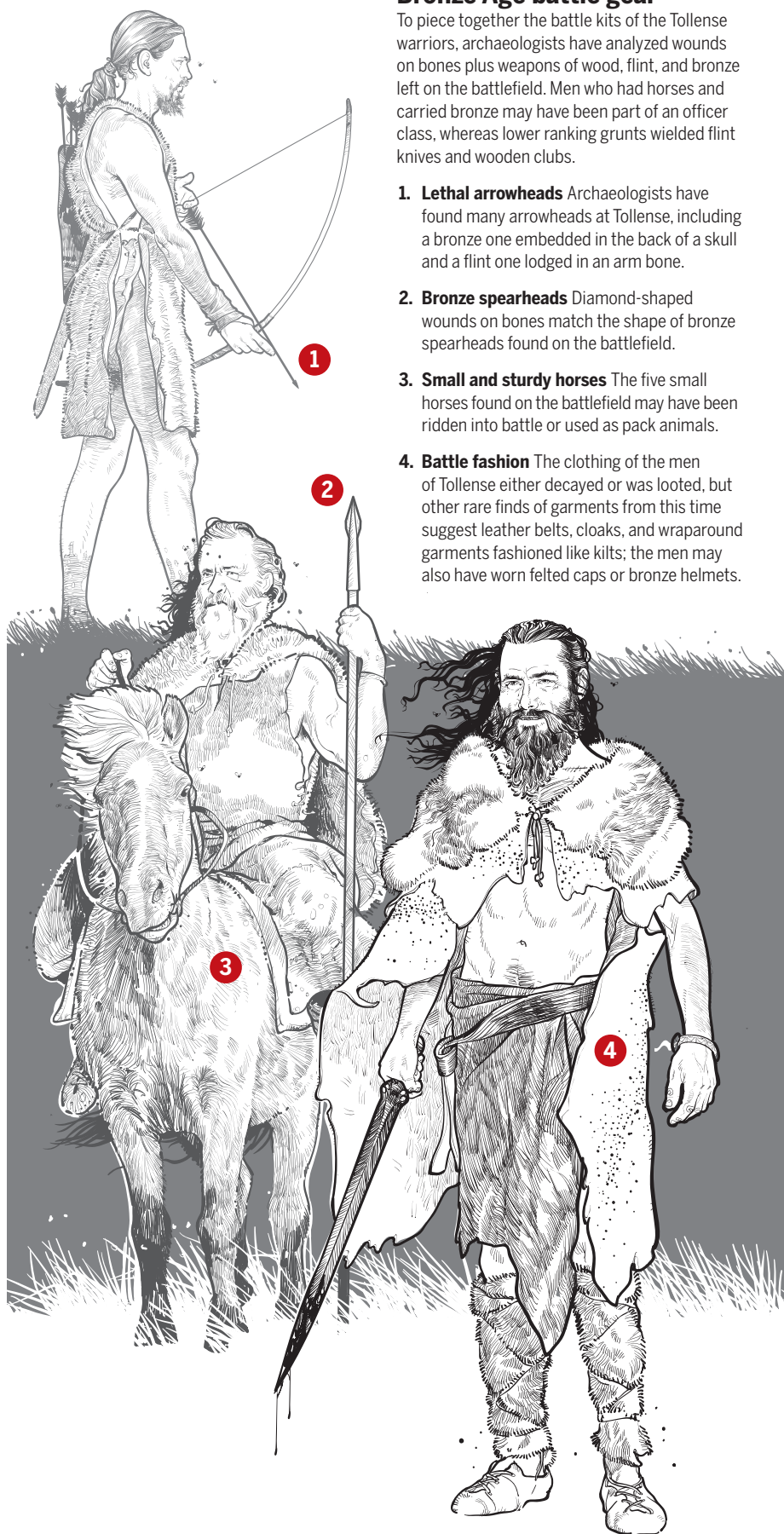
The remains testify to the destructiveness of Bronze Age weapons. A wooden club was likely used to bash in skulls (top), whereas bronze arrows bit deep into bone. This arrow penetrated the skull to the brain.



## Bronze Age battle gear

To piece together the battle kits of the Tollense warriors, archaeologists have analyzed wounds on bones plus weapons of wood, flint, and bronze left on the battlefield. Men who had horses and carried bronze may have been part of an officer class, whereas lower ranking grunts wielded flint knives and wooden clubs.

- 1. Lethal arrowheads** Archaeologists have found many arrowheads at Tollense, including a bronze one embedded in the back of a skull and a flint one lodged in an arm bone.
- 2. Bronze spearheads** Diamond-shaped wounds on bones match the shape of bronze spearheads found on the battlefield.
- 3. Small and sturdy horses** The five small horses found on the battlefield may have been ridden into battle or used as pack animals.
- 4. Battle fashion** The clothing of the men of Tollense either decayed or was looted, but other rare finds of garments from this time suggest leather belts, cloaks, and wraparound garments fashioned like kilts; the men may also have worn felted caps or bronze helmets.



**AT THE TIME OF THE BATTLE**, northern Europe seems to have been devoid of towns or even small villages. As far as archaeologists can tell, people here were loosely connected culturally to Scandinavia and lived with their extended families on individual farmsteads, with a population density of fewer than five people per square kilometer. The closest known large settlement around this time is more than 350 kilometers to the southeast, in Watenstedt. It was a landscape not unlike agrarian parts of Europe today, except without roads, telephones, or radio.

And yet chemical tracers in the remains suggest that most of the Tollense warriors came from hundreds of kilometers away. The isotopes in your teeth reflect those in the food and water you ingest during childhood, which in turn mirror the surrounding geology—a marker of where you grew up. Retired University of Wisconsin, Madison, archaeologist Doug Price analyzed strontium, oxygen, and carbon isotopes in 20 teeth from Tollense. Just a few showed values typical of the northern European plain, which sprawls from Holland to Poland. The other teeth came from farther afield, although Price can't yet pin down exactly where. "The range of isotope values is really large," he says. "We can make a good argument that the dead came from a lot of different places."

Further clues come from isotopes of another element, nitrogen, which reflect diet. Nitrogen isotopes in teeth from some of the men suggest they ate a diet heavy in millet, a crop more common at the time in southern than northern Europe.

Ancient DNA could potentially reveal much more: When compared to other Bronze Age samples from around Europe at this time, it could point to the homelands of the warriors as well as such traits as eye and hair color. Genetic analysis is just beginning, but so far it supports the notion of far-flung origins. DNA from teeth suggests some warriors are related to modern southern Europeans and others to people living in modern-day Poland and Scandinavia. "This is not a bunch of local idiots," says University of Mainz geneticist Joachim Burger. "It's a highly diverse population."

As University of Aarhus's Vandkilde puts it: "It's an army like the one described in Homeric epics, made up of smaller war bands that gathered to sack Troy"—an event thought to have happened fewer than 100 years later, in 1184 B.C.E. That suggests an unexpectedly widespread social organization, Jantzen says. "To organize a battle like this over tremendous distances and gather all these people in one place was a tremendous accomplishment," he says.

## The things they carried

Archaeologists have recovered a wealth of artifacts from the battlefield, offering a detailed view of the warriors' weapons and jewelry. Because many artifacts were found with metal detectors, bronze and tin objects abound.

### Tin rings and bronze scrolls

These two tin rings may have been worn on warriors' fingers. The small bronze scrolls may have served as tassels or as decorations for garments.



### Wooden clubs

Archaeologists found two clubs at Tollense, likely both carried by lower ranking men. The simple, 73-cm "baseball bat" was made of ash and the 62-cm "croquet mallet" was crafted of sloe wood.



So far the team has published only a handful of peer-reviewed papers. With excavations stopped, pending more funding, they're writing up publications now. But archaeologists familiar with the project say the implications are dramatic. Tollense could force a re-evaluation of the whole period in the area from the Baltic to the Mediterranean, says archaeologist Kristian Kristiansen of the University of Gothenburg in Sweden. "It opens the door to a lot of new evidence for the way Bronze Age societies were organized," he says.

For example, strong evidence suggests this wasn't the first battle for these men. Twenty-seven percent of the skeletons show signs of healed traumas from earlier fights, including three skulls with healed fractures. "It's hard to tell the reason for the injuries, but these don't look like your typical young farmers," Jantzen says.

Standardized metal weaponry and the remains of the horses, which were found intermingled with the human bones at one spot, suggest that at least some of the combatants

were well-equipped and well-trained. "They weren't farmer-soldiers who went out every few years to brawl," Terberger says. "These are professional fighters."

Body armor and shields emerged in northern Europe in the centuries just before the Tollense conflict and may have necessitated a warrior class. "If you fight with body armor and helmet and corselet, you need daily training or you can't move," Hansen says. That's why, for example, the biblical David—a shepherd—refused to don a suit of armor and bronze helmet before fighting Goliath. "This kind of training is the beginning of a specialized group of warriors," Hansen says. At Tollense, these bronze-wielding, mounted warriors might have been a sort of officer class, presiding over grunts bearing simpler weapons.

But why did so much military force converge on a narrow river valley in northern Germany? Kristiansen says this period seems to have been an era of significant upheaval from the Mediterranean to the Baltic. In Greece, the sophisticated Mycenaean

### Bronze ax

Ax heads like this one were used as weapons and also for chores during the Bronze Age. They were traded and even hoarded as a form of wealth.



### Bronze arm ring

Decorated jewelry shows that at least some warriors were high-status.

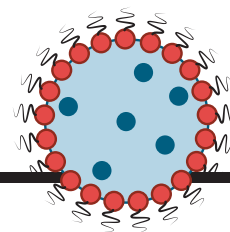


civilization collapsed around the time of the Tollense battle; in Egypt, pharaohs boasted of besting the "Sea People," marauders from far-off lands who toppled the neighboring Hittites. And not long after Tollense, the scattered farmsteads of northern Europe gave way to concentrated, heavily fortified settlements, once seen only to the south. "Around 1200 B.C.E. there's a radical change in the direction societies and cultures are heading," Vandkilde says. "Tollense fits into a period when we have increased warfare everywhere."

Tollense looks like a first step toward a way of life that is with us still. From the scale and brutality of the battle to the presence of a warrior class wielding sophisticated weapons, the events of that long-ago day are linked to more familiar and recent conflicts. "It could be the first evidence of a turning point in social organization and warfare in Europe," Vandkilde says. ■

*Andrew Curry is a freelance writer based in Berlin.*





## PERSPECTIVES

### STRUCTURE

## A Big Bang in spliceosome structural biology

3D snapshots reveal  
dynamics of the  
spliceosome on the  
mRNA splicing pathway

By **Jamie H. D. Cate**

**L**ook at a protein-coding gene in the genome of any eukaryote—be it animal, plant, fungus, or protist—and you will likely find the coding region fragmented by intervening sequences known as introns. When the gene is transcribed, these introns have to be removed from the pre-messenger RNA (pre-mRNA) before a protein can be made. How these introns are removed has been studied intensively for decades without the aid of a three-dimensional map of the highly dynamic machine at the heart of the process: the spliceosome. On page 1416 of this issue, Agafonov *et al.* report the first molecular-resolution reconstruction of a central assembly of the human spliceosome, the U4/U6.U5 triple small nuclear ribonucleoprotein (tri-snRNP) complex, using cryo-electron microscopy (cryo-EM) (1). Together with high-resolution cryo-EM reconstructions of spliceosome assemblies from fungi (2–5) and the x-ray

**Splicing machine.** A major building block of the mRNA splicing machine, as revealed by single-particle electron cryomicroscopy. The 1.8 MDa human U4/U6.U5 triple small nuclear ribonucleoprotein complex is shown at 7 Å resolution. Ribbon diagram representations of some of the molecular components are shown within the cryo-EM structure.

Departments of Molecular and Cell Biology and Chemistry, University of California, Berkeley, CA 94720, USA, and Molecular Biophysics and Integrated Bioimaging, Lawrence Berkeley National Laboratory, Berkeley, CA 94720, USA. E-mail: jcate@lbl.gov

ILLUSTRATION: K. SUTLIF/SCIENCE PROTEIN DATABASE

crystal structure of the U1 snRNP (6), these structural models of the splicing machinery launch a new era in understanding eukaryotic gene regulation.

The spliceosome is an ancient RNA-protein machine in which the RNA is the catalytic engine (7), a property shared with other ancient cellular machines that may be relics from an “RNA world” before proteins and DNA appeared. Splicing out introns from a pre-mRNA is both a highly complex and highly regulated process, and gives a single gene the potential to encode many different protein variants with different properties and functions. Furthermore, evidence is accumulating that defects in the splicing pathway may be responsible for a number of human diseases (8).

Splicing cycles through a series of steps in which the spliceosome assembles on the intron-containing pre-mRNA, defining the boundaries between exons—the sequences ultimately retained in the mature mRNA—and introns (see the figure, panel A). The spliceosome assembles on pre-mRNA to form complexes named A, B, and C, depending on the step in the splicing reaction, using five snRNP complexes, the U1, U2, U4, U5, and U6 snRNPs. Three of these

snRNPs join as a pre-assembled unit called the tri-snRNP (U4/U6.U5), the target of the present structural investigation (1). When the proper boundaries of the intron and flanking exons are located, the spliceosome

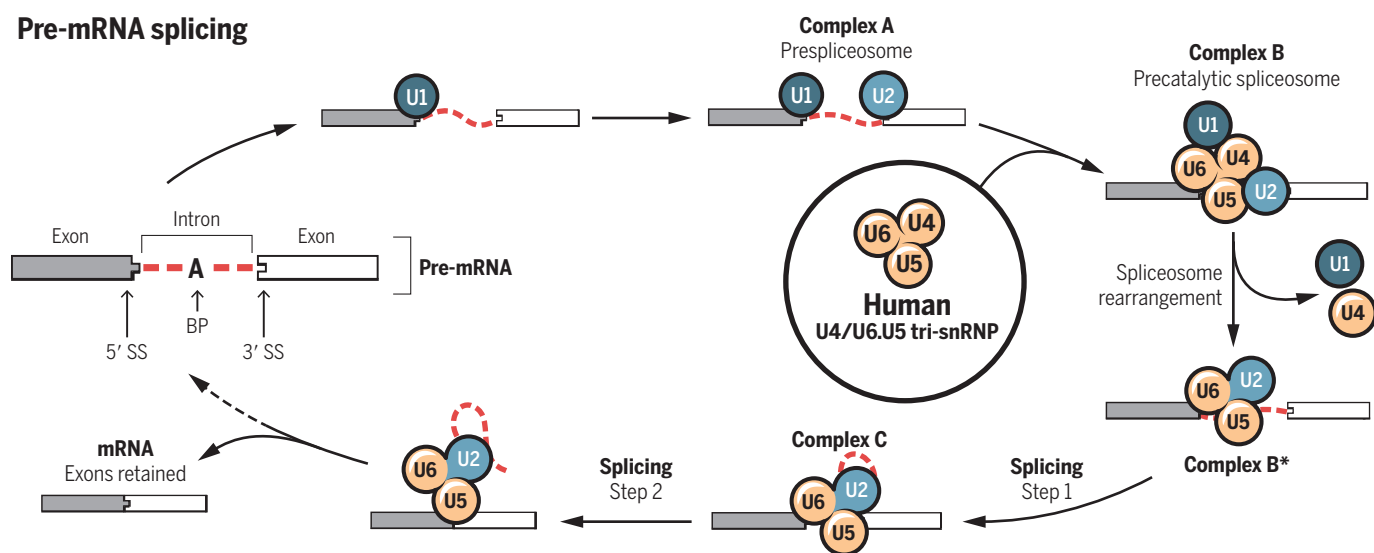
**“...these structural models of the splicing machinery launch a new era in understanding eukaryotic gene regulation.”**

undergoes a sequence of rearrangements leading to ejection of the U4 snRNP and pairing of the U2 snRNP with U6 to activate the splicing reaction.

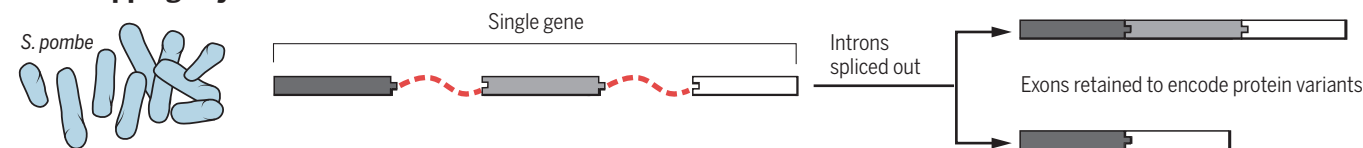
In the structural model of the human tri-snRNP complex, large differences are apparent when compared to the high-resolution reconstructions of splicing assemblies from yeast (1, 4, 5). These differences involve two key protein components of the spliceosome, named Brr2 and Prp8. These two proteins reside within the U5 snRNP and play central roles choreographing the correct assembly

of active spliceosomes and the catalytic cycle of pre-mRNA splicing. Brr2 is a helicase required to remove U4 from the precatalytic spliceosome, thereby allowing U2 to form a base-pairing interaction with U6. In the human U4/U6.U5 tri-snRNP complex, Brr2 is held more than 8 nm away from U4. Results from modeling, protein cross-linking, and comparison to high-resolution yeast U4/U6.U5 tri-snRNPs (4, 5) indicate that another protein, Sad1, acts to sequester Brr2 in this inactive position until Brr2 has to be released, to swing into place for U4 removal and spliceosome activation.

A second major structural rearrangement proposed to be part of the spliceosome catalytic cycle involves the central scaffolding protein Prp8. In the human tri-snRNP complex, which represents a state prior to pre-mRNA binding, Prp8 is in an “open” conformation with its En and NTD1 domains 5 nm apart (1). By contrast, the structure of the U2/U6.U5 spliceosome, which probably represents the reaction immediately after splicing has occurred (9), reveals Prp8 in a closed conformation that brings the En and NTD1 domains of Prp8 together and holds the U2/U6 and U5 snRNAs in an active conformation for splicing (2, 3).



## Exon skipping in yeast



**Splicing the message. (A)** Splicing of adjacent coding sequences (exons) together requires the spliceosome to recognize boundaries between exons and introns (the sequences to be removed). Boundaries are marked as 5' SS and 3' SS (5' and 3' splice sites). The spliceosome uses a branchpoint (BP) adenosine within the intron during the splicing reaction. RNA-protein complexes that assemble to form the spliceosome are named U1, U2, U4, U5, and U6 snRNPs. These assemble in a stepwise manner to form complexes named A, B, B\*, and C. High-resolution structures are now available for U1 snRNP, a preexisting U4/U6.U5 tri-snRNP, and a U2/U6.U5 spliceosome after the splicing reaction. The human U4/U6.U5 tri-snRNP described by Agafonov *et al.* suggests the dynamic structural changes required in this complex to form the U2/U6.U5 core in the active spliceosome. [Adapted from (9)] **(B)** Many pre-mRNAs are alternatively spliced to form many variant mRNAs—for example, by skipping an exon. Exon skipping is ubiquitous from fungi to humans.



The knowledge that large-scale rearrangements in two key proteins in the spliceosome likely play key roles in the cycling of the spliceosome provide a new perspective on prior genetic and biochemical data, and should provide opportunities to further explore the functional consequences of these arrangements. Cryo-EM reconstructions of other steps in the splicing pathway, previously imaged at much lower resolution (2 to 4 nm) (8)—too low for accurate docking of the new models—are now primed to be imaged at resolutions better than 1 nm, given the rapid advances in cryo-EM in the past 3 years (10). Higher-resolution structures of the spliceosome in these other steps are likely to reveal additional conformational changes required for splicing to occur.

The recent structural models of the spliceosome in different steps of the splicing reaction represent a turning point for the field, reminiscent of the change that occurred when structures of the protein-synthesizing machine—the ribosome—were resolved in 2000 (11). Now, dozens of ribosome and ribosomal subunit structures are determined every year. With the advent of high-resolution cryo-EM, the same is likely to be true for the spliceosome over the next decade. New structures will be needed to understand the catalytic cycle and the process by which pre-mRNAs can be alternatively spliced to form many different mature mRNAs encoding different proteins. Model organisms such as fungi, which were needed for the first high-resolution cryo-EM structures (2–5), will likely continue to provide important insights into alternative splicing—for example, into exon skipping (12) (see the figure, panel B). In the meantime, it will be exciting to see how the present burst of spliceosome structural knowledge permeates through the field to inspire new genetic, biochemical, and biophysical experiments aimed at unraveling the fundamental properties of this ancient regulator of gene expression. ■

## REFERENCES

1. D. E. Agafonov *et al.*, *Science* **351**, 1416 (2016).
2. C. Yan *et al.*, *Science* **349**, 1182 (2015).
3. J. Hang, R. Wan, C. Yan, Y. Shi, *Science* **349**, 1191 (2015).
4. T. H. D. Nguyen *et al.*, *Nature* **530**, 298 (2016).
5. R. Wan *et al.*, *Science* **351**, 466 (2016).
6. Y. Kondo, C. Oubridge, A.-M. M. van Roon, K. Nagai, *Elife* **4**, 360 (2015).
7. S. M. Fica *et al.*, *Nature* **503**, 229 (2013).
8. Y. Lee, D. C. Rio, *Annu. Rev. Biochem.* **84**, 291 (2015).
9. T. H. D. Nguyen *et al.*, *Curr. Opin. Struct. Biol.* **36**, 48 (2016).
10. E. Nogales, *Nat. Methods* **13**, 24 (2016).
11. V. Ramakrishnan, *Cell* **159**, 979 (2014).
12. N. Stepankiw, M. Raghavan, E. A. Fogarty, A. Grimson, J. A. Pleiss, *Nucleic Acids Res.* **43**, 8488 (2015).

10.1126/science.aaf3061



## ECOLOGY

# Thermal trouble in the tropics

Tropical species may be highly vulnerable to climate change

By Timothy M. Perez,<sup>1,2</sup> James T. Stroud,<sup>1,2</sup>  
Kenneth J. Feeley<sup>1,2</sup>

Early Victorian naturalists marveled at the profusion of diversity they encountered as they traveled from temperate to tropical latitudes. The inverse relationship between latitude and species richness that these naturalists first observed is now referred to as the latitudinal diversity gradient. Various ecological and evolutionary explanations have been proposed for the latitudinal diversity gradient. Of these, perhaps none are more relevant to contemporary conservation issues than Janzen's hypothesis of latitudinal differences in species' climatic tolerances and thermal selectivity (1). On page 1437 of this issue, Chan *et al.* (2) advance Janzen's early theories by elucidating some of the potential selective pressures imposed by climate and climate variability.

In 1967, Daniel Janzen published his seminal treatise discussing why "mountain passes are higher in the tropics" (1). He argued that in climates with low variability, as occur throughout much of the tropics, species should evolve to have narrow thermal

tolerances. In contrast, the high climatic variability that occurs in most temperate regions should select for broader thermal tolerances. Therefore, species at lower latitudes will generally have smaller elevational ranges because they have narrower thermal tolerances, making mountains less surmountable, and hence "higher," from the perspective of tropical species. The real importance of Janzen's ideas lies in the revelation that thermal tolerances are traits shaped by selection and that they manifest in the realized elevational and geographic ranges of species.

However, climate varies not just with latitude and elevation, but also through time. Increasing atmospheric concentrations of CO<sub>2</sub> and other greenhouse gases are driving rapid changes in Earth's climate. Alongside rising mean annual temperatures, there have been dramatic and complex changes in the temporal variability of climatic conditions over the past century (3). Compared to their temperate counterparts, tropical species are particularly vulnerable to changes in global climate, because they have evolved under stable climates and thus have narrow thermal niches (see the figure) (4, 5). In other words, just as mountain passes are "higher in the tropics," so, too, are the effects of climate change on species predicted to be more severe in the tropics—despite absolute rates of warming being slower there than at higher latitudes (6).

<sup>1</sup>International Center for Tropical Botany, Department of Biological Sciences, Florida International University, Miami, FL 33199, USA. <sup>2</sup>Fairchild Tropical Botanic Garden, Coral Gables, FL 33156, USA. E-mail: kjfeeley@gmail.com





**Thermal specialists.** Tropical species such as those living in these mountains in Pahang, Malaysia, tend to have narrow thermal tolerances and may therefore be especially vulnerable to climate change.

Using data from more than 16,000 vertebrate species and over 150 elevational transects from around the globe, Chan *et al.* provide macroecological evidence supporting Janzen's original thesis, inject the pertinent context of climate change, and—perhaps most importantly—identify how temporal variation in climatic factors is likely to select for the breadths of species' thermal tolerances. More specifically, the authors show that high seasonal temperature variability and low diurnal temperature variability both favor thermal generalist species over specialist species with narrower thermal tolerances.

Several studies have shown that thermal specialists will need to quickly migrate and/or evolve to track the movement of suitable climatic zones (6), potentially leading to extinctions as some species fail to keep pace (7). The results of Chan *et al.* suggest that additional evolutionary pressures may act against thermal specialists at a global scale. Long-term increases in seasonal temperature variability (3) due to the increasing frequency and severity of extreme climatic events (8), coupled with decreases in diurnal temperature variability due to faster nighttime versus daytime warming (9), will both select against thermal specialists. The combined ecological and evolutionary pressures of climate change on specialists may eventually lead to global biodiversity losses and biotic homogenization.

To better predict the impacts of climate change on biodiversity, further research is paramount, especially on tropical species, which are expected to be most sensitive to changes in climate and climate variation. Several influential and oft-cited reviews claim to have uncovered coherent fingerprints of climate change across Earth's ecosystems

(10, 11). In reality, however, a clear understanding of how climate change is affecting tropical species is precluded by a paucity of studies, and hence data, from low-latitude systems. This geographic bias is further magnified by taxonomic biases: Nearly all studies that do exist for the tropics come from just a handful of taxa, generally dominated by endothermic vertebrates, which may be unrepresentative of broader patterns in other species groups. Geographic and taxonomic biases result, in part, from the traditional difficulties of working with diverse taxa in often-inaccessible locations. Growing collaborative data networks, combined with new methods of large-scale data collection (12), are helping researchers to bypass some of these limitations and will hopefully soon provide us with a more complete understanding of how tropical species are responding to climate change.

The potential effects of climate change on natural systems are complex and remain poorly understood. However, the ecological and evolutionary risks to specialist species appear particularly ominous. A lamentable lack of basic ecological and biogeographic data from the tropics limits our ability to extrapolate macroecological patterns or to model future environmental responses to changes in climate. Chan *et al.* present a novel framework for how long-term and short-term climatic variability combine to shape the evolution of thermal niche breadths and hence geographic distributions. Additional studies looking at the adaptability and plasticity of climatic tolerances of species are now required to improve predictions of how these species will respond to increasing environmental variability in a rapidly changing world. ■

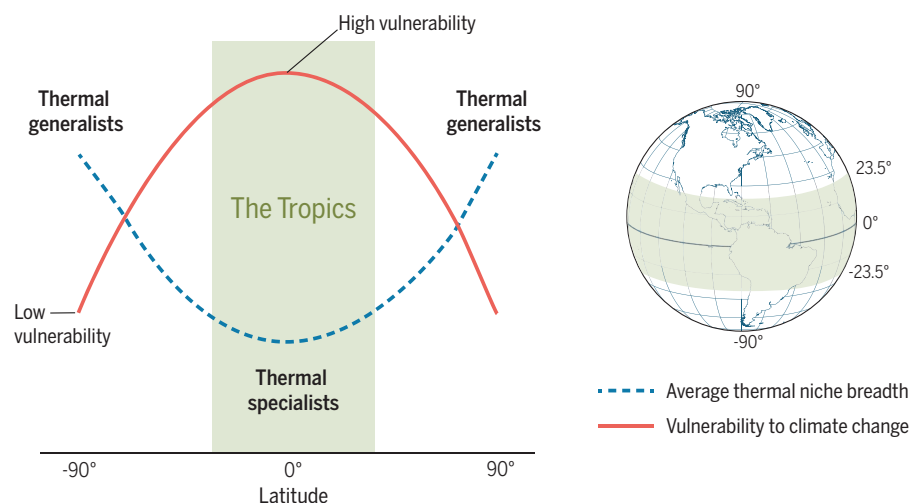
#### REFERENCES AND NOTES

1. D. H. Janzen, *Am. Nat.* **101**, 233 (1967).
2. W.-P. Chan *et al.*, *Science* **351**, 1437 (2016).
3. International Panel on Climate Change (IPCC), *Climate Change 2013: The Physical Science Basis. Contribution of Working Group I to the Fifth Assessment Report of the Intergovernmental Panel on Climate Change*, T. F. Stocker *et al.*, Eds. (Cambridge Univ. Press, New York, 2013).
4. J. J. Tewksbury, R. B. Huey, C. A. Deutsch, *Science* **320**, 1296 (2008).
5. D. A. Vasseur *et al.*, *Proc. R. Soc. B* **281**, 20132612 (2014).
6. J. W. Williams, S. T. Jackson, J. E. Kutzbach, *Proc. Natl. Acad. Sci. U.S.A.* **104**, 5738 (2007).
7. K. J. Feeley, E. M. Rehm, B. Machovina, *Front. Biogeogr.* **4**, 69 (2012).
8. D. R. Easterling *et al.*, *Science* **289**, 2068 (2000).
9. D. R. Easterling *et al.*, *Science* **277**, 364 (1997).
10. G. E. Walther *et al.*, *Nature* **416**, 389 (2002).
11. C. Parmesan, G. Yohe, *Nature* **421**, 37 (2003).
12. D. Schimel *et al.*, *Global Change Biol.* **21**, 1762 (2015).

#### ACKNOWLEDGMENTS

We thank E. J. von Wettberg, A. G. Vincent, M. C. Ladd, and A. A. Shantz for comments that improved the manuscript. The authors are supported by the U.S. National Science Foundation (DEB-1257655 and DEB-1350125).

10.1126/science.aaf3343





## PHYSICS

# A benchmark for materials simulation

Material properties can now be predicted reliably from first-principles calculations

By Chris-Kriton Skylaris

**D**ensity functional theory (DFT) stands out from all first-principles quantum mechanical methods for the simulation of materials, as it enables very good approximations for the complicated components of electronic motion called exchange and correlation. DFT is the method of choice for many materials simulations because of the availability of general-purpose programs that can perform calculations on any material. Results obtained with one DFT program need to be reproducible by any of the other DFT programs, and this has not been straightforward up to now. On page 1415 of this issue, Lejaeghere *et al.* (1) describe an extensive effort by developers of the major solid-state DFT codes to provide a unified and reproducible benchmark of precision for their calculations based on a reliable criterion, the so-called  $\Delta$  gauge. Using the  $\Delta$  gauge, the authors found that the level of precision that can be achieved today in DFT calculations of elemental crystalline solids is comparable to the precision of the most advanced techniques for experimental measurement of the properties of materials. The work leads to the conclusion that the DFT simulation of elemental crystalline solids is a (computationally) solved problem, but also poses the question of whether we can achieve the same levels of validation and reproducibility for more complex simulations of materials involving several elements and/or several methods.

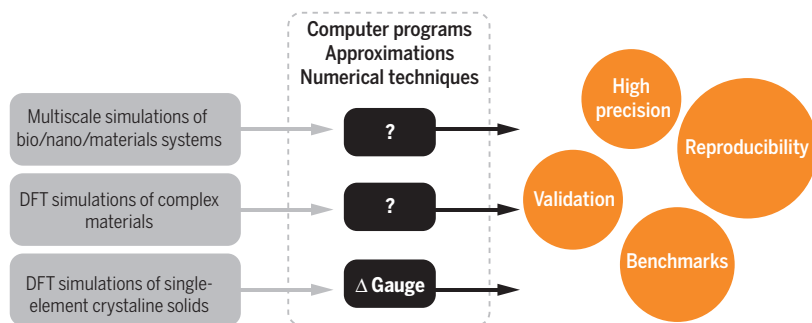
First-principles quantum mechanical calculations use the fundamental equations of quantum theory that govern the behavior of electrons, atoms, and molecules. In principle, quantum theory allows us to compute any observable property of materials with extremely high accuracy. However, this capability can only be realized at the expense of appreciable computational effort; for

most cases, the quantum mechanical equations cannot be solved analytically and must be approximated numerically. A variety of implementations exist that are based on different numerical approximations, and at the theoretical limit of infinite computational power, they are expected to produce the same answers. However, in real calculations it is difficult to know how the numerical approximations used by each program affect its results. Lejaeghere *et al.* demonstrate this by comparing published calculations of the lattice constant of crystalline silicon and

DFT has proved its value in calculations in an impressive range of applications such as drug design (5), catalysis (6), crystal structure prediction (7), nanoelectronics (8), and geophysics (9), to name just a few.

The tremendous success of DFT has been enabled by the development of highly sophisticated programs that are general-purpose and can perform calculations on any material or molecule. These computational tools have a high level of complexity, as a consequence of the fact that a host of numerical techniques are required to solve the DFT

**How the calculations measure up.** The  $\Delta$  gauge approach described by Lejaeghere *et al.* allows us to validate calculations between different DFT programs. Can an equivalent criterion be derived for DFT simulations of complex materials and eventually for multiscale simulations?



showing that in the early years of development of such programs, the error in precision was larger than the difference from the value measured in experiments.

The development of DFT by Kohn (2) was a major breakthrough in first-principles calculations. DFT is an alternative formulation of quantum theory in which the electronic density is the central quantity rather than the wave function. This is a dramatic simplification, as the electronic density is a mathematical function of only three geometrical variables  $x$ ,  $y$ , and  $z$ , whereas the wave function is a function of  $3N$  variables, that is, three variables for each of the  $N$  particles simulated. As a result, DFT, in the form developed by Kohn and Sham (3), has found extensive use in simulations of materials. Although DFT is formally an exact theory, there is no explicit expression for the so-called exchange and correlation energy that describes interactions between the electrons, so this term has to be approximated. Over the past few decades, a hierarchy of increasingly accurate approximations of the term has been developed (4).

equations (10). As a result of this complexity, DFT programs had to be developed over many years by dedicated communities, and each such community has acquired expertise on how to set up calculations with their code to achieve the required level of precision for each application. These codes have now matured and become established, and because they were developed according to a “black-box” philosophy that allows

the user to control the approximations via a small set of input parameters, they are now available as tools for research by non-experts. As this transition from “community products” to general-purpose research tools is taking place, it is imperative to be able to compare and tune the quality of calculations between different codes. Results obtained with one code can only be credible if they can be reproducible by any of the other codes at the same level of DFT theory (that is, the DFT exchange-correlation functional).

Lejaeghere *et al.* outline the extensive efforts by developers of the major solid-state DFT codes to provide a unified and reproducible benchmark of precision for DFT calculations. This multinational consortium evaluated the major codes against each other using a reliable criterion, the  $\Delta$  gauge (see the figure). DFT calculations of the equation of state of elemental crystalline solids have been compared among all the codes in the study. An outcome of this work is that all the DFT codes were able to produce results at the same level of precision as the most advanced experimental techniques for mea-

suring structural and electronic properties of materials. Thus, “computer experiments” can be used on a par with experimental investigation. Users of DFT codes now have a dependable estimate for the level of precision of their results and a confidence of reproducibility by other DFT codes. This work has far-reaching implications, as it affects the entire community of DFT users, in fields as diverse as metallurgy and biochemistry.

Being able to do such accurate quantum calculations is insufficient when the goal is to solve complex problems of technological relevance. Molecules, biomolecules, and materials are neither isolated nor at a temperature of 0 K. On the contrary, they interact heavily with each other and their environment (for example, a solvent) and are in constant thermal motion. To make an impact in grand challenges such as understanding the function of a living cell or a nanodevice, we will need to tackle much larger (thousands to millions of atoms) length scales than can be approached with conventional DFT. Part of the answer to this challenge will be provided by linear-scaling DFT approaches (11), which can treat much larger numbers of atoms. Inevitably, however, multiscale methods that couple DFT with coarser descriptions such as classical atomistic force fields (12), and eventually continuum models, will be needed. These multiscale simulations will also need to describe how the materials evolve in time, so the choice of a configurational sampling problem that can be tackled with methods such as molecular dynamics (13), with implementations able to take advantage of the largest supercomputers (14), is equally important. Thus, a new, greater challenge is posed for the field of materials simulation: Can we have the same confidence in the reproducibility and precision of multiscale simulations as we have now for simple DFT calculations? Only time will tell. ■

#### REFERENCES

1. K. Lejaeghere *et al.*, *Science* **351**, aad3000 (2016).
2. W. Kohn, *Rev. Mod. Phys.* **71**, 1253 (1999).
3. W. Kohn, L. J. Sham, *Phys. Rev.* **140**, A1133 (1965).
4. N. Mardirossian, M. Head-Gordon, *J. Chem. Phys.* **140**, 18A527 (2014).
5. S. J. Fox *et al.*, *Proteins* **82**, 3335 (2014).
6. J. K. Nørskov, F. Abild-Pedersen, F. Studt, T. Bligaard, *Proc. Natl. Acad. Sci. U.S.A.* **108**, 937 (2011).
7. M. J. Lyle, C. J. Pickard, R. J. Needs, *Proc. Natl. Acad. Sci. U.S.A.* **112**, 6898 (2015).
8. J. Junquera, P. Ghosez, *Nature* **422**, 506 (2003).
9. C. Davies, M. Pozzo, D. Gubbins, D. Alfè, *Nat. Geosci.* **8**, 678 (2015).
10. M. C. Payne *et al.*, *Rev. Mod. Phys.* **64**, 1045 (1992).
11. D. R. Bowler, T. Miyazaki, *Rep. Prog. Phys.* **75**, 036503 (2012).
12. A. Warshel, M. Levitt, *J. Mol. Biol.* **103**, 227 (1976).
13. V. Calandrini *et al.*, *J. Inorg. Biochem.* **153**, 231 (2015).
14. N. A. Romero *et al.*, *Computer* **48**, 33 (2015).

## IONIC TRANSPORT

# Two-dimensional nanofluidics

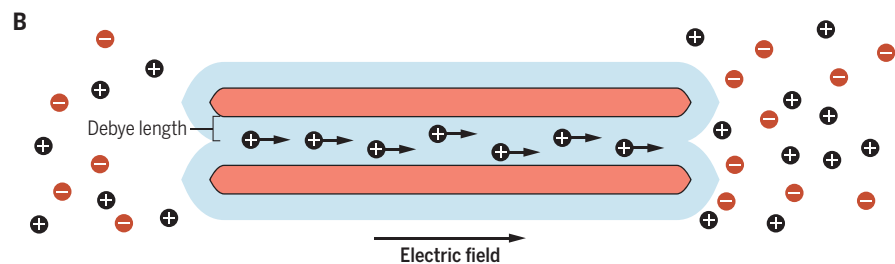
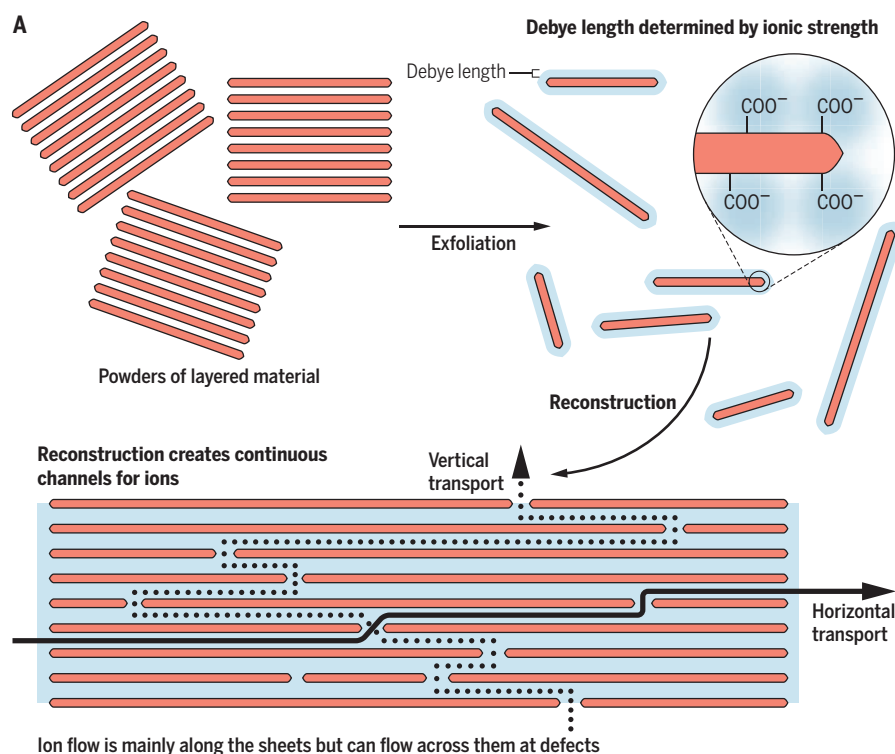
Restacked exfoliated sheets create interconnected nanofluidic channels for ion transport

By Andrew R. Koltonow and Jiaying Huang

**T**he remarkable electronic properties of graphene and related two-dimensional (2D) materials result from the confinement of electrons within the material. Similarly, the interstitial space between 2D materials can enable the 2D confinement of ions and electrolytes and alter their transport. Many different 2D sheets can be obtained by exfoliation of natu-

ral layered materials (1), and an exfoliation-reconstruction strategy can convert powders of layered materials into continuous, robust bulk forms in which lamellar nanochannels occupy a substantial volume fraction (up to several tens of percent). Nanofluidics, which enables the manipulation of confined ions and electrolytes, has applications in electrochemical energy conversion and storage, biosensing, and water purification.

Electrolytes exhibit drastically different properties when confined in nanochannels.



**Confining ion flow.** (A) Lamellar film with massive arrays of 2D nanofluidic channels can be made by the exfoliation-reconstruction approach, as illustrated with models of graphene oxide (GO) sheets that are terminated with negatively charged carboxyl groups. (B) Debye layers of neighboring sheets overlap to create unipolar 2D ion channels with greatly enhanced cation conductivity.



For example, in bulk solution, cations and anions simultaneously move along opposite directions to generate ionic current. However, in channels narrower than the Debye length of the electrolyte (a measure of how far electrostatic effects can persist), the surface charges on the inner walls repel ions of the same charge and attract the counterions, making them the dominating charge carriers (2). Such unipolar ionic transport can enhance ionic conductivity up to several orders of magnitude. Nanochannels that enable such transport can be fabricated in bulk materials, but such “top-down” methods are rather expensive and difficult to scale up. The construction of nanofluidic channels with the 2D sheets, a “bottom-up” approach, can be done simply by casting or filtration of nanosheets dispersed in solution.

The surface properties and the spacing of the 2D nanochannels can be conveniently controlled by modifying the starting sheets. No matter how electrolytes

***“The surface properties and the spacing of the 2D nanochannels can be conveniently controlled by modifying the starting sheets.”***

pass through the film, horizontally or vertically, they flow through the same set of 2D channels, with the only difference being flux (see the figure, panel A). To create a robust film with uniform lamellar spacing, the 2D building blocks should have uniform thickness and high aspect ratios.

A number of 2D materials are already available for this purpose. For example, filtration of graphene oxide (GO) sheets (graphene functionalized with oxygenated groups, such as carboxylates) leads to films with interlayer spacing of ~1 nm that can be tuned by changing the degree of hydration. Anions are excluded by the negatively charged sheets, enabling cation transport controlled by surface charge (see the figure, panel B) (3). Guo *et al.* later demonstrated that mechanically pumping electrolyte through such 2D channels resulted in unipolar flow of cations, generating electrical current on the order of  $0.1 \text{ A m}^{-2} \text{ bar}^{-1}$  (4). Two-dimensional nanochannels constructed with vermiculite clay walls supported high

proton conductivities approaching those of proton-transport polymeric membranes. The vermiculite channels have extraordinary thermal stability and retain their functions even after baking at  $500^\circ\text{C}$  in air (5).

Packing defects such as voids and dislocations are to be expected in the lamellar films made of irregularly shaped sheets with polydisperse sizes (see the figure, panel A). The effective total volume of the 2D nanochannels can be estimated by comparing the value of ionic conductance to that of a bulk channel. Recent work by Cheng *et al.* aims to quantify the impact of these defects on ionic transport (6). Their continuum ion diffusion simulations treat a GO film as a stack of sheets with uniform size and few-nanometer-sized pinholes. This simple model of the nanofluidic channel walls manages to reproduce the unipolar transport observed in experiments, as well as the influence of the membrane's physical parameters on ionic transport. Experimentally, solvent exchange allows the interlayer spacing of the film to be continuously tuned, and results from the corresponding ionic conductivity measurements converged on the model's prediction. Interlayer spacing critically influences the behaviors of confined ions and can be affected by local stacking defects, so it will be useful to adopt a scanning type of x-ray diffraction technique to map the spacing over entire films.

Enhanced ionic conductivity through 2D nanofluidic membranes can be used to create electrochemical devices, especially for those with in-plane geometry (7). It is also very attractive for designing new ion-selective membranes, potentially allowing new applications under unprecedentedly extreme conditions (5). Here, the remaining challenge is to significantly increase the cross-membrane flux, perhaps by realigning the horizontal nanochannels toward the vertical direction without losing the film's structural integrity. New assembly strategies will be needed to create robust bulk lamellar materials with tunable channel orientations. ■

#### REFERENCES AND NOTES

1. V. Nicolosi, M. Chhowalla, M. G. Kanatzidis, M. S. Strano, J. N. Coleman, *Science* **340**, 1226419 (2013).
2. D. Stein, M. Kruithof, C. Dekker, *Phys. Rev. Lett.* **93**, 035901 (2004).
3. K. Raidongia, J. X. Huang, *J. Am. Chem. Soc.* **134**, 16528 (2012).
4. W. Guo *et al.*, *Adv. Mater.* **25**, 6064 (2013).
5. J. J. Shao, K. Raidongia, A. R. Koltonow, J. X. Huang, *Nat. Commun.* **6**, 7602 (2015).
6. C. Cheng *et al.*, *Sci. Adv.* **2**, e1501272 (2016).
7. W. Gao *et al.*, *Nat. Nanotechnol.* **6**, 496 (2011).

#### ACKNOWLEDGMENTS

Seed support from Northwestern MRSEC (NSF DMR-1121262) and the Office of Naval Research (ONR N000141310556).

Department of Materials Science and Engineering,  
Northwestern University, Evanston, IL 60208, USA. E-mail:  
jiaxing-huang@northwestern.edu

#### CLOUDS

## Don't forget the surface

Surface effects play a key role in cloud droplet formation

By Barbara Noziere

Clouds are an essential source of fresh water to continents and all ecosystems (1) and a major cooling factor in the climate budget (2). Yet, predicting their formation remains a challenge (2). In the atmosphere, cloud droplets form not from water vapor alone but through condensation of water on aerosol particles called cloud condensation nuclei (CCN) (3). On page 1447 of this issue, Ruehl *et al.* (4) show experimentally that surface effects play a central role in cloud droplet formation from CCN.

The first step in predicting cloud formation is to accurately predict the concentration of CCN in the air. For the fine aerosol particles in the atmosphere (with radii between 50 and 150 nm), the contribution to the CCN population is determined by the chemical composition. This is because, as first explained by Köhler in a paper published 80 years ago (5), some chemicals present in these particles can reduce the energy barrier limiting cloud droplet formation either by reducing the vapor pressure around them (Raoult effect) or by lowering their surface tension (see the figure). The magnitudes of both effects must be known to predict cloud droplet formation in the atmosphere.

To study the early steps of cloud droplet formation experimentally, scientists have built “on-line” instruments that allow atmospheric or laboratory-generated submicrometer-scale aerosols to be sampled in an air flow. In these instruments, the aerosols can be exposed to a range of controlled relative humidities, followed by measurements of either the growth of the particles upon water uptake or the number of newly formed droplets (6, 7). These measured quantities are indirectly linked to the Raoult effect and surface tension, making accurate prediction difficult. The role of aerosol chemical composition on the Raoult effect is now acknowledged and widely

CNRS and Université Lyon 1, Ircelyon, Villeurbanne, France.  
E-mail: barbara.noziere@ircelyon.univ-lyon1.fr

10.1126/science.aaf5289



**Explaining cloud formation.** Cloud droplets grow from aerosol particles. The chemical composition of these particles is crucial for whether a cloud droplet forms.

studied (6–8), but that of surface tension is more controversial.

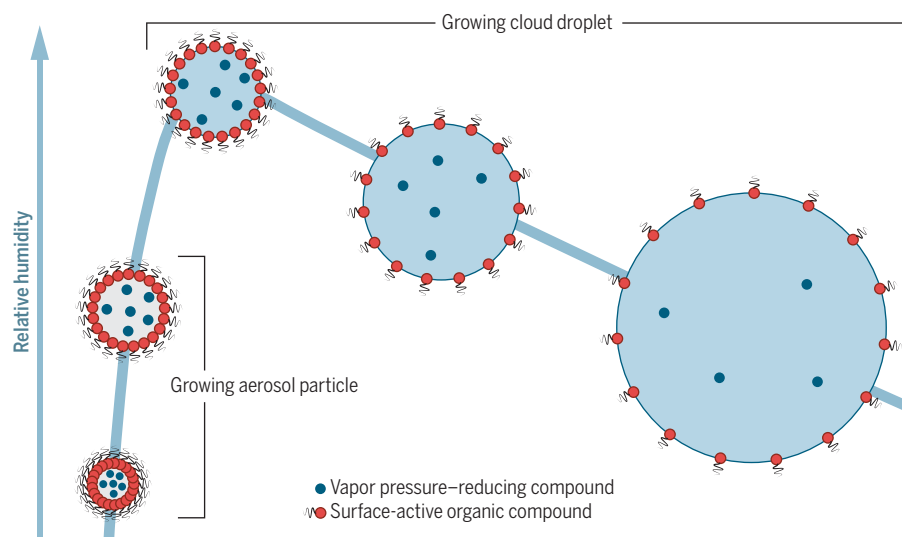
Surface tension—the force that keeps the droplets cohesive—is anomalously large in pure water because of hydrogen bonding. According to Köhler theory (5), surfactants in atmospheric aerosols should lower the surface tension of growing droplets compared to pure water, thereby facilitating their growth and increasing CCN concentrations. However, most instruments built to study cloud droplet formation have been unable to detect surface tension effects on CCN concentrations (6, 7). As a result, the CCN concentrations measured with these instruments can only be explained by assuming that no surface effect is present. Practically all investigations of cloud formation assume that surface tension reduction is nonexistent and that the surface tension of droplets is that of pure water (7, 8).

In their study, Ruehl *et al.* use an original experimental setup that can monitor the growth of droplets until they reach the critical energy barrier (see the figure). The results show that when surface-active organic compounds are present in the aerosol particles, initially as a film, the onset of droplet formation is underestimated by ~50%. This represents the error made by current models that neglect surface effects.

To account for the observations, the authors propose to replace the widely used one-dimensional equation linking the droplet's surface tension and its surfactant concentration gradient with a two-dimensional “compressed film” model that takes into account the area occupied by the molecules at the surface. In stark contrast with the one-dimensional model, the compressed film model predicts that the vast majority of the surfactant molecules are

at the droplet's surface, resulting in substantial surface effects. The results imply that the systematic assumption that the surface tension of growing cloud droplets is that of pure water is at least partly incorrect and that the reported agreements between measured and predicted CCN concentrations in the atmosphere are based on flawed assumptions.

The organic compounds that Ruehl *et al.* investigated are very abundant in atmospheric aerosols (dicarboxylic acids). Furthermore, a recent study has found very low surface tension and large surfactant concentrations in fine atmospheric aerosols (9). Ruehl *et al.*'s results are thus likely to be relevant for the real atmosphere. After decades of investigations with the same types of instruments, their work shows how critical the development of alternative techniques is for a full understanding of cloud formation processes. Techniques that measure directly the effects of the Raoult effect and surface tension on micrometer- or submicrometer-scale particles would be especially valuable by allowing assumptions to be tested. Searching for evidence of the role of surfactants on cloud formation directly in the atmosphere is also a priority. ■



**Formation of a cloud droplet from an aerosol particle.** To grow spontaneously into a cloud droplet, an aerosol particle must overcome the energy barrier represented by the maximum of the blue curve. Chemical compounds in the particle can lower this barrier, thus favoring the formation of cloud droplets, by either reducing the vapor pressure around them (Raoult effect, compounds represented by the blue dots) or reducing their surface tension (organic surfactants, represented by the red dots with organic chains). The effect of aerosol chemical composition on the Raoult effect has been widely studied, but surface tension effects have been harder to detect. Ruehl *et al.* now provide experimental evidence showing that surface-active compounds can also reduce the energy barrier by reducing surface tension.

## REFERENCES

1. B. E. Jiménez Cisneros *et al.*, in *Climate Change 2014: Impacts, Adaptation, and Vulnerability. Part A: Global and Sectoral Aspects. Contribution of Working Group II to the Fifth Assessment Report of the Intergovernmental Panel on Climate Change*, C. B. Field *et al.*, Eds. (Cambridge Univ. Press, Cambridge, UK, 2014), pp. 229–269.
2. O. Boucher *et al.*, in *Climate Change 2013: The Physical Science Basis. Contribution of Working Group I to the Fifth Assessment Report of the Intergovernmental Panel on Climate Change*, T. F. Stocker *et al.*, Eds. (Cambridge Univ. Press, Cambridge, UK, 2013), pp. 571–657.
3. J. Aitken, *Trans. R. Soc. Edinb.* **30**, 337 (1881).
4. C. R. Ruehl, J. F. Davies, K. R. Wilson, *Science* **351**, 1447 (2016).
5. H. Köhler, *Trans. Faraday Soc.* **32**, 1152 (1936).
6. G. McFiggans *et al.*, *Atmos. Chem. Phys.* **6**, 2593 (2006).
7. D. K. Farmer, C. D. Cappa, S. M. Kreidenweis, *Chem. Rev.* **115**, 4199 (2015).
8. M. D. Petters, S. M. Kreidenweis, *Atmos. Chem. Phys.* **7**, 1961 (2007).
9. V. Gérard *et al.*, *Environ. Sci. Technol.* **50**, 2974 (2016).

10.1126/science.aaf3253



## CANCER

# The oncogene makes its escape

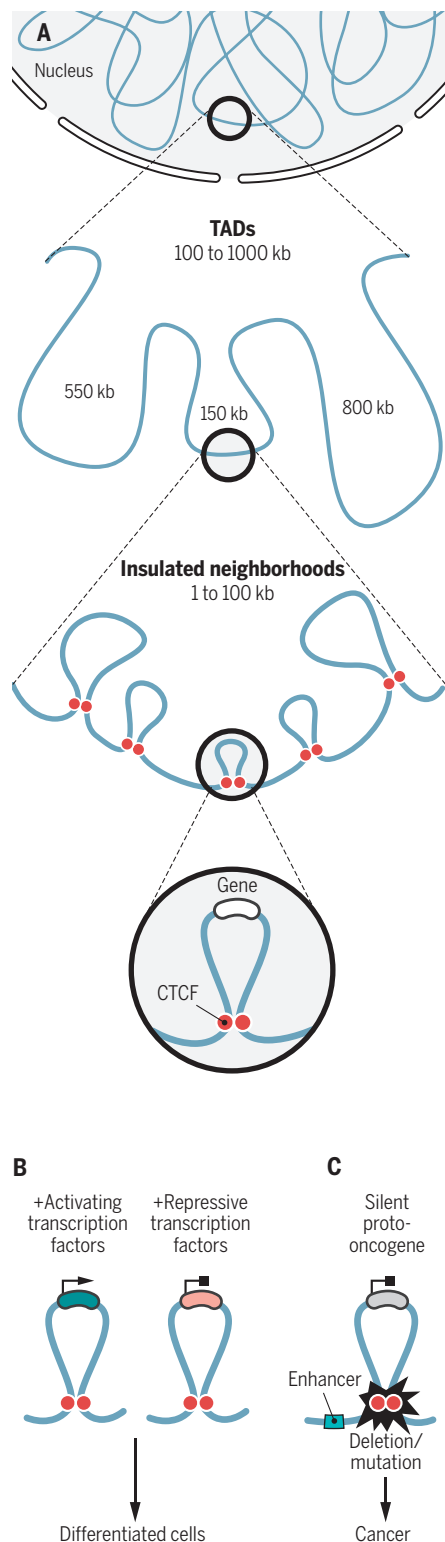
Disruptions in 3D genomic architecture allow cancer genes to evade transcriptional silencing

By Jeremiah Wala and Rameen Beroukhim

**F**ar from a random tangle, cellular DNA is packed into the nucleus with astounding precision. Indeed, there is growing appreciation for how the three-dimensional (3D) organization of the genome contributes to controlling gene expression. For instance, loops of DNA called insulated neighborhoods can protect small groups of genes from silencing or activation (1). If cancer can result from dysregulation of gene expression (2), then an enticing hypothesis is that disrupting insulated neighborhoods may lead to increased transcription of cancer genes. On page 1454 of this issue, Hnisz *et al.* (3) use tumor-derived sequencing data and targeted deletions in cells to show that disruption of insulated neighborhoods leads to activation of proto-oncogenes—genes with the potential to cause cancer. These findings strongly support disruption of chromatin structure as causally linked to tumorigenesis, and suggest that such disruptions may be the hidden culprit driving many tumors.

Physical separation is maintained between transcriptionally active and inactive regions of the genome (4), and recent studies have identified units of hundreds to thousands of kilobases of DNA, called topologically associating domains (TADs), where genes exhibit close spatial proximity and correlated expression (5). The boundaries of these TADs are occupied by CCCTC-binding factor (CTCF), the primary protein that mediates long-range chromatin interactions in mammals (6). Further transcriptional control can occur inside CTCF-mediated DNA loops such as insulated neighborhoods. These loops can stop the spread of silencing heterochromatin, physically separate genes from activating enhancers, or sequester genes together with powerful transcriptional activators known as superenhancers (1).

Hnisz *et al.* asked whether changes to this three-dimensional structure of DNA contribute to the activation of proto-on-



cogenes. Proto-oncogenes are often not expressed, and in a human cell-line model of T cell acute lymphoblastic leukemia (T-ALL), Hnisz *et al.* found that many of these dormant proto-oncogenes lie in insulated neighborhoods. To determine whether opening of these DNA loops is sufficient to allow transcription of the proto-oncogenes, the authors used the DNA editing technique called CRISPR (clustered regularly-interrupted short palindromic repeats)-Cas9 to delete the CTCF sites that mark the boundaries of insulated neighborhoods containing the genes *TAL1* and *LMO2*. *TAL1* and *LMO2* are transcription factors that drive hematopoiesis and can be aberrantly activated in T cell acute lymphoblastic leukemia. Remarkably, despite targeting regions thousands of base pairs away from the gene body, both deletions flanking an insulated neighborhood were sufficient to induce proto-oncogene expression in nonmalignant cells. The authors further made a key connection with patient data: Recurrent focal deletions targeting the same region were associated with increased *TAL1* expression in T cell acute lymphoblastic leukemia.

One model behind the increased expression is that releasing DNA loops allows physical contact between proto-oncogenes and nearby enhancers. Such commandeering of enhancers to drive expression is reminiscent of enhancer hijacking, where superenhancers are brought into proximity of proto-oncogenes through genome rearrangement events (7). Interestingly, the *TAL1* locus can also undergo somatic mutations in T cell acute lymphoblastic leukemia to create a new superenhancer (8), further demonstrating the arsenal of tools with which tumors can dysregulate transcription.

CRISPR-Cas9-mediated deletions of insulated neighborhood boundaries can activate proto-oncogenes in the laboratory, but how prevalent are such disruptions in real tumors? CTCF binding sites are known to be frequently somatically mutated (9); to identify whether this is due to positive selection for chromatin disruption, Hnisz *et al.* separately analyzed mutations in non-boundary CTCF sites and boundary CTCF

## Chromatin architecture and gene expression.

(A) DNA has a hierarchical structure, with units of hundreds to thousands of kilobases organized into topologically associating domains (TADs). Smaller subdomains called insulated neighborhoods are organized by CTCF and cohesin binding at insulators. (B) Insulated neighborhoods provide protected units where genes can be co-regulated. (C) Otherwise well-behaved proto-oncogenes can become activated in cancer by disrupting the structure of insulated neighborhoods through deletions or mutations of boundary CTCF binding sites.

Departments of Medical Oncology and Cancer Biology, Dana-Farber Cancer Institute, Boston, MA 02115, USA, and Broad Institute, Cambridge, MA 02142, USA. E-mail: rameen\_beroukhim@dfci.edu

sites in different cancer types. If the target of CTCF site alterations is destruction of insulated neighborhoods, then only boundary CTCF sites should be enriched for mutations. Across a large pan-cancer cohort, the authors observed a factor of >2 enrichment for boundary CTCF site mutations. This enrichment was particularly strong in liver and esophageal carcinomas, where boundary CTCF site mutations were also significantly more likely to be found near known oncogenes. Whether this enrichment is driven primarily by activation of proto-oncogenes is not clear, and further analyses are needed to uncover the specific gene targets driving CTCF site alterations within different tumor types. Such studies may also be useful for clinical genotyping, where identification of activated oncogenes is a key step in applying the optimal targeted therapy.

Genetic events that disrupt insulated neighborhoods may be just one of many ways that cells alter their 3D chromatin structure to dysregulate gene expression. Recently, Flavahan *et al.* reported that disruption of TADs by DNA methylation of boundary CTCF sites allows a distant active enhancer to interact with and drive a key oncogene in brain tumors (10). Together with the findings of Hnisz *et al.*, these pioneering studies highlight the diversity of mechanisms by which chromatin structure may be targeted and suggest that modulating 3D chromatin structure may be widespread in cancer.

By showing that disruption of insulated neighborhoods leads to activation of proto-oncogenes, Hnisz *et al.* describe a previously unrecognized mechanism by which cancers may escape transcriptional regulation. This study adds to an expanding understanding of the deep impact that alterations outside of protein-coding regions can have in driving the expression of cancer genes (11–13). Future research aimed at deciphering such noncoding alterations in cancer will need to account for perturbations to the 3D architecture of the genome, while also being alert to indications of novel methods of transcriptional dysregulation. ■

## REFERENCES

1. J. M. Downen *et al.*, *Cell* **159**, 374 (2014).
2. D. Hanahan, R. A. Weinberg, *Cell* **144**, 5 (2011).
3. D. Hnisz *et al.*, *Science* **351**, 1454 (2016).
4. E. Lieberman-Aiden *et al.*, *Science* **326**, 289 (2009).
5. J. R. Dixon *et al.*, *Nature* **485**, 376 (2012).
6. J. E. Phillips-Cremins, V. G. Corces, *Mol. Cell* **50**, 461 (2013).
7. P. A. Northcott *et al.*, *Nature* **511**, 428 (2015).
8. M. R. Mansour *et al.*, *Science* **346**, 1373 (2014).
9. R. Katainen *et al.*, *Nat. Genet.* **47**, 818 (2015).
10. W. A. Flavahan *et al.*, *Nature* **529**, 110 (2015).
11. C. F. Davis *et al.*, *Cancer Cell* **26**, 319 (2014).
12. S. Horn *et al.*, *Science* **339**, 959 (2013).
13. F. W. Huang *et al.*, *Science* **339**, 957 (2013).

10.1126/science.aaf5542

## RESEARCH ETHICS

# Ethics review for international data-intensive research

Ad hoc approaches mix and match existing components

By Edward S. Dove,<sup>1\*</sup> David Townend,<sup>2</sup> Eric M. Meslin,<sup>3</sup> Martin Bobrow,<sup>4,5</sup> Katherine Littler,<sup>6</sup> Dianne Nicol,<sup>7</sup> Jantina de Vries,<sup>8</sup> Anne Junker,<sup>9</sup> Chiara Garattini,<sup>10</sup> Jasper Bovenberg,<sup>11</sup> Mahsa Shabani,<sup>12</sup> Emmanuelle Lévesque,<sup>13</sup> Bartha M. Knoppers<sup>13</sup>

**H**istorically, research ethics committees (RECs) have been guided by ethical principles regarding human experimentation intended to protect participants from physical harms and to provide assurance as to their interests and welfare. But research that analyzes large aggregate data sets, possibly including detailed clinical and genomic information of individuals, may require different assessment. At the same time, growth in international data-sharing collaborations adds stress to

a system already under fire for **POLICY** subjecting multisite research to replicate ethics reviews, which can inhibit research without improving the quality of human subjects' protections (1, 2). "Top-down" national regulatory approaches exist for ethics review across multiple sites in domestic research projects [e.g., United States (3, 4), Canada (5), United Kingdom (6), Australia (7)], but their applicability for data-intensive international research has not been considered. Stakeholders around the world have thus been developing "bottom-up" solutions. We scrutinize five such efforts involving multiple countries around the world, including resource-poor settings (table S1), to identify models that could inform a framework for mutual recognition of international

ethics review (i.e., the acceptance by RECs of the outcome of each other's review).

Data-intensive projects often raise ethical concerns for which RECs have little guidance. Data can be collected from consenting participants at one site but stored, analyzed, or linked with data sets elsewhere. Data are typically stored for long periods and can be reused and (re)linked. Particularly problematic is that perceived and legislated ownership of data and the responsibility to authorize data sharing varies across jurisdictions. Investigators and RECs must consider the security of data management, how the privacy of participants will be assured, and the overall governance (e.g., use and access) of a data set.

We exclude from our analysis clinical trials work, which is led by the International Council (formerly Conference) on Harmonisation (8), although we note increasing convergence of clinical trials with large, heterogeneous data sets (9).

**MODELS AND PRINCIPLES.** Our analysis revealed three general ethics review models—reciprocity, delegation, and federation—that clarify and add to what currently exists in some jurisdictions and integrate existing ethics review approaches in innovative ways (see table). Each project used several mechanisms to achieve greater cross-jurisdictional mutual recognition of ethics review (table S2). Prior and ongoing engagement with RECs, institutions, or governmental bodies to achieve REC alignment (e.g., a memorandum of understanding) can be effective. A well-resourced process for developing tools (e.g., customized agreements or face-to-face meetings) for improved REC review is critical, as is (if possible) an opportunity to pilot test them before full implementation.

Ethics review for data-intensive international research should be founded on at least two principles. First, projects imposing similar risks on research participants should be subjected to similar levels of scrutiny by all RECs. Second, if we assume that procedural and regulatory alignment is in place, once an ethics review opinion has been provided, each jurisdiction should not require further de novo review. This does not foreclose local accommodations for is-

<sup>1</sup>J. Kenyon Mason Institute for Medicine, Life Sciences and the Law, School of Law, University of Edinburgh, UK. <sup>2</sup>Department of Health, Ethics & Society, CAPRI Research School, Maastricht University, The Netherlands. <sup>3</sup>Indiana University Center for Bioethics, Indiana University School of Medicine, Indianapolis, Indiana, USA. <sup>4</sup>Honorary Faculty, Wellcome Trust Sanger Institute, Hinxton, UK. <sup>5</sup>Department of Medical Genetics, University of Cambridge, UK. <sup>6</sup>Wellcome Trust, London, UK. <sup>7</sup>Centre for Law and Genetics, Faculty of Law, University of Tasmania, Australia. <sup>8</sup>Department of Medicine, Faculty of Health Sciences, University of Cape Town, South Africa. <sup>9</sup>Department of Pediatrics, Faculty of Medicine, University of British Columbia, Vancouver, British Columbia, Canada. <sup>10</sup>Intel Corporation, Health and Life Sciences, London, UK. <sup>11</sup>Legal Pathways, Aardenhout, The Netherlands. <sup>12</sup>Centre for Biomedical Ethics and Law, KU Leuven, Leuven, Belgium. <sup>13</sup>Centre of Genomics and Policy, Faculty of Medicine, McGill University, Montreal, Quebec, Canada. \*Corresponding author. E-mail: edward.dove@ed.ac.uk



## Three models for building ethics review mutual recognition for data-intensive international research

	ADVANTAGES	DISADVANTAGES	PROJECTS
<b>RECIPROCITY</b> An institution, funder, or regulator/government in one jurisdiction accepts the completed ethics review from another jurisdiction and vice versa through collaborative recognition of equivalent processes and/or standards	Helps build agreement on research participant protections while respecting local context  Flexibility with review standards  Potentially time-saving once a decision on equivalence is reached, if applied to a whole class of projects	Some REC system inefficiencies remain (e.g., inconsistent or incompatible opinions)  Challenge in defining whose protections are “best”  Time-consuming at the initial implementation stage	Human Heredity and Health in Africa (H3Africa): shared ethics consultation meetings to build trust and REC alignment  International Cancer Genome Consortium (ICGC): development of ethics review policies  Personalized Risk Stratification for Prevention and Early Detection of Breast Cancer (PERSPECTIVE): customized tools and agreements approved by each institution
<b>DELEGATION</b> Before review, an institution, funder, or regulator/government delegates ethics review responsibilities to one or several existing designated RECs through agreement	Reduces the potential for inconsistency  Researchers can channel energy and resources into one or a few RECs  Increased possibility for specific areas of ethics expertise in the designated REC(s)	Challenge in determining how a REC is chosen  Challenge in determining how post-approval activities will be handled  All-or-nothing outcome of review; no room for alternative reviews	ICGC: agreements signed between ministries of health
<b>FEDERATION</b> Institutions, funders, or regulators/governments create a central REC with representation from multiple jurisdictions	Reduces costs and duplication of efforts  Reduces inconsistency in REC review  Drives improved standards across sites by encouraging a “herd instinct”	Challenge in developing REC structure and process  Challenge in balancing cultural representation, power differences, or local priorities  Challenge in getting several jurisdictions to agree on policy and standards	Indiana University–Moi University (IU-Moi): proposed REC with members of each institution  Maternal Infant Child & Youth Research Network (MICRYN): federated pediatric REC across Canada

sues pertinent to local context (e.g., data storage or recruitment methods).

RECs are likely to be more supportive of mutual recognition frameworks if acceptable safeguards are in place and there are guarantees that, in case of a personal data breach, participants can bring an action (i) individually in their own jurisdiction and (ii) collectively. RECs could have a role in working with other bodies, such as data access committees, data protection authorities, funding agencies, journals, and research employers to assure that storage and use of data are properly monitored and reported, which includes material data breaches and action taken. Although there will always be some inconsistency within and between RECs, there must also be core opinions and underlying rationales deemed acceptable by researchers, research participants, and society (10).

Any successful model of ethics review for data-intensive international research must sustain key functions: robust protection of research participants; the gatekeeping role of a REC during the research life cycle; integrity of the ethics review system and of each REC; and trust in the ethics review standards and processes to collect, store, share, and access data.

Although no one model will fully suit all data-intensive international research and multiple variations can be devised, we believe that the models identified here can improve on the status quo of replicate REC review.

Until the emergence of a competent and legitimate system for reviewing and steering data-intensive international research, we advocate bottom-up, ad hoc solutions, ideally coupled with official recognition and support by governments and regulators, sponsors, funders, institutions, and data access committees. As models are tested and improved, more systemic solutions can be implemented.

Organizations have a key role to play. For instance, the Global Alliance for Genomics and Health has developed policies on accountability, consent, and privacy and is engaging stakeholders on the research ethics governance of data-intensive projects (11). This may assist RECs that need to check the consistency of secondary data uses with the original consent forms or verify the adequacy of data protection measures or consent processes.

In addition to moving toward common ethics review standards and procedural alignment, common conditions for exchanging data should be developed, which we believe would make RECs more inclined to mutual recognition of ethics review.

Given the global scale of the task and the bottom-up nature of this approach, at this stage, there needs to be international commitment to test these models and variations to determine whether they can achieve the desired alignment in ethics review of data-intensive research. Evidence suggests that the current system is not working well; evi-

dence is now needed to show whether certain alternatives are better. This will necessitate defining metrics to evaluate the quality and efficiency of ethics review both in the current system and in the proposed models (12). Communication with and between RECs will be crucial. The era of collaborative data-intensive international research gives us an opportunity to reform the way in which ethics committees across the world work. ■

### REFERENCES AND NOTES

1. Council of Canadian Academies, *Accessing Health and Health-Related Data in Canada* (CCA, Ottawa, 2015); <http://bit.ly/AccessHealthData>.
2. L. Abbott, C. Grady, *J. Empir. Res. Hum. Res. Ethics* **6**, 3 (2011).
3. U.S. Code of Federal Regulations, 45 CFR §46.101(h).
4. U.S. Code of Federal Regulations, 45 CFR §46.114.
5. Panel on Research Ethics, *Tri-Council Policy Statement: Ethical Conduct for Research Involving Humans* (Government of Canada, 2014); <http://bit.ly/EthicsHumRes>.
6. Health Research Authority, [U.K. National Health Service (NHS) 2016]; <http://www.hra.nhs.uk/>.
7. National Health and Medical Research Council, *National Approach to Single Ethical Review* (Australian Government, 2015); <http://bit.ly/EthicsHealth>.
8. International Council on Harmonisation of Technical Requirements for Registration of Pharmaceuticals for Human Use (ICH, 2015); [www.ich.org/](http://www.ich.org/).
9. D. C. Angus, *JAMA* **314**, 767 (2015).
10. Health Research Authority, *National Research Ethics Advisors' Panel, Consistency in REC Review* (NHS, 2014); <http://bit.ly/RECReview>.
11. Global Alliance for Genomics and Health (2016); [www.genomicsandhealth.org/](http://www.genomicsandhealth.org/).
12. S. G. Nicholls *et al.*, *PLOS One* **10**, e0133639 (2015).

### SUPPLEMENTARY MATERIALS

[www.sciencemag.org/content/351/6280/1399/suppl/DC1](http://www.sciencemag.org/content/351/6280/1399/suppl/DC1)

10.1126/science.aad5269

# Lead halides join the top optoelectronic league

Lead halide materials have the properties needed to reach the highest photovoltaic efficiencies

By **Eli Yablonovitch**

In any solar cell that begins to approach the theoretical limits of performance, an intense internal luminescence photon gas must be present (see the figure) (1). On page 1430 of this issue, Pazos-Outón *et al.* (2) provide evidence for such an internal photon gas in lead halide photovoltaic cells. These materials thus have properties similar to those of GaAs and have the potential to be among the top-performing solar cell materials. This is scientifically remarkable, because these compounds are the first high-quality halide semiconductors. The materials show promise for photovoltaics, light-emitting diodes (LEDs), laser refrigeration, thermophotonics, and a host of other major optoelectronic applications.

Many decades ago, Tom McGill of the California Institute of Technology predicted that the more ionic a semiconductor, the more tolerant it would be of dangling bond defects. In ionic materials, these dangling bond energy levels fall near the band edges, leaving the center of the bandgap relatively free of defect states. The lead halides appear to be a prime example of this effect. There are indications from recent laser cooling experiments (3) that single lead halide crystals can have ~99% internal luminescence yield, a prerequisite for the buildup of an intense internal photon gas. Laser cooling relies on superb efficiency for luminescent extraction and is another strong indication of the potential performance of the lead halides. Laser cooling, LEDs, and solar cells all rely on >95% external extraction of photons from this internal photon gas.

It has been known for over 50 years that the Shockley-Queisser formula (4) for the open-circuit voltage  $V_{oc}$  needs to be corrected from the ideal value if the external

luminescence is less than 100%. The open-circuit voltage is penalized by

$$qV_{oc} = qV_{oc-ideal} - kT \ln |\eta_{ext}| \quad (1)$$

where  $\eta_{ext}$  is the aforementioned external luminescence efficiency (5). The photon gas and the external luminescence are thus essential for achieving high voltage from a solar cell. This has led to the mantra that “a great solar cell needs to be a great LED” (2).

of the open-circuit photons are drawn out of the cell as real current. Good external extraction at open circuit comes at no penalty in current at the optimal operating bias point.

Photon recycling—that is, the reabsorption and reemission of photons—provides numerous opportunities for the photons to find the escape cone and contribute to external luminescence, but it is not the only such mechanism. Many years ago, Lush and Lundstrom (6) identified another mechanism, solar cell surface roughness. Breaking plane parallel symmetry tends to trap the incoming sunlight, boosting incoming current, but the random internal scattering also allows numerous opportunities for luminescence to escape. Photon recycling is a good option for plane parallel solar cells, but multiple elastic scattering events can also produce the same external luminescence and therefore the same voltage boost.

The report by Pazos-Outón *et al.* shows clearly the presence of the internal photon gas and the photon recycling events that are one route to a high-output voltage solar cell (see the figure). The next step will be to show that the superb external luminescent emission is compatible with heterogeneous electrical contacts. Generally, in every step of solar cell fabrication, it is profitable and experimentally straightforward to monitor the external luminescence efficiency, which predicts whether it will be an average or record cell. It is with external luminescence efficiency

monitoring that solar cell efficiency records are broken today. ■

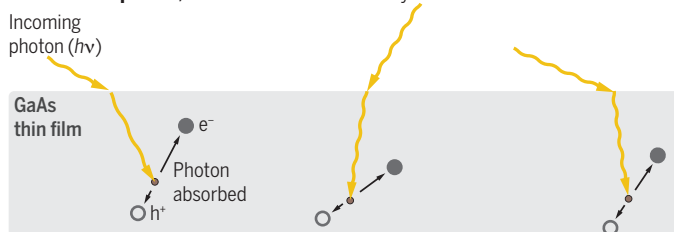
## REFERENCES AND NOTES

1. O. D. Miller, E. Yablonovitch, S. R. Kurtz, *IEEE J. Photovoltaics* **2**, 303 (2012).
2. L. M. Pazos-Outón *et al.*, *Science* **351**, 1430 (2016).
3. S.-T. Ha *et al.*, *Nat. Photonics* **10**, 115 (2016).
4. W. Shockley, H. J. Queisser, *J. Appl. Phys.* **32**, 510 (1961).
5. R. T. Ross, *J. Chem. Physics* **46**, 4590 (1967).
6. G. Lush, M. Lundstrom, *Solar Cells* **30**, 337 (1991).

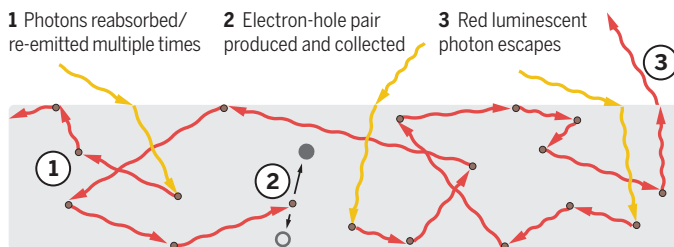
## ACKNOWLEDGMENTS

Supported by U.S. DOE “Light-Material Interactions in Energy Conversion” EFRC under grant DE-AC02-05CH11231.

**Conventional picture, 1990–2007** 25.1% efficiency



**New picture, 2011–present** 28.8% efficiency



**Record breakers.** In the conventional picture (top), a photon in a solar cell produces an electron-hole pair that is collected without need for external luminescence. Recent studies have shown that good luminescence extraction, assisted by photon recycling, is required for the highest open-circuit voltages in solar cells such as those made from GaAs. In this picture (bottom), photons are reabsorbed and re-emitted many times before an electron-hole pair is collected or a luminescent red photon escapes. Pazos-Outón *et al.* now show that lead halide materials have luminescence properties similar to those of GaAs and may, thus, also reach maximum efficiencies.

The idea that increasing light emission improves open-circuit voltage seems paradoxical, as it is tempting to equate light emission with loss. However, basic thermodynamics dictates that materials that absorb sunlight must emit in proportion to their absorptivity. At open circuit, an ideal solar cell would radiate out one photon for every photon that it absorbs. The external luminescence efficiency is a gauge of whether further loss mechanisms in addition to this photon emission are present at open circuit. At the optimum power point, the voltage is reduced by a few  $kT/q$  from open circuit, and fully 98%

Department of Electrical Engineering and Computer Sciences, University of California, Berkeley, CA 94720, USA. E-mail: eliy@eecs.berkeley.edu





Like members of human societies, genes “cooperate” and “compete” to promote survival.

## GENOMICS

# The social gene

Advances in genetic research prompt a pair of scientists to update the “selfish gene” metaphor

By Joseph Swift

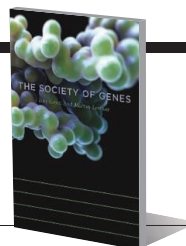
Genetic research has moved rapidly since the publication of Richard Dawkins’s *The Selfish Gene* 40 years ago (1). In the intervening years, we have come to realize that many of the most interesting and important phenomena in human biology are not caused by any single gene. Processes like the immune system’s ability to recognize infection, or the timing of our sleep-wake cycle, for example, are the product of many genes working together in a highly integrated way. Citing a wealth of recent research that explores the ways genes work together to produce complex biological processes, Itai Yanai and Martin Lercher argue that it is time to embrace a new, more holistic, metaphor in their book, *The Society of Genes*.

“Genes do indeed behave in ways that can be described as selfish,” they concede. “But genes, like humans, do not live in isolation.” It is therefore useful to think about our genes as members of a society in which different genes play specific roles.

Rather than focus on any one gene, Yanai and Lercher invite the reader to step back

### The Society of Genes

Itai Yanai and  
Martin Lercher  
Harvard University Press,  
2016. 294 pp.



and observe how genes assemble together to make a global genetic system, or genome. From here, one can see that the labor within the genome is not divided equally. Whereas many genes encode for proteins that perform a single monotonous task, such as breaking down a certain type of sugar or producing a specific skin pigment, there are others that serve such fundamental roles that their removal would lead to the crumbling of the genomic society altogether. Among the latter group are genes that manage the behavior of a host of other genes.

When genes are mismanaged by their masters, organisms can be transformed in dramatic ways. For example, in humans, when *SOX9* fails to direct its wide range of subordinates succinctly, sex reversal and skeletal malformations can occur.

Given that catastrophic things tend to happen when genes don’t work together properly, changes to how the genomic society is run are a rare occurrence. When genes with new abilities evolve, Darwinian

selection determines whether they will join the ranks as productive members of society. Our ancestors obtained genes that could interpret light as color and a gene for a more efficient oxygen-carrying hemoglobin in this very way.

And then there are the genes that don’t contribute to society at all. Instead, they secure their position by hijacking the system. The *LINE1* gene, for example, encodes only for its own dispersal, copying and pasting itself throughout our genome while providing the society with no clear benefit. The “bad behavior” of genes amounts to scandal in the genomic society, and learning about their exploits is one of the most enjoyable elements of reading the book.

There are even genes that work to ensure the survival of individual cells within an organism by wreaking havoc on others. In fruit flies, for example, a pair of genes involved in sperm production work in concert to produce both a poison and its antidote. The toxic compound is released from the cell, while the antidote is retained. In this way, surrounding sperm cells without the gene pair are killed. On reading about such systems, one begins to realize that it’s not quite right to imagine our genome as some idealized republic. This is a society that is easily compromised from within its own ranks.

Despite the genome’s complexity, the authors are careful to keep the text accessible. Indeed, at times the reader may be reminded of those rare high-school teachers who could reveal the simple beauty hidden within abstract scientific theories.

The book’s greatest strength is its remarkable use of metaphor. However, at times, the comparisons confuse rather than clarify. There must be a simpler way to explain retina biology than to compare it to both the structure of an Israeli kibbutz and the design of a color television, for example. But this is a minor shortcoming for a work that largely succeeds in translating the findings of an esoteric science into something that is easily understood.

In the years since *The Selfish Gene* was published, the human genome has been sequenced, along with the genomes of many other species. Indeed, probing one’s own genes is beginning to become routine. Thus, *The Society of Genes* represents a timely and welcome handbook for navigating this post-genomic era.

### REFERENCES

1. R. Dawkins. *The Selfish Gene* (Oxford Univ. Press, Oxford, 2016).

10.1126/science.aaf5297

The reviewer is in the Center for Genomics and Systems Biology, New York University, New York, NY 10003, USA.  
E-mail: jas1310@nyu.edu

## HISTORY OF SCIENCE

# The paradigm shift, in perspective

A new collection of essays takes a fresh look at Thomas Kuhn's classic text

By Sandra D. Mitchell

In his 1962 review of Thomas Kuhn's *The Structure of Scientific Revolutions*, historian Charles Gillispie proclaimed it "a very bold venture, this essay." In hindsight, it seems not just bold but a pivotal point in our understanding of science. Kuhn's book, like the scientific revolutions it documents, initiated a paradigm shift in the way we think about scientific practice. Rather than seeing scientific change solely as rational progress—a slow climb up the mountain of truth—we now view it as a socially produced, psychologically influenced, and somewhat disjointed change of explanatory frameworks. For decades, nearly every undergraduate course in history, philosophy, or sociology of science used *Structure* as a central textbook. The book under review features essays contributed by historians, social scientists, and philosophers that reflect on the development, content, and impact of Kuhn's revolutionary book.

There is much that is new and intriguing in this diverse volume. Some chapters invite us "inside the head" of Kuhn, through personal memories of his unique pedagogical style, his letters and notebooks, and his "Aristotle experience": the moment he realized that Aristotelian physics made sense in the historical context in which it was written. Others explore how psychological theories, Kuhn's scientific work on radar during World War II, and the Cold War culture influenced Kuhn's philosophy. Still others focus on the text itself, examining how Kuhn redefined key concepts, including paradigms, revolutions, exemplars, and progress. The philosophy and sociology chapters offer different lenses through which to view *Structure*, but historical perspectives occupy center stage.

Kuhn studied under the Nobel Prize-winning physicist and mathematician John Van Vleck at Harvard in the 1940s and later

joined Van Vleck and the Radio Research Laboratory in making jamming devices to interfere with German radar. Kuhn's thesis research in solid-state physics led to a new approximation method that is still used today, but it was not field-changing by any stretch of the imagination. As historian Peter Galison puts it: "Kuhn's whole surround was, to grab his own later term, 'normal science.'"

After his election to Harvard's Society of Fellows, Kuhn began teaching the history of science. It is in Kuhn's notebooks from this time that we find key influences on *Struc-*

experiment in which a subject wore a pair of mirrored glasses that completely inverted his view of the world for 10 days. Historian Lorraine Daston's elegantly crafted chapter presents this experiment as parallel to Kuhn's view of structural scientific transformation. Interspersed with her analysis of the rise and fall of the understanding of "structure," she documents the experience of the experimental subject, who gradually progressed from disorientation to adaptation.

Daston argues that Kuhn's search for "structure" in scientific change ultimately undermined his historical project. Historians who embrace Kuhn's campaign against "Whiggishness"—interpreting past science as good or bad through the narrow perspective of contemporary views—have sought to document scientific practice as "resolutely historical." This, Daston argues, has led to the current gulf between philosophy, sociology, and history of science. But this fragmentation need not be Kuhn's final legacy.

Daston challenges Kuhn's view of paradigms as all-encompassing ways of seeing the world that cannot be captured by rules, only

learned through exemplars. Such an interpretation makes paradigm change a necessarily sudden, revolutionary gestalt shift. But perception isn't like that, she argues. As the inverted glasses experiment reveals, adaptation to a radical change in perspective is something that occurs gradually. If those who study science move outside Kuhn's context-inflected interpretations, she writes, "his final conception of paradigm might yet yield a structure capacious enough to bring the history, philosophy and sociology of science—and much else—back together again."

Reflecting on the paradigm shift that Kuhn's influential book initiated gives us new insight into the current and future state of science studies.

## REFERENCES

1. C. Gillispie, *Science* **138**, 1251 (1962).

10.1126/science.aaf2233



Hotly debated among intellectuals and parodied in *The New Yorker*, *The Structure of Scientific Revolutions* caused a sensation in the mid-20th century.

ture. Early on, Kuhn rejected the logical positivist view of science and began to draw parallels between the process of scientific change and the stages of cognitive development, as outlined by the clinical psychologist Jean Piaget. Galison deftly exposes the role that Kuhn's own scientific practice played in framing the questions that motivated *Structure* and documents how experimental psychology became a major resource for answering those questions.

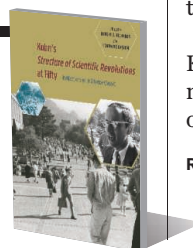
In August 1950, researchers at the University of Innsbruck in Austria conducted an

## Kuhn's *Structure of Scientific Revolutions* at Fifty

Reflections on a Science Classic

Robert J. Richards and  
Lorraine Daston (Eds.)

University of Chicago Press,  
2016. 234 pp.



The reviewer is in the Department of History and Philosophy of Science, University of Pittsburgh, Pittsburgh, PA 15260, USA. E-mail: smitchel@pitt.edu



## LETTERS

Edited by Jennifer Sills

### Basic science: Bedrock of progress

ALMOST 4 YEARS ago, one of us (F.S.C.) wrote an Editorial (1) affirming the continued importance of basic research to the National Institutes of Health (NIH) mission. The Editorial emphasized that basic scientific discovery is the engine that powers the biomedical enterprise, and NIH continues to spend more than half its budget supporting basic research projects. This is critical, because the private sector generally funds projects that yield a more rapid return on investment.

Despite these assurances, some members



of the community believe that NIH's interest in basic science is flagging. For example, investigators have told us that the requirement for a "Public Health Relevance" statement in every NIH research grant application suggests that every project must relate directly to a public health concern—that NIH places less value on projects that cannot be expected to yield an immediate public health benefit. This is simply not true. As we wrote in our Strategic Plan (2), we recognize that many of the most important medical advances trace back to basic research that had no explicit disease link. To address this concern, we have revised our application instructions (3) so that the Public Health Relevance statement reflects the NIH mission and our commitment to supporting a robust, diverse research portfolio, including the pursuit of basic biological knowledge.

We are particularly concerned that misperceptions about NIH's priorities and interests may be causing investigators to submit fewer basic research applications. For example, the National Institute of

Neurological Disorders and Stroke (NINDS) noticed a gradual and significant decline in the number of basic grants awarded between 1997 and 2012 (4). This decrease in awards was not a consequence of peer review given that basic grant applications actually did substantially better in review than applied research proposals. Instead, the major driver of this decline was a decrease in the number of fundamental basic research applications submitted.

The taxpayer investment in NIH has yielded spectacular returns from basic science over the long term. These range from the discoveries of the low-density lipoprotein receptor (5) and the development of CRISPR-associated protein-9 nuclease (6, 7) to recent substantial advances in structural biology through cryo-electron microscopy (8). For this track record of success to continue, we must continue our vigorous support of the pursuit of fundamental knowledge. All of NIH's senior leaders believe strongly that progress toward these goals occurs most rapidly when investigators pursue their passions, whether they lie in basic research or in applied, disease-focused studies. By supporting a broad portfolio of basic, translational, population, and clinical research, NIH will continue to lead the way toward a healthier future.

**Francis S. Collins,<sup>1\*</sup> James M. Anderson,<sup>2</sup> Christopher P. Austin,<sup>3</sup> James F. Battey,<sup>4</sup> Linda S. Birnbaum,<sup>5</sup> Josephine P. Briggs,<sup>6</sup> Janine A. Clayton,<sup>7</sup> Bruce Cuthbert,<sup>8</sup> Robert W. Eisinger,<sup>9</sup> Anthony S. Fauci,<sup>10</sup> John I. Gallin,<sup>11</sup> Gary H. Gibbons,<sup>12</sup> Roger I. Glass,<sup>13</sup> Michael M. Gottesman,<sup>14</sup> Patricia A. Gray,<sup>15</sup> Eric D. Green,<sup>16</sup> Franziska B. Greider,<sup>17</sup> Richard Hodes,<sup>18</sup> Kathy L. Hudson,<sup>1</sup> Betsy Humphreys,<sup>19</sup> Stephen I. Katz,<sup>20</sup> George F. Koob,<sup>21</sup> Walter J. Korshetz,<sup>22</sup> Michael S. Lauer,<sup>23</sup> Jon R. Lorsch,<sup>24</sup> Douglas R. Lowy,<sup>25</sup> John J. McGowan,<sup>26</sup> David M. Murray,<sup>27</sup> Richard Nakamura,<sup>28</sup> Andrea Norris,<sup>29</sup> Eliseo J. Perez-Stable,<sup>30</sup> Roderic I. Pettigrew,<sup>31</sup> William T. Riley,<sup>32</sup> Griffin P. Rodgers,<sup>33</sup> Paul A. Sieving,<sup>34</sup> Martha J. Somerman,<sup>35</sup> Catherine Y. Spong,<sup>36</sup> Lawrence A. Tabak,<sup>1</sup> Nora D. Volkow,<sup>37</sup> Elizabeth L. Wilder<sup>38</sup>**

<sup>1</sup>Office of the Director, NIH, Bethesda, MD 20892, USA. <sup>2</sup>Division of Program Coordination, Planning, and Strategic Initiatives, NIH, Bethesda, MD 20892, USA. <sup>3</sup>National Center for Advancing Translational Science, NIH, Rockville, MD 20850, USA. <sup>4</sup>National Institute on Deafness and Other Communication Disorders, NIH, Bethesda, MD 20892, USA. <sup>5</sup>National Institute of Environmental Health Sciences, NIH, Research Triangle Park, NC 27709, USA. <sup>6</sup>National Center for Complementary and Integrative Health, NIH, Bethesda, MD 20892, USA. <sup>7</sup>Office of Research on Women's Health, NIH, Bethesda, MD 20892, USA. <sup>8</sup>National Institute of Mental Health, NIH, Bethesda, MD 20892, USA.

<sup>9</sup>Office of AIDS Research, NIH, Bethesda, MD 20892, USA. <sup>10</sup>National Institute of Allergy and Infectious Diseases, NIH, Bethesda, MD 20892, USA. <sup>11</sup>Clinical Center, NIH, Bethesda, MD 20892, USA. <sup>12</sup>National Heart, Lung, and Blood Institute, NIH, Bethesda, MD 20892, USA. <sup>13</sup>Fogarty International Center, NIH, Bethesda, MD 20892, USA. <sup>14</sup>Office of Intramural Research, NIH, Bethesda, MD 20892, USA. <sup>15</sup>National Institute of Nursing Research, NIH, Bethesda, MD 20892, USA. <sup>16</sup>National Human Genome Research Institute, NIH, Bethesda, MD 20892, USA. <sup>17</sup>Office of Research Infrastructure Programs, NIH, Bethesda, MD 20892, USA. <sup>18</sup>National Institute on Aging, NIH, Bethesda, MD 20892, USA. <sup>19</sup>National Library of Medicine, NIH, Bethesda, MD 20892, USA. <sup>20</sup>National Institute of Arthritis and Musculoskeletal and Skin Diseases, NIH, Bethesda, MD 20892, USA. <sup>21</sup>National Institute on Alcohol Abuse and Alcoholism, NIH, Bethesda, MD 20892, USA. <sup>22</sup>NINDS, NIH, Bethesda, MD 20892, USA. <sup>23</sup>Office of Extramural Research, NIH, Bethesda, MD 20892, USA. <sup>24</sup>National Institute of General Medical Sciences, NIH, Bethesda, MD 20892, USA. <sup>25</sup>National Cancer Institute, NIH, Bethesda, MD 20892, USA. <sup>26</sup>Office of Management, NIH, Bethesda, MD 20892, USA. <sup>27</sup>Office of Disease Prevention, NIH, Bethesda, MD 20892, USA. <sup>28</sup>Center for Scientific Review, NIH, Bethesda, MD 20892, USA. <sup>29</sup>Center for Information Technology, NIH, Bethesda, MD 20892, USA. <sup>30</sup>National Institute on Minority Health and Health Disparities, NIH, Bethesda, MD 20892, USA. <sup>31</sup>National Institute of Biomedical Imaging and Bioengineering, NIH, Bethesda, MD 20892, USA. <sup>32</sup>Office of Behavioral and Social Sciences Research, NIH, Bethesda, MD 20892, USA. <sup>33</sup>National Institute of Diabetes and Digestive and Kidney Diseases, NIH, Bethesda, MD 20892, USA. <sup>34</sup>National Eye Institute, NIH, Bethesda, MD 20892, USA. <sup>35</sup>National Institute of Dental and Craniofacial Research, NIH, Bethesda, MD 20892, USA. <sup>36</sup>Eunice Kennedy Shriver National Institute of Child Health and Human Development, NIH, Bethesda, MD 20892, USA. <sup>37</sup>National Institute on Drug Abuse, NIH, Bethesda, MD 20892, USA. <sup>38</sup>Office of Strategic Coordination, NIH, Bethesda, MD 20892, USA.

\*Corresponding author. E-mail: collinsf@mail.nih.gov

#### REFERENCES

1. F. S. Collins, *Science* **337**, 503 (2012).
2. NIH, NIH-Wide Strategic Plan ([www.nih.gov/about-nih/nih-wide-strategic-plan](http://www.nih.gov/about-nih/nih-wide-strategic-plan)).
3. NIH, Grant Application Instructions (<http://grants.nih.gov/grants/how-to-apply-application-guide/forms-d/general/g-220-r&r-other-project-information-form.htm#8>).
4. S. Landis, Back to Basics: A call for fundamental neuroscience research (<http://blog.ninds.nih.gov/2014/03/27/back-to-basics/>).
5. M. S. Brown, J. L. Goldstein, *Science* **232**, 34 (1986).
6. M. Jinek et al., *Science* **337**, 816 (2012).
7. L. Cong et al., *Science* **339**, 819 (2013).
8. A. Bartesaghi et al., *Proc. Natl. Acad. Sci. U.S.A.* **111**, 11709 (2014).

### A research symbiont

M. MCNUTT ("I AM A RESEARCH PARASITE," Editorial, 4 March, p. 1005) can be proud to be a "research parasite." The creators of this term, Longo and Drazen (1), miss the very point of scientific research when they write that researchers may "even use the [open] data to try to disprove what the original investigators had posited." It is at the core of the scientific paradigm that researchers take nothing as final truth. In fact, using research data to try to disprove a result is

good scientific practice, especially in light of the replication crisis (2–4).

However, Longo and Drazen are right that scientific data sharing deserves recognition. They suggest that credit for data sharing should take the form of co-authorship, but co-authorship as the sole instrument of credit will unnecessarily restrict the potential of data sharing and could be a detriment to the original researcher (for instance, if the resulting publications lack quality) (5). In the case of replication studies and meta-analyses, co-authorship makes no scientific sense.

A more suitable instrument would be a much higher appraisal of data sharing by research communities through citations of data sets, awards, and the consideration of data “production” in career prospects, funding applications, and evaluations. With this end in mind, research parasites are beneficial for the organism as a whole.

**Benedikt Fecher<sup>1,2,3\*</sup> and  
Gert G. Wagner<sup>1,4</sup>**

<sup>1</sup>German Institute for Economic Research, 10117, Berlin, Germany. <sup>2</sup>Alexander von Humboldt Institute for Internet and Society, 10117, Berlin, Germany.

<sup>3</sup>Leibniz Association, 10115, Berlin, Germany. <sup>4</sup>Max Planck Institute for Human Development, 14195, Berlin, Germany.

\*Corresponding author. E-mail: benedikt.fecher@hiig.de

#### REFERENCES

1. D. L. Longo, J. M. Drazen, *N. Engl. J. Med.* **374**, 276 (2016).
2. Open Science Collaboration, *Science* **349**, aac4716 (2015).
3. C. F. Camerer *et al.*, *Science* **351**, 1433 (2016).
4. C. J. Anderson *et al.*, *Science* **351**, 1037 (2016).
5. T. Rohlfing, J.-B. Poline, *NeuroImage* **59**, 4189 (2012).

## Pseudonymous fame

J. BOHANNON'S In Depth story “Fight over author pseudonyms could flare again” (26 February, p. 902) described problems stemming from authors using the pseudonymous screen names under which they had done their research instead of their real names. The most famous case of pseudonymous authorship occurred over a century ago in the form of William Sealy Gosset's famous 1908 paper “The probable error of a mean,” for which he used the simple pseudonym Student (*1*). This work set the stage for what is now known as Student's *t* test, a hypothesis-testing tool familiar to practically every analyst and statistician. Gosset was employed by Arthur Guinness and Sons brewery in Dublin, and legend holds that his use of a pen name was prompted by the company's concern for secrecy in their use of statistical methods for quality control.

Gosset's case notwithstanding, pseudonyms will hopefully not become a more

regular occurrence. Ephemeral screen names may be acceptable for Internet message boards, but their use in research papers may ultimately lower the public's perception of the transparency, integrity, and timelessness of the permanent scientific record of human knowledge.

**Michael C. Wendt**

McDonnell Genome Institute and Departments of Mathematics and Genetics, Washington University, St. Louis, MO 63108, USA.  
E-mail: mwendt@watson.wustl.edu

#### REFERENCE

1. Student, *Biometrika* **6**, 1 (1908).

## TECHNICAL COMMENT ABSTRACTS

### Comment on “Single-trial spike trains in parietal cortex reveal discrete steps during decision-making”

**Michael N. Shadlen, Roozbeh Kiani, William T. Newsome, Joshua I. Gold, Daniel M. Wolpert, Ariel Zylberberg, Jochen Ditterich, Victor de Lafuente, Tianming Yang, Jamie Roitman**

Latimer *et al.* (Reports, 10 July 2015, p. 184) claim that during perceptual decision formation, parietal neurons undergo one-time, discrete steps in firing rate instead of gradual changes that represent the accumulation of evidence. However, that conclusion rests on unsubstantiated assumptions about the time window of evidence accumulation, and their stepping model cannot explain existing data as effectively as evidence-accumulation models.

Full text at <http://dx.doi.org/10.1126/science.aad3242>

### Response to Comment on “Single-trial spike trains in parietal cortex reveal discrete steps during decision-making”

**Kenneth W. Latimer, Jacob L. Yates, Miriam L. R. Meister, Alexander C. Huk, Jonathan W. Pillow**

Shadlen *et al.*'s Comment focuses on extrapolations of our results that were not implied or asserted in our Report. They discuss alternate analyses of average firing rates in other tasks, the relationship between neural activity and behavior, and possible extensions of the standard models we examined. Although interesting to contemplate, these points are not germane to the findings of our Report: that stepping dynamics provided a better statistical description of lateral intraparietal area spike trains than diffusion-to-bound dynamics for a majority of neurons.

Full text at <http://dx.doi.org/10.1126/science.aad3596>



## TECHNICAL COMMENT

## NEURONAL MODELING

# Comment on “Single-trial spike trains in parietal cortex reveal discrete steps during decision-making”

Michael N. Shadlen,<sup>1\*</sup> Roozbeh Kiani,<sup>2</sup> William T. Newsome,<sup>3</sup> Joshua I. Gold,<sup>4</sup> Daniel M. Wolpert,<sup>5</sup> Ariel Zylberberg,<sup>6</sup> Jochen Ditterich,<sup>7</sup> Victor de Lafuente,<sup>8</sup> Tianming Yang,<sup>9</sup> Jamie Roitman<sup>10</sup>

Latimer *et al.* (Reports, 10 July 2015, p. 184) claim that during perceptual decision formation, parietal neurons undergo one-time, discrete steps in firing rate instead of gradual changes that represent the accumulation of evidence. However, that conclusion rests on unsubstantiated assumptions about the time window of evidence accumulation, and their stepping model cannot explain existing data as effectively as evidence-accumulation models.

Latimer *et al.* (1) analyzed the spiking activity of neurons in the lateral intraparietal (LIP) area of parietal cortex and challenged the hypothesis that these neurons represent the accumulation of noisy evidence bearing on a perceptual choice (e.g., drift diffusion). They conclude that these neurons represent jumps (or steps) from a neutral to a high or low state that represents the upcoming choice. Accordingly, the ramplike activity of LIP neurons is an artifact caused by averaging step functions occurring at different times. Conceptually, their step model implies that LIP activity represents either (i) the outcome of the decision, corresponding to steps synchronized to the end of the process, or (ii) the decision process itself, corresponding to the population average of all-or-none steps contributed by individual neurons at different times. Neither interpretation is consistent with existing data.

The first interpretation is refuted by choice-reaction time (RT) experiments (2). Aligned to the beginning of deliberation, the across-trial averages of such steps would resemble a ramp. However, aligned to the end of the decision, synchronous steps should be obvious [e.g., figures 2A and 3A in (1)]. The LIP data are inconsistent

with this idea (Fig. 1A): trials with long RT do not hover in a neutral state until the end of the decision [see also (3)].

The second interpretation could explain the ramps aligned to saccadic responses in the RT experiments. However, this interpretation is inconsistent with other experiments in which a sequence of shapes replaces random-dot motion to furnish discrete packets of evidence. Under these conditions, LIP neurons do not step to stereotyped high or low states. Instead, they produce graded responses throughout the decision according to the sign and strength of the evidence provided by the current shape (Fig. 1B). Further, the graded population responses are not simply a mixture of high and low steps (4, 5). If they were, the change

in firing rate induced by a shape should diminish for later shapes, because the neuron is more likely to have already stepped. This is clearly incorrect [see figures 3B and 4B in (4)]. Thus, LIP neurons encode multiple small, noisy changes in evidence (not one-time, all-or-nothing steps) in a manner consistent with diffusion or random-walk dynamics.

These points question the conclusions in (1). Then why do their analyses suggest stepping? Parietal activity can step in the context of quickly planned eye movements to visual targets (6, 7). In contrast, diffusion (ramping) dynamics arise when the decision to make such an eye movement results from the temporal integration of evidence over a more prolonged interval. Therefore, before using models to identify (or refute) neural correlates of an integration-based decision process, it is essential to (i) know that the neural activity in question is occurring in a behavioral context that is actually based on prolonged integration and (ii) focus any model comparison on the epoch in which this integration occurs.

Unfortunately, it is difficult to estimate the integration times from the behavioral data in (1). They did not use an RT experiment, and their monkey's accuracy is flat over the viewing durations they tested (Fig. 2, filled stars). It is possible to deduce integration times from a follow-up experiment in the same monkey, using a broader range of durations (Fig. 2, open symbols). Fitting these data with bounded diffusion (curves) yields a median integration time of ~250 ms (across all motion strengths). However, the monkey's accuracy is substantially worse in the earlier data, analyzed in (1). One possibility is that the poorer accuracy is explained by a combination of guessing and overall lower sensitivity—partially compensated by an elevated decision bound—whose net effect is longer integration times (~310 ms). Alternatively, the poor accuracy is explained by brief integration times (~70 ms) or possibly a different

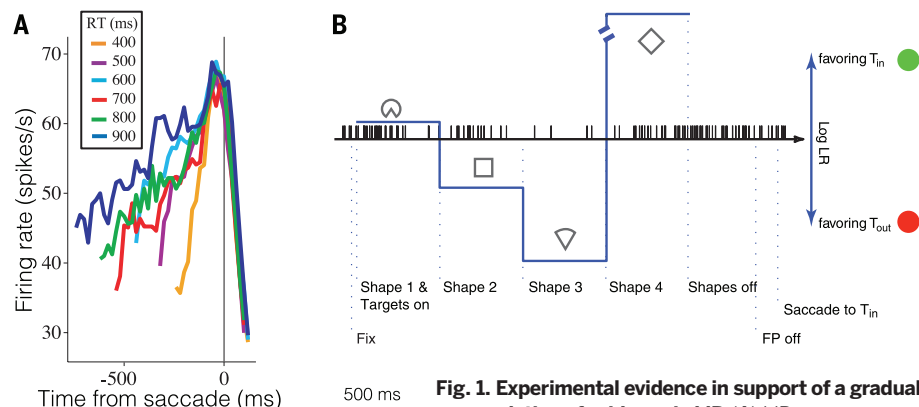


**Fig. 1. Experimental evidence in support of a gradual accumulation of evidence in LIP.** (A) LIP neurons ramp,

on average, during an RT task. Averages are sorted by RT quantile (color), using trials in which the monkey chose the direction associated with the choice target in the neuron's response field. [Modified from (2), showing responses from ~200 ms after stimulus onset; see also figure 2, B and D, in (11)]. (B) LIP neurons undergo multiple incremental changes in firing rate on single trials. On this example trial, the monkey decided in favor of the green target in the neuron's response field, consistent with the accumulated evidence from the sequence of shapes [from movie 3 of (4)]. [For more single-trial examples, see the movies in (4) and movies 1 and 2 in (5). For population analyses, see (4, 5).]

<sup>1</sup>Howard Hughes Medical Institute (HHMI) and Department of Neuroscience, Columbia University, New York, NY, USA.

<sup>2</sup>Center for Neural Science, New York University, New York, NY, USA. <sup>3</sup>HHMI and Stanford University, Stanford, CA, USA.

<sup>4</sup>Department of Neuroscience, University of Pennsylvania, Philadelphia, PA, USA. <sup>5</sup>Department of Engineering, University of Cambridge, Cambridge, UK. <sup>6</sup>HHMI and Department of Neuroscience, Columbia University, New York, NY, USA.

<sup>7</sup>Center for Neuroscience and Department of Neurobiology, Physiology, and Behavior, University of California, Davis, CA, USA. <sup>8</sup>Institute for Neuroscience, National Autonomous University of Mexico, Querétaro, México.

<sup>9</sup>Institute of Neuroscience, Chinese Academy of Sciences, Shanghai, China. <sup>10</sup>Department of Psychology, University of Illinois at Chicago, Chicago, IL, USA.

\*Corresponding author. E-mail: shadlen@columbia.edu

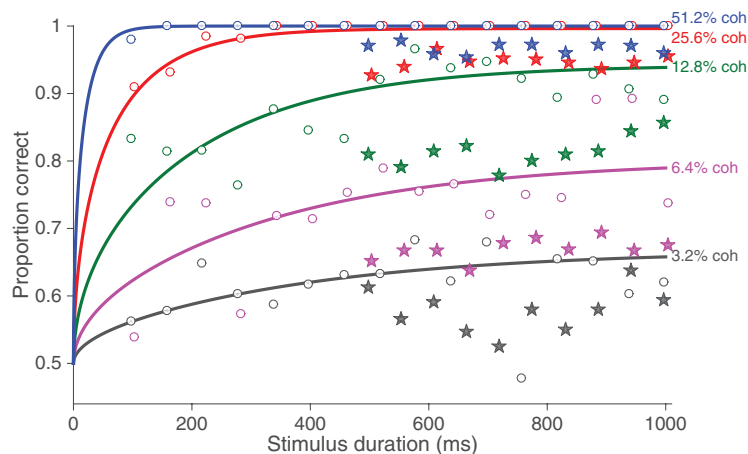


**Fig. 2. Behavioral integration times are difficult to determine from the analyzed data set but are certainly shorter than the full 500- to 1000-ms viewing durations.** Open circles correspond to behavioral data obtained after the collection of the neural recordings [figure 7D in (12)]. Smooth curves show fits of a bounded diffusion model, from which we estimate the median decision time to be ~250 ms across all motion strengths [methods explained in (13, 14)]. The neural data analyzed by Latimer *et al.* (1) accompanied the behavioral data shown by the filled stars [from figure 7A of (12)]. Accuracy was unaffected by viewing duration over the range tested, and overall performance was markedly poorer in this data set. [Data are from figure 7, A and D, in (12), with missing coherences kindly supplied by Latimer *et al.*]

strategy altogether, in which the monkey waits for salient features (extrema) in the random dots. These latter alternatives are consistent with our experience training monkeys on these kinds of tasks.

Most important, regardless of whether the integration times are 70 ms or 300 ms, they are substantially shorter than the 500- to 1000-ms duration of the trials. Accordingly, integration does not need to start at a consistent time within a trial. This potential variability exposes a critical bias in the model comparison: The stepping model is allowed the flexibility to account for random times of transitions, but the diffusion model is tethered to a fixed start time and therefore is unfairly penalized in comparison. A relatively short integration window occurring at random times during motion viewing can also explain other features of (1): the broad distribution of the time of the putative steps, the absence of a dependency of step times on motion strength, the pattern of response variance [figure 4A in (1)], the superior choice predictions of the step mod-

el, and its superior deviance information criterion (DIC).

Latimer *et al.* attempt to mitigate some of these concerns in their supplementary analysis of data from an RT experiment (2). However, that analysis also does not convincingly support a stepping model. Of the 16 neurons (of 54) chosen for analysis, only 10 exhibited the kind of coherence- and choice-dependent ramping that is the focus of the model comparison. Of these, four support diffusion. Moreover, the average  $\Delta$ DIC in favor of steps is small (~19; 10 excluding the outlier), even though the comparison is biased toward that result: (i) the data include many high-motion strength trials with brief integration times (e.g., 12% of included trials have integration times <150 ms) that are likely to be seen as steps; (ii) their integration model assumes that the starting time of integration is fixed, despite the fact that it varies considerably across neurons [see figure S22 in (1)]; and (iii) their own simulations [figure S6 in (1)] show that their analysis can produce evidence for stepping even under simulations of diffusion.

Identifying the sources of these biases, including possibly their model's handling of negative-going rates (which are neither bounded nor stopped like the positive-going rates) [supplementary materials section 2.1, figure 1B, and figure S9 in (1)] and the inability to identify latent firing rates from the parameters of diffusion, should be addressed before applying these methods to richer data sets.

In summary, Latimer *et al.* present a statistical method for inferring discrete steps in firing rate from single neurons [similar to (8–10)] and use it to claim that averages of random steps are responsible for the evolving firing of LIP neurons during deliberative decision-making. However, they have not supported this claim, and they have not provided a plausible explanation for many experimental observations supporting the representation of accumulated noisy evidence by single neurons in LIP. At present, bounded diffusion provides the best account of the ensemble of neural data.

## REFERENCES

1. K. W. Latimer, J. L. Yates, M. L. Meister, A. C. Huk, J. W. Pillow, *Science* **349**, 184–187 (2015).
2. J. D. Roitman, M. N. Shadlen, *J. Neurosci.* **22**, 9475–9489 (2002).
3. A. Bollimunta, D. Totten, J. Ditterich, *J. Neurosci.* **32**, 12684–12701 (2012).
4. T. Yang, M. N. Shadlen, *Nature* **447**, 1075–1080 (2007).
5. S. Kira, T. Yang, M. N. Shadlen, *Neuron* **85**, 861–873 (2015).
6. S. Barash, R. M. Bracewell, L. Fogassi, J. W. Gnadt, R. A. Andersen, *J. Neurophysiol.* **66**, 1095–1108 (1991).
7. J. W. Gnadt, R. A. Andersen, *Exp. Brain Res.* **70**, 216–220 (1988).
8. D. Commenges, J. Seal, *Stat. Med.* **4**, 91–104 (1985).
9. D. Commenges, J. Seal, F. Pinatet, *Math. Biosci.* **80**, 81–108 (1986).
10. R. C. Wilson, M. R. Nassar, J. I. Gold, *Neural Comput.* **22**, 2452–2476 (2010).
11. A. K. Churchland, R. Kiani, M. N. Shadlen, *Nat. Neurosci.* **11**, 693–702 (2008).
12. M. L. Meister, J. A. Hennig, A. C. Huk, *J. Neurosci.* **33**, 2254–2267 (2013).
13. R. Kiani, T. D. Hanks, M. N. Shadlen, *J. Neurosci.* **28**, 3017–3029 (2008).
14. V. de Lafuente, M. Jazayeri, M. N. Shadlen, *J. Neurosci.* **35**, 4306–4318 (2015).

28 August 2015; accepted 4 February 2016  
10.1126/science.aad3242



## TECHNICAL RESPONSE

## NEURONAL MODELING

# Response to Comment on “Single-trial spike trains in parietal cortex reveal discrete steps during decision-making”

Kenneth W. Latimer,<sup>1,2,3</sup> Jacob L. Yates,<sup>1,2</sup> Miriam L. R. Meister,<sup>3</sup>  
Alexander C. Huk,<sup>1,2,4,5</sup> Jonathan W. Pillow<sup>1,2,5,6\*</sup>

Shadlen *et al.*'s Comment focuses on extrapolations of our results that were not implied or asserted in our Report. They discuss alternate analyses of average firing rates in other tasks, the relationship between neural activity and behavior, and possible extensions of the standard models we examined. Although interesting to contemplate, these points are not germane to the findings of our Report: that stepping dynamics provided a better statistical description of lateral intraparietal area spike trains than diffusion-to-bound dynamics for a majority of neurons.

**W**e organize our Response to Shadlen *et al.* (1) around four topics: (i) comparisons to other experiments, (ii) the integration behavior of our animals, (iii) alternative formulations of the drift-diffusion model, and (iv) interpretation of data from Roitman and Shadlen (2), followed by (v) technical comments. (i) Shadlen *et al.* assert that our main finding in Latimer *et al.* (3) is inconsistent with other experiments and analyses. Their figure 1A shows saccade-aligned peristimulus time histograms (PSTHs) from a reaction time (RT) motion discrimination task. First, a PSTH (an average over trials) cannot provide definitive evidence about

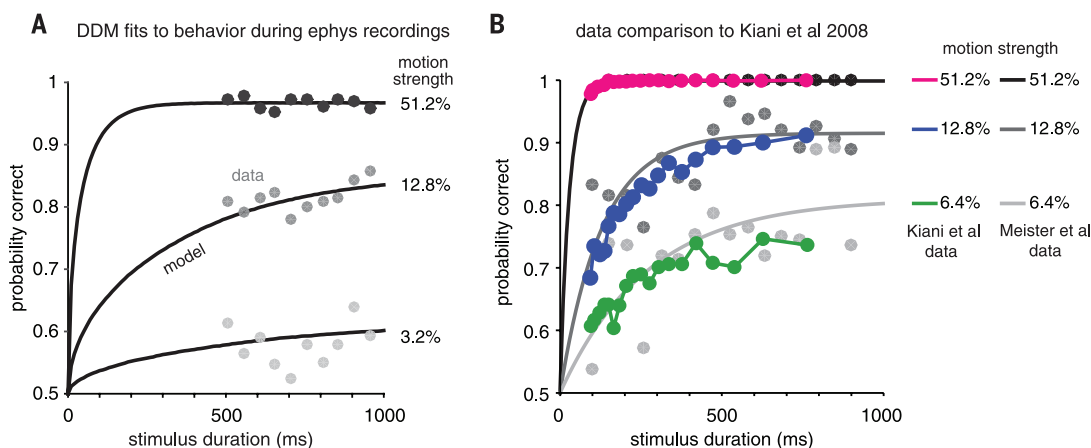
the dynamics governing firing on single trials, a primary point of motivation for our Report. Second, their figure 1A simply shows that spike rate steps are not precisely aligned with saccade times. Our Report made no assumptions and drew no conclusions about the relationship between spike rates and decisions or saccades—in fact, both stepping and ramping models were fit without knowledge of the animal's choices. Moreover, we obtained an identical stepping result with spike trains from this very data set (2), indicating that there is nothing inconsistent about a finding of stepping dynamics with ramping saccade-aligned PSTHs.

Shadlen *et al.* then argue that lateral intraparietal (LIP) area activity during a different decision-making task (4) conflicts with our results. We fail to see the conflict: We did not analyze data from this task, and it is entirely conceivable that LIP neurons exhibit different dynamics in distinct contexts. Regardless, Kira *et al.* (4) analyzed population-averaged responses over many trials, and this cannot provide evidence for or against stepping single-trial dynamics. Although figure 1B from Shadlen *et al.* overlays spikes with instantaneous decision evidence, this spike train appears to be hand-picked, and no single-trial spike trains were analyzed in that paper.

(ii) Shadlen *et al.* argue that our behavioral data (5) might reflect brief or variable evidence accumulation. However, a drift-diffusion model (DDM) fit confirms that the monkey's behavior during electrophysiological recordings met or exceeded conventional periods of integration (Fig. 1A), and is nearly indistinguishable from that in Kiani *et al.* (6) when assessed with shorter viewing durations in sessions outside of electrophysiology (Fig. 1B). The slightly lower accuracy observed during electrophysiology sessions is not evidence that the monkey employed two different decision-making strategies and instead is likely a simple consequence of differences in stimulus geometry. Specifically, our neural recording sessions

**Fig. 1. Our animal's behavior reflects a period of evidence accumulation as long or longer than durations reported previously.**

(A) Monkey's accuracy as a function of stimulus duration during neurophysiological recording sessions (dots) from (5) overlaid with the theoretical curves (solid lines) obtained from a maximum likelihood fit of a DDM. The median durations of behavioral integration under this model are 408, 362, and 152 ms across the range of motion strengths shown. These integration times are in fact longer than those recently reported in (10). A modest lapse rate in the DDM accounts for the asymptotic performance slightly below 100% [e.g., (7, 8, 15)]. The other monkey (not discussed by Shadlen *et al.*) exhibits similar signatures of substantial evidence accumulation. (B) This animal's behavior is also very similar to that of previous studies. Dependency of accuracy on viewing duration and motion strength [same conventions as in (A)] from a purely



behavioral data set collected from the same monkey (5) (gray-scale dots) using a range of shorter durations that closely match those used in a previous study (6) (colored dots). The data from the two studies are very similar (i.e., they overlap and follow matching forms), demonstrating that our monkey achieves performance on the random dots task nearly identical to that reported in a study by some of the authors of Shadlen *et al.*

employed unique target and dot-motion aperture locations and motion directions tailored to each neuron under study, whereas the shorter-duration behavior (shown in Fig. 1B) had consistent cardinal stimulus geometry across sessions. This difference in stimulus geometry strikes us as a more plausible account than Shadlen *et al.*'s suggestion that this monkey only employed conventional temporal integration when we were not recording from LIP. [Additionally, unlike many LIP studies in which dot motion is presented at central fixation—e.g., (2, 6–9)—we presented the dots peripherally, better encouraging broad spatiotemporal integration and avoiding individual dot tracking that is possible in high-resolution central vision.]

(iii) Shadlen *et al.* call for an alternative diffusion-to-bound model with variable per-trial integration start times. We constructed our model to be faithful to previous formulations in the LIP literature. Shadlen and Kiani (10) stated, “There’s a reproducible starting time ~200 ms after the onset of motion.” Applications of the DDM for behavior typically use a fixed start time [e.g., (4, 9, 11)]. Many LIP studies analyze spike counts averaged across trials and neurons, thereby assuming that integration begins at the same time on each trial and in each neuron [e.g., (4, 12)]. Without this assumption, average spike rates would reflect a mixture of temporally shifted ramping trajectories and preintegration activity, instead of a coherent ramping process (13). Moreover, the claim that the fixed start time “unfairly penalized” the ramping model is incorrect. The stepping model does not have a flexible start time. Both models describe spike trains in terms of a conditionally Poisson process beginning at a fixed time after motion onset on every trial and evolves according to discrete stepping or continuous ramping dynamics for the remainder of the trial. We did test a range of start times for both models for every cell, with no noticeable changes to our results [figure S18 in (3)].

(iv) Shadlen *et al.* claim that our supplementary analysis of data from Roitman and Shadlen

(2) included cells inappropriate for studying evidence accumulation. We are perplexed by this argument because it appears to conflict with conclusions about LIP function made by Shadlen *et al.* from this data set (point i above). All the cells that we analyzed were taken from the same data set used to construct Shadlen *et al.*'s figure 1A. Additionally, Shadlen *et al.* posit that trials with integration times under 150 ms biased our results, but we only analyzed trials with RTs of at least 350 ms [see the supplementary materials for (3)]. Shadlen *et al.* assert that the average  $\Delta$ DIC (deviance information criterion) is small ( $\Delta$ DIC = 19), but this value is clearly in favor of stepping;  $\Delta$ DIC  $\geq 10$  is conventionally regarded as “strong” statistical evidence (14).

(v) Shadlen *et al.* assert that our ramping model simulations produce evidence for stepping. The figure in question [figure S6 in (3)] shows that for ramping simulations (based on our fits and trial counts from real data), the distribution of  $\Delta$ DICs strongly supports ramping. A few small positive values indicated that the two models are not always identifiable given limited data (3 of 40 individual-neuron simulations yielded negligible evidence for stepping;  $\Delta$ DICs < 3), which does not undermine the consistency of our analyses. Finally, Shadlen *et al.* argue that our model comparison is biased because we cannot “identify latent firing rates” in the ramping model. Frankly, we do not understand this remark. Our Bayesian fitting methods integrate over all possible latent rates consistent with the data, for both models.

In summary, (i) hypotheses about how LIP dynamics relate to decision formation are intriguing and worthy of future investigation but not relevant to our statistical analyses; (ii) our monkey behavior and modeling assumptions match previous studies of LIP, although we certainly welcome future standardization and generalization of experimental and theoretical protocols; and (iii) our reanalysis of data from Roitman and Shadlen still supported the stepping model. We

stand behind the conclusions of our Report and believe that considering alternative hypotheses to integration will continue to be illuminating. We of course agree with Shadlen *et al.* that extrapolations of our original study's characterizations of single-neuron spike trains to that of population-level dynamics and/or to decision-making would be premature. These important issues require consideration of richer multineuron data sets, which we have recently collected and are currently analyzing. The ongoing introduction of powerful new tools and data sets will likely bring continued constructive debate, and we share Shadlen *et al.*'s enthusiasm for testing and generalizing theories that link brain and cognition.

## REFERENCES

1. M. N. Shadlen *et al.*, *Science* **351**, 1406 (2016).
2. J. D. Roitman, M. N. Shadlen, *J. Neurosci.* **22**, 9475–9489 (2002).
3. K. W. Latimer, J. L. Yates, M. L. R. Meister, A. C. Huk, J. W. Pillow, *Science* **349**, 184–187 (2015).
4. S. Kira, T. Yang, M. N. Shadlen, *Neuron* **85**, 861–873 (2015).
5. M. L. R. Meister, J. A. Hennig, A. C. Huk, *J. Neurosci.* **33**, 2254–2267 (2013).
6. R. Kiani, T. D. Hanks, M. N. Shadlen, *J. Neurosci.* **28**, 3017–3029 (2008).
7. R. Kiani, M. N. Shadlen, *Science* **324**, 759–764 (2009).
8. S. Berru, J. I. Gold, *J. Neurosci.* **31**, 913–921 (2011).
9. V. de Lafuente, M. Jazayeri, M. N. Shadlen, *J. Neurosci.* **35**, 4306–4318 (2015).
10. M. N. Shadlen, R. Kiani, *Neuron* **80**, 791–806 (2013).
11. R. Bogacz, E. Brown, J. Moehlis, P. Holmes, J. D. Cohen, *Psychol. Rev.* **113**, 700–765 (2006).
12. A. C. Huk, M. N. Shadlen, *J. Neurosci.* **25**, 10420–10436 (2005).
13. I. M. Park, M. L. Meister, A. C. Huk, J. W. Pillow, *Nat. Neurosci.* **17**, 1395–1403 (2014).
14. K. P. Burnham, D. R. Anderson, *Model Selection and Multimodel Inference: A Practical Information-Theoretic Approach* (Springer Science and Business Media, New York, 2002).
15. M. N. Shadlen, W. T. Newsome, *J. Neurophysiol.* **86**, 1916–1936 (2001).

17 September 2015; accepted 4 February 2016  
10.1126/science.aad3596





Geri Richmond and Hashemite University molecular biologist Rana Dajani spoke after Richmond's AAAS presidential address to open the 2016 AAAS Annual Meeting.

## AAAS annual meeting demonstrates the critical value of global scientific collaboration

By **Becky Ham**

Some of the most intriguing news at the 2016 AAAS Annual Meeting focused on the tiny: a minuscule cosmic ripple born 1.5 billion years ago, and a millimeters-long mosquito responsible for an emerging health crisis. But the science behind these discoveries is huge in scope and in importance, reflecting the ongoing achievement of international research teams addressing complex challenges in science and society.

Efforts to track the spread of Zika virus in the Americas, and the landmark discovery of gravitational waves, both demonstrate the power and potential—and the need—for global collaborations between scientists, speakers emphasized at the 11 to 15 February event, held in Washington, DC.

In particular, scientists in developing countries must work as equal partners with their counterparts in developed countries to solve border-crossing challenges like climate change and virus

outbreaks, said outgoing AAAS President Geri Richmond in her address at the start of the meeting.

The best science happens, Richmond said, “when everyone is at the table and has an equal voice, when creativity flows with different perspectives from different countries, different institutions, and different backgrounds.”

The increasingly global nature of science became clear to Christopher Dye in 2015 when he walked into an Ebola response team meeting in Monrovia, Liberia. “I counted 12 nationalities in the room,” said Dye, director of strategy in the Office of the Director General at the World Health Organization. “These were people who had never worked together, and never met each other before. They came from very diverse backgrounds, and yet they worked together immediately.”

“And if you want to think about Zika virus—because that’s what worries us at the moment—will



NIAID Director Anthony Fauci proposed new Zika funding.



Zika be a story of global science engagement and global engagement in other forms?” Dye asked in his AAAS plenary address.

Dye joined a panel of public health experts who spoke at the meeting on the troubling increase in Zika virus infections and associated neurological disorders such as microcephaly and Guillain-Barré syndrome in Central and South America. After the World Health Organization (WHO) declared the Zika outbreak a public health emergency of international concern on 1 February, teams of international researchers have traveled to the region to clarify the connections between the virus and the disorders, and to look for ways to prevent Zika’s spread. Panel speakers said the first results from these studies, including a report from Brazil on children with microcephaly, are expected in April.

In a AAAS news briefing, National Institute of Allergy and Infectious Diseases (NIAID) Director Anthony Fauci noted that President Barack Obama has asked the U.S. Congress for a \$1.8 billion budget supplement to fight the virus outbreak, which would include funding to the National Institutes of Health to help develop a Zika vaccine.

Speakers at the meeting also said that challenges such as food shocks associated with the extreme-weather effects of climate change require a coordinated international response. There is a growing likelihood of a weather-driven food shock, where major harvests of a staple crop such as soy, maize, wheat, or rice fail and significantly drive up the crop’s price on the global market, warned Tim Benton of the United Kingdom’s Global Food Security Program. The global food trade network can potentially amplify the risks of weather-driven food shocks, hitting hardest in poor and import-dependent countries such as those in sub-Saharan Africa, he said.

Benton and his colleagues have been working with government leaders and policy-makers around the world to address and manage food shock risks. “We ask, ‘Are you prepared for the consequences?’ And typically the answer is ‘No,’” he said. “Governments are listening, but they aren’t engaged as much as we would like them to be.”

The researchers called for an international plan of action to make the food system more resilient, such as adopting contingency plans to store key crops or divert certain crops from biofuel use when demand reaches a critical level. Biotechnology used to develop drought-resistant crops, better agricultural practices such as crop rotation, and more sustainable use of resources can also help agriculture adapt to extreme weather, they said.

In other sessions throughout the meeting, scientists emphasized how their international collaborations have led to productive diplomatic relationships between countries. In one such gathering, key researchers with the Synchrotron-light for Experimental Science and Applications in the Middle East (SESAME) talked about how their center will nourish both technological expertise and

understanding among people with diverse religions and political systems in the region.

Synchrotron particle accelerators such as SESAME produce electromagnetic radiation that can be useful in probing the structures of complex proteins, identifying the chemicals in a new drug, or developing materials that capture pollutants. SESAME’s current members include Bahrain, Cyprus, Egypt, Iran, Israel, Jordan, Pakistan, the Palestinian Authority, and Turkey. More than a dozen nations, including the United States, act as advisors to the project.

“The first news is that it exists at all,” said Chris Llewellyn-Smith, a former director-general of CERN, the European Organization for Nuclear Research. Llewellyn-Smith is president of the international council that is leading the SESAME project. “I believe I am correct in saying that I chair the only body in the world outside of the United Nations that has representatives of Iran and Israel in the same room.”

When it begins operations later this year, SESAME will join a growing number of other “megascience projects” dotting the globe, including those involved in the blockbuster discovery of gravitational waves by the Laser Interferometer Gravitational-Wave Observatory, or LIGO project.

The existence of gravitational waves—ripples in the fabric of spacetime—were predicted 100 years ago by Albert Einstein, who thought that the effect would be too small to ever detect. At a special session convened at the AAAS meeting, Gabriela González, a professor of physics at Louisiana State University and spokesperson for the LIGO Scientific Collaboration, described how a massive international effort by more than 1000 scientists from 16 countries finally observed the signature of a gravitational wave as it brushed over Earth. The LIGO collaboration is poised to expand globally, González said, with the VIRGO detector in Italy and the KAGRA detector in Japan now under construction. A few days after the historic LIGO an-

nouncement, the cabinet of Indian Prime Minister Shri Narendra Modi gave approval to a new detection facility called LIGO-India.

The 182nd AAAS meeting drew nearly 10,000 attendees from 60 countries to participate in research presentations, career workshops, and special events such as Family Science Days. At that event, more than 3000 children and adults had a chance to engage with dozens of scientists and explore 30 interactive science exhibits. The meeting also included four “edit-a-thons” to encourage attendees to edit and create scientific content for the website Wikipedia, as well as discussions at the forum website Reddit, where scientists attending the meeting fielded the public’s questions on robots, neutrinos, and addiction. ■

*With reporting by Andrea Korte, Earl Lane, Jean Mendoza, and Juan David Romero*



Hands-on experiments are encouraged at AAAS’s annual Family Science Days. This year’s event drew more than 3000 children and their families.



## RESEARCH ARTICLE SUMMARY

## SYNTHETIC BIOLOGY

# Design and synthesis of a minimal bacterial genome

Clyde A. Hutchison III,\*† Ray-Yuan Chuang,† Vladimir N. Noskov, Nacyra Assad-Garcia, Thomas J. Deerinck, Mark H. Ellisman, John Gill, Krishna Kannan, Bogumil J. Karas, Li Ma, James F. Pelletier, Zhi-Qing Qi, R. Alexander Richter, Elizabeth A. Strychalski, Lijie Sun, Yo Suzuki, Billyana Tsvetanova, Kim S. Wise, Hamilton O. Smith, John I. Glass, Chuck Merryman, Daniel G. Gibson, J. Craig Venter\*

**INTRODUCTION:** In 1984, the simplest cells capable of autonomous growth, the mycoplasmas, were proposed as models for understanding the basic principles of life. In 1995, we reported the first complete cellular genome sequences (*Haemophilus influenza*, 1815 genes, and *Mycoplasma genitalium*, 525 genes). Comparison of these sequences revealed a conserved core of about 250 essential genes, much smaller than either genome. In 1999, we introduced the method of global transposon mutagenesis and experimentally demonstrated that *M. genitalium* contains many genes that are nonessential for growth in the laboratory, even though it has the

smallest genome known for an autonomously replicating cell found in nature. This implied that it should be possible to produce a minimal cell that is simpler than any natural one. Whole genomes can now be built from chemically synthesized oligonucleotides and brought to life by installation into a receptive cellular environment. We have applied whole-genome design and synthesis to the problem of minimizing a cellular genome.

**RATIONALE:** Since the first genome sequences, there has been much work in many bacterial models to identify nonessential genes and

define core sets of conserved genetic functions, using the methods of comparative genomics. Often, more than one gene product can perform a particular essential function. In such cases, neither gene will be essential, and neither will necessarily be conserved. Consequently, these approaches cannot, by themselves, identify a set of genes that is sufficient to constitute a viable genome. We set out to define a minimal cellular genome experimentally by designing and building one, then testing it for viability. Our goal is a cell so simple that we can determine the molecular and biological function of every gene.

**RESULTS:** Whole-genome design and synthesis were used to minimize the 1079-kilobase pair (kbp) synthetic genome of *M. mycoides* JCVI-syn1.0. An initial design, based on collective knowledge of molecular biology in combination

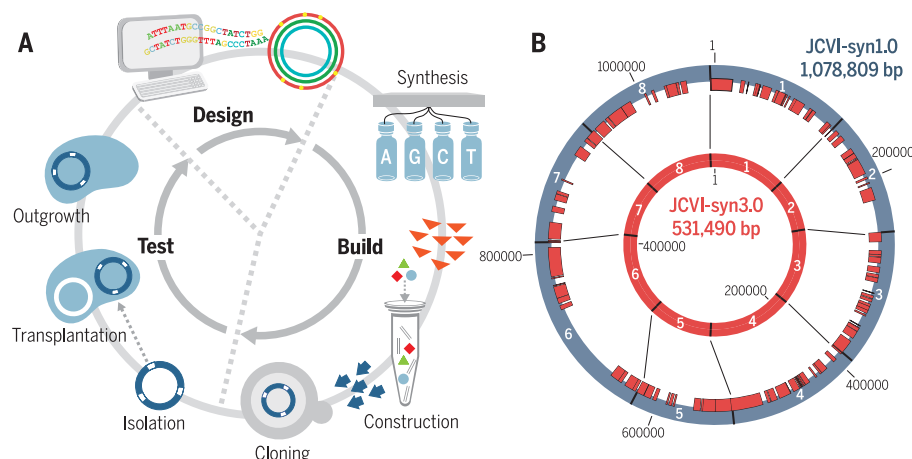
## ON OUR WEB SITE

Read the full article at <http://dx.doi.org/10.1126/science.aad6253>

with limited transposon mutagenesis data, failed to produce a viable cell. Improved transposon mutagenesis methods revealed a class of quasi-essential genes that are needed for

robust growth, explaining the failure of our initial design. Three more cycles of design, synthesis, and testing, with retention of quasi-essential genes, produced JCVI-syn3.0 (531 kbp, 473 genes). Its genome is smaller than that of any autonomously replicating cell found in nature. JCVI-syn3.0 has a doubling time of ~180 min, produces colonies that are morphologically similar to those of JCVI-syn1.0, and appears to be polymorphic when examined microscopically.

**CONCLUSION:** The minimal cell concept appears simple at first glance but becomes more complex upon close inspection. In addition to essential and nonessential genes, there are many quasi-essential genes, which are not absolutely critical for viability but are nevertheless required for robust growth. Consequently, during the process of genome minimization, there is a trade-off between genome size and growth rate. JCVI-syn3.0 is a working approximation of a minimal cellular genome, a compromise between small genome size and a workable growth rate for an experimental organism. It retains almost all the genes that are involved in the synthesis and processing of macromolecules. Unexpectedly, it also contains 149 genes with unknown biological functions, suggesting the presence of undiscovered functions that are essential for life. JCVI-syn3.0 is a versatile platform for investigating the core functions of life and for exploring whole-genome design. ■



## Four design-build-test cycles produced JCVI-syn3.0.

(A) The cycle for genome design, building by means of synthesis and cloning in yeast, and testing for viability by means of genome transplantation. After each cycle, gene essentiality is reevaluated by global transposon mutagenesis. (B) Comparison of JCVI-syn1.0 (outer blue circle) with JCVI-syn3.0 (inner red circle), showing the division of each into eight segments. The red bars inside the outer circle indicate regions that are retained in JCVI-syn3.0. (C) A cluster of JCVI-syn3.0 cells, showing spherical structures of varying sizes (scale bar, 200 nm).

The list of author affiliations is available in the full article online.

\*Corresponding author. E-mail: [chutchis@jcvl.org](mailto:chutchis@jcvl.org) (C.A.H.); [jcventer@jcvl.org](mailto:jcventer@jcvl.org) (J.C.V.)

†These authors contributed equally to this work.

Cite this article as: A. Hutchison III et al., *Science* 351, aad6253 (2016). DOI: 10.1126/science.aad6253

## RESEARCH ARTICLE

## SYNTHETIC BIOLOGY

# Design and synthesis of a minimal bacterial genome

Clyde A. Hutchison III,<sup>1,\*†</sup> Ray-Yuan Chuang,<sup>1,††</sup> Vladimir N. Noskov,<sup>1</sup> Nacyra Assad-Garcia,<sup>1</sup> Thomas J. Deerinck,<sup>2</sup> Mark H. Ellisman,<sup>2</sup> John Gill,<sup>3</sup> Krishna Kannan,<sup>3</sup> Bogumil J. Karas,<sup>1</sup> Li Ma,<sup>1</sup> James F. Pelletier,<sup>4,§</sup> Zhi-Qing Qi,<sup>3</sup> R. Alexander Richter,<sup>1</sup> Elizabeth A. Strychalski,<sup>4</sup> Lijie Sun,<sup>1||</sup> Yo Suzuki,<sup>1</sup> Billyana Tsvetanova,<sup>3</sup> Kim S. Wise,<sup>1</sup> Hamilton O. Smith,<sup>1,3</sup> John I. Glass,<sup>1</sup> Chuck Merryman,<sup>1</sup> Daniel G. Gibson,<sup>1,3</sup> J. Craig Venter<sup>1,3\*</sup>

We used whole-genome design and complete chemical synthesis to minimize the 1079-kilobase pair synthetic genome of *Mycoplasma mycoides* JCVI-syn1.0. An initial design, based on collective knowledge of molecular biology combined with limited transposon mutagenesis data, failed to produce a viable cell. Improved transposon mutagenesis methods revealed a class of quasi-essential genes that are needed for robust growth, explaining the failure of our initial design. Three cycles of design, synthesis, and testing, with retention of quasi-essential genes, produced JCVI-syn3.0 (531 kilobase pairs, 473 genes), which has a genome smaller than that of any autonomously replicating cell found in nature. JCVI-syn3.0 retains almost all genes involved in the synthesis and processing of macromolecules. Unexpectedly, it also contains 149 genes with unknown biological functions. JCVI-syn3.0 is a versatile platform for investigating the core functions of life and for exploring whole-genome design.

Cells are the fundamental units of life. The genome sequence of a cell may be thought of as its operating system. It carries the code that specifies all of the genetic functions of the cell, which in turn determine the cellular chemistry, structure, replication, and other characteristics. Each genome contains instructions for universal functions that are common to all forms of life, as well as instructions that are specific to the particular species. The genome is dependent on the functions of the cell cytoplasm for its expression. In turn, the properties of the cytoplasm are determined by the instructions encoded in the genome. The genome can be viewed as a piece of software; DNA sequencing allows the software code to be read. In 1984, Morowitz proposed the simplest cells capable of autonomous growth, the mycoplasmas, as models for understanding the basic principles of life (1). A key early step in his proposal was the sequencing of a mycoplasma genome, which we accomplished for *Mycoplasma genitalium* in 1995 (2). Even with the sequence in hand,

deciphering the operating system of the cell was a daunting task.

We have long been interested in simplifying the genomic software of a bacterial cell by eliminating genes that are nonessential for cell growth under ideal conditions in the laboratory. This facilitates the goal of achieving an understanding of the molecular and biological function of every gene that is essential for life. To survive in nature, most bacterial cells must be capable of adapting to numerous environments. Typical well-studied bacteria such as *Bacillus subtilis* and *Escherichia coli* carry 4000 to 5000 genes. They are highly adaptable, because many of their genes provide functions that are needed only under certain growth conditions. Some bacteria, however, grow in restricted environments and have undergone genome reduction over evolutionary time. They have lost genes that are unnecessary in a stable environment. The mycoplasmas, which typically grow in the nutrient-rich environment of animal hosts, have the smallest known genomes of any autonomously replicating cells. A comparison of the first two available genome sequences, *Haemophilus influenzae* [1815 genes (3)] and *M. genitalium* [the smallest known mycoplasma genome; 525 genes (2)], revealed a common core of only 256 genes, much smaller than either genome. This was proposed to be the minimal gene set for life (4).

In 1999, to put this comparative study to an experimental test, we introduced the method of global transposon mutagenesis (5), which allowed us to catalog 150 nonessential genes in *M. genitalium* (6) and predict a set of 375 essen-

tial genes. These results showed that it should be possible to produce a minimal genome that is smaller than any found in nature, but that the minimal genome would be larger than the common set of 256 genes. At that time, we proposed to create and test a cassette-based minimal artificial genome (5). We have been working since then to produce the tools needed to accomplish this. We developed methods to chemically synthesize the *M. genitalium* genome (7). However, *M. genitalium* grows very slowly, so we turned to the faster-growing *M. mycoides* genome as our target for minimization. We developed the method of genome transplantation, which allowed us to introduce *M. mycoides* genomes, as isolated DNA molecules, into cells of a different species, *M. capricolum* (8, 9). In this process, the *M. capricolum* genome is lost, resulting in a cell containing only the transplanted genome. In 2010, we reported the complete chemical synthesis and installation of the genome of *M. mycoides* JCVI-syn1.0 [1,078,809 base pairs (bp) (10); hereafter abbreviated syn1.0]. This genome was an almost exact copy of the wild-type *M. mycoides* genome, with the addition of a few watermark and vector sequences.

Genome reduction in bacteria such as *E. coli* and *B. subtilis* has previously been achieved by a series of sequential deletion events (11, 12). After each deletion, viability, growth rate, and other phenotypes can be determined. In contrast to this approach, we set out to design a reduced genome, then build and test it. We initially designed a hypothetical minimal genome (HMG) based on a combination of existing transposon mutagenesis and deletion data (13) and cumulative knowledge of molecular biology from the literature (14).

We designed the genome to be built in eight segments, each of which could be independently tested for viability in the context of a seven-eighths syn1.0 genome (i.e., a syn1.0 genome that is seven-eighths complete). Initially, only one of the designed HMG segments produced a viable genome. Improvements to our global transposon mutagenesis method allowed us to reliably classify genes as essential or nonessential and to identify quasi-essential genes that are needed for robust growth, though not absolutely required [figs. S1 to S4 (9); a similar result in *M. pneumoniae* is presented in (15)]. We also established rules for removing genes from our genome design without disturbing the expression of the remaining genes. Methods that we developed in the course of building syn1.0 (10) provide a way to build a new genome as a centromeric plasmid in yeast and to test it for viability and other phenotypic traits after transplantation into an *M. capricolum* recipient cell. These methods, along with improvements described here, make up a design-build-test (DBT) cycle (Fig. 1).

Here we report a new cell, JCVI-syn3.0 (abbreviated syn3.0), that is controlled by a 531-kilobase pair (kbp) synthetic genome that encodes 438 proteins and 35 annotated RNAs. It is a working approximation to a minimal cell. Its genome is substantially smaller than that of

<sup>1</sup>J. Craig Venter Institute, La Jolla, CA 92037, USA. <sup>2</sup>National Center for Microscopy and Imaging Research, University of California–San Diego, La Jolla, CA 92037, USA. <sup>3</sup>Synthetic Genomics, La Jolla, CA 92037, USA. <sup>4</sup>National Institute of Standards and Technology, Gaithersburg, MD 20899, USA. \*Corresponding author. E-mail: chutchis@jcvl.org (C.A.H.); jcventer@jcvl.org (J.C.V.). †These authors contributed equally to this work. ‡Present address: American Type Culture Collection, 10801 University Boulevard, Manassas, VA 20110, USA. §Present address: Center for Bits and Atoms, Massachusetts Institute of Technology, Room E15-401, 20 Ames Street, Cambridge, MA 02139, USA. ||Present address: CBRITE, 11575 Sorrento Valley Road, Suite 204, San Diego, CA 92121, USA.



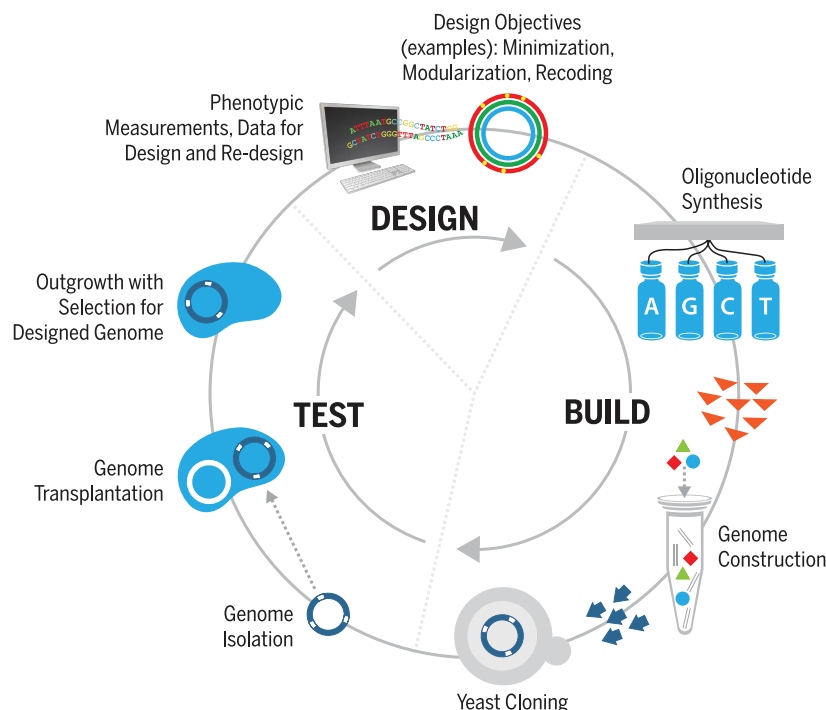


**Fig. 1. The JCVI DBT cycle for bacterial genomes.** At each cycle, the genome is built as a centromeric plasmid in yeast, then tested by transplantation of the genome into an *M. capricolum* recipient. In this study, our main design objective was genome minimization. Starting from syn1.0, we designed a reduced genome by removing nonessential genes, as judged by global Tn5 gene disruption. Each of eight reduced segments was tested in the context of a seven-eighths syn1.0 genome and in combination with other reduced segments. At each cycle, gene essentiality was reevaluated by Tn5 mutagenesis of the smallest viable assembly of reduced and syn1.0 segments that gave robust growth.

*M. genitalium*, and its doubling rate is about five times as fast.

### Preliminary knowledge-based HMG design does not yield a viable cell

In our first attempt to make a minimized cell, we started with syn1.0 (10) and used information from the biochemical literature, as well as some transposon mutagenesis data, to produce a rational design. Genes that could be disrupted by transposon insertions without affecting cell viability were considered to be nonessential. Based on ~16,000 transposon 4001 (Tn4001) and Tn5 insertions into the syn1.0 genome, we were able to find and delete a total of 440 apparently nonessential genes from the syn1.0 genome. The resulting HMG design was 483 kbp in size and contained 432 protein genes and 39 RNA genes (database S1 includes a detailed gene list).

In the course of designing the HMG, we developed a simple set of deletion rules that was used throughout the project. (i) Generally, the entire coding region of each nonessential gene was deleted, including start and stop codons. (Exceptions are described below.) (ii) When a cluster of more than one consecutive gene was deleted, the intergenic regions within the cluster were deleted also. (iii) Intergenic regions flanking a deleted gene or a consecutive cluster of deleted genes were retained. (iv) If part of a gene to be deleted overlapped a retained gene,

that part of the gene was retained. (v) If part of a gene to be deleted contained a ribosome binding site or promoter for a retained gene, that part of the gene was retained. (vi) When two genes were divergently transcribed, we assumed that the intergenic region separating them contained promoters for transcription in both directions. (vii) When a deletion resulted in converging transcripts, a bidirectional terminator was inserted, if one was not already present.

Because of the possibility of design flaws, we divided the genome into eight overlapping segments that could be independently synthesized and tested. We previously used this approach to identify a single lethal point mutation in our synthetic syn1.0 construct (10). As before, each of the eight designed synthetic segments had a corresponding syn1.0 DNA segment. This allowed untested pieces to be mixed and matched with viable syn1.0 pieces in one-pot combinatorial assemblies or to be purposefully assembled in any specified combination (16, 17). Additionally, each of the eight target segments was moved into a seven-eighths syn1.0 background by recombinase-mediated cassette exchange [(RMCE; (18))] (fig. S10) (9). Unique restriction sites (NotI sites) flanked each HMG or syn1.0 segment in the resulting yeast strains (fig. S9 and table S12) (9). Upon transplantation, we obtained a mycoplasma strain carrying any viable HMG segment (flanked by NotI sites) and eight other strains, each carrying one syn1.0

segment (flanked by NotI sites). This facilitated the production of one-eighth genome segments, because they could be recovered from bacterial cultures, which produce much higher yields of better-quality DNA than yeast (9). All eight HMG segments were tested in a syn1.0 background, but only one of the segment designs produced viable colonies (HMG segment 2), and the cells grew poorly.

Perhaps the greatest value that we derived from the HMG work was the refinement of semi-automated DNA synthesis methods by means of error-correcting procedures. We had previously developed a variety of DNA synthesis and assembly methodologies that extend from oligonucleotides to whole chromosomes. In this work, we optimized the methodology to rapidly generate error-free large DNA constructs, starting from overlapping oligonucleotides in a semiautomated DNA synthesis pipeline. This was accomplished by developing robust protocols for (i) single-reaction assembly of 1.4-kbp DNA fragments from overlapping oligonucleotides, (ii) elimination of synthesis errors and facilitation of single-round assembly and cloning of error-free 7-kbp cassettes, (iii) cassette sequence verification to simultaneously identify hundreds of error-free clones in a single run, and (iv) rolling circle amplification (RCA) of large plasmid DNA derived from yeast. Together, these methods substantially increased the rate at which the DBT cycle could be carried out (9).

Figure 2 illustrates the general approach that we used for whole-genome synthesis and assembly, using HMG as an example. An automated genome synthesis protocol was established to generate overlapping oligonucleotide sequences, starting from a DNA sequence design (9). Briefly, the software parameters include the number of assembly stages, overlap length, maximum oligonucleotide size, and appended sequences to facilitate polymerase chain reaction (PCR) amplification or cloning and hierarchical DNA assembly. About 48 oligonucleotides were pooled, assembled, and amplified to generate 1.4-kbp DNA fragments in a single reaction (figs. S12 and S13) (9). The 1.4-kbp DNA fragments were then error corrected, re-amplified, assembled five at a time into a vector, and transformed into *E. coli*. Error-free 7-kbp cassettes were identified on a DNA sequencer (Illumina MiSeq), and as many as 15 cassettes were assembled in yeast to generate one-eighth molecules. Supercoiled plasmid DNA was prepared from positively screened yeast clones, and RCA was performed to generate microgram quantities of DNA for whole-genome assembly in yeast (figs. S14 to S16). This whole-genome synthesis workflow can be carried out in less than three weeks, which is about two orders of magnitude faster than the first reported synthesis of a bacterial genome (by our group) in 2008 (7).

### Tn5 mutagenesis identifies essential, quasi-essential, and nonessential genes

It was clear from the limited success of our HMG design that we needed a better understanding of which genes are essential versus nonessential. To achieve this, we used Tn5 mutagenesis (fig. S1).

An initial Tn5 disruption map was generated by transforming JCVI-syn1.0  $\Delta$ RE  $\Delta$ IS cells [in which all restriction enzyme (RE) genes and six insertion (IS) elements are deleted; table S6] with an activated form of a 988-bp miniature-Tn5 puromycin resistance transposon (fig. S1) (9). Transformed cells were selected on agar plates containing 10  $\mu$ g/ml of puromycin. About 80,000 colonies, each arising from a single Tn5 insertion event, were pooled from the plates. A sample of DNA extracted from this “P0” pool was mechanically sheared and analyzed for the sites of Tn5 insertion using inverse PCR and DNA sequencing. The P0 data set contained ~30,000 unique insertions. To remove slow-growing mutagenized cells, a sample of the pooled P0 cells was serially passaged for more than 40 generations, and DNA was prepared and sequenced to generate a “P4” data set containing ~14,000 insertions. (fig. S2).

Genes fell into three major groups: (i) Genes that were not hit at all, or that were sparsely hit in the terminal 20% of the 3'-end or the first few bases of the 5'-end, were classified as essential (“e-genes”) (5). (ii) Genes that were hit frequently by both P0 and P4 insertions were classified as nonessential (“n-genes”). (iii) Genes hit primarily by P0 insertions but not P4 insertions were classified as quasi-essential, the deletion of which would cause growth impairments (“i-genes”). Cells with i-gene disruptions spanned a continuum of growth impairment, varying from minimal to severe. To differentiate this growth continuum, we designated i-genes with minimal growth disadvantage as “in-genes” and those with severe growth defect as “ie-genes.” Of the 901 annotated protein and RNA coding genes in the syn1.0 genome, 432 were initially classified as n-, 240 as e-, and 229 as i-genes (Fig. 3, A and B, and fig S3).

In viewing a syn1.0 map of P4 insertions (fig. S4), it was evident that nonessential genes tended to occur in clusters far more often than expected by chance. We used deletion analysis to confirm that most of the n-gene clusters could be deleted without losing viability or substantively affecting growth rate (9). Individual gene clusters (or, in some cases, single genes) were replaced by the yeast *URA3* marker as follows. Fifty-base pair sequences flanking the gene(s) to be deleted were added to the ends of the *URA3* marker by PCR, and the DNA was introduced into yeast cells carrying the syn1.0 genome. Yeast clones were selected on plates not containing uracil, confirmed by PCR, and transplanted to determine viability. Deletions fell into three classes: (i) those resulting in no successful transplants, indicating deletion of an essential gene; (ii) those resulting in transplants with normal or near-normal growth rates, indicating deletion of nonessential genes; and (iii) those resulting in transplants with slow growth, indicating deletion of quasi-essential genes.

A large number of deletions, including all of the HMG deletions, were individually tested for viability and yielded valuable information for subsequent reduced-genome designs. The transposon insertion data that were available at the time of the HMG design were all collected from passage

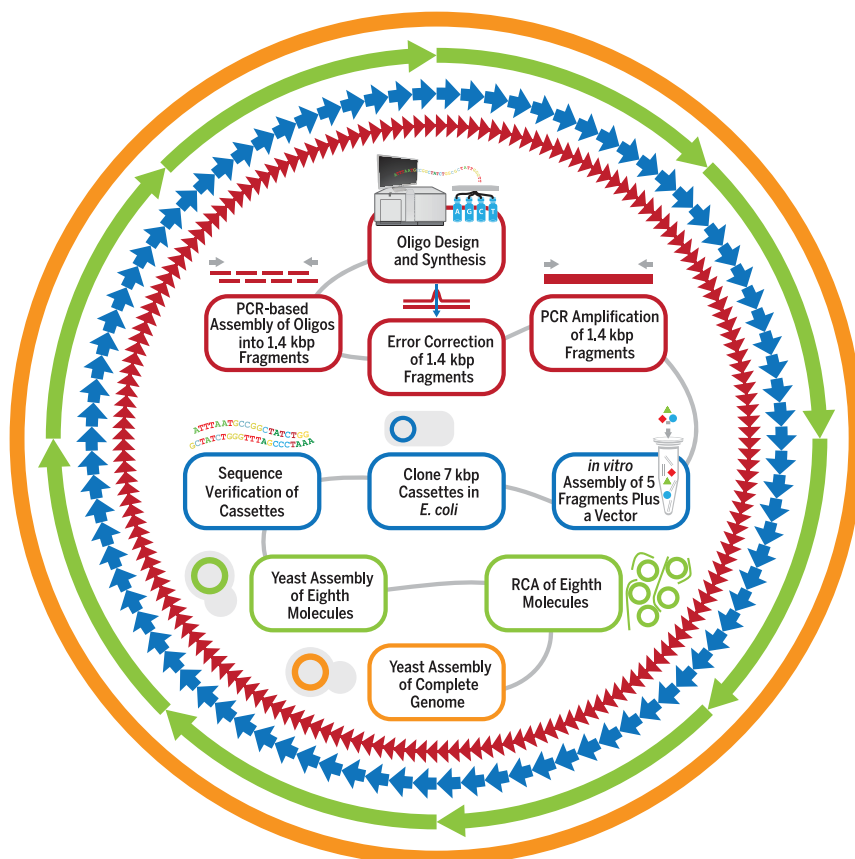


**Fig. 2. Strategy for whole-genome synthesis.** Overlapping oligonucleotides (oligos) were designed, chemically synthesized, and assembled into 1.4-kbp fragments (red). After error correction and PCR amplification, five fragments were assembled into 7-kbp cassettes (blue). Cassettes were sequence-verified and then assembled in yeast to generate one-eighth molecules (green). The eight molecules were amplified by RCA and then assembled in yeast to generate the complete genome (orange).

P0. Consequently, genes with insertions included the genes that were subsequently characterized as quasi-essential i-genes, so some HMG deletions produced very small colonies or were nonviable.

In parallel with iterations of the DBT cycle, described below, we also took the traditional sequential deletion approach to genome reduction. We performed stepwise scarless deletions (fig. S8 and table S11) (9) of medium to large clusters to produce a series of strains with progressively greater numbers of genes removed. Strain D22, with 255 genes and 357 kbp of DNA removed, grew at a rate similar to syn1.0 (table S6). We discontinued this approach when it became clear that the synthesis of redesigned segments at each DBT cycle would yield a minimal cell more quickly. These deletion studies also helped to validate our simple set of deletion rules.

### Retaining quasi-essential genes yields viable segments but no viable complete genome

To improve on the design of the HMG, we redesigned a reduced genome using the Tn5 and deletion data described above. This reduced genome design (RGD1.0) achieved a 50% reduction of syn1.0 by removing ~90% of the n-genes (table S1). In a few cases, n-genes were retained—

specifically, if their biochemical function appeared essential, or if they were singlet n-genes separating two large e- or i-gene clusters. To preserve the expression of genes upstream and downstream of deleted regions, we followed the same design rules that we used in the HMG design.

The eight segments of RGD1.0 were chemically synthesized as described above, and each synthetic reduced segment was inserted into a seven-eighths syn1.0 background in yeast by means of RMCE (fig. S10 and table S13) (9). Each one-eighth RGD–seven-eighths syn1.0 genome was then transplanted out of yeast to test for viability. Each of the eight reduced segments produced a viable transplant; however, segment 6 produced only a very small colony in the first 6 days. On further growth over the next 6 days, sectors of faster-growing cells developed (fig. S18). Several isolates of the faster-growing cells were sequenced and found to have destabilizing mutations in a transcription terminator that had been joined to an essential gene when the non-essential gene preceding it was deleted (figs. S19 and S21). Another mutation produced a consensus TATAAT box in front of the essential gene (fig. S20). This illustrates the potential for expression errors when genes are deleted, but it shows that these errors can sometimes be corrected by



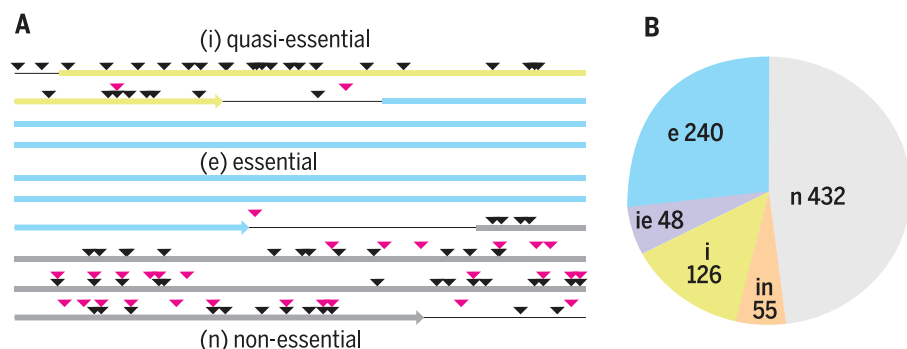


**Fig. 3. Classification of gene essentiality by transposon mutagenesis.** (A) Examples of the three gene classifications, based on Tn5 mutagenesis data. The region of syn1.0 from sequence coordinates 166,735 to 170,077 is shown. The gene *MMSYN1\_0128* (lime arrow) has many P0 Tn5 inserts (black triangles) and is an i-gene (quasi-essential). The next gene, *MMSYN1\_0129* (light blue arrow), has no inserts and is an e-gene (essential). The last gene, *MMSYN1\_0130* (gray arrow), has both P0 (black triangles) and P4 (magenta triangles) inserts and is an n-gene (nonessential). Intergenic regions are indicated by black lines. (B) The number of syn1.0 genes in each Tn5-mutagenesis classification group. The n- and in-genes are candidates for deletion in reduced genome designs.

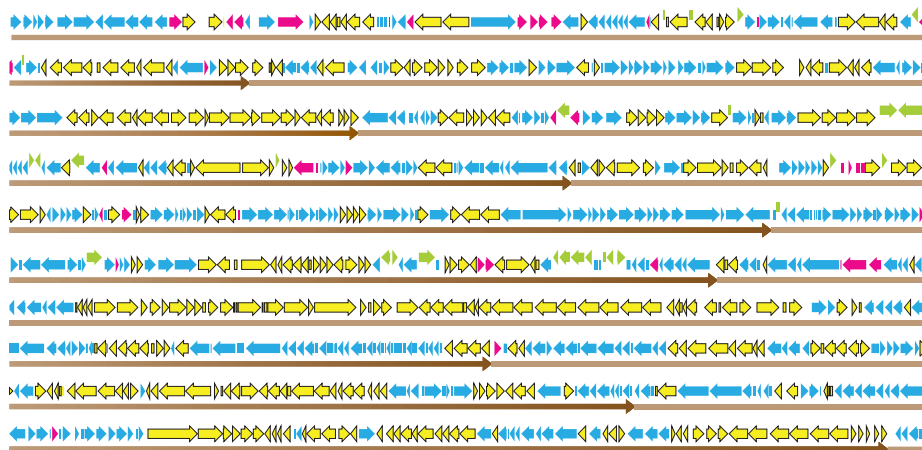


**Fig. 4. The three DBT cycles involved in building syn3.0.** This detailed map shows syn1.0 genes that were deleted or added back in the various DBT cycles leading from syn1.0 to syn2.0 and finally to syn3.0 (compare with fig. S7). The long brown arrows indicate the eight NotI assembly segments. Blue arrows represent genes that were retained throughout the process. Genes that were deleted in both syn2.0 and syn3.0 are shown in yellow. Green arrows (slightly offset) represent genes that were added back. The original RGD1.0 design was not viable, but a combination of syn1.0 segments 1, 3, 4, and 5 and designed segments 2, 6, 7, and 8 produced a viable cell, referred to as RGD2678. Addition of the genes shown in green resulted in syn2.0, which has eight designed segments. Additional deletions, shown in magenta, produced syn3.0 (531,560 bp, 473 genes). The directions of the arrows correspond to the directions of transcription and translation.

subsequent spontaneous mutation. Ultimately, we identified a promoter that had been overlooked and erringly deleted. When this region was resupplied in accordance with the design rules, cells containing designed segment 6 grew rapidly. This solution was incorporated in later designs.

Despite the growth of cells containing each designed segment, combining all eight reduced RGD1.0 segments, including the self-corrected segment 6, into a single genome did not produce a viable cell when transplanted into *M. capricolum* (9). We then mixed the eight RGD1.0 segments with the eight syn1.0 segments to perform combinatorial assembly of genomes in yeast (9). A number of completely

assembled genomes were obtained in yeast that contained various combinations of RGD1.0 segments and syn1.0 segments. When transplanted, several of these combinations gave rise to viable cells (table S7). One of these (RGD2678)—containing RGD1.0 segments 2, 6, 7, and 8 and syn1.0 segments 1, 3, 4, and 5, with an acceptable growth rate (105-min doubling time, compared with 60 min for syn1.0)—was analyzed in more detail.

#### To obtain a viable genome, avoid deleting pairs of redundant genes for essential functions

In bacteria, it is common for certain essential (or quasi-essential) functions to be provided by

more than one gene. The genes may or may not be paralogs. Suppose gene A and gene B each supplies the essential function, E1. Either gene can be deleted without loss of E1, so each gene by itself in a single knockout study is classed as nonessential. However, if both are deleted, the cell will be dead because E1 is no longer provided. Such a lethal combination of mutations is called a “synthetic lethal pair” (19). Redundant genes for essential functions are common in bacterial genomes, although less so in genomes that have undergone extensive evolutionary reduction, such as the mycoplasmas. Our biggest design challenge has been synthetic lethal pairs in which gene A has been deleted from one segment and gene B from another segment. Each segment is viable in the context of a seven-eighths syn1.0 background, but when combined, the resulting cell is nonviable, or, in the case of a shared quasi-essential function, grows more slowly. We do not know how many redundant genes for essential functions are present in each of the eight segments, but when RGD1.0 segments 2, 6, 7, and 8 were combined, the cell was viable.

We subjected RGD2678 to Tn5 mutagenesis and found that some n-genes in the syn1.0 segments 1, 3, 4, and 5 had converted to i- or e-genes in the genetic context of RGD2678 (table S2). This was presumably because these genes encoded essential or quasi-essential functions that were redundant with a gene that had been deleted in RGD2678.

In addition, we examined 39 gene clusters and single genes that had been deleted in the design of RGD1.0 segments 1, 3, 4, and 5 (table S8). These were deleted one at a time in an RGD2678 background (tables S8 and S14) and tested for viability by transplantation. In several cases, this resulted in slow-growth transplants or no transplants, suggesting that they included one or more genes that are functionally redundant with genes that had been deleted in segments 2, 6, 7, or 8.

The combined Tn5 and deletion data identified 26 genes (tables S2 and S9) as candidates for adding back to RGD1.0 segments 1, 3, 4, and 5 to produce a new RGD2.0 design for these segments (fig. S5 and tables S1 and S2). An assembly was carried out in yeast using the newly designed and synthesized RGD2.0 segments 1, 3, 4, and 5, together with RGD1.0 segments 2, 6, 7, and 8 (tables S7 and S15). This assembly was not viable initially, but we found that substituting syn1.0 segment 5 for RGD2.0 segment 5 resulted in a viable transplant. Working with this strain, we deleted a cluster of genes (*MMSYN1\_0454* to *MMSYN1\_0474*) from syn1.0 segment 5 and replaced another cluster of genes (*MMSYN1\_0483* to *MMSYN1\_0492*) with gene *MMSYN1\_0154* (figs. S6 and S11 and table S10) (9). Gene *MMSYN1\_0154* was originally deleted from segment 2 in the RGD1.0 design but was found to increase growth rate when added back to RGD2678. The described revision of syn1.0 segment 5 in the RGD2.0 genetic context yielded a viable cell, which we refer to as JCVI-syn2.0 (abbreviated syn2.0; Fig. 4). With syn2.0, we achieved for the first time a minimized cell with a genome smaller than that of the smallest

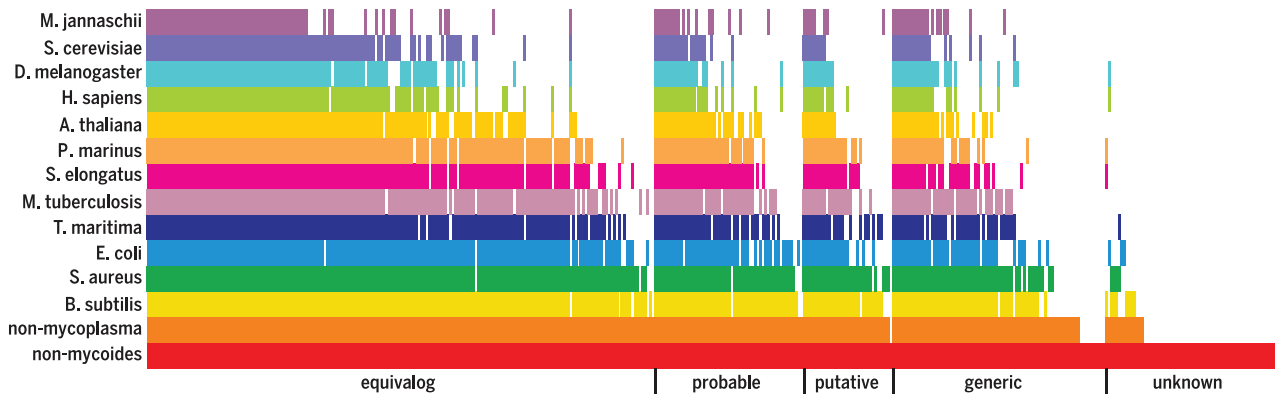


**Fig. 5. Map of proteins in syn3.0 and homologs found in other organisms.** Searches using BLASTP software were performed for all syn3.0 protein-coding genes against a panel of 14 organisms ranging from non-*Mycoides* mycoplasmas to Archaea. A score of  $1e^{-5}$  was used as the similarity cutoff. From left to right, five classes (equivalog, 232 genes; probable, 58 genes; putative, 34 genes; generic, 84 genes; and unknown, 65 genes) proceed from nearly complete certainty about a gene's activity (equivalog) to no functional information (unknown). White space indicates no homologs to syn3.0 in that organism.

known natural bacterium, *M. genitalium*. Syn2.0 doubles in laboratory culture every 92 min. Its total genome size is 576 kbp. It contains 478 protein coding genes and 38 RNA genes from *M. mycoides*, with 12 kbp of vector sequences for selection of the genome and for propagation in yeast and *E. coli*.

#### Removing 42 additional genes yields an approximately minimal cell, syn3.0

We performed a new round of Tn5 mutagenesis on syn2.0. In this new genetic background, transition of some i-genes to apparent n-genes was expected. At this point, the composition of the P4 serial passage population was depleted of original n-genes; the faster-growing i-gene knockouts predominated and were classified as n-genes by our rules. We classified 90 genes as apparently nonessential. These were subdivided into three groups. The first group contained 26 genes that were frequently classed as i- or e-genes in previous rounds of mutagenesis. The second group contained 27 genes that were classified as i- or borderline i-genes in some of the previous Tn5 studies. The third group contained 37 genes that had previously been classified as nonessential in several iterations of Tn5 mutagenesis involving various genome contexts. To create the new RGD3.0 design, these 37 genes were selected for deletion from syn2.0, along with two vector sequences, *bla* and *lacZ*, and the ribosomal RNA (rRNA) operon in segment 6 (Fig. 4 and table S3).

The eight newly designed RGD3.0 segments were synthesized and propagated as yeast plasmids. These plasmids were amplified in vitro by RCA (9). All eight segments were then re-assembled in yeast to obtain several versions of the RGD3.0 genome as yeast plasmids (9). These assembled RGD3.0 genomes were transplanted out of yeast into an *M. capricolum* recipient cell. Several were viable. One of these, RGD3.0 clone g-19 (table S4), was selected for detailed analysis and named JCVI-syn3.0.

A final round of Tn5 mutagenesis was performed on syn3.0 to determine which genes continue to show Tn5 insertions after serial

**Table 1. Syn1.0 genes listed by functional category and whether they were kept or deleted in syn3.0.** Categories with asterisks are mostly kept in syn3.0, whereas those without are depleted in syn3.0. Vector sequences, for selection of the genome and for propagation in other hosts, are not included in these gene tallies.

Functional category	Kept	Deleted
Glucose transport and glycolysis*	15	0
Ribosome biogenesis*	14	1
Protein export*	10	0
Transcription*	9	0
RNA metabolism*	7	0
DNA topology*	5	0
Chromosome segregation*	3	0
DNA metabolism*	3	0
Protein folding*	3	0
Translation*	89	2
RNA (rRNAs, tRNAs, small RNAs)*	35	4
DNA replication*	16	2
Lipid salvage and biogenesis*	21	4
Cofactor transport and salvage*	21	4
rRNA modification*	12	3
tRNA modification*	17	2
Efflux*	7	3
Nucleotide salvage	19	8
DNA repair	6	8
Metabolic processes	10	10
Membrane transport	31	32
Redox homeostasis	4	4
Proteolysis	10	11
Regulation	9	10
Unassigned	79	134
Cell division	1	3
Lipoprotein	15	72
Transport and catabolism of nonglucose carbon sources	2	34
Acylglycerol breakdown	0	4
Mobile elements and DNA restriction	0	73
<b>Total</b>	<b>473</b>	<b>428</b>

passaging (P4). Nonessential vector genes and intergenic sequences are the most frequent insertion sites. As expected, cells with insertions

in genes that were originally classified as quasi-essential make up almost the whole population of P4 cells that have insertions in mycoplasma



genes. The genes in syn3.0 are predominantly e- or i-genes, based on the original syn1.0 classification. Of these, only the i-genes can tolerate Tn5 insertions without producing lethality. The most highly represented in-, i-, and ie-genes are shown in table S5. It might be possible to remove a few of these in a fourth DBT cycle, but there would probably be further erosion of growth rate. In addition, a dozen genes that were originally classified as nonessential continue to retain that classification (table S5 and database S1).

### In syn3.0, 149 genes cannot be assigned a specific biological function

Syn3.0 has 438 protein- and 35 RNA-coding genes. We organized the 473 genes into five classes, based on our level of confidence in their precise functions: equivalog, probable, putative, generic, and unknown (Fig. 5 and database S1). Many of these genes have been studied exhaustively, and their primary biological functions are known.

We used the TIGRfam equivalog family of hidden Markov models (20) to annotate equivalog genes (~49% of the genes). The less certain classes were defined in a stepwise manner (Fig. 5). The probable class included genes that scored well against unambiguous TIGRfam mathematical models but that nevertheless scored below the trusted cutoff. These genes were consistently supported by other lines of evidence. Genomic context and threading alignment to crystal structures both agreed with the assignment. The putative class included genes that were similarly supported by multiple lines of evidence; at the same time, either their scores, genomic context, or alignment to structures with known activities were not convincing. The generic class included genes encoding clearly identifiable proteins (e.g., kinase) but lacking consistent clues as to their substrates or biological role. Unknown genes were those that could not be reliably categorized with regard to a putative activity.

Thus, biological functions could not be assigned for the ~31% of the genes that were placed in the generic and unknown classes. Nevertheless, potential homologs for a number of these were found in diverse organisms. Many of these genes probably encode universal proteins whose functions are yet to be characterized. Each of the five sectors has homologs in species ranging from mycoplasma to humans. However, some of each annotation class is blank, indicating that no homologs for these genes were found among the organisms chosen for display in Fig. 5. Because mycoplasmas evolve rapidly, some of the white space in Fig. 5 corresponds to sequences that have diverged so as to align poorly with representatives from other organisms.

In Table 1, we have assigned syn1.0 genes to 30 functional categories and indicated how many were kept or deleted in syn3.0. Of the 428 deleted genes, the largest group is the functionally unassigned genes; 134 out of 213 have been deleted. All of the 73 mobile element and DNA modification and restriction genes have been removed, as well as most genes encoding lipoproteins (72 out of 87). These three categories alone account for

65% of the deleted genes. In addition, because of the rich growth medium that supplies almost all of the necessary small molecules, many genes involved in transport, catabolism, proteolysis, and other metabolic processes have become dispensable. For example, because glucose is plentiful in the medium, most genes for transport and catabolism of other carbon sources have been deleted (34 out of 36), whereas all 15 genes involved in glucose transport and glycolysis have been retained.

In contrast, almost all of the genes involved in the machinery for reading and expressing the genetic information in the genome and in ensuring the preservation of genetic information across generations have been retained. The first of these two fundamental life processes, the expression of genetic information as proteins, requires the retention of 195 genes in the categories of transcription, regulation, RNA metabolism, translation, protein folding, RNA (rRNA, tRNA, and small RNAs), ribosome biogenesis, rRNA modification, and tRNA modification. The second of these two fundamental processes, the preservation of genome sequence information, requires the retention of 34 genes in the categories of DNA replication, DNA repair, DNA topology, DNA metabolism, chromosome segregation, and cell division. These two processes together require 229 (48%) of the 473 total genes in syn3.0 (Fig. 6).

In addition to the two vital processes just described, another major component of living cells is the cell membrane that separates the outer medium from the cytoplasm and governs molecular traffic into and out of the cell. It is an isolatable structure, and many of the syn3.0 genes code for its protein constituents. Because our minimal cell is largely lacking in biosynthesis of amino acids, lipids, nucleotides, and vitamins, it depends on the rich medium to supply almost all of these required small molecules. This necessitates numerous transport systems within the membrane. In addition, the membrane is rich in lipoproteins. Membrane-related genes account for 84 (18%) of the 473 total syn3.0 genes. Included categories from Table 1 are lipoproteins, cofactor transport, efflux systems, protein transport, and other membrane transport systems.

Lastly, 81 genes (17%) that are primarily involved in cytosolic metabolism are retained in the categories of nucleotide salvage, lipid salvage and biogenesis, proteolysis, metabolic processes, redox homeostasis, transport and catabolism of non-glucose carbon sources, and glucose transport and glycolysis (Fig. 6).

We presume that most of the 79 genes that are not assigned to a functional category belong to one or another of these same four major groups (gene expression, genome preservation, membrane structure and function, and cytosolic metabolism). Among these 79 genes, 65 have completely unknown functions and 24 are classified as generic, such as in the case of a hydrolase for which neither the substrate nor the biological role is discernible. The other 60 of the 84 genes in the generic class were assigned to a functional category on the basis of their generic classification. For example, an ABC transporter is assigned to membrane transport, even though the substrate is unknown. Some of the unassigned essential genes match domains of unknown function that have been found in a wide variety of organisms.

### Syn3.0 has a doubling time of 3 hours and is polymorphic in appearance

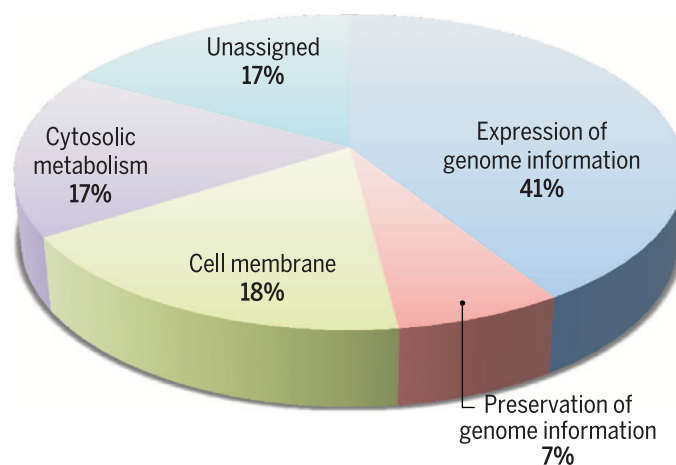
Comparison of syn3.0 with the starting cell, syn1.0 (Fig. 7A) (9), showed that they have similar colony morphologies, which are characteristic of the natural, wall-less *Mycoplasma mycoides* subspecies *capri* on which the synthetic syn1.0 genome was originally based (10). The smaller colony size of syn3.0 suggested a slower growth rate and perhaps an altered colony architecture on the solid medium. A corresponding reduction in the growth rate of syn3.0 in static liquid culture (Fig. 7B), from a doubling time of ~60 min for syn1.0 to ~180 min, confirmed the lower intrinsic rate of propagation for syn3.0. This rate, however, greatly exceeds the 16-hour doubling time of *M. genitalium* (21).

In contrast to the anticipated reduction in growth rate, we found unexpected changes in macro- and microscopic growth properties of syn3.0 cells. Whereas syn1.0 grew in static culture as nonadherent planktonic suspensions of

**Fig. 6. Partition of genes into four major functional groups.**

Syn3.0 has 473 genes. Of these, 79 have no assigned functional category (Table 1). The remainder can be assigned to four major functional groups:

(i) expression of genome information (195 genes); (ii) preservation of genome information (34 genes); (iii) cell membrane structure and function (84 genes); and (iv) cytosolic metabolism (81 genes). The percentage of genes in each group is indicated.



predominantly single cells with a diameter of ~400 nm (10), syn3.0 cells formed matted sediments under the same conditions. Microscopic images of these undisturbed cells revealed extensive networks of long, segmented filamentous structures, along with large vesicular bodies (Fig. 7C), which were particularly prevalent at late stages of growth. Both of these structures were easily disrupted by physical agitation, yet such suspensions contained small replicative forms that passed through 0.2- $\mu$ m filters to render colony-forming units (CFU). This same procedure retained 99.9% of the CFU in planktonic syn1.0 cultures.

### Exploring the design of reorganized genomes

To further refine our genome-design rules, we also investigated prospects for logically organizing genomes and recoding them at the nu-

cleotide level. This effort was meant to clarify whether gene order and gene sequence are major contributors to cell viability. The ability to invert large sections of DNA in many genomes has demonstrated that overall, gene order is not critical. We showed that fine-scale gene order is also not a major factor in cell survival. About an eighth of the genome was reconfigured into seven contiguous DNA cassettes, six of which represented known biological systems; the seventh cassette contained genes whose system-level assignment was somewhat equivocal. The vertical bar on the right side of Fig. 8 specifies the biological systems. Individual genes (colored horizontal lines) and intergenic regions (black lines) can be traced from their native location to their new positions by following a line from left to right. Intersecting lines represent a change in the relative position

of two genetic elements. Despite extensive reorganization, the resulting cell grew about as fast as syn1.0, as judged by colony size. Thus, the details of genetic organization impinge upon survival in hypercompetitive natural environments, but the finer details are apparently not critical for life.

### Recoding and rRNA gene replacement provide examples of genome plasticity

Our DBT cycle for bacterial genomes allows us to assess the plasticity of gene content in terms of sequence and functionality. This includes testing modified versions of genes that are fundamentally essential for life. We tested whether an altered 16S rRNA gene (*rrs*), which is essential, could support life (Fig. 9A). The single copy of the syn3.0 *rrs* gene was designed and synthesized to include seven single-nucleotide changes

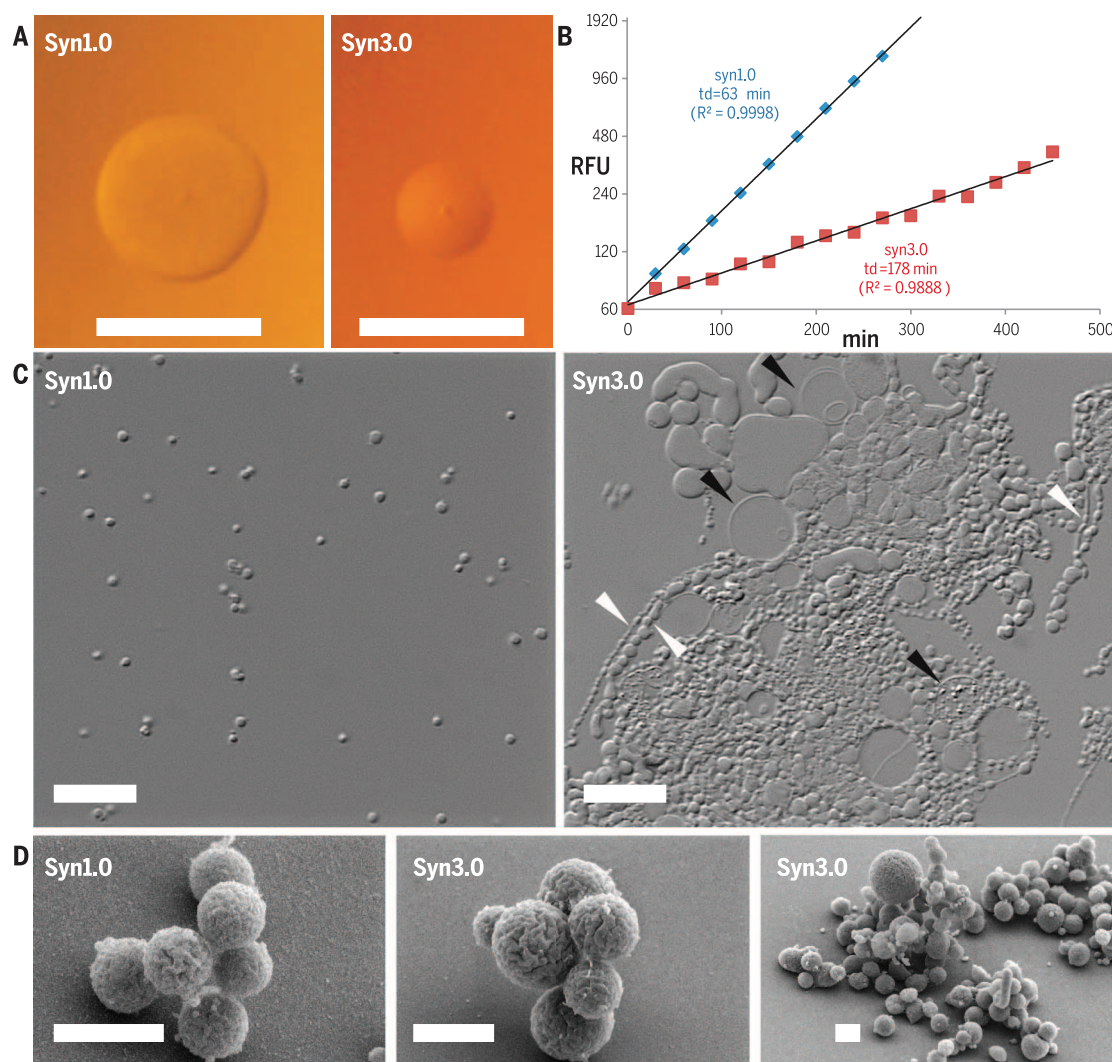


**Fig. 7. Comparison of syn1.0 and syn3.0 growth features.** (A) Cells derived from 0.2  $\mu$ m-filtered liquid cultures were diluted and plated on agar medium to compare colony size and morphology after 96 hours (scale bars, 1.0 mm). (B) Growth rates in liquid static culture were determined using a fluorescent measure (relative fluorescent units, RFU) of double-stranded DNA accumulation over time (minutes) to calculate doubling times (td). Coefficients

of determination ( $R^2$ ) are shown. (C) Native cell morphology in liquid culture was imaged in wet mount preparations by means of differential interference contrast microscopy (scale bars, 10  $\mu$ m). Arrowheads indicate assorted forms of segmented filaments (white) or large vesicles (black). (D) Scanning electron microscopy of syn1.0 and syn3.0 (scale bars, 1  $\mu$ m). The picture on the right shows a variety of the structures observed in syn3.0 cultures.



corresponding to those contained in the *rrs* gene of *M. capricolum*. In addition, we replaced helix h39 (35 nucleotides) with that from a phylogenetically distant *E. coli rrs* counterpart. This unique 16S gene was successfully incorporated into syn3.0 without noticeably affecting growth rate. Some other variants of the *rrs* gene were constructed but proved nonviable. This demonstrates our ability to test the plasticity of a gene sequence and, at the same time, provides a watermark by which to quickly identify this strain.

We also tested the underlying codon usage principles in the *M. mycoides* genome, which has extremely high adenine and thymine (AT) content. *M. mycoides* uses TGA as a codon for the amino acid tryptophan, instead of a stop codon, and occasionally uses nonstandard start codons; in addition, the codon usage is heavily biased toward high-AT content. We modified this uncommon codon usage in a 5-kbp region

containing three essential genes (*era*, *recO*, and *glyS*) to determine its role. Specifically, we modified this region to include (i) *M. mycoides* codon adaptation index (CAI), but with the unusual start codons recoded and tryptophan encoded by the TGG codon, instead of by TGA; (ii) *E. coli* CAI, with tryptophan still encoded by TGA; or (iii) *E. coli* CAI with standard codon usage (TGG encoding tryptophan) (Fig. 9B). Unexpectedly, we found that all three versions were functional and resulted in *M. mycoides* cells without noticeable growth differences. However, large-scale changes in codon usage may need to accompany modifications in the tRNA dosage levels to ensure efficient translation.

## Discussion and conclusions

Genomics is moving from a descriptive phase, in which genomes are sequenced and analyzed, to a synthetic phase, in which whole genomes

can be built by chemical synthesis. As the detailed genetic requirements for life are discovered, it will become possible to design whole genomes from first principles, build them by chemical synthesis, and then bring them to life by installation into a receptive cellular environment. We have applied this whole-genome design and synthesis approach to the problem of minimizing a cellular genome.

A minimal cell is usually defined as a cell in which all genes are essential. This definition is incomplete, because the genetic requirements for survival, and therefore the minimal genome size, depend on the environment in which the cell is grown. The work described here has been conducted in medium that supplies virtually all the small molecules required for life. A minimal genome determined under such permissive conditions should reveal a core set of environment-independent functions that are necessary and sufficient for life. Under less permissive conditions, we expect that additional genes will be required.

There is a large body of literature concerning the minimal cell concept and minimal sets of essential genes in a number of organisms [for a review, see (22)]. Work in the area has focused on comparative genomic analyses and on experiments in which genes are individually knocked out or disrupted by transposon insertion. Such studies identify a core of essential genes, often about 250 in number. But this is not a set of genes that is sufficient to constitute a viable cellular genome, because redundant genes for essential functions are scored as nonessential in these studies.

In contrast, we set out to construct a minimal cellular genome in order to experimentally determine a core set of genes for an independently replicating cell. We designed a genome using genes from *M. mycoides* JCVI-syn1.0 (10). This mycoplasma cell has several advantages for this purpose. First, the mycoplasmas already have very small genomes. They have evolved from gram-positive bacteria with larger genomes by losing genes that are unnecessary in their niche as mammalian parasites. They are already far along an evolutionary pathway to a minimal genome, and consequently they are likely to have fewer functionally redundant genes than other bacteria. We also have a highly developed set of tools for building this genome and for assembling and manipulating the genome as an extra chromosome in yeast.

Our initial attempt to design a minimal genome was based on the current collective knowledge of molecular biology, in combination with limited data concerning transposon disruption of genes, which provided additional information about gene essentiality. This information was particularly valuable with respect to the genes of unknown function. Specific experimental proposals for minimal genome construction have been made solely on the basis of accumulated knowledge concerning the genes that are involved in fundamental biological processes (14). Our HMG was assembled from eight segments

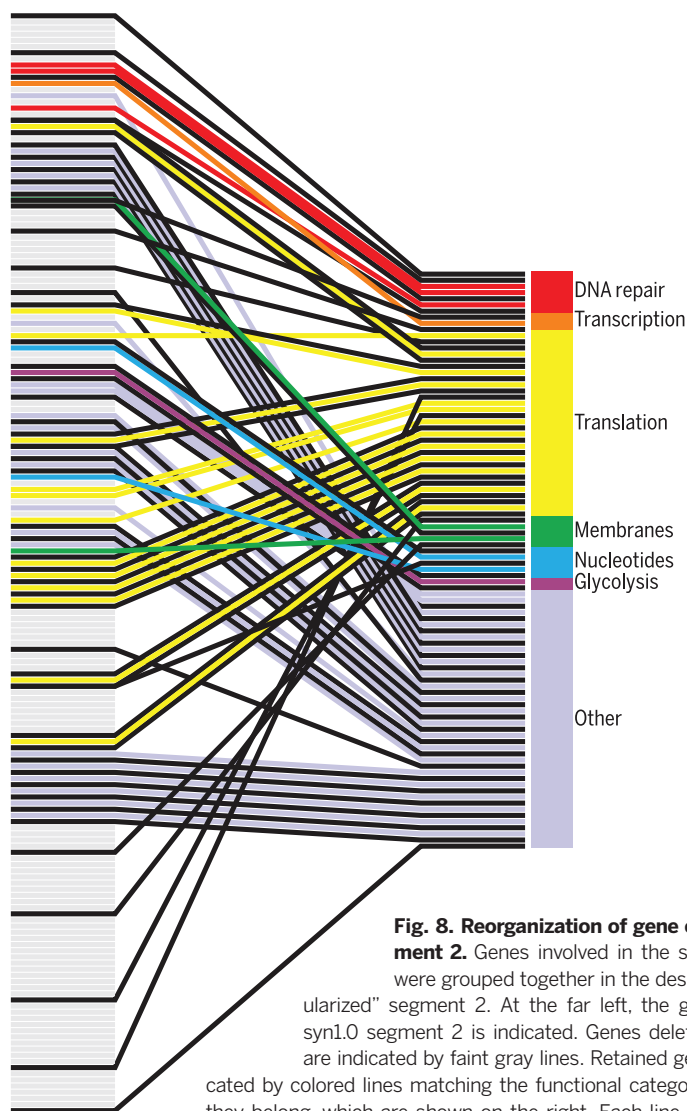


**Fig. 8. Reorganization of gene order in segment 2.** Genes involved in the same process

were grouped together in the design for “modularized” segment 2. At the far left, the gene order of syn1.0 segment 2 is indicated. Genes deleted in syn3.0 are indicated by faint gray lines. Retained genes are indicated by colored lines matching the functional categories to which they belong, which are shown on the right. Each line connects the position of the corresponding gene in syn1.0 with its position in the modularized segment 2. Black lines represent intergenic sequences containing promoters or transcriptional terminators.

and proved nonviable, although one of the segments (segment 2) was functional when tested in the context of the other seven syn1.0 segments. These results convinced us that initially, we did not have sufficient knowledge to design a functional minimal genome from first principles. There-

fore, to obtain better information concerning gene essentiality, we made major improvements in our transposon mutagenesis methods.

To produce a genome containing all of the essential and quasi-essential genes, we developed a DBT cycle for bacterial genomes (Fig. 1).

Any design, viable or not, can be built in yeast and then tested to determine whether it can function as the genome of a viable bacterium. After four DBT cycles (genome designs HMG, RGD1.0, RGD2.0, and RGD3.0), we obtained a viable genome with all eight segments reduced,

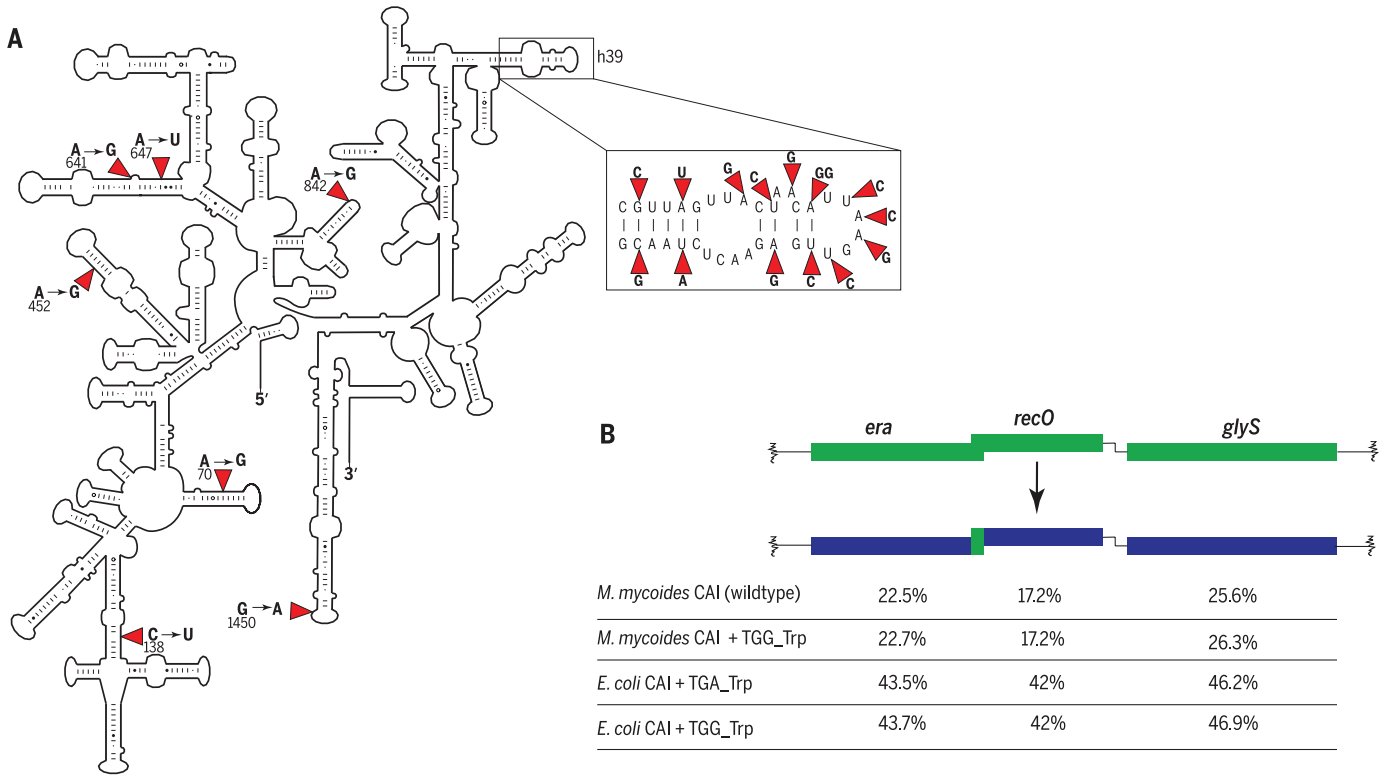


**Fig. 9. Gene content and codon usage principles, tested using the DBT cycle.** (A) Secondary structure of the modified *rrs* gene that was successfully incorporated into the syn3.0 genome; this gene was carrying *M. capricolum* mutations and had its h39 (inset) swapped with that of *E. coli*. Positions with nucleotide changes are indicated by red arrows, and *E. coli* numbering is used to indicate the position of *M. capricolum* mutations. (B) The sequences of the essential genes *era*, *recO*, and *glyS*

were modified in three different ways: using *M. mycoides* CAI with TGG encoding tryptophan, *E. coli* CAI with TGG encoding tryptophan, or *E. coli* CAI with TGA encoding tryptophan. GC content of the wild-type and modified genes is noted. The JCat codon adaptation tool was used for this exercise ([www.jcat.de](http://www.jcat.de)) to optimize the three open reading frames, with the exception of the overlapping gene fragment. Green and purple indicate wild-type and codon-optimized sequences, respectively.

Table 2. Reduced genomes resulting from the DBT cycles, ultimately leading to syn3.0. Column 1 indicates the round of genome design (dashes indicate the starting genome, syn1.0), column 2 gives the size of the designed genome (in kilobase pairs), and column 3 gives the number of mycoplasma genes in the design. Column 4 shows the genome composition for key viable cell strains; for nonviable designs, a viable strain with the highest number of segments from the design is shown, as well as a more robust alternative for RGD1.0 (fourth row) and a smaller derivative for RGD2.0 (sixth row, syn2.0). Column 5 gives the size of the genome corresponding to column 3, and column 6 shows a quantitative or qualitative estimate of the growth rate of cells with the genome described in column 4.					
1. Genome design	2. Design size	3. Number of design genes	4. Cellular genome segment composition for key viable strains	5. Cellular genome size	6. Growth rate
-		901	syn1.0: all eight syn1.0 segments	1079 kbp	Doubling time, td = 60 min
HMG	483 kbp	460	HMG segment 2 + 7/8 syn1.0	1003 kbp	Slow-growing
RGD1.0	544 kbp	483	RGD1.0 segments 2,6,7,8 + syn1.0 segments 1,3,4,5	758 kbp	Slow-growing
"	"	"	RGD1.0 segments 1,2,4,6,8 + syn1.0 segments 3,5,7	718 kbp	Slow-growing
RGD2.0	575 kbp	512	RGD2.0 segments 1,2,3,4,6,7,8 + syn1.0 segment 5	617 kbp	?
"	"	"	syn2.0: RGD2.0 segments 1,2,3,4,6,7,8 + syn1.0 segment 5 with genes <i>MMSYN1_0454</i> to <i>-0474</i> and <i>MMSYN1_0483</i> to <i>-0492</i> deleted	576 kbp	td = 92 min
RGD3.0	531 kbp	473	syn3.0: all eight segments of RGD3.0	531 kbp	td = 180 min



syn3.0. Table 2 summarizes the process leading to syn3.0. The first three designs did not yield complete viable cellular genomes. But in each case, one or more of the eight segments yielded a viable genome when combined with syn1.0 segments for the remainder of the genome. The composition of several of these intermediate strains is listed in the table. The viable syn3.0 cell is our best approximation to a minimal cell. We obtained another strain with a genome smaller than any free-living cell found in nature (syn2.0). This cell has a genome consisting of seven RGD2.0 segments plus a syn1.0 segment 5 with 31 genes deleted.

Syn3.0 has a 531-kbp genome that encodes 473 gene products. It is substantially smaller than *M. genitalium* (580 kbp), which has the smallest genome of any naturally occurring cell that has been grown in pure culture. The syn3.0 genome contains the core set of genes that are required for cellular life, but it is only half the size of syn1.0 (10). In comparing the HMG to the subsequently derived viable syn3.0 genome, we found agreement among 329 deleted genes and 365 retained genes. However, 111 genes that were kept in syn3.0 were deleted from HMG, and 100 genes deleted in syn3.0 were kept in HMG. The discrepancies were primarily due to the sparseness and quality of the initial transposon data, which resulted in incorrect identification of a number of essential or nonessential genes and did not identify quasi-essential genes that affect growth rate (discussed below). One example of the importance of the quasi-essential gene classification was the case of four genes (*MMSYN\_0008* to *MMSYN\_0011*) that make up the transport system for nucleosides. The original annotation of the system was as a ribose/galactose ABC transporter, which led us to target it for deletion in the HMG. Our initial transposon data showed that all four genes were hit heavily and appeared to confirm that the genes were nonessential. However, in later transposon mapping experiments, P0 transposon data confirmed that they were hit heavily, but after serial passage to deplete slow-growing cells, all four genes received zero hits, confirming that they were quasi-essential and should have been retained.

### Gene content of syn3.0

Syn3.0 is a working approximation of a minimal cell. Our first synthetic cell, syn1.0, contained 901 mycoplasma genes plus some watermarks and vector sequences. Of these, 428 have been removed in syn3.0, leaving 438 protein-coding genes and 35 RNA genes. More genes could probably be removed while retaining viability, but it seems likely that growth rate would be compromised. The slower growth rate of syn3.0 is not due to the removal of one of the rRNA operons. We also constructed a strain with the same gene complement, except that it retained both rRNA operons, and this strain grew at close to the same rate as syn3.0.

The largest group of genes retained in syn3.0 is involved in gene expression (195 genes, 41%). Approximately equal numbers of genes are involved in the cell membrane (84 genes, 18%) and

in metabolism (81 genes, 17%). During reductive evolution as a mycoplasma, many biosynthetic genes were lost and replaced by transporters residing in the membrane, resulting in a trade-off between these two categories. A relatively small number of genes function in the replication of the genome and the preservation of genomic information through cell division (36 genes, 7%). Unexpectedly, there are 79 genes (17%) that we have been unable to assign to a functional category. Of these, 19 are in the essential category (e-genes), 36 are needed for rapid growth (i- or ie-genes), and 24 are nonessential or nearly so (n- or in-genes). We presume that most of these will fall into one of the four major categories described above (gene expression, membrane structure and function, cytosolic metabolism, and genome preservation), but it seems likely that some of them may perform previously undescribed biological functions. In particular, 13 of the 19 functionally unassigned e-genes are of completely unknown function. Some of these match genes of unknown function in other bacteria or even in eukaryotes, and these are prime candidates for proteins with novel functions. Genes of unknown function that are required in syn3.0 and present in most organisms must represent nearly universal functions and thus can provide biological insights. Likewise, unknown genes without homologs may be novel, or they may represent unusual sequences but well-understood functions. In contrast to the wholly unknown genes, it is easy to oversimplify a gene's putative role in cell survival if it has a generic functional assignment. For example, some of the numerous hydrolases and kinases will undoubtedly contribute to processes such as nucleotide or cofactor salvage. The question is, will all of the generic functions of the unknown genes be so commonplace, or do some of them represent fundamentally new processes? There are genes whose generic annotations are perplexing even though they are needed for survival. For example, there are six different efflux systems, encoded by the genes *MMSYNL\_0034*, *MMSYNL\_0371* and *MMSYNL\_0372*, *MMSYNL\_0399*, *MMSYNL\_0531*, *MMSYNL\_0639*, and *MMSYNL\_0691*. Except for the heterodimeric pair, *MMSYNL\_0371* and *MMSYNL\_0372*, which may be a flippase, the substrates and functions of these proteins are unclear. It is somewhat disconcerting to imagine that all of these exclude or remove toxic substances. Similarly, a rather complex pathway (23) for producing and exporting glycolipids was required. Although there is some evidence that galactofuranose residues are important for membrane integrity (24), a detailed explanation for the biological role fulfilled by glycolipids remains obscure.

### Phenotype of the syn3.0 cell

The replication of genomic information and its coordinated distribution into segregated membrane-bound cellular compartments are hallmarks of extant living systems that are commonly considered to be among the attributes that define cellular life (25). The minimal requirements for this process are not known, but evidence from disparate fields of study suggests that mecha-

nisms far simpler than the complex division apparatus in most eubacteria may be sufficient.

First, several types of bacterial cells, both natural (26) and experimentally manipulated (27, 28), have been shown to divide in the absence of key cytoskeletal components, most notably the FtsZ cytoskeletal scaffolding and force-generating component. Through our empirically based design process, a nonessential gene cluster present in syn1.0 (*MMYSYNL\_0520* through *MMYSYNL\_0522*) was removed during construction of syn3.0 cells. This contained orthologs of *ftsZ* and *sepF* [encoding a membrane-anchoring component that interacts with FtsZ (29)]. An adjacent gene, *ftsA*, which is reported to share some redundant functions with *sepF* in other systems (30), remained essential in progressively reduced constructs that lacked *ftsZ*.

Second, completely synthetic lipid vesicles have been shown to spontaneously segregate without the involvement of macromolecular scaffolding or catalysis (31). In propagating cell wall-deficient bacteria, alteration of the lipid content and properties of the plasma membrane have been shown to elicit analogous membrane vesicle segregation (32). In several wall-less mycoplasma species, filamentous and large-vesicle morphotypes similar to those in syn3.0 have long been observed under certain growth conditions, depending in part on the nature of lipid precursors available to these cells (33). Ultimately, understanding the genetic and mechanistic basis for the phenotype of syn3.0 propagation may shed light on the minimal requirements for segregation of the membrane-bounded cellular compartment that is essential for a living cell.

### Use of the DBT cycle for applications other than genome minimization

Our main focus here has been the application of the whole-genome DBT cycle to a specific problem, the construction of a minimal cellular genome. However, the approach we describe can be applied to the construction of a cell with any desired properties. For example, a cell could be designed with added metabolic pathways (34), an altered genetic code (35), or dramatically altered gene arrangements. We have begun to design genomes with modified 16S rRNA sequences and to assess the effects of dramatic alterations in codon usage. Application of our DBT cycle is limited only by our ability to produce designs with a reasonable chance of success. With increasing knowledge of the functions of essential genes that are presently unknown, and with increasing experience in reorganizing the genome, we expect that our design capabilities will strengthen. The ability to design cells in which the function of every gene is known should facilitate complete computational modeling of the cell (36). This would make it possible to calculate the consequences of adding pathways for the production of useful products, such as drugs or industrial chemicals, and would lead to greater efficiency in development.

### Methods summary

Our methods for the identification of nonessential genes by global Tn5 mutagenesis, manipulation

of bacterial genomes in yeast by the scarless TREC (tandem repeat coupled with endonuclease cleavage) deletion method, synthesis and assembly of reduced genomes, genome transplantation, microscopic analysis of cells with reduced genomes, and observation of their growth characteristics are described in detail in the supplementary materials. General information about our methods, accompanied by specific references to the supplementary materials, is included throughout the text.

## REFERENCES AND NOTES

- H. J. Morowitz, The completeness of molecular biology. *Isr. J. Med. Sci.* **20**, 750–753 (1984). PMID: 6511349
- C. M. Fraser *et al.*, The minimal gene complement of *Mycoplasma genitalium*. *Science* **270**, 397–404 (1995). doi: 10.1126/science.270.5235.397; PMID: 7569993
- R. D. Fleischmann *et al.*, Whole-genome random sequencing and assembly of *Haemophilus influenzae* Rd. *Science* **269**, 496–512 (1995). doi: 10.1126/science.7542800; PMID: 7542800
- A. R. Mushegian, E. V. Koonin, A minimal gene set for cellular life derived by comparison of complete bacterial genomes. *Proc. Natl. Acad. Sci. U.S.A.* **93**, 10268–10273 (1996). doi: 10.1073/pnas.93.19.10268; PMID: 8816789
- C. A. Hutchison III *et al.*, Global transposon mutagenesis and a minimal *Mycoplasma* genome. *Science* **286**, 2165–2169 (1999). doi: 10.1126/science.286.5447.2165; PMID: 10591650
- J. I. Glass *et al.*, Essential genes of a minimal bacterium. *Proc. Natl. Acad. Sci. U.S.A.* **103**, 425–430 (2006). doi: 10.1073/pnas.0510013103; PMID: 16407165
- D. G. Gibson *et al.*, Complete chemical synthesis, assembly, and cloning of a *Mycoplasma genitalium* genome. *Science* **319**, 1215–1220 (2008). PMID: 18218864
- C. Lartigue *et al.*, Genome transplantation in bacteria: Changing one species to another. *Science* **317**, 632–638 (2007). doi: 10.1126/science.1144622; PMID: 17600181
- Materials and methods are available as supplementary materials on Science Online.
- D. G. Gibson *et al.*, Creation of a bacterial cell controlled by a chemically synthesized genome. *Science* **329**, 52–56 (2010). PMID: 20488990
- M. Juhas, D. R. ReuB, B. Zhu, F. M. Commichau, *Bacillus subtilis* and *Escherichia coli* essential genes and minimal cell factories after one decade of genome engineering. *Microbiology* **160**, 2341–2351 (2014). doi: 10.1099/mic.0.079376-0; PMID: 25092907
- G. Pósfai *et al.*, Emergent properties of reduced-genome *Escherichia coli*. *Science* **312**, 1044–1046 (2006). doi: 10.1126/science.1126439; PMID: 16645050
- Y. Suzuki *et al.*, Bacterial genome reduction using the progressive clustering of deletions via yeast sexual cycling. *Genome Res.* **25**, 435–444 (2015). doi: 10.1101/gr.182477.114; PMID: 25654978
- A. C. Forster, G. M. Church, Towards synthesis of a minimal cell. *Mol. Syst. Biol.* **2**, 45 (2006). doi: 10.1038/msb4100090; PMID: 16924266
- M. Lluch-Senar *et al.*, Defining a minimal cell: Essentiality of small ORFs and ncRNAs in a genome-reduced bacterium. *Mol. Syst. Biol.* **11**, 780 (2015). PMID: 25609650
- A. Ramon, H. O. Smith, Single-step linker-based combinatorial assembly of promoter and gene cassettes for pathway engineering. *Biotechnol. Lett.* **33**, 549–555 (2011). doi: 10.1007/s10529-010-0455-x; PMID: 21107654
- C. Merryman, D. G. Gibson, Methods and applications for assembling large DNA constructs. *Metab. Eng.* **14**, 196–204 (2012). doi: 10.1016/j.mbs.2012.02.005; PMID: 22629570
- V. N. Noskov, L. Ma, S. Chen, R. Y. Chuang, Recombinase-mediated cassette exchange (RMCE) system for functional genomics studies in *Mycoplasma mycoides*. *Biol. Proced. Online* **17**, 6 (2015). doi: 10.1186/s12575-015-0016-8; PMID: 25774095
- T. Dobzhansky, Genetics of natural populations. XIII. Recombination and variability in populations of *Drosophila pseudoobscura*. *Genetics* **31**, 269–290 (1946).
- D. H. Haft, J. D. Selengut, O. White, The TIGRFAMs database of protein families. *Nucleic Acids Res.* **31**, 371–373 (2003). doi: 10.1093/nar/gkg128; PMID: 12520025
- J. S. Jensen, H. T. Hansen, K. Lind, Isolation of *Mycoplasma genitalium* strains from the male urethra. *J. Clin. Microbiol.* **34**, 286–291 (1996). PMID: 8789002
- R. Gil, F. J. Silva, J. Peretó, A. Moya, Determination of the core of a minimal bacterial gene set. *Microbiol. Mol. Biol. Rev.* **68**, 518–537 (2004). doi: 10.1128/MMBR.68.3.518-537.2004; PMID: 15353568
- J. Romero-García, C. Francisco, X. Biarnés, A. Planas, Structure-function features of a *Mycoplasma* glycolipid synthase derived from structural data integration, molecular simulations, and mutational analysis. *PLOS ONE* **8**, e81990 (2013). doi: 10.1371/journal.pone.0081990; PMID: 24312618
- E. Schieck *et al.*, Galactofuranose in *Mycoplasma mycoides* is important for membrane integrity and conceals adhesins but does not contribute to serum resistance. *Mol. Microbiol.* **99**, 55–70 (2016). PMID: 26354009
- J. C. Xavier, K. R. Patil, I. Rocha, Systems biology perspectives on minimal and simpler cells. *Microbiol. Mol. Biol. Rev.* **78**, 487–509 (2014). doi: 10.1128/MMBR.00050-13; PMID: 25184563
- R. Bernander, T. J. Ettema, FtsZ-less cell division in archaea and bacteria. *Curr. Opin. Microbiol.* **13**, 747–752 (2010). doi: 10.1016/j.mib.2010.10.005; PMID: 21050804
- R. Mercier, Y. Kawai, J. Errington, Excess membrane synthesis drives a primitive mode of cell proliferation. *Cell* **152**, 997–1007 (2013). doi: 10.1016/j.cell.2013.01.043; PMID: 23452849
- M. Lluch-Senar, E. Querol, J. Piñol, Cell division in a minimal bacterium in the absence of ftsZ. *Mol. Microbiol.* **78**, 278–289 (2010). doi: 10.1111/j.1365-2958.2010.07306.x; PMID: 20735775
- S. Gola, T. Munder, S. Casonato, R. Manganello, M. Vicente, The essential role of SepF in mycobacterial division. *Mol. Microbiol.* **97**, 560–576 (2015). doi: 10.1111/mmi.13050; PMID: 25943244
- R. Duman *et al.*, Structural and genetic analyses reveal the protein SepF as a new membrane anchor for the Z ring. *Proc. Natl. Acad. Sci. U.S.A.* **110**, E4601–E4610 (2013). doi: 10.1073/pnas.1313978110; PMID: 24218584
- J. C. Blain, J. W. Szostak, Progress toward synthetic cells. *Annu. Rev. Biochem.* **83**, 615–640 (2014). doi: 10.1146/annurev-biochem-080411-124036; PMID: 24606140
- R. Mercier, P. Domínguez-Cuevas, J. Errington, Crucial role for membrane fluidity in proliferation of primitive cells. *Cell Reports* **1**, 417–423 (2012). doi: 10.1016/j.celrep.2012.03.008; PMID: 22832271
- S. Razin, B. J. Cosenza, M. E. Tourtellotte, Filamentous growth of mycoplasma. *Ann. N. Y. Acad. Sci.* **143**, 66–72 (1967). doi: 10.1111/j.1749-6632.1967.tb27645.x; PMID: 4861145
- M. J. Smanski *et al.*, Functional optimization of gene clusters by combinatorial design and assembly. *Nat. Biotechnol.* **32**, 1241–1249 (2014). doi: 10.1038/nbt.3063; PMID: 25419741
- M. J. Lajoie *et al.*, Genomically recoded organisms expand biological functions. *Science* **342**, 357–360 (2013). PMID: 24136966
- J. R. Karr *et al.*, A whole-cell computational model predicts phenotype from genotype. *Cell* **150**, 389–401 (2012). doi: 10.1016/j.cell.2012.05.044; PMID: 22817898

## ACKNOWLEDGMENTS

We thank Synthetic Genomics (SGI) and the Defense Advanced Research Projects Agency's Living Foundries program (contract HRO011-12-C-0063) for funding this work. Microscopy work at the University of California–San Diego was supported by NIH grant P41GM103412 from the National Institute of General Medical Sciences to M.H.E. J.F.P. was supported by a Fannie and John Hertz Graduate Fellowship, the Massachusetts Institute of Technology (MIT) Center for Bits and Atoms, and the MIT Department of Physics. E.A.S. was supported by the National Institute of Standards and Technology (certain commercial equipment, instruments, or materials are identified in this paper to foster understanding; such identification does not imply recommendation or endorsement by the National Institute of Standards and Technology, nor does it imply that the materials or equipment identified are necessarily the best available for the stated purpose). We thank M. D. Adams, M. A. Algire, D. Bami, D. Brown, L. Brinkac, N. Caiazza, O. Fetzer, L. Fu, D. Haft, S. Kaushal, M. Lapointe, A. Lee, M. Lewis, D. Lomelin, C. Ludka, M. Montague, C. Orsco, T. Peterson, A. Ramon, T. Richardson, A. Schwartz, D. Smith, S. Vashee, and T. Yee for their contributions to this work and for helpful discussions. J.C.V. is chairman of the Board of Directors and co-chief scientific officer of SGI. H.O.S. is on the Board of Directors and co-chief scientific officer of SGI. C.A.H. is chairman of the SGI Scientific Advisory Board. D.G.G. is a vice president of SGI. J.C.V., H.O.S., C.A.H., D.G.G., J.G., K.K., and the J. Craig Venter Institute (JCVI) hold SGI stock and/or stock options. SGI and JCVI have filed patent applications on some of the methods and concepts described in this paper.

## SUPPLEMENTARY MATERIALS

[www.sciencemag.org/content/351/6280/aad6253/suppl/DC1](http://www.sciencemag.org/content/351/6280/aad6253/suppl/DC1)  
Materials and Methods  
Figs. S1 to S21  
Tables S1 to S15  
References (37–59)  
Database S1

13 October 2015; accepted 5 February 2016  
10.1126/science.aad6253



## RESEARCH ARTICLE SUMMARY

## DFT METHODS

# Reproducibility in density functional theory calculations of solids

Kurt Lejaeghere,\* Gustav Bihlmayer, Torbjörn Björkman, Peter Blaha, Stefan Blügel, Volker Blum, Damien Caliste, Ivano E. Castelli, Stewart J. Clark, Andrea Dal Corso, Stefano de Gironcoli, Thierry Deutsch, John Kay Dewhurst, Igor Di Marco, Claudia Draxl, Marcin Dulak, Olle Eriksson, José A. Flores-Livas, Kevin F. Garrity, Luigi Genovese, Paolo Giannozzi, Matteo Giantomassi, Stefan Goedecker, Xavier Gonze, Oscar Grånäs, E. K. U. Gross, Andris Gulans, François Gygi, D. R. Hamann, Phil J. Hasnip, N. A. W. Holzwarth, Diana Iușan, Dominik B. Jochym, François Jollet, Daniel Jones, Georg Kresse, Klaus Koepf, Emine Küçükbenli, Yaroslav O. Kvashnin, Inka L. M. Locht, Sven Lubeck, Martijn Marsman, Nicola Marzari, Ulrike Nitzsche, Lars Nordström, Taisuke Ozaki, Lorenzo Paulatto, Chris J. Pickard, Ward Poelmans, Matt I. J. Probert, Keith Refson, Manuel Richter, Gian-Marco Rignanese, Santanu Saha, Matthias Scheffler, Martin Schlipf, Karlheinz Schwarz, Sangeeta Sharma, Francesca Tavazza, Patrik Thunström, Alexandre Tkatchenko, Marc Torrent, David Vanderbilt, Michiel J. van Setten, Veronique Van Speybroeck, John M. Wills, Jonathan R. Yates, Guo-Xu Zhang, Stefaan Cottenier\*

**INTRODUCTION:** The reproducibility of results is one of the underlying principles of science. An observation can only be accepted by the scientific community when it can be confirmed by independent studies. However, reproducibility does not come easily. Recent works have painfully exposed cases where previous conclusions were not upheld. The scrutiny of the scientific community has also turned to research involving computer programs, finding that reproducibility depends more strongly on implementation than commonly thought. These problems are especially relevant for property predictions of crystals and molecules, which hinge on precise computer implementations of the governing equation of quantum physics.

**RATIONALE:** This work focuses on density functional theory (DFT), a particularly popular quan-

tum method for both academic and industrial applications. More than 15,000 DFT papers are published each year, and DFT is now increasingly used in an automated fashion to build large databases or apply multiscale techniques with limited human supervision. Therefore, the reproducibility of DFT results underlies the scientific credibility of a substantial fraction of current work in the natural and engineering sciences. A plethora of DFT computer codes are available, many of them differing considerably in their details of implementation, and each yielding a certain “precision” relative to other codes. How is one to decide for more than a few simple cases which code predicts the correct result, and which does not? We devised a procedure to assess the precision of DFT methods and used this to demonstrate reproducibility among many of the most widely used

DFT codes. The essential part of this assessment is a pairwise comparison of a wide range of methods with respect to their predictions of the equations of state of the elemental crystals. This effort required the combined expertise of a large group of code developers and expert users.

**RESULTS:** We calculated equation-of-state data for four classes of DFT implementations, totaling 40 methods. Most codes agree very well, with pairwise differences that are comparable to those between different high-precision exper-

## ON OUR WEB SITE

Read the full article at <http://dx.doi.org/10.1126/science.aad3000>

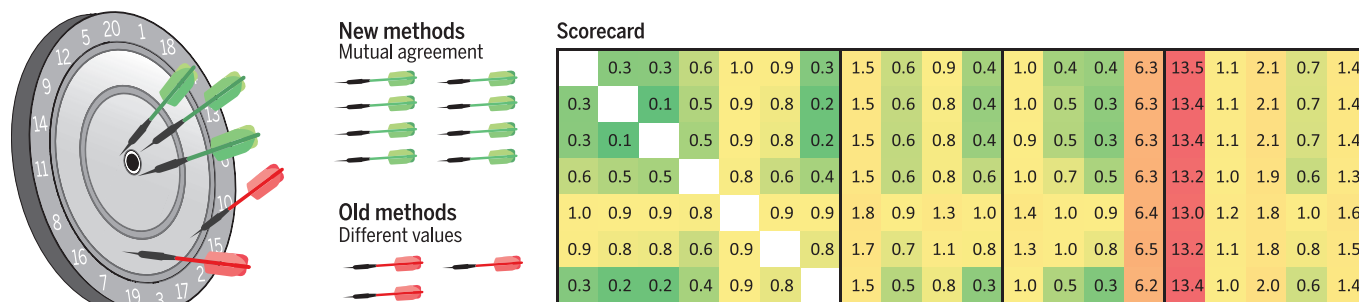
iments. Even in the case of pseudization approaches, which largely depend on the atomic potentials used, a similar precision can be obtained as when using the full potential. The remaining deviations are due to subtle effects, such as specific numerical implementations or the treatment of relativistic terms.

**CONCLUSION:** Our work demonstrates that the precision of DFT implementations can be determined, even in the absence of one absolute reference code. Although this was not the case 5 to 10 years ago, most of the commonly used codes and methods are now found to predict essentially identical results. The established precision of DFT codes not only ensures the reproducibility of DFT predictions but also puts several past and future developments on a firmer footing. Any newly developed methodology can now be tested against the benchmark to verify whether it reaches the same level of precision. New DFT applications can be shown to have used a sufficiently precise method. Moreover, high-precision DFT calculations are essential for developing improvements to DFT methodology, such as new density functionals, which may further increase the predictive power of the simulations. ■

The list of author affiliations is available in the full article online.  
\*Corresponding author. E-mail: [kurt.lejaeghere@ugent.be](mailto:kurt.lejaeghere@ugent.be) (K.L.); [stefaan.cottenier@ugent.be](mailto:stefaan.cottenier@ugent.be) (S.C.)

Cite this article as K. Lejaeghere *et al.*, *Science* **351**, aad3000 (2016). DOI: 10.1126/science.aad3000

**Recent DFT methods yield reproducible results.** Whereas older DFT implementations predict different values (red darts), codes have now evolved to mutual agreement (green darts). The scoreboard illustrates the good pairwise agreement of four classes of DFT implementations (horizontal direction) with all-electron results (vertical direction). Each number reflects the average difference between the equations of state for a given pair of methods, with the green-to-red color scheme showing the range from the best to the poorest agreement.



## RESEARCH ARTICLE

## DFT METHODS

# Reproducibility in density functional theory calculations of solids

Kurt Lejaeghere,<sup>1\*</sup> Gustav Bihlmayer,<sup>2</sup> Torbjörn Björkman,<sup>3,4</sup> Peter Blaha,<sup>5</sup> Stefan Blügel,<sup>2</sup> Volker Blum,<sup>6</sup> Damien Caliste,<sup>7,8</sup> Ivano E. Castelli,<sup>9</sup> Stewart J. Clark,<sup>10</sup> Andrea Dal Corso,<sup>11</sup> Stefano de Gironcoli,<sup>11</sup> Thierry Deutsch,<sup>7,8</sup> John Kay Dewhurst,<sup>12</sup> Igor Di Marco,<sup>13</sup> Claudia Draxl,<sup>14,15</sup> Marcin Dulak,<sup>16</sup> Olle Eriksson,<sup>13</sup> José A. Flores-Livas,<sup>12</sup> Kevin F. Garrity,<sup>17</sup> Luigi Genovese,<sup>7,8</sup> Paolo Giannozzi,<sup>18</sup> Matteo Giantomassi,<sup>19</sup> Stefan Goedecker,<sup>20</sup> Xavier Gonze,<sup>19</sup> Oscar Grånäs,<sup>13,21</sup> E. K. U. Gross,<sup>12</sup> Andris Gulans,<sup>14,15</sup> François Gygi,<sup>22</sup> D. R. Hamann,<sup>23,24</sup> Phil J. Hasnip,<sup>25</sup> N. A. W. Holzwarth,<sup>26</sup> Diana Iuşan,<sup>13</sup> Dominik B. Jochym,<sup>27</sup> François Jollet,<sup>28</sup> Daniel Jones,<sup>29</sup> Georg Kresse,<sup>30</sup> Klaus Koepnick,<sup>31,32</sup> Emine Küçükbenli,<sup>9,11</sup> Yaroslav O. Kvashnin,<sup>13</sup> Inka L. M. Loch,<sup>13,33</sup> Sven Lubeck,<sup>14</sup> Martijn Marsman,<sup>30</sup> Nicola Marzari,<sup>9</sup> Ulrike Nitzsche,<sup>31</sup> Lars Nordström,<sup>13</sup> Taisuke Ozaki,<sup>34</sup> Lorenzo Paulatto,<sup>35</sup> Chris J. Pickard,<sup>36</sup> Ward Poelmans,<sup>1,37</sup> Matt I. J. Probert,<sup>25</sup> Keith Refson,<sup>38,39</sup> Manuel Richter,<sup>31,32</sup> Gian-Marco Rignanese,<sup>19</sup> Santanu Saha,<sup>20</sup> Matthias Scheffler,<sup>15,40</sup> Martin Schlipf,<sup>22</sup> Karlheinz Schwarz,<sup>5</sup> Sangeeta Sharma,<sup>12</sup> Francesca Tavazza,<sup>17</sup> Patrik Thunström,<sup>41</sup> Alexandre Tkatchenko,<sup>15,42</sup> Marc Torrent,<sup>28</sup> David Vanderbilt,<sup>23</sup> Michiel J. van Setten,<sup>19</sup> Veronique Van Speybroeck,<sup>1</sup> John M. Wills,<sup>43</sup> Jonathan R. Yates,<sup>29</sup> Guo-Xu Zhang,<sup>44</sup> Stefaan Cottenier<sup>1,45\*</sup>

The widespread popularity of density functional theory has given rise to an extensive range of dedicated codes for predicting molecular and crystalline properties. However, each code implements the formalism in a different way, raising questions about the reproducibility of such predictions. We report the results of a community-wide effort that compared 15 solid-state codes, using 40 different potentials or basis set types, to assess the quality of the Perdew-Burke-Ernzerhof equations of state for 71 elemental crystals. We conclude that predictions from recent codes and pseudopotentials agree very well, with pairwise differences that are comparable to those between different high-precision experiments. Older methods, however, have less precise agreement. Our benchmark provides a framework for users and developers to document the precision of new applications and methodological improvements.

Scientific results are expected to be reproducible. When the same study is repeated independently, it should reach the same conclusions. Nevertheless, some recent articles have shown that reproducibility is not self-evident. A widely resounding *Science* article (1), for example, demonstrated a lack of reproducibility among published psychology experiments. Although the hard sciences are believed to perform better in this respect, concerns about reproducibility have emerged in these fields as well (2–4). The issue is of particular interest when computer programs are involved. Undocumented approximations or undetected bugs can lead to wrong conclusions (5). In areas where academic codes compete with commercial software, the unavailability of source code can hinder assessment of the relevance of conclusions (6, 7).

Density functional theory (DFT) calculations (8, 9) are a prominent example of an area that depends on the development and appropriate use of complex software. With rigorous foundations in the quantum theory of matter, DFT

describes the structure and properties of molecules and solids at the atomic scale. Over the years, many academic groups have developed implementations of DFT in computer codes, and several of these have been adopted by large user communities. Commercial alternatives are entering this area as well. At present, more than 15,000 papers are published each year that make use of DFT codes (10), with applications varying from metallurgy to drug design. Moreover, DFT calculations are used nowadays to build large databases (11, 12) and in multiscale calculations in which they serve as one part of the tool chain (13, 14). The precision of DFT codes thus underlies the scientific credibility and reproducibility of a substantial fraction of current work in the natural and engineering sciences, and therefore it has implications that reach far beyond the traditional electronic-structure research community.

The main idea of DFT is to solve the intractable many-particle Schrödinger equation by replacing the complete electron wave function with the much simpler ground-state electron density as

the fundamental variable. Although this reformulation is in principle exact, it is not fully known how the interaction between individual electrons should be transformed. As a result, the specific form of the unknown part of the interaction energy, the exchange-correlation functional, has been the focus of many investigations, leading to a plethora of available functionals in both solid-state physics (15–19) and quantum chemistry (15, 20–23).

Once a particular exchange-correlation functional has been chosen, the mathematical problem is completely specified as a set of Kohn-Sham equations, whose solution yields orbitals and energies from which the total electronic energy can be evaluated. A variety of such numerical solution schemes have been implemented in different computer codes. Comparisons of their performance are much less frequent or extensive than those of exchange-correlation functionals, however (21, 24–29). One might reasonably expect that because they solve the same equations, they all produce similar answers for a given crystal structure, but a glance at the literature shows that this assumption is by no means always true. Figure 1 demonstrates that even for a well-studied material such as silicon, deviations between predictions from different codes (the “precision”) are of the same order of magnitude as the deviation from the 0 K experimental value (the “accuracy”) (26, 30). Because all of the codes shown in Fig. 1 treat silicon at the same level of theory, using the same exchange-correlation functional, they yield the same accuracy by definition. However, the particular predictions vary from one code to another because of approximations that are unrelated to the exchange-correlation functional. These approximations decrease the computational load but limit the precision.

What level of precision can we now achieve? Discussion of precision-related issues is uncommon in reports of solid-state DFT studies. The reproducibility of predictions is sometimes checked by cross-validation with other codes (21, 24–28), but we are not aware of any systematic assessments of precision (also called “verification”), even though such studies would reinforce confidence in practical DFT calculations.

As a group of 69 code developers and expert users, we determined the error bar associated with energy-versus-volume  $[E(V)]$  predictions of elemental solids by running the same benchmark protocol with various DFT codes. Parameters of these equations of state (EOS), such as the lattice parameter or the bulk modulus, are commonly used for accuracy assessments (15–19). By considering elemental solids, we have established a broad and comprehensive test for precision. Elemental solids have a wide range of chemical environments and constitute a reasonable first approximation to sampling the broad compositional space of multicomponent systems. Our effort has resulted in 18,602 DFT calculations, which we aimed to execute with a rigorously determined precision. This exercise might seem simple, but each code tackles the Kohn-Sham equations and subsequent energy evaluation in its own way, requiring different approaches to



deal with difficulties in different parts of the computational procedure.

## Kohn-Sham solution techniques

The Kohn-Sham equations describe a many-electron system in terms of a density built from single-particle wave functions. By expressing these wave functions as a linear combination of pre-defined basis functions, the Kohn-Sham equations reduce to a matrix equation, which can in principle be solved exactly. Their solutions should yield identical results, irrespective of the form of the basis functions, provided that the basis set is complete. However, achieving technical convergence of the complete Kohn-Sham problem is not feasible in practice. Consider silicon, whose electronic structure is schematically illustrated in Fig. 2. The Aufbau principle requires first populating the lowest energy level, which is the  $1s$  band. This is much lower in energy than the valence and conduction bands, and the localization of the orbitals close to the nuclei demands high spatial resolution. These core electrons do not contribute directly to chemical bonding, so they can be separated out and represented using a different basis that is better suited to describe localized atomic-like states. Core orbitals may be either computed in an isolated atom environment, with their effect on valence transferred unaltered to the crystal, or relaxed self-consistently in the full crystal field. They can moreover be treated using a relativistic Hamiltonian, which is essential for core electrons in heavy atoms. Different relativistic schemes may lead to differences in the predicted  $E(V)$  curves.

To stitch together a complete solution, the wave functions of the semi-core and valence electrons ( $2s\ 2p$  and  $3s\ 3p$ , respectively, in the case of silicon) must be constructed to include the effect of orthogonality to the core electrons. This central problem can be solved in a number of different

ways, depending on the choice of numerical method. For methods that are based on plane-wave expansions or uniform real-space grids, the oscillatory behavior near the nucleus cannot be accurately represented because of the limited spatial resolution. The need for unmanageably large basis sets can be mitigated by adding a carefully designed repulsive part to the Kohn-Sham potential, a so-called pseudopotential. This pseudopotential affects only a small region around the nuclei (gray zones in Fig. 2) and may conserve the core-region charge [norm-conserving pseudopotentials (31, 32)], giving rise to an analytically straightforward formalism, or it may break norm conservation by including a compensating augmentation charge [ultrasoft pseudopotentials (33)], allowing for smoother wave functions and hence smaller basis sets. Alternatively, the projector-augmented wave (PAW) approach defines an explicit transformation between the all-electron and pseudopotential wave functions by means of additional partial-wave basis functions (34, 35). This allows PAW codes to obtain good precision for small numbers of plane waves or large grid spacings, but choosing suitable partial-wave projectors is not trivial. Here we refer to both pseudopotential and PAW methods as pseudization approaches. In contrast to these approaches, all-electron methods explicitly construct basis functions that are restricted to a specific energy range [linearized augmented plane wave (LAPW) (36–39) and linear muffin-tin orbital (LMTO) (40) methods] or treat core and valence states on equal footing (e.g., by using numerical atomic-like orbitals) (41, 42). Avoiding pseudization enables better precision but inevitably increases the computation time. In these codes, the ambiguity in solving the Kohn-Sham problem shifts from the choice of the pseudization scheme to the choice of the basis functions. This choice leads to a variety of methods as well, which, despite solving the same Kohn-Sham

equations, differ in many other details. Because each all-electron or pseudization method has its own fundamental advantages, it is highly desirable to achieve high precision for all of them.

## The $\Delta$ matrix

The case study for silicon (Fig. 1) demonstrates that different approaches to the potential or basis functions may lead to noticeably different predictions, even for straightforward properties such as the lattice parameter. There is no absolute reference against which to compare these methods; each approach has its own intricacies and approximations. To determine whether the same results can be obtained irrespective of the code or (pseudo)potential, we instead present a large-scale pairwise code comparison using the  $\Delta$  gauge. This criterion was formulated by Lejaeghere *et al.* (26) to quantify differences between DFT-predicted  $E(V)$  profiles in an unequivocal way. That study proposed a benchmark set of 71 elemental crystals and defined, for every element  $i$ , the quantity  $\Delta_i$  as the root-mean-square difference between the EOS of methods  $a$  and  $b$  over a  $\pm 6\%$  interval around the equilibrium volume  $V_{0,i}$ . The calculated EOS are lined up with respect to their minimum energy and compared in an interval that is symmetrical around the average equilibrium volume (Fig. 3).

$$\Delta_i(a, b) = \sqrt{\frac{\int_{0.94V_{0,i}}^{1.06V_{0,i}} (E_{b,i}(V) - E_{a,i}(V))^2 dV}{0.12V_{0,i}}} \quad (1)$$

A comparison of  $\Delta_i$  values allows the expression of EOS differences as a single number, and a small  $\Delta_i$  automatically implies small deviations between equilibrium volumes, bulk moduli, or any other EOS-derived observables. The overall difference  $\Delta$  between methods  $a$  and  $b$  is

<sup>1</sup>Center for Molecular Modeling, Ghent University, Technologiepark 903, BE-9052 Zwijnaarde, Belgium. <sup>2</sup>Peter Grünberg Institute and Institute for Advanced Simulation, Forschungszentrum Jülich and JARA (Jülich Aachen Research Alliance), D-52425 Jülich, Germany. <sup>3</sup>Department of Physics, Åbo Akademi, FI-20500 Turku, Finland. <sup>4</sup>Centre of Excellence in Computational Nanoscience (COMP) and Department of Applied Physics, Aalto University School of Science, Post Office Box 11100, FI-00076 Aalto, Finland. <sup>5</sup>Institute of Materials Chemistry, Vienna University of Technology, Getreidemarkt 9/165-TC, A-1060 Vienna, Austria. <sup>6</sup>Department of Mechanical Engineering and Materials Science, Duke University, Durham, NC 27708, USA. <sup>7</sup>Université Grenoble Alpes, Institut Nanosciences et Cryogénie-Modeling and Material Exploration Department (INAC-MEM), Laboratoire de Simulation Atomistique (L-Sim), F-38042 Grenoble, France. <sup>8</sup>Commissariat à l'Énergie Atomique et aux Énergies Alternatives (CEA), INAC-MEM, L-Sim, F-38054 Grenoble, France. <sup>9</sup>Theory and Simulation of Materials (THEOS) and National Centre for Computational Design and Discovery of Novel Materials (MARVEL), École Polytechnique Fédérale de Lausanne, CH-1015 Lausanne, Switzerland. <sup>10</sup>Department of Physics, University of Durham, Durham DH1 3LE, UK. <sup>11</sup>International School for Advanced Studies (SISSA) and DEMOCRITOS, Consiglio Nazionale delle Ricerche-Istituto Officina dei Materiali (CNR-IOM), Via Bonomea 265, I-34136 Trieste, Italy. <sup>12</sup>Max-Planck-Institut für Mikrostrukturphysik, Weinberg 2, D-06120 Halle, Germany. <sup>13</sup>Department of Physics and Astronomy, Division of Materials Theory, Uppsala University, Post Office Box 516, SE-75120 Uppsala, Sweden. <sup>14</sup>Institut für Physik und Integrative Research Institute for the Sciences (IRIS)-Adlershof, Humboldt-Universität zu Berlin, Zum Großen Windkanal 6, D-12489 Berlin, Germany. <sup>15</sup>Fritz-Haber-Institut der Max-Planck-Gesellschaft, Faradayweg 4-6, D-14195 Berlin, Germany. <sup>16</sup>Center for Atomic-Scale Materials Design, Department of Physics, Technical University of Denmark, DK-2800 Kongens Lyngby, Denmark. <sup>17</sup>Material Measurement Laboratory, National Institute of Standards and Technology, 100 Bureau Drive, Stop 8553, Gaithersburg, MD 20899, USA. <sup>18</sup>Department of Mathematics, Computer Science, and Physics, University of Udine, Via delle Scienze 206, I-33100 Udine, Italy. <sup>19</sup>Institute of Condensed Matter and Nanosciences-Nanoscopy Physics (NAPS), Université Catholique de Louvain, Chemin des Étoiles 8, BE-1348 Louvain-la-Neuve, Belgium. <sup>20</sup>Institut für Physik, Universität Basel, Klingelbergstrasse 82, CH-4056 Basel, Switzerland. <sup>21</sup>School of Engineering and Applied Sciences, Harvard University, Cambridge, MA 02138, USA. <sup>22</sup>Department of Computer Science, University of California-Davis, Davis, CA 95616, USA. <sup>23</sup>Department of Physics and Astronomy, Rutgers University, Piscataway, NJ 08854-8019, USA. <sup>24</sup>Mat-Sim Research, Post Office Box 742, Murray Hill, NJ 07974, USA. <sup>25</sup>Department of Physics, University of York, Heslington, York YO10 5DD, UK. <sup>26</sup>Department of Physics, Wake Forest University, Winston-Salem, NC 27109, USA. <sup>27</sup>Scientific Computing Department, Science and Technology Facilities Council, Rutherford Appleton Laboratory, Didcot OX11 0QX, UK. <sup>28</sup>CEA, DAM, DIF, F-91297 Arpajon, France. <sup>29</sup>Department of Materials, University of Oxford, 16 Parks Road, Oxford OX1 3PH, UK. <sup>30</sup>Faculty of Physics and Center for Computational Materials Science, University of Vienna, Sensengasse 8/12, A-1090 Vienna, Austria. <sup>31</sup>Leibniz-Institut für Festkörper- und Werkstoffforschung (IFW) Dresden, Post Office Box 270 116, D-01171 Dresden, Germany. <sup>32</sup>Dresden Center for Computational Materials Science (DCMS), Technische Universität Dresden, D-01069 Dresden, Germany. <sup>33</sup>Institute for Molecules and Materials, Radboud University, Heyendaalseweg 135, 6525 AJ Nijmegen, Netherlands. <sup>34</sup>Institute for Solid State Physics, The University of Tokyo, Kashiwa 277-8581, Japan. <sup>35</sup>Institut de Minéralogie, de Physique des Matériaux, et de Cosmochimie (IMPMC), Sorbonne Universités-Pierre et Marie Curie Université Paris 06, Centre National de la Recherche Scientifique (CNRS) Unité Mixte de Recherche (UMR) 7590, Muséum National d'Histoire Naturelle, Institut de Recherche pour le Développement (IRD) Unité de Recherche 206, 4 Place Jussieu, F-75005 Paris, France. <sup>36</sup>Department of Materials Science and Metallurgy, University of Cambridge, 27 Charles Babbage Road, Cambridge CB3 0FS, UK. <sup>37</sup>High Performance Computing Unit, Ghent University, Krijgslaan 281 S9, BE-9000 Ghent, Belgium. <sup>38</sup>Department of Physics, Royal Holloway, University of London, Egham TW20 0EX, UK. <sup>39</sup>ISIS Facility, Science and Technology Facilities Council, Rutherford Appleton Laboratory, Didcot OX11 0QX, UK. <sup>40</sup>Department of Chemistry and Biochemistry and Materials Department, University of California-Santa Barbara, Santa Barbara, CA 93106-5050, USA. <sup>41</sup>Institute for Solid State Physics, Vienna University of Technology, A-1040 Vienna, Austria. <sup>42</sup>Physics and Materials Science Research Unit, University of Luxembourg, L-1511 Luxembourg. <sup>43</sup>Theoretical Division, Los Alamos National Laboratory, Los Alamos, NM 87545, USA. <sup>44</sup>Institute of Theoretical and Simulation Chemistry, School of Chemistry and Chemical Engineering, Harbin Institute of Technology, Harbin 150001, People's Republic of China. <sup>45</sup>Department of Materials Science and Engineering, Ghent University, Technologiepark 903, BE-9052 Zwijnaarde, Belgium.

\*Corresponding author. E-mail: kurt.lejaeghere@ugent.be (K.L.); stefaan.cottenier@ugent.be (S.C.)

obtained by averaging  $\Delta_i$  over all 71 crystals in the benchmark set. Alternative definitions of  $\Delta$  essentially render the same information (27, 28). In this work, we applied the original  $\Delta$  protocol to 40 DFT implementations of the Perdew-Burke-Ernzerhof (PBE) functional (43). Appropriate numerical settings were determined separately for each method, ensuring converged results. In all calculations, valence and semi-core electrons were treated on a scalar-relativistic level, because not all codes support spin-orbit coupling. This is not a limitation, because the aim is to compare codes with each other rather than to experiment. We do not elaborate here on speed and memory requirements, for which we refer to the documentation of the respective codes.

Figure 4 presents an overview of the most important  $\Delta$  values, categorized by method: all-electron, PAW, ultrasoft pseudopotentials, and norm-conserving pseudopotentials. Approaches with a similar intrinsic precision are clustered together in this way. Both the full results and the most important numerical settings are included in tables S3 to S42. A complete specification would have to include code defaults and hard-coded values, so a reasonable compromise was chosen. A full specification could be realized by recent endeavors in full-output databases (44, 45) or workflow scripting (46, 47), but this capacity is not yet available for several of the codes used in this study. We have, however, tried to provide generation scripts for as many methods as possible (48), and we emphasize the need for these tools as an important future direction.

### Comparing all-electron methods

Although the definition of  $\Delta$  does not favor a particular reference, it is instructive to first examine the  $\Delta$  values with respect to all-electron methods (Fig. 4). They generally come at a computationally higher cost, but all-electron approaches are often considered to be a standard for DFT calculations, because they implement the potential without pseudization. By comparing pseudopotential or PAW methods with all-electron codes, we can therefore get an idea of the error bar associated with each pseudization scheme. The  $\Delta$  values between different all-electron methods reflect the remaining discrepancies, such as a different treatment of the scalar-relativistic terms or small differences in numerical methods.

To gain some insight into typical values of  $\Delta$ , we should first establish which values for  $\Delta$  can be qualified as “small,” so that we know which results can be considered equivalent. A first indication comes from converting differences between high-precision measurements of EOS parameters into a  $\Delta$  format. Comparing the high-quality experimental data of Holzapfel *et al.* for Cu, Ag, and Au (49) with those of Kittel (50) and Knittle (51), for example, shows a small difference  $\Delta_{exp}$  of 1.0 meV per atom. Because the average all-electron  $\Delta$  for these materials is only 0.8 meV per atom, this implies that the precision of many DFT codes outperforms experimental precision.

Secondly, we also considered the differences between codes in terms of commonly reported EOS parameters. The 1.0 meV-per-atom maximum  $\Delta$  among all-electron codes (Fig. 4, top) corresponds to an average volume deviation of 0.14 Å<sup>3</sup> per atom (0.38%) or a median deviation of 0.05 Å<sup>3</sup> per atom (0.24%) over the entire 71-element test set. For the bulk modulus, the average deviation is 1.6 GPa (4.0%), and the median deviation 0.8 GPa (1.6%).

Compared with the scatter on experimental values, which can amount to up to 35% for the bulk moduli of the rare earth metals [for instance, see (52)], these values are very small. The difference between EOS obtained by independent all-electron codes is hence smaller than the spread between independent experimental EOS. We conclude that, unless some elements deviate substantially from the overall trend, codes with a

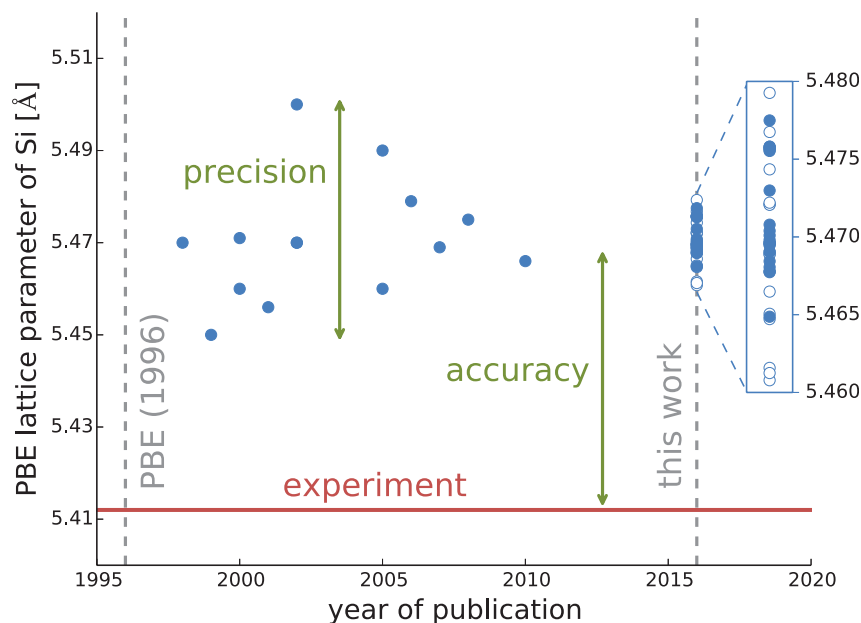


**Fig. 1. Historical evolution of the predicted equilibrium lattice parameter for silicon.** All data points represent calculations within the DFT-PBE framework. Values from literature (data points before 2016) (15, 16, 18, 56–62, 63–65) are compared with (i) predictions from the different codes used in this study (2016 data points, magnified in the inset; open circles indicate data produced by older methods or calculations with lower numerical settings) and (ii) the experimental value, extrapolated to 0 K and corrected for zero-point effects (red line) (26). The concepts of precision and accuracy are illustrated graphically.

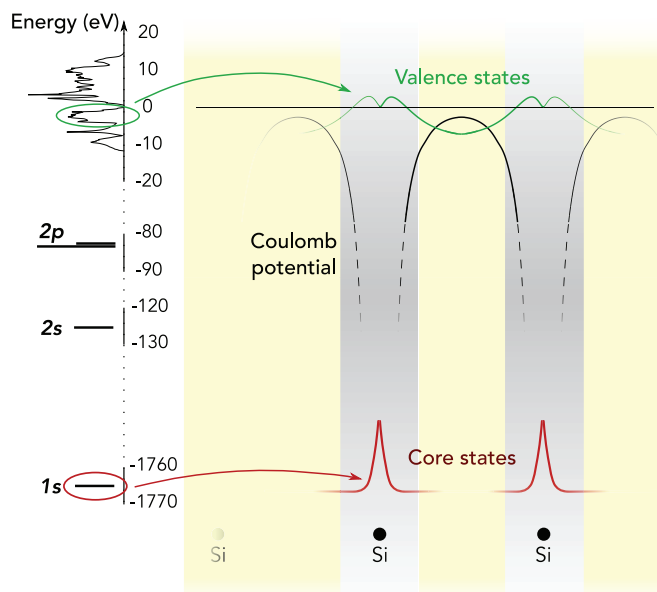
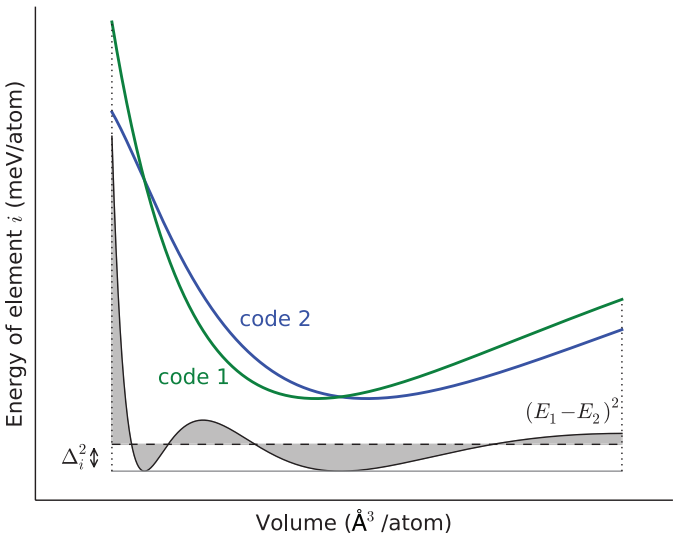


**Fig. 2. Electronic states in solid silicon.**

The valence states are delocalized over the solid (green line), because the wave functions overlap from one atom to the next. The lowest-energy 1s state (red) is at an energy two orders of magnitude lower than the valence states and is strongly localized near the nucleus, with no overlap between the atoms. The gray regions around the atoms indicate approximately where the wave function, density, and potential are smoothed in pseudized methods.



**Fig. 3. Graphical representation of the  $\Delta$  gauge.** The black curve depicts the quadratic energy difference between two EOS  $[(E_1 - E_2)^2]$ , where the subscripts correspond to the two codes shown], and  $\Delta_i$  corresponds to the root-mean-square average. This is demonstrated by the shaded area, which is equally large above and below the  $\Delta_i^2$  line.



<b>Table 1. Agreement between osmium crystal predictions at nearly identical settings.</b> The top group includes $\Delta_i$ values for the osmium crystal (in millielectron volts per atom) produced by four APW+lo calculations that tried to mimic the same settings as well as possible. These settings are therefore different from the ones used for Fig. 4 and reported in tables S3, S4, S8, and S15. The bottom group includes the corresponding equilibrium volumes $V_0$ , bulk moduli $B_0$ , and bulk modulus derivatives $B_1$ .				
	Elk	FLEUR	WIEN2K	exciting
$\Delta(\text{Elk})$	–	0.03	0.02	0.20
$\Delta(\text{FLEUR})$	0.03	–	0.04	0.22
$\Delta(\text{WIEN2K})$	0.02	0.04	–	0.18
$\Delta(\text{exciting})$	0.20	0.22	0.18	–
$V_0$ ( $\text{\AA}^3$ per atom)	14.276	14.276	14.276	14.274
$B_0$ (GPa)	397.5	397.9	397.6	397.4
$B_1$ (unitless)	4.86	4.89	4.83	4.82

<b>Table 2. Precision evolution of PAW and pseudopotential sets over time.</b> The $\Delta$ values are expressed as an average over the all-electron methods (in millielectron volts per atom) and are listed chronologically per code. The corresponding code settings and the DFT-predicted EOS parameters are listed in tables S17, S19 to S26, S30, S31, and S33. The most recent potentials are the ones used to generate the data shown in Fig. 4.		
	Year	$\langle \Delta \rangle$ versus AE
JTH01/ABINIT	2013	1.1
JTH02/ABINIT	2014	0.6
Vdb/CASTEP	1998	6.5
OTFG7/CASTEP	2013	2.6
OTFG9/CASTEP	2015	0.7
GPAW06/GPAW	2010	3.6
GPAW09/GPAW	2012	1.6
PSlib031/QE	2013	1.7
PSlib100/QE	2013	1.0
VASP2007/VASP	2007	2.0
VASP2012/VASP	2012	0.8
VASPGW2015/VASP	2015	0.6

mutual  $\Delta$  of 1 or even 2 meV per atom can be deemed to yield indistinguishable EOS for all practical purposes.

The above-mentioned differences correspond to the best attainable precision for each all-electron code, using highly converged or “ultimate” compu-

tational settings. However, particular choices for these settings may still slightly change the  $\Delta$  values. It is not always necessary to set such stringent requirements, because efficient codes are able to perform well with less-than-perfect settings. Nevertheless, the difference between default- and ultimate-precision EOS may sometimes reach a few millielectron volts per atom (table S2). To eliminate the effect of numerical convergence altogether, we used the osmium crystal to test whether it is possible to obtain exactly the same result with different codes. Rather than aiming for the best representation of the ideal PBE results, as in the rest of this work, the goal in this case was to choose input settings as consistently as possible (using the same basis functions, grids, and other parameters). Comparing four APW+lo (augmented plane waves plus local orbitals) calculations in this way yielded the results in Table 1. Whereas numerical noise in various subroutines gives rise to fluctuations of only 0.02 to 0.04 meV per atom, the larger deviation of  $\sim 0.2$  meV per atom in comparisons involving the code known as “exciting” can partly be attributed to a different scalar-relativistic treatment of the valence electrons in this code. There is no single universal method to account for the relativistic change of the electron mass in the kinetic energy. The “exciting” code uses the infinite-order regular approximation (53), whereas the other three APW+lo codes use the Koelling-Harmon scheme (54). A third possibility is to use the atomic zero-order regular approximation, as was done in the FHI-aims code package (tables S5 to S7) (42, 55).

**Comparing (pseudo)potential libraries**

In comparison with all-electron codes, pseudization approaches are generally faster, because fewer states are considered, and explicit construction and diagonalization of the Hamiltonian matrix is avoided. Among these, PAW and ultrasoft pseudopotentials require fewer basis functions than the norm-conserving variety, but advanced features such as linear response theory or hybrid functionals sometimes may not be available because of the increased complexity of the implementation. However, pseudization approaches all perform very well in terms of precision when compared with all-electron results (Fig. 4). For EOS, the precision of current potentials is able to compete with that of all-electron methods, yielding  $\Delta$  values of about 1 meV per atom, with a low approaching 0.3 meV per atom. This has not always been the case. As suggested by the example of silicon (Fig. 1), the available potentials have improved considerably over time. In Table 2, it can be seen that for several codes, the  $\Delta$  value is smaller for newer potential sets. Moreover, older potentials such as the Troullier-Martins FHI98pp norm-conserving set in ABINIT or the Vanderbilt-type ultrasoft sets in Dacapo and CASTEP all have a substantially larger  $\Delta$  (Fig. 4). This evolution is evidence of internal quality-control mechanisms used by developers of potentials in the past, as well as of additional, more recent efforts based on the  $\Delta$  gauge [e.g., the Jollet-Torrent-Holzwarth (JTH) and Standard Solid-State Pseudopotentials

		AE							
		average $\langle \Delta \rangle$	Elk	exciting	FHI-aims/tier2	FLEUR	FPLO/T+Fs	RSpt	WIEN2k/acc
AE	Elk	0.6		0.3	0.3	0.6	1.0	0.9	0.3
	exciting	0.5	0.3		0.1	0.5	0.9	0.8	0.2
	FHI-aims/tier2	0.5	0.3	0.1		0.5	0.9	0.8	0.2
	FLEUR	0.6	0.6	0.5	0.5		0.8	0.6	0.4
	FPLO/T+Fs	0.9	1.0	0.9	0.9	0.8		0.9	0.9
	RSpt	0.8	0.9	0.8	0.8	0.6	0.9		0.8
	WIEN2k/acc	0.5	0.3	0.2	0.2	0.4	0.9	0.8	
PAW	GBRV12/ABINIT	0.9	0.9	0.8	0.8	0.9	1.3	1.1	0.8
	GPAW09/ABINIT	1.4	1.3	1.3	1.3	1.3	1.7	1.5	1.3
	GPAW09/GPAW	1.6	1.5	1.5	1.5	1.5	1.8	1.7	1.5
	JTH02/ABINIT	0.6	0.6	0.6	0.6	0.6	0.9	0.7	0.5
	PSlib100/QE	0.9	0.9	0.8	0.8	0.8	1.3	1.1	0.8
	VASPGW2015/VASP	0.6	0.4	0.4	0.4	0.6	1.0	0.8	0.3
USPP	GBRV14/CASTEP	1.1	1.1	1.1	1.0	1.0	1.4	1.3	1.0
	GBRV14/QE	1.1	1.0	1.0	0.9	1.0	1.4	1.3	1.0
	OTFG9/CASTEP	0.7	0.4	0.5	0.5	0.7	1.0	1.0	0.5
	SSSP/QE	0.5	0.4	0.3	0.3	0.5	0.9	0.8	0.3
	Vdb2/DACAPO	6.3	6.3	6.3	6.3	6.3	6.4	6.5	6.2
NCPP	FHI98pp/ABINIT	13.3	13.5	13.4	13.4	13.2	13.0	13.2	13.4
	HGH/ABINIT	2.2	2.2	2.2	2.2	2.0	2.3	2.2	2.1
	HGH-NLCC/BigDFT	1.1	1.1	1.1	1.1	1.0	1.2	1.1	1.0
	MBK2013/OpenMX	2.0	2.1	2.1	2.1	1.9	1.8	1.8	2.0
	ONCVSP (PD0.1) /ABINIT	0.7	0.7	0.7	0.7	0.6	1.0	0.8	0.6
	ONCVSP (SG15) 1/QE	1.4	1.4	1.3	1.3	1.3	1.6	1.5	1.3
ONCVSP (SG15) 2/CASTEP	1.4	1.4	1.4	1.4	1.3	1.6	1.5	1.4	

**Fig. 4.  $\Delta$  values for comparisons between the most important DFT methods considered (in millielectron volts per atom).** Shown are comparisons of all-electron (AE), PAW, ultrasoft (USPP), and norm-conserving pseudopotential (NCP) results with all-electron results (methods are listed in alphabetical order in each category). The labels for each method stand for code, code/specification (AE), or potential set/code (PAW, USPP, and NCP) and are explained in full in tables S3 to S42. The color coding illustrates the range from small (green) to large (red)  $\Delta$  values. The mixed potential set SSSP was added to the ultrasoft category, in agreement with its prevalent potential type. Both the code settings and the DFT-predicted EOS parameters behind these numbers are included in tables S3 to S42, and fig. S1 provides a full  $\Delta$  matrix for all methods mentioned in this article.

(SSSP) libraries]. The considerable difference in the older potentials, even for the predefined structures in this relatively simple test set, provides a compelling argument to use only the most recent potential files of a given code.

In addition to the comparison with all-electron codes, it is also interesting to assess how the same PAW or pseudopotential recipes are implemented in different ways. When both the GPAW and ABINIT codes use the GPAW 0.9 PAW set,

for example, they agree to within a  $\Delta$  of 0.6 meV per atom. A similar correspondence is found for the Schlipf-Gygi 2015-01-24 optimized norm-conserving Vanderbilt pseudopotentials (ONCVSP) (0.3 meV per atom between Quantum ESPRESSO and CASTEP), the Garrity-Bennett-Rabe-Vanderbilt (GBRV) 1.4 ultrasoft pseudopotentials (0.3 meV per atom between Quantum ESPRESSO and CASTEP) and the GBRV 1.2 set (0.7 meV per atom between PAW potentials in ABINIT and ultrasoft poten-

tials in Quantum ESPRESSO). In this case, too, the small  $\Delta$  values indicate a good agreement between codes. This agreement moreover encompasses varying degrees of numerical convergence, differences in the numerical implementation of the particular potentials, and computational differences beyond the pseudization scheme, most of which are expected to be of the same order of magnitude or smaller than the differences among all-electron codes (1 meV per atom at most).

## Conclusions and outlook

Solid-state DFT codes have evolved considerably. The change from small and personalized codes to widespread general-purpose packages has pushed developers to aim for the best possible precision. Whereas past DFT-PBE literature on the lattice parameter of silicon indicated a spread of 0.05 Å, the most recent versions of the implementations discussed here agree on this value within 0.01 Å (Fig. 1 and tables S3 to S42). By comparing codes on a more detailed level using the  $\Delta$  gauge, we have found the most recent methods to yield nearly indistinguishable EOS, with the associated error bar comparable to that between different high-precision experiments. This underpins the validity of recent DFT EOS results and confirms that correctly converged calculations yield reliable predictions. The implications are moreover relevant throughout the multidisciplinary set of fields that build upon DFT results, ranging from the physical to the biological sciences.

In spite of the absence of one absolute reference code, we were able to improve and demonstrate the reproducibility of DFT results by means of a pairwise comparison of a wide range of codes and methods. It is now possible to verify whether any newly developed methodology can reach the same precision described here, and new DFT applications can be shown to have used a method and/or potentials that were screened in this way. The data generated in this study serve as a crucial enabler for such a reproducibility-driven paradigm shift, and future updates of available  $\Delta$  values will be presented at <http://molmod.ugent.be/deltacodesdft>. The reproducibility of reported results also provides a sound basis for further improvement to the accuracy of DFT, particularly in the investigation of new DFT functionals, or for the development of new computational approaches. This work might therefore substantially accelerate methodological advances in solid-state DFT.

Future work can examine the reproducibility of different codes even further. Such work might involve larger benchmark sets (describing different atomic environments per element), other functionals, an exhaustive comparison of different relativistic treatments, and/or a more detailed account of computational differences (using databases or scripts, for example). The precision of band gaps, magnetic anisotropies, and other non-EOS properties would also be of interest. However, the current investigation of EOS parameters provides the most important pass-fail test of the quality of different implementations of Kohn-Sham theory. A method that is not able to reach



an acceptable precision with respect to the EOS of the elemental crystals will probably not fulfill even more stringent demands.

## Methods summary

This study relied on the collective efforts of a large group of developers and expert users to make pairwise comparisons of widely used DFT codes. We compared 40 DFT methods in terms of  $\Delta$ , which expresses the root-mean-square difference between the EOS of two codes, averaged over a benchmark set of 71 elemental crystals (Eq. 1). Our approach, including details about the codes used, is described further in the supplementary materials. The reported settings yield highly converged results but may not be necessary for typical DFT applications. In particular, the use of sometimes very small electronic smearing widths requires much higher numbers of k-points than routine DFT calculations warrant.

## REFERENCES AND NOTES

- Open Science Collaboration, Estimating the reproducibility of psychological science. *Science* **349**, aac4716 (2015). doi: [10.1126/science.aac4716](https://doi.org/10.1126/science.aac4716); pmid: [26315443](https://pubmed.ncbi.nlm.nih.gov/26315443/)
- A checklist for photovoltaic research. *Nat. Mater.* **14**, 1073 (2015). pmid: [25613704](https://pubmed.ncbi.nlm.nih.gov/25613704/)
- W. F. van Gunsteren, The seven sins in academic behavior in the natural sciences. *Angew. Chem. Int. Ed.* **52**, 118–122 (2013). doi: [10.1002/anie.201204076](https://doi.org/10.1002/anie.201204076); pmid: [23203439](https://pubmed.ncbi.nlm.nih.gov/23203439/)
- C. Drummond, N. Japkowicz, W. Klement, S. Macskassy, "Replicability is not reproducibility: Nor is it good science," in *Proceedings, Twenty-Sixth International Conference on Machine Learning*, L. Bottou, M. Littman, Eds. (2009); [www.csi.uottawa.ca/~cdrummon/pubs/ICMLws09.pdf](http://www.csi.uottawa.ca/~cdrummon/pubs/ICMLws09.pdf).
- G. Miller, A scientist's nightmare: Software problem leads to five retractions. *Science* **314**, 1856–1857 (2006). doi: [10.1126/science.314.5807.1856](https://doi.org/10.1126/science.314.5807.1856); pmid: [17185570](https://pubmed.ncbi.nlm.nih.gov/17185570/)
- M. Viñhien, No more hidden solutions in bioinformatics. *Nature* **521**, 261 (2015). doi: [10.1038/521261a](https://doi.org/10.1038/521261a); pmid: [25993922](https://pubmed.ncbi.nlm.nih.gov/25993922/)
- D. C. Ince, L. Hatton, J. Graham-Cumming, The case for open computer programs. *Nature* **482**, 485–488 (2012). doi: [10.1038/nature10836](https://doi.org/10.1038/nature10836); pmid: [22358837](https://pubmed.ncbi.nlm.nih.gov/22358837/)
- P. Hohenberg, W. Kohn, Inhomogeneous electron gas. *Phys. Rev.* **136**, B864–B871 (1964). doi: [10.1103/PhysRev.136.B864](https://doi.org/10.1103/PhysRev.136.B864)
- W. Kohn, L. J. Sham, Self-consistent equations including exchange and correlation effects. *Phys. Rev.* **140**, A1133–A1138 (1965). doi: [10.1103/PhysRev.140.A1133](https://doi.org/10.1103/PhysRev.140.A1133)
- R. O. Jones, Density functional theory: Its origins, rise to prominence, and future. *Rev. Mod. Phys.* **87**, 897–923 (2015). doi: [10.1103/RevModPhys.87.897](https://doi.org/10.1103/RevModPhys.87.897)
- S. Curtarolo et al., AFLOW: An automatic framework for high-throughput materials discovery. *Comput. Mater. Sci.* **58**, 218–226 (2012). doi: [10.1016/j.commatsci.2012.02.005](https://doi.org/10.1016/j.commatsci.2012.02.005)
- A. Jain et al., Commentary: The Materials Project: A materials genome approach to accelerating materials innovation. *APL Mater.* **1**, 011002 (2013). doi: [10.1063/1.4812323](https://doi.org/10.1063/1.4812323)
- C.-C. Fu, J. Dalla Torre, F. Willaime, J.-L. Bocquet, A. Barbu, Multiscale modelling of defect kinetics in irradiated iron. *Nat. Mater.* **4**, 68–74 (2005). doi: [10.1038/nmat1286](https://doi.org/10.1038/nmat1286)
- M. Friák et al., Methodological challenges in combining quantum-mechanical and continuum approaches for materials science applications. *Eur. Phys. J. Plus* **126**, 101 (2011). doi: [10.1140/epjp/i2011-11101-2](https://doi.org/10.1140/epjp/i2011-11101-2)
- S. Kurth, J. P. Perdew, P. Blaha, Molecular and solid-state tests of density functional approximations: LSD, GGAs, and Meta-GGAs. *Int. J. Quantum Chem.* **75**, 889–909 (1999). doi: [10.1002/\(SICI\)1097-461X\(1999\)75:4<889::AID-QUA54>3.0.CO;2-8](https://doi.org/10.1002/(SICI)1097-461X(1999)75:4<889::AID-QUA54>3.0.CO;2-8)
- V. N. Staroverov, G. E. Scuseria, J. Tao, J. P. Perdew, Tests of a ladder of density functionals for bulk solids and surfaces. *Phys. Rev. B* **69**, 075102 (2004). doi: [10.1103/PhysRevB.69.075102](https://doi.org/10.1103/PhysRevB.69.075102)
- P. Haas, F. Tran, P. Blaha, Calculation of the lattice constant of solids with semilocal functionals. *Phys. Rev. B* **79**, 085104 (2009). doi: [10.1103/PhysRevB.79.085104](https://doi.org/10.1103/PhysRevB.79.085104)
- G. I. Csonka et al., Assessing the performance of recent density functionals for bulk solids. *Phys. Rev. B* **79**, 155107 (2009). doi: [10.1103/PhysRevB.79.155107](https://doi.org/10.1103/PhysRevB.79.155107)
- P. Pernot, B. Civalieri, D. Presti, A. Savin, Prediction uncertainty of density functional approximations for properties of crystals with cubic symmetry. *J. Phys. Chem. A* **119**, 5288–5304 (2015). doi: [10.1021/jp509980w](https://doi.org/10.1021/jp509980w); pmid: [25626469](https://pubmed.ncbi.nlm.nih.gov/25626469/)
- L. A. Curtiss, K. Raghavachari, P. C. Redfern, J. A. Pople, Assessment of Gaussian-2 and density functional theories for the computation of enthalpies of formation. *J. Chem. Phys.* **106**, 1063 (1997). doi: [10.1063/1.473182](https://doi.org/10.1063/1.473182)
- J. Paier, R. Hirschl, M. Marsman, G. Kresse, The Perdew-Burke-Ernzerhof exchange-correlation functional applied to the G2-1 test set using a plane-wave basis set. *J. Chem. Phys.* **122**, 234102 (2005). doi: [10.1063/1.1926272](https://doi.org/10.1063/1.1926272); pmid: [16008425](https://pubmed.ncbi.nlm.nih.gov/16008425/)
- Y. Zhao, D. G. Truhlar, Density functionals with broad applicability in chemistry. *Acc. Chem. Res.* **41**, 157–167 (2008). doi: [10.1021/ar700111a](https://doi.org/10.1021/ar700111a); pmid: [18186612](https://pubmed.ncbi.nlm.nih.gov/18186612/)
- L. Goerigk, S. Grimme, A thorough benchmark of density functional methods for general main group thermochemistry, kinetics, and noncovalent interactions. *Phys. Chem. Chem. Phys.* **13**, 6670–6688 (2011). doi: [10.1039/c0cp02984j](https://doi.org/10.1039/c0cp02984j); pmid: [21384027](https://pubmed.ncbi.nlm.nih.gov/21384027/)
- A. Kiejna et al., Comparison of the full-potential and frozen-core approximation approaches to density-functional calculations of surfaces. *Phys. Rev. B* **73**, 035404 (2006). doi: [10.1103/PhysRevB.73.035404](https://doi.org/10.1103/PhysRevB.73.035404)
- B. Grabowski, T. Hickel, J. Neugebauer, *Ab initio* study of the thermodynamic properties of nonmagnetic elementary fcc metals: Exchange-correlation-related error bars and chemical trends. *Phys. Rev. B* **76**, 024309 (2007). doi: [10.1103/PhysRevB.76.024309](https://doi.org/10.1103/PhysRevB.76.024309)
- K. Lejaeghere, V. Van Speybroeck, G. Van Oost, S. Cottenier, Error estimates for solid-state density-functional theory predictions: An overview by means of the ground-state elemental crystals. *Crit. Rev. Solid State* **39**, 1–24 (2014). doi: [10.1080/10408436.2013.772503](https://doi.org/10.1080/10408436.2013.772503)
- F. Jollet, M. Torrent, N. Holzwarth, Generation of Projector Augmented-Wave atomic data: A 71 element validated table in the XML format. *Comput. Phys. Commun.* **185**, 1246–1254 (2014). doi: [10.1016/j.cpc.2013.12.023](https://doi.org/10.1016/j.cpc.2013.12.023)
- E. Küçükbenli et al., <http://arxiv.org/abs/1404.3015> (2014).
- S. Poncé et al., Verification of first-principles codes: Comparison of total energies, phonon frequencies, electron-phonon coupling and zero-point motion correction to the gap between ABINIT and QE/Yambo. *Comput. Mater. Sci.* **83**, 341–348 (2014). doi: [10.1016/j.commatsci.2013.11.031](https://doi.org/10.1016/j.commatsci.2013.11.031)
- The studies of accuracy and precision for DFT calculations are often referred to as validation and verification (V&V), respectively.
- D. R. Hamann, M. Schlüter, C. Chiang, Norm-conserving pseudopotentials. *Phys. Rev. Lett.* **43**, 1494–1497 (1979). doi: [10.1103/PhysRevLett.43.1494](https://doi.org/10.1103/PhysRevLett.43.1494)
- L. Kleinman, D. M. Bylander, Efficacious form for model pseudopotentials. *Phys. Rev. Lett.* **48**, 1425–1428 (1982). doi: [10.1103/PhysRevLett.48.1425](https://doi.org/10.1103/PhysRevLett.48.1425)
- D. Vanderbilt, Soft self-consistent pseudopotentials in a generalized eigenvalue formalism. *Phys. Rev. B* **59**, 1758–1775 (1999). doi: [10.1103/PhysRevB.59.1758](https://doi.org/10.1103/PhysRevB.59.1758)
- J. C. Slater, Wave functions in a periodic potential. *Phys. Rev.* **51**, 846–851 (1937). doi: [10.1103/PhysRev.51.846](https://doi.org/10.1103/PhysRev.51.846)
- O. K. Andersen, Linear methods in band theory. *Phys. Rev. B* **12**, 3060–3083 (1975). doi: [10.1103/PhysRevB.12.3060](https://doi.org/10.1103/PhysRevB.12.3060)
- E. Sjöstedt, L. Nordström, D. J. Singh, An alternative way of linearizing the augmented plane-wave method. *Solid State Commun.* **114**, 15–20 (2000). doi: [10.1016/S0038-1098\(99\)00577-3](https://doi.org/10.1016/S0038-1098(99)00577-3)
- G. K. H. Madsen, P. Blaha, K. Schwarz, E. Sjöstedt, L. Nordström, Efficient linearization of the augmented plane-wave method. *Phys. Rev. B* **64**, 195134 (2001). doi: [10.1103/PhysRevB.64.195134](https://doi.org/10.1103/PhysRevB.64.195134)
- J. M. Wills et al., *Full-Potential Electronic Structure Method*, vol. 167 of *Springer Series in Solid-State Sciences* (Springer-Verlag, 2010).
- K. Koepernik, H. Eschrig, Full-potential nonorthogonal local-orbital minimum-basis band-structure scheme. *Phys. Rev. B* **59**, 1743–1757 (1999). doi: [10.1103/PhysRevB.59.1743](https://doi.org/10.1103/PhysRevB.59.1743)
- V. Blum et al., *Ab initio* molecular simulations with numeric atom-centered orbitals. *Comput. Phys. Commun.* **180**, 2175–2196 (2009). doi: [10.1016/j.cpc.2009.06.022](https://doi.org/10.1016/j.cpc.2009.06.022)
- J. P. Perdew, K. Burke, M. Ernzerhof, Generalized gradient approximation made simple. *Phys. Rev. Lett.* **77**, 3865–3868 (1996). doi: [10.1103/PhysRevLett.77.3865](https://doi.org/10.1103/PhysRevLett.77.3865); pmid: [10062328](https://pubmed.ncbi.nlm.nih.gov/10062328/)
- G. Yuan, F. Gygi, ESTEST: A framework for the validation and verification of electronic structure codes. *Comput. Sci. Discov.* **3**, 015004 (2010). doi: [10.1088/1749-4699/3/1/015004](https://doi.org/10.1088/1749-4699/3/1/015004)
- The NoMaD Repository, <http://nomad-repository.eu>.
- S. R. Bahn, K. W. Jacobsen, An object-oriented scripting interface to a legacy electronic structure code. *Comput. Sci. Eng.* **4**, 56–66 (2002). doi: [10.1109/5992.998641](https://doi.org/10.1109/5992.998641)
- G. Pizzi, A. Cepellotti, R. Sabatini, N. Marzari, B. Kozinsky, AiiDA: Automated interactive infrastructure and database for computational science. *Comput. Mater. Sci.* **111**, 218–230 (2016). doi: [10.1016/j.commatsci.2015.09.013](https://doi.org/10.1016/j.commatsci.2015.09.013)
- Scripts are available at <https://cmr.fysik.dtu.dk/dcdft/dcdft.html>.
- W. B. Holzapfel, M. Hartwig, W. Sievers, Equations of state for Cu, Ag, and Au for wide ranges in temperature and pressure up to 500 GPa and above. *J. Phys. Chem. Ref. Data* **30**, 515 (2001). doi: [10.1063/1.1370170](https://doi.org/10.1063/1.1370170)
- C. Kittel, *Introduction to Solid State Physics* (Wiley, ed. 8, 2005).
- E. Knittle, in *Mineral Physics and Crystallography: A Handbook of Physical Constants*, T. Ahrens, Ed. (American Geophysical Union, 1995), pp. 98–142.
- W. A. Grosshans, W. B. Holzapfel, Atomic volumes of rare-earth metals under pressures to 40 GPa and above. *Phys. Rev. B* **45**, 5171–5178 (1992). doi: [10.1103/PhysRevB.45.5171](https://doi.org/10.1103/PhysRevB.45.5171); pmid: [10000231](https://pubmed.ncbi.nlm.nih.gov/10000231/)
- K. G. Dyall, E. van Lenthe, Relativistic regular approximations revisited: An infinite-order relativistic approximation. *J. Chem. Phys.* **111**, 1366 (1999). doi: [10.1063/1.479395](https://doi.org/10.1063/1.479395)
- D. D. Koelling, B. N. Harmon, A technique for relativistic spin-polarized calculations. *J. Phys. C Solid State Phys.* **10**, 3107–3114 (1977). doi: [10.1088/0022-3719/10/16/019](https://doi.org/10.1088/0022-3719/10/16/019)
- E. van Lenthe, E. Baerends, J. Snijders, Relativistic total energy using regular approximations. *J. Chem. Phys.* **101**, 9783 (1994). doi: [10.1063/1.467943](https://doi.org/10.1063/1.467943)
- I.-H. Lee, R. M. Martin, Applications of the generalized-gradient approximation to atoms, clusters, and solids. *Phys. Rev. B* **56**, 7197–7205 (1997). doi: [10.1103/PhysRevB.56.7197](https://doi.org/10.1103/PhysRevB.56.7197)
- T. Miyake, T. Ogitsu, S. Tsuneyuki, Quantum distributions of muonium and hydrogen in crystalline silicon. *Phys. Rev. Lett.* **81**, 1873–1876 (1998). doi: [10.1103/PhysRevLett.81.1873](https://doi.org/10.1103/PhysRevLett.81.1873)
- W. Windl, M. M. Bunea, R. Stumpf, S. T. Dunham, M. P. Masquellier, First-principles study of boron diffusion in silicon. *Phys. Rev. Lett.* **83**, 4345–4348 (1999). doi: [10.1103/PhysRevLett.83.4345](https://doi.org/10.1103/PhysRevLett.83.4345)
- L. Vitos, B. Johansson, J. Kollár, H. Skriver, Exchange energy in the local Airy gas approximation. *Phys. Rev. B* **62**, 10046–10050 (2000). doi: [10.1103/PhysRevB.62.10046](https://doi.org/10.1103/PhysRevB.62.10046)
- R. Miotto, G. P. Srivastava, A. C. Ferraz, Dissociative adsorption of PH<sub>3</sub> on the Si(001) surface. *Phys. Rev. B* **63**, 125321 (2001). doi: [10.1103/PhysRevB.63.125321](https://doi.org/10.1103/PhysRevB.63.125321)
- L. E. Ramos et al., Structural, electronic, and effective-mass properties of silicon and zinc-blende group-III nitride semiconductor compounds. *Phys. Rev. B* **63**, 165210 (2001). doi: [10.1103/PhysRevB.63.165210](https://doi.org/10.1103/PhysRevB.63.165210)
- L. V. C. Assali, W. V. M. Machado, J. F. Justo, Titanium impurities in silicon, diamond, and silicon carbide. *Braz. J. Phys.* **34**, 602–604 (2004). doi: [10.1590/S0103-97332004000400016](https://doi.org/10.1590/S0103-97332004000400016)
- J. Heyd, J. E. Peralta, G. E. Scuseria, R. L. Martin, Energy band gaps and lattice parameters evaluated with the Heyd-Scuseria-Ernzerhof screened hybrid functional. *J. Chem. Phys.* **123**, 174101 (2005). doi: [10.1063/1.2085170](https://doi.org/10.1063/1.2085170); pmid: [16375511](https://pubmed.ncbi.nlm.nih.gov/16375511/)
- J. Paier et al., Screened hybrid density functionals applied to solids. *J. Chem. Phys.* **124**, 154709 (2006). doi: [10.1063/1.2187006](https://doi.org/10.1063/1.2187006); pmid: [16674253](https://pubmed.ncbi.nlm.nih.gov/16674253/)
- F. Tran, R. Laskowski, P. Blaha, K. Schwarz, Performance on molecules, surfaces, and solids of the Wu-Cohen GGA exchange-correlation energy functional. *Phys. Rev. B* **75**, 115131 (2007). doi: [10.1103/PhysRevB.75.115131](https://doi.org/10.1103/PhysRevB.75.115131)

## ACKNOWLEDGMENTS

This research benefited from financial support from the Research Board of Ghent University; the Fond de la Recherche Scientifique de Belgique (FRS-FNRS), through Projet de Recherches (PDR) grants T.0238.13-AIXPHO and T.1031.14-HIT4FIT; the Communauté Française de Belgique, through the BATTAB project (grant ARC

14/19-057); the U.S. NSF (grant DMR-14-08838); the Swedish Research Council; the Knut and Alice Wallenberg Foundation (grants 2013.0020 and 2012.0031); the Fund for Scientific Research–Flanders (FWO) (project no. G0E0116N); and the U.S. Department of Energy (grant DOE-BES DE-SC0008938). N.A.W.H. was supported by U.S. NSF grant DMR-1105485. J.A.F.-L. acknowledges financial support from the European Union's 7th Framework Marie-Curie Scholarship Program within the ExMaMa Project (project no. 329386). I.D.M., O.E., O.G., D.I., Y.O.K., I.L.M.L., and L.N. acknowledge support from eSENCE. T.B. was supported by the Academy of Finland (grant 263416) and the COMP Centre of Excellence. C.D., A.G., and S.L. acknowledge support from the Deutsche Forschungsgemeinschaft (DFG) and the Einstein Foundation, Berlin. M.Sche. and C.D. received funding from the European Union's Horizon 2020 research and innovation program under grant agreement no. 676580 with The Novel Materials Discovery (NOMAD) Laboratory, a European Center of Excellence. A.D.C., S.d.G., and E.K. acknowledge support from the Italian Ministry of Education, Universities, and Research (MIUR) through PRIN (Projects of National Interest) 2010–2011 (registration no. 20105ZZTSE\_005). P.J.H., D.B.J., and M.I.J.P. are grateful for financial support by the Engineering and Physical Sciences Research Council (EPSRC) under UK Car-Parrinello (UKCP) grant EP/K013564/1. C.J.P. and J.R.Y. acknowledge support from the Collaborative Computational Project for NMR Crystallography under EPSRC grant EP/J010510/1. W.P. acknowledges funding by

FWO. D.J. is grateful for financial support by EPSRC under grant EP/J017639/1. S.Sa. acknowledges support from the Swiss National Science Foundation (SNSF). G.-M.R. is thankful for personal financial support from FRS-FNRS. The work by I.E.C. and N.M. was supported by the SNSF's National Centre of Competence in Research MARVEL. G.K. and P.B. acknowledge support by the Austrian Science Fund, project SFB-F41 (ViCoM). S.C. acknowledges financial support from OCAS NV by an OCAS-endowed chair at Ghent University. Computational resources were as follows: The Ghent University contributors used the Stevin Supercomputer Infrastructure at Ghent University, which is funded by Ghent University, FWO, and the Flemish Government (Economy, Science, and Innovation Department). The Université Catholique de Louvain contributors used the Tier-1 supercomputer of the Fédération Wallonie-Bruxelles (funded by the Walloon Region under grant agreement no. 1117545), the Centre de Calcul Intensif et de Stockage de Masse–Université Catholique de Louvain supercomputing facilities, and the Consortium des Équipements de Calcul Intensif en Fédération Wallonie-Bruxelles (CÉCI) (funded by the FRS-FNRS under convention 2.5020.11). The Science and Technology Facilities Council, Scientific Computing Department's SCARF (Scientific Computing Application Resource for Facilities) cluster was used for the CASTEP calculations. The Basel University and École Polytechnique Fédérale de Lausanne contributors used the Swiss National Supercomputing Center in Lugano. Finland's IT Centre for Science was used for the RSPT calculations. K.L. and

F.T. thank C. Becker for instructive discussions on the comparison of atomic-scale simulations. K.L. and S.C. thank W. Dewitte for drafting the summary figure. S.J.C., P.J.H., C.J.P., M.I.J.P., K.R., and J.R.Y. declare the receipt of income from commercial sales of CASTEP by Biovia. N.M. and M.Sche. are members of the Board of Trustees of the Psi-k Electronic Structure Network. P.G. is director of the Quantum ESPRESSO Foundation, and N.M. is a representative member. X.G., D.R.H., M.T., D.C., F.J., and G.-M.R. are members of the Advisory Board of ABINIT, an organization that develops and publishes open-source software related to this article. Commercial software is identified to specify procedures. Such identification does not imply recommendation by the National Institute of Standards and Technology. Atomic Simulation Environment scripts (46) for several of the codes are available online (48). All data are listed in tables S3 to S42.

#### SUPPLEMENTARY MATERIALS

[www.sciencemag.org/content/351/6280/aad3000/suppl/DC1](http://www.sciencemag.org/content/351/6280/aad3000/suppl/DC1)

Materials and Methods

Fig. S1

Tables S1 to S42

References (66–115)

27 August 2015; accepted 19 February 2016  
10.1126/science.aad3000



## RESEARCH ARTICLE

## STRUCTURAL BIOLOGY

## Molecular architecture of the human U4/U6.U5 tri-snRNP

Dmitry E. Agafonov,<sup>1\*</sup> Berthold Kastner,<sup>1\*</sup> Olexandr Dybkov,<sup>1\*</sup> Romina V. Hofele,<sup>2,3,†</sup> Wen-Ti Liu,<sup>4,5</sup> Henning Urlaub,<sup>2,3,†</sup> Reinhard Lührmann,<sup>1,†</sup> Holger Stark<sup>4,5,†</sup>

The U4/U6.U5 triple small nuclear ribonucleoprotein (tri-snRNP) is a major spliceosome building block. We obtained a three-dimensional structure of the 1.8-megadalton human tri-snRNP at a resolution of 7 angstroms using single-particle cryo-electron microscopy (cryo-EM). We fit all known high-resolution structures of tri-snRNP components into the EM density map and validated them by protein cross-linking. Our model reveals how the spatial organization of Brr2 RNA helicase prevents premature U4/U6 RNA unwinding in isolated human tri-snRNPs and how the ubiquitin C-terminal hydrolase-like protein Sad1 likely tethers the helicase Brr2 to its preactivation position. Comparison of our model with cryo-EM three-dimensional structures of the *Saccharomyces cerevisiae* tri-snRNP and *Schizosaccharomyces pombe* spliceosome indicates that Brr2 undergoes a marked conformational change during spliceosome activation, and that the scaffolding protein Prp8 is also rearranged to accommodate the spliceosome's catalytic RNA network.

The spliceosome is formed stepwise by recruitment of the U1 and U2 snRNPs (small nuclear ribonucleoproteins) and the U4/U6.U5 tri-snRNP, plus numerous other proteins, to the pre-mRNA (1). Initially, U1 and U2 interact with the pre-mRNA's 5' splice site (SS) and branch site (BS), respectively, generating the A complex. The tri-snRNP then joins, leading to formation of the precatalytic spliceosomal B complex. Subsequent catalytic activation of the spliceosome involves major structural rearrangements of multiple tri-snRNP components (1).

The 1.8-MDa tri-snRNP is the largest preformed building block of the human spliceosome. It contains three snRNA molecules (U4, U6, and U5), two heteroheptameric rings of Sm proteins bound to the U4 and U5 snRNAs' 3'-terminal Sm sites, the LSm ring bound to the 3' end of U6 snRNA, plus 16 additional proteins (1) (fig. S1). In the tri-snRNP and B complex, U4 and U6 snRNA are extensively base-paired. During activation, the U4/U6 duplex is disrupted and a highly structured RNA interaction network forms among the U2, U6, and U5 snRNAs and the pre-mRNA, generat-

ing the spliceosome's catalytic RNA core (2, 3). Three large U5 proteins—Prp8, the RNA helicase Brr2, and the guanosine triphosphatase (GTPase) Snu114—play key roles during catalytic activation. Prp8 is a major scaffolding protein that interacts with Brr2 and Snu114 (4) and all reactive sites of the intron (5'SS, 3'SS, and BS) and is thus located at the heart of the spliceosome's catalytic core (5, 6). Brr2 unwinds the U4/U6 snRNA helices and is the major driving force for catalytic activation (7, 8). However, as Brr2 and its RNA substrate are present in the tri-snRNP and precatalytic B complex, a mechanism must exist to prevent premature dissociation of the U4/U6 helices by Brr2.

Here, we report a 3D cryo-electron microscopy (cryo-EM) structure of the human tri-snRNP at a resolution of 7 Å and resolve its spatial organization with the aid of protein cross-linking. Comparison with the recently reported cryo-EM structure of the yeast tri-snRNP (9) reveals unexpected, large differences in the position of the helicase Brr2, including its position relative to its RNA substrate, the U4/U6 duplex. Our model also reveals the nature of tri-snRNP rearrangements that must occur during spliceosome maturation, including a major conformational change within the Prp8 protein, which adopts an open conformation in the human tri-snRNP and a closed one in the *Schizosaccharomyces pombe* spliceosome at late stages of splicing (10).

## Structure determination and model building

Human tri-snRNPs were affinity-purified from HeLa nuclear extract and prepared for cryo-EM by a modification of the GraFix protocol involving chemical cross-linking of the particles (fig. S1B) (11).

The 3D structure was determined from ~141,000 particle images after several steps of computational sorting, starting with an initial data set of ~1,150,000 selected particle images (fig. S2). The calculated 3D structure of the tri-snRNP was determined at a final overall resolution of 7 Å with better-resolved parts in the center and somewhat lower-resolution areas in the U4/U6 part of the structure (fig. S3). Overall, the structure is entirely consistent with an earlier, lower-resolution 3D structure (12) showing the tri-snRNP as a roughly tetrahedral particle with dimensions of approximately 300 Å × 200 Å × 175 Å (Fig. 1). At this resolution, structured protein domains and double-stranded RNA (dsRNA) elements can be identified clearly, allowing us to fit known x-ray structures or homology models of structured regions of tri-snRNP components into the EM density map (see table S1 for details regarding how proteins were fit into the EM density map). Additionally, we performed chemical protein cross-linking of purified tri-snRNPs together with mass spectrometry (CX-MS) (table S2). These data allowed us to validate the locations of large tri-snRNP proteins and facilitated docking of smaller proteins. Although we could place all snRNAs and structured protein domains in the EM density map in a manner consistent with our protein cross-linking data, ~30% of the calculated stoichiometric mass of human tri-snRNP proteins are very likely intrinsically unstructured regions that could not be localized (table S1).

## Structural organization of the U5 Sm core and the U4/U6 snRNP

The helical regions of U4/U6 and U5 snRNA allowed their unambiguous placement in the EM density map (Fig. 1). The U5 Sm core is located at the lower tip of the tri-snRNP, with the 5'-terminal m<sup>3</sup>G cap of U5 snRNA positioned close to it, whereas U5 loop 1 is located more centrally and stems 1b and 1c are coaxially stacked (Fig. 1B). The U4/U6 snRNAs are located in the upper, broader region of the human tri-snRNP. Their dsRNA regions are connected by a three-way junction and are located in a deeper, solvent-accessible cleft. The difference in length of U4/U6 stems I and II and the clearly visible three-way junction define the orientation of U4/U6 snRNA in the model and indicate coaxial stacking of stems I and II (Fig. 1). The U4/U6 snRNAs also define the positions of the U4 Sm and U6 LSm protein rings, which are found at two corners in the upper part of the tri-snRNP (Fig. 1B).

The geometry of the U4/U6 snRNA three-way junction allowed us to fit the crystal structures of (i) the U4 snRNA 5' stem-loop in complex with Snu13 and a large part of the U4/U6 Prp31 protein, (ii) a large part of Prp3 (Prp3-CTF) in complex with U4/U6 stem II and the U6 single-stranded 3' overhang, (iii) the WD40 domain of the Prp3-associated Prp4 protein, and (iv) the cyclophilin H (CypH) protein into nearby density elements (Fig. 2A). The position of the various U4/U6 proteins was confirmed by protein-protein cross-linking (fig. S4). There is an overall similarity in the organization of U4/U6 proteins in human and yeast

<sup>1</sup>Department of Cellular Biochemistry, Max Planck Institute for Biophysical Chemistry, D-37077 Göttingen, Germany.

<sup>2</sup>Bioanalytical Mass Spectrometry, Max Planck Institute for Biophysical Chemistry, D-37077 Göttingen, Germany.

<sup>3</sup>Bioanalytics Group, Institute for Clinical Chemistry, University Medical Center Göttingen, D-37075 Göttingen, Germany.

<sup>4</sup>Department of 3D Electron Cryomicroscopy, Georg-August Universität Göttingen, D-37077 Göttingen, Germany.

<sup>5</sup>Department of Structural Dynamics, Max Planck Institute for Biophysical Chemistry, D-37077 Göttingen, Germany.

\*These authors contributed equally to this work. †Present address: Medimmune, Gaithersburg, MD, USA. ‡Corresponding author. E-mail: reinhard.luehrmann@mpi-bpc.mpg.de (R.L.); hstark1@gwdg.de (H.S.); henning.urlaub@mpi-bpc.mpg.de (H.U.)

tri-snRNPs, with differences in the architectural details of some proteins (fig. S5) (see below).

The Prp6 protein contains 19 tetratricopeptide repeats (TPRs) in its C-terminal region and is required

for stable tri-snRNP formation (13, 14). Consistent with this, Prp6 forms a bridge across a deep cleft at the top of the tri-snRNP that connects the U4/U6 and U5 snRNPs (Fig. 2B). This is supported by

numerous cross-links, whereby Prp6's N-terminal and C-terminal TPRs exclusively form cross-links to U5 and U4/U6 proteins, respectively. Consistent with intramolecular cross-links between TPR 19

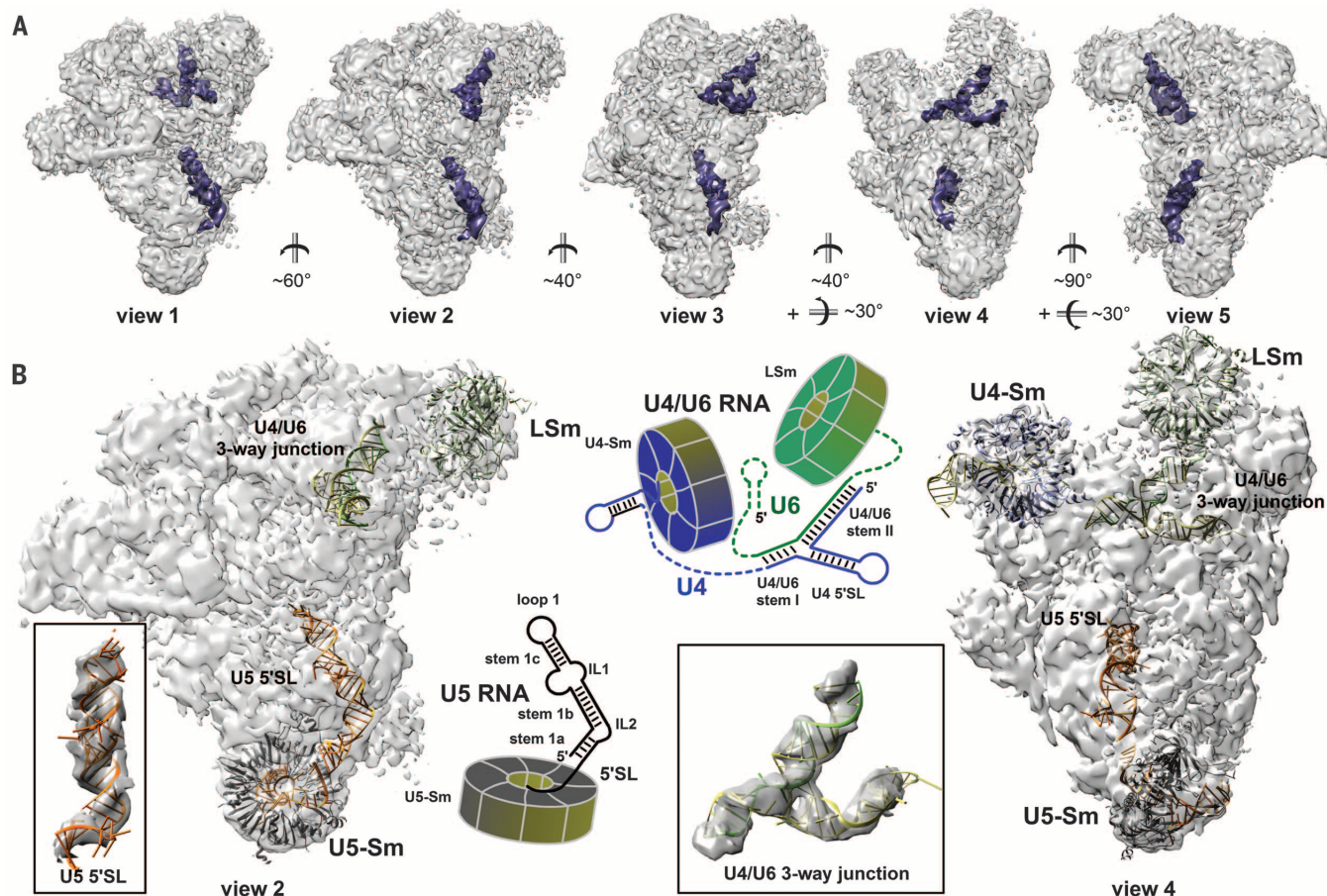


**Fig. 1. Three-dimensional cryo-EM structure of the human U4/U6.U5 tri-snRNP and location of U5 and U4/U6 snRNAs and their Sm/LSm cores.** (A) Different views of the tri-snRNP EM density map with helical high-density elements (blue) representing U5 (in lower region) and U4/U6 snRNA (upper region). (B) Position of the U5 Sm, U4 Sm, and U6 LSm cores. A schematic of U5 and U4/U6 snRNA with their Sm/LSm rings is shown. The double-stranded regions of U4/U6 and U5, and their heptameric Sm/LSm rings, are modeled into the cryo-EM map. Insets: RNA elements shown separately.

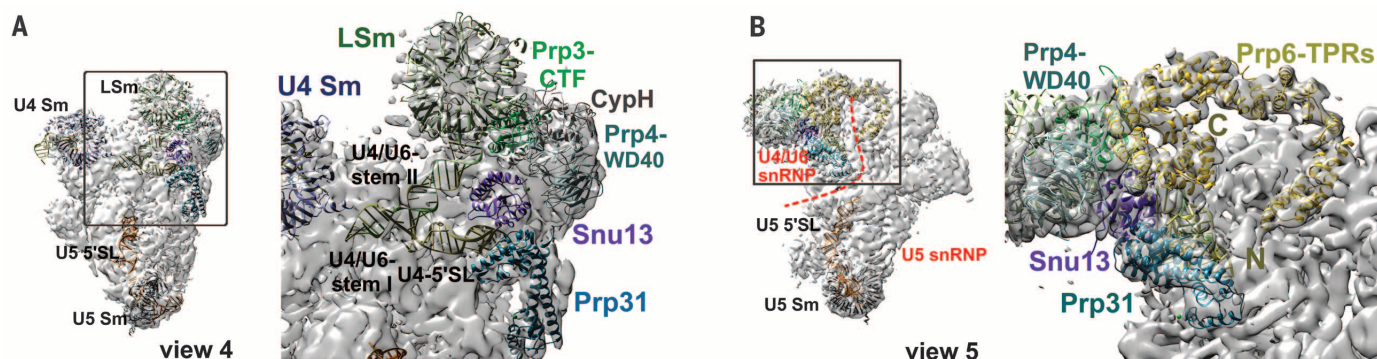


**Fig. 2. Structural organization of U4/U6 proteins and Prp6 and their locations in the human tri-snRNP.** (A) Positions of the U4/U6 proteins and snRNA. Right: Expanded view of boxed region showing the U4/U6 snRNA three-way junction, the crystal structures of Prp31, Snu13, CypH, and the C-terminal fragment (CTF) of Prp3, and a modeled structure of Prp4's WD40 domain, fit into the EM density map. (B) Prp6 forms a bridge connecting the U4/U6 and U5 snRNPs. Right: Expanded view of boxed region showing Prp6 TPR repeats and U4/U6 proteins.



and TPRs 9 to 13 (fig. S4), the C-terminal TPRs fit as a circularly arranged ensemble into a large ringlike density that is connected to U4/U6 proteins (Fig. 2B).

### The architecture of Snu114 and Prp8

Aside from its 115-residue N-terminal domain, the 116-kDa Snu114 protein is highly homologous to ribosomal elongation factor EF-2/EF-G (15), and we could fit domains D1 to D5 of Snu114 into the lower part of the tri-snRNP, with D1 and D2 located closer to the U5 Sm core and D3 to D5 located more centrally (Fig. 3A). Thus, in the isolated human tri-snRNP, Snu114 adopts a compact form similar to the compact structure of EF-2 (fig. S6) (16).

The crystal structure of a large fragment of yeast Prp8 (~110 kDa) containing a reverse transcriptase (RT)-like domain, connected through a linker region to a restriction endonuclease (En)-like domain, fits into a central density element at the base of the upper part of the tri-snRNP; the En domain points outward and is positioned below the U4 Sm core (Fig. 3A). Prp8's C-terminal RNase H (RH)-like domain could be docked into a density element located just above the linker region of the RT/En domain (Fig. 3A), and its orientation was confirmed by cross-linking (tables S1 and S2). The architecture of Prp8's RT/En domain and its position are essentially the same in the human and yeast tri-snRNP models, whereas Prp8's RH domain is rotated by ~180° in yeast relative to human (fig. S7) (9).

In the *S. pombe* spliceosome, Prp8's N-terminal 800 amino acids consist of two domains, henceforth termed NTD1 and NTD2, that contain mainly  $\alpha$  helices and are separated by a short linker region, termed NTDL (Fig. 3A) (10). The larger NTD1 structure fits into a density element in the lower part of the tri-snRNP model and has a substantial interface with Snu114 and also contacts stem1 of U5 snRNA (Fig. 3A) (see below). Consistent with our cross-linking data, the smaller NTD2 is located more toward the U4/U6 three-way junction and interacts with Prp8's RT domain (Fig. 3B and fig. S8A). The crystal structure of Dim1 fits into a density element between NTD1 and NTD2 (Fig. 3B), a position supported by cross-linking (fig. S8A). The overall structure of Prp8's NTD1 and Snu114 is similar in the human tri-snRNP and *S. pombe* spliceosome, including the lasso-like protrusion of NTD1 that interacts with Snu114's D1 domain in a similar manner in both complexes (fig. S8B) (10). Guided by multiple cross-links of the RecA2 domain of the Prp28 helicase to Prp8's NTD1 and RT/En domains (fig. S8A), we could fit the crystal structure of the two RecA domains into nearby density elements (Fig. 3C). Prp28, which is not present in isolated *Saccharomyces cerevisiae* tri-snRNPs, exists in an open (inactive) conformation, very similar to its conformation in the crystal structure of isolated Prp28 (17, 18). Finally, we could place the WD40 domain of U5-40K, which is conserved in *S. pombe* but not *S. cerevisiae*, into a density element close to U5's ILS1 (fig. S8C)—a position where it is also found in the *S. pombe* spliceosome (10).

### Brr2 helicase is found at very different positions in human and yeast tri-snRNPs

The 245-kDa RNA helicase Brr2 contains two tandemly organized helicase cassettes, but only the N-terminal cassette (NC) actively unwinds the U4/U6 duplex during catalytic activation (19). The C-terminal Prp8-Jab1 domain binds tightly to Brr2's active NC and regulates its helicase activity (20, 21). The crystal structure of the complete 200-kDa helicase unit of Brr2 bound to Prp8 Jab1 fits very well, as a rigid body, into a major density element in the upper part of the tri-snRNP, near the RT end of the Prp8-RT/En domain, opposite the U4 Sm and U6 LSm rings (Fig. 4A).

Besides this Brr2 NC-Prp8-Jab1 interaction, there appear to be at least two additional density elements connecting the helicase cassettes to other tri-snRNP proteins (Fig. 4, A to C). The N-terminal region of Brr2 contains a noncanonical PWI domain (22) and a helical domain (23). The PWI domain fits into the density element connecting Brr2's C-terminal cassette (CC) to Snu114 and Sad1 (Fig. 4B), while the N-terminal helical domain

(NHD) fits into a density element connecting Brr2's NC to Prp8's RH domain and to the N-terminal-most three TPR repeats of Prp6 (Fig. 4C and table S1). Interestingly, Brr2's NHD is located in front of the RNA binding channel between the RecA2 and helical bundle (HB) domain of Brr2's NC (Fig. 4C), consistent with this element acting like a plug, autoinhibiting Brr2 via substrate recognition (23). Brr2's architecture and its connections to the above-mentioned proteins were confirmed by a network of cross-links between Brr2's NHD and NC/CC domains, and between these domains and the Prp8's RH and Jab1 domains, as well as Prp6's N-terminal TPRs (fig. S9), and additionally between Brr2's PWI and CC domains and the Snu114 and Sad1 proteins (fig. S10).

Strikingly, Brr2 is located at radically different positions in the human and yeast tri-snRNP models (Fig. 4D). Human (h)Brr2 (bound to hPrp8 Jab1) is located close to the N-terminal TPR repeats of Prp6 and Prp8's RT end, and its general position in the tri-snRNP is not dependent on the use of a chemical cross-linking reagent during EM sample preparation (fig. S11). In contrast, yeast (y)Brr2 (bound to the yPrp8 Jab1 domain) is found near

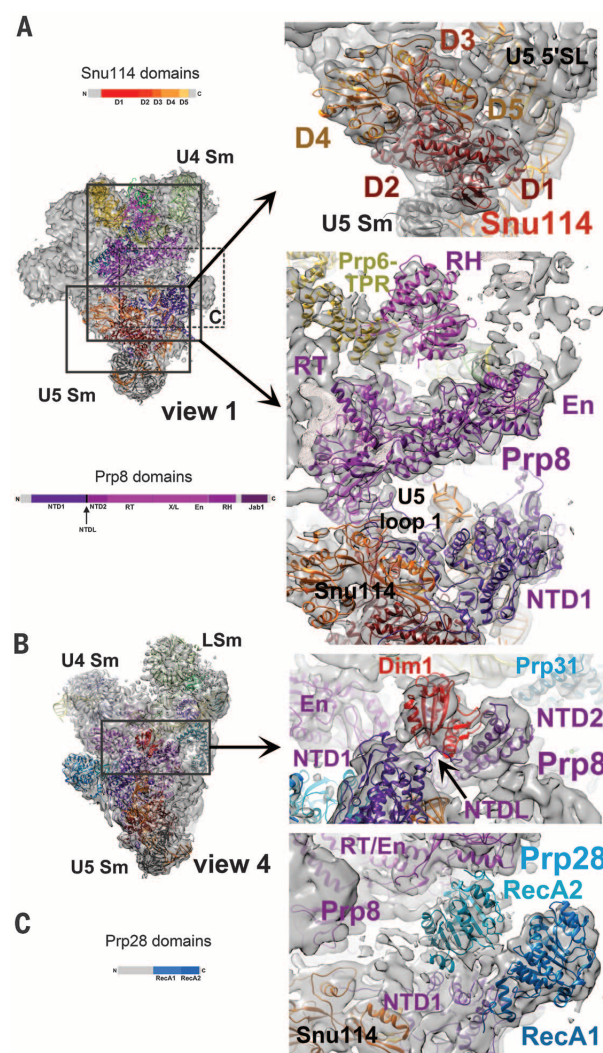


**Fig. 3. Structures and positions of Snu114, Prp8, Dim1, and Prp28 in the human tri-snRNP.** (A) Location and structural organization of Snu114 and Prp8. Left: Organization of Snu114 (domains D1 to D5 homologous to EF-G/EF-2) and Prp8 (NTD1 and NTD2, N-terminal domains 1 and 2; NTDL, NTD linker; RT, reverse transcriptase-like; X/L, linker; En, endonuclease-like; RH, RNase H-like; Jab1, Jab1/MPN-like). Upper right: Fit of Snu114 domains D1 to D5 as a compact structure. Lower right: Fit of Prp8 NTD1, RT/En, and RH domains, with front global clipping to improve Prp8 visibility. (B) U5 Dim1 between Prp8's NTD1 and NTD2 domains (extended view at right). (C) Structural organization of the RNA helicase Prp28. Left: Domain organization of Prp28. Right: Expanded view of dashed box labeled C in view 1 of (A), showing Prp28's RecA domains fit into two neighboring density elements.

yPrp8's En domain, which is ~20 nm away from the position of hBrr2. In addition, it is rotated by ~180° around the long axis of the tri-snRNP (Fig. 4D and fig. S12). In the yeast model, yBrr2 appears to be connected to the tri-snRNP primarily via the yPrp8 Jab1 domain (which contacts the tip of yPrp8's EN domain) and the U4 Sm core (Fig. 4D and fig. S12) (9). Unfortunately, because of the less well-defined density at the interface between yBrr2 and other tri-snRNP proteins, the locations of yBrr2's N-terminal PWI and helical domains cannot be identified in the yeast structure. Another striking difference is that the yeast U4 Sm core is located at the interface between yBrr2's helicase cassettes, and the central single-stranded region of U4 snRNA, to which Brr2 is thought to dock prior to unwinding the U4/U6 duplex (fig. S1C) (24), is positioned at/near the RecA domains of the active NC of yBrr2 (Fig. 4D) (9). In contrast, in the human tri-snRNP structure, hBrr2's active NC is located 8 to 10 nm away from its U4/U6 snRNA substrate (Fig. 4D).

### Structural basis for how Sad1 likely tethers Brr2 in a preactivation position

The very different position of Brr2 suggests either that there is a substantial difference in the spatial organization of the yeast and human tri-snRNPs, or potentially that the human and yeast structures represent two different conformational states that are obtained by rearrangements in protein architecture. Although the first possibility cannot be rigorously excluded, we consider it unlikely, as the structures of Brr2 and all other major U5 proteins

are evolutionarily highly conserved between yeast and human (1, 5). Instead, differences in the protein composition of the purified human and yeast tri-snRNPs potentially lead to different conformations. That is, in the presence of adenosine triphosphate (ATP), isolated human tri-snRNPs are stable, whereas yeast tri-snRNPs are not (9, 25, 26). This is likely because the evolutionarily conserved Sad1 protein is stoichiometrically present in purified human tri-snRNPs (25) but is lost during purification of the yeast complex (26, 27). Sad1 plays a key role in stabilizing the tri-snRNP, as depletion of Sad1 from yeast cell extracts leads to dissociation of the otherwise stable tri-snRNP in an ATP- and Brr2-dependent manner into a U4/U6 di-snRNP (where U6 and U4 are still base-paired) and U5 snRNP (28). Consistent with it contributing to tri-snRNP stability, human Sad1 is located at a strategically important position at the interface between the U4/U6 and U5 snRNPs. The Sad1 UCH domain contacts U4/U6-Prp31 and the Prp8 NTD2 and RT domains, whereas Sad1's Zf-UBP domain has a substantial interface with domains D2, D3, and D4 of Snu114 and is tightly connected to Brr2's PWI domain (Fig. 5, table S1, and fig. S10).

Thus, Sad1 not only potentially acts as a clamp stabilizing the interaction of U4/U6 and U5, it might also help to tether Brr2 in a preactivation position (i.e., away from the U4/U6 duplex) within the human tri-snRNP. This in turn suggests that dissociation of Sad1—as observed during activation of the human B complex (1)—might allow Brr2 to undergo a major conformational change

that is required for it to interact with its U4/U6 snRNA substrate. Because Sad1 is absent from purified yeast tri-snRNPs, the very different position of Brr2 in the yeast tri-snRNP may therefore represent a conformational state similar to the one that Brr2 normally adopts at a later stage during spliceosome activation. Whereas the yeast cryo-EM model lacks density in the corresponding regions where Sad1 and Brr2 are located in the human tri-snRNP structure, the crystal structures of Sad1 and Brr2 can be docked well onto the surface of the yeast tri-snRNP at the corresponding positions (fig. S13). It will be of interest to determine the 3D structure of the yeast tri-snRNP in the presence of ySad1.

### Remodeling of the human tri-snRNP during spliceosome assembly and activation

The spatial architecture of the human tri-snRNP provides important insight into the function of several proteins and also reveals the likely docking site of the tri-snRNP with the spliceosomal A complex during B complex formation. That is, the 3' end of U6 and Prp8's RH domain, which interact with U2 snRNA to form U2/U6 helix II (fig. S1C) and with the pre-mRNA's 5'SS, respectively, during A complex docking, are located at accessible positions at the “top” of the tri-snRNP (fig. S14A), consistent with the general architecture of the spliceosomal B complex previously revealed by EM (29).

The architecture of the human tri-snRNP also indicates that several of its proteins and RNA

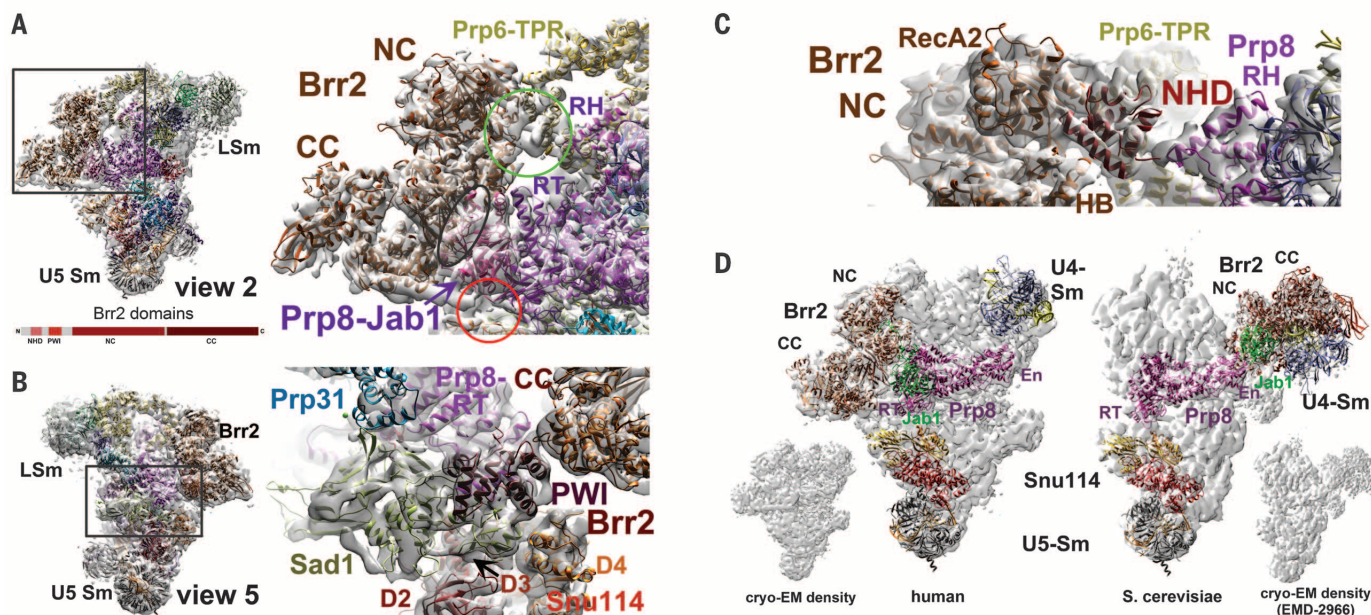


**Fig. 4. Structure and location of the RNA helicase Brr2 and Prp8 Jab1 domain.**

(A) Location and structural organization of Brr2. Left: Organization of hBrr2. NHD, N-terminal helical domain; PWI, N-terminal, noncanonical PWI domain; NC/CC, N-terminal/C-terminal helicase cassette. Right: Expanded view showing fit of hBrr2's helicase region in complex with Prp8-Jab1. Circles: Brr2-Jab1 interface (black oval), additional density elements connecting Brr2's NC (green circle) and CC (red circle)

to the tri-snRNP [see (B) and (C)]. (B) Right: Expanded view showing fit of Brr2's N-terminal PWI domain [red circle in (A)]. (C) Expanded view showing fit of Brr2's NHD [green circle in (A)]. (D) Brr2 is located at radically different positions in the human and yeast tri-sNRNPs, and is found at opposite ends of Prp8's RT/En domain in the two models. The cryo-EM densities of the human (left) and yeast (right) tri-sNRNPs (9) are shown in corresponding views as insets.



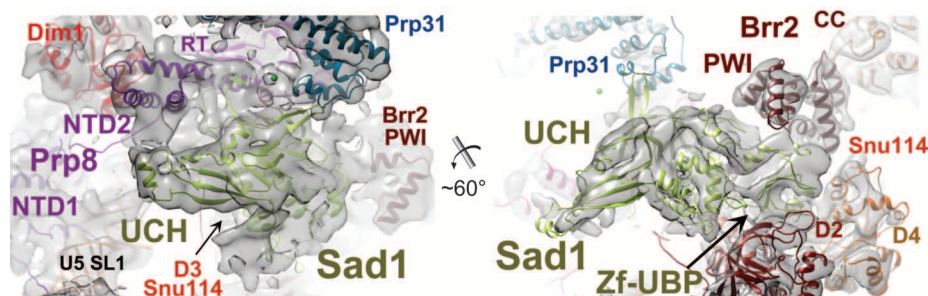


**Fig. 5. Sad1 is located in a position bridging U5 and U4/U6 proteins. (Left)** Fit of Sad1's ubiquitin C-terminal hydrolase (UCH)-like domain (including linker) into a density element that is connected to several U5 proteins and the U4/U6 protein Prp31. **(Right)** Sad1's ubiquitin protease (Zf-UBP)-like domain fits into a neighboring density that is connected to Snu114's D2-D4 domains and Brr2's PWI domain.

elements must undergo major, sequential conformational changes during B complex formation and spliceosome activation. One major rearrangement concerns Prp28, which catalyzes the transfer of the 5'SS from U1 to the ACAGA box of U6 snRNA. As this likely occurs at the Prp8 RH domain (30), Prp28 must move from its outward position through the cleft between Brr2 and the U4 Sm domain toward the RH domain (fig. S14A). In fact, the Prp28 "stalk" appears to be intrinsically flexible and undergoes movements within the isolated tri-snRNP consistent with this proposed rearrangement (31). For catalytic activation of the spliceosome, Brr2's NC and the U4/U6 duplex must be juxtaposed. This could be achieved by movement of Brr2's helicase domain across the cleft between Brr2 and the U4 Sm core toward the U4/U6 snRNAs (fig. S14A).

Additionally, Prp8 appears to undergo a substantial structural change during spliceosome activation. That is, whereas the overall structure of Prp8's large N-terminal NTD1 domain is similar in the human tri-snRNP and *S. pombe* spliceosome models, the RT/En domain adopts a clearly different position in both complexes (figs. S14B and S15) (10). In the tri-snRNP it points upward, whereby the tip of the En domain is ~5 nm away from NTD1, resulting in an open conformation. In contrast, in the *S. pombe* spliceosome, Prp8 adopts a closed conformation where the En domain interacts closely with NTD1 (figs. S14B and S15). As the overall structure of the RT/En domain does not change, Prp8 achieves the closed conformation by a downward movement of the RT/En domain, whereby the pivoting point appears to be located at the interface between the RT and NTD1 domains (figs. S14B and S15A). The position of Prp8's RH domain undergoes a similar downward shift (fig. S14B). This structural change within Prp8 is required to create the pocket into which the rearranged catalytic U2/U6 RNA network and U5 snRNA loop 1 are docked in the *S. pombe* spliceosome (fig. S15, B and C) (32). Interestingly, the U5 snRNA loop 1, which also interacts with the 3' end of the pre-mRNA's 5' exon in the activated spliceosome (33), is already located in the tri-snRNP near Prp8's emerging active-site region,

and thus it must not be substantially repositioned (fig. S14B).

The aforementioned rearrangements can only occur when several proteins are displaced concomitantly from their positions in the tri-snRNP. For example, in the tri-snRNP, Dim1 is located in the same area where the center of the U2/U6 catalytic RNA network is found in the *S. pombe* spliceosome (fig. S15, B and C) (32). Possibly Dim1 and the RecA2 domain of Prp28, which are both located between Prp8's RT/En and NTD domains (fig. S15B), may stabilize the open conformation of Prp8 in the tri-snRNP. Prp31, Prp3, and Prp4 must also be displaced from the U4 and/or U6 snRNAs. Indeed, except for Prp8, all of these proteins, plus Sad1 and Prp6, are displaced from the spliceosome during activation (1). How these multiple rearrangements are orchestrated is currently not clear. Snu114 has been implicated in the activation process (34), and if it should undergo a conformational switch from a compact to an elongated state, similar to EF-2/EF-G in the ribosome during translocation (16, 35, 36), several coordinated movements of other tri-snRNP proteins would result (figs. S6 and S14A). For example, Brr2's PWI domain, which (together with Brr2's NHD) provides major contact points between Brr2 and other U5 proteins as well as Sad1, would likely be destabilized; this could potentially facilitate movement of Brr2 toward U4/U6. The elucidation of the structural dynamics of the various events that take place during spliceosome activation will require numerous cryo-EM "snapshots" of the spliceosome during its multistep assembly pathway.

## REFERENCES AND NOTES

- M. C. Wahl, C. L. Will, R. Lührmann, *Cell* **136**, 701–718 (2009).
- T. W. Nilsen, in *RNA Structure and Function*, R. Simons, M. Grunberg-Manago, Eds. (Cold Spring Harbor Laboratory Press, Cold Spring Harbor, NY, 1998), pp. 279–307.
- S. M. Fica, M. A. Mefford, J. A. Piccirilli, J. P. Staley, *Nat. Struct. Mol. Biol.* **21**, 464–471 (2014).
- T. Achsel, K. Ahrens, H. Brahm, S. Teigelkamp, R. Lührmann, *Mol. Cell. Biol.* **18**, 6756–6766 (1998).
- W. P. Galej, T. H. D. Nguyen, A. J. Newman, K. Nagai, *Curr. Opin. Struct. Biol.* **25**, 57–66 (2014).
- R. J. Grainger, J. D. Beggs, *RNA* **11**, 533–557 (2005).

- B. Laggenbauer, T. Achsel, R. Lührmann, *Proc. Natl. Acad. Sci. U.S.A.* **95**, 4188–4192 (1998).
- P. L. Raghunathan, C. Guthrie, *Curr. Biol.* **8**, 847–855 (1998).
- T. H. D. Nguyen et al., *Nature* **523**, 47–52 (2015).
- C. Yan et al., *Science* **349**, 1182–1191 (2015).
- B. Kastner et al., *Nat. Methods* **5**, 53–55 (2008).
- B. Sander et al., *Mol. Cell* **24**, 267–278 (2006).
- E. M. Makarov, O. V. Makarova, T. Achsel, R. Lührmann, *J. Mol. Biol.* **298**, 567–575 (2000).
- F. Galisson, P. Legrain, *Nucleic Acids Res.* **21**, 1555–1562 (1993).
- P. Fabrizio, B. Laggenbauer, J. Lauber, W. S. Lane, R. Lührmann, *EMBO J.* **16**, 4092–4106 (1997).
- R. Jørgensen et al., *Nat. Struct. Biol.* **10**, 379–385 (2003).
- S. Möhlmann et al., *Acta Crystallogr. D* **70**, 1622–1630 (2014).
- A. Jacewicz, B. Schwer, P. Smith, S. Shuman, *Nucleic Acids Res.* **42**, 12885–12898 (2014).
- K. F. Santos et al., *Proc. Natl. Acad. Sci. U.S.A.* **109**, 17418–17423 (2012).
- S. Mozaffari-Jovin et al., *Science* **341**, 80–84 (2013).
- C. Maeder, A. K. Kutach, C. Guthrie, *Nat. Struct. Mol. Biol.* **16**, 42–48 (2009).
- E. Absmeier et al., *Acta Crystallogr. D* **71**, 762–771 (2015).
- E. Absmeier et al., *Genes Dev.* **29**, 2576–2587 (2015).
- S. Mozaffari-Jovin et al., *Genes Dev.* **26**, 2422–2434 (2012).
- S. E. Behrens, R. Lührmann, *Genes Dev.* **5**, 1439–1452 (1991).
- S. W. Stevens et al., *RNA* **7**, 1543–1553 (2001).
- P. Fabrizio, S. Esser, B. Kastner, R. Lührmann, *Science* **264**, 261–265 (1994).
- Y.-H. Huang, C.-S. Chung, D.-I. Kao, T.-C. Kao, S.-C. Cheng, *Mol. Cell. Biol.* **34**, 210–220 (2014).
- H. Stark, R. Lührmann, *Annu. Rev. Biophys. Biomol. Struct.* **35**, 435–457 (2006).
- J. L. Reyes, E. H. Gustafson, H. R. Luo, M. J. Moore, M. M. Konarska, *RNA* **5**, 167–179 (1999).
- B. Sander, M. M. Golas, R. Lührmann, H. Stark, *Structure* **18**, 667–676 (2010).
- J. Hang, R. Wan, C. Yan, Y. Shi, *Science* **349**, 1191–1198 (2015).
- E. J. Sontheimer, J. A. Steitz, *Science* **262**, 1989–1996 (1993).
- E. C. Small, S. R. Leggett, A. A. Winans, J. P. Staley, *Mol. Cell* **23**, 389–399 (2006).
- C. M. T. Spahn et al., *EMBO J.* **23**, 1008–1019 (2004).
- J. Lin, M. G. Gagnon, D. Bulkeley, T. A. Steitz, *Cell* **160**, 219–227 (2015).

## ACKNOWLEDGMENTS

We thank T. Conrad for HeLa cell production in a bioreactor; H. Kohansal for preparing HeLa cell nuclear extract; I. Öchsner, U. Steuerwald, W. Lendeckel, M. Raabe, and U. Pleßmann for excellent technical assistance; and C. L. Will, K. Hartmuth, N. Fischer, D. Haselbach, M. Wahl, and A. Chari for advice and many helpful discussions. Supported by Deutsche Forschungsgemeinschaft grant SFB 860 (R.L., H.S., and H.U.). EM raw data are available at the Electron Microscopy Pilot Image Archive under the code EMPIAR-10056. The EM map has been deposited in the Electron Microscopy Data Bank with accession code EMD-6581. The atomic coordinates have been deposited in the Protein Data Bank with accession code 3JCR.

## SUPPLEMENTARY MATERIALS

[www.sciencemag.org/content/351/6280/1416/suppl/DC1](http://www.sciencemag.org/content/351/6280/1416/suppl/DC1)  
Materials and Methods  
Figs. S1 to S16  
Tables S1 and S2  
Movie S1  
References (37–54)

7 August 2015; accepted 4 February 2016  
Published online 18 February 2016  
10.1126/science.12085

## REPORTS

## C–H BOND ACTIVATION

## Catalyst-controlled selectivity in the C–H borylation of methane and ethane

Amanda K. Cook, Sydonie D. Schimler, Adam J. Matzger, Melanie S. Sanford\*

The C–H bonds of methane are generally more kinetically inert than those of other hydrocarbons, reaction solvents, and methane functionalization products. Thus, developing strategies to achieve selective functionalization of CH<sub>4</sub> remains a major challenge. Here, we report transition metal–catalyzed C–H borylation of methane with bis-pinacolborane (B<sub>2</sub>pin<sub>2</sub>) in cyclohexane solvent at 150 °C under 2800 to 3500 kilopascals of methane pressure. Iridium, rhodium, and ruthenium complexes all catalyze the reaction. Formation of mono- versus diborylated methane is tunable as a function of catalyst, with the ruthenium complex providing the highest ratio of CH<sub>3</sub>Bpin to CH<sub>2</sub>(Bpin)<sub>2</sub>. Despite the high relative concentration of cyclohexane, minimal quantities of borylated cyclohexane products are observed. Furthermore, all three metal complexes catalyze borylation of methane with >3.5:1 selectivity over ethane.

Over the past 50 years, numerous homogeneous transition-metal catalysts have been developed for the C–H functionalization of liquid alkanes [for example, via dehydrogenation (1), oxygenation (2), carbonylation (3), borylation (4–7), and C, N-, and O-atom insertion (8, 9)]. However, relatively few of these catalysts have been translated to analogous reactions of methane (10–14). This is largely due to the particular challenges associated with methane C–H functionalization. First, the C–H bonds

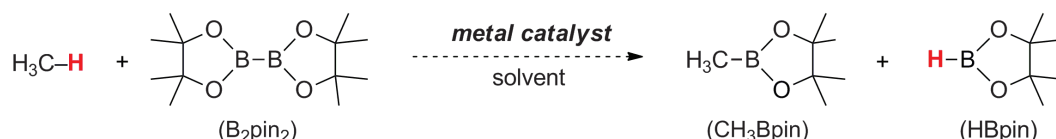
of methane are stronger than those of most liquid alkanes [the C–H bond dissociation energies (BDEs) of methane, *n*-hexane (1 °C–H), and cyclohexane are 105, 101, and 99.5 kcal/mol, respectively (15, 16)]. As such, methane C–H bond cleavage is prohibitively slow with many catalysts. Second, homogeneous alkane functionalization reactions are typically conducted by using neat alkane as the solvent (4, 5, 14), so the use of methane gas as a substrate poses challenges with respect to identifying a compatible reaction solvent (12, 17). Last, the reaction solvent and the CH<sub>3</sub>X products of methane functionalization typically contain more reactive C–H bonds than those of CH<sub>4</sub>. As such, developing strategies to achieve selective

functionalization of CH<sub>4</sub> in the presence of solvent and CH<sub>3</sub>X remains a challenging problem (10–14).

We sought to identify a methane C–H functionalization process in which selectivity (both for CH<sub>4</sub> versus CH<sub>3</sub>X functionalization and for CH<sub>4</sub> versus solvent C–H functionalization) could be tuned through modification of the homogeneous transition-metal catalyst. To accomplish this goal, we focused on the catalytic C–H borylation of methane with B<sub>2</sub>pin<sub>2</sub> (Fig. 1A). Over the past 15 years, there has been tremendous progress in the development of transition-metal catalysts for the C–H borylation of liquid alkane substrates. Catalysts based on iridium (Ir) (18, 19), rhodium (Rh) (20–22), rhenium (Re) (23), and ruthenium (Ru) (24) have been reported for liquid alkane C–H borylation, typically by using the alkane substrate as the solvent and B<sub>2</sub>pin<sub>2</sub> as the borylating reagent (19, 21, 23–25). With the vast majority of liquid alkane substrates, the selectivity of C–H borylation is dominated by steric factors, with terminal (primary) C(sp<sup>3</sup>)–H bonds undergoing selective functionalization over secondary or tertiary C–H sites (25, 26). This selectivity has been reported to be largely independent of the nature of the transition-metal catalyst. For example, the C–H borylation of *n*-alkanes (*n*-C<sub>n</sub>H<sub>2n+2</sub>) with B<sub>2</sub>pin<sub>2</sub> affords 1-Bpin-C<sub>n</sub>H<sub>2n+1</sub> as the sole detectable product with Ir-, Rh-, Re-, and Ru-based catalysts (18, 20, 23, 24).

In certain contexts, the introduction of a Bpin substituent has been shown to electronically activate adjacent C–H bonds toward further C–H borylation by rendering them more acidic (27, 28). This electronic activation has been best studied in the context of benzylic substrates, in which the C–H borylation of 1°-benzylic C–H bonds is often slower than that of the 2°  $\alpha$ -boryl benzylic C–H bonds of the products (29, 30). However, the interplay between these steric and electronic effects has not been extensively explored in the C–H borylation literature, especially as a function of catalyst metal identity. As discussed below, these

## A Proposed selective mono-C–H borylation of methane:



## B Selectivity challenges:

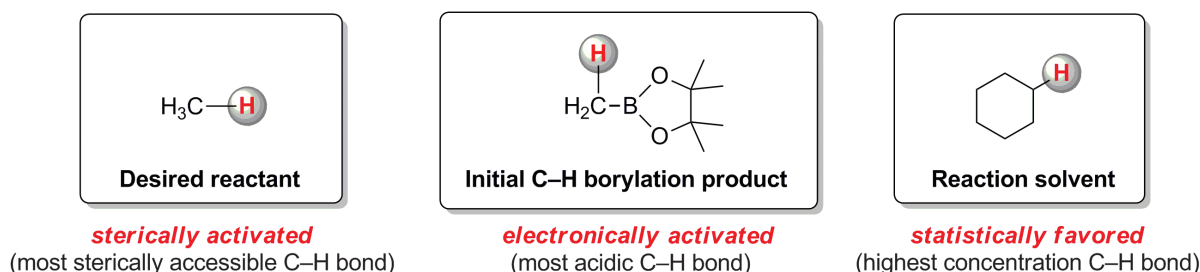


**Fig. 1. Reactivity and selectivity challenges in the C–H borylation of methane.** (A) Proposed methane C–H borylation reaction. (B) Challenges with selectivity in methane C–H borylation.



issues are expected to be particularly salient in the context of methane C–H borylation (Fig. 1B).

In 2005, Hall and co-workers reported density functional theory (DFT) calculations that suggest that Cp<sup>+</sup>Rh complexes (Cp<sup>+</sup>, pentamethylcyclopentadienyl) should be capable of catalyzing the C–H borylation of CH<sub>4</sub> (22). Despite these encouraging computational results, there have been no subsequent experimental studies establishing the feasibility and/or exploring the selectivity of methane C–H borylation with these or any other catalysts. In a methane C–H borylation reaction, three major C–H bond-containing molecules will be present in solution: methane, CH<sub>3</sub>Bpin, and solvent (cyclohexane) (Fig. 1B). Among these three molecules, methane has the most sterically accessible C–H bonds, CH<sub>3</sub>Bpin has the most electronically activated (acidic) C–H bonds, and the reaction solvent, cyclohexane, is statistically favored because of its high concentration. Our studies sought to (i) experimentally establish the feasibility of metal-catalyzed methane C–H borylation; (ii) determine which factor (or factors) dominate selectivity in this transformation (sterics, electronics, or statistics); and (iii) probe whether different catalysts can be used to tune the selectivity of the reaction.

We selected Rh complex **1** for our initial investigations of methane C–H borylation on the basis of Hall and co-workers' DFT calculations, which predicted a relatively low barrier for CH<sub>4</sub> activation with this complex (22). The initial reactions were conducted in a Parr high-pressure batch reactor (45 mL volume) at 150 °C, using 1.5 mole percent (mol %) of **1**, 3500 kPa of methane, and 0.89 mmol of B<sub>2</sub>pin<sub>2</sub> as the limiting reagent (31). As discussed above, the choice of solvent is particularly critical because any C–H bonds in the solvent must be less reactive with **1** than those of CH<sub>4</sub>. Thus, we first examined solvents without C–H bonds [perfluoromethylcyclohexane (PFMCH) and perfluorohexane (PFH)]. However, modest yields of methane C–H borylation products were obtained (Table 1, entries 1 and 2), likely because of the low solubility of the Rh catalyst in these media. We next examined cyclopentane (*c*-C<sub>5</sub>H<sub>10</sub>) and cyclohexane (*c*-C<sub>6</sub>H<sub>12</sub>) as solvents (Table 1, entries 3 and 4). These cycloalkanes are both known to be poor substrates for Rh-catalyzed C–H borylation (6, 20, 21) because the 2° C–H bonds are relatively sterically congested and weakly acidic (32). Cyclohexane proved to be optimal, affording CH<sub>3</sub>Bpin in 74% yield with only traces (~2%) of the solvent C–H borylation product *c*-C<sub>6</sub>H<sub>11</sub>Bpin (Table 1, entry 4). Under these conditions, high selectivity was also observed for the mono-borylation of methane [ratio of CH<sub>3</sub>Bpin to bis-borylated CH<sub>2</sub>(Bpin)<sub>2</sub> was 10:1]. Increasing the loading of catalyst **1** to 3 mol % resulted in 99% yield of CH<sub>3</sub>Bpin, while maintaining excellent selectivity for CH<sub>3</sub>Bpin over *c*-C<sub>6</sub>H<sub>11</sub>Bpin and CH<sub>2</sub>(Bpin)<sub>2</sub> (entry 6). Lowering the catalyst loading to 0.75 mol % resulted in decreased yield of CH<sub>3</sub>Bpin (51%) but increased turnover number (68 turnovers) (entry 5) relative to the standard conditions.

We next examined Ir and Ru complexes **2/3** and **4** as potential catalysts for methane C–H borylation. These complexes were selected on the basis of their

**Table 1. Methane C–H borylation catalyzed by **1**.**

Entry	Mol % <b>1</b>	Solvent	Yield*	TON	CH <sub>3</sub> Bpin:solventBpin*	CH <sub>3</sub> Bpin:CH <sub>2</sub> (Bpin) <sub>2</sub> *
1	1.5	PFMCH	<1%	<1	na†	na†
2	1.5	PFH	26%	17	na†	8:1
3	1.5	<i>c</i> -C <sub>5</sub> H <sub>10</sub>	69%	46	8:1	10:1
4	1.5	<i>c</i> -C <sub>6</sub> H <sub>12</sub>	74%	49	48:1	10:1
5	0.75	<i>c</i> -C <sub>6</sub> H <sub>12</sub>	51%	68	46:1	18:1
6	3	<i>c</i> -C <sub>6</sub> H <sub>12</sub>	99%	33	59:1	9:1

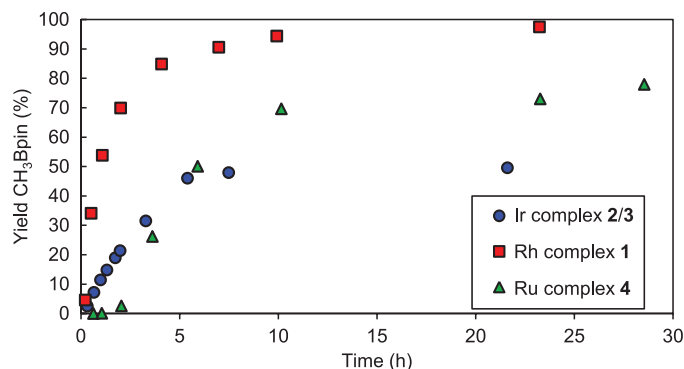
\*Yields and ratios of all products were determined by means of gas chromatography–flame ionization detector (GC-FID) and are based on B<sub>2</sub>pin<sub>2</sub> as the limiting reagent. †na, not applicable.

**Table 2. Impact of catalyst on the yield and selectivity of methane C–H borylation.**

Entry	Catalyst	Time (hours)	Yield*	TON	CH <sub>3</sub> Bpin:CyBpin*	CH <sub>3</sub> Bpin:CH <sub>2</sub> (Bpin) <sub>2</sub> *
1	2/3	14	45%	15	3:1	4:1
2	4	14	67%	22	83:1	21:1
3	4†	6	50%	17	82:1	31:1
4	1†	1	54%	18	36:1	20:1

\*Yields and ratios of all products were determined by means of GC-FID and are based on B<sub>2</sub>pin<sub>2</sub> as the limiting reagent. †Reactions stopped before completion in order to compare selectivity at similar yields.

**Fig. 2. Time studies showing formation of CH<sub>3</sub>Bpin using 2800 kPa of CH<sub>4</sub>.** Rh complex **1** is indicated with red squares, Ir complex **2/3** with blue circles, and Ru complex **4** with green triangles.



known catalytic activity for the C–H borylation of liquid alkanes (18, 19, 24, 33, 34). Under the optimal conditions for catalyst **1**, the combination of Ir complex **2** and ligand **3** (18) afforded moderate yield (45%) of CH<sub>3</sub>Bpin, whereas Ru complex **4** provided 67% yield (Table 2, entries 1 and 2). To more quantitatively compare these three catalysts, their reaction progress was monitored as a function of

time, and the results are shown in Fig. 2. These studies show that all of the reactions achieve a maximum yield within 10 hours. However, the initial reaction rate with Rh catalyst **1** is approximately four times faster than that with **2/3**. Furthermore, **4** displays a lengthy induction period (~2 hours), suggesting that it serves as a precatalyst for this transformation (24, 35).

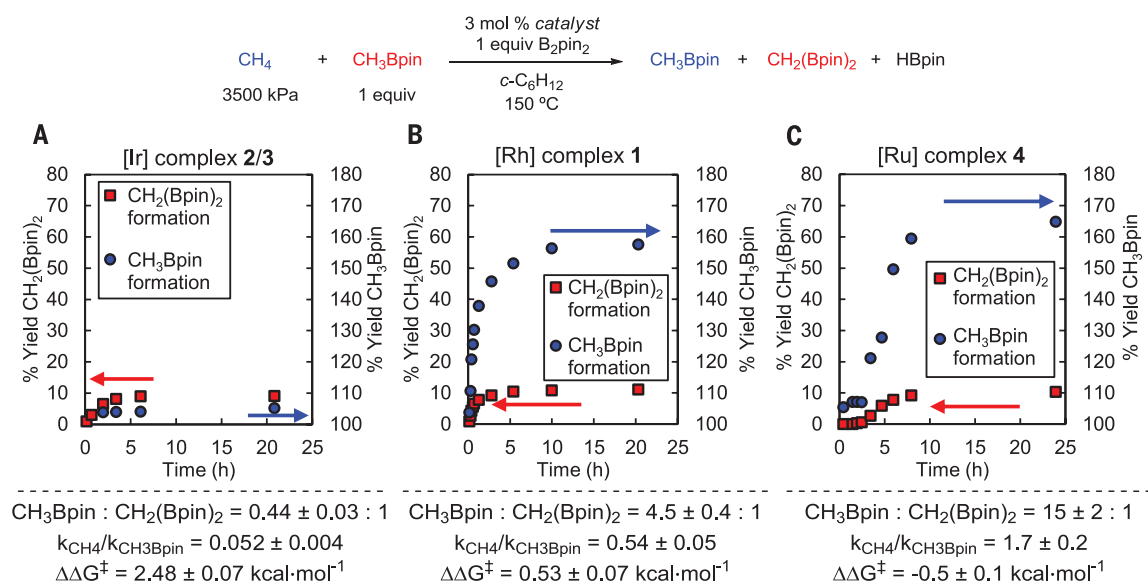


**Fig. 3. Evaluation of the selectivity in  $\text{CH}_4/\text{CH}_3\text{Bpin}$  borylation.** (A to C) Reaction time profiles (top) for (A) Ir catalyst **2/3**, (B) Rh catalyst **1**, and (C) Ru catalyst **4**. Red squares (left y axes) represent formation of  $\text{CH}_2(\text{Bpin})_2$ , and blue circles (right y axes) represent formation of  $\text{CH}_3\text{Bpin}$ .  $\text{CH}_3\text{Bpin} : \text{CH}_2(\text{Bpin})_2$  ratios at early time points, relative rates, and  $\Delta\Delta G^\ddagger$  values for the three catalyst systems are given below their respective time profile graphs.

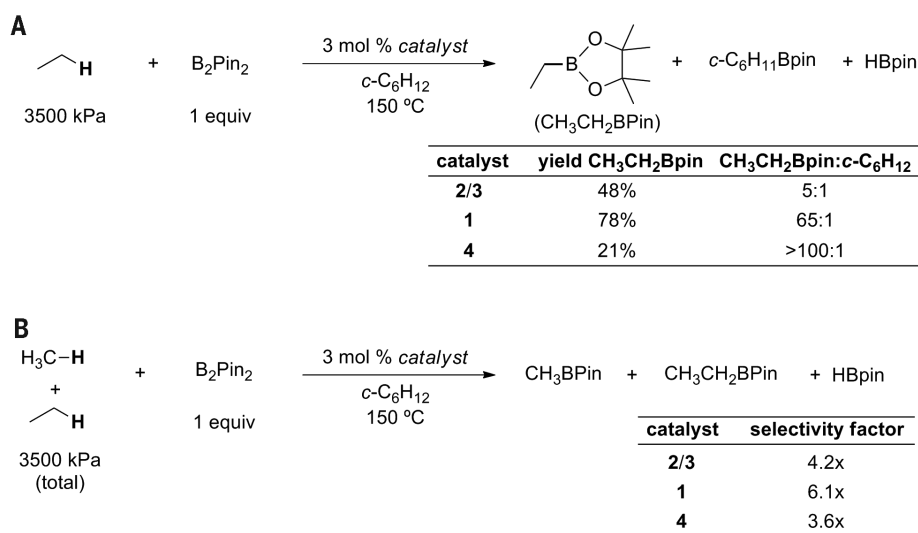


**Fig. 4. Comparison of catalysts for ethane borylation.** (A) Batch ethane borylation results for catalysts **2/3**, **1**, and **4**. (B) Methane and ethane one-pot competition. Selectivity factor is the preference for methane over ethane borylation corrected for statistics and solubility.

In the Table 2 data, the choice of catalyst has a major impact on the selectivity of C–H borylation, both for methane versus cyclohexane and for methane versus  $\text{CH}_3\text{Bpin}$ . In particular, Rh and Ru catalysts **1** and **4** exhibit much higher selectivity for  $\text{CH}_4$  than does the Ir catalyst system **2/3**. This effect is observed even when the reactions are stopped at similar yield of  $\text{CH}_3\text{Bpin}$  (~50% yield; Table 2, entries 1, 3, and 4 for comparison). The ratio of  $\text{CH}_3\text{Bpin}$  to  $\text{c-C}_6\text{H}_{11}\text{Bpin}$  ranged from 82:1 (with catalyst **4**) to 3:1 (with catalyst **2/3**). Similarly, the  $\text{CH}_3\text{Bpin}$  to  $\text{CH}_2(\text{Bpin})_2$  ratio ranged from 31:1 (with catalyst **4**) to 4:1 (with catalyst **2/3**). These results indicate that tuning of the catalyst structure can be used to control this undesired overfunctionalization reaction.

To more quantitatively evaluate selectivity as a function of catalyst, we conducted competition experiments between  $\text{CH}_4$  (3500 kPa, 1.1 M)

(36) and  $\text{CH}_3\text{Bpin}$  (0.13 M, 1 equivalent relative to  $\text{B}_2\text{pin}_2$ ) with each of the catalysts **1**, **2/3**, and **4**. The time course of each reaction is shown in Fig. 3. The yield of  $\text{CH}_3\text{Bpin}$  (Fig. 3, blue circles, right y axes) represents the additional  $\text{CH}_3\text{Bpin}$  formed from the C–H borylation of  $\text{CH}_4$  (measured in excess of 100%, given the  $\text{CH}_3\text{Bpin}$  equivalent added at the outset), whereas the yield of  $\text{CH}_2(\text{Bpin})_2$  (Fig. 3, red squares, left y axes) represents the product of C–H borylation of  $\text{CH}_3\text{Bpin}$ .

With Ir catalyst **2/3** (Fig. 3A), the quantity of diborylated product present exceeds that of  $\text{CH}_3\text{Bpin}$  at all time points. In contrast, the concentration of  $\text{CH}_3\text{Bpin}$  is much greater than that of  $\text{CH}_2(\text{Bpin})_2$  throughout the reactions catalyzed by Rh complex **1** and Ru complex **4** (Fig. 3, B and C, respectively). Using the ratio of  $\text{CH}_3\text{Bpin} : \text{CH}_2(\text{Bpin})_2$  obtained at early time points and the concentrations of  $\text{CH}_4$  and  $\text{CH}_3\text{Bpin}$  added at the

onset, we can estimate  $k_{\text{CH}_4}/k_{\text{CH}_3\text{Bpin}}$  (and thus approximate  $\Delta\Delta G^\ddagger$ ) for the C–H borylation of  $\text{CH}_4$  versus  $\text{CH}_3\text{Bpin}$  for each catalyst (complete details of these calculations are provided in the supplementary materials). As shown in the bottom of Fig. 3, positive  $\Delta\Delta G^\ddagger$  values are observed for catalysts **1** and **2/3**, reflecting faster C–H borylation of  $\text{CH}_3\text{Bpin}$  versus  $\text{CH}_4$ . The values of  $\Delta\Delta G^\ddagger$  are estimated as 0.53 and 2.48 kcal/mol for **1** and **2/3**, respectively. In contrast, Ru catalyst **4** shows a reversal in selectivity, exhibiting a preference for  $\text{CH}_4$  over  $\text{CH}_3\text{Bpin}$ , with an estimated  $\Delta\Delta G^\ddagger$  of  $-0.5$  kcal/mol.

The relative reactivity of methane and ethane is another important issue (given that ethane is the secondmost abundant component of natural gas) but is rarely addressed in alkane C–H functionalization reactions. In the few reported systems in which this has been studied, ethane is usually found to be much more reactive (17, 37–39). As shown in Fig. 4A, catalysts **1**, **2/3**, and **4** all catalyze the C–H borylation of ethane at  $150^\circ\text{C}$  in cyclohexane. Again, ethane borylation occurs in preference to cyclohexane borylation and shows a similar dependence on metal catalyst as with methane, with selectivities ranging from 5:1 (with **2/3**) to >100:1 (with **4**).

To probe catalyst selectivity for methane versus ethane, known molar quantities of each gas were added to the high-pressure reactor. The reactions were run to complete conversion of  $\text{B}_2\text{pin}_2$ , and the ratio of  $\text{CH}_3\text{Bpin}$  to  $\text{CH}_3\text{CH}_2\text{Bpin}$  was determined with each catalyst. These ratios were then corrected for the number of C–H bonds in each substrate as well as the relative solubilities of the two gases (36). As shown in Fig. 4B, all three catalysts exhibit a >3.5:1 preference for the C–H borylation of methane relative to ethane, which is consistent with sterically controlled selectivity. Additionally, the level of selectivity varies with the catalyst. The Ir catalyst **2/3** and Ru catalyst **4** both react approximately fourfold faster with methane C–H bonds, whereas **1** is more selective for methane (approximately sixfold faster). These



results further highlight the impact of catalyst on both reactivity and selectivity in the C–H borylation of light alkanes.

Overall, we have demonstrated that catalyst structure has a major impact on reaction rates and selectivities in the C–H borylation of methane. Over-functionalization of the initial product, CH<sub>3</sub>Bpin, can be limited through the appropriate selection of catalyst. These results open up exciting possibilities for catalyst design (to further modulate reactivity and selectivity in methane C–H borylation) as well as the application of the concepts delineated here for other light alkane C–H functionalization reactions.

## REFERENCES AND NOTES

- J. Choi, A. H. R. MacArthur, M. Brookhart, A. S. Goldman, *Chem. Rev.* **111**, 1761–1779 (2011).
- A. E. Shilov, G. B. Shul'pin, *Chem. Rev.* **97**, 2879–2932 (1997).
- T. Sakakura, T. Sodeyama, K. Sasaki, K. Wada, M. Tanaka, *J. Am. Chem. Soc.* **112**, 7221–7229 (1990).
- T. Ishiyama, N. Miyaura, *J. Organomet. Chem.* **680**, 3–11 (2003).
- I. A. I. Mkhaliid, J. H. Barnard, T. B. Marder, J. M. Murphy, J. F. Hartwig, *Chem. Rev.* **110**, 890–931 (2010).
- J. F. Hartwig, *Chem. Soc. Rev.* **40**, 1992–2002 (2011).
- J. F. Hartwig, *Acc. Chem. Res.* **45**, 864–873 (2012).
- H. M. L. Davies, J. R. Manning, *Nature* **451**, 417–424 (2008).
- D. Mansuy, *Coord. Chem. Rev.* **125**, 129–141 (1993).
- H. Schwarz, *Angew. Chem. Int. Ed.* **50**, 10096–10115 (2011).
- V. N. Cavaliere, B. F. Wicker, D. J. Mindiola, *Adv. Organomet. Chem.* **60**, 1–47 (2012).
- N. J. Gunzsalus, M. M. Konnick, B. G. Hashiguchi, R. A. Periana, *Isr. J. Chem.* **54**, 1467–1480 (2014).
- P. Tang, Q. Zhu, Z. Wu, D. Ma, *Environ. Sci.* **7**, 2580–2591 (2014).
- A. Caballero, P. J. Pérez, *Chem. Soc. Rev.* **42**, 8809–8820 (2013).
- D. R. Lide, *CRC Handbook of Chemistry and Physics* (CRC Press, ed. 96, 2015).
- S. J. Blanksby, G. B. Ellison, *Acc. Chem. Res.* **36**, 255–263 (2003).
- A. Caballero *et al.*, *Science* **332**, 835–838 (2011).
- C. W. Liskay, J. F. Hartwig, *J. Am. Chem. Soc.* **134**, 12422–12425 (2012).
- C. W. Liskay, J. F. Hartwig, *J. Am. Chem. Soc.* **135**, 3375–3378 (2013).
- H. Chen, S. Schlecht, T. C. Semple, J. F. Hartwig, *Science* **287**, 1995–1997 (2000).
- C. S. Wei, C. A. Jiménez-Hoyos, M. F. Vide, J. F. Hartwig, M. B. Hall, *J. Am. Chem. Soc.* **132**, 3078–3091 (2010).
- J. F. Hartwig *et al.*, *J. Am. Chem. Soc.* **127**, 2538–2552 (2005).
- H. Chen, J. F. Hartwig, *Angew. Chem. Int. Ed.* **38**, 3391–3393 (1999).
- J. M. Murphy, J. D. Lawrence, K. Kawamura, C. Incarvito, J. F. Hartwig, *J. Am. Chem. Soc.* **128**, 13684–13685 (2006).
- Q. Li, C. W. Liskay, J. F. Hartwig, *J. Am. Chem. Soc.* **136**, 8755–8765 (2014).
- J. D. Lawrence, M. Takahashi, C. Bae, J. F. Hartwig, *J. Am. Chem. Soc.* **126**, 15334–15335 (2004).
- B. A. Vanchura II *et al.*, *Chem. Commun. (Camb.)* **46**, 7724–7726 (2010).
- H. Tajuddin *et al.*, *Chem. Sci.* **3**, 3505–3515 (2012).
- S. Shimada, A. S. Batsanov, J. A. K. Howard, T. B. Marder, *Angew. Chem. Int. Ed.* **40**, 2168–2171 (2001).
- M. A. Larsen, C. V. Wilson, J. F. Hartwig, *J. Am. Chem. Soc.* **137**, 8633–8643 (2015).
- These initial conditions were selected on the basis of (i) published conditions for alkane borylation reactions (20, 21, 24, 26) as well as (ii) the fixed volume of our Parr high-pressure reactor.
- The Ir-catalyzed background reaction of *c*-C<sub>5</sub>H<sub>10</sub> and *c*-C<sub>6</sub>H<sub>12</sub> with B<sub>2</sub>pin<sub>2</sub> in the absence of methane afforded 20.3 and 4.2% yield of the solvent C–H borylation products, respectively.
- G. A. Chotana *et al.*, *Chem. Commun. (Camb.)* **38**, 5731–5733 (2009).
- P. Nguyen, H. P. Blom, S. A. Westcott, N. J. Taylor, T. B. Marder, *J. Am. Chem. Soc.* **115**, 9329–9330 (1993).
- All three of these reactions passed the Hg drop test (supplementary materials), which is consistent with homogeneous catalysis.
- The concentrations of methane and ethane under the reaction conditions were determined by using Raman spectroscopic analysis of solutions of CH<sub>4</sub> or CH<sub>3</sub>CH<sub>3</sub> in C<sub>6</sub>D<sub>12</sub> (supplementary materials).
- M. Lin, T. E. Hogan, A. Sen, *J. Am. Chem. Soc.* **118**, 4574–4580 (1996).
- O. Demoulin, B. Le Clef, M. Navez, P. Ruiz, *Appl. Catal. A Gen.* **344**, 1–9 (2008).
- P. O. Graf, B. L. Mojet, L. Lefferts, *Appl. Catal. A Gen.* **346**, 90–95 (2008).

## ACKNOWLEDGMENTS

The work conducted by A.K.C. (primarily involving evaluation of catalysts **1** and **2/3**) was supported by NSF under the Centers for Chemical Innovation (CCI) Center for Enabling New Technologies through Catalysis (CENTC) Phase II Renewal, CHE-1205189. The work conducted by S.D.S. (primarily involving evaluation of catalyst **4** and gas solubility measurements) was supported by the U.S. Department of Energy Office of Basic Energy Sciences (contract DE-FG02-08ER 15997). The Parr reactors used in this work were

purchased with funds from the NSF, under the CCI CENTC Phase II Renewal, CHE-1205189. We gratefully acknowledge D. Samblanet for assistance with the gas solubility measurements. The University of Michigan has filed for a provisional patent on this work.

## SUPPLEMENTARY MATERIALS

www.sciencemag.org/content/351/6280/1421/suppl/DC1  
Materials and Methods  
Supplementary Text  
Figs. S1 to S19  
Tables S1 to S14  
References (40–57)

24 November 2015; accepted 18 February 2016  
10.1126/science.aad9289

## C–H BOND ACTIVATION

## Catalytic borylation of methane

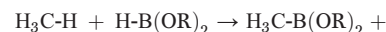
Kyle T. Smith,<sup>1</sup> Simon Berritt,<sup>1</sup> Mariano González-Moreiras,<sup>1</sup> Seihwan Ahn,<sup>2,3</sup> Milton R. Smith III,<sup>4\*</sup> Mu-Hyun Baik,<sup>2,3\*</sup> Daniel J. Mindiola<sup>1\*</sup>

Despite steady progress in catalytic methods for the borylation of hydrocarbons, methane has not yet been subject to this transformation. Here we report the iridium-catalyzed borylation of methane using bis(pinacolborane) in cyclohexane solvent. Initially, trace amounts of borylated products were detected with phenanthroline-coordinated Ir complexes. A combination of experimental high-pressure and high-throughput screening, and computational mechanism discovery techniques helped to rationalize the foundation of the catalysis and identify improved phosphine-coordinated catalytic complexes. Optimized conditions of 150°C and 3500-kilopascal pressure led to yields as high as ~52%, turnover numbers of 100, and improved chemoselectivity for monoborylated versus diborylated methane.

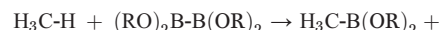
Activation of methane is challenging because it is nonpolar, has strong sp<sup>3</sup> C–H bonds, is sparingly soluble in both polar and nonpolar solvents, and has very high ionization energies and very low triple, boiling, and flashing points (*I*–*8*). Homogeneous catalysts that convert methane to products that could be used as liquid fuels are known, but these systems often require strong electrophiles and, in some cases, superacids and/or powerful oxidants (*1*, *2*, *9*–*17*). Chemoselectivity is another limitation in methane activation and functionalization. For instance, H<sub>3</sub>C–R (R = functional group) products resulting from methane activation and functionalization have more reactive C–H bonds than methane itself, hence often resulting in poor selectivity, overfunctionalization, and overoxidation.

The pioneering work by Hartwig, Marder, and Smith on C–H bond borylation inspired our investigation into the catalytic functionalization of methane using a similar approach (*18*). Whereas stoichiometric and catalytic borylations of alkanes show marked selectivity for monoborylation of terminal methyl groups (*18*), analogous reac-

tions with methane have not been thoroughly explored, despite this reaction being known for more than a decade. Fundamentally important is that the methyl-derived product is arguably a form of a mildly nucleophilic methyl transfer reagent, which complements the chemistry observed in electrophilic activation reactions in Shilov-type chemistry (*9*). Theory predicts that borylation of hydrocarbons with a borane (Eq. 1) is thermoneutral, whereas the weaker B–B bond in diboron reagents provides an enthalpic driving force of at least 12 kcal/mol, as shown in Eq. 2 (*18*). These considerations led us to pursue the catalytic borylation of methane using diboron reagents such as B<sub>2</sub>pin<sub>2</sub> (pin = pinacolate).



$$\text{H-H } \Delta H_o = -1 \text{ to } +1 \text{ kcal/mol} \quad (1)$$



$$\text{H-B(OR)}_2 \Delta H_o = -13 \text{ kcal/mol} \quad (2)$$

Iridium systems are particularly promising for C–H activation of methane (*1*, *2*), and some of the most active borylation catalysts use this transition metal (*18*). Therefore, we focused our attention on the commercially available iridium reagents [Ir(COD)(μ-Cl)]<sub>2</sub>, [Ir(COD)(μ-OMe)]<sub>2</sub> (COD = 1,5-cyclooctadiene), and (MesH)Ir(Bpin)<sub>3</sub> (MesH = mesitylene) (*19*), modifying them with a range of

<sup>1</sup>Department of Chemistry, University of Pennsylvania, 231 South 34th Street, Philadelphia, PA 19104, USA. <sup>2</sup>Institute for Basic Science—Center for Catalytic Hydrocarbon Functionalizations, Daejeon, Korea. <sup>3</sup>Department of Chemistry, Korea Advanced Institute of Science and Technology, Daejeon, Korea. <sup>4</sup>Department of Chemistry, Michigan State University, 578 South Shaw Lane, East Lansing, MI 48824, USA.  
\*Corresponding author. E-mail: smithm@msu.edu (M.R.S.); mbaiik2805@kaist.ac.kr (M.-H.B.); mindiola@sas.upenn.edu (D.J.M.)

nitrogen-based ligands, some of which are summarized in Table 1. Suitable catalyst and reaction conditions were identified systematically by means of a high-pressure, high-throughput reactor (see fig. S1 for details). Both  $[\text{Ir}(\text{COD})(\mu\text{-OMe})_2]$  and  $(\text{MesH})\text{Ir}(\text{Bpin})_3$  complexes gave some conversion to borylated methane products in cyclohexane (CyH) or tetrahydrofuran (THF) at pressures as low as 2068 kPa. Product yields were determined by gas chromatography–mass spectrometry (GC–MS) techniques with mesitylene as an internal standard.

$\text{Ir}(\text{I})$  precatalysts with supporting ligand combinations were exposed for 16 hours at 120°C to 2068 kPa of methane and  $\text{B}_2\text{pin}_2$ . Our results indicate that L3 (3,4,7,8-tetramethyl-1,10-phenanthroline) is the best nitrogen ligand. Among the products detected in the reaction mixture were  $\text{H}_3\text{CBpin}$  (**1**),  $\text{H}_2\text{C}[\text{Bpin}]_2$  (**2**),  $\text{HBpin}$  (**3**), and  $\text{H}_3\text{COBpin}$ . We also observed the production of  $\text{O}[\text{Bpin}]_2$ . Because hydrolysis of **1** and **2** is very slow on the basis of control experiments, we propose  $\text{O}[\text{Bpin}]_2$  to derive from a combination of hydrolysis of **3** during aerobic workup and analysis by GC–MS, as well as decomposition of  $\text{B}_2\text{pin}_2$  or **3**. The decomposition of  $\text{B}_2\text{pin}_2$  may be metal-catalyzed, as ring-opening of pinacolborane with Ir catalysts has been documented recently (20). We did not observe any tri- or tetraborylated methyl products,  $\text{H}_{4-x}\text{C}[\text{Bpin}]_x$  ( $x = 3$  or 4), whereas borylation of the solvent is barely detected under our conditions. Increasing  $\text{CH}_4$  pressures in small increments to 8274 kPa did not improve the mono- or diborylation reaction appreciably. Although gem-diborylation of alkanes is unknown, the gem-diborylation of benzylic groups has been documented (21, 22). Because three boryl moieties become incorporated into the active catalyst, as illustrated in Fig. 1, the diboron additive has an immediate impact on the reactivity. For instance, no reaction takes place when  $\text{B}_2\text{cat}_2$  (cat: catechol) is used instead of  $\text{B}_2\text{pin}_2$ , which is consistent with previous experimental and computational studies showing that borylation is favored for more electron-rich catalysts (23, 24).

The observed lower yield of **3** compared to **1** and **2** may be due to a second, slower borylation cycle that consumes **3** (Eq. 1). Consistent with our findings, we have observed that **3** can be used as a reactant replacing  $\text{B}_2(\text{pin})_2$ , but this reaction is much slower at 120°C (table S7). Other diboron reagents, such as  $\text{B}_2(\text{OH})_4$  or  $\text{B}_2(\text{NMe}_2)_4$ , produced complex mixtures of products with intractable precipitates.

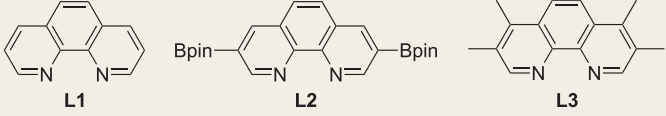
Table 1 summarizes some of our screening results with the most promising chelating polypyridyl ligands. The use of ligands L1 and L2 gave detectable amounts of  $\text{H}_3\text{CBpin}$ , whereas the best results were obtained with L3 (3,4,7,8-tetramethyl-1,10-phenanthroline), which showed yields as high as 4.1% and chemoselectivity ratios of mono- versus diborylated products **1**:**2** as high as 4:1. Surprisingly, even  $[\text{Ir}(\text{COD})(\mu\text{-OMe})_2]$  without exogenous ligand resulted in some borylation (<1%) but overall (25), the results listed in Table 1 suggest these systems to be stoichiometric with respect to methane borylation

(supplementary text). Likewise, increasing the temperature to 150°C did not improve the reaction (table S6).

The mechanism of methane borylation was modeled with density functional theory calculations

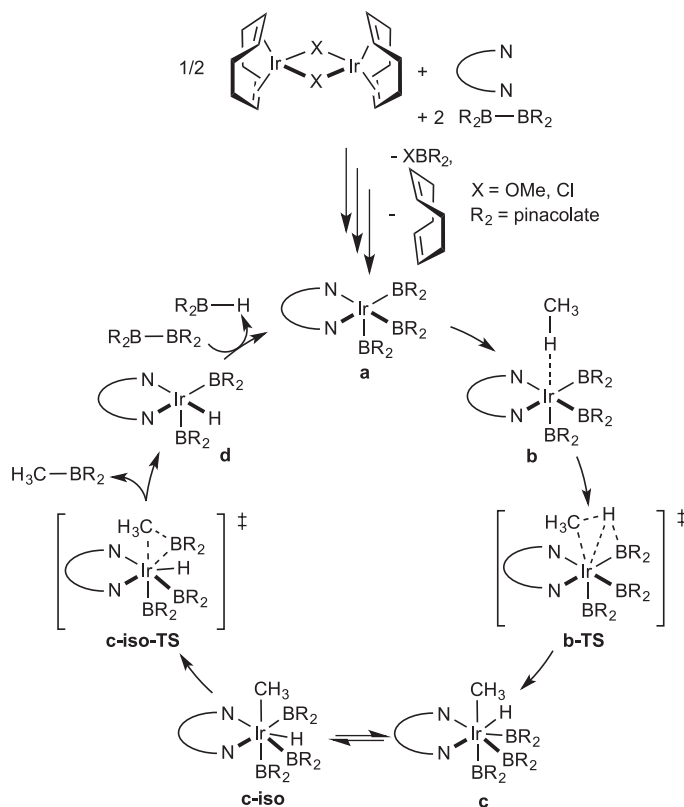
on the Ir-phenanthroline system, and the proposed catalytic cycle is summarized in Fig. 1. Before catalysis can take place, the  $[\text{Ir}(\text{COD})(\mu\text{-X})_2]$  ( $\text{X}^- = \text{OMe}$  or  $\text{Cl}$ ) undergoes a series of ligand substitutions to ultimately yield  $(\text{phen})\text{Ir}(\text{Bpin})_3$

**Table 1. 1,10-phenanthroline ligands used in the borylation of methane.** The ligands were added in a 2:1 ratio relative to dimeric Ir reagent and in a 1:1 ratio relative to independently prepared  $(\text{MesH})\text{Ir}(\text{Bpin})_3$ . Solvent was either tetrahydrofuran (THF) or cyclohexane (CyH). Results with other ligands are shown in table S4.



Reaction scheme:  $\text{CH}_4 + \text{B}_2\text{pin}_2 \xrightarrow[\text{solvent, 16 hours, 120 °C, - MeOBpin}]{\text{Ir reagent, Ligand, 2068 kPa}}$   $\text{H}_3\text{C-Bpin}$  (**1**) +  $\text{H}_2\text{C}(\text{Bpin})_2$  (**2**) +  $\text{HBpin}$  (**3**) +  $\text{O}(\text{Bpin})_2$

Entry	Ir reagent	Loading (mol %)	Ligand	Solvent	Percent yield <b>1</b>	Ratio <b>1</b> : <b>2</b>
1	$[\text{Ir}(\text{COD})(\mu\text{-OMe})_2]$	2.5	L3	THF	2.6	n/a
2	$[\text{Ir}(\text{COD})(\mu\text{-OMe})_2]$	5.0	L1	THF	1.5	n/a
3	$[\text{Ir}(\text{COD})(\mu\text{-OMe})_2]$	5.0	L2	THF	1.5	n/a
4	$[\text{Ir}(\text{COD})(\mu\text{-OMe})_2]$	5.0	L3	THF	2.7	n/a
5	$[\text{Ir}(\text{COD})(\mu\text{-OMe})_2]$	2.5	L3	CyH	2.0	3.9:1
6	$[\text{Ir}(\text{COD})(\mu\text{-OMe})_2]$	5.0	L3	CyH	2.3	2.5:1
7	$(\text{MesH})\text{Ir}(\text{Bpin})_3$	2.5	L3	THF	4.1	n/a
8	$(\text{MesH})\text{Ir}(\text{Bpin})_3$	5.0	L5	THF	2.4	n/a
9	$(\text{MesH})\text{Ir}(\text{Bpin})_3$	2.5	L5	CyH	1.7	2.9:1







$1\text{-}^{13}\text{C}$  as the only product derived from  $^{13}\text{CH}_4$  borylation (fig. S7), excluding the possibility of pinacol or solvent degradation as possible sources of  $\text{CH}_3$ . Mechanistically, we expect the phosphine system to follow the same route outlined above for the polypyridyl systems.

## REFERENCES AND NOTES

- V. N. Cavaliere, B. F. Wicker, D. J. Mindiola, *Adv. Organomet. Chem.* **60**, 1–47 (2012).
- V. N. Cavaliere, D. J. Mindiola, *Chem. Sci.* **3**, 3356–3365 (2012).
- R. H. Crabtree, *Chem. Rev.* **85**, 245–269 (1985).
- G. Parshall, *Homogeneous Catalysis* (Wiley, New York, 1982).
- H. Arakawa et al., *Chem. Rev.* **101**, 953–996 (2001).
- W. A. Chupka, J. Berkowitz, *J. Chem. Phys.* **54**, 4256–4266 (1971).
- J. Berkowitz, J. P. Greene, H. Cho, B. Ruscic, *J. Chem. Phys.* **86**, 674–676 (1987).
- S. J. Blanksby, G. B. Ellison, *Acc. Chem. Res.* **36**, 255–263 (2003).
- A. E. Shilov, G. B. Shul'pin, *Chem. Rev.* **97**, 2879–2932 (1997).
- A. Caballero, P. J. Pérez, *Chem. Soc. Rev.* **42**, 8809–8820 (2013).
- R. A. Periana et al., *Science* **280**, 560–564 (1998).
- R. A. Periana, O. Mironov, D. Taube, G. Bhalla, C. J. Jones, *Science* **301**, 814–818 (2003).
- A. D. Sadow, T. D. Tilley, *Angew. Chem. Int. Ed.* **42**, 803–805 (2003).
- A. D. Sadow, T. D. Tilley, *J. Am. Chem. Soc.* **127**, 643–656 (2005).
- M. V. Kirilova et al., *J. Am. Chem. Soc.* **129**, 10531–10545 (2007).
- A. Caballero et al., *Science* **332**, 835–838 (2011).
- M. Lin, A. Sen, *Nature* **368**, 613–615 (1994).
- I. A. I. Mkhaliid, J. H. Barnard, T. B. Marder, J. M. Murphy, J. F. Hartwig, *Chem. Rev.* **110**, 890–931 (2010).
- G. A. Chotana et al., *Chem. Commun. (Camb.)* **45**, 5731–5733 (2009).
- B. Ghaffari et al., *Organometallics* **34**, 4732–4740 (2015).
- S. Shimad, A. S. Batsanov, J. A. K. Howard, T. B. Marder, *Angew. Chem. Int. Ed.* **40**, 2168–2171 (2001).
- W. N. Palmer, J. V. Obligation, I. Pappas, P. J. Chirik, *J. Am. Chem. Soc.* **138**, 766–769 (2016).
- C. W. Liskey, C. S. Wei, D. R. Pahls, J. F. Hartwig, *Chem. Commun. (Camb.)* **45**, 5603–5605 (2009).
- B. A. Vanchur II et al., *Chem. Commun. (Camb.)* **46**, 7724–7726 (2010).
- P. Nguyen, H. P. Blom, S. A. Westcott, N. J. Taylor, T. B. Marder, *J. Am. Chem. Soc.* **115**, 9329–9330 (1993).
- All energies discussed are obtained from calculations without any corrections for concentration differences. That is, all calculations assume standard conditions. In reality, the substrate concentrations are a few orders of magnitude higher than the concentration of the catalyst. Thus, Le Chatelier's principle will give rise to a lowering of all free energies by a few kcal/mol. As a result, our computed barrier of 25.9 kcal/mol must be considered an upper bound estimate. The real barrier will be a few kcal/mol lower because of the concentration differential.
- H. Tamura, H. Yamazaki, H. Sato, S. Sakaki, *J. Am. Chem. Soc.* **125**, 16114–16126 (2003).
- Q. Li, C. W. Liskey, J. F. Hartwig, *J. Am. Chem. Soc.* **136**, 8755–8765 (2014).
- T. Tagata, M. Nishida, *Adv. Synth. Catal.* **346**, 1655–1660 (2004).
- A. B. Crooks et al., *ACS Catalysis* **5**, 3342–3353 (2015).
- Z. Yinghuai et al., *Inorg. Chem.* **47**, 5756–5761 (2008).
- J. Wei, E. Iglesia, *Angew. Chem. Int. Ed.* **43**, 3685–3688 (2004).

## ACKNOWLEDGMENTS

A U.S. provisional patent has been filed for this work. Financial support of this research was provided to D.J.M. by the University of Pennsylvania. M.G.-M. thanks the Ministry of Education of Spain for sponsoring his work in the United States. M.-H.B. thanks the Institute for Basic Science (IBS-R10-D1) in Korea for support. M.R.S. thanks the NIH (GM63188) for support. We thank B. Ghaffari and K. Gore for providing some catalysts and ligands and B.-C. Lee for help in some catalytic reactions. Experimental procedures, spectroscopic measurements, and theoretical calculations are provided in the supplementary materials.

## SUPPLEMENTARY MATERIALS

www.sciencemag.org/content/351/6280/1424/suppl/DC1  
Materials and Methods  
Supplementary Text  
Figs. S1 to S15  
Tables S1 to S8  
References (33–43)

30 November 2015; accepted 18 February 2016  
10.1126/science.aad9730

## MAGNETOHYDRODYNAMICS

# Large-scale magnetic fields at high Reynolds numbers in magnetohydrodynamic simulations

H. Hotta,<sup>1,2\*</sup> M. Rempel,<sup>2</sup> T. Yokoyama<sup>3</sup>

The 11-year solar magnetic cycle shows a high degree of coherence in spite of the turbulent nature of the solar convection zone. It has been found in recent high-resolution magnetohydrodynamics simulations that the maintenance of a large-scale coherent magnetic field is difficult with small viscosity and magnetic diffusivity ( $\lesssim 10^{12}$  square centimeters per second). We reproduced previous findings that indicate a reduction of the energy in the large-scale magnetic field for lower diffusivities and demonstrate the recovery of the global-scale magnetic field using unprecedentedly high resolution. We found an efficient small-scale dynamo that suppresses small-scale flows, which mimics the properties of large diffusivity. As a result, the global-scale magnetic field is maintained even in the regime of small diffusivities—that is, large Reynolds numbers.

The Sun shows an 11-year magnetic activity cycle that exhibits a large degree of coherence. The Sun's activity has been recorded in terms of number of sunspots, whose record has a long observation history dating from 1610 (1). The coherence of the large-scale field is evident from the 11-year polar field reversals and parity rules of sunspot pairs (2) that show only very few violations. The solar magnetic field and its cyclic activity is thought to be maintained by dynamo action: the transformation of kinetic energy to magnetic energy by the turbulent motion of the ionized plasma in the solar convection zone (3). A remaining mystery is the generation process of the coherent large-scale magnetic field in the presence of chaotic small-scale fields, which are expected because of the large magnetic and fluid Reynolds numbers of the solar convection zone. Some studies have already succeeded in reproducing a magnetic cycle in three-dimensional (3D) convection calculations (4–6). Recent calculations, however, suggest that large fluid and magnetic Reynolds numbers—small viscosity and magnetic diffusivity—lead to a reduction of the energy and coherence of the global-scale magnetic field (7). 2.5D kinematic dynamo calculations with high magnetic Reynolds numbers suggest that the construction of the global-scale magnetic field requires the suppression of the small-scale dynamo (8, 9). Although the suppression of the small-scale dynamo is caused by the strong shear in these investigations, they suggested a possibility of the nonlinear Lorentz feedback that can suppress the small-scale phenomena and cannot be included in these investigations because of kinematic assumption—that is, ignoring the Lorentz force. The global dynamo cal-

culations that show the coherent global-scale magnetic field (4–6) use relatively large viscosity and magnetic diffusivity ( $\geq 10^{12}$  cm<sup>2</sup> s<sup>-1</sup> in solar cases) or small number of grid points in ILES (implicit large-eddy simulation) approaches in order to suppress the small-scale chaotic magnetic field. However, the sun has very small viscosity and magnetic diffusivity (1 and 10<sup>4</sup> cm<sup>2</sup> s<sup>-1</sup> at the base of the convection zone, respectively) (10, 11). Thus, we need to understand the construction mechanism of the global-scale magnetic field in the presence of small viscosity and diffusivity.

A hint is seen in recent high-resolution calculations for the small-scale dynamo in the solar convection zone (12). For sufficiently high resolution, the small-scale dynamo becomes efficient, and the magnetic energy exceeds the kinetic energy on small scales. Then, the Lorentz force feedback becomes significant—the kinematic assumption is no longer valid, and the small-scale flow is suppressed. This process requires a high resolution to resolve the inertial scale of the turbulence well. Because of the substantial scale separation between the global scale of the sun (circumference is  $4.4 \times 10^9$  m) and the energy injection scale of the turbulence (density scale height is  $6 \times 10^7$  m at the base of the convection zone), resolving an efficient small-scale dynamo in global simulations requires a large number of grid points and/or efficient numerical schemes that resolve small-scale turbulence.

Here, we present high-resolution calculations that resolve the turbulence inertial scale well and maintain an efficient small-scale dynamo even in the global domain. We adopt the reduced speed of sound technique (13) and solve the 3D magnetohydrodynamics equations in spherical geometry ( $r, \theta, \phi$ ) with gravity and rotation. The solar standard model (Model S) is used for the background stratification (14). We have previously performed similar calculations, but without rotation (15) or magnetic field (16). In addition, the calculation time is much longer in this study. In

<sup>1</sup>Department of Physics, Graduate School of Science, Chiba University, 1-33 Yayoi-cho, Inage-ku, Chiba 263-8522, Japan.

<sup>2</sup>High Altitude Observatory, National Center for Atmospheric Research (NCAR), Post Office Box 3000, Boulder, CO 80307, USA.

<sup>3</sup>Department of Earth and Planetary Science, University of Tokyo, 7-3-1, Hongo, Bunkyo-ku, Tokyo, 113-0033, Japan.

\*Corresponding author. E-mail: hotta@chiba-u.jp



order to focus on the interaction of large- and small-scale dynamo, we restrict our radial extent to  $0.715R_{\odot} < r < 0.96R_{\odot}$ , where  $R_{\odot}$  is the solar radius and the full sphere is covered by using the Yin-Yang grid (17). Here, we focus on four cases, which we name “Low,” “Medium,” “High,” and “High-S” in the following discussion. The grid size for the cases Low and Medium is  $64(r) \times 96(\theta) \times 288(\phi) \times 2(\text{Yin} - \text{Yang})$ . For the case Low, we adopt a relatively large explicit viscosity and magnetic diffusivity. The values are  $10^{12} \text{ cm}^2 \text{ s}^{-1}$  at the top boundary with a dependence of  $1/\sqrt{\rho_0}$ , where  $\rho_0$  is the background density, which is same as in the previous study with cyclic magnetic activity (6). For the case Medium, we exclude explicit viscosity and magnetic diffusivity and use only a slope-limited numerical diffusivity (18) in order to increase the effective resolution. Then, we increase the number of grid points by a factor of 4 in the case High,  $256(r) \times 384(\theta) \times 1152(\phi) \times 2(\text{Yin} - \text{Yang})$ , without explicit viscosity and magnetic diffusivity. In the ordinary spherical geometry, this number of the grid points corresponds to  $256(r) \times 768(\theta) \times 1536(\phi)$ . Case High-S has twice the resolution of case High, with a grid size of  $512(r) \times 768(\theta) \times 2304(\phi) \times 2(\text{Yin} - \text{Yang})$ . Because we use the same values for the explicit viscosity and magnetic diffusivity in the case Low, the magnetic Prandtl number is unity. In addition, we use completely the same slope-limited diffusion for the velocities and magnetic fields, and we expect that the effective magnetic Prandtl number would be unity for the cases Medium, High, and High-S. This is estimated and confirmed in the supplementary materials, section 2. We calculate 50 years for cases Low, Medium, and High, and we restrict the calculation time for High-S to 500 days. Case High-S is restarted from a snapshot of case High at 3000 days. The advection time scale at the base of the convection zone is estimated as  $H_p/v_{\text{rms}} \sim 7$  days, where  $H_p \sim 6 \times 10^7$  m and  $v_{\text{rms}} \sim 100 \text{ m s}^{-1}$  are the pressure scale height and root-mean-square velocity at the base of the convection zone, respectively. Thus, 500 days correspond to 70 advection time. Although the calculation time for High-S is not enough to investigate the evolution of the large-scale magnetic field, we include this case to further study the dependence of the small-scale dynamo on resolution. In all cases, we use the solar rotation rate  $\Omega_0/(2\pi) = 413 \text{ nHz}$  (19) and a large thermal conductivity  $\kappa = 2 \times 10^{13} \text{ cm}^2 \text{ s}^{-1}$  with a radial dependence of  $1/\sqrt{\rho_0}$  (6). Large thermal conductivity reduces the convective velocity and increases the rotational constraint, which leads to solar-like differential rotation—that is, equatorial acceleration (20, 21). These settings are summarized in Table 1.

Energy flux and differential rotation are shown in the supplementary materials (figs. S1 and S2). When we increase the resolution, magnetic energy increases, and Lorentz force feedback leads to a reduction of differential rotation. Regarding the energy flux, using our parameters the enthalpy (convective) flux transports 60% of solar luminosity. This behavior does not depend on the resolution. The amplitude of the enthalpy flux

possibly changes the location of the large-scale dynamo. For example, when the enthalpy flux is reduced, the convective velocity becomes small, and the rotational constraint becomes strong. In our study, the large-scale magnetic field is concentrated near the base of the convection zone. Strong rotational constraint possibly changes this location to the middle of the convection zone (22).

Shown in Fig. 1 and movie S1 are the contour of radial velocity  $v_r$  at  $r = 0.95R_{\odot}$  (Fig. 1, A, C, and E) and longitudinal magnetic field  $B_{\phi}$  at  $r = 0.72R_{\odot}$  (Fig. 1, B, D, and F). Although the overall convection patterns among the cases are similar,

the case High clearly includes the small-scale turbulence (Fig. 1E). Similar to the previous study (6), the global-scale coherent magnetic field is maintained at the base of the convection zone in the case Low (Fig. 1B). This is weakened with smaller diffusivities in the case Medium (Fig. 1D). The large-scale magnetic field seems recovered in the higher resolution (Fig. 1F). This finding is more clearly seen in butterfly diagram-type figures. The zonally averaged toroidal magnetic field  $\langle B_{\phi} \rangle$  at the base of the convection zone ( $r = 0.72R_{\odot}$ ) is shown in Fig. 2, where angle brackets denote the zonal average. In the case Low, coherent magnetic field and its cyclic

Table 1. List of calculated cases. In the first three lows, the number of grid points, type of diffusivities, and calculation time are shown. The numbers of grid points are in the Yin-Yang grid. Thus, the total number of the grid points is $N_r \times N_{\theta} \times N_{\phi} \times 2$ . In the final two lows, the turbulent and mean magnetic energy density averaged from $0.715R_{\odot}$ to $0.73R_{\odot}$ are shown. The averaged period for the cases Low, Medium, and High is from 5000 to 12,500 days. The period for the case High-S is from 300 to 500 days. The value in parentheses for the case High shows the value from 3300 day to 3500 day, the same period for the High-S. The unit for energy is erg per cubic centimeter.				
Case	Low	Medium	High	High-S
$(N_r, N_{\theta}, N_{\phi})$	(64,96,288)	(64,96,288)	(256,384,1152)	(512,768,2304)
Diffusivities	Explicit	Implicit	Implicit	Implicit
Run time	50 years	50 years	50 years	500 days
Turbulent $E_{\text{mag}}$	$1.2 \times 10^6$	$1.6 \times 10^6$	$2.4(3.0) \times 10^6$	$3.4 \times 10^6$
Mean $E_{\text{mag}}$	$2.0 \times 10^6$	$6.7 \times 10^6$	$1.1(2.7) \times 10^6$	$2.3 \times 10^5$

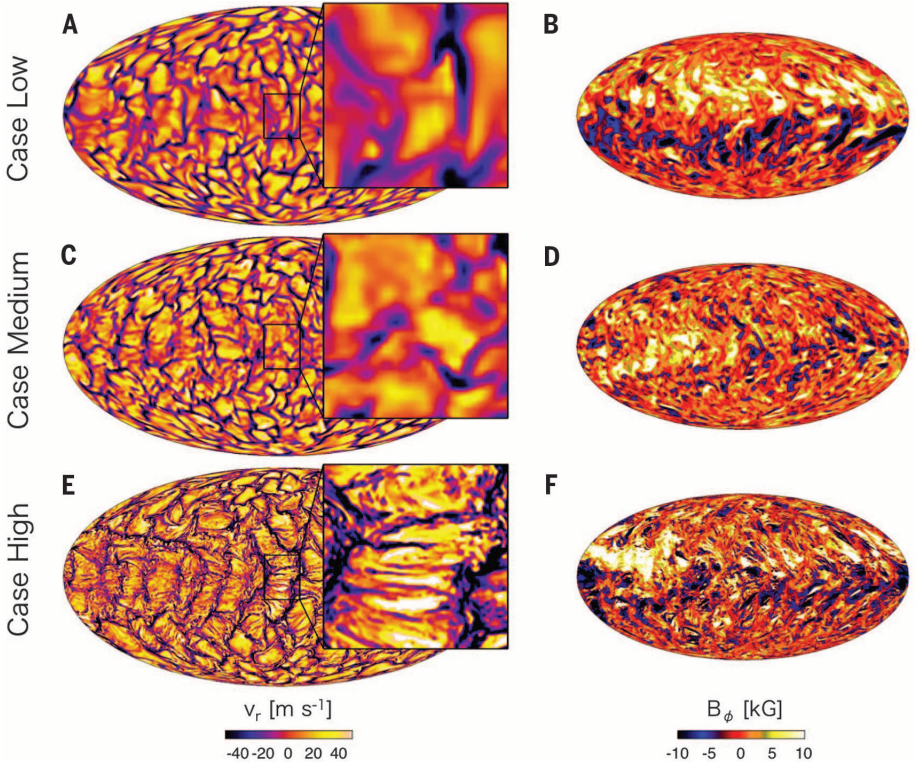


**Fig. 1. Comparison of the different resolutions.** (A, C, and E) The radial velocity at  $r = 0.95R_{\odot}$ . (B, D, and F) The longitudinal magnetic field  $B_{\phi}$  at  $r = 0.72 R_{\odot}$ . The top, middle, and bottom rows show the results from the cases Low, Medium, and High, respectively.

variation is seen (Fig. 2A). Then, these features become weak in the case Medium (Fig. 2B). When the resolution is increased further, the coherent magnetic field and its cycle are recovered (Fig. 2C). Shown in Table 1 are the turbulent

magnetic energy density  $B'^2/(8\pi)$ , where  $B' = B - \langle B \rangle$ , and mean magnetic energy  $\langle B \rangle^2/(8\pi)$  averaged from  $0.715R_\odot$  to  $0.73R_\odot$ , where the mean magnetic field is concentrated. Whereas the turbulent magnetic energy (dominant con-

tribution to total magnetic energy) increases monotonically with increasing the resolution, the mean magnetic energy has a different behavior. From Low to Medium, the energy decreases by a factor of 3, and half of the mean magnetic energy from the case Low is recovered in the case High.

Our finding can be understood with Fig. 3, which shows the energy spectra at the base of the convection zone ( $r = 0.72R_\odot$ ). Whereas in case Medium, the magnetic energy is always smaller than the kinetic energy, indicating an inefficient small-scale dynamo, the small-scale ( $l > 40$ , where  $l$  is the spherical harmonic degree) magnetic energy exceeds the kinetic energy in the case High. This is an indication of an efficient small-scale dynamo. The possibility that the strong small-scale magnetic field is generated by the small-scale dynamo is supported by fig. S3. From the calculation without rotation (only small-scale dynamo action), we find a ratio ( $E_{\text{mag}}/E_{\text{kin}}$ ) comparable with that of the case High. From this, we conclude that the small-scale magnetic field in the case High is mostly generated by the small-scale dynamo.

The velocity amplitude in the small scale is significantly suppressed by the small-scale magnetic field. In the case Medium, the small-scale flow leads to destruction of the global magnetic field. This is confirmed with an additional calculation for the case Medium with the same explicit viscosity as the case Low, but no explicit magnetic diffusivity (fig. S4). That calculation also shows a similar level of coherent global-scale magnetic field as the case Low. In this control experiment, the large viscosity suppresses the small-scale flow, which tends to destruct the global-scale magnetic field, whereas in the case High, the suppression is a consequence of feedback from the strong small-scale magnetic field. Previous studies suggested that the nonlinearity of the magnetic field can suppress the exponential growth of the small-scale dynamo and set a finite amplitude of the magnetic field, which may be essential in allowing the reproduction of the large-scale magnetic field (8, 9). Because our calculation is nonlinear, this effect is included. Our new finding here is that the suppression of the small-scale flow supports the construction of large-scale magnetic field, and small-scale dynamo is still efficient. Because the case High-S continues only a short time owing to the restriction of our computer resource, we cannot conclude that the large-scale magnetic field in the case High-S is self-consistently generated by the large-scale dynamo. However, we can check the numerical convergence and the tendency of the small-scale dynamo in the currently unreachable high-resolution calculation. The kinetic and magnetic energy spectra of the cases High and High-S are shown in fig. S5. This figure shows that when we adopt higher resolution, the small-scale velocity is more reduced; our obtained effect is more promoted in higher resolution.

Our result demonstrates that a global-scale coherent magnetic field can be maintained even with small viscosity and magnetic diffusivity, provided that the Lorentz-force feedback from a small-scale magnetic field is strong enough. We roughly

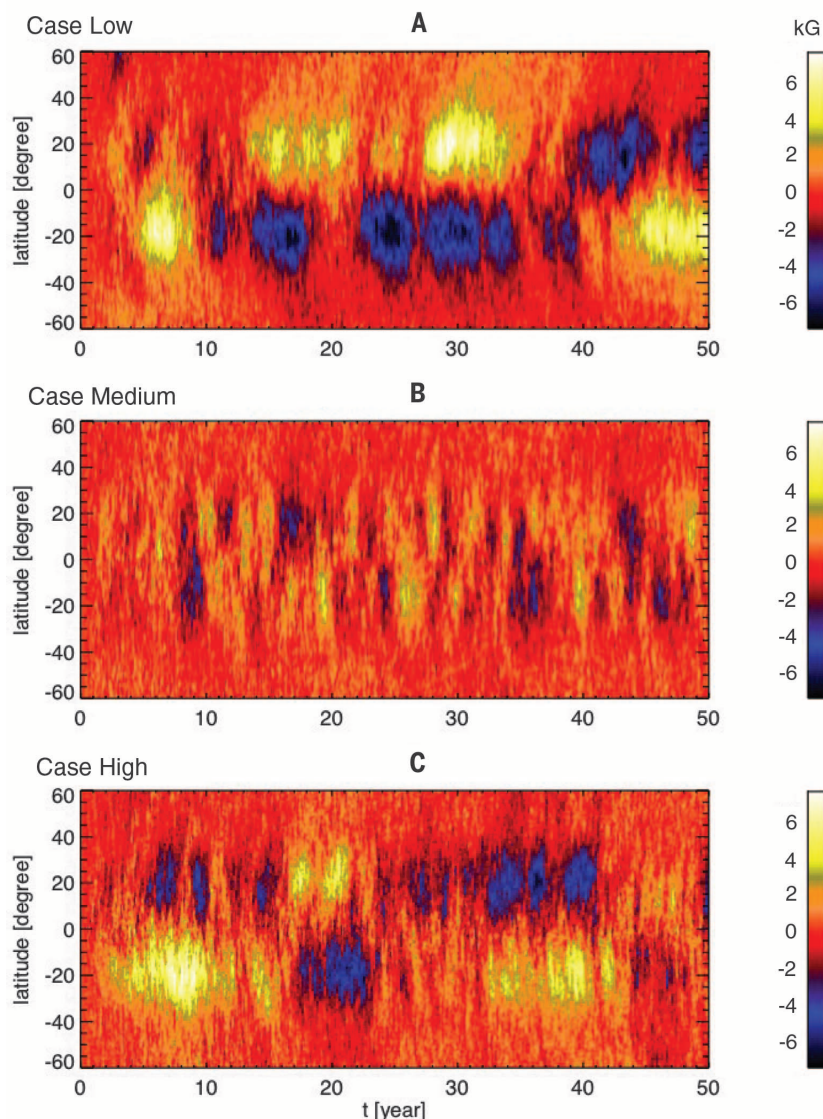
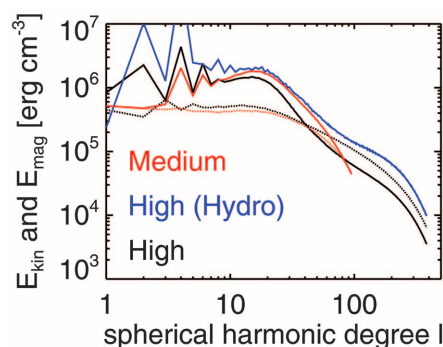


**Fig. 2. Toroidal magnetic field at the base of the convection zone.** (A to C) Zonally averaged toroidal magnetic field ( $B_\phi$ ) at  $r = 0.72R_\odot$ . The result from the cases Low, Medium, and High are shown in (A), (B), and (C), respectively.

### Fig. 3. Spectra of the cases Medium and High.

The kinetic (solid) and magnetic (dotted) energy spectra at  $r = 0.72R_\odot$ . The red line shows the result from the case Medium. The blue and black lines show the result from the cases High without magnetic field (hydrodynamic) and High with magnetic field, respectively. The averaged period is the same as Table 1, from 5000 to 12,500 days.





estimate the Reynolds number for the cases High and High-S. The values are 2000 and 7000 for the cases High and High-S, respectively (the detailed explanation for the estimation is given in the supplementary materials). Thus, the effective diffusivities for the cases High and High-S are  $1.6 \times 10^{11}$  and  $4.6 \times 10^{10} \text{ cm}^2 \text{ s}^{-1}$ , respectively. Because it was found in (23) that the critical Reynolds number for exciting the dynamo is  $\sim 100$ , our achieved Reynolds numbers are  $\sim 20$  and 70 times larger than the threshold. Although the presented calculation has still a much larger viscosity and magnetic diffusivity than those of the real Sun ( $< 10^4 \text{ cm}^2 \text{ s}^{-1}$ ), the obtained mechanism does not require any assumption of large “turbulent” diffusivities because Maxwell stresses from the small-scale field can mimic their effect.

## REFERENCES AND NOTES

1. I. G. Usoskin, K. Mursula, G. A. Kovaltsov, *Sol. Phys.* **218**, 295–305 (2003).
2. G. E. Hale, S. B. Nicholson, *Astrophys. J.* **62**, 270 (1925).
3. E. N. Parker, *Astrophys. J.* **122**, 293 (1955).
4. M. Ghizaru, P. Charbonneau, P. K. Smolarkiewicz, *Astrophys. J.* **715**, L133–L137 (2010).
5. B. P. Brown, M. S. Miesch, M. K. Browning, A. S. Brun, J. Toomre, *Astrophys. J.* **731**, 69 (2011).
6. Y. Fan, F. Fang, *Astrophys. J.* **789**, 35 (2014).
7. N. J. Nelson, B. P. Brown, A. S. Brun, M. S. Miesch, J. Toomre, *Astrophys. J.* **762**, 73 (2013).
8. S. M. Tobias, F. Cattaneo, *Nature* **497**, 463–465 (2013).
9. F. Cattaneo, S. M. Tobias, *Astrophys. J.* **789**, 70 (2014).
10. S. Chapman, *Astrophys. J.* **120**, 151 (1954).
11. T. G. Cowling, “Solar Electrodynamics,” in *The Sun*, G. P. Kuiper, Ed. (Univ. Chicago Press, Chicago, 1953), pp. 532–591.
12. H. Hotta, M. Rempel, T. Yokoyama, *Astrophys. J.* **803**, 42 (2015).
13. H. Hotta, M. Rempel, T. Yokoyama, Y. Iida, Y. Fan, *Astron. Astrophys.* **539**, A30 (2012).
14. J. Christensen-Dalsgaard *et al.*, *Science* **272**, 1286–1292 (1996).
15. H. Hotta, M. Rempel, T. Yokoyama, *Astrophys. J.* **786**, 24 (2014).
16. H. Hotta, M. Rempel, T. Yokoyama, *Astrophys. J.* **798**, 51 (2015).
17. A. Kageyama, T. Sato, *Geochim. Geophys. J.* **5**, 9005 (2004).
18. M. Rempel, *Astrophys. J.* **789**, 132 (2014).
19. M. J. Thompson, J. Christensen-Dalsgaard, M. S. Miesch, J. Toomre, *Annu. Rev. Astron. Astrophys.* **41**, 599–643 (2003).
20. T. Gastine, R. K. Yadav, J. Morin, A. Reiners, J. Wicht, *Mon. Not. R. Astron. Soc.* **438**, L76–L80 (2014).
21. N. A. Featherstone, M. S. Miesch, *Astrophys. J.* **804**, 67 (2015).
22. B. P. Brown, M. K. Browning, A. S. Brun, M. S. Miesch, J. Toomre, *Astrophys. J.* **711**, 424–438 (2010).
23. A. S. Brun, M. S. Miesch, J. Toomre, *Astrophys. J.* **614**, 1073–1098 (2004).

## ACKNOWLEDGMENTS

We are grateful to M. Miesch, R. Cameron, and M. Schüssler for helpful comments. H.H. is supported by a Japan Society for the Promotion of Science Postdoctoral Fellowship for Research Abroad. The National Center for Atmospheric Research is sponsored by the National Science Foundation. The results were obtained by using the K computer at the RIKEN Advanced Institute for Computational Science (Proposal no. hpl40212 and hpl50226) and the Yellowstone Supercomputer at NCAR (project code NHA00005). This work was supported by the Ministry of Education, Culture, Sports, Science and Technology Strategic Program for Innovative Research, Joint Institute for Computational Fundamental Science, and Project for Solar-Terrestrial Environment Prediction. Statistical data from the calculations and executable software are available in the supplementary materials.

## SUPPLEMENTARY MATERIALS

www.sciencemag.org/content/351/6280/1427/suppl/DC1  
Supplementary Text

Table S1  
Figs. S1 to S5  
References (24–26)  
Movie S1

Calculation result in IDL format (science.idl)  
Executable file compiled with Fujitsu Fortran

5 August 2015; accepted 10 February 2016  
10.1126/science.aad1893

## SOLAR CELLS

## Photon recycling in lead iodide perovskite solar cells

Luis M. Pazos-Outón,<sup>1</sup> Monika Szumilo,<sup>1</sup> Robin Lamboll,<sup>1\*</sup> Johannes M. Richter,<sup>1\*</sup> Micaela Crespo-Quesada,<sup>2</sup> Mojtaba Abdi-Jalebi,<sup>1</sup> Harry J. Beeson,<sup>1</sup> Milan Vrućinić,<sup>1</sup> Mejd Alsari,<sup>1</sup> Henry J. Snaith,<sup>3</sup> Bruno Ehrler,<sup>4</sup> Richard H. Friend,<sup>1†</sup> Felix Deschler<sup>1‡</sup>

Lead-halide perovskites have emerged as high-performance photovoltaic materials. We mapped the propagation of photogenerated luminescence and charges from a local photoexcitation spot in thin films of lead tri-iodide perovskites. We observed light emission at distances of  $\geq 50$  micrometers and found that the peak of the internal photon spectrum red-shifts from 765 to  $\geq 800$  nanometers. We used a lateral-contact solar cell with selective electron- and hole-collecting contacts and observed that charge extraction for photoexcitation  $> 50$  micrometers away from the contacts arose from repeated recycling between photons and electron-hole pairs. Thus, energy transport is not limited by diffusive charge transport but can occur over long distances through multiple absorption-diffusion-emission events. This process creates high excitation densities within the perovskite layer and allows high open-circuit voltages.

Since 2009 (1), hybrid lead halide perovskite photovoltaics have shown a marked rise in power conversion efficiency to values that are almost comparable to that of crystalline silicon (2–7). This improved photovoltaic performance has been attributed to well-suited material properties such as high absorption cross sections (8), long charge-carrier lifetimes (9), and high emission yields (10). Recent studies in single crystals have reported charge diffusion lengths of 175  $\mu\text{m}$  (11, 12); in polycrystalline thin films, vertical diffusion lengths have been found to be longer than 1  $\mu\text{m}$  (13, 14). Together with high radiative recombination yields and long carrier lifetimes, these properties raise the question of whether absorption and reemission of excited carriers can occur during the transport. We report that such “photon recycling” does indeed play a central role, allowing considerable increases over current descriptions in the characteristic lengths for charge and energy transport.

Highly crystalline inorganic semiconductors with high internal quantum yields, such as GaAs, demonstrate the current record efficiencies in single-junction solar cells (15, 16). The low non-radiative recombination rates and high photoluminescence (PL) yields of these materials allow one photoexcited state to undergo multiple radiative emission-absorption events before it is lost through nonradiative decay (17, 18). This photon recycling effect, together with photonic confinement caused by the difference in refractive index between the active material and its surroundings, leads to a buildup of excited-state population in the bulk of the material, similar to a solar

concentration effect (17). Additionally, the length scales for energy transport are not limited to a single charge diffusion length but can occur through multiple recombination-emission events in an interchange between light and charge states, which markedly enhances the transport length scales.

Previous studies of lead iodide perovskites have shown a sharp absorption onset at the optical band edge, with an Urbach tail slope close to that of GaAs (8, 19), whereas the PL spectrum is homogeneously broadened by interaction with phonons, leading to a considerable intensity beyond the band edge (20). Additionally, long carrier lifetimes and low nonradiative losses have been reported (9, 10). These conditions could support photon recycling.

We studied thin perovskite films (with a thickness of  $\sim 100$  nm) on glass substrates [details of preparation and characterization can be found in the supplementary materials (21)]. Under these conditions, only 10 to 15% of internally generated PL escaped to the air above or to the glass below [calculation in the supplementary materials (21)], and the remaining emission was guided within the film (22). To measure the spatial distribution of photogenerated emission, we used a confocal optical microscope setup with separately controlled excitation and collection objectives and a spatial resolution of  $\sim 1.5 \mu\text{m}$  (Fig. 1A and fig. S1) (21). Photons propagating in the film could be scattered out of the film or be absorbed and re-emitted isotropically. We measured the emission from the edge of the film, maximizing out-scattering and allowing the detection of both components. These results provide a direct probe of the internal photon distribution traveling through the film. Figure 1B shows spatial emission mapping. When excitation is near the edge ( $\leq 4 \mu\text{m}$ ), the observed spectrum is similar to the macroscopic PL of this film, centered at  $\sim 765$  nm (Fig. 1C). However, when the excitation objective was moved farther away from the collection spot, the internal spectrum continuously red-shifted to

<sup>1</sup>Cavendish Laboratory, University of Cambridge, JJ Thomson Avenue, CB3 0HE Cambridge, UK. <sup>2</sup>Department of Chemistry, University of Cambridge, CB2 1EW Cambridge, UK. <sup>3</sup>Clarendon Laboratory, Department of Physics, University of Oxford, OX1 3PU Oxford, UK. <sup>4</sup>Center for Nanophotonics, FOM Institute AMOLF, Science Park 104, 1098 XG Amsterdam, Netherlands.

\*These authors contributed equally to this work. †Corresponding author. E-mail: rhl10@cam.ac.uk (R.H.F.); fd297@cam.ac.uk (F.D.)

beyond 800 nm after the separation increased to 50  $\mu\text{m}$ . Unexpectedly, at these distances we still detected a blue (765-nm) component in the spectrum at a wavelength similar to those of the initial emission spectrum, the origin of which we discuss below.

We used photothermal deflection spectroscopy to measure the absorption coefficients  $\alpha_\lambda$  (where  $\lambda$  is the wavelength) of the films and then compared our findings with the photoluminescence excitation spectrum (Fig. 1C). Under conditions in which photons are mostly confined within a slab (formed here by the glass-perovskite-air structure), the Beer-Lambert law gives a decay

in spectral photon population  $I_\lambda$  away from a pointlike excitation spot with radius  $r_0$

$$I_\lambda(r) = \frac{r_0}{r} I_{\lambda 0} \cdot e^{-(\alpha_\lambda \cdot r)} \quad (1)$$

This relation indicates that the decay is mono-exponential for each wavelength, with an additional radial factor. Using Eq. 1, the predicted spectral decay map following this law is plotted in Fig. 1D. The measured decay in the different spectral regions was substantially slower than the prediction from the Beer-Lambert law. To illustrate the difference, the decay for selected wavelengths was extracted (Fig. 1E) and compared

with Beer-Lambert predictions. Beer-Lambert predictions do not take scattering into account, which further accelerates the decay, particularly in spectral regions of very low absorption.

We attribute the main red-shifted peak to guided photons that out-scattered at the edge of the film. Scattering is nondispersive, so we expect these out-scattered photons to match the internal spectral distribution of photons travelling inside the film. The internal photon spectral distribution was biased toward longer-wavelength photons that travelled farther between emission and absorption events due to the sharp decay of the absorption coefficient at the band tail. These

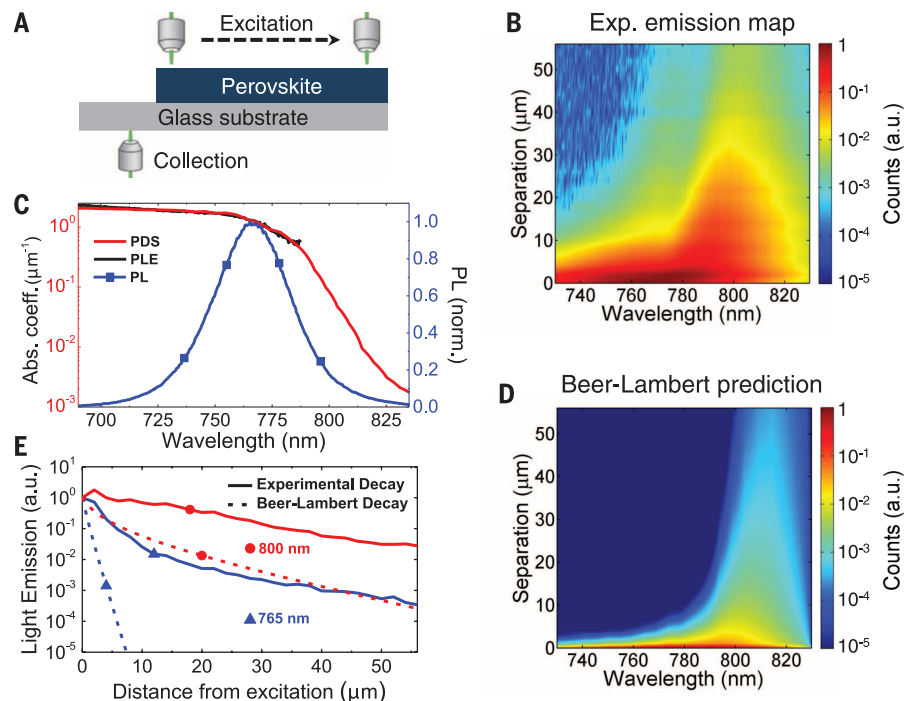


**Fig. 1. Spatial mapping of emission and photon spectrum.** (A) Graphical representation of microscope setup and measurement geometry. (B) Experimentally measured light emission map for different separation distances between excitation and collection. (a.u., arbitrary units) (C) Comparison of normalized PL with PL excitation (PLE) and photothermal deflection spectra. (D) Predicted spatial light emission spectra from the cylindrically decaying Beer-Lambert law. (E) Comparison between experiment (solid lines) and expected decay (dashed lines) from the Beer-Lambert law at 765 and 800 nm. The experimental data are not in agreement with simple linear absorption, which suggests that additional processes, such as photon recycling, maintain substantial photon intensity at large distances.

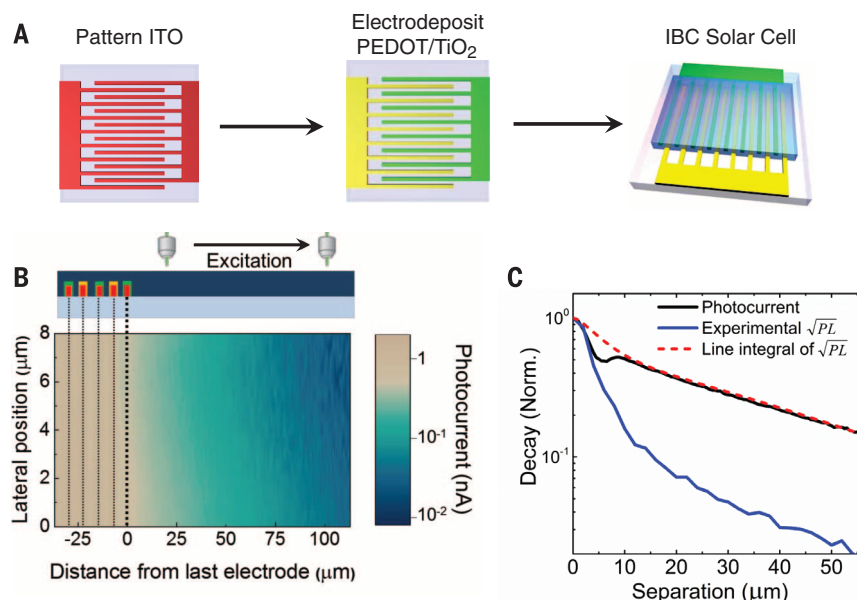


**Fig. 2. Photocurrent mapping of an interdigitated back-contact (IBC) perovskite solar cell.** (A) Fabrication process of the IBC device: (left) pattern a flat sheet of ITO, (middle) electrodeposit  $\text{TiO}_2$  on half of the “fingers” and PEDOT on the other half, and (right) spin-coat the photoactive perovskite layer. (B) Photocurrent map at the edge of the active area of an IBC perovskite device. The lateral position is along the electrode direction. We observed photocurrent several tens of micrometers beyond the last electrode (x-axis position 0  $\mu\text{m}$ , bold dashed line). (C) Comparison between normalized spatial decay of the photocurrent and square root of PL. These results suggest that photon densities, which propagate over large distances through the material assisted by photon recycling, can be extracted as photocurrent.



long-wavelength photons were absorbed and generated electron-hole ( $e^-h^+$ ) pairs far from the original excitation spot. When these  $e^-h^+$  pairs recombined, they regenerated the original emission spectrum that peaks near 765 nm, giving rise to the second observed peak. The photon energy gain between absorption and re-emission occurred via phonon-assisted thermalization.

With the observed spatial decay of photon intensity, charges are expected to be generated at comparable distances. To measure the spatial charge distribution directly, we designed a lateral solar cell with electron- and hole-selective electrodes. The fabrication process of this back-contacted device (Fig. 2A) began with a plain sheet of indium tin oxide (ITO) covering a glass substrate. Photolithography was used to make a pattern of ITO with interdigitated electrodes. The channel and electrode width was  $\sim 4 \mu\text{m}$  (a pitch of  $8 \mu\text{m}$ ). Electrodeposition was used to selectively deposit electron- and hole-blocking layers. On half of the electrodes,  $\text{TiO}_2$  was deposited from a solution of  $\text{Ti}(\text{O}_2)\text{SO}_4$ , and poly-3,4-ethylenedioxythiophene (PEDOT) from a 3,4-ethylenedioxythiophene monomer-based solution was deposited in the remaining electrode surface. The  $\text{TiO}_2$  layer was formed by hydrolysis, whereas the PEDOT film formed by polymerization under an external bias. Finally, a layer of perovskite was spin-coated from a standard precursor solution based on methylammonium iodide mixed with lead acetate in  $N,N'$ -dimethylformamide (23), and uniform film formation was detected on both electrodes [see supplementary materials and methods (27)].

The electric response of this device measured in the dark revealed a diode-like rectifying behavior. Under solar irradiation, a photovoltaic response with an open-circuit voltage of 0.5 V was observed (fig. S14), showing effective carrier selectivity at the electrodes. Photocurrent extraction appeared to be limited in our device compared with vertical solar cells, possibly due to energy barriers at the electrodes and an unfavorable charge collection geometry. For comparison, a lateral solar cell without selective

layers (fig. S15) (21) showed a reduced charge selectivity, as well as very limited voltage and photocurrent.

We used confocal microscopy to map the spatially resolved photocurrent generation in these devices with an excitation resolution below  $1 \mu\text{m}$ . The photocurrent probed the number of photoexcited carriers that reached the electrodes. Figure 2B shows a spatial map of photocurrent, both across the interdigitated electrodes ( $\leq 1 \mu\text{m}$ ) and for photoexcitation beyond the electrodes (0 to  $100 \mu\text{m}$ ). The very slow falloff in photocurrent for excitation beyond the edge of the electrode structure (see also Fig. 2C) extends well beyond the reported diffusion lengths of lead halide perovskite thin films.

In the range of excitation fluences used in our experiment, PL in perovskites mainly arises from bimolecular recombination of charge carriers with volume density  $n$  (i.e.,  $PL \propto n^2$ ), consistent with  $e^-h^+$  recombination (10, 24). Hence, we can relate the locally generated PL, taken around the PL emission peak (765 nm), with the local charge density, and  $\sqrt{PL} \propto n$  is a probe of the spatial charge distribution. Because  $\sqrt{PL}$  decays cylindrically, it must be geometrically corrected by performing a line integral of  $\sqrt{PL}$  over the length of the electrode, to compare it with the photocurrent measurements.

In Fig. 2C, we compare the decay of the integrated  $\sqrt{PL}$  with the measured spatial decay of the photocurrent. We observed a similar decay in photocurrent and integrated  $\sqrt{PL}$  beyond  $8 \mu\text{m}$ , which is the resolution set by the electrode geometry. The agreement between these two quantities indicates that the redshifted component of the recycled photons allows excitation transport over long distances, beyond carrier diffusion lengths, which eventually can be extracted as photocurrent from a solar cell.

To model this, we set up and solved a system of cylindrically symmetric partial differential equations based on existing theoretical approaches for photon recycling (25–27). We expanded these concepts (21) to account for local

excitation and calculate the local photon distribution in the film

$$\frac{dn}{dt} = D\nabla^2 n + G + \frac{c}{n_s} \sum_{\lambda} \alpha_{\lambda} \gamma_{\lambda} - k_1 n - k_2 n^2 \quad (2)$$

$$\frac{d\gamma_{\lambda}}{dt} = D_{\lambda} \nabla^2 \gamma_{\lambda} - \frac{c}{n_s} \alpha_{\lambda} \gamma_{\lambda} + (k_2 n^2 P_{\text{stay}}) P_{\lambda} \quad (3)$$

The charge-carrier concentration  $n$  and the photon density  $\gamma$  were modeled (at different wavelengths  $\lambda$ ) as a function of distance from the excitation spot. Input parameters are reported experimental values for carrier diffusion [diffusion constant  $D = 0.5 \text{ cm}^2 \text{ s}^{-1}$  (9, 11, 12)], mono- and bimolecular recombination rates of carriers [ $k_1 = 10^6 \text{ s}^{-1}$  and  $k_2 = 10^{-10} \text{ cm}^3 \text{ s}^{-1}$ ; from our own measurements and (10, 28)], and the measured wavelength-dependent absorption coefficients  $\alpha_{\lambda}$  (Fig. 1C). (Additionally,  $t$  is time,  $G$  is the generation rate,  $c$  is the speed of light,  $n_s$  is the refractive index,  $P_{\text{stay}}$  is the optical probability of photon escape, and  $P_{\lambda}$  is the probability that light will be emitted with a given wavelength.) The experimentally measured external bimolecular rate had to be adjusted to account for photon recycling (29, 30). All absorption of photons is assumed to result in the creation of  $e^-h^+$  pairs, but only the bimolecular channel is radiative (with the spectrum as shown in Fig. 1C), and a proportion  $1 - P_{\text{stay}}$  [modeled to be 12.5% (21)] of these photons is lost through optical transmission out of the perovskite at the interfaces. The external PL quantum efficiency (PLQE) results from multiple internal recycling events and is related to the internal PLQE by the geometric series

$$PLQE_{\text{ext}} =$$

$$\sum_{r=1}^{\infty} (PLQE_{\text{int}})^r (1 - P_{\text{escape}})^{r-1} P_{\text{escape}} = \frac{PLQE_{\text{int}} P_{\text{escape}}}{1 - PLQE_{\text{int}} (1 - P_{\text{escape}})} \quad (4)$$

The external PLQE varies with distance from the excitation spot and the carrier density (Fig. 3A). Photon recycling could be very efficient near the excitation spot but dropped off at larger distances for which charge-carrier densities are smaller. From Eq. 4, we find that internal PLQEs can exceed 50% for 1-sun illumination (here, sun is defined as the solar spectrum standard ASTM G173) (internal carrier density  $\sim 10^{15} \text{ cm}^{-3}$ ), corresponding to lower measured external PLQEs of  $\sim 10\%$ . The observed recycling effect on extraction would be increased in a solar cell with homogeneous illumination, which produces constant carrier densities over the full active area.

In order for this model to match the experimental photocurrent, recycling must be taken into account to explain the observed long spatial decays (Fig. 3B). On average, the model predicts one recycling event per photoexcited charge carrier under 1-sun illumination before the carrier decays

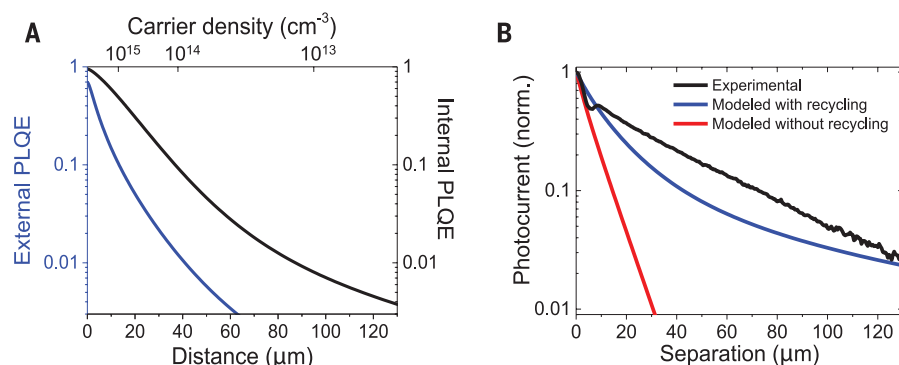


**Fig. 3. Predicted effects of photon recycling.** (A) Change in external and internal PLQE as a function of distance derived from a photon recycling diffusion model as presented in the text, with reported mono- and bimolecular recombination ( $k_{\text{mono}} = 10^6 \text{ s}^{-1}$ ,  $k_{\text{bi}} = 10^{-10} \text{ cm}^3 \text{ s}^{-1}$ ) and diffusion constants ( $D = 0.5 \text{ cm}^2 \text{ s}^{-1}$ ) of photoexcited carriers. (B) Predicted spatial photocurrent decay for the model with and without photon recycling.

nonradiatively [calculation in the supplementary materials (27)] in a perovskite film in air on glass. This value relates to a photon recycling-assisted average excitation travel distance of 20  $\mu\text{m}$  (fig. S18). The average travel distance could be enhanced at larger charge densities (for example, under high fluences) and can reach values beyond 50  $\mu\text{m}$ .

In terms of  $e^-h^+$  transport, our results suggest that the average distance a charge carrier can travel in a perovskite is not limited by the charge-carrier diffusion length, for as long as recombination is radiative and the photon stays in the film, the  $e^-h^+$  pair can be regenerated and can propagate over large distances. This process creates a distinction between extraction and charge diffusion lengths and allows us to solve the existing contradiction of reported high recombination rates and long diffusion lengths.

What are the implications of the observations presented here for standard thin-film perovskite solar cells (3, 6)? The thin-film samples from our work provide valuable model systems for these structures. Using the model and parameters developed above, we estimate that, under open-circuit conditions, in a device with a thickness of 350 nm and nonquenching electrodes, recycling produces a doubling of the internal photon density under 1-sun illumination. These effects can be enhanced further by minimizing nonradiative decay channels and being subjected to higher fluences, such as in solar concentrators, where high bimolecular recombination rates dominate. In the ideal case of unity PLQE and a perfect back mirror, photon recycling can produce internal photon densities up to 25 suns ( $4n^2$  with  $n = 2.5$ ) (31) in perovskite solar cells under open-circuit conditions. Photon management, such as the use of highly reflective back mirrors to minimize photonic losses and texturing of the top surface, offers promising approaches for using photon recycling to improve photoconversion efficiencies of perovskite solar cells toward the Shockley-Queisser limit. Higher photon densities lead to higher internal luminescence and a build-up of excited charges, which increase the split of quasi-Fermi levels and enhance the achievable open-circuit voltage in a solar cell.

## REFERENCES AND NOTES

- A. Kojima, K. Teshima, Y. Shirai, T. Miyasaka, *J. Am. Chem. Soc.* **131**, 6050–6051 (2009).
- J.-H. Im, C.-R. Lee, J.-W. Lee, S.-W. Park, N.-G. Park, *Nanoscale* **3**, 4088–4093 (2011).
- M. M. Lee, J. Teuscher, T. Miyasaka, T. N. Murakami, H. J. Snaith, *Science* **338**, 643–647 (2012).
- M. Liu, M. B. Johnston, H. J. Snaith, *Nature* **501**, 395–398 (2013).
- H.-S. Kim et al., *Sci. Rep.* **2**, 591 (2012).
- N. J. Jeon et al., *Nature* **517**, 476–480 (2015).
- J. Burschka et al., *Nature* **499**, 316–319 (2013).
- S. De Wolf et al., *J. Phys. Chem. Lett.* **5**, 1035–1039 (2014).
- C. Wehrenfennig, G. E. Eperon, M. B. Johnston, H. J. Snaith, L. M. Herz, *Adv. Mater.* **26**, 1584–1589 (2014).
- F. Deschler et al., *J. Phys. Chem. Lett.* **5**, 1421–1426 (2014).
- Q. Dong et al., *Science* **347**, 967–970 (2015).
- D. Shi et al., *Science* **347**, 519–522 (2015).
- G. Xing et al., *Science* **342**, 344–347 (2013).
- S. D. Stranks et al., *Science* **342**, 341–344 (2013).
- E. Yablonovitch, O. D. Miller, S. R. Kurtz, in *Conference Record of the 38th IEEE Photovoltaic Specialists Conference*, Austin, TX, 3 to 8 June 2012 (IEEE, 2012), pp. 1556–1559.
- L. S. Mattos et al., in *Conference Record of the 38th IEEE Photovoltaic Specialists Conference*, Austin, TX, 3 to 8 June 2012 (IEEE, 2012), pp. 3187–3190.
- O. D. Miller, E. Yablonovitch, S. R. Kurtz, *IEEE J. Photovoltaics* **2**, 303–311 (2012).
- E. Dupont, H. C. Liu, M. Buchanan, S. Chiu, M. Gao, *Appl. Phys. Lett.* **76**, 4 (2000).
- A. Sadhanala et al., *J. Phys. Chem. Lett.* **5**, 2501–2505 (2014).
- C. Wehrenfennig, M. Liu, H. J. Snaith, M. B. Johnston, L. M. Herz, *J. Phys. Chem. Lett.* **5**, 1300–1306 (2014).
- Full details can be found in the supplementary materials on Science Online.
- I. Suárez, E. J. Juárez-Pérez, J. Bisquert, I. Mora-Seró, J. P. Martínez-Pastor, *Adv. Mater.* **27**, 6157–6162 (2015).
- W. Zhang et al., *Nat. Commun.* **6**, 6142 (2015).
- Y. Yamada, T. Nakamura, M. Endo, A. Wakamiya, Y. Kanemitsu, *J. Am. Chem. Soc.* **136**, 11610–11613 (2014).
- J. L. Balenzategui, A. Martí, *Sol. Energy Mater. Sol. Cells* **90**, 1068–1088 (2006).
- S. M. Durbin, J. L. Gray, *IEEE Trans. Electron. Dev.* **41**, 239–245 (1994).
- R. Graaff, J. J. Ten Bosch, *Opt. Lett.* **25**, 43–45 (2000).
- M. B. Johnston, L. M. Herz, *Acc. Chem. Res.* **49**, 146–154 (2016).
- R. K. Ahrenkiel et al., *Appl. Phys. Lett.* **55**, 1088–1090 (1989).
- P. Renaud, F. Raymond, B. Bensaid, C. Vérié, *J. Appl. Phys.* **71**, 1907–1913 (1992).
- Q. Lin, A. Armin, R. C. R. Nagiri, P. L. Burn, P. Meredith, *Nat. Photonics* **9**, 106–112 (2014).

## ACKNOWLEDGMENTS

We acknowledge financial support from the Engineering and Physical Sciences Research Council of the UK (EPSRC) and King Abdulaziz City for Science and Technology. L.M.P.-O. thanks the Cambridge Home European Scheme for financial support. L.M.P.-O. and H.J.B. also thank the Nano Doctoral Training Center (NanoDTC) of the EPSRC for financial support. M.S., M.V., and J.M.R. thank the Winton Programme for the Physics of Sustainability (University of Cambridge). M.C.-Q. would like to thank the Marie Curie Actions (FP7-PEOPLE-IEF2013) for funding. M.A. acknowledges financial support from the President of the UAE's Distinguished Student Scholarship Program (DSS), granted by the UAE's Ministry of Presidential Affairs. M.A.-J. thanks Nyak Technology Limited for a Ph.D. scholarship. B.E. acknowledges the Foundation for Fundamental Research on Matter (FOM), which is part of the Netherlands Organisation for Scientific Research (NWO). F.D. acknowledges funding from a Herchel Smith Research Fellowship. We thank H. Sirringhaus, N. Greenham, U. Steiner, E. Reisner, and R. Phillips for providing support and access to their facilities. Experimental data are available at [www.repository.cam.ac.uk/handle/1810/253689](http://www.repository.cam.ac.uk/handle/1810/253689).

## SUPPLEMENTARY MATERIALS

[www.sciencemag.org/content/351/6280/1430/suppl/DC1](http://www.sciencemag.org/content/351/6280/1430/suppl/DC1)  
Materials and Methods  
Supplementary Text  
Figs. S1 to S19  
References (32–46)

22 December 2015; accepted 2 February 2016  
10.1126/science.aaf1168

## ECONOMICS

# Evaluating replicability of laboratory experiments in economics

Colin F. Camerer,<sup>1,\*†</sup> Anna Dreber,<sup>2,†</sup> Eskil Forsell,<sup>2,†</sup> Teck-Hua Ho,<sup>3,4,†</sup> Jürgen Huber,<sup>5,†</sup> Magnus Johannesson,<sup>2,†</sup> Michael Kirchler,<sup>5,6,†</sup> Johan Almenberg,<sup>7</sup> Adam Altmejd,<sup>2</sup> Taizan Chan,<sup>8</sup> Emma Heikensten,<sup>2</sup> Felix Holzmeister,<sup>5</sup> Taisuke Imai,<sup>1</sup> Siri Isaksson,<sup>2</sup> Gideon Nave,<sup>1</sup> Thomas Pfeiffer,<sup>9,10</sup> Michael Razen,<sup>5</sup> Hang Wu<sup>4</sup>

The replicability of some scientific findings has recently been called into question. To contribute data about replicability in economics, we replicated 18 studies published in the *American Economic Review* and the *Quarterly Journal of Economics* between 2011 and 2014. All of these replications followed predefined analysis plans that were made publicly available beforehand, and they all have a statistical power of at least 90% to detect the original effect size at the 5% significance level. We found a significant effect in the same direction as in the original study for 11 replications (61%); on average, the replicated effect size is 66% of the original. The replicability rate varies between 67% and 78% for four additional replicability indicators, including a prediction market measure of peer beliefs.

The deepest trust in scientific knowledge comes from the ability to replicate empirical findings directly and independently. Although direct replication is widely applauded (1), it is rarely carried out in empirical social science. Replication is now more important than ever, because the quality of results has been questioned in many fields, such as medicine (2–5), neuroscience (6), and genetics (7, 8). In economics, concerns about inflated findings in empirical (9) and experimental analyses (10, 11) have also been raised. In the social sciences, psychology has been the most active in both self-diagnosing the forces that create “false positives” and conducting direct replications (12–15). Several high-profile replication failures

(16, 17) quickly led to changes in journal publication practices (18). The recent Reproducibility Project: Psychology (RPP) replicated 100 original studies published in three top journals in psychology. The vast majority (97) of the original studies reported “positive findings,” but in the replications, the RPP only found a significant effect in the same direction for 36% of these studies (19).

In this report, we provide insights into the replicability of laboratory experiments in economics. Our sample consists of all 18 between-subject laboratory experimental papers published in the *American Economic Review* and the *Quarterly Journal of Economics* between 2011 and 2014. The most important statistically significant finding,



as emphasized by the authors of each paper, was chosen for replication (see section 1 of the supplementary materials and tables S1 and S2). We used replication sample sizes with at least 90% power (mean = 92%; median = 91%) to detect the original effect size at the 5% significance level. All of the replication and analysis plans were made public on the project website (supplementary materials, section 1) and were also sent to the original authors for verification.

There are different ways of assessing replication, with no universally agreed-upon standard of excellence (19–23). We present results for the same replication indicators that were used in the RPP (19). As our first indicator of replication, we used a “significant effect in the same direction as in the original study” [Gelman and Stern (20) discuss the challenges of comparing significance levels across experiments].

The results of the replications are shown in Fig. 1A and table S1. We found a significant effect

in the same direction as in the original study for 11 replications (61.1%). This is considerably lower than the replication rate of 92% (mean power) that would be expected if all original effects were true and accurately estimated (one-sample binomial test,  $P < 0.001$ ).

A complementary method for assessing replicability is to test whether the 95% confidence interval (CI) of the replication effect size includes the original effect size (19) [Cumming (21) discusses the interpretation of CIs for replications]. This is the case in 12 of our replications (66.7%). If we also include the study in which the entire 95% CI exceeds the original effect size, the number of replicable studies increases to 13 (72.2%). An alternative measure, which acknowledges sampling error in both the original study and the replications, is to count how many replicated effects lie in a 95% “prediction interval” (24). This count is higher (83.3%) and increases to 88.9% if we also include the replication whose effect size exceeds the upper bound of the prediction interval (fig. S2 and supplementary materials, section 2).

The mean standardized effect size (correlation coefficient,  $r$ ) of the replications is 0.279, compared with 0.474 in the original studies (fig. S3). This difference is significant [Wilcoxon signed-rank test;  $z = -2.98$ ,  $P = 0.003$ ,  $n = 18$ ]. The replicated effect sizes tend to be of the same sign as the original ones but not as large. The mean relative effect size of the replications is 65.9%.

The original and replication studies can also be combined in a meta-analytic estimate of the effect size (19). As shown in Fig. 1B, in the meta-analysis, 14 studies (77.8%) have a significant effect in the same direction as in the original study. These results should be interpreted cau-

tiously, because the estimates assume that the results of the original studies do not have publication or reporting biases.

To measure peer beliefs about the replicability of original results, we set up prediction markets before the 18 replications were performed (25). Dreber *et al.* (26), in a recent study that presented evidence for a subset of the replications in the RPP, proposed the use of prediction markets as an additional replicability indicator. In the prediction market for a particular target study, peers who were likely to be familiar with experimental methods in economics could buy or sell shares whose monetary value depended on whether the target study was replicated (fig. S4 and tables S1 and S2). The prediction markets produce a collective market probability of replication (27) that can be interpreted as a replicability indicator (26). The traders' ( $n = 97$ ) survey beliefs about replicability were also collected before market trading as an additional measure of peer beliefs.

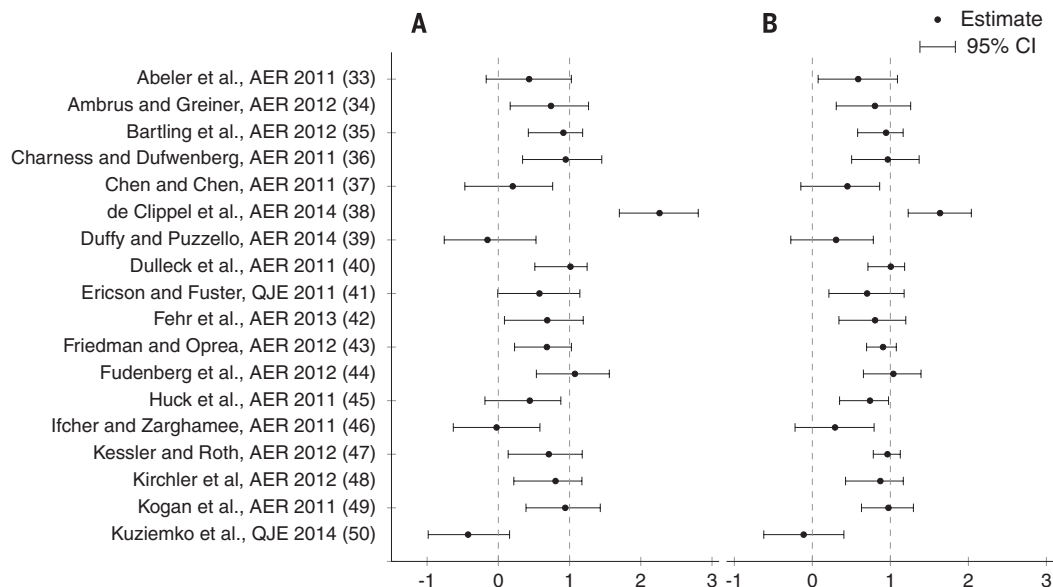
The average prediction market belief is a replication rate of 75.2%, and the average survey belief is 71.1% (Fig. 2, fig. S5, and tables S3 and S4). Both are higher than the observed replication rate of 61.1%, but neither difference is significant (supplementary Materials, section 5). The prediction market beliefs and the survey beliefs are highly correlated, and both are positively correlated with the ranked degree of replication success, although the correlation does not reach significance for the prediction market beliefs (Fig. 2 and fig. S6). Contrary to Dreber *et al.* (26), prediction market beliefs are not a more accurate indicator of replicability than survey beliefs.

We also tested whether replicability is correlated with two observable characteristics of

## Fig. 1. Replication results.

(A) Plotted are 95% CIs of replication effect sizes (standardized to correlation coefficients). The standardized effect sizes are normalized so that 1 equals the original effect size (fig. S1 shows a nonnormalized version). Eleven replications have a significant effect in the same direction as in the original study [61.1%; 95% CI = (36.2%, 86.1%)]. The 95% CI of the replication effect size includes the original effect size for 12 replications [66.7%; 95% CI = (42.5%, 90.8%)]; if we also include the study in which the entire 95% CI exceeds the original effect size, this increases to 13 replications [72.2%; 95% CI = (49.3%, 95.1%)]. AER denotes the *American Economic Review* and QJE denotes the *Quarterly Journal of Economics*.

(B) Meta-analytic estimates of effect sizes, combining the original and replication studies. Plotted are 95% CIs of combined effect sizes (standardized to correlation coefficients). The standardized effect sizes are normalized as in (A) (fig. S1 shows a nonnormalized version). Fourteen studies have a significant effect in the same direction as the original study in the meta-analysis [77.8%; 95% CI = (56.5%, 99.1%)].



published studies: the  $P$  value and the sample size (number of participants) of the original study. These two characteristics are likely to be correlated with each other, which is the case for our 18 studies (Spearman correlation coefficient =  $-0.61$ ,  $P = 0.007$ ,  $n = 18$ ). We expected the replicability to be negatively correlated with the original  $P$  value and positively correlated with the sample size, because the risk of false positives increases with the original  $P$  value and decreases with the original sample size (statistical power) (6, 11). The correlations are presented in Fig. 3 and table S5, and the results are in line with our expectations. The correlations are typically around 0.5 in the expected direction and significant. Only one study out of eight with a  $P$  value  $< 0.01$  in the original study was not replicable at the 5% level in the original direction.

We report the first systematic replications of laboratory experiments in economics, with the aim of contributing much-needed data to the larger question of the replicability of empirical findings in all areas of science. The results provide provisional answers to two questions: (i) Are laboratory experiments in economics generally replicable, and (ii) do statistical measures of research quality, including peer beliefs about replicability, help predict which studies will be replicable?

The provisional answer to the first question is that, based on this sample of experiments, replication is generally possible, although there is room for improvement. Eleven out of 18 (61.1%) studies were replicable with  $P < 0.05$  in the original direction, and three more studies were relatively close to being replicated (all have sig-

nificant effects in the meta-analysis). Four replications (22.2%) had effect sizes close to zero, somewhat more than the 1.4 replication failures expected by pure chance (given the mean power of 92%). Moreover, the original effect sizes in the studies that we replicated could have been inflated, a phenomenon that could stem from publication bias (28). If there is publication bias, our prospective power analyses will have overestimated the replication power.

The answer to the second question is that peer surveys and market beliefs did contain some information about which experiments were more likely to replicate, but sample sizes and  $P$  values in the original studies were even more strongly correlated with replicability (Fig. 3).

To learn from successes and failures in different scientific fields, it is useful to compare our results with recent results from studies of robustness in experimental psychology and empirical economics. Our results can be compared with the recent RPP project in the psychological sciences (19), which was also accompanied by prediction market beliefs and survey beliefs (26). All measures of replication success are somewhat higher for the economics experiments than for the sampled psychology experiments (Fig. 4). Peer beliefs in our study are also significantly higher than in the RPP study (Fig. 4). Acknowledging the limits of this two-study comparison, and particularly our small sample of 18 replications, there appears to be some difference in replication success between these fields. However, it is premature to draw strong conclusions about disciplinary differences; other methodological factors potentially could explain why the replication rates differed. For example, in the RPP replications, interaction effects were less likely to be replicable than main or simple effects (19).

In economics, several studies have shown that statistical findings from nonexperimental data are not always easy to replicate (29). Two studies of macroeconomic findings, reported in the *Journal of Money, Credit and Banking* in 1986 and 2006, respectively found that only 13% and 23% of original results were replicable, even when the data and code were easily accessible (30, 31). An analysis of 50,000  $P$  values reported between 2005 and 2011 in three widely cited general economics journals found that  $P$  values between 0.10 and 0.25 were less common than might be expected. (32). However, the frequency of these “missing”  $P$  values is smaller in laboratory and field experiments. Taken together, these analyses and our replication sample suggest that laboratory experiments are at least as robust, and perhaps more robust, than other kinds of empirical economics.

Two methodological research practices in laboratory experimental economics may contribute to relatively high replication success. First, experimental economists have strong norms about motivating subjects with substantial financial incentives and avoiding the use of deception. These norms make subjects more responsive and may reduce variability in how experiments are performed across different research teams,

**Fig. 2. Prediction market and survey beliefs.**

A plot of prediction market beliefs and survey beliefs, in relation to whether the original result was replicated with  $P < 0.05$  in the original direction. The mean prediction market belief in a successful replication is 75.2% [range, 59% to 94%; 95% CI = (69.7%, 80.6%)], and the mean survey belief is 71.1% [range, 54% to 86%; 95% CI = (66.4%, 75.8%)]. The prediction market beliefs and survey beliefs are highly correlated (Spearman correlation coefficient = 0.79,  $P < 0.001$ ,  $n = 18$ ). Both the prediction market beliefs (Spearman correlation coefficient = 0.30,  $P = 0.232$ ,  $n = 18$ ) and the survey beliefs (Spearman correlation coefficient 0.52,  $P = 0.028$ ,  $n = 18$ ) are positively correlated with the ranked degree of replication success.

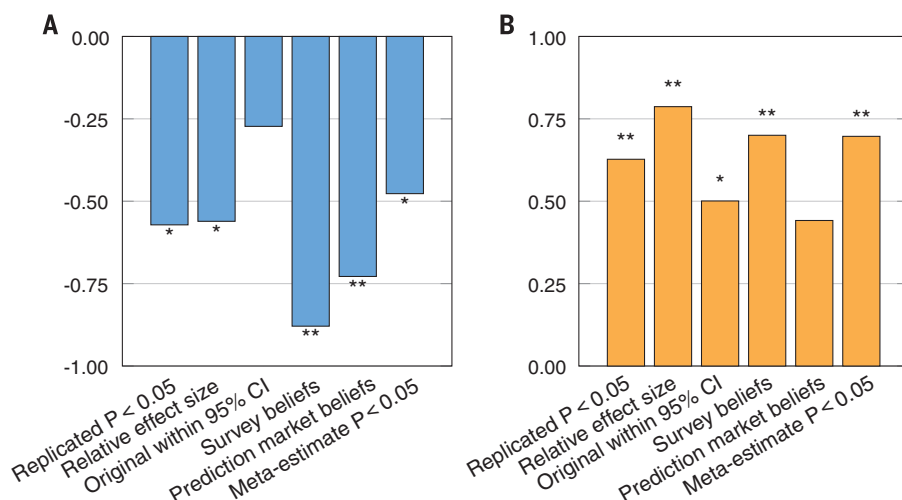
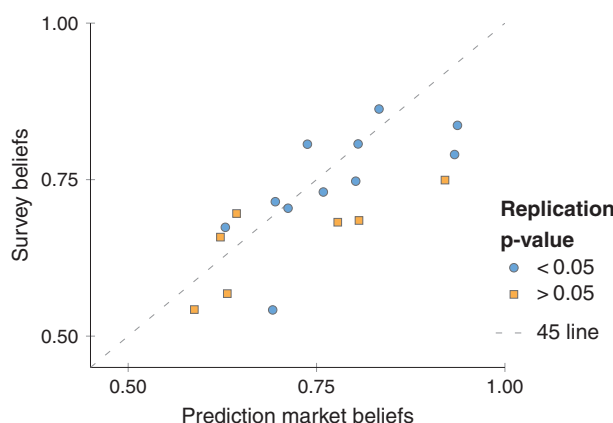


**Fig. 3. Correlations between  $P$  values and sample sizes in original studies and replicability indicators.** (A) The original  $P$  value is negatively correlated with all six replicability indicators, and five of these correlations are significant. (B) The original sample size is positively correlated with all six replicability indicators, and five of these correlations are significant. Spearman correlation coefficients are shown on the vertical axes. \* $P < 0.05$ ; \*\* $P < 0.01$ .



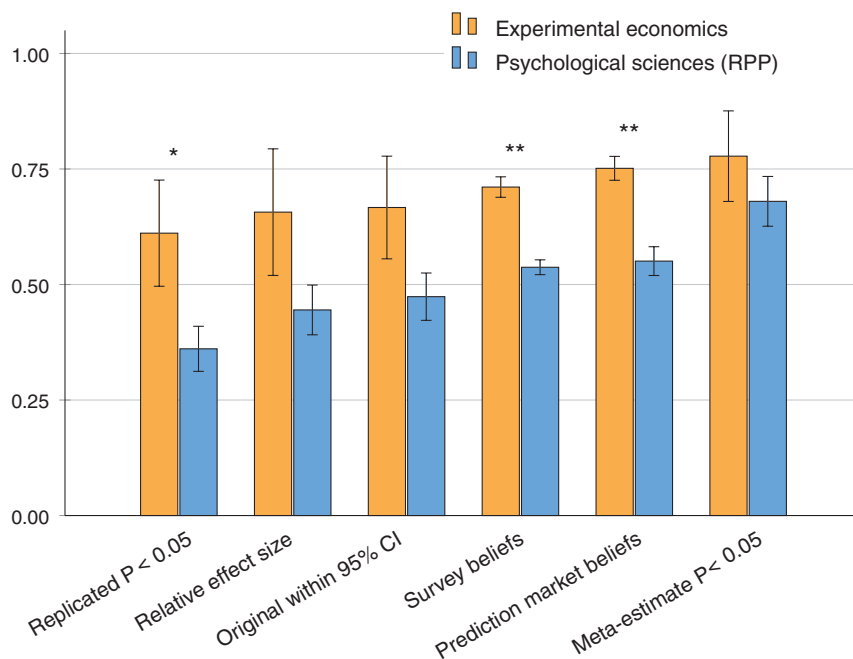


**Fig. 4. A comparison of replicability indicators in experimental economics (this study) and psychological sciences (RPP).** The graph shows means  $\pm$  SE for replicability indicators. All six replicability indicators are higher for experimental economics; this difference is significant for three of the replicability indicators. The average difference in replicability across the six indicators is 19 percentage points. Details about the statistical tests are included in the supplementary materials. \* $P < 0.05$ ; \*\* $P < 0.01$ .

thereby improving replicability. Second, pioneering experimental economists were eager for others to adopt their methods; to this end, they persuaded journals to print instructions and even original data. These editorial practices created norms of transparency and have made replication and reanalysis relatively easy.

There is every reason to be optimistic that science in general, and social science in particular, will emerge much improved after the current period of critical self-reflection. Our study suggests that laboratory experiments published in top economic journals have relatively high rates of replicability. Challenges still remain: For example, executing replications can be laborious, even when scientific journals require online posting of data and computer code to make things easier. This is a reminder that as scientists, we should design and document our methods to anticipate replication and make it easy to do. Our results also show that there is some information in post-publication peer beliefs (revealed in both markets and surveys), and perhaps even more information in simple statistics from published results, about whether studies are likely to be replicable. All of these developments suggest that the cultivation of good professional norms, discouragement of bad norms, policing of disclosure requirements by journals, and simple evidence-based editorial policies can improve scientific replicability, perhaps very quickly.

## REFERENCES AND NOTES

1. M. McNutt, *Science* **343**, 229 (2014).
2. J. P. A. Ioannidis, *PLOS Med.* **2**, e124 (2005).

3. F. Prinz, T. Schlange, K. Asadullah, *Nat. Rev. Drug Discov.* **10**, 712 (2011).
4. C. G. Begley, L. M. Ellis, *Nature* **483**, 531–533 (2012).
5. L. P. Freedman, I. M. Cockburn, T. S. Simcoe, *PLOS Biol.* **13**, e1002165 (2015).
6. K. S. Button et al., *Nat. Rev. Neurosci.* **14**, 365–376 (2013).
7. J. K. Hewitt, *Behav. Genet.* **42**, 1–2 (2012).
8. M. S. Lawrence et al., *Nature* **499**, 214–218 (2013).
9. E. E. Leamer, *Am. Econ. Rev.* **73**, 31 (1983).
10. A. E. Roth, *Empir. Econ.* **19**, 279–289 (1994).
11. Z. Maniatis, F. Tufano, J. A. List, *Am. Econ. Rev.* **104**, 277–290 (2014).
12. J. P. Simmons, L. D. Nelson, U. Simonsohn, *Psychol. Sci.* **22**, 1359–1366 (2011).
13. S. Carpenter, *Science* **335**, 1558–1561 (2012).
14. Open Science Collaboration, *Perspect. Psychol. Sci.* **7**, 657–660 (2012).
15. J. Bohannon, *Science* **344**, 788–789 (2014).
16. S. Doyen, O. Klein, C.-L. Pichon, A. Cleeremans, *PLOS ONE* **7**, e29081 (2012).
17. S. J. Ritchie, R. Wiseman, C. C. French, *PLOS ONE* **7**, e33423 (2012).
18. B. A. Nosek et al., *Science* **348**, 1422–1425 (2015).
19. Open Science Collaboration, *Science* **349**, aac4716 (2015).
20. A. Gelman, H. Stern, *Am. Stat.* **60**, 328–331 (2006).
21. G. Cumming, *Perspect. Psychol. Sci.* **3**, 286–300 (2008).
22. J. Verhagen, E.-J. Wagenmakers, *J. Exp. Psychol. Gen.* **143**, 1457–1475 (2014).
23. U. Simonsohn, *Psychol. Sci.* **26**, 559–569 (2015).
24. J. T. Leek, P. Patil, R. D. Peng, <http://arxiv.org/abs/1509.08968> (2015).
25. K. J. Arrow et al., *Science* **320**, 877–878 (2008).
26. A. Dreber et al., *Proc. Natl. Acad. Sci. U.S.A.* **112**, 15343–15347 (2015).
27. J. Wolfers, E. Zitzewitz, *Interpreting Prediction Market Prices as Probabilities* (Working Paper No. 12200, National Bureau of Economic Research, 2006).
28. J. P. A. Ioannidis, *Epidemiology* **19**, 640–648 (2008).
29. B. D. McCullough, H. D. Vinod, *Am. Econ. Rev.* **93**, 873–892 (2003).
30. W. G. Dewald, J. G. Thursby, R. G. Anderson, *Am. Econ. Rev.* **76**, 587 (1986).
31. B. D. McCullough, K. A. McGeary, T. D. Harrison, *J. Money Credit Bank.* **38**, 1093–1107 (2006).

32. A. Brodeur, M. Lé, M. Sangnier, Y. Zylberberg, *AJ Applied* **8**, 1–32 (2016).
33. J. Abeler, A. Falk, L. Goette, D. Huffman, *Am. Econ. Rev.* **101**, 470–492 (2011).
34. A. Ambrus, B. Greiner, *Am. Econ. Rev.* **102**, 3317–3332 (2012).
35. B. Bartling, E. Fehr, K. M. Schmidt, *Am. Econ. Rev.* **102**, 834–864 (2012).
36. G. Charness, M. Dufwenberg, *Am. Econ. Rev.* **101**, 1211–1237 (2011).
37. R. Chen, Y. Chen, *Am. Econ. Rev.* **101**, 2562–2589 (2011).
38. G. de Clippel, K. Eliaz, B. G. Knight, *Am. Econ. Rev.* **104**, 3434–3458 (2014).
39. J. Duffy, D. Puzello, *Am. Econ. Rev.* **104**, 1735–1776 (2014).
40. U. Dulleck, R. Kerschbamer, M. Sutter, *Am. Econ. Rev.* **101**, 526–555 (2011).
41. K. M. Marzilli Ericson, A. Fuster, *Q. J. Econ.* **126**, 1879–1907 (2011).
42. E. Fehr, H. Herz, T. Wilkening, *Am. Econ. Rev.* **103**, 1325–1359 (2013).
43. D. Friedman, R. Oprea, *Am. Econ. Rev.* **102**, 337–363 (2012).
44. D. Fudenberg, D. G. Rand, A. Dreber, *Am. Econ. Rev.* **102**, 720–749 (2012).
45. S. Huck, A. J. Seltzer, B. Wallace, *Am. Econ. Rev.* **101**, 819–843 (2011).
46. J. Ifcher, H. Zarghamee, *Am. Econ. Rev.* **101**, 3109–3129 (2011).
47. J. B. Kessler, A. E. Roth, *Am. Econ. Rev.* **102**, 2018–2047 (2012).
48. M. Kirchler, J. Huber, T. Stöckl, *Am. Econ. Rev.* **102**, 865–883 (2012).
49. S. Kogan, A. M. Kwasnica, R. A. Weber, *Am. Econ. Rev.* **101**, 927–947 (2011).
50. I. Kuziemko, R. W. Buell, T. Reich, M. I. Norton, *Q. J. Econ.* **129**, 105–149 (2014).

## ACKNOWLEDGMENTS

For financial support, we thank the Austrian Science Fund (START grant Y617-G11), the Austrian National Bank (grant OeNB 14953), the Behavioral and Neuroeconomics Discovery Fund (grant to C.F.C.), the Jan Wallander and Tom Hedelius Foundation (grants P2015-0001:1 and P2013-0156:1), the Knut and Alice Wallenberg Foundation (Wallenberg Academy Fellows grant to A.D.), the Swedish Foundation for Humanities and Social Sciences (grant NHS14-1719:1), and the Sloan Foundation (grant G-2015-13929). We thank the following experimental laboratories for kindly allowing us to use them for replication experiments: the Center for Behavioral Economics at the National University of Singapore, the Center for Neuroeconomics Studies at Claremont Graduate University, the Frankfurt Laboratory for Experimental Economic Research, the Harvard Decision Science Laboratory, the Innsbruck EconLab, and the Nuffield Centre for Experimental Social Sciences. We thank the following persons for assistance with the experiments: J. Barraza, A. Berge, R. Bhui, A. Born, N. Cohodes, H. K. Dat, C. Dohmen, Z. Faiyad, M. Heissel, A. Henderson, G. Mansur, J. Preussler, L. Schultze, G. Thoenen, and E. Warner. The data reported in this paper are tabulated in tables S1, S3, and S4, and the replication reports, analyses code, and the data from the replications are available at [www.experimentaleconreplications.com](http://www.experimentaleconreplications.com) and at Open Science Framework ([osf.io/bzm54](https://osf.io/bzm54)). The authors report no potential conflicts of interest. No material transfer agreements, patents, or patent applications apply to methods or data in the paper. C.F.C., A.D., J.H., T.-H.H., M.J., and M.K. designed the research; C.F.C., A.D., E.F., J.H., T.-H.H., M.J., and M.K. wrote the paper; E.F., J.A., T.C., T.-H.H., and T.P. helped design the prediction market part; E.F., F.H., J.H., M.K., M.R., T.P., and H.W. analyzed data; A.A., E.H., F.H., T.J., S.I., G.N., M.R., and H.W. carried out the replications (including re-estimating the original estimate with the replication data); and all authors approved the final manuscript.

## SUPPLEMENTARY MATERIALS

[www.sciencemag.org/content/351/6280/1433/suppl/DC1](http://www.sciencemag.org/content/351/6280/1433/suppl/DC1)  
Materials and Methods  
Figs. S1 to S6  
Tables S1 to S5  
References (51–66)

16 December 2015; accepted 19 February 2016  
Published online 3 March 2016  
10.1126/science.aaf0918

## PHYSIOLOGICAL ECOLOGY

# Seasonal and daily climate variation have opposite effects on species elevational range size

Wei-Ping Chan,<sup>1\*</sup> I-Ching Chen,<sup>1,2\*</sup> Robert K. Colwell,<sup>3,4,5</sup> Wei-Chung Liu,<sup>6</sup> Cho-ying Huang,<sup>7</sup> Sheng-Feng Shen<sup>1†</sup>

The climatic variability hypothesis posits that the magnitude of climatic variability increases with latitude, elevation, or both, and that greater variability selects for organisms with broader temperature tolerances, enabling them to be geographically widespread. We tested this classical hypothesis for the elevational range sizes of more than 16,500 terrestrial vertebrates on 180 montane gradients. In support of the hypothesis, mean elevational range size was positively correlated with the scope of seasonal temperature variation, whereas elevational range size was negatively correlated with daily temperature variation among gradients. In accordance with a previous life history model and our extended versions of it, our findings indicate that physiological specialization may be favored under shorter-term climatic variability.

Changes in patterns of climatic variability with global warming are progressively more conspicuous (1). Increasing seasonal variability and asymmetric changes of daily maximum and minimum temperatures have altered the thermal environment that organisms experience (2–4). So far, little is known about how species respond physiologically to climate variation (5, 6), yet these responses are crucial for survival in an era of rapid climate change. The climatic variability hypothesis suggests that organisms experiencing higher thermal variability, and thus having broader physiological thermal tolerances, tend to be geographically widely distributed as a consequence (7). This hypothesis is regarded as a broad macrophysiological principle, as it brings together climate patterns and mechanisms of adaptation to explain macroecological phenomena (8, 9). Although species face environmental fluctuations on the scale of hours to days to years to decades and beyond, how the interplay between climatic variability at these various temporal scales contributes to shaping the evolution of species' physiological traits and geographical range sizes has rarely been addressed.

Consideration of how species range size relates to climatic variation has deep roots (10). Janzen (11) explained that “mountain passes are higher in the tropics” because species inhabiting tropi-

cal mountains experience relatively lower seasonal variation in temperature than species at comparable elevations at higher latitudes and may therefore evolve narrower physiological tolerances. Temperature gradients in tropical mountains thus become effective dispersal barriers and result in relatively smaller elevational range sizes (11, 12). Stevens went on to propose Rapoport's rule, which postulates a positive correlation between species range size and latitude or elevation, suggesting that climatic variability may be the underlying mechanism (13, 14). Empirical support for these components of the climate variability hypothesis has been equivocal (15–17), partly due to the use of latitude or elevation as a rough proxy for climatic variability (18–21). Previous studies often neglected considerable variation in climate components within latitudes (22), as well as associated distinct biological influences.

Here we assess how climatic variability on contrasting temporal scales—seasonal and diurnal— influences the elevational range size of terrestrial vertebrates across the world. We obtained data for climatic variables potentially associated with species range size from CRU TS2.1 and other open sources (23) (table S1) and adopted McCain's carefully vetted database of elevational range size for 16,592 species of rodents, bats, birds, lizards, snakes, salamanders, and frogs on 180 montane gradients spanning from 36.5°S to 48.2°N latitude (19) (fig. S1). We calculated mean elevational range size for each taxonomic group on each gradient. These means, not individual ranges, formed the basis for all analyses and are henceforth referred to simply as “elevational range size.”

We first applied hierarchical partitioning (24) to select the environmental and geographic variables with the highest explanatory power for elevational range size. The nine variables retained were daily temperature maximum, diurnal tem-

perature range (DTR), mean annual temperature, seasonal temperature range (STR), minimum and maximum monthly mean temperature, mean annual precipitation (MAP), latitude, and mountain height (fig. S2). We then applied structural equation modeling (SEM) (25) to assess the relationships among these variables in explaining range size. SEM is capable of including non-mutually exclusive hypotheses in a system of relationships (25) and, hence, is particularly suitable to structure the multiple pathways of highly correlated climatic variables that shape elevational range size (23) (fig. S3).

On the basis of the preliminary hierarchical partitioning and subsequent SEM analysis, we found that latitude alone explained little of the variation in elevational range size (Fig. 1, A and B), in accord with other studies that used latitude as a proxy for climatic variability (15, 17, 19). However, when we considered all possible combinations of proxies, drivers, and relevant climate components, the final model retained latitude, MAP, STR, and DTR as the best model (Fig. 1, A and C). In this model, STR had a significantly positive relationship with elevational range size for our vertebrate data set (correlation coefficient  $R = 0.29$ , probability  $P = 0.006$ ) (Fig. 1A and table S3). Not surprisingly, latitude had a strong and significant positive relationship with STR ( $R = 0.88$ ,  $P < 0.001$ ) (Fig. 1A and fig. S4A) and thus indirectly influenced elevational range size through its effect on STR in the model. Together, these results support the climate variability hypothesis and corroborate previous results (11, 12, 19).

However, elevational range size had a significantly negative relationship with DTR ( $R = -0.25$ ,  $P = 0.012$ ) (Fig. 1, A and D). Moreover, DTR and STR are each negatively correlated with MAP (fig. S4, D and E;  $R = -0.54$ ,  $P < 0.001$  and  $R = -0.07$ ,  $P = 0.025$ , respectively; panels A, B, and C in fig. S4 display the global patterns between each climatic factor and latitude). In contrast, MAP showed only a weak correlation with elevational range size itself (Fig. 1E), as demonstrated previously by McCain (19). Our final model fits better than a model with only latitude and STR [root mean square error of approximation = 0.076; comparative fit index = 0.981; standard root mean square residual = 0.073 (table S2); note that SEM penalizes for each additional parameter]. When we used climate variables for which climate data are currently available at finer spatial resolutions (5 arc min and 30 arc sec) (fig. S5), the structured relationships remained robust, except that the effect of STR became insignificant in one model variant.

In our analysis, latitude and MAP emerged as the geographical and environmental factors that indirectly shape elevational range size through their influence on climatic variability (DTR and STR). We used a stationary bootstrap method to assess whether STR and/or DTR is more explanatory than expected at random along latitude and MAP gradients (23). We found that MAP gradients, but not latitude, influenced the relative importance of DTR versus STR with regard to the elevational range size (Fig. 2, A and B). The explanatory

<sup>1</sup>Biodiversity Research Center, Academia Sinica, Taipei 11529, Taiwan. <sup>2</sup>Department of Life Sciences, National Cheng Kung University, Tainan 70101, Taiwan. <sup>3</sup>Department of Ecology and Evolutionary Biology, University of Connecticut, Storrs, CT 06269, USA. <sup>4</sup>University of Colorado Museum of Natural History, Boulder, CO 80309, USA. <sup>5</sup>Departamento de Ecologia, Universidade Federal de Goiás, CP 131, 74.001-970 Goiânia, Goiás, Brazil. <sup>6</sup>Institute of Statistical Science, Academia Sinica, Taipei 11529, Taiwan. <sup>7</sup>Department of Geography, National Taiwan University, Taipei 10617, Taiwan.

\*These authors contributed equally to this work. †Corresponding author. E-mail: shensf@sinica.edu.tw



power of MAP was generally higher than random expectation along the precipitation gradient, whereas latitude showed considerably less deviation from random expectations. Because precipitation influences global energy flow through its correlation with cloudiness and latent heat flux, MAP has been identified as a dominant factor governing Earth's thermodynamics (26). At lower precipitation levels, DTR was the dominant influence on geographic variation in mean elevational range size, whereas STR dominated at moderate precipitation levels. At high precipitation levels, the effects of both DTR and STR were diminished (Fig. 2A). This complex relationship was generally concealed when the proxy approach was directly applied. As shown by the blue lines in Fig. 2, A and B, the locally weighted scatterplot smoothing (LOESS) lines for elevational range size did not respond noticeably to either gradient.

Our structural equation model demonstrated that STR and DTR have opposite effects on species elevational range size. Although organisms must evolve to survive all conditions that they experience (tolerance range), they can nonetheless focus reproductive activity on a narrow range of conditions (optimum performance range), as long as they experience those conditions often enough within their life span (27). Using a phenotypic optimality model, Gilchrist (27) demonstrated that greater among-generation temperature variation should favor a wider performance range (thermal generalists), whereas a narrower performance range (thermal specialists) will be favored by selection when within-generation temperature variation is great. Recent empirical studies also show that the scope of tolerance range limits for motor function and survival, as determined experimentally, may be a poor predictor of elevational range size for thermal generalists (28).

Nevertheless, because Gilchrist's model focused on within- and among-generation environmental variation, an organism's life span should have a pronounced influence on the evolution of thermal performance range. Thus, it is perhaps surprising to see the strong relationships among STR, DTR, and range size for the vertebrate species in our analysis, given that most have multiyear generation times. We therefore extended Gilchrist's approach to general forms of environmental variation to investigate the expected effects of longer- and shorter-term environmental variations on the expected evolution of performance range (23) (figs. S6 to S9). We found that Gilchrist's principal predictions still hold, even when we replaced among- and within-generation variations with a more general form of longer- and shorter-term variation, respectively. This result arises simply because longer-term variation (including STR) occurs more frequently among generations than within generations, whereas shorter-term variation (e.g., DTR) tends to occur within generations (23). Moreover, we found that average STR was highly correlated with multiyear temperature variation ( $R = 0.87$ ,  $P < 0.001$ ) (23) (fig. S10). Together, these results help to explain the important roles of STR and DTR in shaping the

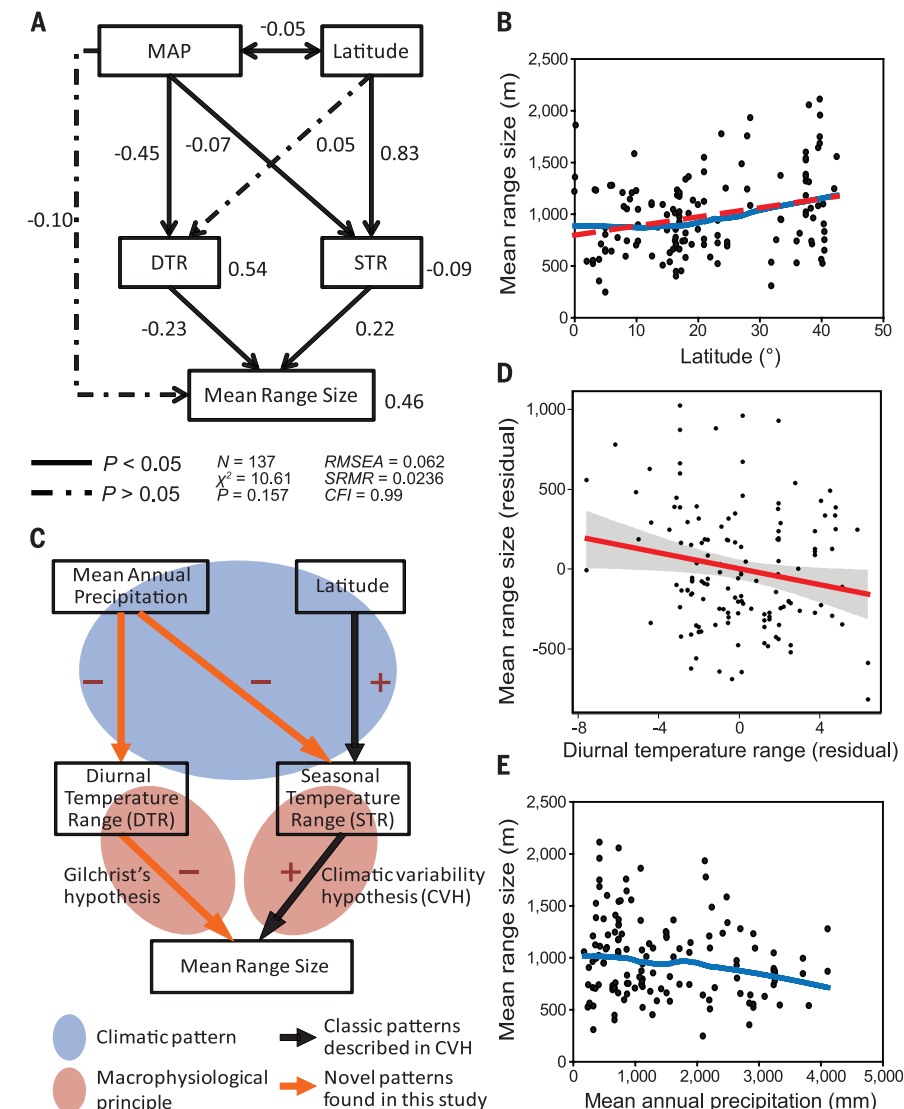


**Fig. 1. Relationships among MAP, DTR, latitude, and STR in explaining the elevational range sizes of terrestrial vertebrates.** (A) Structural equation statistical model.  $N$ , number of mountain gradients; RMSEA, root mean square error of approximation; SRMR, standard root mean square residual; CFI, comparative fit index. (B) Direct relationship between elevational range size and latitude. The blue line represents the LOESS mean; the red dashed line represents a significant linear relationship. (C) Conceptual scheme of this study. Plus and minus symbols represent positive and negative relationships, respectively. (D) Partial residual plots of elevational range size and DTR. The red line represents the regression curve, which controls for the effect of STR and the interaction between DTR and STR. The gray shaded area represents the smoothed 95% confidence interval. (E) Direct relationship between elevational range size and MAP. The blue line represents the LOESS mean. In (A), the structural equation model, numbers next to arrows and boxes are unstandardized slopes and intercepts, respectively. The double-headed arrow indicates correlations between factors. For this analysis, taxonomic differences were statistically controlled by setting taxon as a variable, but taxa were also analyzed separately (fig. S11). For details, see tables S3 to S5.

elevational range sizes of the vertebrate species in this study.

In addition, taxon-specific analysis showed that MAP and DTR synergistically shape elevational range sizes of rodents and birds (but not bats, the third endotherm group considered), with increasing range size associated with greater MAP (fig. S11). For endotherms, water availability is crucial for evaporative cooling in

a hot environment (29). The role of water in adaptation to cold remains largely unexplored in ecological studies, but water may be important in blood circulation and metabolic heat (30). Further studies of the relationship between water availability and shorter-term temperature variation could prove fruitful, especially for endotherms, including bats (see supplementary text and fig. S12).

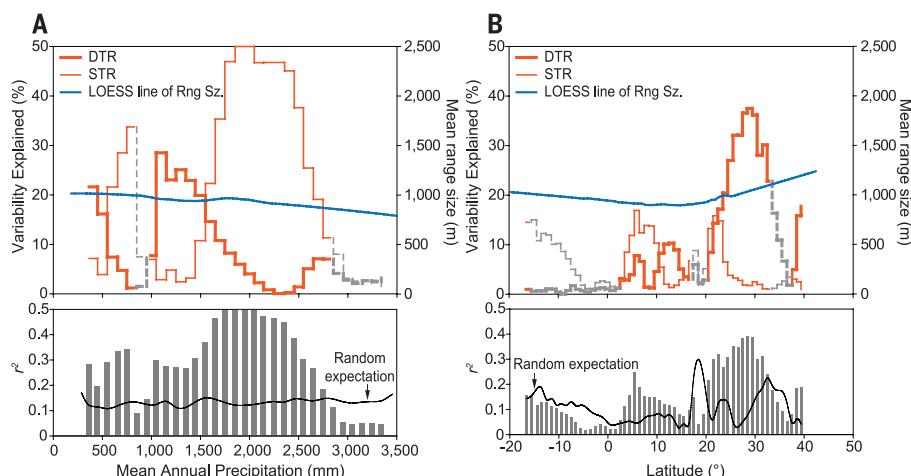


**Fig. 2. Influence of DTR and STR along environmental gradients.** Panels show the relative explanatory power of DTR and STR for elevational range size along (A) the MAP gradient and (B) the latitudinal gradient. In the upper panels, blue lines represent LOESS lines of the plots in Fig. 1, B and E. Total explanatory power is indicated by bars in the lower panels, plotted against random expectations (black lines). Rng Sz., range size;  $r^2$ , coefficient of determination.

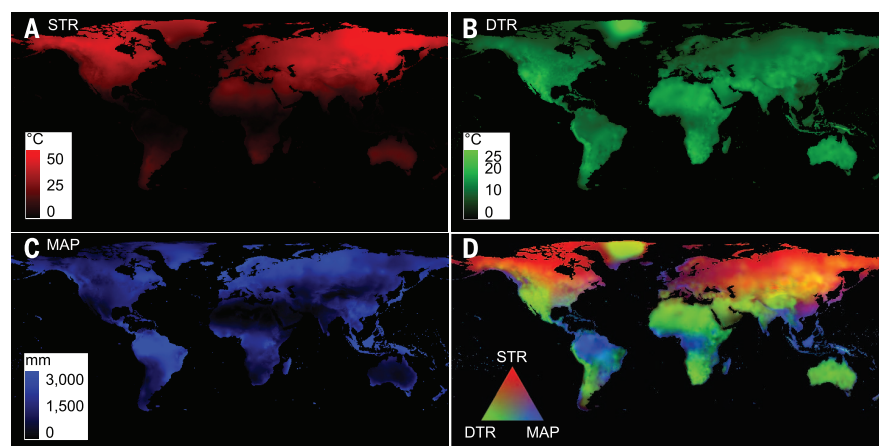


**Fig. 3. Global maps of temperature variability.** (A) Seasonal temperature range (STR). (B) Diurnal temperature range (DTR). (C) Mean annual precipitation (MAP). (D) RGB (red-green-blue) color spectra presenting STR, DTR, and MAP. For example, the northern Amazon basin within the tropical region has very high MAP with low STR and DTR, yielding bluish pixels in (D). All maps are at 0.5° spatial resolution.

On the basis of our empirical and modeling results, we propose a new macroecological principle. Introducing temporal scale offers a new perspective on the physical influence of climatic variability. STR dominates the thermal profile at high latitudes in the Northern Hemisphere, whereas tropical areas with high amounts of rainfall weaken the contrast between DTR and STR (Fig. 3). DTR dominates the majority of the rest of the land surface, including arid land masses, mountainous areas, and most of the terrestrial Southern Hemisphere (Fig. 3D). We conclude that the relevance of each climatic factor to the range size of species should be carefully evaluated for organisms of different taxonomic groups, characterized by different generation times and thermoregulatory systems.

Our study may have implications for understanding biological responses to climate change. For example, tropical species are expected to be thermal specialists because they are adapted to low STR (5, 6). Nevertheless, because of their adaptation to higher DTR, both tropical and temperate montane species (of some groups) may be thermal specialists and, thus, vulnerable to changing climates.

#### REFERENCES AND NOTES

1. IPCC, "Summary for policymakers," in *Climate Change 2013: The Physical Science Basis. Contribution of Working Group I to the Fifth Assessment Report of the Intergovernmental Panel on Climate Change*, T. F. Stocker et al., Eds. (Cambridge Univ. Press, 2013), pp. 1–30.
2. D. R. Easterling et al., *Science* **277**, 364–367 (1997).

3. T. R. Karl et al., *Geophys. Res. Lett.* **18**, 2253–2256 (1991).
4. G. Wang, M. E. Dillon, *Nat. Clim. Chang.* **4**, 988–992 (2014).
5. I. Khaliq, C. Hof, R. Prinzing, K. Böhmig-Gaese, M. Pfenniger, *Proc. Biol. Sci.* **281**, 20141097 (2014).
6. D. A. Vasseur et al., *Proc. Biol. Sci.* **281**, 20132612 (2014).
7. J. Spicer, K. Gaston, *Physiological Diversity and Its Ecological Implications* (Blackwell Science, 1999).
8. F. Bozinovic, P. Calosi, J. I. Spicer, *Annu. Rev. Ecol. Syst.* **42**, 155–179 (2011).
9. K. J. Gaston et al., *Am. Nat.* **174**, 595–612 (2009).
10. K. J. Gaston, *The Structure and Dynamics of Geographic Ranges* (Oxford Univ. Press, 2003).
11. D. H. Janzen, *Am. Nat.* **101**, 233–249 (1967).
12. C. K. Ghalambor, R. B. Huey, P. R. Martin, J. J. Tewksbury, G. Wang, *Integr. Comp. Biol.* **46**, 5–17 (2006).
13. G. C. Stevens, *Am. Nat.* **133**, 240–256 (1989).
14. G. C. Stevens, *Am. Nat.* **140**, 893–911 (1992).
15. K. J. Gaston, S. L. Chown, *Oikos* **84**, 309–312 (1999).
16. C. M. McCain, K. Bracy Knight, *Glob. Ecol. Biogeogr.* **22**, 750–759 (2013).
17. F. J. Whittton, A. Purvis, C. D. L. Orme, M. Á. Olalla-Tárraga, *Glob. Ecol. Biogeogr.* **21**, 179–190 (2012).
18. A. Addo-Bediako, S. L. Chown, K. J. Gaston, *Proc. Biol. Sci.* **267**, 739–745 (2000).
19. C. M. McCain, *Ecol. Lett.* **12**, 550–560 (2009).
20. A. Ruggiero, V. Wrenk, *Glob. Ecol. Biogeogr.* **16**, 401–414 (2007).
21. J. M. Sunday, A. E. Bates, N. K. Dulvy, *Proc. Biol. Sci.* **278**, 1823–1830 (2011).
22. K. S. Sheldon, J. J. Tewksbury, *Ecology* **95**, 2134–2143 (2014).
23. Materials and methods are available as supplementary materials on Science Online.
24. U. Grömping, *J. Stat. Software* **17**, 1 (2006).
25. J. B. Grace, *Structural Equation Modeling and Natural Systems* (Cambridge Univ. Press, 2006).
26. J. T. Kiehl, K. E. Trenberth, *Bull. Am. Meteorol. Soc.* **78**, 197–208 (1997).
27. G. W. Gilchrist, *Am. Nat.* **146**, 252–270 (1995).
28. J. M. Sunday et al., *Proc. Natl. Acad. Sci. U.S.A.* **111**, 5610–5615 (2014).
29. L. B. Buckley, A. H. Hurlbert, W. Jetz, *Glob. Ecol. Biogeogr.* **21**, 873–885 (2012).
30. C. M. Beall, N. G. Jablonski, A. Steegmann, *Human Biology: An Evolutionary and Biocultural Perspective* (Blackwell Science, 2012).

#### ACKNOWLEDGMENTS

We thank T. Amano and anonymous referees for insightful comments and Y.-S. Jang for help with assembling the data for fig. S10. The sources for the data sets used in this paper can be found in table S1. S.-F.S. was supported by Academia Sinica (Career Development Award) and the Ministry of Science and Technology, Taiwan (grant NSC101-2313-B001-008-MY3). I.-C.C. was funded by the Ministry of Science and Technology, Taiwan (grant 103-3114-C-006-001-ESR). R.K.C. was supported by the U.S. NSF (grants DEB-0639979 and DBI-0851245) and Coordenação de Aperfeiçoamento de Pessoal de Nível Superior (CAPES, Brazil). C.H. was sponsored by National Taiwan University and the Ministry of Science and Technology, Taiwan (grant NSC100-2621-B-002-001-MY3).

#### SUPPLEMENTARY MATERIALS

www.sciencemag.org/content/351/6280/1437/suppl/DC1  
Materials and Methods  
Supplementary Text  
Figs. S1 to S12  
Tables S1 to S5  
References (31–37)

23 April 2015; accepted 17 February 2016  
10.1126/science.aab4119



## MEMORY FORMATION

# Diversity in neural firing dynamics supports both rigid and learned hippocampal sequences

Andres D. Grosmark<sup>1,2</sup> and György Buzsáki<sup>2,3\*</sup>

Cell assembly sequences during learning are “replayed” during hippocampal ripples and contribute to the consolidation of episodic memories. However, neuronal sequences may also reflect preexisting dynamics. We report that sequences of place-cell firing in a novel environment are formed from a combination of the contributions of a rigid, predominantly fast-firing subset of pyramidal neurons with low spatial specificity and limited change across sleep-experience-sleep and a slow-firing plastic subset. Slow-firing cells, rather than fast-firing cells, gained high place specificity during exploration, elevated their association with ripples, and showed increased bursting and temporal coactivation during postexperience sleep. Thus, slow- and fast-firing neurons, although forming a continuous distribution, have different coding and plastic properties.

**T**he restructuring of hippocampal networks through synaptic plasticity is necessary for the formation of new episodic memories. Replay of hippocampal place-cell (1) sequences during sharp wave ripples (SPW-Rs) of waking immobility (2–5) and non-rapid eye movement sleep (6–13) after learning has been proposed to support memory consolidation (10–13). Replay is conceptualized and typically studied as a phenomenon with higher-order interactions within populations of neurons taken to have similar properties (10, 14). However, networks built from similar neurons are unstable (15), and recent findings demonstrate that biophysical properties of cortical pyramidal neurons are highly diverse and characterized by lognormal distributions of synaptic weights, long-term firing rates, and spike bursts (16). Furthermore, temporal correlations of hippocampal neurons are largely preserved across brain states and environmental situations, suggesting that learning-induced changes are constrained within a dynamically stable network (16, 17). An example of a preexisting bias between place-cell sequences in a novel environment and sleep before the novel experience (preplay) has been described (18–20), although its computational relevance has been questioned recently (14). To clarify the relationship between preexisting biophysical properties of neurons and their contribution to learning, characterization of individual neurons is necessary. We performed such analyses during sleep in rats before and after they explored a novel environment.

Simultaneous recordings of well-isolated CA1 pyramidal single units were performed in four rats. Several methods were used to assess the relationship between firing patterns during explo-

ration of one of two linear or a circular track (MAZE) in rooms B, C and D, respectively, and candidate SPW-R sequences during preexperience sleep (PRE) and postexperience sleep (POST) in the home cage in room A (fig. S1) (21). First, a spatial Bayesian decoder (2), constructed from the firing-rate vectors of place cells ( $n = 491$  cells) during track running (eight novel exploration sessions), was applied to all candidate ripple events (21) (figs. S2 to S4) of PRE, MAZE, and POST immobility epochs to estimate the posterior probabilities of position in forward (2, 5, 9) or reverse virtual traversals of the track (3, 4) (Fig. 1, A and B). These virtual traversals were measured as weighted correlations over the Bayesian derived posteriors for place across all 20-ms bins in each ripple event (21) and normalized as Z scores [ $rZ$  (sequence score) (21)] (figs. S5 to S8).

To determine each place cell's contribution to PRE and POST sequences [per cell contribution (PCC)], a PCC score was defined as the neuron's mean contribution across all PRE and POST putative events as determined by a cell-specific shuffling technique (21). Neurons that showed significant PCC scores in either PRE or POST were considered to be strongly contributing to sequence formation ( $n = 216$  neurons (Fig. 2B) (21). Importantly, the majority of neurons strongly contributing to PRE (73%) also contributed to POST sequences (Fig. 2C and fig. S19), suggesting that these neurons represent rigid network elements. Strongly contributing neurons < 50 percentile of that session's PRE to POST sleep PCC change ( $\Delta PCC$ ) were classified as rigid cells (blue x's in Fig. 2B), whereas those > 50 percentile as plastic cells (red x's in Fig. 2A and figs. S9 to 11). Rigid and plastic neurons were similarly distributed along the track (fig. S2). The contribution of individual neurons to the overall population  $\Delta POST$ -PRE score ( $POST\ rZ - PRE\ rZ$ ) was assessed by either shuffling or excluding neurons with increasing or decreasing  $\Delta PCC$  scores from the analysis (Fig. 2C and fig. S12) (21). Replay ( $POST > PRE$ )

was eliminated after shuffling or removal of the top 10 to 20% of cells with the highest  $\Delta PCC$  scores, whereas it remained after shuffling or removal of the bottom 75% (Figs. 2, C and D, and fig. S12). These results suggest that from the PRE to the POST sleep, plastic neurons are added to a pre-existing backbone structure, leading to an increase in maze-related sequential activity (replay) associated with learning (Fig. 2C).

Although both rigid and plastic neurons contributed to replay sequences, the nature of their representation was different. Plastic neurons had higher place-specific indices and fewer place fields compared with rigid cells (Fig. 3A), and plastic but not rigid neurons increased their spatial specificity steadily during learning (Fig. 3B and fig. S13). Neither overall firing-rate changes (figs. S14 and S15) nor potential errors in neuronal clustering or neuron classification (figs. S2 and S11) could account for the above differences. These findings suggest that precision in spatial coding is a property developed during maze running by a small plastic subset of cells.

Next, we asked whether rigid and plastic neurons have different biophysical and network properties. Session-wide firing rates of rigid neurons were significantly higher compared with plastic neurons (Fig. 4, A and B, and figs. S14 and S15). Ripple-related spiking, bursting, and pair-wise coactivation were higher in plastic versus rigid neurons (Fig. 4A and figs. S14 to S16). In PRE sleep, coactivity was dominated by fast-firing neurons, and these correlations remained unchanged into POST sleep. In contrast, slow-firing neurons showed the strongest increases in coactivation from PRE to POST sleep (Fig. 4B). Pair-wise coactivity and temporal bias patterns were stable from PRE to POST for pairs of rigid cells, whereas plastic cell pair interactions were modified by experience on the novel maze (10) (figs. S16 and S17).

Because the above analyses indicated that overall firing rates and ripple-related activity of neurons predicted their coding and plastic features, in our final analysis we divided place cells into equal subgroups by either “off-line” sleep-firing rate or ripple-rate gain and repeated the Bayesian place decoding analysis for each group. Low-rate neurons (median, 0.39 Hz) contributed more spatial information per spike on the maze and displayed increased within-ripple firing-rate gains from PRE to POST sleep than high-rate cells (median, 1.12 Hz) (fig. S16). Slow-firing, but not fast-firing, neurons increased their contribution to neuronal sequences from PRE to POST sleep (Fig. 4D). Conversely, PRE to POST increases in sequence content were limited to cells that showed a high degree of ripple-specific recruitment (gain) (Fig. 4E and figs. S20 to S22), suggesting that ripples are privileged windows for learning-related changes in excitability. Similar results were obtained using several Bayesian and non-Bayesian replay methods (figs. S19 to S22).

Using several established and newly developed methods, we demonstrate that sequences of place cells in a novel environment are formed from a combination of relatively fast-firing group of pyramidal neurons with relatively unchanging temporal dynamics and a slow-firing plastic subset of

<sup>1</sup>Department of Neuroscience, Columbia University Medical Center, New York, NY 10019, USA. <sup>2</sup>The Neuroscience Institute, School of Medicine, New York University, New York, NY 10016, USA. <sup>3</sup>Center for Neural Science, New York University, New York, NY 10016, USA.

\*Corresponding author. E-mail: gyorgy.buzsaki@nyumc.org

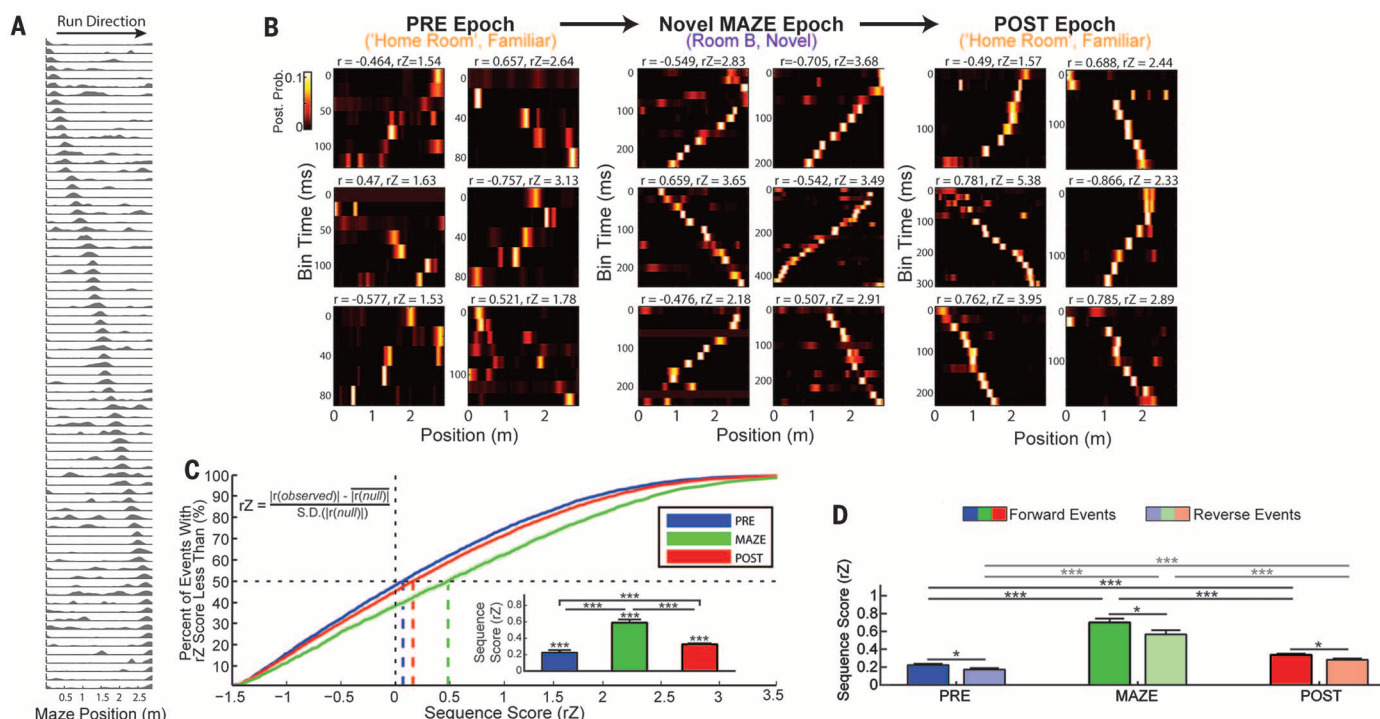


**Fig. 1. PRE and POST maze sequence events.** (A) Simultaneous recording of 77 place cells (rightward runs) used to generate a sequence template. (B) Representative forward and reverse sequences during PRE maze sleep, immobility in the novel MAZE, and POST-learning sleep. (C) Cumulative distribution of  $rZ$  for PRE, MAZE, and POST events, and 95% confidence intervals. Vertical dashed lines, medians. Inset, mean  $\pm$  SE of sequence scores in each condition. \* $P < 0.05$ ; \*\* $P < 0.005$ ; \*\*\* $P < 0.0005$  (Kruskal-Wallis test, followed by post hoc Tukey-Kramer tests). Sign-rank tests were used for within-condition significance testing. (D) As inset in (C), but events with forward and reverse sequences are shown separately (within epoch comparisons, ranked-sum test).

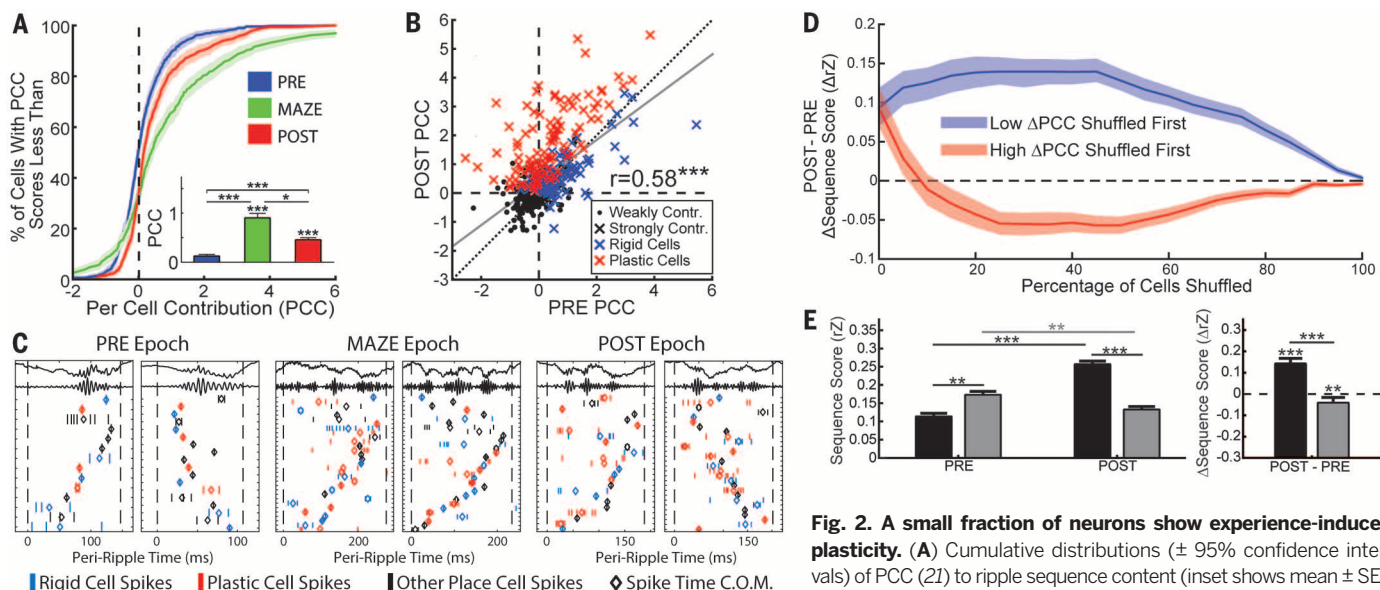


**Fig. 2. A small fraction of neurons show experience-induced plasticity.** (A) Cumulative distributions ( $\pm$  95% confidence intervals) of PCC (2I) to ripple sequence content (inset shows mean  $\pm$  SE). (B) Relationship between each neuron's contribution to PRE and POST PCC scores. Neurons strongly contributing to either PRE or POST (2I) are marked with X; others are marked with dots. Strongly contributing neurons in the lower 50th percentile of that session's PRE versus POST change ( $\Delta$ PCC) were considered rigid cells and those in the upper 50th percentile as plastic cells. (C) Raster and local field potential (LFP) plots of example ripple events from the PRE, MAZE, and POST epochs (diamonds show within-ripple spike-time center of mass). These six events correspond to the top row of Fig. 1B. Rigid and plastic cell spikes are shown in blue and red, respectively. Although rigid cells tend to predominate in the PRE epoch, the marked increase in sequence content observed in the MAZE and POST epochs is driven by the recruitment of plastic cells. (D) To assess the contribution of neurons with differing  $\Delta$ PCC scores to the change in virtual travel content from the PRE to the POST epoch, the replay analysis was repeated using templates in which an increasing percentage (x axis) of neuron's place fields were shuffled either beginning with those that showed the lowest  $\Delta$ PCC values (blue line) (shaded area shows bootstrapped 95% confidence interval) or beginning with neurons with the highest  $\Delta$ PCC scores (red line). (E) Effect on sequence content of removal of rigid (black) or plastic (gray) neurons. The PRE to POST increase in sequence content is attributable to only a small number of plastic cells.

POST sequence content. Gray line, least-squared regression between all PRE and POST PCC scores. Neurons strongly contributing to either PRE or POST (2I) are marked with X; others are marked with dots. Strongly contributing neurons in the lower 50th percentile of that session's PRE versus POST change ( $\Delta$ PCC) were considered rigid cells and those in the upper 50th percentile as plastic cells. (C) Raster and local field potential (LFP) plots of example ripple events from the PRE, MAZE, and POST epochs (diamonds show within-ripple spike-time center of mass). These six events correspond to the top row of Fig. 1B. Rigid and plastic cell spikes are shown in blue and red, respectively. Although rigid cells tend to predominate in the PRE epoch, the marked increase in sequence content observed in the MAZE and POST epochs is driven by the recruitment of plastic cells. (D) To assess the contribution of neurons with differing  $\Delta$ PCC scores to the change in virtual travel content from the PRE to the POST epoch, the replay analysis was repeated using templates in which an increasing percentage (x axis) of neuron's place fields were shuffled either beginning with those that showed the lowest  $\Delta$ PCC values (blue line) (shaded area shows bootstrapped 95% confidence interval) or beginning with neurons with the highest  $\Delta$ PCC scores (red line). (E) Effect on sequence content of removal of rigid (black) or plastic (gray) neurons. The PRE to POST increase in sequence content is attributable to only a small number of plastic cells.



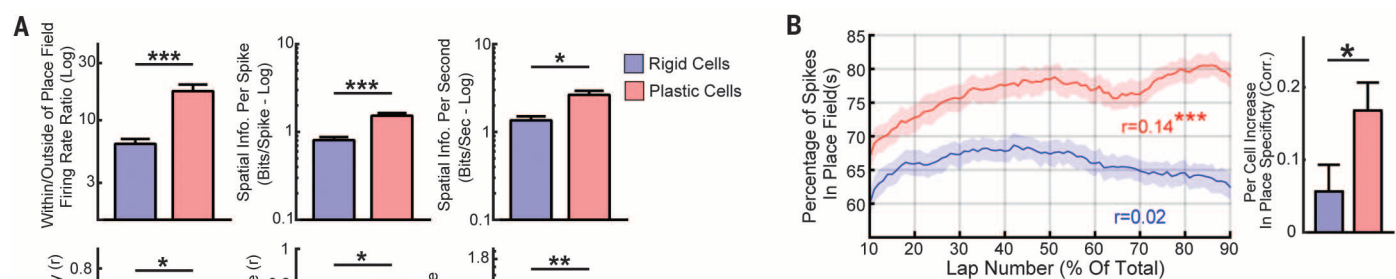


**Fig. 3. Properties of rigid and plastic neurons differ on the novel maze.** (A) Differences in spatial coding properties (top panels, log-mean  $\pm$  log-SE; bottom panels, mean  $\pm$  SE, rank-sum tests). (B) Within-session improvement of plastic neurons' in-field versus outside field firing ratios. Plastic cells improved spatial coding overlaps on the maze; left panel shows the within-session changes of place field representation changes (mean  $\pm$  SE) (21).

for rigid (blue) or plastic (red) neurons (shaded region shows bootstrapped 95% confidence interval). Right panel, per cell summary of within-field firing specificity changes (mean  $\pm$  SE) (21).

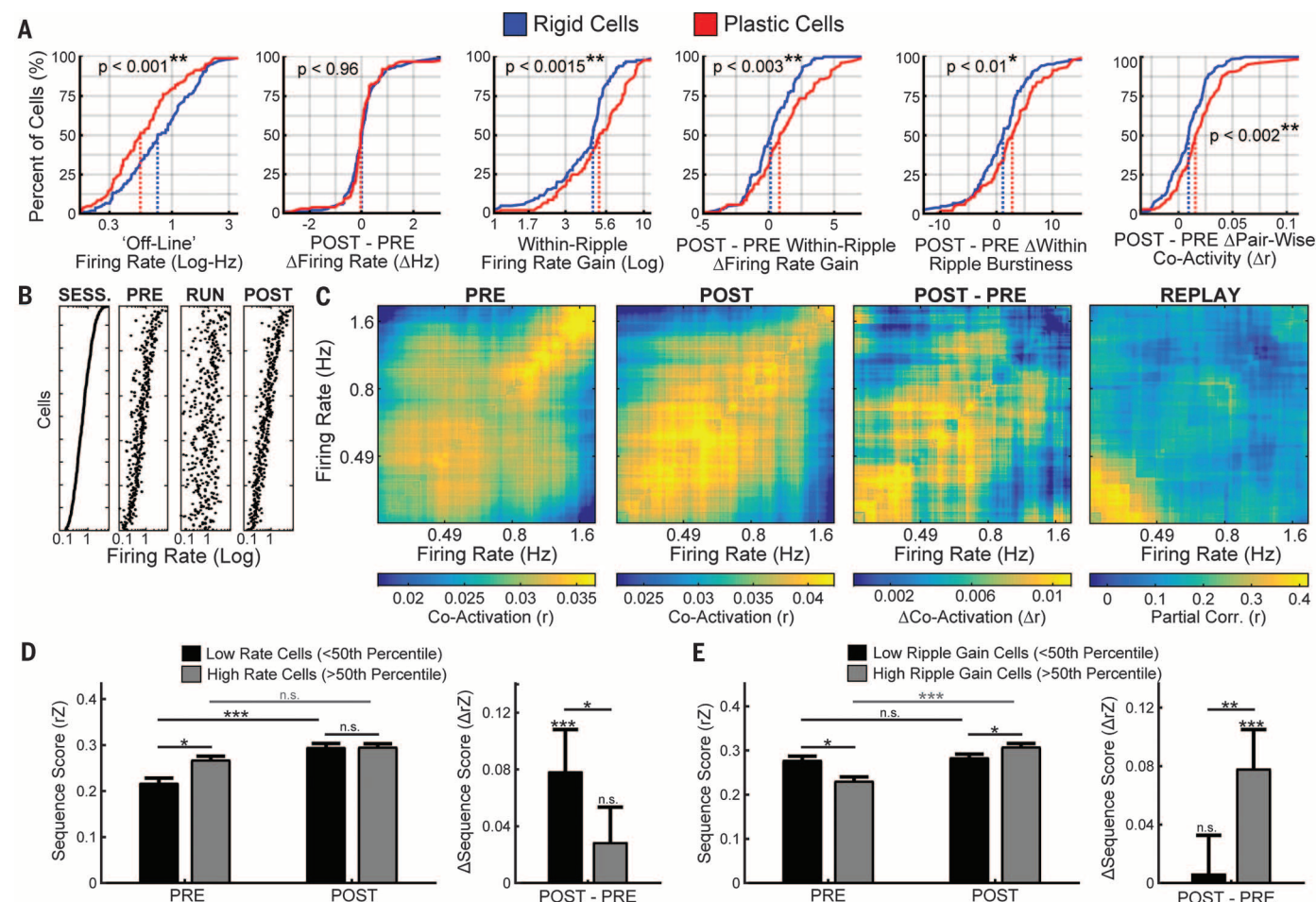


**Fig. 4. Low-firing-rate, high-ripple-recruitment neurons show high learning-related plasticity.** (A) Summary of excitability and synchrony profiles of rigid and plastic cells. Each panel shows the cumulative distributions of the two groups; dashed lines show medians ( $P$  values, rank-sum tests). (B) To examine the relationship between firing rates and learning-related changes in pair-wise coactivation (Pearson's correlation of firing rates in 100-ms bins), neurons in PRE, MAZE, and POST were sorted by their overall session (SESS) firing rates [(B), left panel]. (C) Coactivation was assessed across overlapping groups each containing 20% of place cells with similar firing rates (step size,

1% of cells). Although fast-firing cells dominated the coactivation structure during the PRE (left panel), it was the slow-firing cells that showed the highest increase in coactivation from PRE to POST (middle two panels). Moreover, it was the slow-firing cells that showed the greatest replay (partial correlation across coactivation values between RUN and POST, accounting for PRE). (D and E) An additional replay analysis restricted to place cells with either low or high firing rates (D) or within-ripple firing-rate gains [(E), annotation same as in Fig. 2D] confirms the findings obtained using the PCC method.

neurons (22). Firing properties of neurons predicted their rigid (18, 19) and plastic (10) features. Slow-firing neurons gained high place specificity during maze exploration (23, 24) and showed increased ripple-related recruitment during POST-experience sleep. In contrast, fast-firing neurons had low selectivity (16, 25), have been shown previously to project to multiple targets (26) and to form an interactive subnetwork responsible for global stability, thus allowing plasticity to take place in the remaining majority of slow-firing cells (16, 17). Fast-firing neurons may generalize across situations, whereas slow-firing neurons may differentiate among them (27). Because replay sequence-forming neurons are drawn from the wide span of a continuous log-rate distribution (16) with varying coding, biophysical, circuit, and plasticity properties, these events can forward a synthesis of preexisting and new information to downstream observer neurons.

## REFERENCES AND NOTES

1. L. N. John O'Keefe, *The Hippocampus as a Cognitive Map* (Oxford Univ. Press, 1978).
2. T. J. Davidson, F. Kloosterman, M. A. Wilson, *Neuron* **63**, 497–507 (2009).
3. K. Diba, G. Buzsáki, *Nat. Neurosci.* **10**, 1241–1242 (2007).
4. D. J. Foster, M. A. Wilson, *Nature* **440**, 680–683 (2006).
5. B. E. Pfeiffer, D. J. Foster, *Nature* **497**, 74–79 (2013).
6. D. Dupret, J. O'Neill, B. Pleydell-Bouverie, J. Csicsvari, *Nat. Neurosci.* **13**, 995–1002 (2010).
7. G. Girardeau, K. Benchenane, S. I. Wiener, G. Buzsáki, M. B. Zugaro, *Nat. Neurosci.* **12**, 1222–1223 (2009).
8. H. S. Kudrimoti, C. A. Barnes, B. L. McNaughton, *J. Neurosci.* **19**, 4090–4101 (1999).
9. A. K. Lee, M. A. Wilson, *Neuron* **36**, 1183–1194 (2002).
10. M. A. Wilson, B. L. McNaughton, *Science* **265**, 676–679 (1994).
11. G. Buzsáki, *Neuroscience* **31**, 551–570 (1989).
12. M. E. Hasselmo, *Trends Cogn. Sci.* **3**, 351–359 (1999).
13. G. Buzsáki, *Hippocampus* **25**, 1073–1188 (2015).
14. D. Silva, T. Feng, D. J. Foster, *Nat. Neurosci.* **18**, 1772–1779 (2015).
15. W. Gerstner, W. M. Kistler, R. Naud, L. Paninski, *Neuronal Dynamics: From Single Neurons to Networks and Models of Cognition* (Cambridge Univ. Press, 2014).
16. K. Mizuseki, G. Buzsáki, *Cell Rep.* **4**, 1010–1021 (2013).
17. D. A. Panatier, et al., *J. Neurosci.* **35**, 8480–8492 (2015).
18. G. Dragoi, S. Tonegawa, *Nature* **469**, 397–401 (2011).
19. G. Dragoi, S. Tonegawa, *Proc. Natl. Acad. Sci. U.S.A.* **110**, 9100–9105 (2013).
20. H. F. Ólafsson, C. Barry, A. B. Saleem, D. Hassabis, H. J. Spiers, *eLife* **4**, e06063 (2015).
21. Materials and methods are available as supplementary materials on Science Online.
22. G. Dragoi, K. D. Harris, G. Buzsáki, *Neuron* **39**, 843–853 (2003).
23. K. C. Bittner et al., *Nat. Neurosci.* **18**, 1133–1142 (2015).
24. S. Cheng, L. M. Frank, *Neuron* **57**, 303–313 (2008).
25. P. D. Rich, H.-P. Liaw, A. K. Lee, *Science* **345**, 814–817 (2014).
26. S. Cioocchi, J. Passecker, H. Malagon-Vina, N. Mikus, T. Klausberger, *Science* **348**, 560–563 (2015).
27. G. Buzsáki, *Science* **347**, 612–613 (2015).

## ACKNOWLEDGMENTS

This work was supported by NIH grants NS075015, MH54671, and MH102840; the Simons Foundation; and the G. Harold and Leila Y. Mathers Foundation. We thank J. Long for invaluable experimental support and B. Watson, S. McKenzie, L. Roux, and S. Tuncdemir for discussion and advice. Spike and LFP data are available at CRCNS.org.

## SUPPLEMENTARY MATERIALS

www.sciencemag.org/content/351/6280/1440/suppl/DC1  
Materials and Methods  
Figs. S1 to S22  
References (28–36)

6 August 2015; accepted 11 February 2016  
10.1126/science.1231935

## NEURODEVELOPMENT

# Sequential transcriptional waves direct the differentiation of newborn neurons in the mouse neocortex

Ludovic Telley,<sup>1,7\*</sup> Subashika Govindan,<sup>1,7\*</sup> Julien Prados,<sup>1,7</sup>  
Isabelle Stevant,<sup>2,7</sup> Serge Nef,<sup>2,7</sup> Emmanouil Dermitzakis,<sup>2,5,6,7</sup>  
Alexandre Dayer,<sup>1,3,7</sup> Denis Jabaudon<sup>1,4,7†</sup>

During corticogenesis, excitatory neurons are born from progenitors located in the ventricular zone (VZ), from where they migrate to assemble into circuits. How neuronal identity is dynamically specified upon progenitor division is unknown. Here, we study this process using a high-temporal-resolution technology allowing fluorescent tagging of isochronic cohorts of newborn VZ cells. By combining this *in vivo* approach with single-cell transcriptomics in mice, we identify and functionally characterize neuron-specific primordial transcriptional programs as they dynamically unfold. Our results reveal early transcriptional waves that instruct the sequence and pace of neuronal differentiation events, guiding newborn neurons toward their final fate, and contribute to a road map for the reverse engineering of specific classes of cortical neurons from undifferentiated cells.

**D**uring neocortical development, distinct classes of neurons assemble to form local and long-range circuits. Although class-specific genes and features identify cortical neuron types relatively late in differentiation (1–5), early postmitotic fate specification programs have been inaccessible. Here, we describe the dynamic transcriptional activity controlling layer 4 (L4) excitatory neuron birth and differentiation in the mouse neocortex.

Mammalian cortical progenitor cells in the ventricular zone (VZ) undergo DNA synthesis [S-phase, susceptible to bromodeoxyuridine (BrdU) labeling] at the basal border of the VZ and mitosis (M-phase, lasting about an hour at midcorticogenesis in mice) when their soma is apically located, adjacent to the ventricular space (6, 7). At this location, mitotic cells are susceptible to labeling by intraventricular injection of carboxy-fluorescein esters [“FlashTag” (FT)], which bind to and fluorescently label intracellular proteins (8). The short extracellular half-life of FT in the mouse ventricular space ensures effective pulse-labeling of juxtaventricular dividing cells (Fig. 1A and fig. S1). Intracellularly, FT is linearly diluted at each mitosis, such that fluorescence reflects the number of cell divisions that have occurred since the time of labeling (fig. S1,

D and E, and movie S1) (8). FT<sup>+</sup> newborn cells synchronously moved away from the ventricular wall within 3 hours of labeling (Fig. 1A, bottom), reached the subventricular zone (SVZ) within 12 hours, and entered the cortical plate (CP) 24 to 48 hours after mitosis (Fig. 1B). Isochronic cohorts of VZ cells born at the time of injection can thus be specifically identified and tracked during their initial differentiation.

The laminar fate of FT<sup>+</sup> neurons was linked to the day of FT injection at all ages examined [embryonic day (E) 11.5 to 17.5] (fig. S2 and Fig. 1C). At postnatal day (P) 7, when neuronal migration is complete, E14.5-labeled FT<sup>+</sup> neurons were restricted to a sublamina of L4 (Fig. 1C). These neurons were born at the time of the FT pulse, not later, because they mostly remained unlabeled after continuous BrdU administration beginning at the time of the FT pulse (fig. S1, B to D). Injection of FT at E14 and E14.5 using two dye colors in the same embryo showed two distinct populations of labeled neurons within L4 at P7, revealing a tight relationship between time of birth and final radial location, even within a single layer (Fig. 1D). Thus, we used E14.5 FT injections to label L4 neurons *in vivo* from the time of mitosis in the VZ and track their early molecular differentiation.

We observed that newborn cells sequentially expressed PAX6, a VZ marker, TBR2 a SVZ marker, and the early neuronal protein TBR1 (9, 10) within the first 48 hours after mitosis (fig. S3). This reveals a highly dynamic cellular process characterized by overlapping signature shifts in protein expression. For an unbiased account of the transcriptional programs active just after cell birth in single cells, we isolated E14.5-born FT<sup>+</sup> cells 6, 12, 24, and 48 hours after mitosis by using cortical microdissection followed by fluorescence-activated cell sorting

<sup>1</sup>Department of Basic Neurosciences, University of Geneva, Switzerland. <sup>2</sup>Department of Genetic Medicine and Development, University of Geneva, Switzerland.

<sup>3</sup>Department of Psychiatry, Geneva University Hospital, Switzerland. <sup>4</sup>Clinic of Neurology, Geneva University Hospital, Switzerland. <sup>5</sup>Biomedical Research Foundation Academy of Athens, Greece. <sup>6</sup>Center of Excellence in Genomic Medicine Research, King Abdulaziz University, Saudi Arabia. <sup>7</sup>Institute for Genetics and Genomics in Geneva (iG3), University of Geneva, Switzerland.

\*These authors contributed equally to this work. †Corresponding author. E-mail: denis.jabaudon@unige.ch



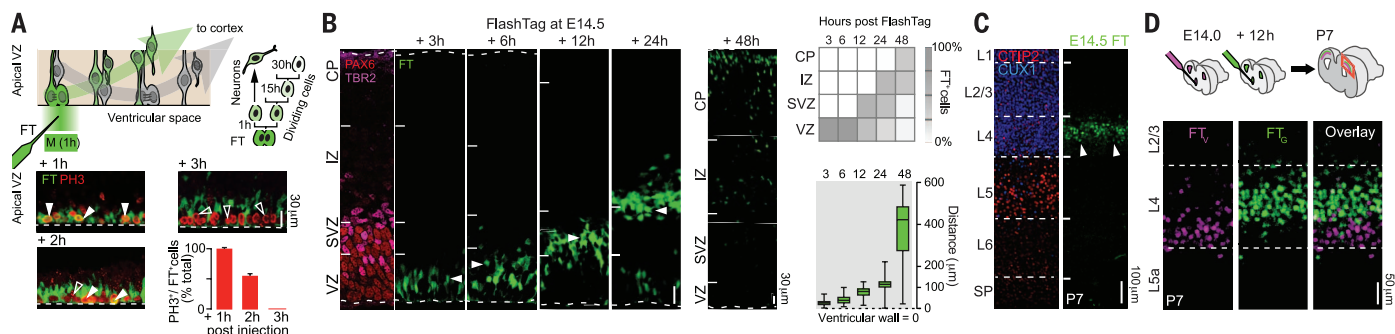


**Fig. 1. FT labels time-locked cohorts of newborn VZ cells during corticogenesis.** (A) (Top) Schematic representation of the FT labeling principle. (Bottom) Pulse-labeling of isochronic mitotic cells using FT at E14.5. PH3, phospho-histone 3, an M-phase marker. (B) Isochronic cohorts of FT<sup>+</sup> cells radially migrate from the VZ to the CP. PAX6 and TBR2 delineate the VZ and SVZ. (C) E14.5 FT labeling identifies a subset of L4 neurons at P7. (D) E14 (FT<sub>v</sub><sup>+</sup>) and E14.5 (FT<sub>c</sub><sup>+</sup>) VZ-born neurons occupy distinct sublaminae within L4. Cx, cortex; IZ, intermediate zone. See also figs. S1 and S2.

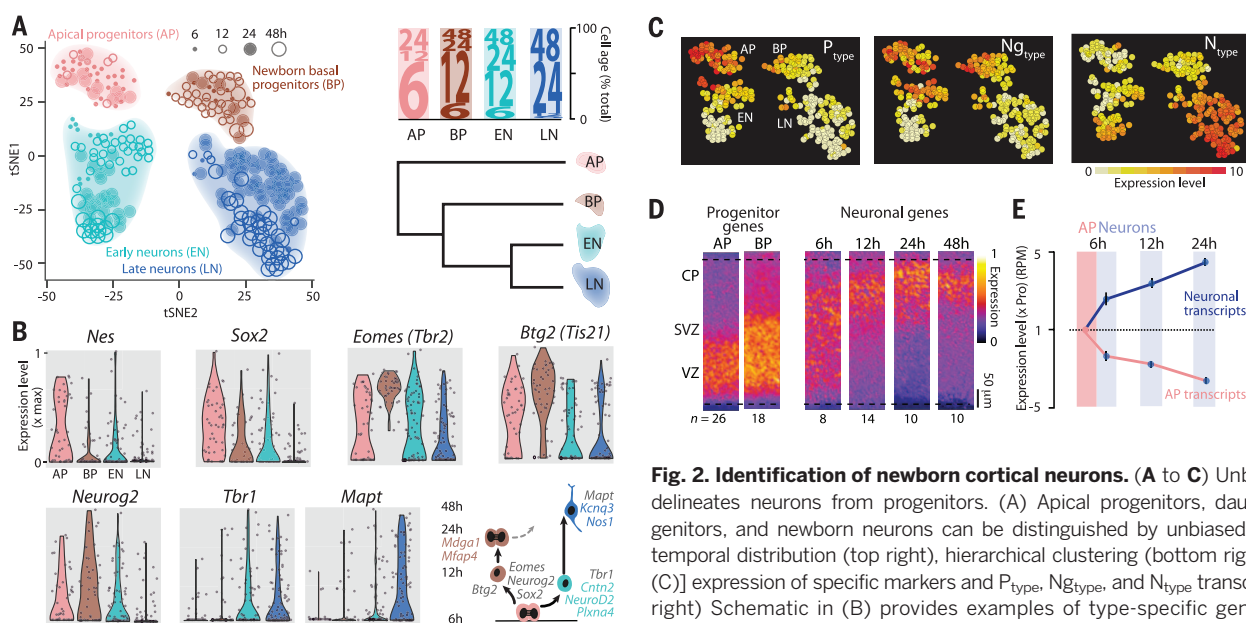


**Fig. 2. Identification of newborn cortical neurons.** (A to C) Unbiased clustering delineates neurons from progenitors. (A) Apical progenitors, daughter basal progenitors, and newborn neurons can be distinguished by unbiased clustering (left), temporal distribution (top right), hierarchical clustering (bottom right), and [(B) and (C)] expression of specific markers and P<sub>type</sub>, Ng<sub>type</sub>, and N<sub>type</sub> transcripts. (B, bottom right) Schematic in (B) provides examples of type-specific genes presented in figs. S6 to S9. Although basal progenitors eventually give rise to neurons (dotted arrow), this progeny is not included in the current data set because FT<sup>+</sup> cells are essentially VZ-born (see fig. S1). (D) Spatial segregation of progenitor and neuron-specific transcripts with in situ hybridization (24). Values represent median expressions for several transcripts. (E) Rapid segregation of cell-type-specific transcripts after cytokinesis.  $P < 0.0001$  for all values compared to 6-hour apical progenitor (AP) values.

essentially VZ-born (see fig. S1). (D) Spatial segregation of progenitor and neuron-specific transcripts with in situ hybridization (24). Values represent median expressions for several transcripts. (E) Rapid segregation of cell-type-specific transcripts after cytokinesis.  $P < 0.0001$  for all values compared to 6-hour apical progenitor (AP) values.

(FACS). We characterized transcriptional activity using single-cell RNA sequencing in microfluidically isolated single cells (fig. S4, A and B) (1, 11, 12).

To determine the sequence and pace of early differentiation processes, we first examined the expression dynamics of a core set of genes involved in proliferation, neurogenesis (i.e., which promote differentiative divisions), and neuronal differentiation. We found that proliferative (P), neurogenic (Ng), and neuronal (N) transcripts were sequentially expressed: All P transcripts were repressed first, Ng transcripts showed delayed repression, and N transcripts were induced after cell division (see fig. S4C and table S1). The closely timed repression of P and Ng transcripts reveals that exit from the cell cycle and initial

postmitotic specification are partially overlapping rather than strictly sequential processes. We used these program-specific dynamics to identify a broader set of proliferative-type (P<sub>type</sub>), neurogenic-type (Ng<sub>type</sub>), and neuronal-type (N<sub>type</sub>) transcripts (fig. S4D and data table S1). The functional relevance of these three programs was supported by the enrichment of P<sub>type</sub>, Ng<sub>type</sub>, and N<sub>type</sub> transcripts in the VZ, SVZ, and CP, respectively; differential enrichment in specific gene ontology terms; and sequential expression in single cells (fig. S4, D and E, and fig. S5). These findings reveal the highly dynamic unfolding of proliferative, neurogenic, and neuronal programs after mitosis in vivo.

Two main classes of juxtaventricular cells are initially labeled by FT in the VZ: (i) pro-

genitor cells and (ii) newborn neurons (Fig. 1A and fig. S1D). We sought to identify neuron-specific transcriptional programs by distinguishing neurons from progenitors. For this purpose, we used a machine-learning approach to cluster cells based on transcriptional expression signatures (13).

This approach delineated distinct groups of cells, which were identified as progenitors [genuine apical progenitors and daughter basal progenitors (14)] and neurons (early and late populations) (Fig. 2A). Apical progenitors and daughter basal progenitors were distinguished based on differential expression of markers such as *Eomes* and *Btg2* [which are enriched in basal progenitors (see references in table S1)] (Fig. 2B) and differential enrichment in P<sub>type</sub> genes

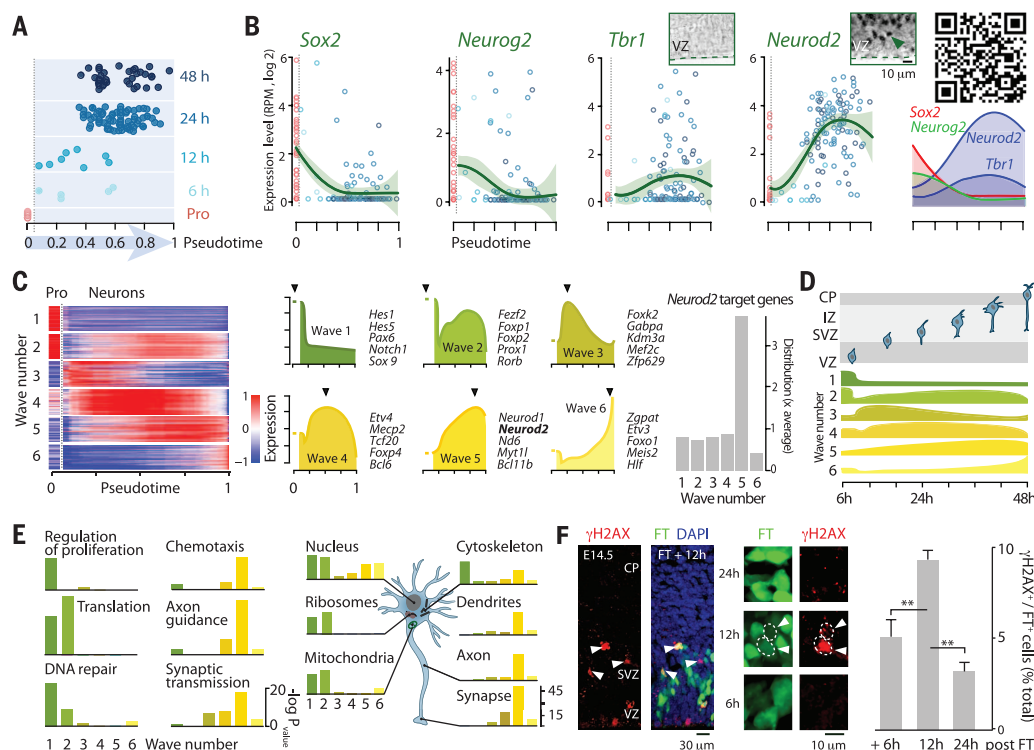


**Fig. 3. Real-time functional transcriptomics of early postmitotic neurons in vivo.** (A) Neurons are staggered by age along the pseudotime axis. (B) Gene expression dynamics for classical proliferative (*Sox2*), neurogenic (*Neurog2*), and neuronal (*Tbr1*) genes. *Neurog2* is expressed more strongly and earlier than *Tbr1*. QR code, <http://genebrowser.unige.ch/science2016>, for access to dynamics of all transcripts. (C) Unbiased clustering of genes based on expression dynamics reveals distinct transcriptional waves with sequential expression peaks (black arrowheads). Illustrative transcription factors are provided for each wave (see also fig. S10 and data table S3). (Right) Chromatin immunoprecipitation sequencing–identified targets of NEUROD2 (18) are enriched in its own wave but also are present across waves (see also fig. S11). (D) Summary of wave dynamics related to developmental time. (E) Gene ontology term-based analysis. Colors correspond to wave numbers. (F) Double-strand DNA breaks are transiently increased in 12-hour-old cells, as indicated by the presence of phosphorylated histone 2AX ( $\gamma$ H2AX) (25).  $^{**}P < 0.001$ .

(apical > basal progenitors), including *Nes* and *Sox2* (Fig. 2C). Accordingly, cells in the apical progenitor cluster were mostly 6 hours old, whereas newborn basal progenitor identity was more distinct after 12 hours (Fig. 2A, top right). Neurons expressed core neuronal genes such as *Tbr1* and *Mapt*, and were enriched in  $N_{type}$  genes (Fig. 2, B and C). With apical progenitors and their daughter neurons now distinguishable, we identified cell-type specific, stage-specific transcripts by comparing gene expression at each developmental age (data table S2 and fig. S8). Consistent with this classification, apical progenitor genes were predominantly expressed in the VZ, basal progenitor genes extended into the SVZ, and neuronal transcripts showed stage-specific sequential expression in the VZ, SVZ, and CP (Fig. 2D and fig. S9). Hierarchical relationship analysis revealed that apical progenitors are clearly distinct from daughter basal progenitors and neurons (Fig. 2A, bottom right), further supporting the lineage relationships identified above. Segregation of type-specific transcripts between newborn neurons and their progenitors was detected as early as 6 hours after mitosis (Fig. 2E). This suggests that type-specific transcripts can be premitotically segregated or differentially stabilized in nascent postmitotic neurons versus progenitors. Together, these data

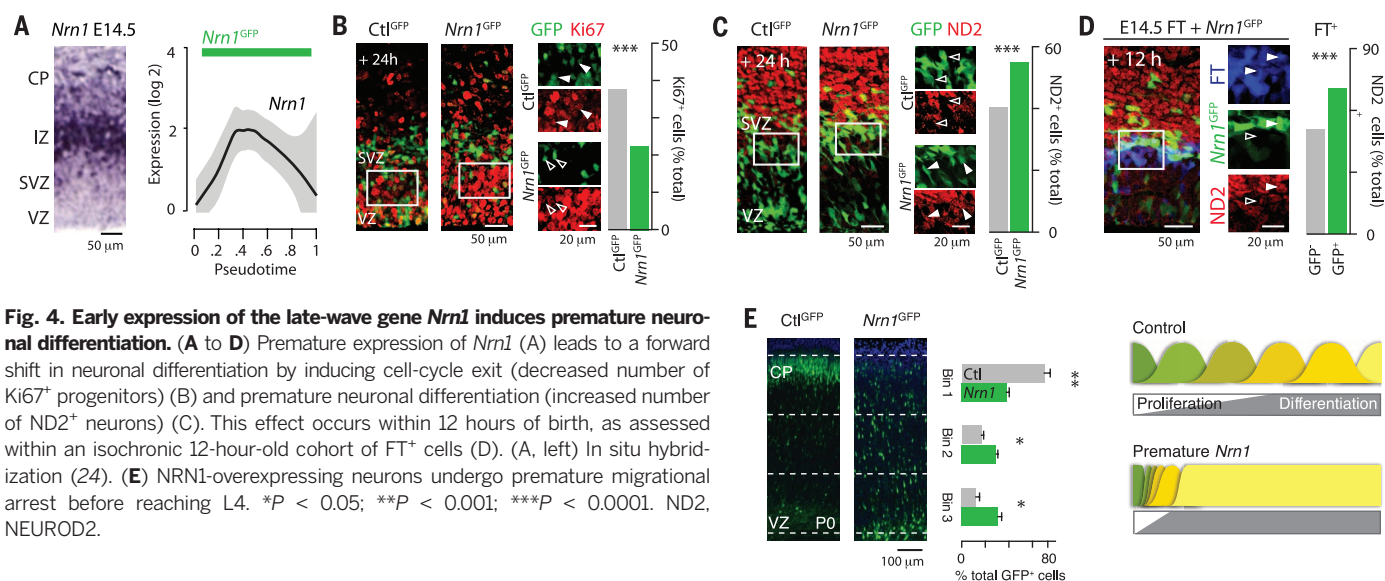


**Fig. 4. Early expression of the late-wave gene *Nrn1* induces premature neuronal differentiation.** (A to D) Premature expression of *Nrn1* (A) leads to a forward shift in neuronal differentiation by inducing cell-cycle exit (decreased number of  $Ki67^{+}$  progenitors) (B) and premature neuronal differentiation (increased number of  $ND2^{+}$  neurons) (C). This effect occurs within 12 hours of birth, as assessed within an isochronic 12-hour-old cohort of  $FT^{+}$  cells (D). (A, left) In situ hybridization (24). (E) *NRN1*-overexpressing neurons undergo premature migrational arrest before reaching L4.  $^{*}P < 0.05$ ;  $^{**}P < 0.001$ ;  $^{***}P < 0.0001$ .  $ND2$ , NEUROD2.



identify progenitor and neuron-specific transcripts activated after cell division and reveal rapid cell-type specific segregation and regulation of transcripts after mitosis.

To establish a real-time quantitative account of differentiation programs in newborn neurons, we used an unsupervised approach in which single-cell expression profiles are temporally ordered based on distinct intermediate differentiation states (Fig. 3A) (15, 16). This method appropriately ordered neurons along a pseudotime axis, with 6-, 12-, 24-, and 48-hour-old neurons being progressively staggered along this time line (Fig. 3A). This allowed us to reconstruct the expression dynamics of all transcripts across this pseudotime axis and generate a high-resolution transcriptomic atlas of the first 48 hours of L4 cortical neuron development (Fig. 3B) (see <http://genebrowser.unige.ch/science2016> for the data set of all transcripts). The expression dynamics of classical P (*Sox2*), Ng (*Neurog2*), and N (*Tbr1*) transcripts were consistent with their function (Fig. 3B). *Neurod2* was identified as an early-onset neuronal transcript; accordingly, NEUROD2 protein was detected in newborn apical VZ neurons, whereas this was not the case for TBR1 (Fig. 3B, inset).

Clustering of expressed transcripts based on their expression dynamics showed how transcriptional networks are organized in newborn neurons. Directly after mitosis, waves of transcriptional programs sequentially unfold, each including temporally distinct complements of transcription factors and networks (Fig. 3, C and D, fig. S10, data table S3, and movie S2). To understand the temporal organization of the molecular pathways across differentiation, we focused on the genetic network of *Neurod2*, a wave 5 transcription factor required for L4 neuron maturation and whose target genes have been identified in the E14.5 neocortex (17, 18). The temporal distribution of NEUROD2 target genes across the distinct waves was not random (Fig. 3C, right, and data table S4). Instead, NEUROD2 targets were strongly enriched in its own wave (e.g., *Nrn1* and *EphB2*), in line with its role in neuritogenesis, but also present across waves, including in wave 1, where targets include cyclins and cyclin-dependent kinases such as *Cnd2*, *Cnd3*, and *Cdk13*, which control cell cycle progression. NEUROD2 may therefore act not only on isochronically expressed genes but also across differentiation. Consistent with a repressive action on wave 1 targets, overexpression of NEUROD2 through in utero electroporation into VZ progenitors induced exit from the cell cycle, as indicated by decreased numbers of Ki67<sup>+</sup> VZ cells (fig. S11). Single transcription factors can therefore control distinct differentiation events through combinatorial actions on a variety of temporally gated genetic targets and networks.

Ontology term analysis of the transcriptional waves identified successive functional differentiation events in newborn neurons (Fig. 3E). We observed an initial rapid (6 to 12 hours after mitosis) repression of proliferation-associated

transcripts (e.g., *Arx*, *Notch1*, and *Sox9*) and a surge in transcripts associated with ribosome biogenesis and translation (e.g., *Etf1*, *Rpl13a*, and *Rpl12*), which might reflect nucleolar reassembly and increased protein synthesis. Transcripts associated with DNA repair (e.g., *DNA2*, *Ddb1*, and *Exo1*) were transiently increased after mitosis, suggesting postmitotic genetic instability. Consistent with this possibility, DNA double-strand breaks were significantly increased in 12-hour-old neurons (Fig. 3F). This reveals a critical period after mitosis during which neocortical neurons are susceptible to somatic mutations and where clonal mosaicism could be generated (19, 20). Twelve-hour-old neurons already initiated differentiation programs related to late-occurring processes such as synaptogenesis, revealing an early transcriptional poise in anticipation of terminal differentiation events. Finally, chemotaxis-associated transcripts (e.g., *Ephb1*, *LICAM*, and *Nrp1*) peaked around 42 hours after birth, while neurons are reaching the CP, providing a molecular framework for input-dependent differentiation processes (21).

Finally, we examined whether the distribution of transcript expression across waves instructs the sequence and pace of neuronal differentiation events. For this purpose, we prematurely expressed a late-wave transcript, *Nrn1*, which normally peaks ~30 hours after mitosis (wave 5, Fig. 4A) and controls L4 neuron maturation through promotion of neuritogenesis (22, 23). We hypothesized that heterochronic expression of this normally late-occurring gene could bypass early processes and accelerate neuronal differentiation. Indeed, in utero electroporation of *Nrn1* led to premature transition to neuronal identity and precocious expression of NEUROD2 (Fig. 4, B and C). Premature acquisition of this neuronal trait was detectable as early as 12 hours after cell birth, as revealed by assessing NEUROD2 expression within an isochronic 12-hour-old cohort of FT<sup>+</sup> cells with mosaic overexpression of NRN1 (Fig. 4D). Finally, precocious molecular maturation was associated with an early loss of migrational capacity, leading to neuronal mispositioning at birth (Fig. 4E). Therefore, the precise timing of early differentiation programs is critical not only for the execution of single-cell differentiation events but also for the successful organization of the cortical networks to which it belongs. Precise and dynamic temporal control over the expression of even single genes thus controls the sequence and pace of neuronal differentiation, which is essential for circuit assembly.

Our data provide a comprehensive transcriptional blueprint outlining the dynamic acquisition of neuronal identity in vivo. We show that early neuronal differentiation is directed by a series of transcriptional waves whose proper sequence is critical for normal progression through development. These waves provide discrete time windows during which specific transcriptional complexes are present simultaneously and can interact. These transient combinatorial transcriptional niches could act as sequential checkpoints

during the course of differentiation, combinatorially coding for specific cell fates. These results build a road map for reverse engineering of cortical neuron subtypes from undifferentiated cells and provide a set of genetic targets for identification and directed differentiation of progenitors and nascent neurons.

## REFERENCES AND NOTES

1. A. Zeisel et al., *Science* **347**, 1138–1142 (2015).
2. T. G. Belgard et al., *Neuron* **71**, 605–616 (2011).
3. P. Ariotta et al., *Neuron* **45**, 207–221 (2005).
4. B. J. Molyneaux et al., *Neuron* **85**, 275–288 (2015).
5. S. Fertuzinhos et al., *Cell Rep.* **6**, 938–950 (2014).
6. Y. Kosodo et al., *EMBO J.* **30**, 1690–1704 (2011).
7. E. Taverna, M. Götz, W. B. Huttner, *Annu. Rev. Cell Dev. Biol.* **30**, 465–502 (2014).
8. B. J. C. Quah, C. R. Parish, *J. Vis. Exp.* **2010**, e2259 (2010).
9. M. Götz, A. Stoykova, P. Gruss, *Neuron* **21**, 1031–1044 (1998).
10. C. Englund et al., *J. Neurosci.* **25**, 247–251 (2005).
11. A. A. Pollen et al., *Cell* **163**, 55–67 (2015).
12. A. A. Pollen et al., *Nat. Biotechnol.* **32**, 1053–1058 (2014).
13. E. Z. Macosko et al., *Cell* **161**, 1202–1214 (2015).
14. M. Florio, W. B. Huttner, *Development* **141**, 2182–2194 (2014).
15. C. Trapnell et al., *Nat. Biotechnol.* **32**, 381–386 (2014).
16. J. Shin et al., *Cell Stem Cell* **17**, 360–372 (2015).
17. G. Ince-Dunn et al., *Neuron* **49**, 683–695 (2006).
18. E. Bayam et al., *BMC Genomics* **16**, 681 (2015).
19. P. J. McKinnon, *Nat. Neurosci.* **16**, 1523–1529 (2013).
20. M. A. Lodato et al., *Science* **350**, 94–98 (2015).
21. T. Namba et al., *Neuron* **81**, 814–829 (2014).
22. G. Pouchelon et al., *Nature* **511**, 471–474 (2014).
23. H. Sato et al., *J. Neurosci.* **32**, 15388–15402 (2012).
24. G. Diez-Roux et al., *PLOS Biol.* **9**, e1000582 (2011).
25. E. P. Rogakou, D. R. Pilch, A. H. Orr, V. S. Ivanova, W. M. Bonner, *J. Biol. Chem.* **273**, 5858–5868 (1998).

## ACKNOWLEDGMENTS

Annotated data are available at <http://genebrowser.unige.ch/science2016>. We thank R. Hevner for the gift of the TBR1 antibody; A. Benoit, M. Lanzillo, and the Genomics Platform and FACS Facility of the University of Geneva for technical assistance; and E. Azim, A. Carleton, S. Tole, and the members of the Jabaudon laboratory for comments on the manuscript. Work in the Jabaudon laboratory is supported by the Swiss National Science Foundation (PP00P3\_123447), the Synapsis Foundation, and the Brain and Behavior Foundation (NARSAD Grant). S.N. is funded by the Swiss SystemsX Interdisciplinary PhD Grant 51PH10–141994. S.G. and I.S. are supported by the iGe3 PhD Award. A.D. is funded by the Swiss National Science Foundation and the National Center of Competence in Research (NCCR) Synapsis. The authors declare no competing interests. The supplementary materials contain additional data.

## SUPPLEMENTARY MATERIALS

[www.sciencemag.org/content/351/6280/1443/suppl/DC1](http://www.sciencemag.org/content/351/6280/1443/suppl/DC1)  
Materials and Methods  
Figs. S1 to S11  
Table S1  
Movies S1 and S2  
Data Tables S1 to S4  
Database S1  
Reference (26)

11 November 2015; accepted 15 February 2016  
Published online 3 March 2016  
10.1126/science.1248361

## CLOUD FORMATION

# An interfacial mechanism for cloud droplet formation on organic aerosols

Christopher R. Ruehl,<sup>\*,†</sup> James F. Davies, Kevin R. Wilson<sup>†</sup>

Accurate predictions of aerosol/cloud interactions require simple, physically accurate parameterizations of the cloud condensation nuclei (CCN) activity of aerosols. Current models assume that organic aerosol species contribute to CCN activity by lowering water activity. We measured droplet diameters at the point of CCN activation for particles composed of dicarboxylic acids or secondary organic aerosol and ammonium sulfate. Droplet activation diameters were 40 to 60% larger than predicted if the organic was assumed to be dissolved within the bulk droplet, suggesting that a new mechanism is needed to explain cloud droplet formation. A compressed film model explains how surface tension depression by interfacial organic molecules can alter the relationship between water vapor supersaturation and droplet size (i.e., the Köhler curve), leading to the larger diameters observed at activation.

Accurate predictions of the impact of aerosols on cloud properties, and thus the radiative balance of the atmosphere, rely on simple parameterizations of cloud droplet formation. Despite the simplicity required of such parameterizations, they must be based on robust chemistry and physics to ensure the validity of climate predictions. From Köhler theory (1), the cloud condensation nuclei (CCN) activity of an aerosol is governed both by its size and its molecular constituents that can lower the water activity and/or surface tension of aqueous droplets below that of pure water. There are a number of extensively used empirical parameterizations of Köhler theory that neglect surface tension depression and assume that cloud droplets form on particles that contain sufficient solute (2, 3). In our study, droplet sizes measured up to and including the point of cloud droplet activation reveal that most organic aerosol (OA) contributes to CCN by adsorbing to the air/droplet interface.

One popular parameterization of Köhler theory, known as  $\kappa$ -Köhler theory (3), describes the lowering of water activity by a solute using a single parameter,  $\kappa$ : a dimensionless ratio of the molar volume of water to the average osmolar volume of the aerosol.  $\kappa$ -Köhler theory is used to interpret field observations and laboratory experiments in an effort to relate aerosol composition to hygroscopicity (4). Although many field studies, including those in Colorado (5), Ontario (6), coastal California (7), and the Amazon (8), yield reasonable values for the hygroscopicity of the organic component of the aerosol ( $\kappa_{\text{org}}$ ) when interpreted via  $\kappa$ -Köhler theory, there are observations that suggest more complex behavior (non-ideal solution and surface tension effects) not captured in current water activity-based parameterizations of CCN activity (9, 10).

Neglecting surface activity in CCN parameterizations appears consistent with predictions of surface-bulk partitioning models (e.g., Szyszkowski-Langmuir adsorption theory). When using parameters obtained for macroscopic solutions, the bulk concentrations of surface-active solutes are predicted to be strongly depleted in microscopic droplets, thus increasing water activity and negating any increase in CCN activity caused by a reduction in surface tension (11). This has led many to conclude that accounting for surface activity is not necessary to accurately predict the CCN activity of OA, despite measurements of reduced surface tension in macroscopic aqueous solutions of atmospheric OA and relevant model compounds (12, 13). Furthermore, partitioning models fail to predict concentrations of surfactants in submicrometer droplets, suggesting significant limitations of current approaches to accurately describe surface activity at that length scale (14).

Using a continuous-flow streamwise thermal gradient chamber [section S1 of (15)], we measured the diameter of droplets ( $D_{\text{wet}}$ ) that form on mixed organic-ammonium sulfate (AS) particles at water vapor supersaturation [ $S$ , or relative humidity (RH) – 100%] approaching and including the point of CCN activation. Although it is common to compute Köhler curves to predict the critical supersaturation ( $S_c$ ) of aerosols, direct measurements of  $D_{\text{wet}}$  as a function of  $S$  (15) allow OA CCN activity to be additionally constrained by droplet activation diameter ( $D_{\text{wet,c}}$ ).

As shown in Fig. 1A, pure 200-nm-diameter ( $D_{\text{dry}}$ ) AS particles activate at  $D_{\text{wet,c}} \sim 2.5 \mu\text{m}$ , consistent with  $\kappa$ -Köhler theory. Mixed aerosols of AS and sucrose (known to be surface-inactive) activate at  $D_{\text{wet,c}} = 0.8 \mu\text{m}$ , consistent with a water activity-based parameterization (Fig. 1B). These results are in contrast to AS aerosol coated with a series of small dicarboxylic acid (Fig. 1, C and D, and figs. S5 to S7) and  $\alpha$ -pinene secondary OA (SOA, Fig. 2). The functional form of  $D_{\text{wet}}$  versus  $S$  deviates substantially from  $\kappa$ -Köhler predictions, with a  $D_{\text{wet,c}}$  that is  $\sim 50\%$  larger than

predicted by constant  $\kappa_{\text{org}}$  for a given  $S_c$ . For succinic acid-coated AS (Fig. 1D),  $D_{\text{wet,c}}$  is observed to be  $1.8 \mu\text{m}$ , which is substantially larger than predicted ( $D_{\text{wet,c}} = 1.4 \mu\text{m}$ ), assuming  $\kappa_{\text{org}} = 0.31$ . A similar difference was observed for malonic acid (Fig. 1C). For SOA-coated AS in Fig. 2,  $D_{\text{wet,c}} = 1.3$  to  $1.4 \mu\text{m}$ , which is much larger than the  $\kappa_{\text{org}}$  predictions of  $D_{\text{wet,c}} = 0.9 \mu\text{m}$ .

For pure AS aerosol, the evolution of  $D_{\text{wet}}$  with  $S$ , and the size of  $D_{\text{wet,c}}$ , are exactly what is predicted by  $\kappa$ -Köhler theory and serve to validate the experimental approach. The mixed AS/sucrose observations show that  $\kappa$ -Köhler theory correctly predicts  $D_{\text{wet}}$  versus  $S$  and  $D_{\text{wet,c}}$  in the case of a highly water-soluble organic compound that does not depress surface tension (i.e., is surface-inactive). In contrast, AS aerosols coated with a series of dicarboxylic acids, some of which are known to be surface-active, exhibit much larger activation diameters and a different functional form of  $D_{\text{wet}}$  versus  $S$  than is predicted by  $\kappa$ -Köhler theory (Figs. 1 and 2 and figs. S3 to S7). Although limited organic solubility can alter the shape of the Köhler curve (16), it cannot explain the consistently large droplet activation diameters observed for these dicarboxylic acids, whose bulk solubility varies from near that of sucrose (i.e., malonic acid) to over two orders of magnitude smaller (table S1). The mixed SOA/AS aerosols exhibit the same deviation from  $\kappa$ -Köhler theory as the dicarboxylic acids. Collectively, the observed differences between  $D_{\text{wet,c}}$  for the organic acids (also SOA) and sucrose suggest that the discrepancies with  $\kappa$ -Köhler theory originate from surface effects rather than non-ideal behavior of mixtures.

To account for the surface activity of organics within Köhler theory, an equation of state is required to relate the bulk and surface concentrations of the various solution components. Associated with the equation of state is an isotherm that relates organic surface concentration to surface tension. Previously, the Szyszkowski-Langmuir equation (13, 17) was used to compute Köhler curves (i.e., to predict  $S_c$ ) for model organic compounds (16). This particular treatment of bulk-surface partitioning [section S2 of (15)] cannot fully explain the observed  $D_{\text{wet}}$  as a function of  $S$ . Instead, an equation of state that allows for a two-dimensional (2D) phase transition is required. To provide a self-consistent model description of the observations shown in Figs. 1 and 2, a compressed film model (18) was used to describe the relationship between surface tension depression and organic surface coverage or thickness on the droplet (figs. S3 to S7). Model details can be found in section S2 of (15) and are described conceptually here. The model contains a 2D phase transition between “gaseous” and “compressed” surface states, which depends on surface concentration (i.e., molecular packing). Because the quantity of organic material is fixed by the composition of the original dry aerosol, changes in surface tension occur when  $S$  increases and the droplet grows, decreasing the surface concentration by providing a larger surface area per molecule. At low  $S$  (below  $S_c$ ),

Chemical Sciences Division, Lawrence Berkeley National Laboratory, Berkeley, CA 94720, USA.

<sup>\*</sup>Present address: California Air Resources Board, Sacramento, CA 95814, USA. <sup>†</sup>Corresponding author. E-mail: chris.ruehl@arb.ca.gov (C.R.R.); krwilson@lbl.gov (K.R.W.)



the surface organic concentration is high, and the molecules adopt a compressed state, which lowers the droplet's surface tension below that of liquid water. At higher  $S$  (near  $S_c$ ), the droplets are larger, the surface concentration is lower, and the molecules at the interface are non-interacting (i.e., in a gaseous surface state), with a droplet surface tension nearly equal to that of pure water. The data shown in Figs. 1 and 2 (and figs. S3 to S7) are best replicated if it is assumed that the surface tension increases linearly with decreasing surface concentration (18). As shown in Figs. 1 and 2 and figs. S3 to S7, the compressed film model can reasonably account for the functional form of  $S$  versus  $D_{\text{wet}}$ . Although the compressed film model shows that some of the organic material is dissolved in the droplet bulk, the model reveals that for SOA and most of the model compounds [section S3 of (15)] most of the organic material is at the droplet surface (Fig. 2B and figs. S3 to S7), in stark contrast with the underlying assumption of  $\kappa$ -Köhler theory.

The compressed film model predicts that a particle will reach  $S_c$  when the surface film decreases in thickness to the point that individual molecules begin to separate; i.e., a 2D phase transition occurs, and the surface tension no longer varies with increasing  $D_{\text{wet}}$  (15). This occurs at an  $S$  and  $D_{\text{wet}}$  that lies on the post-activation portion of the Köhler curve for the bare inorganic AS seed. At this intersection point, all of the hygroscopicity can be attributed to the reduction of water activity by AS. The compressed film model explains this by predicting that the organic material is adsorbed to the interface (hence no decrease in water activity by the organic), but  $D_{\text{wet}}$  is large enough to lower the organic surface concentration to a point where the resulting surface tension is near that of pure water. Although there are several parameters needed to constrain the model, a single-parameter approximation to the compressed film model can be used if it is assumed that all the organic material resides at the droplet surface. This parameter, termed  $\delta_{\text{org}}$ , corresponds to a film thickness (in nanometers) on the droplet surface where the 2D phase transition occurs (i.e., where the surface tension depression goes to zero). Although surface concentration is used more often than film thickness for monolayers of known composition, film thickness is preferable for discussions of particle hygroscopicity, because aerosol composition is often complex and poorly constrained molecularly, and because sizes (particle and droplet diameters) are measured in CCN experiments.

The  $S_c$  for a particle is computed from  $\delta_{\text{org}}$  if both the organic fraction ( $f_{\text{org}}$ ) and  $\kappa_{\text{inorg}}$  (inorganic hygroscopicity) are known [section S2 of (15)], which is the same set of parameters required to predict  $S_c$  given  $\kappa_{\text{org}}$ . In Fig. 3, the surface ( $\delta_{\text{org}}$ ) and bulk activity ( $\kappa_{\text{org}}$ ) parameterizations are compared with additional measurements of  $S_c$  versus dry organic coating thickness on AS seed particles for the same series of dicarboxylic acids and SOA. The measured critical supersaturation ( $S_c$ ) decreases with increasing dry organic coating thickness for all particles measured. The data

for each compound/SOA in Fig. 3 are fit with both a constant organic osmolar volume (related to  $\kappa_{\text{org}}$ ) and film thickness ( $\delta_{\text{org}}$ ).

In most cases, constant  $\kappa_{\text{org}}$  does not replicate the observed curvature in  $S_c$  versus coated diameter (Fig. 3), generally predicting a more shallow slope than is observed. There are two exceptions: malonic and suberic acid. However, the molar volumes required to replicate these data are much smaller than what is reported in the literature: malonic acid by 36%, and suberic acid by 3.7 times. Such a dramatic increase in hygroscopicity cannot be explained by the dissociation of these weak acids. In contrast, the  $\delta_{\text{org}}$  approximation does capture the curvature observed in most plots of  $S_c$  versus  $f_{\text{org}}$  shown in Fig. 3. Thus, the  $\delta_{\text{org}}$  approximation to the compressed film model correctly accounts for

both the droplet size at activation (Figs. 1 and 2 and figs. S3 to S7) and the evolution of  $S_c$  with dry OA fraction (Fig. 3).

The compressed film model offers an explanation for some recent ambient CCN observations. In CCN closure studies, agreement between observations and predictions is often best when the OA fraction is assumed to be insoluble, as recently reported in California (19). In particles that have similar amounts of organic and inorganic material, or are predominantly inorganic, there is not enough organic material to form a compressed film on the droplet at or near the point of activation. Although this organic material will be adsorbed to the droplet surface, there is an insufficient concentration at the interface to reduce surface tension; instead, the organic will effectively behave as insoluble material with

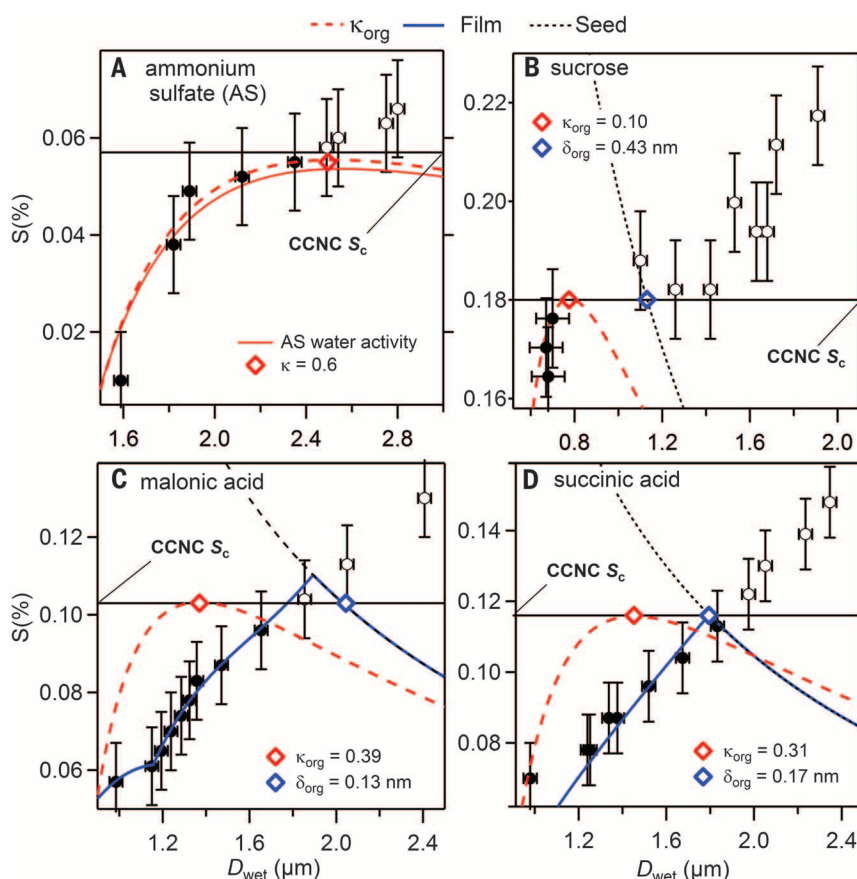


**Fig. 1. Köhler curve observations for (A) pure AS, (B) sucrose + AS, (C) malonic acid + AS, and (D) succinic acid + AS particles.**  $D = 200$  nm for pure AS particles, and for all other particles  $D = 150$  nm (a 50-nm AS seed + a 50-nm radial coating thickness, corresponding to 89% organic by volume). As described in section S1 of (15),  $D_{\text{wet}}$  is measured by phase Doppler interferometry, along the centerline of a thermal gradient chamber (29) after  $\sim 10$  s of exposure to RH  $\sim 100\%$  and is therefore not sensitive to decreases in surface tension that might occur over longer time scales as recently observed for aerosol and biological surfactants (14). Solid and open circles represent unactivated and activated droplets, respectively. Because it is not always apparent when activation occurs solely from measurements of  $D_{\text{wet}}$ ,  $S_c$  (horizontal solid black lines) is measured using a separate CCN counter (CCNC, Droplet Measurement Technologies). Dashed red lines are the Köhler curves predicted using a water activity parameterization ( $\kappa_{\text{org}}$ ). Solid blue lines are those predicted by the compressed film model [section S2 of (15)], and dashed black lines are those for the AS seed particles. The solid red line in (A) is the Köhler curve obtained with a parameterization of the water activity of dilute AS (30). Also shown are the points of CCN activation predicted by  $\kappa_{\text{org}}$  (red diamonds) and  $\delta_{\text{org}}$  (blue diamonds).

respect to CCN activation. Recently, activation diameters inferred from particle and droplet size distributions in urban fog were unexpectedly large (20), similar to what was observed in this study. Finally, observations of enhanced OA hygroscopicity that were recently reported for a coastal site on Vancouver Island (9) do not seem

reasonable for marine organic material, suggesting, in light of our results, that a major contribution to CCN activity from surface activity could be likely.

The compressed film model also offers an explanation for some unresolved questions arising from laboratory CCN studies, including several

single-component OAs that exhibit anomalously large CCN activity despite limited bulk solubility (21–24). For example, pimelic acid is CCN-active ( $\kappa = 0.14$  to  $0.16$ ), despite its low solubility that suggests that  $\kappa$  should be five times smaller than observed (25). This model predicts that most OA (especially OA of limited solubility) is adsorbed to the surface of microscopic droplets. Thus, the relatively small bulk concentrations may not, in fact, exceed solubility limits. Although Raoult (water activity) effects may also be important for aerosol with unknown or more complex composition (26), it is an unlikely explanation for the anomalously high CCN activity of individual compounds. The compressed film model also resolves the “gap” between  $\kappa_{\text{org}}$  values derived from CCN activity experiments, which are often much larger than those derived from subsaturated measurements of hygroscopic growth (27). The surface tension reduction by a compressed film will only increase hygroscopicity at high RH (near 100%) (28), whereas at lower RH, where the water activity term dominates, the effect of the film will be to lower hygroscopicity relative to the fully soluble assumption.

These results point to an alternative mechanism for cloud droplet formation in mixed organic/inorganic aerosol. Although a water activity-based parameterization correctly predicts the droplets' sizes under supersaturated conditions for pure AS and sucrose (a non-surface-active compound), it fails to correctly account for the larger cloud droplets that form on AS coated with a series of dicarboxylic acids (with a broad range of water solubility) and SOA. Thus it is unlikely that our results can be attributed to bulk solubility effects, but rather can be explained if most of the organic material exists as an interfacial compressed film, which reduces surface tension, allowing larger droplets to form before activation. At activation, the compressed film transitions to a gaseous state, and the surface tension of the droplet is nearly equal to that of pure water. Although the assumption that organic material dissolved in the droplet bulk may yield reasonable CCN predictions, in field measurements and in the laboratory these results can help explain several outstanding questions and highlight the potential importance of interfacial organics in the formation of cloud droplets on OA.

**Fig. 2. Köhler curve observations for AS +  $\alpha$ -pinene SOA particles ( $D = 175$  nm) prepared in a flow tube reactor.**

As described in section S1 of (15), SOA was generated by ozonolysis in a flow tube reactor and coated onto 85-nm-diameter AS seeds (91% SOA by volume). (A) Dashed red lines are the Köhler curves predicted using a water activity parameterization; solid blue lines are those predicted with the compressed film model [details in section S2 of (15)]; and dotted black lines are those for the AS seed particles.

The horizontal black line indicates the  $S_c$  observed with a conventional CCN instrument (CCNC, Droplet Measurement Technologies). Also indicated is the point of CCN activation predicted by  $\kappa_{\text{org}}$  (red) and  $\delta_{\text{org}}$  (blue) symbols. Included are the (B) surface tension ( $\sigma$ ) and (C) fraction of SOA at the surface ( $f_{\text{surf}}$ ), as predicted by the compressed film model.

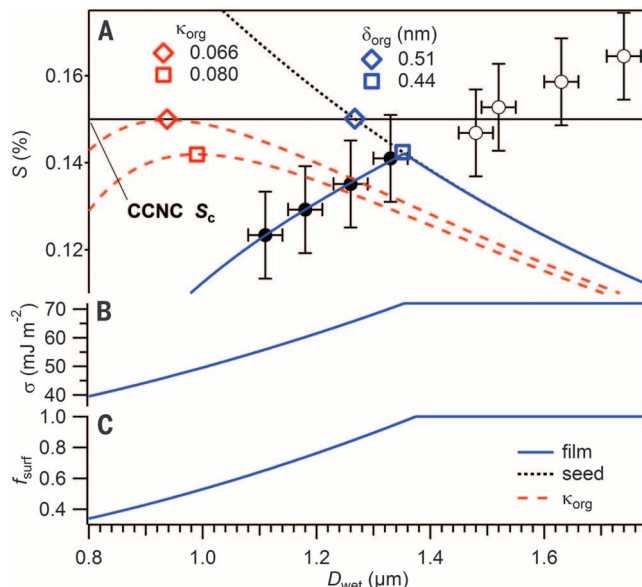
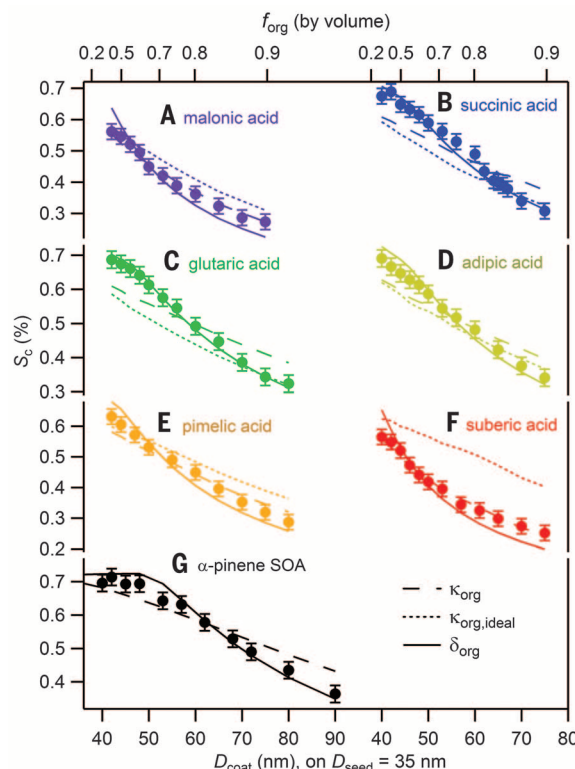


**Fig. 3.  $S_c$  as a function of coated dry diameter for (A to F) a series of dicarboxylic acids or (G) SOA generated via ozonolysis of  $\alpha$ -pinene coated onto AS seed particles ( $D = 35$  nm). Both seed and coated diameters were size-selected by a differential mobility analyzer (TSI, Model 3080). Dashed and solid lines are the best fits for each substance, using a single parameter for organic hygroscopicity ( $\kappa_{\text{org}}$  and  $\delta_{\text{org}}$ , respectively), and dotted lines indicate predictions assuming an ideal solution ( $\kappa_{\text{org,ideal}}$ ). These values are listed in table S1 of (15).**



## REFERENCES AND NOTES

1. H. Köhler, *Trans. Faraday Soc.* **32**, 1152–1161 (1936).
2. H. Abdul-Razzak, S. J. Ghan, *J. Geophys. Res. Atmos.* **107**, AAC 1-1-AAC 1-6 (2002).
3. M. D. Petters, S. M. Kreidenweis, *Atmos. Chem. Phys.* **7**, 1961–1971 (2007).
4. J. L. Jimenez et al., *Science* **326**, 1525–1529 (2009).
5. E. J. T. Levin et al., *Atmos. Chem. Phys.* **14**, 2657–2667 (2014).
6. R. Y. W. Chang et al., *Atmos. Chem. Phys.* **10**, 5047–5064 (2010).
7. J. Wang, Y. N. Lee, P. H. Daum, J. Jayne, M. L. Alexander, *Atmos. Chem. Phys.* **8**, 6325–6339 (2008).
8. S. S. Gunthe et al., *Atmos. Chem. Phys.* **9**, 7551–7575 (2009).
9. J. D. Yakobi-Hancock et al., *Atmos. Chem. Phys.* **14**, 12307–12317 (2014).
10. N. Good et al., *Atmos. Chem. Phys.* **10**, 3189–3203 (2010).



11. R. Sorjamaa *et al.*, *Atmos. Chem. Phys.* **4**, 2107–2117 (2004).
12. S. Ekström, B. Nozière, H. C. Hansson, *Atmos. Chem. Phys.* **9**, 973–980 (2009).
13. M. C. Facchini, M. Mircea, S. Fuzzi, R. J. Charlson, *Nature* **401**, 257–259 (1999).
14. B. Nozière, C. Baduel, J.-L. Jaffrezo, *Nat. Commun.* **5**, 3335 (2014).
15. Materials and methods and supporting analysis of the experimental data are available as supplementary materials on Science Online.
16. M. L. Shulman, M. C. Jacobson, R. J. Carlson, R. E. Synovec, T. E. Young, *Geophys. Res. Lett.* **23**, 277–280 (1996).
17. S. Henning *et al.*, *Atmos. Chem. Phys.* **5**, 575–582 (2005).
18. G. Jura, W. D. Harkins, *J. Am. Chem. Soc.* **68**, 1941–1952 (1946).
19. R. H. Moore *et al.*, *J. Geophys. Res. Atmos.* **117**, D00V12 (2012).
20. E. Hammer *et al.*, *Atmos. Chem. Phys.* **14**, 10517–10533 (2014).
21. K. Broekhuizen, P. P. Kumar, J. P. D. Abbatt, *Geophys. Res. Lett.* **31**, L01107 (2004).
22. K. E. H. Hartz *et al.*, *Atmos. Environ.* **40**, 605–617 (2006).
23. M. Hori, S. Ohta, N. Murao, S. Yamagata, *J. Aerosol Sci.* **34**, 419–448 (2003).
24. A. Kristensson, T. Rosenørn, M. Bilde, *J. Phys. Chem. A* **114**, 379–386 (2010).
25. M. Kuwata, W. Shao, R. Lebouteiller, S. T. Martin, *Atmos. Chem. Phys.* **13**, 5309–5324 (2013).
26. M. D. Petters *et al.*, *Tellus B Chem. Phys. Meteorol.* **58**, 196–205 (2006).
27. H. Wex *et al.*, *Atmos. Chem. Phys.* **9**, 3987–3997 (2009).
28. C. R. Ruehl, K. R. Wilson, *J. Phys. Chem. A* **118**, 3952–3966 (2014).
29. G. C. Roberts, A. Nenes, *Aerosol Sci. Technol.* **39**, 206–221 (2005).
30. K. C. Young, A. J. Warren, *J. Atmos. Sci.* **49**, 1138–1143 (1992).

## ACKNOWLEDGMENTS

This work is supported by the Office of Science Early Career Research Program, through the Office of Energy Research, Office of Basic Energy Science of the U.S. Department of Energy under contract no. DE-AC02-05CH11231. The continuous-flow streamwise thermal gradient chamber was originally developed by Patrick Chuang and Anthanasios Nenes with support from NASA's Atmospheric Radiation Measurement program.

## SUPPLEMENTARY MATERIALS

www.sciencemag.org/content/351/6280/1447/suppl/DC1  
Materials and Methods  
Supplementary Text  
Figs. S1 to S7  
Tables S1 to S3  
References (31–39)

18 September 2015; accepted 18 February 2016  
10.1126/science.aad4889

## PROTEIN EVOLUTION

# Survey of variation in human transcription factors reveals prevalent DNA binding changes

Luis A. Barrera,<sup>1,2,3,4</sup> Anastasia Vedenko,<sup>1\*</sup> Jesse V. Kurland,<sup>1\*</sup> Julia M. Rogers,<sup>1,2</sup> Stephen S. Gisselbrecht,<sup>1</sup> Elizabeth J. Rossin,<sup>3,5,6</sup> Jaie Woodard,<sup>1,2</sup> Luca Mariani,<sup>1</sup> Kian Hong Kock,<sup>1,7</sup> Sachi Inukai,<sup>1</sup> Trevor Siggers,<sup>1†</sup> Leila Shokri,<sup>1</sup> Raluca Gordân,<sup>1‡</sup> Nidhi Sahni,<sup>8,9,10§</sup> Chris Cotsapas,<sup>5,6||</sup> Tong Hao,<sup>8,9,10</sup> Song Yi,<sup>8,9,10</sup> Manolis Kellis,<sup>4,6</sup> Mark J. Daly,<sup>5,6,11</sup> Marc Vidal,<sup>8,9,10</sup> David E. Hill,<sup>8,9,10</sup> Martha L. Bulyk<sup>1,2,3,6,7,8,12¶</sup>

Sequencing of exomes and genomes has revealed abundant genetic variation affecting the coding sequences of human transcription factors (TFs), but the consequences of such variation remain largely unexplored. We developed a computational, structure-based approach to evaluate TF variants for their impact on DNA binding activity and used universal protein-binding microarrays to assay sequence-specific DNA binding activity across 41 reference and 117 variant alleles found in individuals of diverse ancestries and families with Mendelian diseases. We found 77 variants in 28 genes that affect DNA binding affinity or specificity and identified thousands of rare alleles likely to alter the DNA binding activity of human sequence-specific TFs. Our results suggest that most individuals have unique repertoires of TF DNA binding activities, which may contribute to phenotypic variation.

Exome sequencing studies have identified many nonsynonymous single-nucleotide polymorphisms (nsSNPs) in transcription factors (TFs) (1). Genetic variants that alter transcript expression levels have been associated with human disease risk and are widespread in human populations (2, 3). Numerous Mendelian diseases are attributable to mutations in TFs (4). Missense SNPs that change the amino acid sequence of TF DNA binding domains (DBDs) might disrupt their DNA binding activities and thus have detrimental effects on their gene regulatory functions. Despite their medical importance, the consequences of coding variation in DBDs for TF function have remained largely unexplored.

We identified 53,384 unique DBD polymorphisms (DBDPs) (table S1) (here, defined as missense variants) in a curated, high-confidence set of 1254 sequence-specific human TFs (5, 6) (table

S2) from genotype data for 64,706 individuals encompassing African, Asian, and European ancestries (Fig. 1A) (1, 2, 7). We also identified 4552 unique nonsense mutations that result in partial or full DBD truncation (table S3).

We found a median of 60 heterozygous and 20 homozygous DBDPs (Fig. 1B) per genome. We found a significant depletion (odds ratio = 3.7,  $P = 0.005$ , Fisher's exact test) of DBDPs among TFs with known Mendelian disease mutations (6, 8), suggesting that DBDPs in disease-associated TFs have phenotypic consequences.

We developed a computational approach (6) to evaluate missense substitutions in TF DBDs for their impact on DNA binding activity. Existing methods for predicting the impact of missense mutations (9, 10) do not adequately consider the roles of residues in protein-DNA interactions, which we reasoned should improve predictions. We first focused on homeodomain DBDs, as

most known Mendelian disease mutations in TFs occur in homeodomain proteins. We analyzed homeodomain-DNA cocrystal structures in the Protein Data Bank to assemble a composite protein-DNA “contact map” (fig. S1). As anticipated, residues that contact DNA bases or phosphate backbone, or that immediately neighbor base-contacting residues, are enriched among Mendelian disease mutations ( $P < 0.005$ , permutation test). In contrast, individuals in the population are depleted for variants at base- or backbone-contacting positions ( $P = 0.0134$  or  $0.0312$ , respectively, permutation test) (Fig. 1C). This highlights the value of considering protein-DNA contacts in predicting the impact of variants.

On the basis of these results, we expanded our approach to other TF families. For each variant we considered multiple criteria, including (i) position of the residue relative to the protein-DNA interface in homologous cocrystal structures (fig.

<sup>1</sup>Division of Genetics, Department of Medicine, Brigham and Women's Hospital and Harvard Medical School, Boston, MA 02115, USA. <sup>2</sup>Committee on Higher Degrees in Biophysics, Harvard University, Cambridge, MA 02138, USA. <sup>3</sup>Harvard-MIT Division of Health Sciences and Technology, Harvard Medical School, Boston, MA 02115, USA. <sup>4</sup>Computer Science and Artificial Intelligence Laboratory, Massachusetts Institute of Technology, Cambridge, MA 02139, USA. <sup>5</sup>Analytic and Translational Genetics Unit, Department of Medicine, Massachusetts General Hospital and Harvard Medical School, Boston, MA 02114, USA. <sup>6</sup>Broad Institute of Harvard and MIT, Cambridge, MA 02139, USA. <sup>7</sup>Program in Biological and Biomedical Sciences, Harvard University, Cambridge, MA 02138, USA. <sup>8</sup>Center for Cancer Systems Biology (CCSB), Dana-Farber Cancer Institute, Boston, MA 02215, USA. <sup>9</sup>Department of Cancer Biology, Dana-Farber Cancer Institute, Boston, MA 02215, USA. <sup>10</sup>Department of Genetics, Harvard Medical School, Boston, MA 02115, USA. <sup>11</sup>Center for Human Genetics Research and Center for Computational and Integrative Biology, Massachusetts General Hospital, Boston, MA 02114, USA. <sup>12</sup>Department of Pathology, Brigham and Women's Hospital and Harvard Medical School, Boston, MA 02115, USA.

\*These authors contributed equally to this work. †Present address: Department of Biology, Boston University, Boston, MA 02215, USA. ‡Present address: Departments of Biostatistics and Bioinformatics, Computer Science, and Molecular Genetics and Microbiology, Institute for Genome Sciences and Policy, Duke University, Durham, NC 27708, USA. §Present address: Department of Systems Biology, The University of Texas MD Anderson Cancer Center, Houston, TX 77030, USA. ||Present address: Department of Neurology and Department of Genetics, Yale School of Medicine, New Haven, CT 06520, USA. ¶Corresponding author. E-mail: mlbulyk@receptor.med.harvard.edu

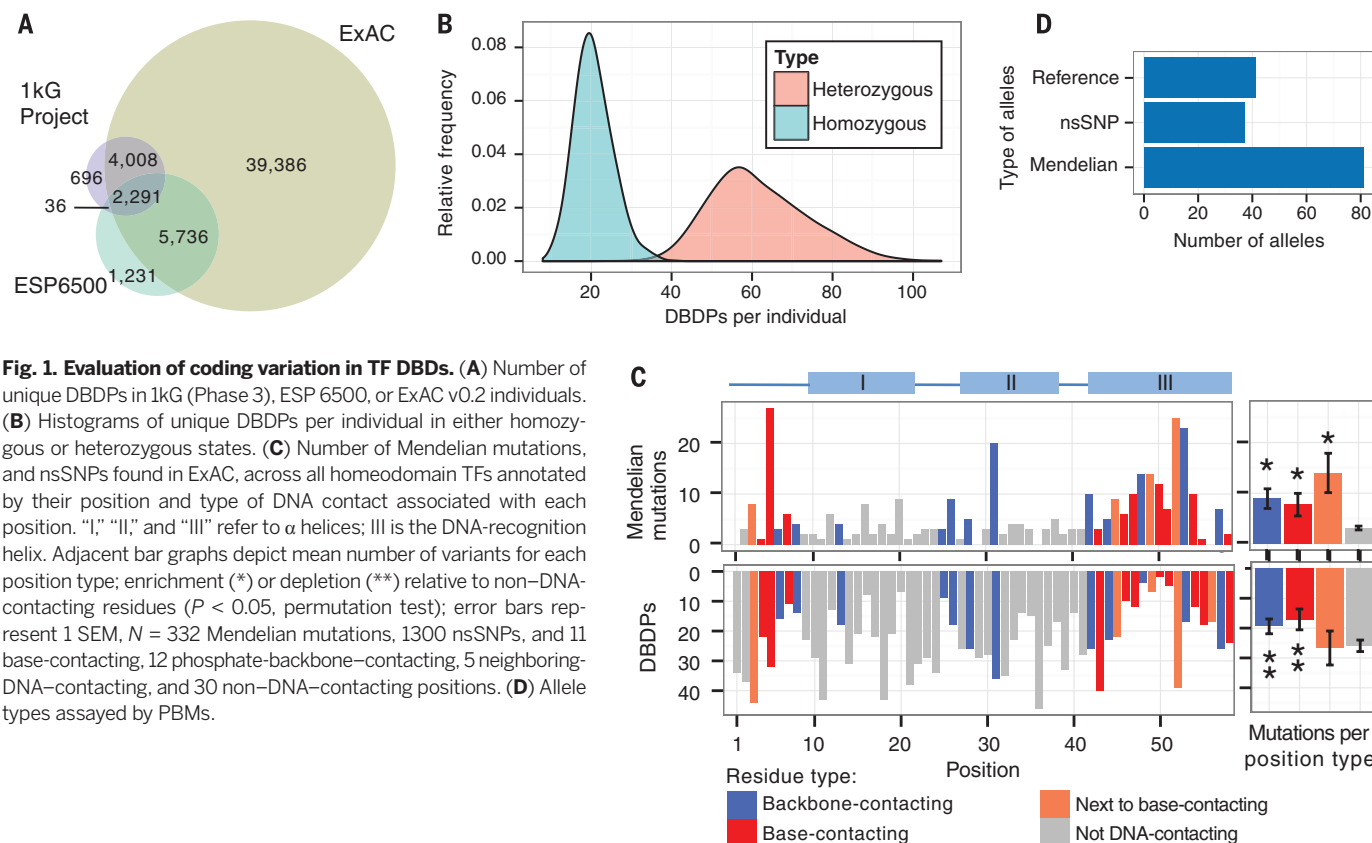


**Fig. 1. Evaluation of coding variation in TF DBDs.** (A) Number of unique DBDPs in 1kG (Phase 3), ESP 6500, or ExAC v0.2 individuals. (B) Histograms of unique DBDPs per individual in either heterozygous or homozygous states. (C) Number of Mendelian mutations, and nsSNPs found in ExAC, across all homeodomain TFs annotated by their position and type of DNA contact associated with each position. "I," "II," and "III" refer to  $\alpha$  helices; III is the DNA-recognition helix. Adjacent bar graphs depict mean number of variants for each position type; enrichment (\*) or depletion (\*\*) relative to non-DNA-contacting residues ( $P < 0.05$ , permutation test); error bars represent 1 SEM,  $N = 332$  Mendelian mutations, 1300 nsSNPs, and 11 base-contacting, 12 phosphate-backbone-contacting, 5 neighboring-DNA-contacting, and 30 non-DNA-contacting positions. (D) Allele types assayed by PBMs.

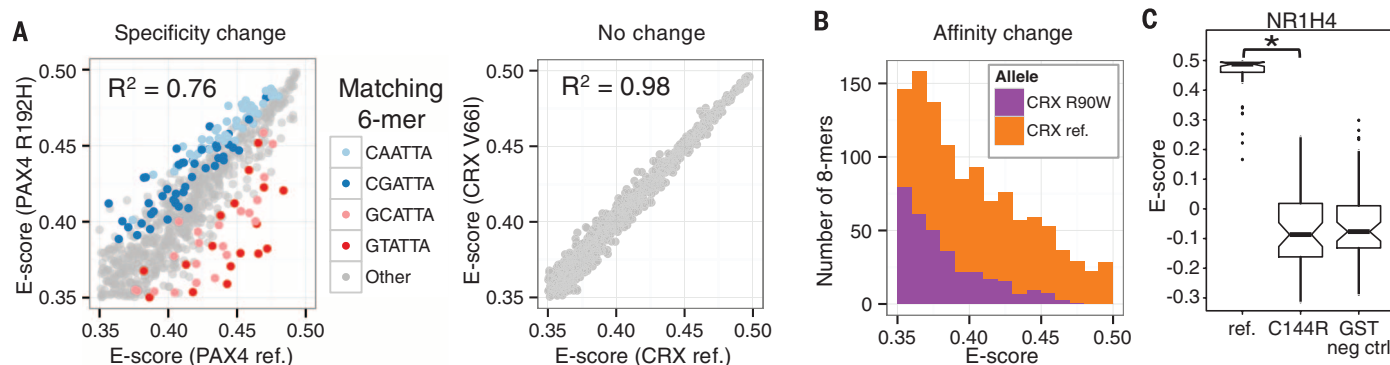
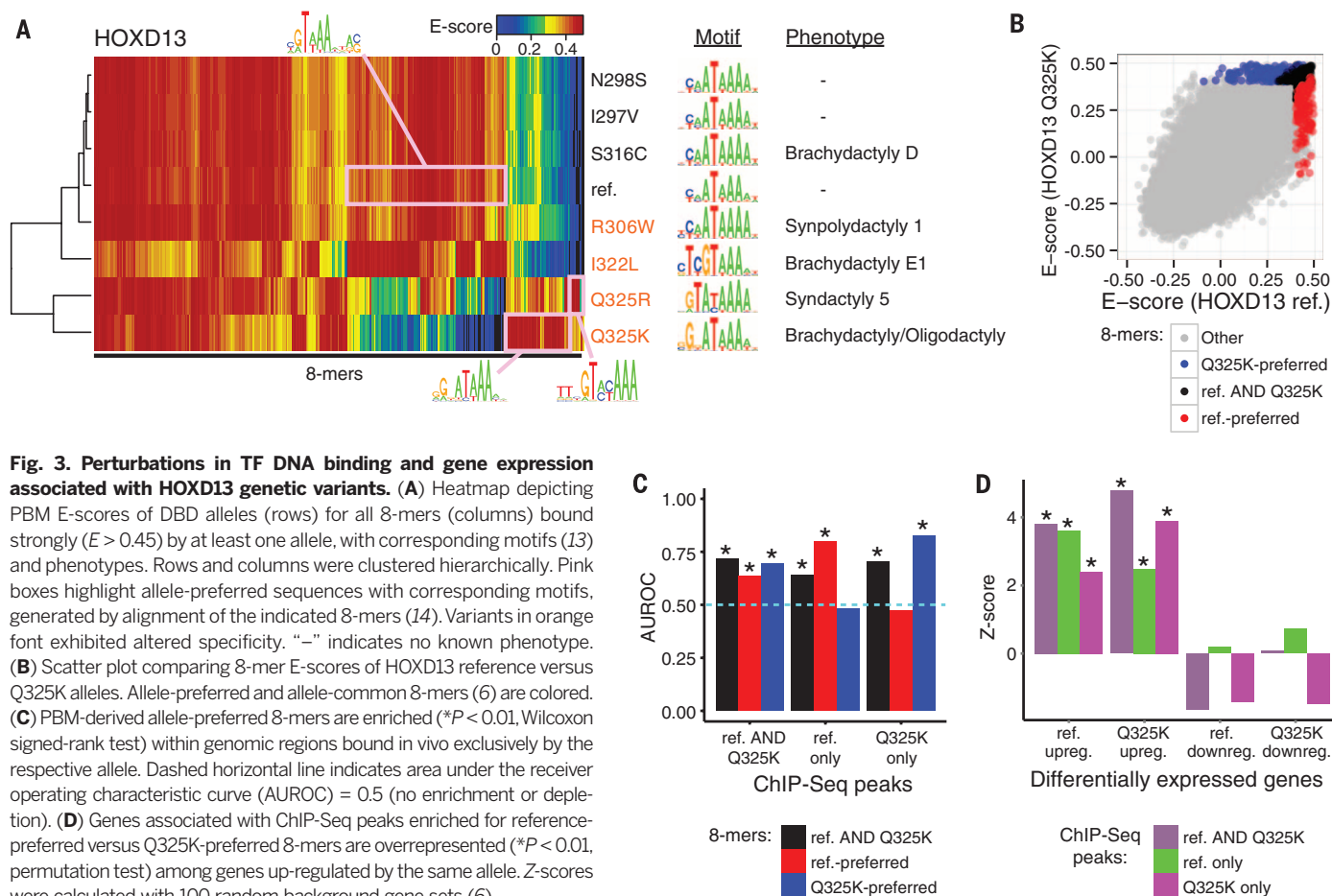


**Fig. 2. Perturbed DNA binding caused by nsSNPs or Mendelian disease mutations.** (A) Specificity change in PAX4 R192H allele (left) compared to no change in CRX V66I allele (right). Colored 6-mers are allele-preferred ( $Q < 0.05$ , intersection-union test with Benjamini-Hochberg correction). (B) Altered E-score distribution of CRX R90W allele relative to the reference allele indicates altered DNA binding affinity. (C) Box plots depict E-scores of NR1H4 reference allele and C144R alleles and glutathione S-transferase (GST) negative controls (6) for the top 50 8-mers bound by NR1H4 reference allele. C144R abolished binding specificity ( $*P < 2.2 \times 10^{-16}$ , Wilcoxon rank-sum test), resulting in E-scores indistinguishable from GST negative controls (table S7). (D) Fraction of alleles with observed changes in DNA binding affinity, specificity, both, or neither as determined from PBM binding profiles. Prioritized nsSNPs exclude those predicted as benign by both PolyPhen-2 and SIFT. (E) Violin plots depicting fraction of 8-mer binding sites gained or lost by variants relative to the number of 8-mers bound by the reference allele. Gains or losses were defined as  $E \geq 0.4$  for one allele and  $E < 0.4$  for the other allele.  $*P = 0.0044$ , Wilcoxon rank-sum test.





S1); (ii) DNA binding specificity—determining residues for particular DBD classes (fig. S2); (iii) scores from tools that predict mutation pathogenicity (9, 10); (iv) minor allele frequencies; and (v) phenotypic associations from genome-wide association studies (11) or known Mendelian disease mutations (8).

Using these criteria, we selected 37 TF DBDPs (6) to assay for direct, sequence-specific DNA binding activity (fig. S3). These DBDPs were obtained from the 1000 Genomes Project (1kG) Phase 2, the Exome Sequencing Project (ESP 6500), and the Exome Aggregation Consortium (ExAC). To calibrate the effects of these nsSNPs, we selected 80 Mendelian disease mutations, which are known or believed to be pathogenic (Fig. 1D) (8, 12). The 117 variant DBD alleles span six major structural classes, representing 41 distinct TF allelic series (fig. S4). We assayed these 158 DBD alleles using universal protein-binding microarrays (PBMs) (6), on which each nonpalindromic 8-base pair sequence (8-mer) occurs on at least 32 spots (13) (table S4).

We identified variant-induced changes in DNA binding specificity (14) (Fig. 2A) or affinity (Fig. 2B) by comparing the enrichment (E) scores of each of 32,768 nonredundant, ungapped 8-mers represented on universal PBMs to those of the corresponding reference allele (6, 13). DNA binding changes were reproducible across replicate PBM

experiments and support previously reported DNA binding affinity differences (table S5 and fig. S5). We categorized all 117 variant alleles as having altered DNA binding specificity, affinity, both, or neither (table S6). Three nsSNPs completely abrogated sequence-specific DNA binding (Fig. 2C and fig. S6). In total, 77 variants altered DNA binding affinity and/or specificity (Fig. 2D). Several nsSNPs predicted to be damaging but not scored here as having altered DNA binding might cause subtle changes beyond the sensitivity of our approach or alternatively affect protein-protein interactions.

Compared to DBDPs, Mendelian disease mutants lost a larger fraction of 8-mers bound by the corresponding reference alleles ( $P = 0.0044$ , Wilcoxon rank-sum test), consistent with more extreme phenotypes being associated with more drastic in vitro binding changes. The overall difference in gained 8-mers was not significantly different between these two sets of variants ( $P = 0.32$ , Wilcoxon rank-sum test; Fig. 2E).

PBM binding profiles within an allelic series differed for variants associated with distinct disease phenotypes (fig. S7), supporting results from a yeast one-hybrid screen of Mendelian disease TF mutants (15). They also provided molecular insights into the molecular basis of clinical heterogeneity of disease mutations affecting the same genes. For example, *CRX* is associated with Men-

delian diseases of retinal degeneration (16). The R90W allele, associated with the severe disease Leber congenital amaurosis 7 (17), lost the ability to bind most 8-mers bound by wild-type CRX. In contrast, the R41W allele, associated with cone-rod dystrophy 2 (18), resulted in a moderate specificity change (fig. S7B).

The 8-mer binding profiles of HOXD13 alleles displayed a range of effects; several of these alleles are associated with various limb malformations (19) (Fig. 3A). The I297V and N298S variants, predicted to be benign, did not alter DNA binding activity. The Q325K and Q325R alleles gained recognition of novel motifs, consistent with those learned from chromatin immunoprecipitation with high-throughput sequencing (ChIP-Seq) data (12). Allele-preferred 8-mers (Fig. 3B and fig. S8A) are enriched within ChIP-Seq peaks bound exclusively by the respective allele (Fig. 3C and figs. S8B and S9) ( $P < 0.01$ , Wilcoxon signed-rank test). Putative target genes, associated with ChIP-Seq peaks enriched ( $P < 2.2 \times 10^{-16}$ , one-tailed Wilcoxon signed-rank test) for Q325K- or Q325R-preferred versus reference-preferred 8-mers (fig. S10) (6), are overrepresented among genes up-regulated by the corresponding allele ( $P < 0.01$ , permutation test) (Fig. 3D and figs. S8C and S11), consistent with HOXD13 acting as a transcriptional activator (20). These results suggest that these variants' changes in binding specificity alter genomic

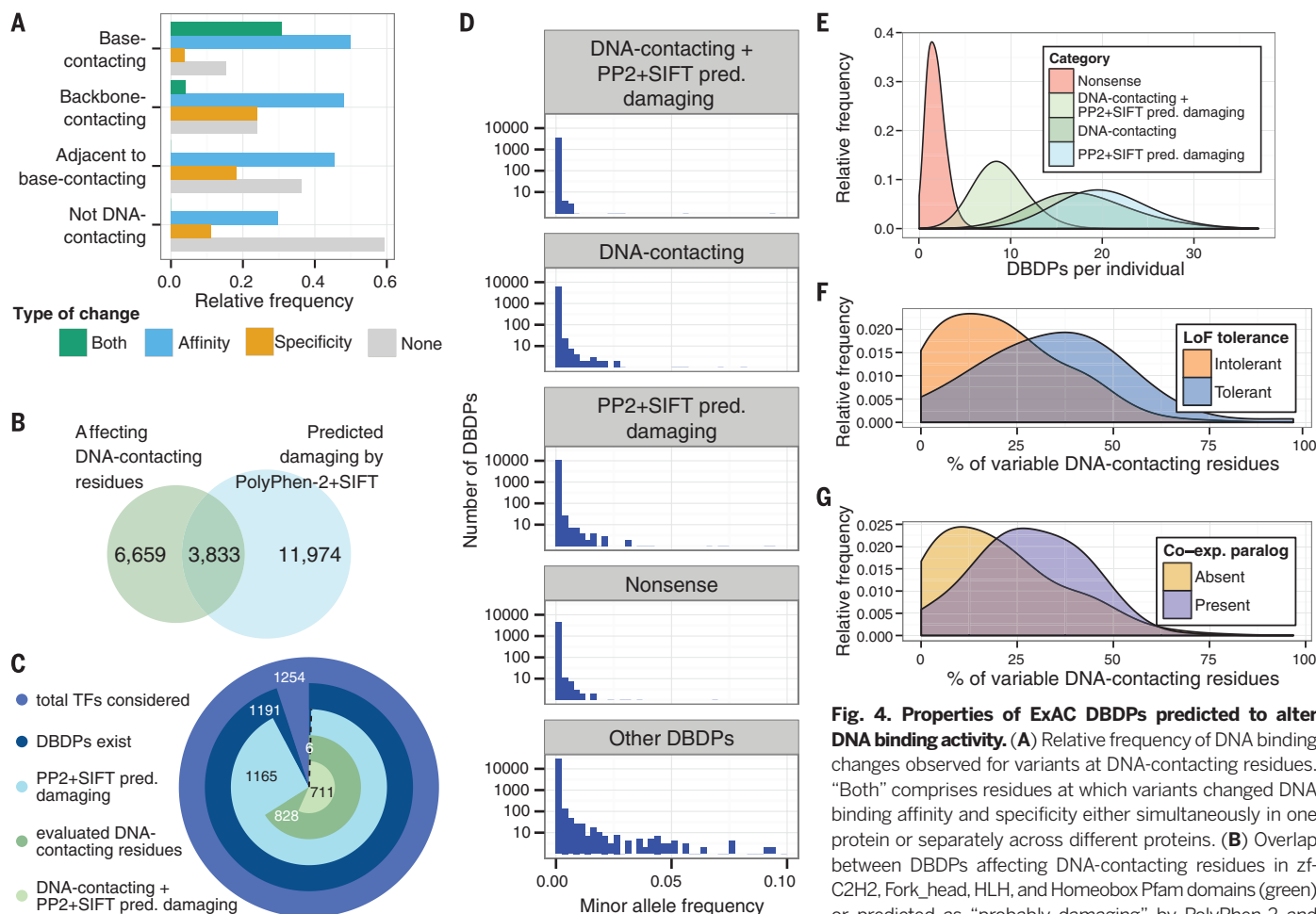


**Fig. 4. Properties of ExAC DBDPs predicted to alter DNA binding activity.** (A) Relative frequency of DNA binding changes observed for variants at DNA-contacting residues. “Both” comprises residues at which variants changed DNA binding affinity and specificity either simultaneously in one protein or separately across different proteins. (B) Overlap between DBDPs affecting DNA-contacting residues in *zf-C2H2*, *Fork\_head*, *HLH*, and *Homeobox* Pfam domains (green) or predicted as “probably damaging” by PolyPhen-2 and their evaluation, as in (B). (D) Minor allele frequencies (ExAC v0.2) of nsSNPs in DBDs. (E) Histogram of DBD variants per individual (1000 Genomes Project Phase 3), annotated as in (C). (F) Fraction of DNA-contacting residues per TF altered by at least one nsSNP (ExAC) for genes tolerant of homozygous or compound heterozygous LoF mutations versus genes for which LoF tolerance was not observed (21). (G) Fraction of variable DNA-contacting residues (ExAC) in TFs with versus without at least one coexpressed paralog.

occupancy, leading to inappropriate gene expression through gained binding sites.

As expected, mutations in residues that either contact DNA or neighbor a base-contacting residue were enriched (odds ratio = 4.3,  $P = 0.003$ , Fisher’s exact test) among DBDPs with altered DNA binding affinity or specificity (Fig. 4A). We also found variants at non-DNA-contacting positions that altered DNA binding, potentially by affecting protein conformation or stability. We identified 3833 unique missense variants that are predicted to be damaging by both PolyPhen-2 (9) and SIFT (10) and occur at DNA-contacting residues (Fig. 4B). These values are likely an underestimate of damaging DBDPs across all human TFs (Fig. 4C). These damaging nsSNPs occur at lower frequencies in the ExAC population than do nsSNPs for which no change in DNA binding is predicted ( $P < 0.05$ , permutation test) (Fig. 4D), suggesting that they are more likely to be deleterious.

Per individual, there were very few (median = 2) nonsense DBD variants but a wide range in the number of putatively damaging missense variants (median = 9, DBDPs at DNA-contacting residues

and predicted as damaging by PolyPhen-2 and SIFT) (Fig. 4E and fig. S12). Hence, we investigated what mechanisms might allow damaged DBDPs to be tolerated. TFs reported to tolerate homozygous loss-of-function (LoF) mutations in Icelanders (21) had a significantly higher fraction of DNA-contacting residues altered by our identified nsSNPs ( $P = 6.63 \times 10^{-8}$ , permutation test) (Fig. 4F). TFs with a coexpressed paralog (22) had a significantly higher fraction of variable DNA-contacting residues ( $P = 6.11 \times 10^{-8}$ , permutation test) (Fig. 4G); this enrichment was significant independent of LoF-tolerance status ( $P < 0.005$ ,  $t$  test) (6). Additional compensation could arise from epistasis with cis-regulatory variants (23). Damaged DBDPs might be associated with undiagnosed or subclinical phenotypes, variably penetrant phenotypes due to epistatic or gene-environment interactions, or phenotypes that present in later life.

Our results highlight the utility of PBM profiling to reveal changes in the DNA binding activities of variant DBDs. PBM profiling of DBDPs identified through additional sequencing studies may elucidate disease pathologies by revealing

alterations in DNA binding that result in transcriptional dysregulation.

Our analyses suggest that most unrelated individuals have a unique repertoire of TF alleles with a distinct landscape of DNA binding activities. Variants with subtle changes in DNA binding activities may confer reduced deleteriousness and thus have greater potential for giving rise to phenotypic variation. Analysis of genetic interactions among TFs, TF variants, and noncoding regulatory variation likely will provide insights into the structure of genetic variation that leads to phenotypic differences among people.

## REFERENCES AND NOTES

- Exome Aggregation Consortium, *bioRxiv* (2015); <http://dx.doi.org/10.1101/030338>.
- G. R. Abecasis *et al.*, *Nature* **467**, 1061–1073 (2010).
- H.-J. Westra *et al.*, *Nat. Genet.* **45**, 1238–1243 (2013).
- A. Veraksa, M. Del Campo, W. McGinnis, *Mol. Genet. Metab.* **69**, 85–100 (2000).
- J. M. Vaquerizas, S. K. Kummerfeld, S. A. Teichmann, N. M. Luscombe, *Nat. Rev. Genet.* **10**, 252–263 (2009).
- Materials and methods are available as supplementary materials on Science Online.
- W. Fu *et al.*, *Nature* **493**, 216–220 (2013).
- UniProt Consortium, *Nucleic Acids Res.* **43**, D204–D212 (2015).



9. I. A. Adzhubei *et al.*, *Nat. Methods* **7**, 248–249 (2010).
10. P. C. Ng, S. Henikoff, *Nucleic Acids Res.* **31**, 3812–3814 (2003).
11. D. Welter *et al.*, *Nucleic Acids Res.* **42**, D1001–D1006 (2014).
12. D. M. Ibrahim *et al.*, *Genome Res.* **23**, 2091–2102 (2013).
13. M. F. Berger *et al.*, *Nat. Biotechnol.* **24**, 1429–1435 (2006).
14. B. Jiang, J. S. Liu, M. L. Bulyk, *Bioinformatics* **29**, 1390–1398 (2013).
15. J. I. Fuxman Bass *et al.*, *Cell* **161**, 661–673 (2015).
16. C. L. Freund *et al.*, *Cell* **91**, 543–553 (1997).
17. A. Swaroop *et al.*, *Hum. Mol. Genet.* **8**, 299–305 (1999).
18. P. K. Swain *et al.*, *Neuron* **19**, 1329–1336 (1997).
19. N. Brison, P. Debeer, P. Tylzanowski, *Dev. Dyn.* **243**, 37–48 (2014).
20. V. Salsi, M. A. Vignano, F. Cocchiarella, R. Mantovani, V. Zappavigna, *Dev. Biol.* **317**, 497–507 (2008).
21. P. Sulem *et al.*, *Nat. Genet.* **47**, 448–452 (2015).
22. M. Ouedraogo *et al.*, *PLOS ONE* **7**, e50653 (2012).
23. T. Lappalainen, S. B. Montgomery, A. C. Nica, E. T. Dermitzakis, *Am. J. Hum. Genet.* **89**, 459–463 (2011).

#### ACKNOWLEDGMENTS

We thank M. Hume, Y.-H. Hsu, Y. Shen, and D. Balcha for technical assistance and A. Gimelbrant for helpful discussions. We are grateful to the Exome Aggregation Consortium for making its data publicly available prior to publication. This work was supported by the National Institutes of Health (grants NHGRI R01 HG003985 to M.L.B. and T.H. and P50 HG004233 to M.V. and D.E.H.), an A\*STAR National Science Scholarship to K.H.K., and National Science Foundation Graduate Research Fellowships to L.A.B. and J.M.R. TF PBM data have been deposited into UniPROBE (publication data set accession BARI5A). GST negative control PBM 8-mer data are provided in table S7. M.L.B. is a coinventor on U.S. patents no. 6,548,021 and no. 8,530,638 on PBM technology and corresponding universal sequence designs, respectively. Universal PBM array designs used in this study are available via a

materials transfer agreement with The Brigham and Women's Hospital. A.V., J.V.K., J.M.R., N.S., T.H., and S.Y. performed experiments; L.A.B., J.V.K., J.M.R., S.S.G., E.J.R., J.W., L.M., K.H.K., S.I., T.S., L.S., R.G., and C.C. performed data analysis; M.K., M.J.D., M.V., D.E.H., and M.L.B. supervised research; L.A.B., L.M., K.H.K., D.E.H., and M.L.B. designed the study and wrote the manuscript; and L.A.B., J.V.K., J.M.R., S.S.G., L.M., K.H.K., S.I., and M.L.B. prepared figures and tables.

#### SUPPLEMENTARY MATERIALS

www.sciencemag.org/content/351/6280/1450/suppl/DC1  
Materials and Methods  
Figs. S1 to S12  
Tables S1 to S7  
References (24–55)

21 September 2015; accepted 18 February 2016  
10.1126/science.aad2257

## CANCER

# Activation of proto-oncogenes by disruption of chromosome neighborhoods

Denes Hnisz,<sup>1\*</sup> Abraham S. Weintraub,<sup>1,2\*</sup> Daniel S. Day,<sup>1</sup> Anne-Laure Valton,<sup>3</sup> Rasmus O. Bak,<sup>4</sup> Charles H. Li,<sup>1,2</sup> Johanna Goldmann,<sup>1</sup> Bryan R. Lajoie,<sup>3</sup> Zi Peng Fan,<sup>1,5</sup> Alla A. Sigova,<sup>1</sup> Jessica Reddy,<sup>1,2</sup> Diego Borges-Rivera,<sup>1,2</sup> Tong Ihn Lee,<sup>1</sup> Rudolf Jaenisch,<sup>1,2</sup> Matthew H. Porteus,<sup>4</sup> Job Dekker,<sup>3,6</sup> Richard A. Young<sup>1,2†</sup>

Oncogenes are activated through well-known chromosomal alterations such as gene fusion, translocation, and focal amplification. In light of recent evidence that the control of key genes depends on chromosome structures called insulated neighborhoods, we investigated whether proto-oncogenes occur within these structures and whether oncogene activation can occur via disruption of insulated neighborhood boundaries in cancer cells. We mapped insulated neighborhoods in T-cell acute lymphoblastic leukemia (T-ALL) and found that tumor cell genomes contain recurrent microdeletions that eliminate the boundary sites of insulated neighborhoods containing prominent T-ALL proto-oncogenes. Perturbation of such boundaries in nonmalignant cells was sufficient to activate proto-oncogenes. Mutations affecting chromosome neighborhood boundaries were found in many types of cancer. Thus, oncogene activation can occur via genetic alterations that disrupt insulated neighborhoods in malignant cells.

**T**umor cell gene expression programs are typically driven by somatic mutations that alter the coding sequence or expression of proto-oncogenes (1) (Fig. 1A), and identifying such mutations in patient genomes is a major goal of cancer genomics (2, 3). Dysregulation of proto-oncogenes frequently involves mutations that bring transcriptional enhancers into proximity of these genes (4). Transcriptional enhancers normally interact with their target genes through the formation of DNA loops (5–7), which

typically are constrained within larger CCCTC-binding factor (CTCF) cohesin-mediated loops called insulated neighborhoods (8–10), which in turn can form clusters that contribute to topologically associating domains (TADs) (11, 12) (fig. S1A). This recent understanding of chromosome structure led us to hypothesize that silent proto-oncogenes located within insulated neighborhoods might be activated in cancer cells via loss of an insulated neighborhood boundary, with consequent aberrant activation by enhancers that are normally located outside the neighborhood (Fig. 1A, lowest panel).

To test this hypothesis, we used chromatin interaction analysis by paired-end tag sequencing (ChIA-PET) to map neighborhoods and other cis-regulatory interactions in a cancer cell genome (Fig. 1B and table S1). A T-cell acute lymphoblastic leukemia (T-ALL) Jurkat cell line was selected for these studies because key T-ALL oncogenes and genetic alterations are well known (13, 14). The ChIA-PET technique gener-

ates a high-resolution (~5 kb) chromatin interaction map of sites in the genome bound by a specific protein factor (8, 15, 16). Cohesin was selected as the target protein because it is involved in both CTCF-CTCF interactions and enhancer-promoter interactions (5–7) and has proven useful for identifying insulated neighborhoods (8, 10) (fig. S1, A and B). The cohesin ChIA-PET data were processed using multiple analytical approaches (figs. S1 to S4 and table S2), and their analysis identified 9757 high-confidence interactions, including 9038 CTCF-CTCF interactions and 379 enhancer-promoter interactions (fig. S4C). The CTCF-CTCF loops had a median length of 270 kb, contained on average two or three genes, and covered ~52% of the genome (table S2). Such CTCF-CTCF loops have been called insulated neighborhoods because disruption of either CTCF boundary causes dysregulation of local genes due to inappropriate enhancer-promoter interactions (8, 10). Consistent with this, the Jurkat chromosome structure data showed that the majority of cohesin-associated enhancer-promoter interactions had end points that occurred within the CTCF-CTCF loops (Fig. 1C and fig. S2H). These results provide an initial map of the three-dimensional (3D) regulatory landscape of a tumor cell genome.

We next investigated the relationship between genes that have been implicated in T-ALL pathogenesis and the insulated neighborhoods. The majority of genes (40 of 55) implicated in T-ALL pathogenesis, as curated from the Cancer Gene Census and individual studies (table S3), were located within the insulated neighborhoods identified in Jurkat cells (Fig. 2A and fig. S5); 27 of these genes were transcriptionally active and 13 were silent, as determined by RNA sequencing (RNA-seq) (Fig. 2A and table S4). Active oncogenes are often associated with super-enhancers (17, 18), and we found that 13 of the 27 active T-ALL pathogenesis genes were associated with superenhancers (Fig. 2, A and B, and fig. S5A). Silent genes have also been shown to be protected by insulated neighborhoods from active enhancers located outside the neighborhood, and we found multiple instances of silent proto-oncogenes located within CTCF-CTCF loop structures in the Jurkat genome (Fig. 2, A and C, and fig. S5B). Thus, both active oncogenes and

<sup>1</sup>Whitehead Institute for Biomedical Research, Cambridge, MA 02142, USA. <sup>2</sup>Department of Biology, Massachusetts Institute of Technology, Cambridge, MA 02139, USA.

<sup>3</sup>Program in Systems Biology, Department of Biochemistry and Molecular Pharmacology, University of Massachusetts Medical School, Worcester, MA 01605, USA. <sup>4</sup>Department of Pediatrics, Stanford University, Stanford, CA, USA.

<sup>5</sup>Computational and Systems Biology Program, Massachusetts Institute of Technology, Cambridge, MA 02139, USA. <sup>6</sup>Howard Hughes Medical Institute.

\*These authors contributed equally to this work. †Corresponding author. E-mail: young@wi.mit.edu

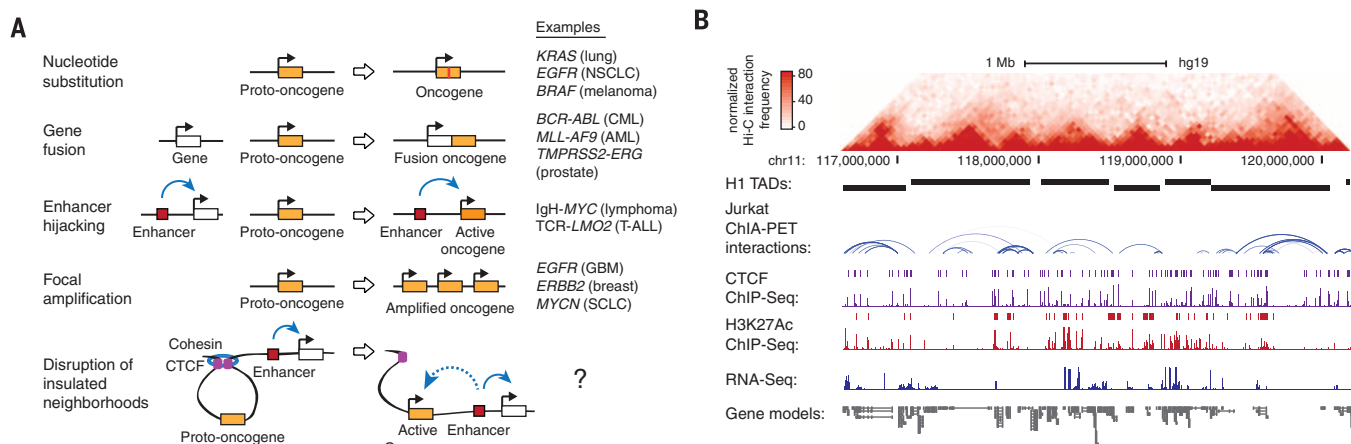


**Fig. 1. 3D regulatory landscape of the T-ALL genome.** (A) Mechanisms activating proto-oncogenes. (B) Hi-C interaction map, TADs defined in human embryonic stem cells (H1), cohesin ChIA-PET interactions (intensity of blue arc represents interaction significance), CTCF and H3K27Ac chromatin immunoprecipitation sequencing (ChIP-seq) profiles and peaks, and RNA-seq in Jurkat cells at the *CD3D* locus. ChIP-seq peaks are denoted as bars above ChIP-seq profiles. (C) ChIA-PET interactions at the *RUNX1* locus displayed above the ChIP-seq profiles of CTCF, cohesin (SMC1), and H3K27Ac. FDR, false discovery rate.

silent proto-oncogenes are located within insulated neighborhoods in these T-ALL cells.

If some insulated neighborhoods function to prevent proto-oncogene activation, some T-ALL tumor cells may have genetic alterations that perturb the CTCF boundaries of neighborhoods containing T-ALL oncogenes. To investigate this possibility, we identified recurrent deletions in T-ALL genomes that span insulated neighborhood boundaries, using data from multiple studies (table S5A) and filtered for relatively short deletions (<500 kb) so as to minimize collection of deletions that affect multiple genes (fig. S6A). Among the 438 recurrent deletions identified with this approach, 113 overlapped at least one boundary of insulated neighborhoods identified in T-ALL, and 6 of these affected neighborhoods containing T-ALL pathogenesis genes (fig. S6B and table S5B). Examples of two such genes, *TAL1* and *LMO2*, are shown in Fig. 3, A and G.

If deletions overlapping neighborhood boundaries can cause activation of proto-oncogenes within the loops, then site-specific deletion of a loop boundary CTCF site at the *TAL1* locus should be sufficient to activate these proto-oncogenes in nonmalignant cells. *TAL1* encodes a transcription factor that is overexpressed in ~50% of T-ALL cases and is a key oncogenic driver of this cancer (19, 20). *TAL1* can be activated by deletions that fuse a promoterless *TAL1* gene to the promoter of *STIL* (19), and this was observed in many patient deletions (Fig. 3A). Several patient deletions, however, retained the *TAL1* promoter

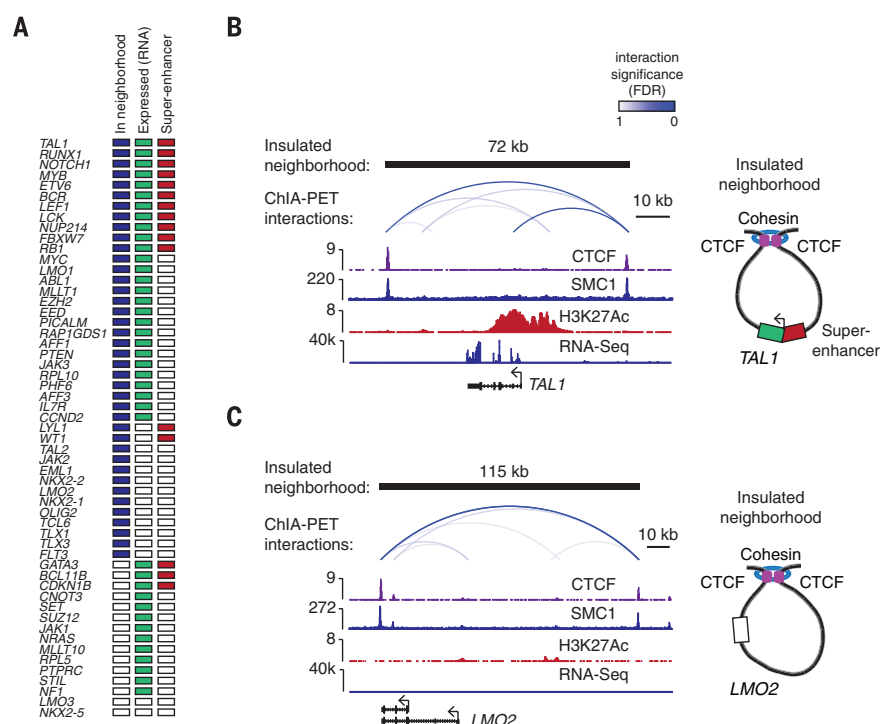
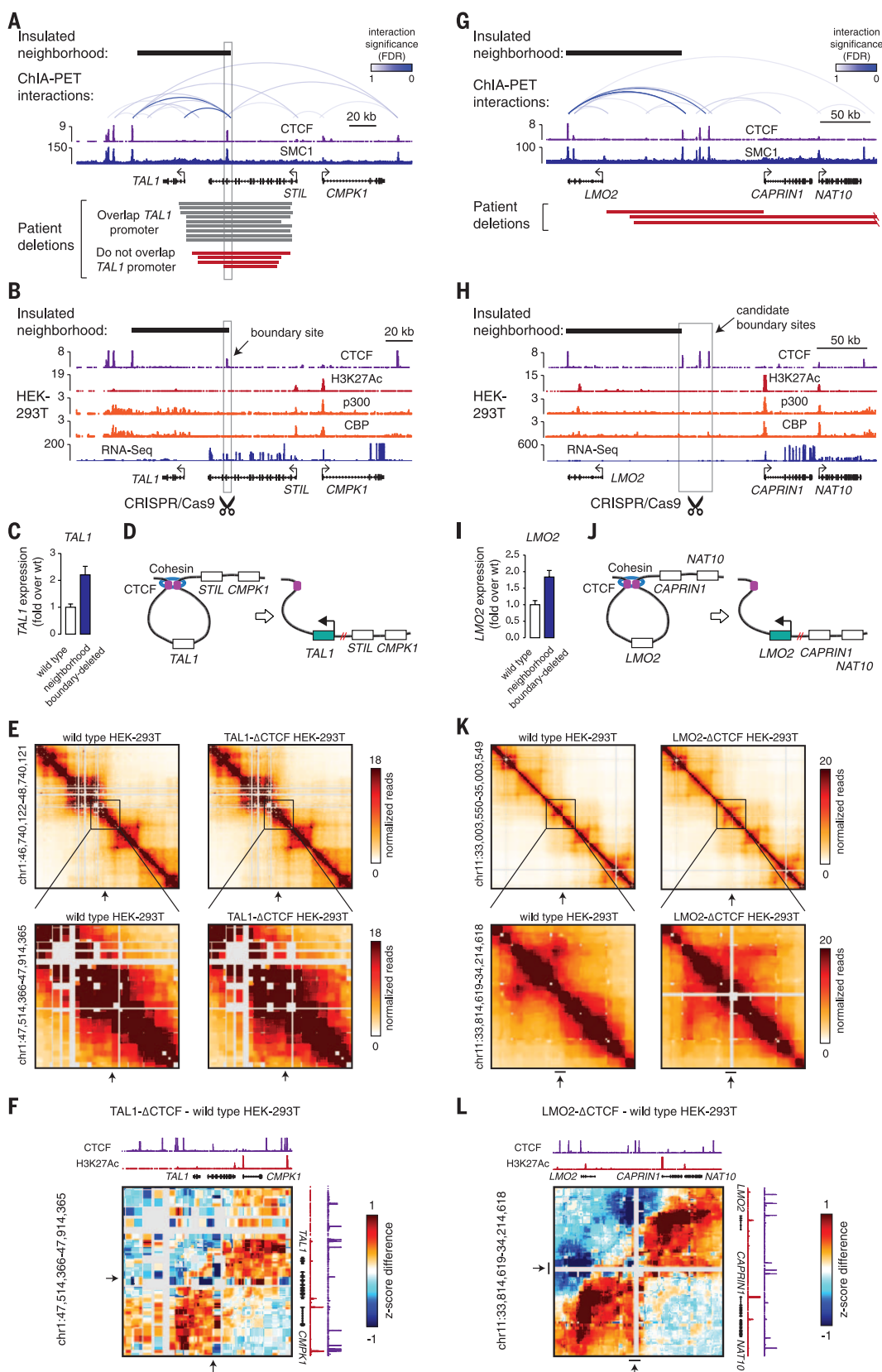


**Fig. 2. Active oncogenes and silent proto-oncogenes occur in insulated neighborhoods.** (A) T-ALL pathogenesis genes. Colored boxes indicate whether a gene is located within a neighborhood, expressed, and associated with a superenhancer. (B) Insulated neighborhood at the active *TAL1* locus. The cohesin ChIA-PET interactions are displayed above the ChIP-seq profiles of CTCF, cohesin (SMC1), H3K27Ac, and RNA-seq profile. A model of the insulated neighborhood is shown on the right. (C) Insulated neighborhood at the silent *LMO2* locus.



### Fig. 3. Disruption of insulated neighborhood boundaries is linked to proto-oncogene activation. (A)

Cohesin ChIA-PET interactions and CTCF and cohesin (SMC1) binding profiles at the *TAL1* locus in Jurkat cells. Patient deletions described in (22) are shown as bars below the gene models. The deletion on the bottom indicates the minimally deleted region identified in (26). (B) ChIP-seq profiles of CTCF, H3K27Ac, p300, CBP, and RNA-seq at the *TAL1* locus in HEK-293T cells. The region deleted using a CRISPR/Cas9-based approach is highlighted in a gray box. (C) Quantitative reverse transcription polymerase chain reaction (qRT-PCR) analysis of *TAL1* expression in wild-type HEK-293T cells (wt) and in cells where the neighborhood boundary highlighted in (B) was deleted. (D) Model of the neighborhood and perturbation at the *TAL1* locus. (E) 5C contact matrices in wild-type HEK-293T cells and *TAL1* neighborhood boundary-deleted cells. An arrow indicates the position of the region removed in the mutant cells. (F) Distance-adjusted z-score difference (5C) maps at the *TAL1* locus ( $\Delta$ CTCF – wild-type HEK-293T). Note the increase in the 5C signal adjacent to the deleted region. CTCF and H3K27Ac binding profiles in wild-type cells are displayed for orientation. (G) Cohesin ChIA-PET interactions and CTCF and cohesin (SMC1) binding profiles at the *LMO2* locus. Patient deletions described in (22) are shown as bars below the gene models. (H) ChIP-Seq binding profile of CTCF, H3K27Ac, p300, CBP, and RNA-seq at the *LMO2* locus in HEK-293T cells. The region deleted by a CRISPR/Cas9-based approach is highlighted in a gray box. (I) qRT-PCR analysis of *LMO2* expression in wild-type HEK-293T cells and in cells where the neighborhood boundary highlighted in (H) was deleted. (J) Model of the neighborhood and perturbation at the *LMO2* locus. (K) 5C contact matrices in wild-type HEK-293T cells and *LMO2* neighborhood boundary-deleted cells. An arrow indicates the position of the region removed in the mutant cells. (L) Distance-adjusted z-score difference (5C) maps at the *LMO2* locus ( $\Delta$ CTCF – wild-type HEK-293T). Note the increase in the 5C signal adjacent to the deleted region. CTCF and H3K27Ac binding profiles in wild-type cells are displayed for orientation. In (C) and (I), data from  $n = 3$  independent biological replicates are displayed as means  $\pm$  SD;  $P < 0.01$  between wild-type and boundary-deleted cells (two-tailed  $t$  test).



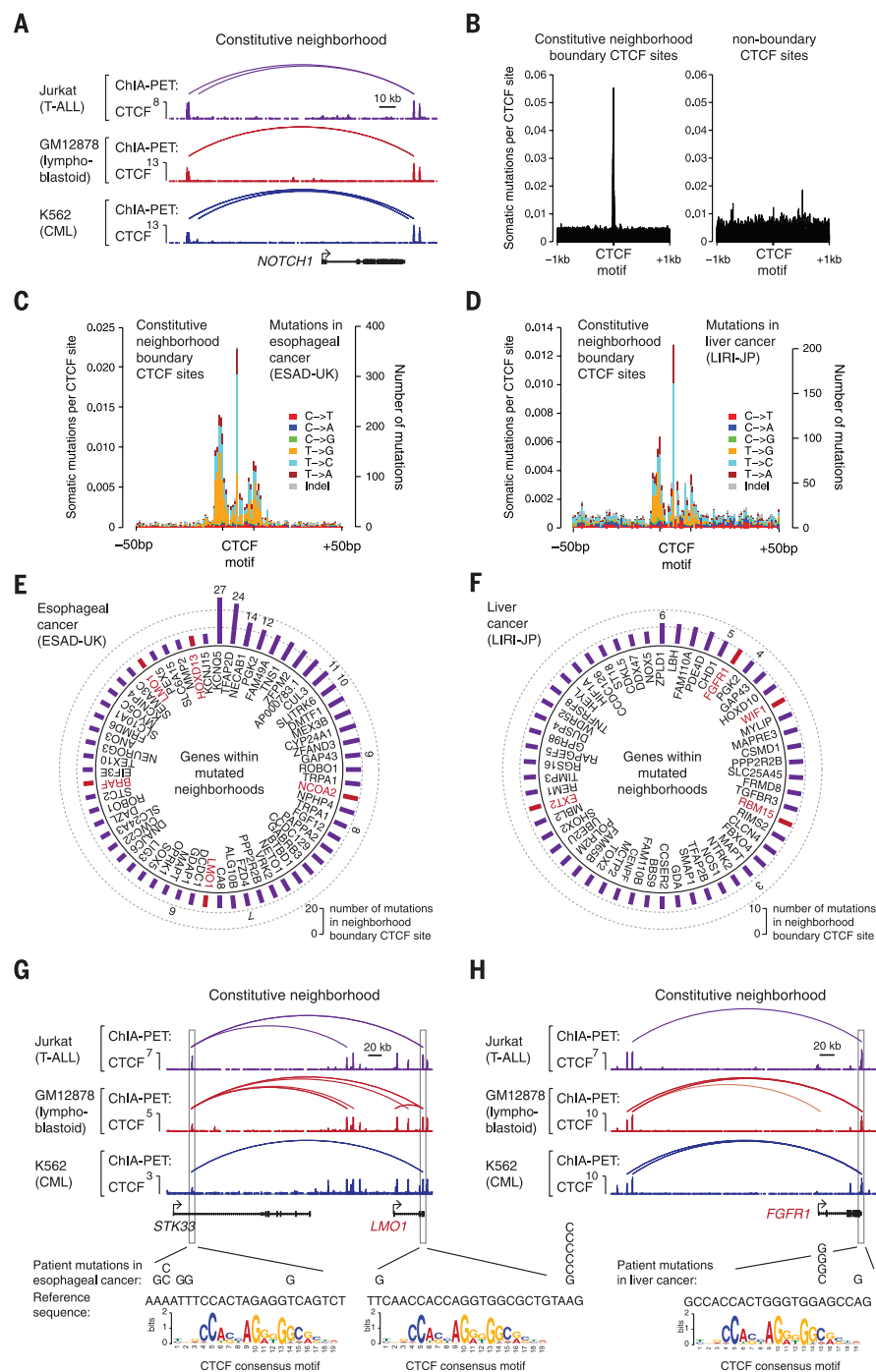


**Fig. 4. Somatic mutations of neighborhood boundaries occur in many cancers.** (A) “Constitutive neighborhood” at the *NOTCH1* locus. CTCF ChIP-seq and cohesin ChIA-PET interactions in Jurkat (T-ALL), GM12878 (lymphoblastoid), and K562 (CML) cells are displayed. (B) Frequency of somatic mutations in the ICGC database at CTCF sites that form constitutive neighborhood boundaries (left) and CTCF sites that do not form neighborhood boundaries (right). (C) Somatic mutations in esophageal adenocarcinoma (ESAD-UK) at constitutive neighborhood boundary CTCF sites. (D) Somatic mutations in hepatocellular carcinoma (LIRI-JP) at constitutive neighborhood boundary CTCF sites. (E and F) Genes in constitutive neighborhoods whose boundary is recurrently mutated in esophageal adenocarcinoma (E) and in hepatocellular carcinoma (F). The bars depict the number of mutations in the neighborhood boundary site. Proto-oncogenes annotated in the Cancer Gene Census are highlighted in red. (G and H) Mutations in the boundary sites of the neighborhood containing the *LMO1* proto-oncogene in esophageal adenocarcinoma (G) and the *FGFR1* proto-oncogene in hepatocellular carcinoma (H). The enrichment of mutations at the constitutive neighborhood boundary sites ( $\pm 5$  bp of the motif) shown in (B) to (D) relative to regions flanking the binding sites has a  $P$  value of  $<10^{-4}$  (permutation test).

(end point  $>5$  kb from promoter) but overlapped the CTCF boundary site of the *TALI* neighborhood (Fig. 3A), and *TALI* was active in the samples harboring these deletions (fig. S7, A and B). This suggests disruption of the insulated neighborhood, allowing activation of *TALI* by regulatory elements outside of the loop.

We tested this idea by CRISPR/Cas9-mediated deletion of the *TALI* neighborhood boundary in human embryonic kidney (HEK-293T) cells (Fig. 3B). In these cells the *TALI* proto-oncogene is silent, as evidenced by low H3K27Ac (histone H3 acetylated Lys<sup>27</sup>) occupancy and RNA-seq (Fig. 3B). However, at least one active regulatory element occurs  $\sim 60$  kb upstream of *TALI*, adjacent to the *CMPI1* promoter, as evidenced by high levels of H3K27Ac and p300/CBP (Fig. 3B) and enhancer reporter assays (fig. S8, A and B). Deletion of a  $\sim 400$ -base pair (bp) segment encompassing the boundary CTCF site, which abolished CTCF binding (fig. S8A), caused a factor of 2.3 induction of the *TALI* transcript (Fig. 3C), which suggests that the integrity of the neighborhood contributes to the silent state of *TALI* (Fig. 3D). In support of this model, contacts between DNA regions that are normally within and outside of the neighborhood were increased (Fig. 3, E and F, and fig. S10). Furthermore, deletion of the CTCF site in primary human T cells also caused a small but detectable activation of *TALI* (fig. S8, C to G). These results are consistent with the idea that the silent state of the *TALI* proto-oncogene is dependent on the integrity of the insulated neighborhood (Fig. 3D).

We further tested the model that site-specific perturbation of a loop boundary is sufficient to activate a proto-oncogene at the *LMO2* locus. The *LMO2* gene encodes a transcription factor that is overexpressed and oncogenic in some forms of T-ALL (14, 20). The region upstream of the *LMO2* promoter is recurrently deleted in T-ALL, and these deletions are linked to *LMO2* activation (Fig. 3G); a previous study proposed that deletion of cryptic repressors located in the deleted region enables activation of *LMO2* (21). Analysis of a T-ALL patient cohort (22) revealed deletions that overlap the CTCF boundary site of the *LMO2* neighborhood, and patient cells harboring these deletions had generally high levels of *LMO2* expression (fig. S9, A and B). CRISPR/Cas9-mediated deletion in HEK-293T cells of a  $\sim 25$ -kb segment encompassing the insulated neighborhood boundary CTCF site and two additional CTCF sites that could act as boundary elements caused a factor of 2 increase in the *LMO2* transcript (Fig. 3, H to J) and a large-scale rearrangement of interactions around *LMO2*, as evidenced by chromosome conformation capture carbon copy (5C) analysis (Fig. 3, K and L, and fig. S10). These results indicate that the deleted CTCF sites contribute to the silent state of the *LMO2* proto-oncogene (Fig. 3J).

The boundaries of chromosome neighborhoods may be disrupted in other cancers. A recent study noted that mutations in CTCF binding sites occur frequently in cancers (23), but it is unclear whether mutations in boundaries are



common, as only a subset of CTCF sites form insulated neighborhoods (8, 10, 24). CTCF cohesin-bound loops are largely preserved across cell types (8, 9, 24), and a set of ~10,000 constitutive CTCF-CTCF loops shared by GM12878 lymphoblastoid, Jurkat, and K562 (CML) cells (24) were identified for comparison (Fig. 4A, fig. S11, and table S8). We used the International Cancer Genome Consortium (ICGC) database—which contains data for ~50 cancer types, ~2300 whole-genome sequence (WGS) samples, and ~13 million unique somatic mutations—to examine the boundaries of these neighborhoods for somatic point mutations found in cancer genomes (table S9). We found a striking enrichment of mutations at the CTCF boundaries of constitutive neighborhoods (Fig. 4B, fig. S12A, and table S10) relative to regions flanking the boundary CTCF sites ( $\pm 1$  kb of the CTCF binding motif;  $P < 10^{-4}$ , permutation test) (fig. S12B), and in many instances these created a change in the consensus CTCF binding motif (fig. S12C). Nonboundary CTCF sites did not show such enrichment (Fig. 4B and figs. S12D and S14). The genomes of esophageal and liver carcinoma samples were particularly enriched for boundary CTCF site mutations (Fig. 4, C and D, fig. S12, D and E, fig. S13, and table S10), and there was no similar enrichment of mutations at the binding sites of other transcription factors (fig. S15). In these cancers, a considerable fraction of the mutated neighborhood boundary CTCF sites were affected by multiple mutations ( $\geq 3$  mutations per site) [280/1826 (15%) in esophageal carcinoma, 54/1030 (5%) in liver carcinoma] (table S10), and recurrent mutations occurred more frequently in neighborhood boundary CTCF sites relative to nonboundary CTCF sites (fig. S16, A to C). The genes located within the most frequently mutated neighborhoods included known cellular proto-oncogenes annotated in the Cancer Gene Census and other genes that have not been associated with these cancers (Fig. 4, E and F, and tables S11 and S12). Shown in Fig. 4, G and H, are two examples of proto-oncogene-containing neighborhoods where the activation of the gene located in the neighborhood has been observed in the respective cancer type. These results suggest that somatic mutations of insulated neighborhood boundaries occur in the genomes of many different cancers.

Our findings indicate that disruption of insulated neighborhood boundaries can cause oncogene activation in cancer cells. With maps of 3D chromosome structure such as those described here, cancer genome analysis can consider how recurrent perturbations of boundary elements may affect the expression of genes with roles in tumor biology. Our understanding of 3D chromosome structure and its control is rapidly advancing and should be considered for potential diagnostic and therapeutic purposes. Because control of 3D chromosome structure involves binding of specific sites by CTCF and cohesin, which is affected by protein cofactors, DNA methylation, and local RNA synthesis (25), advances in our understanding of these regulatory processes may provide new approaches to therapeutics

that have an impact on aberrant chromosome structures.

#### REFERENCES AND NOTES

1. B. Vogelstein, K. W. Kinzler, *Nat. Med.* **10**, 789–799 (2004).
2. B. Vogelstein *et al.*, *Science* **339**, 1546–1558 (2013).
3. L. A. Garraway, E. S. Lander, *Cell* **153**, 17–37 (2013).
4. C. M. Croce, *N. Engl. J. Med.* **358**, 502–511 (2008).
5. M. H. Kagey *et al.*, *Nature* **467**, 430–435 (2010).
6. J. H. Gibcus, J. Dekker, *Mol. Cell* **49**, 773–782 (2013).
7. D. U. Gorkin, D. Leung, B. Ren, *Cell Stem Cell* **14**, 762–775 (2014).
8. J. M. Downen *et al.*, *Cell* **159**, 374–387 (2014).
9. J. E. Phillips-Cremens *et al.*, *Cell* **153**, 1281–1295 (2013).
10. X. Ji *et al.*, *Cell Stem Cell* **18**, 262–275 (2016).
11. J. R. Dixon *et al.*, *Nature* **485**, 376–380 (2012).
12. E. P. Nora *et al.*, *Nature* **485**, 381–385 (2012).
13. S. A. Armstrong, A. T. Look, *J. Clin. Oncol.* **23**, 6306–6315 (2005).
14. P. Van Vlierberghe, A. Ferrando, *J. Clin. Invest.* **122**, 3398–3406 (2012).
15. M. J. Fullwood *et al.*, *Nature* **462**, 58–64 (2009).
16. Z. Tang *et al.*, *Cell* **163**, 1611–1627 (2015).
17. D. Hnisz *et al.*, *Cell* **155**, 934–947 (2013).
18. J. Lovén *et al.*, *Cell* **153**, 320–334 (2013).
19. L. Brown *et al.*, *EMBO J.* **9**, 3343–3351 (1990).
20. J. O'Neil, A. T. Look, *Oncogene* **26**, 6838–6849 (2007).
21. P. Van Vlierberghe *et al.*, *Blood* **108**, 3520–3529 (2006).
22. J. Zhang *et al.*, *Nature* **481**, 157–163 (2012).
23. R. Katainen *et al.*, *Nat. Genet.* **47**, 818–821 (2015).
24. N. Heidari *et al.*, *Genome Res.* **24**, 1905–1917 (2014).
25. C. T. Ong, V. G. Corces, *Nat. Rev. Genet.* **15**, 234–246 (2014).
26. C. G. Mullighan *et al.*, *Nature* **446**, 758–764 (2007).

#### ACKNOWLEDGMENTS

Supported by NIH grants HG002668 (R.A.Y.), CA109901 (R.A.Y.), NS088538 (R.J.), MH104610 (R.J.), and AI120766 (M.H.P.); an Erwin Schrödinger Fellowship (J3490) from the Austrian Science Fund (FWF) (D.H.); Ludwig Graduate Fellowship funds (A.S.W.); the Laurie Kraus Jacob Faculty Scholar Award in Pediatric Translational Research (M.H.P.); Hyundai Hope on Wheels (M.H.P.); and Danish Council for Independent Research, Medical Sciences, individual postdoctoral grant DFF-1333-00106B and Sapere Aude Research Talent grant DFF-1331-00735B (R.O.B.). Work in the Dekker lab is supported by the National Human Genome Research Institute (R01 HG003143, U54 HG007010, U01 HG007910), the National Cancer Institute (U54 CA193419), the NIH Common Fund (U54 DK107980, U01 DA 040588), the National Institute of General Medical Sciences (R01 GM 112720), and the National Institute of Allergy and Infectious Diseases (U01 R01 AI 117839). J.D. is an investigator of the Howard Hughes Medical Institute. We thank R. Fitzgerald, S. Grimmond, and the ICGC Genome Projects ESAD-UK and OV-AU for permission to use genome sequence data. Data sets generated in this study have been deposited in the Gene Expression Omnibus under accession number GSE68978. The Whitehead Institute filed a patent application based on this paper. R.A.Y. is a founder of Syros Pharmaceuticals, and R.J. is a founder of Fate Therapeutics.

#### SUPPLEMENTARY MATERIALS

www.sciencemag.org/content/351/6280/1454/suppl/DC1  
Materials and Methods

Figs. S1 to S16  
Tables S1 to S13  
References (27–71)

19 November 2015; accepted 18 February 2016  
Published online 3 March 2016  
10.1126/science.1230924

#### HIV-1 VACCINES

## HIV-1 broadly neutralizing antibody precursor B cells revealed by germline-targeting immunogen

Joseph G. Jardine,<sup>1,2,3\*</sup> Daniel W. Kulp,<sup>1,2,3\*</sup> Colin Havenar-Daughton,<sup>3,4\*</sup> Anita Sarkar,<sup>2,3,5\*</sup> Bryan Briney,<sup>1,2,3\*</sup> Devin Sok,<sup>1,2,3\*</sup> Fabian Sesterhenn,<sup>1†</sup> June Ereño-Orbea,<sup>6</sup> Oleksandr Kalyuzhnyi,<sup>1,2,3</sup> Isaiah Deresa,<sup>3,4</sup> Xiaozhen Hu,<sup>1,3</sup> Skye Spencer,<sup>1,3</sup> Meaghan Jones,<sup>1,3</sup> Erik Georgeson,<sup>1,3</sup> Yumiko Adachi,<sup>1,2,3</sup> Michael Kubitz,<sup>1,2,3</sup> Allan C. deCamp,<sup>7</sup> Jean-Philippe Julien,<sup>2,3,5,6,8</sup> Ian A. Wilson,<sup>2,3,5,9</sup> Dennis R. Burton,<sup>1,2,3,10</sup> Shane Crotty,<sup>3,4,11†</sup> William R. Schief<sup>1,2,3,10†</sup>

Induction of broadly neutralizing antibodies (bnAbs) is a major HIV vaccine goal. Germline-targeting immunogens aim to initiate bnAb induction by activating bnAb germline precursor B cells. Critical unmet challenges are to determine whether bnAb precursor naïve B cells bind germline-targeting immunogens and occur at sufficient frequency in humans for reliable vaccine responses. Using deep mutational scanning and multitarget optimization, we developed a germline-targeting immunogen (eOD-GT8) for diverse VRC01-class bnAbs. We then used the immunogen to isolate VRC01-class precursor naïve B cells from HIV-uninfected donors. Frequencies of true VRC01-class precursors, their structures, and their eOD-GT8 affinities support this immunogen as a candidate human vaccine prime. These methods could be applied to germline targeting for other classes of HIV bnAbs and for Abs to other pathogens.

**D**evelopment of an HIV vaccine is a global health priority. Recent discoveries of potent broadly neutralizing antibodies (bnAbs) that bind to relatively conserved epitopes on the HIV Env glycoprotein trimer and protect against challenge in animal models have

reinvigorated vaccine design efforts to induce bnAbs (1). However, bnAbs have not been elicited in standard animal models or humans.

Germline targeting, a vaccine priming strategy to initiate the affinity maturation of select germline-precursor B cells, has promise to initiate

bnAb induction. The goals for a germline-targeting prime are to activate B cell precursors with bnAb potential, select productive (bnAb-like) somatic mutations, and generate an expanded population of memory B cells that can be boosted and matured subsequently to shepherd the response further toward bnAb development (2, 3). For a few HIV bnAbs, next-generation sequencing of antibody populations during bnAb development in infected individuals has allowed bioinformatic inference of likely human germline precursors (4, 5). For most bnAbs, however, true human precursors are not known but are usually approximated by “germline-reverted” antibodies that use inferred germline V and J genes and retain mature CDR3 (complementarity-determining region 3) loops. Because CDR3 loops typically play a major role in antibody affinity and specificity, germline-reverted bnAbs are not known to be reliable proxies for true germline precursors.

VRC01-class bnAbs are an important test case for germline targeting, because they are among the most broad and potent of HIV bnAbs and because their germline-reverted forms show no detectable affinity for HIV Env glycoproteins (6–10). Knock-in mice transgenic for a germline-reverted VRC01-class heavy chain responded to immunization with the germline-targeting eOD-GT8 60-subunit self-assembling nanoparticle (60mer) but not with native-like Env trimers, providing proof of principle that germline-targeting immunogens can initiate a VRC01-class response if well-matched B cells are present and competing B cells are strongly reduced in frequency (2, 3). Here, we address further critical knowledge gaps that obstruct the development of this (or any) germline-targeting immunogen as a human vaccine: Do the targeted bnAb precursors exist in humans? What is the frequency and person-to-person variation of germline-targeting immunogen-specific bnAb precursors? Can the germline-targeting immunogen bind the targeted human bnAb precursors in competition with other B cells in the fully complex human B cell repertoire? We exam-

ined these questions by developing new ex vivo approaches and protein design methods.

When we used the VRC01-class germline-targeting immunogen eOD-GT6 (9) as bait to screen human naïve B cells via a two-phase multiple-validation methodology (11) (fig. S1), we failed to isolate VRC01-class B cells. We did, however, isolate non-VRC01-class naïve B cells with Ab affinities as low as 120  $\mu$ M for eOD-GT6 (fig. S1). We therefore set out to develop an improved variant of eOD-GT6 with higher affinity and breadth for germline-reverted VRC01-class Abs, hypothesizing that such improvements might translate into improved affinity for diverse true VRC01-class precursor Abs.

To improve on eOD-GT6, we used yeast display library screening coupled with next-generation sequencing (12). We screened a library of every point mutation at the 58 eOD:Ab interface positions on eOD-GT7, a slightly improved version of eOD-GT6 (11), against each of 29 VRC01-class Abs (18 germline-reverted and 11 mature bnAbs). By measuring binding enrichments for each mutation and antibody (Fig. 1A and fig. S2), we identified 12 positions in eOD-GT7 at which one or more mutations were favorable (enriched by at least a factor of 2) for binding to the majority (at least 10 of 18) of germline-reverted bnAbs, and another four positions at which one or more mutations were enriched by at least a factor of 1.25 for binding to the vast majority (at least 17 of 18) of germline-reverted bnAbs (Fig. 1B). To identify combinations of mutations predicted to confer the greatest binding cross-reactivity, we then created a library encompassing all combinations of a filtered set of the favorable mutations at those 16 positions (13) (Fig. 1C). Upon screening this combinatorial library against the panel of 29 VRC01-class Abs, we identified a sequence, eOD-GT8, predicted to have optimal breadth against the entire panel (Fig. 1C, figs. S3 and S4, and table S1).

Relative to eOD-GT6, eOD-GT8 demonstrated superior affinity and breadth of binding to germline-reverted Abs (Fig. 1D and table S2). eOD-GT8 bound to all germline-reverted Abs in the panel, whereas eOD-GT6 bound to only 8 of 14 Abs with dissociation constants ( $K_D$ ) of less than 100  $\mu$ M. For those eight germline-reverted Abs, the geometric mean affinity of eOD-GT8 was higher than that of eOD-GT6 by a factor of 2100; eOD-GT8 also had improved affinity (factor of 3) for VRC01-class bnAbs. The tightest eOD-GT8 binding detected was for germline-reverted PGV20, with a  $K_D$  of 508 fM (95% confidence interval, 234 to 943 fM) (Fig. 1D and fig. S5), a factor of 5900 improvement over eOD-GT6 ( $K_D$  = 3 nM) and a factor of 33 million improvement over the original eOD construct, eOD Base [ $K_D$  = 17  $\mu$ M (9)]—a remarkable affinity improvement for a protein-protein interface.

To examine whether VRC01-class precursors targeted by eOD-GT8 exist in humans, we performed epitope-specific B cell sorting from a pool of peripheral blood mononuclear cells from healthy, HIV-seronegative donors. Epitope-specific B cells bound tetramers of eOD-GT8 but not tetramers

of eOD-GT8-KO, a variant of eOD-GT8 with mutations abrogating binding by VRC01-class germline-reverted Abs. After sequencing immunoglobulin (Ig) genes from single sorted cells, we searched for VRC01-class antibody sequences—that is, those with a heavy chain that used VH1-2 alleles \*02, \*03, or \*04 and a light chain with a 5-amino acid CDR3 (9, 14). After sorting 2.4 million IgM<sup>+</sup>/IgG<sup>−</sup>/CD19<sup>+</sup> B cells pooled from nine donors, we recovered a single GT8<sup>+</sup>/GT8-KO<sup>−</sup> Ab that qualified as a VRC01-class precursor. This Ab, VRC01c-HuGLI, bound to eOD-GT8 with a  $K_D$  of 22  $\mu$ M and had no detectable affinity for eOD-GT8-KO (fig. S6).

To assess both the percentage of people who possess VRC01-class germline precursor B cells and the frequency of VRC01-class germline precursor B cells within a given donor, we screened naïve B cells from 15 healthy, HIV-seronegative donors individually rather than pooled. For 7 of 15 samples, we used the two-phase multiple-validation methodology that first assesses specificity by probe binding in flow cytometry and then confirms specificity and lack of polyreactivity by single-cell secreted IgM (fig. S7); for eight subsequent donors, we relied on sorting specificity alone. For optimal cell sorting sensitivity, B cells were required to simultaneously bind two eOD-GT8 probes multimerized differently [trimer (“tri”) and streptavidin tetramers (“SA”)] while not binding eOD-GT8-KO-SA (Fig. 2A and fig. S7). For the 15 donors, the mean frequency of eOD-GT8<sup>tri+/SA+</sup> B cells among 61.6 million naïve B cells sorted was 0.0056% (Fig. 2B). Strikingly, a vast majority (84  $\pm$  14%) of these eOD-GT8<sup>tri+/SA+</sup> B cells did not bind eOD-GT8-KO-SA (Fig. 2C), which suggests that naïve B cell reactivity to eOD-GT8 is highly focused to the CD4 binding site (CD4bs) (15).

Paired heavy and kappa light chain sequences were recovered from 173 eOD-GT8<sup>tri+/SA+</sup>/eOD-GT8-KO<sup>−</sup> B cells. All sequences were essentially germline, confirming the naïve B cell sorts. Half (50%) of these B cells were VH1-2, whereas only 4% of control B cells from reference (16) were VH1-2 ( $\chi^2$  = 29.9,  $P$  < 0.0001; Fig. 2D and fig. S8). Among these 87 VH1-2<sup>+</sup> B cells, 26 had a light chain CDR3 (L-CDR3) length of 5 amino acids, a factor of 85 enrichment relative to control B cells ( $\chi^2$  = 32.6,  $P$  < 0.0001; Fig. 2E). Twenty-five of the 26 used the VH1-2\*02 allele and one used VH1-2\*04 (table S3); thus, 15% (26/173) of GT8<sup>tri+/SA+</sup>/eOD-GT8-KO<sup>−</sup> B cells were VRC01-class. In total, we identified 27 independent VRC01-class naïve B cells, including VRC01c-HuGLI.

In addition to the VH1-2 alleles and critical 5-amino acid L-CDR3, VRC01-class bnAbs possess several additional defining features, including a consensus L-CDR3 of Gln-Gln-Tyr-Glu-Phe (QQYEF). The majority of VRC01-class precursors we isolated contained a QQYxx partial VRC01-class consensus motif that was significantly enriched relative to control B cells (67% versus 11%;  $\chi^2$  = 8.2,  $P$  < 0.0001; Fig. 2F). Furthermore, 11% contained a QQYEx L-CDR3 motif (versus 1.5% of control B cells), one mutation away from a perfect mature VRC01-class L-CDR3 (Fig. 2F). In addition, the L-CDR1 loop is under strong selective

<sup>1</sup>Department of Immunology and Microbial Science, The Scripps Research Institute, La Jolla, CA 92037, USA. <sup>2</sup>IAVI Neutralizing Antibody Center, The Scripps Research Institute, La Jolla, CA 92037, USA. <sup>3</sup>Center for HIV/AIDS Vaccine Immunology and Immunogen Discovery, The Scripps Research Institute, La Jolla, CA 92037, USA. <sup>4</sup>Division of Vaccine Discovery, La Jolla Institute for Allergy and Immunology, La Jolla, CA 92037, USA. <sup>5</sup>Department of Integrative Structural and Computational Biology, The Scripps Research Institute, La Jolla, CA 92037, USA. <sup>6</sup>Program in Molecular Structure and Function, Hospital for Sick Children Research Institute, Toronto, Ontario M5G 0A4, Canada. <sup>7</sup>Vaccine and Infectious Disease Division, Statistical Center for HIV/AIDS Research and Prevention (SCHARP), Fred Hutchinson Cancer Research Center, Seattle, WA 98109, USA. <sup>8</sup>Departments of Biochemistry and Immunology, University of Toronto, Toronto, Ontario M5S 1A8, Canada. <sup>9</sup>Skaggs Institute for Chemical Biology, The Scripps Research Institute, La Jolla, CA 92037, USA. <sup>10</sup>Ragon Institute of MGH, MIT, and Harvard, Cambridge, MA 02129, USA. <sup>11</sup>Division of Infectious Diseases, Department of Medicine, University of California San Diego School of Medicine, La Jolla, CA, USA.

\*These authors contributed equally to this work. †Present address: Institute of Bioengineering, École Polytechnique Fédérale de Lausanne, CH-1015 Lausanne, Switzerland. ‡Corresponding author. E-mail: schief@scripps.edu (W.R.S.); shane@iji.org (S.C.)



pressure during VRC01-class bnAb affinity maturation to minimize clashes with gp120 (6, 17). VRC01-class bnAb L-CDR1 loops generally become very short (2 to 6 amino acids) through deletion, or retain a germline length of 6 amino acids and add flexible glycines (17). Of the 27 VRC01-class precursors isolated by eOD-GT8, 23 used V $\kappa$  genes containing L-CDR1 loops of 6 or 7 amino acids (Fig. 2G), thus confirming potential to develop into VRC01-class bnAbs. Indeed, 17 of the VRC01-class naïve B cells had V $\kappa$  genes used in known VRC01-class bnAbs (Fig. 2H). At least 24 of the VRC01-class precursors had H-CDR3 lengths of 10 to 19 amino acids (Fig. 2I) (18), consistent with known VRC01-class bnAb lengths of 10 to 19

amino acids. Thus, not only are the eOD-GT8 isolated naïve B cells highly enriched for VRC01-class core characteristics of VH1-02 and a 5-amino acid L-CDR3, they possess further refined sequence attributes of VRC01-class bnAbs.

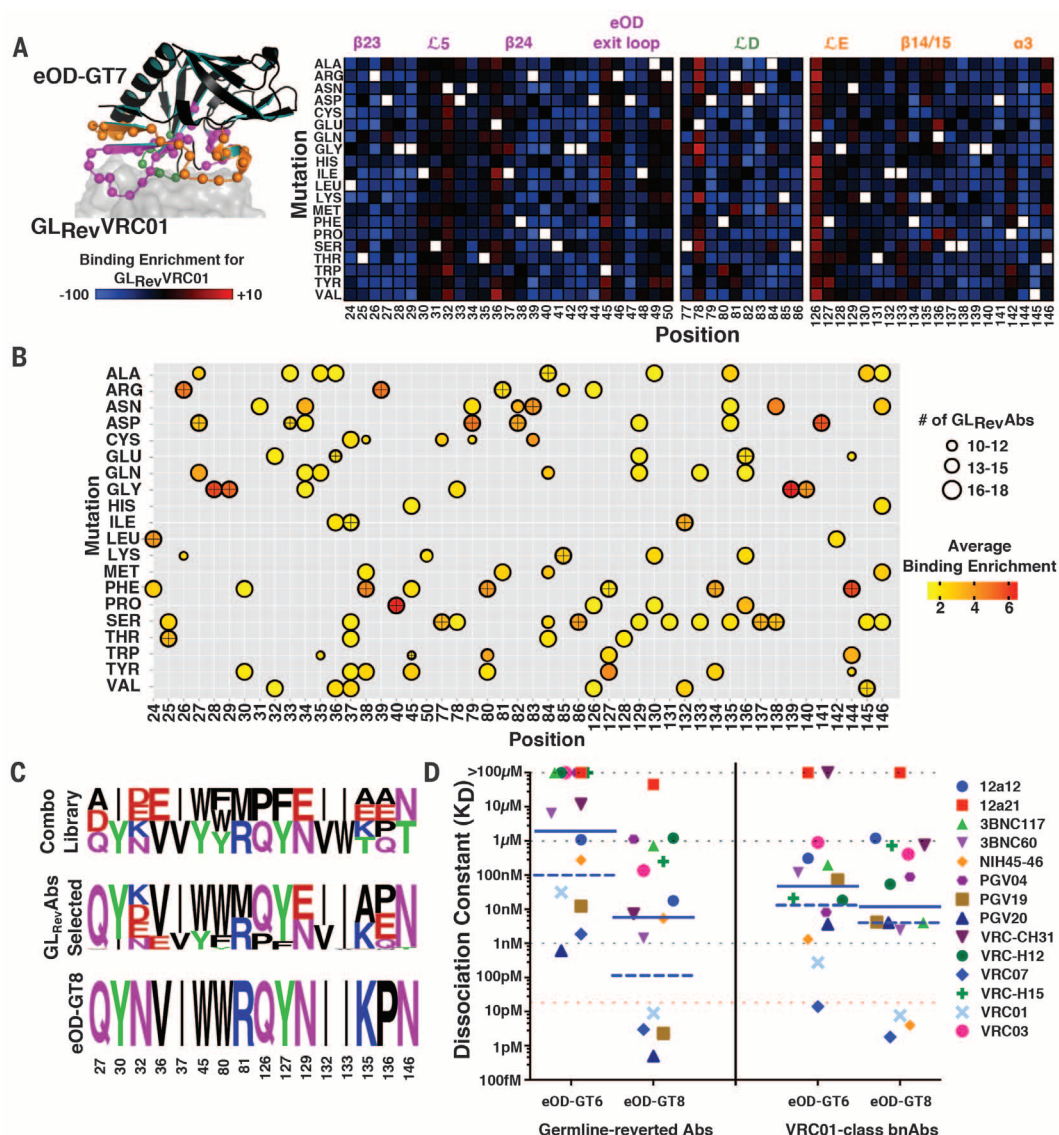
Combining data from the 15 donors analyzed individually, the overall frequency of recovered VRC01-class precursors was 1 in 2.4 million naïve B cells (Fig. 2J), consistent with both our first pooled sort and a previous bioinformatically estimated range (17). The observed counts were consistent with a Poisson distribution with constant frequency of 1 in 2.4 million (Fig. 2K) (17), which suggests that VRC01-class precursors occur at a consistent rate among 96% of humans possess-

ing the necessary VH1-2 alleles (9). Adults have an estimated  $10^{10}$  to  $10^{11}$  B cells, and lymph nodes each have ~50 million B cells, of which ~65 to 75% are naïve B cells (19). Thus, our results indicate that VRC01-class precursor B cells are relatively common in humans: At least 2700 to 31,000 eOD-GT8-reactive VRC01-class naïve B cells are likely present in nearly all potential human vaccine recipients, with ~15 such B cells in each lymph node, at any given time (20).

The  $K_D$  values of 24 isolated VRC01-class precursors for monovalent eOD-GT8 ranged from 57  $\mu$ M to 125 nM, with a geometric mean  $K_D$  of 3.4  $\mu$ M (Fig. 2L and table S4), weaker than germline-reverted VRC01-class Abs by a factor of

**Fig. 1. Development of**

**eOD-GT8. (A)** Model of germline-reverted VRC01 (gray surface) interacting with eOD-GT7 (cartoon) with the 58 positions subjected to deep mutational scanning shown as magenta, green, and orange spheres representing the three mutagenized linear segments. Binding enrichments, the ratio of the frequency of a mutation in the top 10% binding population to the frequency of the same mutation in all cells displaying eOD-GT7, were computed for each mutation on eOD-GT7 for germline-reverted VRC01 and are shown as a heat map on the right, in which blue denotes unfavorable mutations, red denotes favorable mutations, and white denotes the amino acid residue in eOD-GT7. **(B)** The combined binding enrichments from independent yeast display screens for 18 germline-reverted VRC01-class bnAbs are shown as a multidimensional heat map in which the color scale from yellow to red indicates increasing favorable average enrichment. Symbol sizes reflect the breadth of enrichment (the number of germline-reverted Abs with enriched binding for each point mutation). If enriched, the eOD-GT7 amino acid residue is indicated by a cross. **(C)** Sequence logos depicting amino acids at each of 16 positions in the combinatorial library (top), the sequences selected from the combinatorial library for improved binding to germline-reverted VRC01-class bnAbs (middle), and the final sequence of eOD-GT8 (bottom). Abbreviations: A, Ala; C, Cys; D, Asp; E, Glu; F, Phe; G, Gly; H, His; I, Ile; K, Lys; L, Leu; M, Met; N, Asn; P, Pro; Q, Gln; R, Arg; T, Thr; V, Val; W, Trp; Y, Tyr. **(D)** Surface plasmon resonance (SPR) dissociation constants measured for both germline-reverted and mature VRC01-class bnAbs against eOD-GT6 and eOD-GT8. Solid blue



590 (geometric mean  $K_D = 5.8$  nM for the panel), most likely due to the naïve CDR3 loops in the former as opposed to the affinity-matured CDR3 loops in the latter. The VRC01-class naïve B cell affinities are in the range expected to allow a multivalent eOD-GT8 immunogen, such as eOD-GT8 60mer (2, 9), to activate B cells and initiate germinal centers (21, 22). Our data also suggest that eOD-GT8 has promise to produce VRC01-class memory even given competition from non-VRC01-class B cells, as eOD-GT8 exhibited a high degree of CD4bs immunofocusing (Fig. 2C) and

VRC01-class precursors had an affinity advantage (factor of  $\geq 3$ ) over non-VRC01-class CD4bs epitope-binding precursors (Fig. 2L). The frequencies and eOD-GT8 affinities of bona fide VRC01-class precursors isolated here warrant human immunization studies with eOD-GT8 60mer nanoparticles.

Only 2 of 20 tested VRC01-class precursors had detectable affinity for eOD-GT6 (Fig. 2L). Equilibrium binding  $K_D$  values were 36  $\mu$ M and 69  $\mu$ M, and these Abs had two of the highest affinities for eOD-GT8 at 506 nM and 258 nM, re-

spectively (table S4). These data, combined with the failure of eOD-GT6 probe B cell screens to isolate VRC01-class precursors, suggest that the engineered breadth and affinity improvements in eOD-GT8 represent a major advance toward practical utility in human vaccination.

We sought to confirm that the isolated VRC01-class precursors engage the CD4bs in the same structural binding mode as VRC01-class bnAbs (6, 17, 23–25) and germline-reverted VRC01 (9). We solved the crystal structure of isolated precursor VRC01c-HuGL2 (eOD-GT8  $K_D = 368$  nM)

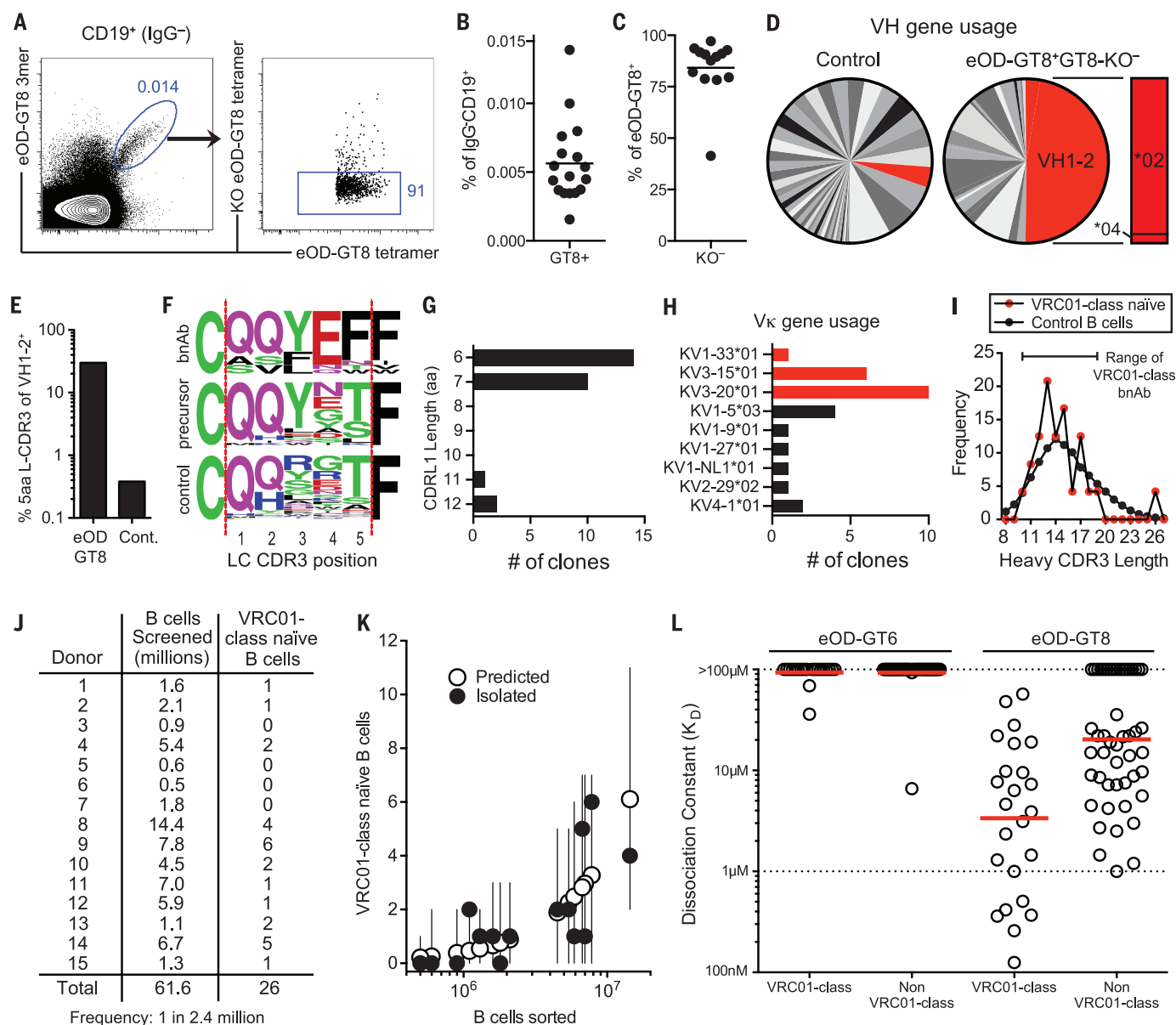


**Fig. 2. eOD-GT8-binding VRC01-class naïve B cells exist in healthy human donors.** (A) eOD-GT8<sup>+</sup> naïve CD19<sup>+</sup>IgG<sup>-</sup> B cells. (B and C) eOD-GT8<sup>+</sup> B cell frequency (B) and eOD-GT8 KO<sup>-</sup> cells (C) among eOD-GT8<sup>+</sup> B cells in individual donors. (D) VH1-2 usage among eOD-GT8<sup>+</sup>/eOD-GT8 KO<sup>-</sup> sorted B cells ( $n = 173$ ) versus control B cells. VH1-2 (red) allele frequencies are indicated. (E) B cells expressing a 5-amino acid L-CDR3 among VH1-2<sup>+</sup> B cells isolated by eOD-GT8 versus control B cells. (F) L-CDR3 sequence logos of VRC01-class bnAbs (top), VRC01-class naïve precursors (middle), and control B cells (bottom).

(G) L-CDR1 lengths of 27 VRC01-class naïve B cells. (H) Light chain V gene usage of 27 VRC01-class naïve B cells. Known VRC01-class bnAb V $\kappa$  genes are in red. (I) H-CDR3 lengths of VRC01-class naïve B cells versus control B cells. (J) Total B cells screened and VRC01-class naïve B cells found in 15 individuals. (K) Poisson distribution modeling of the number of VRC01-class naïve B cells. Vertical lines show the 2.5% and 97.5% quantiles. (L) SPR dissociation constants for eOD-GT6 or eOD-GT8 binding to VRC01-class or non-VRC01-class Abs derived from eOD-GT8-sorted human naïve B cells. Solid red lines indicate geometric mean.



in complex with eOD-GT8 in two crystal forms (I222, 2.16 Å, and C2, 2.44 Å; table S5). Comparison of this structure with the complex of core-gp120 bound to VRC01 [PDB ID: 3NGB (6)] shows the same binding mode (Fig. 3A), including specific H-CDR2 and L-CDR3 conformations (Fig. 3B) (26) that together account for more than 67.2% of the Fv domain buried surface area (Fig. 3C and table S6). When interface residues of eOD-GT8 and core-gp120 are aligned,  $V_H$  and  $V_L$  of VRC01c-HuGL2 and VRC01 have high similarity ( $C\alpha$  RMSD 0.7 Å; Fig. 3A and fig. S9). These structural observations confirm VRC01c-HuGL2 as a bona fide VRC01-class precursor and support

the conclusion that all of the eOD-GT8-specific naïve B cells using VH1-2 and a 5-amino acid L-CDR3 are bona fide VRC01-class precursors. Comparison of the eOD-GT8-VRC01c-HuGL2 structure with a 1.82 Å unliganded VRC01c-HuGL2 structure shows that the important H-CDR2 and L-CDR3 loops are preconfigured in the unbound state and do not require any conformational changes for engagement with gp120 CD4bs (Fig. 3D), heightening the appeal of VRC01-class germline targeting. A 2.9 Å unliganded structure of eOD-GT8 (Fig. 3E and fig. S10) demonstrates faithful mimicry of the VRC01-class antibody-bound conformation (27), thus helping to explain

the increased affinity of eOD-GT8 for true VRC01-class bnAb precursors.

The interaction of the naïve human B cell repertoire with vaccine antigens has not been characterized previously. Given the vast immunoglobulin sequence space, direct probing of the human naïve B cell repertoire was a critical test of the physiologically relevant binding potential of the germline-targeting immunogen. The antibody sequence features, binding affinities, and high structural similarity of the eOD-GT8-specific naïve B cell-derived antibodies to VRC01 all demonstrate the power of germline-targeting design when combined with human B cell probing. Similar

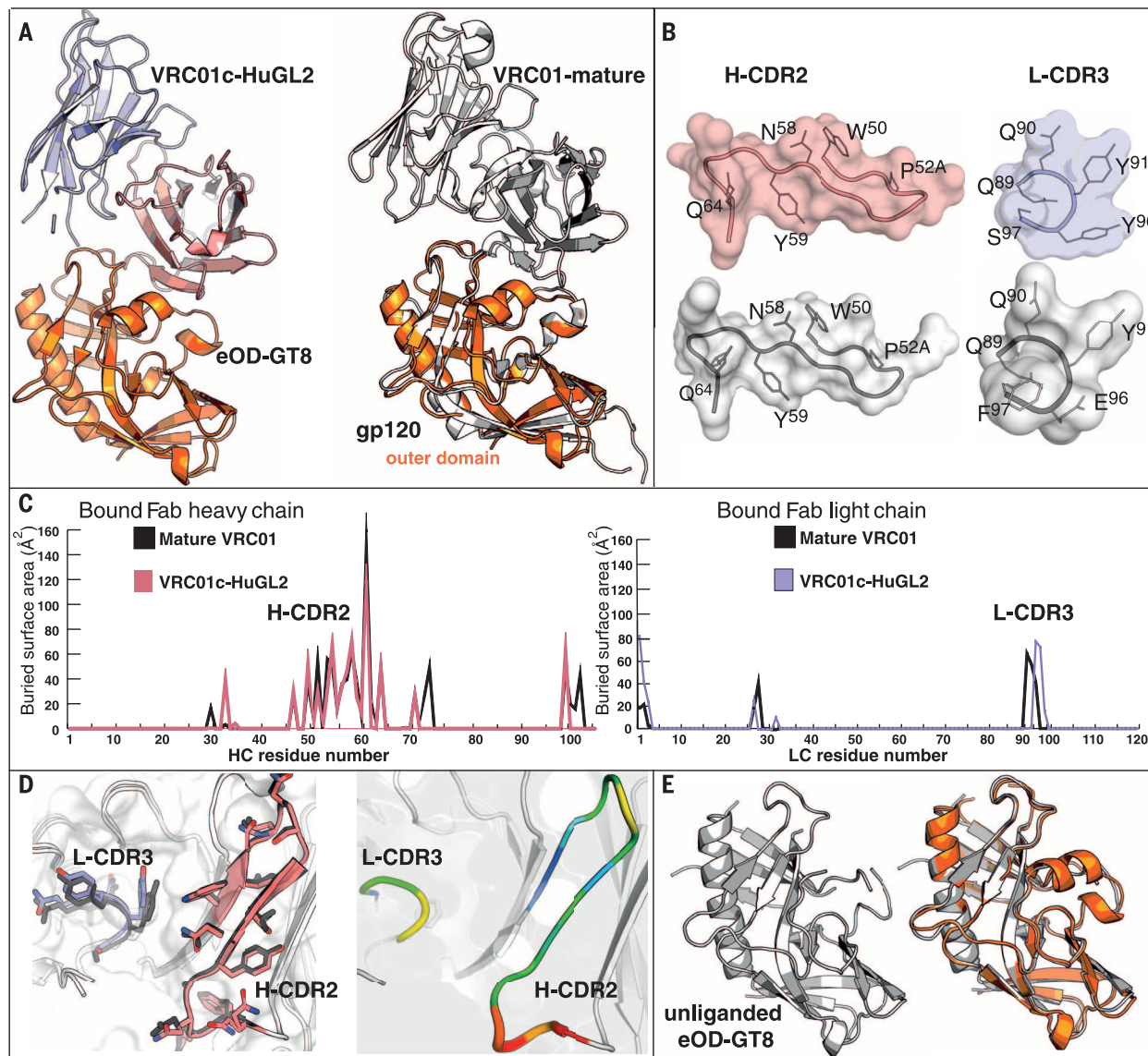


**Fig. 3. Structural analysis of eOD-GT8 and human germline antibody VRC01c-HuGL2 complex.** (A) Crystal structures of VRC01c-HuGL2 + eOD-GT8 (blue, LC; salmon, HC; orange, eOD-GT8) and of mature VRC01 + gp120 (PDB ID: 3NGB, in white) shown in the same orientation, showing eOD-GT8 superimposed on gp120, and showing only the antibody Fv regions for clarity. (B) Comparison of the H-CDR2 and L-CDR3 conformations from the structures in (A). (C) Comparison of buried surface areas for the  $V_H$  and  $V_L$  residues of VRC01c-HuGL2 and mature VRC01 + gp120, in their bound forms. (D) Comparison of H-CDR2 and

L-CDR3 conformations of unliganded and eOD-GT8-liganded VRC01c-HuGL2 Fab. All atoms of  $V_H$  and  $V_L$  were aligned. In the left image, H-CDR2 and L-CDR3 are shown as sticks; in the right image the CDRs are shown according to B-factors reporting local structural flexibility using a relative scale in which increasing wire thickness and warmth of color (blue to red) indicates increasing mobility. (E) Crystal structure of unliganded eOD-GT8 shown in cartoon representation (left) and a superposition of unliganded and VRC01c-HuGL2-bound forms of eOD-GT8 (right;  $C\alpha$  RMSD = 0.4 Å).

methods, including both protein design and human B cell probing methods, could be used to improve and evaluate germline-targeting immunogens for other classes of HIV bnAbs and for Abs against other pathogens. These methods may be particularly important to develop and test germline-targeting approaches for bnAbs that rely heavily on HCDR3 and hence may have lower precursor frequencies.

## REFERENCES AND NOTES

1. D. R. Burton, J. R. Mascola, *Nat. Immunol.* **16**, 571–576 (2015).
2. J. G. Jardine *et al.*, *Science* **349**, 156–161 (2015).
3. P. Dosenovic *et al.*, *Cell* **161**, 1505–1515 (2015).
4. H. X. Liao *et al.*, *Nature* **496**, 469–476 (2013).
5. N. A. Doria-Rose *et al.*, *Nature* **509**, 55–62 (2014).
6. T. Zhou *et al.*, *Science* **329**, 811–817 (2010).
7. J. F. Scheid *et al.*, *Science* **333**, 1633–1637 (2011).
8. S. Hoot *et al.*, *PLOS Pathog.* **9**, e1003106 (2013).
9. J. Jardine *et al.*, *Science* **340**, 711–716 (2013).
10. A. T. McGuire *et al.*, *J. Exp. Med.* **210**, 655–663 (2013).
11. See supplementary materials on Science Online.
12. T. A. Whitehead *et al.*, *Nat. Biotechnol.* **30**, 543–548 (2012).
13. Filtering was done to limit library size, to exclude mutations detrimental to binding the majority of mature bnAbs, to reduce hydrophobic exposure, to exclude unpaired cysteines, and to minimize nonconservative changes to epitope components.
14. A. P. West Jr., R. Diskin, M. C. Nussenzweig, P. J. Bjorkman, *Proc. Natl. Acad. Sci. U.S.A.* **109**, E2083–E2090 (2012).
15. Several design features of eOD-GT8 are likely responsible for this immunofocusing, including the relatively small size of eOD-GT8 (175 amino acids) and its compact structure (no exposed loops except Loop D and V5 within the CD4bs), as well as the glycan shielding by 10 glycans covering much of the eOD-GT8 surface outside the CD4bs.
16. B. J. DeKosky *et al.*, *Nat. Med.* **21**, 86–91 (2015).
17. T. Zhou *et al.*, *Immunity* **39**, 245–258 (2013).
18. Two of the isolated VRC01-class precursors had incomplete H-CDR3 sequences preventing determination of H-CDR3 length.
19. H. Morbach, E. M. Eichhorn, J. G. Liese, H. J. Girschick, *Clin. Exp. Immunol.* **162**, 271–279 (2010).
20. The frequency of 1 in 2.4 million is an underestimate of the true frequency among naive B cells, because not all B cells counted by the sorter as eOD-GT8<sup>trn+/SA+</sup>/eOD-GT8-KO<sup>-</sup> were sorted into a well (cell sorter loss), paired heavy chain and light chain (HC and LC) sequences were recovered from fewer than half of eOD-GT8<sup>trn+/SA+</sup>/eOD-GT8-KO<sup>-</sup> B cells sorted into wells [a result of the inherent limitations of single-cell polymerase chain reaction (PCR)], and B cells bearing lambda light chains were not analyzed. By correcting for cell sorter and PCR losses, the frequency of VRC01-class naive B cell precursors is calculated as 1 in 400,000 naive B cells (11). VRC01-class precursors may also exist in the memory B cell population in healthy humans, but their frequency remains to be measured.
21. T. A. Shih, E. Meffre, M. Roederer, M. C. Nussenzweig, *Nat. Immunol.* **3**, 570–575 (2002).
22. J. M. Dal Porto, A. M. Haberman, G. Kelsoe, M. J. Shlomchik, *J. Exp. Med.* **195**, 1215–1221 (2002).
23. X. Wu *et al.*, *Science* **333**, 1593–1602 (2011).
24. R. Diskin *et al.*, *Science* **334**, 1289–1293 (2011).
25. R. Diskin *et al.*, *J. Exp. Med.* **210**, 1235–1249 (2013).
26. T. Zhou *et al.*, *Cell* **161**, 1280–1292 (2015).
27. We conclude that mutations that led to the design of eOD-GT8 from eOD-GT6 further stabilize the antibody-bound state, based on a higher similarity between the VRC01c-HuGL2-bound and unliganded eOD-GT8 (all-atom RMSD = 0.98 Å, alignment of 1206 atoms) versus GL-VRC01-bound eOD-GT6 (PDBID: 4JPK) and unliganded eOD-GT6 (PDBID: 4JPJ) (all-atom RMSD = 3.0 Å, alignment of 1343 atoms) (fig. S10).

## ACKNOWLEDGMENTS

We thank L. Stamatatos, T. Whitehead, and M. Nussenzweig for discussions; the Flow Cytometry Core at the La Jolla Institute for Allergy and Immunology and L. Nosworthy for expert cell-sorting assistance; H. Tien for technical support with crystallization robots; and A. Irimia for discussions and technical help. This work was supported by the International AIDS Vaccine Initiative Neutralizing Antibody Consortium and Center (W.R.S., I.A.W., D.R.B.); CAVD funding for the IAVI NAC Center (W.R.S., I.A.W., D.R.B.); CAVD

Vaccine Immunology Statistical Center (VISC) (A.C.D.); the Ragon Institute of MGH, MIT, and Harvard (D.R.B. and W.R.S.); the Bayer Science and Education Foundation (F.S.); the Helen Hay Whitney Foundation and Howard Hughes Medical Institute (J.G.J.); and National Institute of Allergy and Infectious Diseases grants P01 AI094419 (W.R.S.), CHAVI-ID U01 AI100663 (W.R.S., S.C., I.A.W., D.R.B.), P01 AI10657 (I.A.W.), and R01 AI084817 (I.A.W.). Portions of this research were carried out at the Stanford Synchrotron Radiation Lightsource (SSRL), a Directorate of SLAC National Accelerator Laboratory and an Office of Science User Facility operated for the U.S. Department of Energy (DOE) Office of Science by Stanford University. The SSRL Structural Molecular Biology Program is supported by the DOE Office of Biological and Environmental Research, and by the National Institute of General Medical Sciences (including P41GM103393). The data presented in this manuscript are tabulated in the main paper and in the supplementary materials. Coordinates and structure factors for VRC01c-HuGL2 Fab, VRC01c-HuGL2+eOD-GT8 (2.44 Å), and VRC01c-HuGL2+eOD-GT8 (2.16 Å) have been deposited with the Protein Data Bank with accession codes 5IFA, 5IF0, and 5IES,

respectively. Sequences for heavy and light chains of HuGL1 through HuGL27 have been deposited at NCBI with GenBank accession codes KU760929 to KU760982. Materials and information are available by MTA from the Scripps Research Institute. IAVI and the Scripps Research Institute have filed a patent relating to the eOD-GT8 immunogens in this manuscript, which included inventors J.G.J., D.W.K., and W.R.S. W.R.S. is a co-founder and stockholder in Compuvax Inc., which has programs in non-HIV vaccine design that might benefit indirectly from this research.

## SUPPLEMENTARY MATERIALS

www.sciencemag.org/content/351/6280/1458/suppl/DC1  
Materials and Methods

Figs. S1 to S14

Tables S1 to S7

References (28–41)

21 November 2015; accepted 24 February 2016  
10.1126/science.aad9195

## TUMOR IMMUNOLOGY

# Clonal neoantigens elicit T cell immunoreactivity and sensitivity to immune checkpoint blockade

Nicholas McGranahan,<sup>1,2,3\*</sup> Andrew J. S. Furness,<sup>3,4\*</sup> Rachel Rosenthal,<sup>3\*</sup> Sofie Ramskov,<sup>5</sup> Rikke Lyngaa,<sup>5</sup> Sunil Kumar Saini,<sup>5</sup> Mariam Jamal-Hanjani,<sup>3</sup> Gareth A. Wilson,<sup>1,3</sup> Nicolai J. Birkbak,<sup>1,3</sup> Crispin T. Hiley,<sup>1,3</sup> Thomas B. K. Watkins,<sup>1,3</sup> Seema Shafi,<sup>3</sup> Nirupa Murugesu,<sup>3</sup> Richard Mitter,<sup>1</sup> Ayse U. Akarca,<sup>4,6</sup> Joseph Linares,<sup>4,6</sup> Teresa Marafioti,<sup>4,6</sup> Jake Y. Henry,<sup>3,4</sup> Eliezer M. Van Allen,<sup>7,8,9</sup> Diana Miao,<sup>7,8</sup> Bastian Schilling,<sup>10,11</sup> Dirk Schadendorf,<sup>10,11</sup> Levi A. Garraway,<sup>7,8,9</sup> Vladimir Makarov,<sup>12</sup> Naiyer A. Rizvi,<sup>13</sup> Alexandra Snyder,<sup>14,15</sup> Matthew D. Hellmann,<sup>14,15</sup> Taha Merghoub,<sup>14,16</sup> Jedd D. Wolchok,<sup>14,15,16</sup> Sachet A. Shukla,<sup>7,8</sup> Catherine J. Wu,<sup>7,8,17,18</sup> Karl S. Peggs,<sup>3,4</sup> Timothy A. Chan,<sup>12</sup> Sine R. Hadrup,<sup>5</sup> Sergio A. Quezada,<sup>3,4</sup> Charles Swanton<sup>1,3,†</sup>

As tumors grow, they acquire mutations, some of which create neoantigens that influence the response of patients to immune checkpoint inhibitors. We explored the impact of neoantigen intratumor heterogeneity (ITH) on antitumor immunity. Through integrated analysis of ITH and neoantigen burden, we demonstrate a relationship between clonal neoantigen burden and overall survival in primary lung adenocarcinomas. CD8<sup>+</sup> tumor-infiltrating lymphocytes reactive to clonal neoantigens were identified in early-stage non-small cell lung cancer and expressed high levels of PD-1. Sensitivity to PD-1 and CTLA-4 blockade in patients with advanced NSCLC and melanoma was enhanced in tumors enriched for clonal neoantigens. T cells recognizing clonal neoantigens were detectable in patients with durable clinical benefit. Cytotoxic chemotherapy-induced subclonal neoantigens, contributing to an increased mutational load, were enriched in certain poor responders. These data suggest that neoantigen heterogeneity may influence immune surveillance and support therapeutic developments targeting clonal neoantigens.

Recent studies have highlighted the relevance of tumor neoantigens in the recognition of cancer cells by the immune system (1–4), prompting a renewed interest in personalized vaccines and cell therapies that target cancer mutations (5, 6). However, although genomic data are revealing the extent of genetic heterogeneity within single tumors (7), the influence of intratumor heterogeneity (ITH) upon the neoantigen landscape and sensitivity to immune modulation is unclear.

To explore neoantigen heterogeneity and its influence on antitumor immunity in early-stage non-small cell lung cancer (NSCLC), we applied a bioinformatics pipeline to seven primary NSCLCs subjected to multiregion sequence analysis (table S1) (8, 9). In total, 2860 putative neoantigens were predicted across the cohort, with a median of 326 neoantigens predicted per tumor (range of 80 to 741) (Fig. 1A). Neoantigen heterogeneity varied considerably, with an average of 44% neoantigens found



heterogeneously, in a subset of tumor regions (range of 10 to 78%).

To address the clinical relevance of neoantigen burden and, specifically, the importance of clonal (present in all tumor cells) versus subclonal (present only in a subset) neoantigens, we subjected a predominantly early-stage cohort of 106 stage I/II, 43 stage III/IV, and 1 unknown-stage lung adenocarcinoma (LUAD) and 92 stage I/II and 32 stage III/IV lung squamous cell carcinoma (LUSC) cases from The Cancer Genome Atlas (TCGA) to neoantigen and clonality analysis (10–12) (Fig. 1B). In this setting, to determine clonality from sequencing of a single sample, the cancer cell fraction, which describes the proportion of cancer cells harboring a mutation, was determined for each neoantigen (13).

A high neoantigen burden, defined as the upper quartile of neoantigen load, was associated with significantly longer overall survival in LUAD ( $P = 0.025$ ) (Fig. 1, C and D, and fig. S1A), and a trend for homogeneous tumors (neoantigen ITH  $\leq 1\%$ ) to have longer overall survival times as compared with that of heterogeneous tumors was also observed ( $P = 0.061$ ) (fig. S1B). Although tumors with a high burden of neoantigens were found to be significantly more homogeneous than those with a low burden of neoantigens ( $P < 0.0001$ , Wilcoxon rank-sum test) (fig. S1C), a combination of neoantigen ITH and neoantigen burden (as outlined in the schematic in Fig. 1C) was more significant than simply considering either metric alone and was observed across multiple different neoantigen ITH thresholds (without ITH threshold,  $P = 0.025$ ; ITH threshold = 0,  $P = 0.019$ ; ITH threshold = 0.01,  $P = 0.0096$ ; ITH threshold = 0.05,  $P = 0.021$ ) (Fig. 1D), remaining significant in multivariate analysis when including the tumor stage (table S2).

Despite a comparable range of predicted neoantigens in LUSC, no statistically significant association between overall survival and neoantigen load was observed in this subtype, even when incorporating neoantigen ITH (fig. S2, A to D). To investigate the reason for this disparity, we explored whether any immune-regulatory genes were differentially expressed between these two cancer types. Human lymphocyte antigen (HLA) class I genes—including *HLA-A*, *HLA-B*, *HLA-C*, *HLA-E*, *HLA-F*, and *HLA-G*, as well as  $\beta_2$  microglobulin ( $\beta_2M$ ), a component of the major histocompatibility complex (MHC) class I molecule—were expressed at a significantly lower level in LUSC as compared with LUAD (fig. S3A and table S3A), and this difference was observed across all levels of neoantigen burden (fig. S3B and table S3B). HLA class I genes were also down-regulated compared with matched normal samples in LUSC (table S3C). These data suggest that the presence of a high number of clonal neoantigens in homogeneous LUAD may favor effective immune surveillance, whereas in LUSC, immune escape may be more prevalent through HLA down-regulation.

We next evaluated whether immune-related genes were differentially expressed between homogeneous LUAD tumors ( $\leq 1\%$  neoantigen ITH) with a high clonal neoantigen burden (greater than or equal to upper-quartile clonal neoantigens) compared with heterogeneous ( $>1\%$  neoantigen ITH) or low clonal neoantigen burden tumors (less than upper-quartile clonal neoantigens). Eight genes were found to be significantly differentially expressed between these two groups (table S4A). Programmed cell death ligand-1 (PD-L1) and the proinflammatory cytokine interleukin-6 (IL-6) were the most significantly differentially expressed genes, up-regulated in the homogeneous and high clonal neoantigen group. When we specifically compared tumors in the upper quartile of clonal neoantigen burden with tumors in the lower quartile, we identified an additional 25 significantly differentially expressed genes (table S4B and fig. S4A). *CD8A*, *CD8B*, and genes associated with antigen presentation (*TAP-1*, *TAP-2*, and *STAT-1*), T cell migration (*CXCL-10* and *CXCL-9*), and effector T cell function [interferon- $\gamma$  (IFN- $\gamma$ ) and granzymes B, H, and A] were up-regulated in the high clonal neoantigen cohort and found to cluster together, indicating coexpression (fig. S4B). PD-1 and lymphocyte activation gene 3 (LAG-3)—negative regulators of T cell function (14)—were also identified in this cluster, as were the ligands PD-L1 and PD-L2.

These data suggest that a high clonal neoantigen burden in LUAD is associated with an inflamed tumor microenvironment enriched with activated effector T cells, potentially regulated by inhibitory immune checkpoint molecules and their ligands. We therefore attempted to identify and characterize T cells reactive to neoantigens in patients with early-stage NSCLC. We focused on two tumors, L011 and L012, with a comparable number of predicted neoantigens and a similar smoking history, but divergent levels of neoantigen ITH (8 versus 74% heterogeneous predicted neoantigens) (Fig. 2, A to C). We used 288 and 354

putative neoantigen-loaded, HLA-matched multimers derived from L011 and L012, respectively, to screen CD8<sup>+</sup> T cells expanded from individual tumor regions and adjacent normal lung tissue, using a previously described high-throughput method (Fig. 2, D and E) (15).

CD8<sup>+</sup> T cells reactive to mutant MTFR2<sup>D326Y</sup> (FAFQEYDSF) were identified in L011, whereas in L012, two distinct CD8<sup>+</sup> T cell responses to mutant CHTF18<sup>L769V</sup> (LLDIVAPK) and MYADM<sup>R30W</sup> (SPMIVGSPW) were observed (Fig. 2, D and E, and fig. S5, A and B). MTFR2<sup>D326Y</sup>, CHTF18<sup>L769V</sup>, and MYADM<sup>R30W</sup> all represent clonal neoantigens, suggesting that immune-reactivity against clonal neoantigens can be detected in both homogeneous and heterogeneous NSCLC. High HLA binding affinity was predicted for MTFR2<sup>D326Y</sup> and CHTF18<sup>L769V</sup> in both wild-type and mutant forms, but only the mutant peptide was found to elicit a T cell response. Higher binding affinity to mutant versus wild-type form was predicted for MYADM<sup>R30W</sup>; however, in this case, reactivity toward wild-type peptide was also observed (fig. S5C). The mutation in the MYADM<sup>R30W</sup> peptide lies in the anchor residue, primarily affecting HLA binding and not T cell recognition. Although the data suggest that T cells in this patient can recognize both mutant and wild-type peptides when stabilized within a MHC-multimer system, the very low predicted affinity of the wild-type peptide to HLA would be expected to prevent adequate presentation in vivo.

We next used MHC multimers that identify neoantigen-reactive T (NAR-T) cells to characterize NAR-T cells in unexpanded samples (Fig. 3, A to D). MTFR2<sup>D326Y</sup>-reactive CD8<sup>+</sup> T cells, identified in unexpanded L011, were analyzed by means of multicolor flow cytometry. We assessed relative expression of co-inhibitory immune checkpoint molecules and effector cytokines between tumor-infiltrating CD4<sup>+</sup>FoxP3<sup>+</sup> (regulatory T cell), CD4<sup>+</sup>FoxP3<sup>−</sup> (CD4<sup>+</sup> helper T cell), CD8<sup>+</sup> multimer negative, and CD8<sup>+</sup> multimer-reactive (MTFR2<sup>D326Y</sup>) T cell subsets. MTFR2<sup>D326Y</sup>-reactive CD8<sup>+</sup> T cells expressed high levels of co-inhibitory receptors PD-1 and LAG-3 (Fig. 3C), which is consistent with our bioinformatics findings (fig. S4). Almost all NAR-T cells (97%) expressed high levels of PD-1, compared with 49% of multimer-negative tumor-infiltrating CD8<sup>+</sup> T cells. CTLA-4 expression was largely confined to CD4<sup>+</sup>FoxP3<sup>+</sup> regulatory T cells, which is consistent with preclinical findings (16). PD-1<sup>+</sup> MTFR2<sup>D326Y</sup>-reactive CD8<sup>+</sup> T cells coexpressed high levels of granzyme B (GzmB) (74.8%) (Fig. 3D). Characterization of CHTF18<sup>L769V</sup>- and MYADM<sup>R30W</sup>-reactive CD8<sup>+</sup> T cells mirrored findings in L011, with high expression of PD-1 observed in 97% and 99.6% of CHTF18<sup>L769V</sup>- and MYADM<sup>R30W</sup>-reactive CD8<sup>+</sup> T cells, respectively (fig. S5, D and E).

Given the potential ability of clonal neoantigens to promote priming and infiltration by neoantigen reactive T cells expressing high levels of PD-1, we explored whether response to PD-1 blockade in patients with advanced NSCLC may be influenced by neoantigen ITH. Exome sequencing data from a recent study in which

<sup>1</sup>The Francis Crick Institute, London WC2A 3LY, UK. <sup>2</sup>Centre for Mathematics and Physics in the Life Sciences and Experimental Biology (CoMPLEX), University College London (UCL), London WC1E 6BT, UK. <sup>3</sup>Cancer Research UK Lung Cancer Centre of Excellence, UCL Cancer Institute, London WC1E 6BT, UK. <sup>4</sup>Cancer Immunology Unit, UCL Cancer Institute, UCL, London WC1E 6BT, UK. <sup>5</sup>Section for Immunology and Vaccinology, National Veterinary Institute, Technical University of Denmark, 1870 Frederiksberg C, Denmark. <sup>6</sup>Department of Cellular Pathology, UCL, London WC1E 6BT, UK. <sup>7</sup>Department of Medical Oncology, Dana-Farber Cancer Institute, Boston, MA 02215, USA. <sup>8</sup>Broad Institute of MIT and Harvard, Cambridge, MA 02142, USA. <sup>9</sup>Center for Cancer Precision Medicine, Dana-Farber Cancer Institute, Boston, MA 02215, USA. <sup>10</sup>Department of Dermatology, University Hospital, University Duisburg-Essen, 45147 Essen, Germany. <sup>11</sup>German Cancer Consortium (DKTK), 69121 Heidelberg, Germany. <sup>12</sup>Human Oncology and Pathogenesis Program, Memorial Sloan Kettering Cancer Center, New York, NY 10065, USA. <sup>13</sup>Hematology/Oncology Division, 177 Fort Washington Avenue, Columbia University, New York, NY 10032, USA. <sup>14</sup>Department of Medicine, Memorial Sloan Kettering Cancer Center, New York, NY 10065, USA. <sup>15</sup>Weill Cornell Medical College, New York, NY 10065, USA. <sup>16</sup>Ludwig Collaborative Laboratory, Memorial Sloan Kettering Cancer Center, New York, NY 10065, USA. <sup>17</sup>Department of Medicine, Harvard Medical School, Boston, MA 02215, USA. <sup>18</sup>Department of Internal Medicine, Brigham and Women's Hospital, Boston, MA 02215, USA.

\*These authors contributed equally to this work. †Corresponding author. E-mail: s.quezada@ucl.ac.uk (S.A.Q.); charles.swanton@crick.ac.uk (C.S.)

34 patients were treated with pembrolizumab—an antibody targeting PD-1—was obtained (table S5) (2), and the clonal architecture of each tumor estimated (possible for 31 of 34 tumors).

Neoantigen burden was related to clinical response to pembrolizumab, with a high neoantigen repertoire associated with improved outcome, as previously reported (Fig. 4A). However, consist-

ent with the importance of clonal neoantigens, the clinical efficacy of PD-1 blockade also appeared related to the clonal architecture of each tumor (Fig. 4A), with tumors derived from patients with no durable benefit [defined as in (2)] exhibiting significantly higher neoantigen ITH than that of tumors from patients with a durable clinical benefit ( $P = 0.006$ , Wilcoxon rank sum

test). Almost every tumor (12 of 13) that exhibited a low neoantigen subclonal fraction ( $<5\%$  subclonal) and high mutation burden ( $\geq 70$ , median clonal neoantigens of the cohort) demonstrated durable clinical benefit with anti-PD-1 therapy. Conversely, only 2 out of 18 tumors with a high subclonal neoantigen fraction ( $>5\%$ ) or low clonal neoantigen burden benefited from pembrolizumab

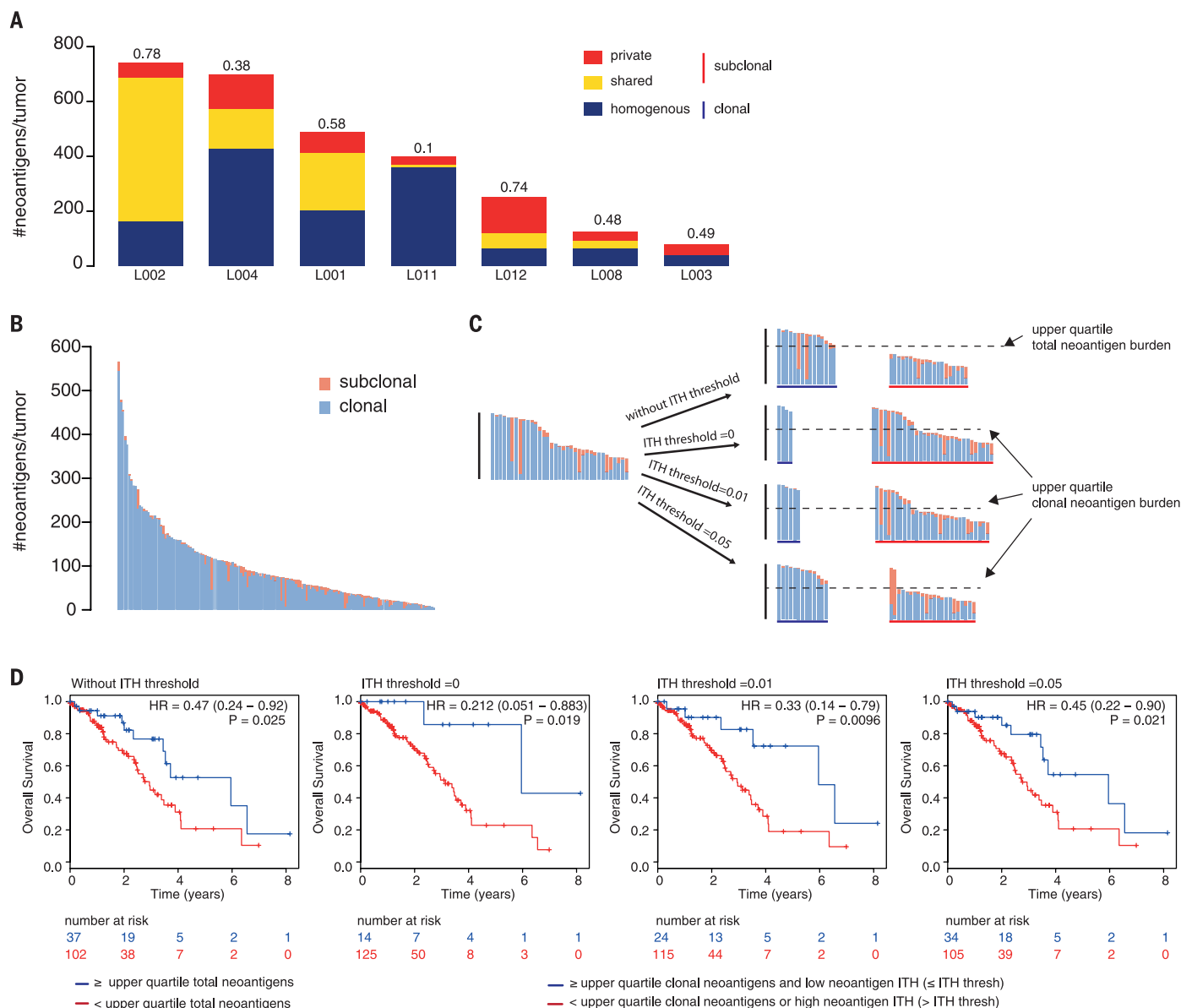


**Fig. 1. Heterogeneity and prognostic value of neoantigen landscape in primary NSCLC.**

(A) Total putative neoantigen burden in multiregion sequenced NSCLC tumors. Proportion of clonal neoantigens, identified ubiquitously in every tumor region, are shown in blue; shared subclonal neoantigens, identified as shared in multiple tumor regions but not all, are shown in yellow; and private subclonal neoantigens, identified in only one tumor region, are in red. (B) Total putative neoantigen burden in TCGA LUAD tumors. Proportion of neoantigens arising from clonal (blue) or subclonal (red) mutations is shown. (C) Schematic illustrating use of different neoantigen ITH thresholds, with bar plot showing separation into the two groups. Without an ITH threshold, samples are simply grouped according to upper quartile of total neoantigen burden. For

each ITH threshold, the upper quartile of clonal neoantigens is used to separate tumors with high and low clonal neoantigen burden, and the neoantigen ITH threshold further groups samples. For example, an ITH threshold = 0 involves grouping tumors with high clonal neoantigen burden and zero neoantigen heterogeneity separately from those with low clonal neoantigen burden or any neoantigen heterogeneity. (D) Overall survival curves for samples by using different ITH thresholds. Shown are without an ITH threshold [log-rank,  $P = 0.025$ , HR = 0.47 (0.24–0.92)]; ITH threshold = 0 [log-rank,  $P = 0.019$ , HR = 0.21 (0.051–0.88)]; ITH threshold = 0.01 [log-rank,  $P = 0.0096$ , HR = 0.33 (0.14–0.79)]; and ITH threshold = 0.05 [log-rank,  $P = 0.021$ , HR = 0.45 (0.22–0.90)]. The number of patients in each group is listed below the survival curves.



(Y2087 and SB10944). For example, despite a large neoantigen burden, ZA6505 exhibited progressive disease, relapsing after 2 months. ZA6505 was one of the most heterogeneous tumors within the cohort, with over 80% of mutations classified as subclonal.

Tumors with both a high clonal neoantigen burden and low neoantigen ITH were associated with significantly longer progression-free survival, and this relationship remained robust to the choice of ITH threshold, with lower hazard ratios observed as compared with the use of neoantigen burden alone (Fig. 4B). The majority of clonal neoantigens could be attributed to smoking-induced mutations (Fig. 4A). Greater PD-L1 expression was observed in tumors harboring a large clonal neoantigen burden and low neoantigen heterogeneity compared with the remaining tumors ( $P = 0.0017$ ,  $\chi^2$  test) (Fig. 4A and fig. S6).

Next, we obtained data from 64 melanoma patients treated with either ipilimumab or tremelimumab, which are antibodies against CTLA-4 (4). Clonal architecture analysis was possible for 57 of 64 tumors, and significantly improved overall survival was observed in tumors exhib-

iting a low neoantigen ITH and a high clonal neoantigen burden. This relationship was observed when multiple different ITH thresholds were used, similar to the NSCLC cohort (ITH threshold = 0.01,  $P = 0.008$ ; ITH threshold = 0.02,  $P = 0.011$ ; ITH threshold = 0.05,  $P = 0.083$ ) (Fig. 4C). The relationship between neoantigen burden and survival outcome was not statistically significant without an ITH threshold ( $P = 0.083$ ) (Fig. 4C).

To address whether radiation or cytotoxic exposure might stimulate production of subclonal neoantigens that could contribute to total neoantigen burden but not the efficacy of checkpoint blockade, sequencing data from a more heavily pretreated melanoma cohort, comprising 110 tumors, were obtained (17). For the subset of tumors for which clonal analysis was possible (78 of 110 tumors, a smaller and less adequately powered cohort as compared with the published analysis), total neoantigen burden was not significantly associated with efficacy of immune checkpoint inhibition [classified as in (17)], although a trend was observed ( $P = 0.24$ , Wilcoxon rank sum test) (fig. S7A). However, an enrichment for tumors

exhibiting high neoantigen heterogeneity or low clonal neoantigen burden (both stratified according to the median of the cohort) reached borderline significance in patients with minimal or no benefit compared with patients exhibiting a clinical benefit ( $P = 0.06$ , Fisher's exact test). Neoantigen burden was not found to be significantly associated with overall survival in this cohort (fig. S7B). Two of the most heterogeneous tumors (Pat58 and Pat151) with minimal or no benefit were among those treated with the alkylating agent dacarbazine (DTIC) before anti-CTLA therapy, and for both, >98% of subclonal mutations were attributable to mutational Signature 11, a signature associated with prior exposure to alkylating agents (18, 19). One patient with stable disease—Pat80, who was also treated with DTIC before anti-CTLA-4 therapy—also harbored an increase in Signature 11 and progressed by 6 months [classified as no durable benefit according to (2)]. These data suggest that therapy may induce subclonal mutations that fail to drive an efficient antitumor response, although further data are needed to confirm this observation.

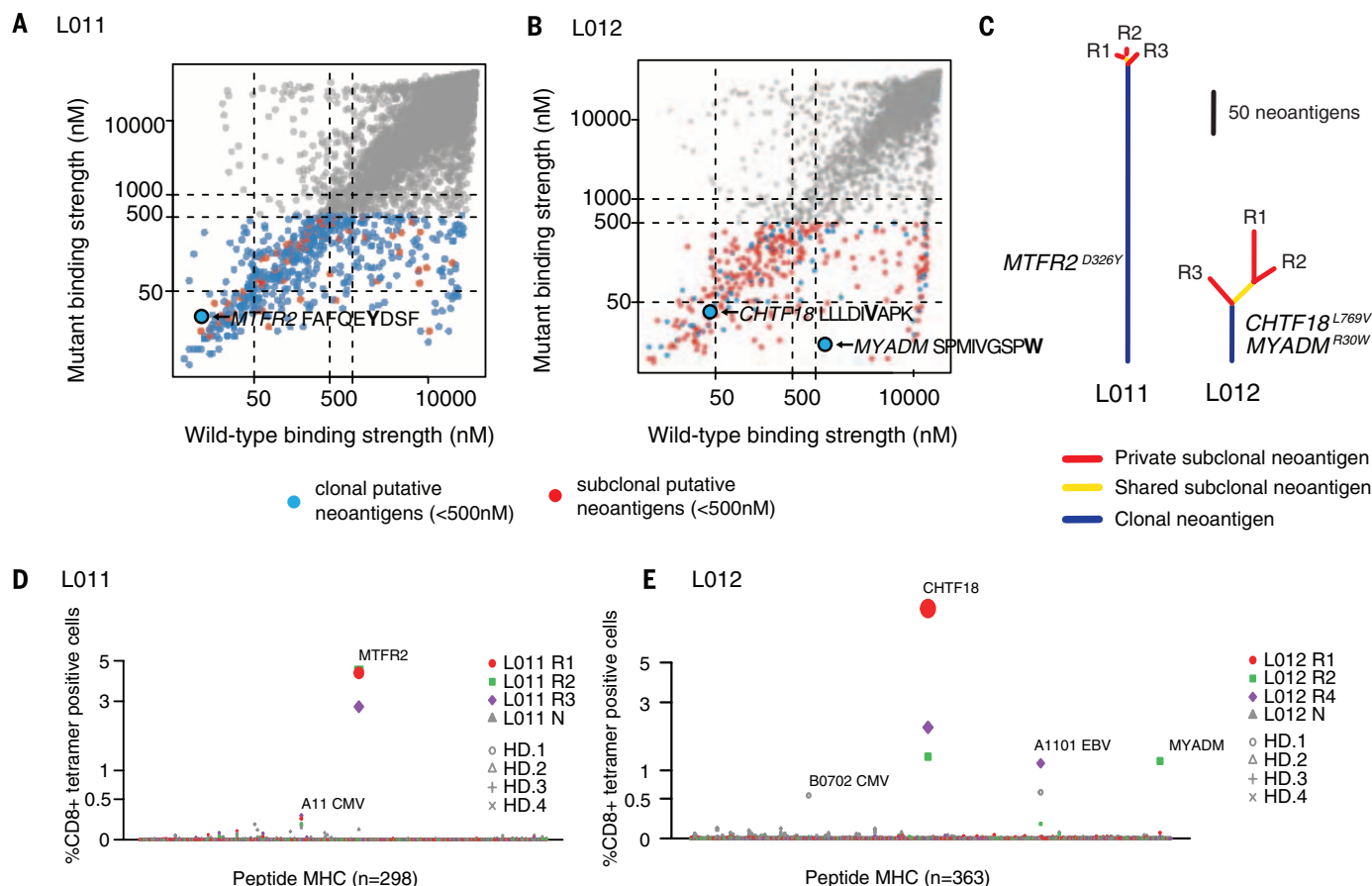


**Fig. 2. Prediction and identification of neoantigen-reactive T cells in NSCLC samples.** (A) Putative neoantigens predicted for all missense mutations in L011. The MTFR2<sup>D326Y</sup> neoantigen (FAFQEYDSF) is highlighted. (B) Putative neoantigens predicted for all missense mutations in L012. The CHTF18<sup>L769V</sup> neoantigen (LLLDIVAPK) and MYADM<sup>R30W</sup> neoantigen (SPMIVGSPW) are indicated. (C) Evolutionary trees for L011 and L012 based on predicted neoantigens. (D and E) MHC-

multimer screening of expanded, region-specific, tumor-infiltrating CD8<sup>+</sup> T lymphocytes and healthy donor (HD) CD8<sup>+</sup> PBMC controls with candidate neoantigens (L011,  $n = 288$ ; L012,  $n = 354$ ) and control HLA-matched viral peptides (L011,  $n = 10$ ; L012,  $n = 9$ ). Frequency of CD8<sup>+</sup> MHC-multimer-positive cells out of total CD3<sup>+</sup>CD8<sup>+</sup> tumor-infiltrating lymphocyte (TILs) is displayed for (D) and (E), with size of symbol increasing with frequency.

Last, we reasoned that T cells recognizing clonal antigens should be detectable in patients deriving favorable responses to checkpoint blockade. Previous analysis of peripheral blood lymphocytes (PBLs) from CA9903, a LUAD patient with an exceptional response to pembrolizumab, identified a CD8<sup>+</sup> T cell population in autologous PBLs, recognizing a predicted neoantigen resulting from a HERC1<sup>P3278S</sup> mutation (ASNASSAAK) (2). Consistent with the relevance of clonal neoantigens, this mutation was found to be present in 100% of cancer cells within the sequenced tumor (Fig. 4D). Similarly, analysis of peripheral blood mononuclear cells (PBMCs) from the patients with CR9309 and CR0095—melanomas that responded to anti-CTLA-4 therapy, resulting in prolonged patient survival—identified CD8<sup>+</sup> T cell populations, recognizing tumor-specific neoantigens (4). In both cases, the neoantigens linked to a T cell response were derived from clonal mutations, predicted to be present in 100% of cancer cells (Fig. 4, E and F).

Previous studies have reported that neoantigen burden influences sensitivity to immune checkpoint blockade in NSCLC and melanoma (2, 4, 17). However, the influence of ITH on this relationship has not been investigated. Our results, although limited by access to small and diverse patient cohorts and single-site biopsy data that likely overestimate the number of clonal mutations, suggest that clonal and subclonal neoantigens do not drive equally effective antitumor immunity. Indeed, using the described approach, despite screening more than 250 peptides against putative subclonal neoantigens, we were only able to detect T cells that recognize clonal neoantigens. Conceivably, higher-neoantigen ITH may result in lower antigen dosage as compared with homogeneous tumors with high clonal neoantigen burden, thus reducing the chances of identifying T cells reactive to subclonal neoantigens. Furthermore, in cases in which T cells reactive to subclonal neoantigens are generated, these will be unable to target all tumor cells, limiting overall tumor control.

The observation that certain anti-CTLA-4 refractory tumors were enriched for subclonal mutations caused by alkylating agents suggests that mutations induced by therapy may enhance total neoantigen burden but might not elicit an effective antitumor response, possibly because of the subclonal nature of the neoantigens that results from cytotoxic exposure. These results highlight the need to consider both the antitumor effects of alkylating agents as well as the potential risk of inducing subclonal mutations (19).

The identification of cytotoxic tumor-infiltrating T cells that recognize clonal mutations, shared by all tumor cells, might hold promise for adoptive therapy strategies to address the challenges of ITH (20). The extensive clonal mutational repertoire present in smoking-associated NSCLC (8, 21) could render this disease vulnerable to vaccination or T cell therapies targeting multiple clonal neoantigens, in combination with appropriate immune checkpoint modulation.

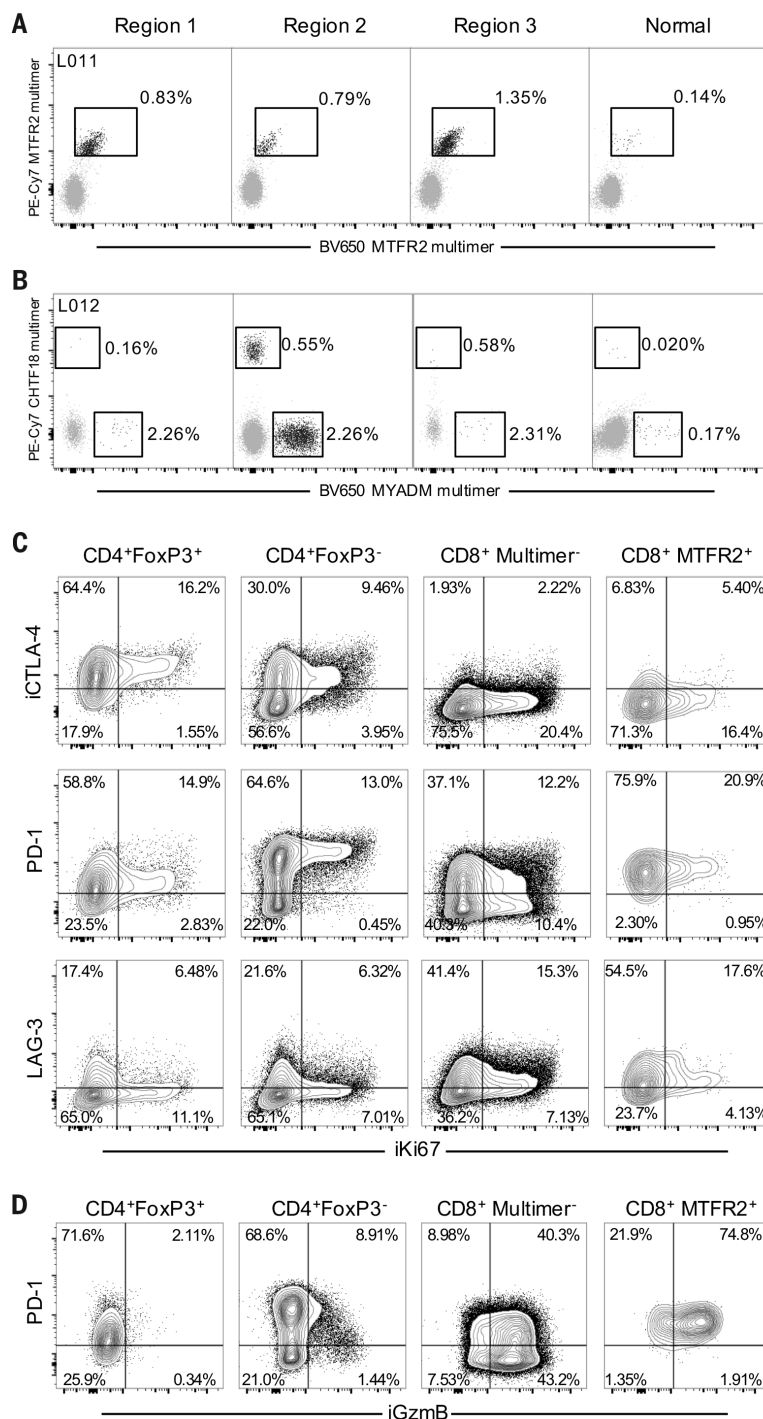
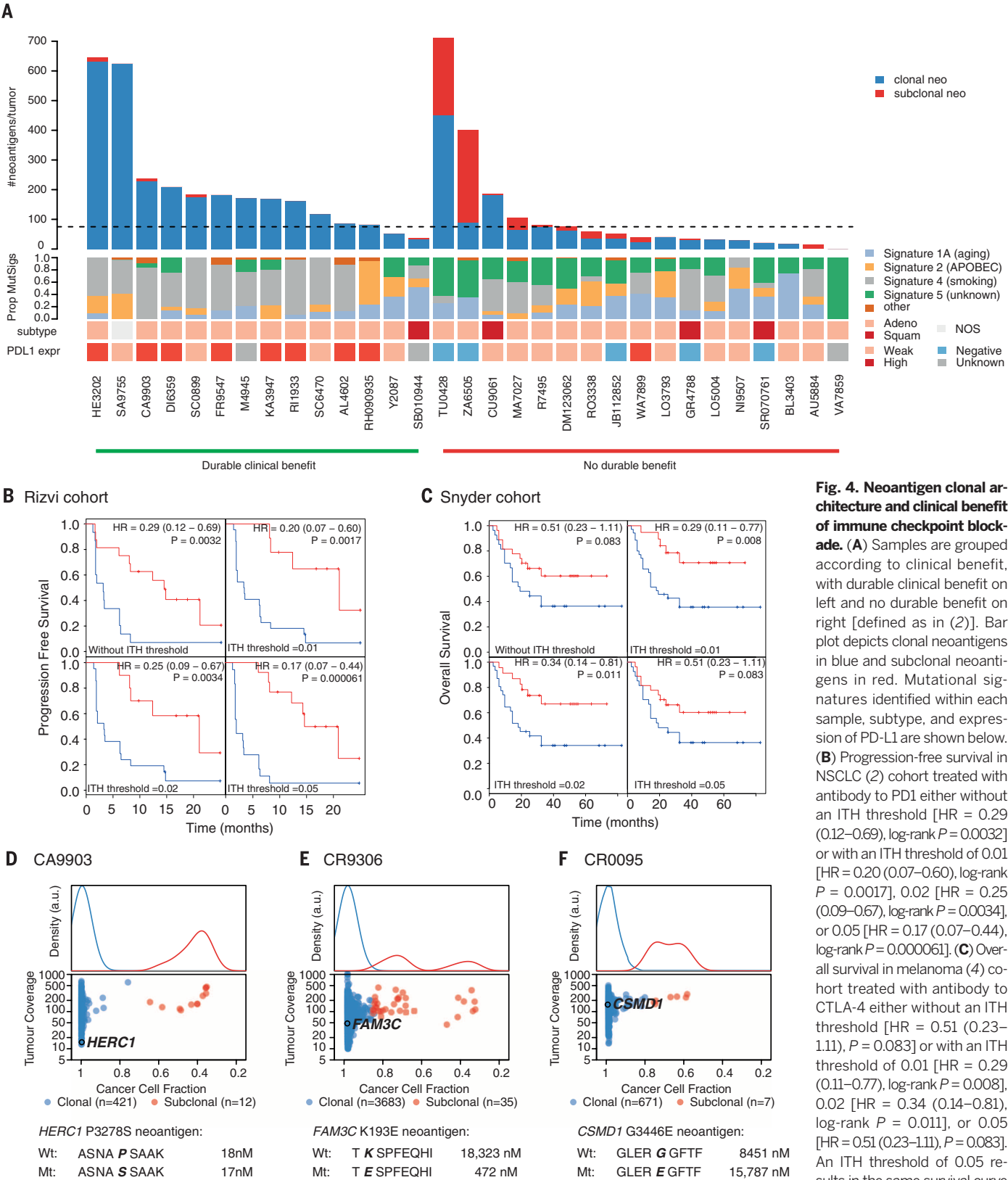


**Fig. 3. Identification and characterization of tumor-infiltrating neoantigen-reactive CD8<sup>+</sup> T cells in early-stage NSCLC.** (A) MHC-multimer analysis of nonexpanded, tumor-infiltrating CD8<sup>+</sup> T lymphocytes isolated from tumor regions 1 to 3 and normal lung tissue of patient L011 identifies CD8<sup>+</sup> TILs reactive to mutant MTRF2 peptide. (B) MHC-multimer analysis of nonexpanded, tumor-infiltrating CD8<sup>+</sup> T lymphocytes isolated from tumor regions 1 to 3 and normal lung tissue of patient L012 identifies two distinct populations of CD8<sup>+</sup> TILs reactive to mutant CHTF18 and MYADM peptide. The frequency of CD8<sup>+</sup> MHC-multimer-positive cells out of total CD3<sup>+</sup>CD8<sup>+</sup> TILs is displayed for (A) and (B). (C) Multiparametric flow cytometric analysis of tumor-infiltrating T lymphocyte subsets isolated from L011 region 3. Phenotypic data are representative of all tumor regions. Relative expression of iCTLA-4 (intracellular CTLA-4), surface PD-1, and surface LAG-3 by CD4<sup>+</sup>FoxP3<sup>+</sup> (regulatory T cell), CD4<sup>+</sup>FoxP3<sup>-</sup> (CD4 helper T cell), CD8<sup>+</sup> multimer-negative, and CD8<sup>+</sup> multimer-reactive (CD8<sup>+</sup> MTRF2<sup>+</sup>) T cells is displayed, plotted against iKi67 (intracellular Ki67). (D) Coexpression of PD-1 and iGzmB (intracellular granzyme B) by tumor-infiltrating T lymphocyte subsets isolated from L011 region 3.





## REFERENCES AND NOTES

1. H. Matsushita *et al.*, *Nature* **482**, 400–404 (2012).
2. N. A. Rizvi *et al.*, *Science* **348**, 124–128 (2015).
3. J. C. Castle *et al.*, *Cancer Res.* **72**, 1081–1091 (2012).
4. A. Snyder *et al.*, *N. Engl. J. Med.* **371**, 2189–2199 (2014).
5. P. F. Robbins *et al.*, *Nat. Med.* **19**, 747–752 (2013).
6. T. N. Schumacher, R. D. Schreiber, *Science* **348**, 69–74 (2015).
7. M. Greaves, *Cancer Discovery* **5**, 806–820 (2015).
8. E. C. de Bruin *et al.*, *Science* **346**, 251–256 (2014).
9. M. Jamal-Hanjani *et al.*, *Ann. Oncol.* **mdw037** (2016).
10. M. S. Lawrence *et al.*, *Nature* **505**, 495–501 (2014).
11. M. S. Rooney, S. A. Shukla, C. J. Wu, G. Getz, N. Hacohen, *Cell* **160**, 48–61 (2015).
12. S. A. Shukla *et al.*, *Nat. Biotechnol.* **33**, 1152–1158 (2015).
13. Materials and methods are available as supplementary materials on Science Online.
14. L. T. Nguyen, P. S. Ohashi, *Nat. Rev. Immunol.* **15**, 45–56 (2015).
15. S. R. Hadrup *et al.*, *Nat. Methods* **6**, 520–526 (2009).
16. S. Read, V. Malmström, F. Powrie, *J. Exp. Med.* **192**, 295–302 (2000).
17. E. M. Van Allen *et al.*, *Science* **350**, 207–211 (2015).
18. L. B. Alexandrov *et al.*, *Nature* **500**, 415–421 (2013).
19. B. E. Johnson *et al.*, *Science* **343**, 189–193 (2014).
20. T. A. Yap, M. Gerlinger, P. A. Futreal, L. Pusztai, C. Swanton, *Sci. Transl. Med.* **4**, 127ps10 (2012).
21. J. Zhang *et al.*, *Science* **346**, 256–259 (2014).

## ACKNOWLEDGMENTS

C.S. is a senior Cancer Research UK (CRUK) clinical research fellow and is funded by CRUK (TRACERx), the CRUK Lung Cancer Centre of Excellence, Stand Up 2 Cancer Laura Ziskin prize (SU2C), the Rosetrees Trust, NovoNordisk Foundation (ID 16584), the Prostate Cancer Foundation, the Breast Cancer Research Foundation, the European Research Council (THESEUS), and EU FP7 (PREDICT). S.A.Q. is funded by a CRUK Career Development Fellowship, CRUK Biotherapeutic Programme Grant, World Wide Cancer Research, and a Cancer Research Institute Investigator Award. A.J.S.F. receives support from the Sam Keen Foundation. R.R., N.M., N.J.B., and G.A.W. are funded by the TRACERx CRUK grant. T.B.K.W. is funded by the FP7-People-2013-ITN [grant (2013)607722 – PloidyNet]. C.T.H. is funded by the Rosetrees Trust. C.J.W. is a Scholar of the Leukemia and Lymphoma Society and acknowledges support from the Blavatnik Family Foundation, NIH/National Heart, Lung, and Blood Institute (grant 1R01CA155010-02) and NIH/National Cancer Institute (grants 1R01CA182461-01 and 1R01CA184922-01). S.S. is funded by the Cancer Research UK–UCL Centre, and M.J.H. is funded by a CRUK–UCL Centre Clinical Research Fellowship. A.A. is funded by the Cancer Research UK–UCL Centre Cancer Immuno-Therapy Accelerator Award. We thank N. Hacohen and S. Turajlic for helpful advice on the manuscript. This research is supported by the National Institute for Health Research, the University College London Hospitals Biomedical Research Centre, and the Cancer Research UK University College London Experimental Cancer Medicine Centre. Certain data were received under a material transfer agreement with Memorial Sloan Kettering Cancer Center. Data from multiregion sequenced NSCLC are available at the European Bioinformatics Institute (accession no. EGAS00001000809). Data from the Rizvi cohort (2) are available at the database of Genotypes and Phenotypes (dbGAP) (accession no. phs000980.v1.p1). Data from the Snyder cohort (4) are available at dbGAP (accession no. phs001041.v1.p1). Data from the Van Allen cohort (17) are available at dbGAP (accession no. phs000452.v2.p1). The results published here are in part based on data generated by a TCGA pilot project established by the National Cancer Institute and National Human Genome Research Institute. The data were retrieved through dbGAP authorization (accession no. phs000178.v9.p8). Information about TCGA and the investigators and institutions that constitute the TCGA research network can be found at <http://cancergenome.nih.gov>. C.S. is a paid advisor for Janssen, Boehringer Ingelheim, Ventana, Novartis, Roche, Sequenom, Natera, Grail, Apogen Biotechnologies, Epic Biosciences, and the Sarah Cannon Research Institute. D.S. is a paid advisor for Bristol-Myers Squibb, Roche, Novartis, Merck, and Amgen. B.S. is a paid advisor for Bristol-Myers Squibb. T.A.C. is a cofounder of and holds equity in Gritstone Oncology; is a paid

advisor for Geneocea, OncoSpire, and Cancer Genetics; and receives funding from Bristol-Myers Squibb for research on the genomics of immune response. N.A.R. is a cofounder of and holds equity in Gritstone Oncology. E.M.V.A. is a paid advisor for Syapse, Roche Ventana, Takeda, and Third Rock Ventures. M.D.H. is a paid advisor for Bristol-Myers Squibb, Merck, Genentech, AstraZeneca, and Neon. J.D.W. is a paid advisor for Bristol-Myers Squibb. L.A.G. is a paid scientific advisor for Novartis, Boehringer Ingelheim, Foundation Medicine, and Warp Drive Bio. C.S., N.M., R.R., S.A.Q., and K.S.P. are co-inventors on UK patent applications (1516047.6, 1601098.5, 1601098.5, and 1601099.3) filed by Cancer Research Technology relating to methods for identifying and targeting neoantigens, methods of predicting prognosis of cancer

patients, and/or identifying cancer patients who will benefit from treatment that involves determining the number of neoantigens.

## SUPPLEMENTARY MATERIALS

[www.sciencemag.org/content/351/6280/1463/suppl/DC1](http://www.sciencemag.org/content/351/6280/1463/suppl/DC1)  
Materials and Methods  
Figs. S1 to S7  
Tables S1 to S5  
References (22–38)

15 August 2015; accepted 11 February 2016  
Published online 3 March 2016  
10.1126/science.aaf1490

## TRANSPORTER FUNCTION

# Direct observation of proton pumping by a eukaryotic P-type ATPase

Salome Veshaguri,<sup>1,2,3,4</sup> Sune M. Christensen,<sup>1,2,3,4\*</sup> Gerdi C. Kemmer,<sup>5</sup> Garima Ghale,<sup>1,2,3,4</sup> Mads P. Møller,<sup>1,2,3,4</sup> Christina Lohr,<sup>1,2,3,4</sup> Andreas L. Christensen,<sup>1,2,3,4</sup> Bo H. Justesen,<sup>5</sup> Ida L. Jørgensen,<sup>5</sup> Jürgen Schiller,<sup>6</sup> Nikos S. Hatzakis,<sup>1,2,3,4</sup> Michael Grabe,<sup>7</sup> Thomas Günther Pomorski,<sup>5</sup> Dimitrios Stamou<sup>1,2,3,4,†</sup>

In eukaryotes, P-type adenosine triphosphatases (ATPases) generate the plasma membrane potential and drive secondary transport systems; however, despite their importance, their regulation remains poorly understood. We monitored at the single-molecule level the activity of the prototypic proton-pumping P-type ATPase *Arabidopsis thaliana* isoform 2 (AHA2). Our measurements, combined with a physical nonequilibrium model of vesicle acidification, revealed that pumping is stochastically interrupted by long-lived (~100 seconds) inactive or leaky states. Allosteric regulation by pH gradients modulated the switch between these states but not the pumping or leakage rates. The autoinhibitory regulatory domain of AHA2 reduced the intrinsic pumping rates but increased the dwell time in the active pumping state. We anticipate that similar functional dynamics underlie the operation and regulation of many other active transporters.

Electrochemical gradients across cellular membranes control many essential biological processes. These gradients are generated by primary active transporters and are used to drive the exchange of other solutes through secondary active transporters and to facilitate signaling through ion channels (1). Patch clamp recording has made it possible to observe the functional dynamics of single ion channels, revealing discrete on and off states, subconductance states, and other mechanistically important features that macroscopic experiments cannot probe (2). However, despite extensive structural

and biochemical efforts (3), we currently lack a similar depth of understanding of transporters, because they in general do not produce electrically detectable single-molecule transport signals (4–8). We monitored at the single-molecule level the functional dynamics of a eukaryotic primary active transporter, *Arabidopsis thaliana* H<sup>+</sup>-adenosine triphosphatase (ATPase) isoform 2 (AHA2, referred to as the proton pump), which is responsible for energizing the plasma membrane of plants and fungi (figs. S1 and S2) (3, 9). This provided insights into how the activity of P-type ATPases is modulated by autoregulatory terminal domains (R domains) and pH gradients (10, 11).

We used total internal reflection fluorescence (TIRF) microscopy to image with high throughput single nanoscopic lipid vesicles tethered to a solid support (Fig. 1, A and B, and figs. S3 and S4). Tethering was accomplished with a biotin/neutravidin protocol (12), which maintains the native function and diffusivity of reconstituted transmembrane proteins (13) and the vesicles' spherical morphology (14) and low passive ion permeability (15). The fluorescence intensity of all single vesicles was quantitatively converted to pH (fig. S5) and tracked over periods of up to 30 min.

Initial studies were carried out on the well-studied activated form of AHA2, which lacks the

<sup>1</sup>Bionanotechnology and Nanomedicine Laboratory, University of Copenhagen, Copenhagen, Denmark. <sup>2</sup>Department of Chemistry, University of Copenhagen, Copenhagen, Denmark. <sup>3</sup>Nano-Science Center, University of Copenhagen, Copenhagen, Denmark. <sup>4</sup>Lundbeck Foundation Center Biomembranes in Nanomedicine, University of Copenhagen, Copenhagen, Denmark. <sup>5</sup>Centre for Membrane Pumps in Cells and Disease - PUMPKIN, Department of Plant and Environmental Sciences, University of Copenhagen, Frederiksberg, Denmark. <sup>6</sup>Institute of Medical Physics and Biophysics, Faculty of Medicine, University of Leipzig, Leipzig, Germany. <sup>7</sup>Cardiovascular Research Institute, Department of Pharmaceutical Chemistry, University of California, San Francisco, CA 94143, USA.

\*Present address: Novozymes A/S, 2880 Bagsvaerd, Denmark.

†Corresponding author. E-mail: [stamou@nano.ku.dk](mailto:stamou@nano.ku.dk)



flexible C-terminal autoinhibitory R domain (AHA2<sup>R</sup>) (Fig. 1A and figs. S1 to S3) (9). Initialization of H<sup>+</sup> pumping into the vesicle lumen was triggered by the addition of ATP and Mg<sup>2+</sup>, which are non-membrane-permeable and thus only activate proton pumps with an outward-facing ATP-binding domain (Fig. 1A) (12). Consistent with this, we never observed luminal alkalinization (Fig. 1C). Acidification kinetics reached a plateau of well-defined pH ( $\Delta\text{pH}_{\text{max}}$ ) as a result of a dynamic steady state, in which active pumping (influx) of protons matched the passive leakage (efflux) of protons through the membrane due to the buildup of a proton motive force (16). As expected, addition of the protonophore CCCP collapsed the H<sup>+</sup> gradients (Fig. 1C), whereas controls performed without Mg<sup>2+</sup>, ATP, or AHA2<sup>R</sup> showed no response (fig. S6D). Furthermore, the activity of the pump was blocked by the addition of the specific inhibitor vanadate (11), and it decayed after ATP and Mg<sup>2+</sup> were flushed out (fig. S7). To control for potential artifacts arising from the surface tethering of vesicles, we performed a side-by-side comparison with vesicles suspended in solution, which proved indistinguishable within experimental uncertainties (Fig. 1C and fig. S6). Taken together, these results demonstrate that we were able to observe the AHA2<sup>R</sup>-mediated and ATP-fueled pumping of protons against their concentration gradient into the lumen of single vesicles. The single-vesicle experiments revealed a heterogeneity of acidification rates and  $\Delta\text{pH}_{\text{max}}$  values between vesicles (Fig. 1C) that remain masked in the ensemble averages (16).

At the low protein-to-lipid molar ratio (1:12,000) used in our experiments, 84% of vesicles exhibited no detectable pH changes (Fig. 1C and Fig. 2A, top trace) indicating the absence of active pumps and thus suggesting that there are only a few active pumps in each of the remaining vesicles whose pH changed over time (hereafter termed active vesicles). We inspected the pH changes in the 16% of active vesicles and indeed found that all of them exhibited the hallmark of single-molecule behavior; i.e., stochastic changes between discrete states (Fig. 2A). Because the passive leakage rates of the vesicles are constant over time (fig. S10), these data demonstrate that the individual proton pumps are stochastically transitioning between active and inactive states. This behavior is termed functional dynamics (17–24) and is key to the function and regulation of ion channels (25).

Further examination of all active vesicle traces revealed that ~60% of them reverted back to the zero  $\Delta\text{pH}$  baseline after switching off, strongly suggesting the presence of only one molecule, because it is improbable for many molecules to switch off simultaneously (Fig. 2A). In the remaining traces (~40%), we observed two or three discrete plateaus, a feature that has been observed in all studies of single channels to date and has been interpreted to demonstrate that the activity of multiple single molecules can be discretely resolved. The latter conclusion was further supported by experiments in which titration of the protein-to-lipid ratio modulated the percentage of multiple plateaus (fig. S5G), excluding the possibility that

multiple plateaus represent multiple single-molecule activity states. These observations allowed us to unambiguously identify the traces resulting from a single active proton pump, which we then selected for further analysis. The activity of single proton pumps was amplified and reported by ~10<sup>3</sup> pH-sensitive fluorophores (figs. S3 and S4) (16), circumventing the issue of photobleaching that fundamentally restricts most fluorescence studies of single molecules.

Dynamic transitions between active and inactive states were also observed in experiments with wild-type AHA2 (Fig. 2C), demonstrating that they are not solely a property of the truncated version. Here ~80% of all vesicles were inactive, whereas ~73% of those that showed activity had a single plateau indicating a single molecule (Fig. 2D). With wild-type AHA2, we succeeded in using a SNAP-tag to fluorescently label the protein and count directly the number of proteins per vesicle (Fig. 2E). This allowed us to observe activity dynamics and directly count the number of labeled proteins at the same time on the same

vesicles (Fig. 2C and 2E). We then estimated the labeling efficiency and the probability that a proton pump was active (12). We were thus able to quantitatively convert the bleach-step distribution to a distribution of active molecules per vesicle and demonstrated that  $70 \pm 15\%$  of active proteoliposomes carried one active molecule (Fig. 2F). This was in quantitative agreement with the distribution of activity plateaus (~73%) (Fig. 2D), providing an additional demonstration that we can resolve and record the functional dynamics of the proton pump at the single-molecule level.

The activity of the proton pump, and probably other active transporters, is thus not constant in time (Fig. 2). Therefore, for transporters (just like ion channels), the rates measured in macroscopic experiments are the product of the active-state probability and the intrinsic pumping rate. To quantitatively analyze the kinetics and dynamics of pumping, we constructed a physical model of a single vesicle (12), which accounts for several parameters that affect the acidification kinetics, including passive and active ionic fluxes across

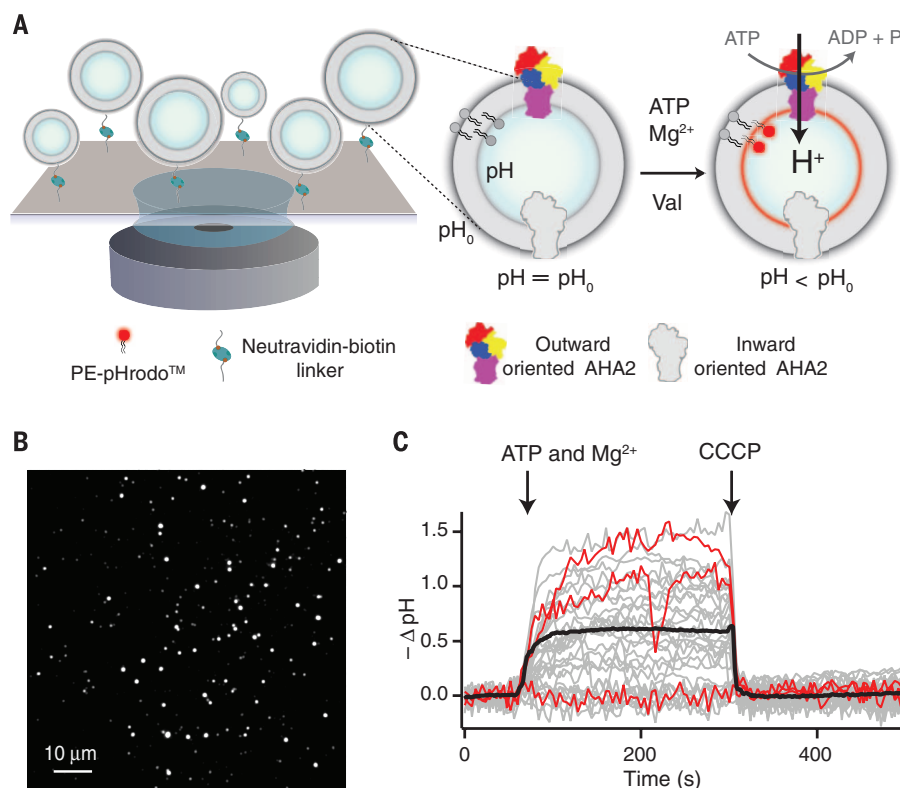


**Fig. 1. Imaging proton pumping into the lumen of single surface-tethered vesicles using TIRF microscopy.** (A) Illustration of AHA2 reconstituted vesicles tethered to a passivated glass surface and imaged on and individual basis with TIRF microscopy. Zoom: Extravesicular addition of both ATP and Mg<sup>2+</sup> activated exclusively outward-facing AHA2 molecules, triggering H<sup>+</sup> pumping in the vesicle lumen. We quantified changes in the vesicular H<sup>+</sup> concentration by calibrating the response of the lipid-conjugated pH-sensitive fluorophore pHrodo. Valinomycin was always present to mediate K<sup>+</sup>/H<sup>+</sup> exchange and prevent the buildup of a transmembrane electrical potential. (B) TIRF image of single vesicles tethered on a passivated glass slide. (C) Acidification kinetics of single vesicles upon addition of ATP and Mg<sup>2+</sup>. Red traces highlight three representative signals from single vesicles, showcasing the absence of transport activity, the continuous pumping of protons, and fluctuations in proton-transport activity. The black trace is the average of ~600 single-vesicle traces. As expected, addition of the protonophore CCCP collapsed the proton gradient established by AHA2<sup>R</sup>.

the membrane, proton buffering in the lumen, vesicle size, and buildup of membrane potential (Fig. 3A) (26). Proton pumping is modeled with a fixed rate ( $I_p$ ), a lifetime ( $t_{on}$ ), and time between pumping events ( $t_{off}$ ) (Fig. 3, A and B). The vesicle is assumed to have a passive membrane permeability to protons ( $P_{leak}$ ), which is constant over time, as revealed by control experiments (fig. S10). The stochastic switching of the pump between active and inactive states was extracted directly from the traces and used as time-dependent input to the model. The model is constrained to fit the entire trace, and it provides a realistic description of the full electrochemical gradient and a direct estimation of the absolute numbers of pumped and leaked ions.

Initially, all experimental traces were fit with the model by varying two parameters:  $I_p$  and

$P_{leak}$ . This provided a good quantitative description of the majority of AHA2<sup>R</sup> traces (~65% of 126 counts, fig. S8); however, it systematically underestimated the observed leaking rates for the remaining traces (Fig. 3B, blue line), suggesting the existence of an additional proton-leaking route apart from passive leakage through the membrane (fig. S8). Indeed, leakage of ions through transporters has been reported before; e.g., for P- and V-type ATPases (27, 28). To test this hypothesis, we collected all lifetimes of exponential fits to the leakage kinetics from traces transitioning between active and inactive states. The histogram of leakage lifetimes (fig. S9C) had two clearly separated peaks: one that according to control experiments corresponded to passive leakage through the membrane (a transmembrane leak) and another that was approximately 20

times faster (figs. S9 and S10). The latter peak was specifically inhibited by the addition of vanadate, which locked the pump in the E2 state (11) (fig. S9D), demonstrating that the leak is not passively mediated by the membrane (or the protein/membrane interface) but by the pump itself. Because vanadate is membrane-impermeable, we can exclude the possibility that the fast-leak component originated from pumps with the opposite orientation, because they would not be blocked by vanadate. We thus modified the model to include a time-dependent transprotein proton leak ( $P_{AHA2}$ ), which turns on once pumping stops and turns off at the beginning of the next pumping cycle (Fig. 3C, blue dotted line). As expected, the revised model considerably improved the fits of the remaining traces (Fig. 3B, red line, and fig. S8).

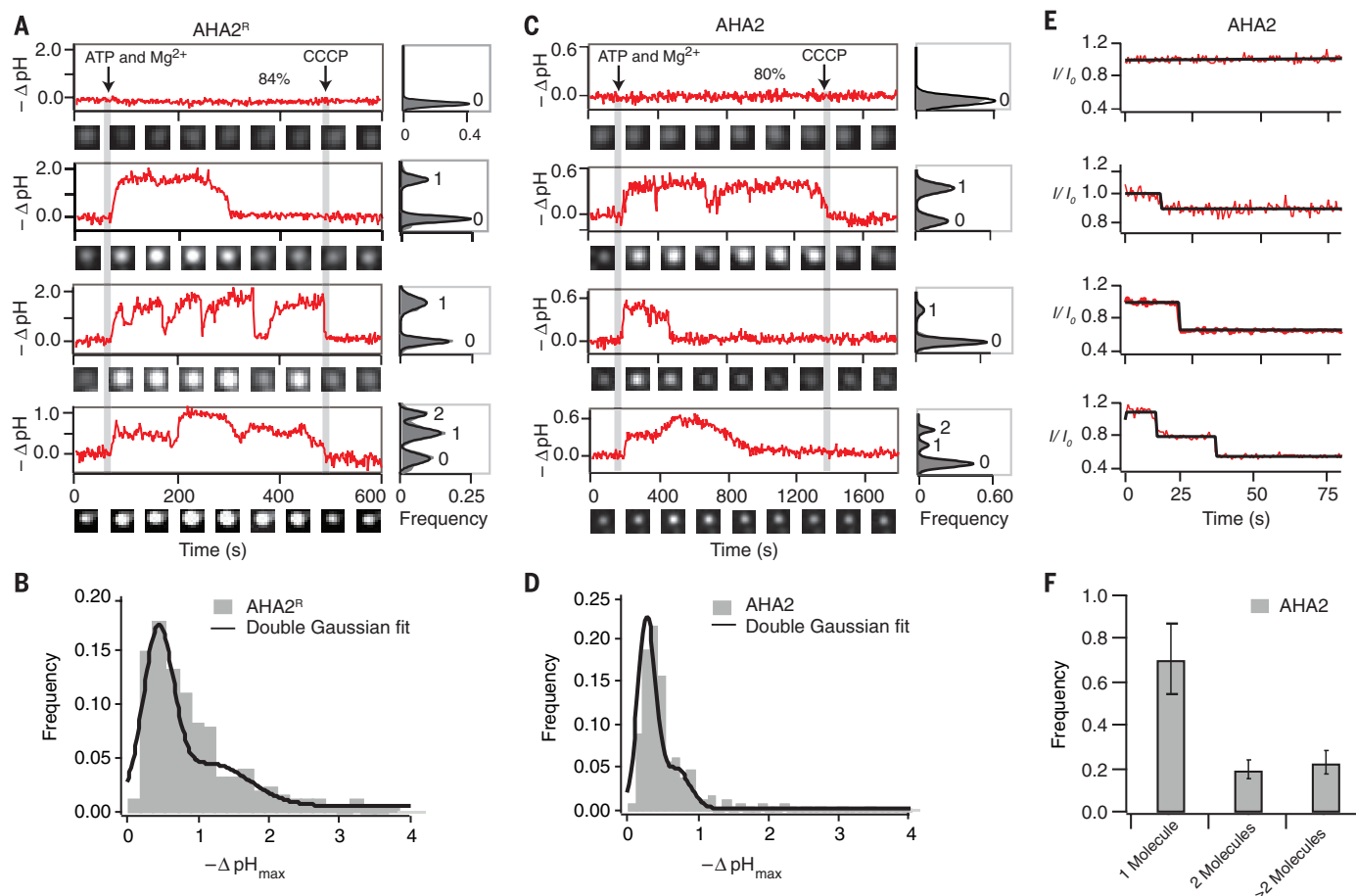


**Fig. 2. Single-molecule observation of proton pumping reveals active and inactive states.** (A) Typical examples of pH changes inside individual AHA2<sup>R</sup> reconstituted vesicles. ATP and Mg<sup>2+</sup> (2 mM) were added to initiate proton pumping, and CCCP (5  $\mu$ M) was added to collapse the pH gradients. Traces show  $-\Delta$ pH defined as a difference between the initial and final pH. Images of each respective liposome at different time points are shown below each trace. At the right-hand side of the traces, we plotted histograms of pH plateaus numbered to indicate the number of active pumps per vesicle. The pH inside the majority of vesicles showed no changes indicating the absence of functional transporter molecules (top panel). For the majority of active vesicles, we observed intermittent H<sup>+</sup> pumping, indicating the presence of single molecules (middle panels). The observation of two discrete steady-state pH plateaus in

single-vesicle traces indicated the occasional presence of two active pumps per single vesicle (bottom panel). (B) Population histogram of pH plateaus for AHA2<sup>R</sup>-reconstituted vesicles ( $n = 3$ , where hereafter  $n$  is the number of independent experiments). (C and D) Same as in (A) and (B) but for full-length AHA2. For (D),  $n = 2$ . Labeling of AHA2 with Alexa Fluor 647 enabled counting on the same vesicles of both the number of labeled AHA2 proteins (E) and of the respective activity dynamics (C). (F) The histogram of active proteins per vesicle was calculated from step-bleaching analysis of the data in (E) that was corrected for labeling efficiency and the probability that a proton pump is active (12). The two independent methods for estimating the number of active molecules agreed that ~70% of vesicles containing a protein have one active proton pump.



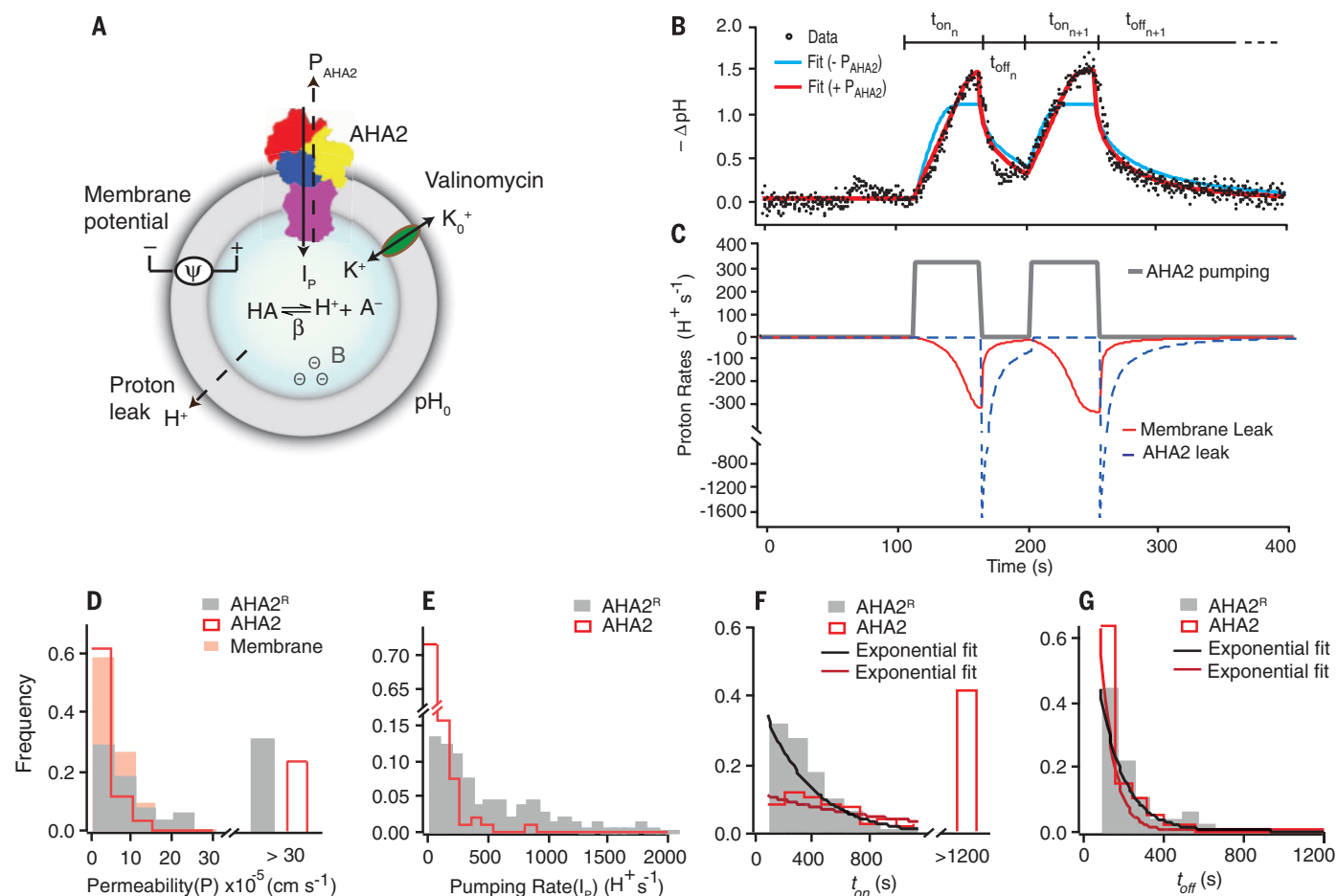
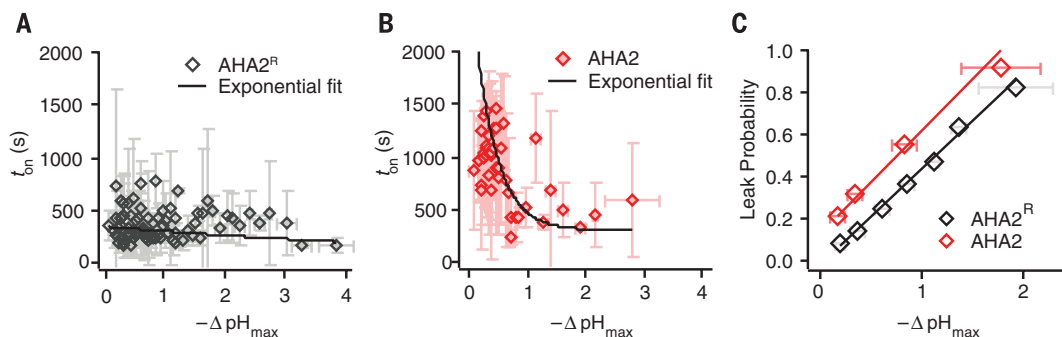


**Fig. 3. Modeling active, inactive, and leaky states and their role in auto-inhibiting proton pumps.** (A) The main parameters of the physical model we used to fit changes in the vesicular pH were pumping rate ( $I_p$ ), protein-associated leak ( $P_{\text{AHA2}}$ ), membrane leak ( $P_{\text{leak}}$ ), valinomycin-induced  $\text{K}^+$  permeability ( $P_{\text{K}^+}$ ), buffering capacity in the interior of the vesicle ( $\beta$ ), and electrical potential across the membrane ( $\Psi$ ) (12). (B) Example of a typical proton pumping trace and respective fits without (blue) and with (red) a transprotein proton leak. A threshold in the first derivative of the pH kinetics (12) was used to define the lifetime of the active state  $t_{\text{on}}$  and the time between pumping events  $t_{\text{off}}$ . (C) Temporal evolution of the proton pumping rate (gray) and the proton

efflux rates due to passive membrane (red) leakage and transprotein backflow (blue) for the pH trace shown in (B). (D) Histogram of proton permeability associated with the membrane, AHA2, and AHA2<sup>R</sup>. Respective counts were 95, 37, and 45. (E) Histogram of pumping rates for AHA2<sup>R</sup> and AHA2. Respective counts were 126 and 95. (F) Histogram of  $t_{\text{on}}$  for AHA2<sup>R</sup> and AHA2. Respective counts were 241 and 134. The bar at  $>1200$  s shows the number of traces that did not switch in the duration of the experiment. (G) Histogram of  $t_{\text{off}}$  for AHA2<sup>R</sup> and AHA2. Respective counts were 69 and 39. For AHA2<sup>R</sup> and AHA2, respectively, the number of independent experiments was 3 and 2 and the number of individual proteoliposomes analyzed was 126 and 95.

#### Fig. 4. Regulation of proton pumping by pH gradients.

(A and B) Relation between  $t_{\text{on}}$  and the maximal pH gradient for AHA2<sup>R</sup> and AHA2, respectively. Each data point represents the average of three consecutive values. Error bars represent corresponding standard deviations. The decay constants from the error-weighted exponential fits to the data are  $6.9 \pm 2.0$  s and  $0.4 \pm 0.1$  s for (A) and (B), respectively, where uncertainties represent 95% confidence intervals from the fits. (C) Probability of observing a transprotein leak as a function of pH gradient. For AHA2<sup>R</sup> and AHA2, data were binned with 0.25 and 0.5 pH units; the number of independent experiments and individual proteoliposomes analyzed was the same as in Fig. 3. Spearman's rank order correlation coefficients  $\rho$  (126) = 0.40,  $P = 10^{-4}$ , and  $\rho$  (95) = 0.30,  $P = 0.03$  indicated a strong positive correlation between leakage probability and  $\Delta\text{pH}_{\text{max}}$  for both AHA2<sup>R</sup> and AHA2.



respectively, where uncertainties represent 95% confidence intervals from the fits. (C) Probability of observing a transprotein leak as a function of pH gradient. For AHA2<sup>R</sup> and AHA2, data were binned with 0.25 and 0.5 pH units; the number of independent experiments and individual proteoliposomes analyzed was the same as in Fig. 3. Spearman's rank order correlation coefficients  $\rho$  (126) = 0.40,  $P = 10^{-4}$ , and  $\rho$  (95) = 0.30,  $P = 0.03$  indicated a strong positive correlation between leakage probability and  $\Delta\text{pH}_{\text{max}}$  for both AHA2<sup>R</sup> and AHA2.

Next, we quantitated proton permeabilities by fitting the kinetics with the model. The average transmembrane leak  $P_{\text{leak}}$  (Fig. 3D and fig. S11) was  $\sim 7 \times 10^{-5}$  cm/s, which is in line with previous measurements and estimates (26), and the average transprotein leak  $P_{\text{AHA2}}$  had a similar value ( $\sim 46 \times 10^{-5}$  cm/s) (Fig. 3D). However, when normalized for surface area, the transprotein proton current was greater than the transmembrane by a factor of  $\sim 10^4$ .

The inhibitory R domain of AHA2 has been shown to reduce the net macroscopic proton transport rate by  $\sim$ twofold (10, 11). In order to elucidate the mechanisms underlying this regulation, we characterized the activity of the proton pump with and without the R domain. Counterintuitively, the autoinhibitory R domain increased the total time the transporter spent in the active state, both by increasing  $t_{\text{on}}$   $\sim$ threefold (from 337 to 951 s,  $P = 10^{-19}$ ) and by decreasing  $t_{\text{off}}$   $\sim$ 0.5-fold (from 121 to 65 s,  $P = 0.05$ ) (decay constants of exponential fits to the distributions in Fig. 3, F and G; unless otherwise stated,  $P$  is a Kolmogorov-Smirnov test of statistical similarity between two distributions). Thus, the probability of finding the pump in an active state  $P_{\text{on}} = t_{\text{on}}/(t_{\text{on}} + t_{\text{off}})$  increased  $\sim 200\%$  for AHA2 (from  $0.35 \pm 0.05$  to  $0.76 \pm 0.06$ ). Importantly, 100% of AHA2<sup>R</sup> and  $\sim 60\%$  of AHA2 molecules switched on/off during our observation period, highlighting the fact that functional dynamics is a dominant property of this system (Fig. 3F). The R domain also had a pronounced effect on the overall intrinsic transport rates of the pump, which were reduced by  $\sim 10$ -fold as compared to AHA2<sup>R</sup> (from 928 to 85 protons/s, average values,  $P = 10^{-20}$ ) (Fig. 3E). In addition, the R domain promoted an overall decrease in the transprotein leak ( $\sim 1.4$ -fold,  $P = 0.005$ ) (Fig. 3D).

The activity of the pump was also regulated by the pH gradients established across the membrane during proton pumping. Increasing  $\Delta\text{pH}_{\text{max}}$  decreased by  $>$ twofold the lifetime of the active state, but only for the wild type (Fig. 4A, B). This regulation seems to be transmitted allosterically across the bilayer, because the R domain of AHA2 is facing the vesicle exterior, where the pH remains constant. In addition, traces with larger  $\Delta\text{pH}_{\text{max}}$  had a dramatic eightfold increase (from 0.1 to 0.8) in the probability of a transprotein leak for both forms of AHA2 (Fig. 4C). Thus, regulation by pH gradients can manifest through two mechanistically distinct processes that reduce the net average proton transport: reduction of the pumping lifetime and increase of the probability of a transprotein leak, whereby only the former is encoded in the R domain.

Our observations of proton transport and leakage dynamics at the single-molecule level also provide critical insights into the ATP/H<sup>+</sup> stoichi-

ometry (27, 28). Ensemble average experiments have reported that the buildup of pH gradients can in general alter the stoichiometry of transport and therefore pumping rates (27, 28). Contrary to expectation, we found that the intrinsic (single-molecule) pumping rate remained constant for gradients as large as 2 pH units (Fig. 3, B and C, and fig. S12C). As discussed above, pH gradients did reduce the net proton transport, but primarily by increasing the probability of a downhill transprotein leak (Fig. 4C). However, because the transprotein leak takes place once the pump has switched to the inactive state (Fig. 3C, S9), it does not affect the actual stoichiometry of active transport. In contrast, the R domain reduced the intrinsic pumping rates by  $\sim 10$ -fold (Fig. 4E). Because the R domain does not significantly affect the ensemble average ATPase activity (10, 29), our measurements suggest that the R domain can reduce the stoichiometry of active transport by a factor of  $\sim 10$  (or 20 if we correct for the change in  $P_{\text{on}}$ ) (11). Finally, we note that our measurements of proton transport were integrated over thousands of Post-Albers catalytic cycles per second per single molecule. A better mechanistic understanding of these processes would ultimately require direct measurement of the stoichiometry at the level of single turnover cycles or careful molecular simulations.

We have developed a technique to observe, in a highly parallel manner, uphill substrate transport mediated by single transporter molecules into single nanoscopic lipid vesicles. Our measurements revealed the existence and the dynamics of several distinct functional states (active, inactive, and leaky) that together defined the activity and regulation of the proton pump, and that, we anticipate, underlie the operation of many other primary and secondary active transporters. The assays introduced here render these processes accessible to direct experimental observation.

## REFERENCES AND NOTES

1. F. Ashcroft, D. Gadsby, C. Miller, *Philos. Trans. R. Soc. London Ser. B* **364**, 145–147 (2009).
2. E. Neher, B. Sakmann, *Nature* **260**, 799–802 (1976).
3. J. P. Morth et al., *Nat. Rev. Mol. Cell Biol.* **12**, 60–70 (2011).
4. L. J. DeFelice, T. Goswami, *Annu. Rev. Physiol.* **69**, 87–112 (2007).
5. R. Peters, *Annu. Rev. Biophys. Biomol. Struct.* **32**, 47–67 (2003).
6. A. Tonnesen, S. M. Christensen, V. Tkach, D. Stamou, *Biophys. J.* **106**, 201–209 (2014).
7. R. Watanabe et al., *Nat. Commun.* **5**, 4519 (2014).
8. M. Li et al., *J. Am. Chem. Soc.* **137**, 16055–16063 (2015).
9. B. P. Pedersen, M. J. Buch-Pedersen, J. P. Morth, M. G. Palmgren, P. Nissen, *Nature* **450**, 1111–1114 (2007).
10. M. G. Palmgren, C. Larsson, M. Sommarin, *J. Biol. Chem.* **265**, 13423–13426 (1990).
11. M. G. Palmgren, P. Nissen, *Annu. Rev. Biophys.* **40**, 243–266 (2011).

12. See materials and methods and supplementary information on Science Online.
13. S. Mathiasen et al., *Nat. Methods* **11**, 931–934 (2014).
14. P. M. Bendix, M. S. Pedersen, D. Stamou, *Proc. Natl. Acad. Sci. U.S.A.* **106**, 12341–12346 (2009).
15. D. Stamou, C. Duschl, E. Delamarque, H. Vogel, *Angew. Chem. Int. Ed. Engl.* **42**, 5580–5583 (2003).
16. G. C. Kemmer et al., *Analyst* **140**, 6313–6320 (2015).
17. L. Iversen et al., *Science* **345**, 50–54 (2014).
18. M. J. Comstock et al., *Science* **348**, 352–354 (2015).
19. T. Yanagida, Y. Ishii, Eds., *Single Molecule Dynamics in Life Science* (Wiley-VCH, Weinheim, Germany, 2009).
20. X. S. Xie, in *Single Molecule Spectroscopy in Chemistry, Physics and Biology*, A. Graslund, R. Rigler, J. Widengren, Eds. (Springer-Verlag Berlin, 2010), vol. 96, pp. 435–448.
21. N. Akyuz et al., *Nature* **518**, 68 (2015).
22. C. E. Aitken, J. D. Puglisi, *Nat. Struct. Mol. Biol.* **17**, 793–800 (2010).
23. G.-W. Li, E. Oh, J. S. Weissman, *Nature* **484**, 538–541 (2012).
24. A. R. Subramaniam, B. M. Zid, E. K. O'Shea, *Cell* **159**, 1200–1211 (2014).
25. B. Sakmann, E. Neher, Eds., *Single-Channel Recording* (Springer, New York, ed. 2, 2009).
26. M. Grabe, G. Oster, *J. Gen. Physiol.* **117**, 329–344 (2001).
27. M. C. Berman, *Biochim. Biophys. Acta* **1513**, 95–121 (2001).
28. N. Nelson, A. Sacher, H. Nelson, *Nat. Rev. Mol. Cell Biol.* **3**, 876–881 (2002).
29. M. G. Palmgren, M. Sommarin, R. Serrano, C. Larsson, *J. Biol. Chem.* **266**, 20470–20475 (1991).

## ACKNOWLEDGMENTS

This work was supported by the Lundbeck Foundation (Center of Excellence Biomembranes in Nanomedicine); the Danish Councils for Independent (grant number 1323-00297) and Strategic Research; the Danish National Research Foundation (Center of Excellence PUMPKIN, grant number DNRF85); the University of Copenhagen programs of excellence Single Molecule Nanoscience, BioScaRT, and UNIK-Synthetic Biology; and the National Institutes of Health (grant number R21-GM100224). We are grateful to M. G. Palmgren, J. Mindell, and P. Nissen for stimulating discussions and comments on the manuscript; M. G. Palmgren for generously providing plasmids; U. Gether for instrumentation; and A.-M. Bjerg Petersen for excellent technical assistance. D.S. conceived the strategy and was responsible for the overall project supervision. B.H.J. performed cloning. G.C.K., B.H.J., and I.L.J. expressed, purified, and reconstituted AHA2<sup>R</sup> and AHA2 and performed macroscopic measurements and data analysis under the supervision of T.G.P. T.G.P. synthesized and G.C.K. purified pHrodo-PE; J.S. performed and analyzed mass spectrometry experiments of pHrodo-PE. S.M.C. wrote software for analyzing time-lapse sequences of single vesicles. S.V. designed, performed, and analyzed most single-vesicle experiments, with help from M.P.M. and G.G., under the supervision of S.M.C. and D.S.. C.L., A.L.C., and N.S.H. contributed with preliminary single-vesicle acidification measurements. M.G. contributed the model of vesicle acidification. D.S. wrote the manuscript, and S.V., G.G., M.P.M., B.H.J., G.C.K., I.L.J., and T.G.P. helped prepare figures and supplementary materials. All authors discussed the results and commented on the manuscript.

## SUPPLEMENTARY MATERIALS

www.sciencemag.org/content/351/6280/1469/suppl/DC1  
Materials and Methods  
Supplementary Text  
Figs. S1 to S12  
Tables S1 and S2  
References (30–47)

15 October 2015; accepted 23 February 2016  
10.1126/science.aad6429



BOYALIFE  
博雅控股集团

# All about BIOTECHNOLOGY

## All for Human Development and Health Improvement

Boyalife Group is an enterprise centered on innovation in the biotechnology field covering stem cell technology and bio-pharm. Found in 2009, Boyalife Group has more than 30 wholly-owned subsidiaries and holding companies currently, becoming the leading brand in healthcare and pharmaceutical center in China.

Our operative segments all for better health are including:

- Stem Cell Technology
- Pharmaceutical
- Gene Harbor
- Cloning Factory
- Health Management
- Regenerative Medicine
- Disease Models

For more information, visit : [www.boyalifegroup.com](http://www.boyalifegroup.com)



# 300



BIO-RAD'S DROPLET DIGITAL™ PCR SYSTEMS

## Over 300 Peer-Reviewed Droplet Digital PCR (ddPCR™) Publications\*

From detection of rare mutations and cancer biomarkers to quantification of gene editing events and miniscule viral loads, the QX100™ and QX200™ Droplet Digital PCR Systems have been used to redefine the limits of absolute nucleic acid quantification. With over 300 peer-reviewed publications, ddPCR platforms have outperformed other digital PCR systems by several orders of magnitude. The third-generation QX200™ AutoDG™ System now brings automation and scalability to digital PCR.

Visit [bio-rad.com/info/science300](http://bio-rad.com/info/science300) for the publication list and to learn more.

**BIO-RAD**

\* Based on PubMed data, October 2015.

# Let your work flow.

Introducing MiniSeq. Our simplest, most affordable sequencing solution yet.



The MiniSeq System makes the power of Illumina next-generation sequencing (NGS) accessible for every lab, every day. Now you can examine multiple targets or entire pathways in a single run, eliminating the iterative testing of Sanger sequencing and qPCR. Perform the most popular NGS applications in your own lab with this walk-away, library-to-results solution.


Explore NGS that fits your bench and your budget.

[www.illumina.com/miniseq](http://www.illumina.com/miniseq)

For Research Use Only. Not for use in diagnostic procedures.

©2016 Illumina, Inc. All rights reserved.

**illumina**<sup>®</sup>



Call for entries:  
a global award in  
stem cells and  
regenerative medicine

**BOYALIFE**  
& Science  
Science Translational Medicine  
**Award in**  
**Stem Cells**  
and Regenerative  
Medicine

Stem cells and regenerative medicine  
is the new frontier in life sciences.

Boyalife, Science and Science Translational  
Medicine jointly establish a global award to  
recognize significant contributions in advancing  
basic science to clinical applications in this field.

The award is to recognize and reward scientists in the fields of stem cells and/or regenerative medicine with a focus on developing cell-based treatments for cancer, degenerative disorders, immunotherapy and stem cells transplantation.

You could be next to win this prize and to receive

- ★ A Grand Prize of **\$25,000** and a Runner-Up Prize of **\$5,000** will be awarded.
- ★ The Grand Prize Winning Essay will be published in Science; a brief abstract of the Runner-Up Essay will be published in Science.

The 2016 Award is now open. The award ceremony will be held in San Francisco, on 23rd June, 2016.

For more information, please visit: <http://www.sciencemag.org/prizes/boyalife>



**BOYALIFE**  
StemCell

**Science**  
AAAS

Science  
Translational  
Medicine  
AAAS





The Transfection Experts

# X2 for CRISPR

See the NEW  
**CRISPR/Cas9**  
Transfection Video  
[www.mirusbio.com/CRISPR](http://www.mirusbio.com/CRISPR)

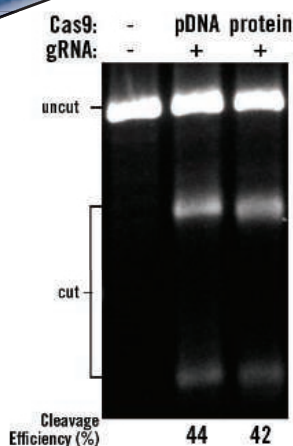


## *TransIT*-X2<sup>®</sup> Dynamic Delivery System

Now you can use the same transfection reagent for your knockout, knockdown or expression experiments. The *TransIT*-X2<sup>®</sup> Dynamic Delivery System takes CRISPR genome editing a step further with an advanced polymeric technology that efficiently delivers plasmid DNA, small RNAs such as siRNA and CRISPR guide RNA or RNP complexes.

The *TransIT*-X2<sup>®</sup> Dynamic Delivery System delivers CRISPR/Cas components in multiple formats:

- DNA**—deliver plasmid DNA expressing Cas9 or guide RNA
- RNA**—deliver sgRNA or crRNA:tracrRNA
- Protein**—deliver Cas9:sgRNA RNP complexes

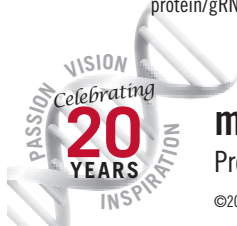


T7E1 cleavage efficiency in 293T/17 cells transfected with Cas9 pDNA/gRNA or Cas9 protein/gRNA (RNP) using *TransIT*-X2<sup>®</sup>.

### ADVANCE YOUR TRANSFECTIONS.

Request a FREE SAMPLE of  
*TransIT*-X2<sup>®</sup> Dynamic Delivery System.

Visit [www.mirusbio.com](http://www.mirusbio.com), call 888.530.0801 (U.S. only) or +1.608.441.2852

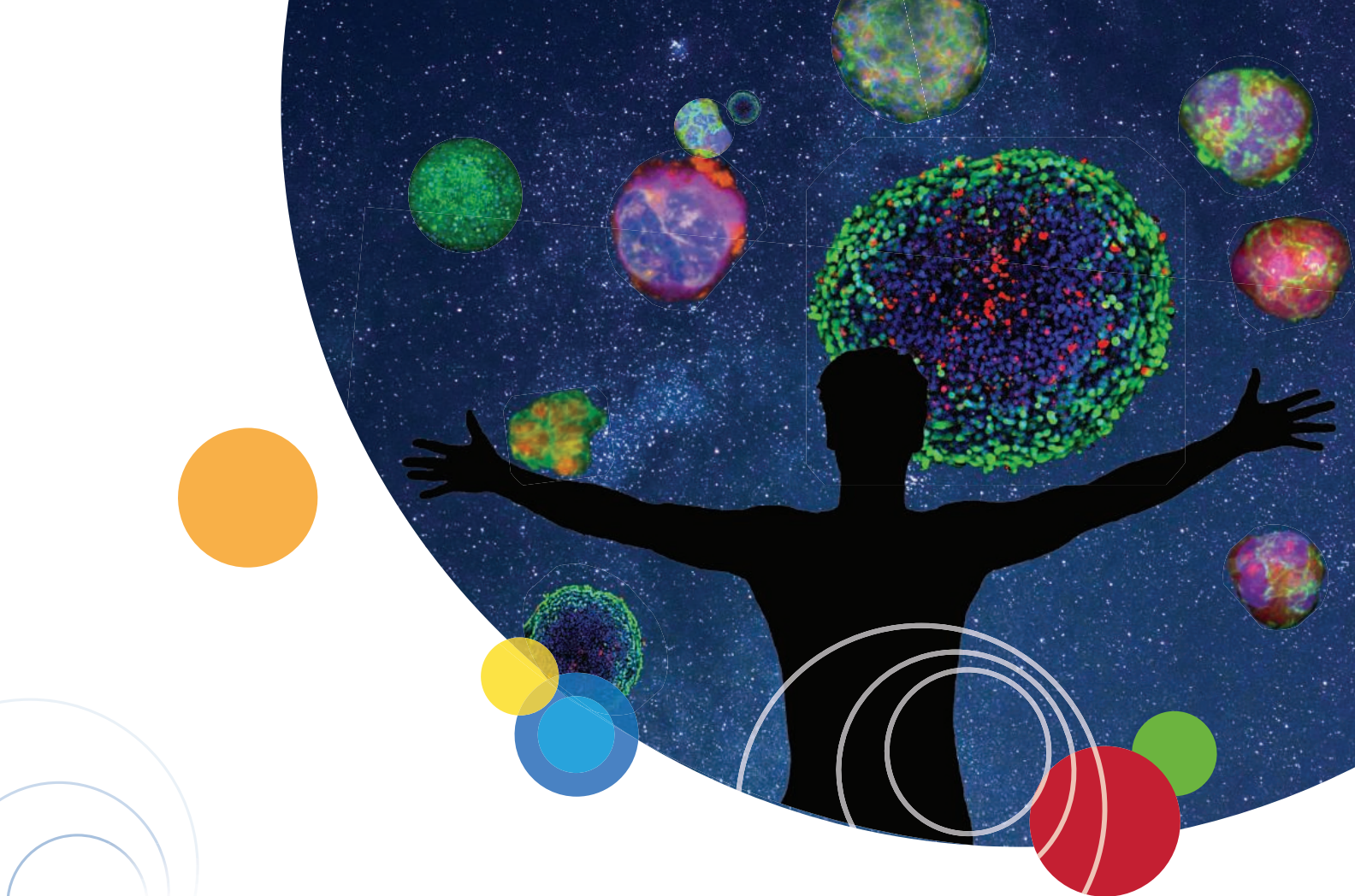


**mirusbio.com**

Providing gene delivery expertise since 1995

©2016 All rights reserved Mirus Bio LLC. Mirus Bio and *TransIT*-X2 are registered trademarks of Mirus Bio LLC. All trademarks are the property of their respective owners.





# Explore the new dimension

## The confocal system for your complex biology

Explore the complexities of biology faster while generating better results. With our new ImageXpress® Micro Confocal High-Content Imaging System, you can run 3D cellular assays and obtain confocal results—at a speed you'd only expect from widefield screening. Easily quantify images and generate statistically relevant data by selecting an optical geometry from crisp confocal or whole-well widefield options to match your application requirements. Built on the reliable, field-proven ImageXpress Micro platform, the ImageXpress Micro Confocal is our most versatile system yet.

*Discover more.*

[moleculardevices.com/IXMConfocal](http://moleculardevices.com/IXMConfocal)



ImageXpress® Micro Confocal system



Unleash your brilliance™

For Research Use Only. Not for use in diagnostic procedures.  
© 2015 Molecular Devices, LLC. All Rights Reserved. The trademarks mentioned herein are the property of Molecular Devices, LLC or their respective owners.



advantage New Promotion March 1 – June 30, 2016



US\$25  
OFF

# Macro-offers for Microbiologists

Premium solutions for your microbiological processes – now save up to 25 %!

Our new Eppendorf Advantage™ special offers include Eppendorf premium products ideally suited for the most important steps of your microbiology workflow.

> Buy a Mastercycler® nexus gradient PCR cycler and save 25 %

> Purchase any Eppendorf Xplorer® or Xplorer plus electronic pipette with 20 % off

> Save 20 % on the epMotion® 96

> Get the Eppendorf HeatSealer S100 with 20 % savings

[www.eppendorf.com/advantage](http://www.eppendorf.com/advantage)

Eppendorf®, the Eppendorf logo, epMotion®, Eppendorf Xplorer®, and Mastercycler® are registered trademarks of Eppendorf AG, Hamburg, Germany. Eppendorf Advantage™ is a trademark of Eppendorf AG, Hamburg, Germany. U.S. Design Patents are listed on [www.eppendorf.com/ip](http://www.eppendorf.com/ip). Offers may vary by country. All rights reserved, including graphics and images. Copyright © 2016 by Eppendorf AG.





2015 Winner  
Shigeki Watanabe, Ph.D.  
Johns Hopkins University  
For research on synaptic  
vesicle endocytosis

# Call for Entries

**Application Deadline**  
**June 15, 2016**

## **Eppendorf & Science Prize for Neurobiology**

The annual Eppendorf & Science Prize for Neurobiology is an international award which honors young scientists for their outstanding contributions to neurobiological research based on methods of molecular and cell biology. The winner and finalists are selected by a committee of independent scientists, chaired by Science's Senior Editor, Dr. Peter Stern. Researchers who are not older than 35 years are invited to apply.

## **You could be next to win this prize and to receive**

- > Prize money of US\$25,000
- > Publication of your work in Science
- > Full support to attend the Prize Ceremony held in conjunction with the Annual Meeting of the Society for Neuroscience in the USA
- > An invitation to visit Eppendorf in Hamburg, Germany

It's easy to apply!

Learn more about the Prize and its past winners at:

[www.eppendorf.com/prize](http://www.eppendorf.com/prize)

eppendorf  
& Science

PRIZE FOR  
NEURO  
BIOLOGY



2015 年获奖者  
渡边茂树博士  
美国约翰·霍普金斯大学  
专注突触囊泡内吞现象的研究

## 欢迎申请

申请截止日期  
2016 年 6 月 15 日

### Eppendorf & Science 神经生物学奖

一年一度的 Eppendorf & Science 神经生物学奖是一项国际奖项，授予用分子与细胞生物学方法在神经生物学领域取得非凡成果的青年科学家。冠军及入围候选人均是由《Science》杂志高级编辑 Peter Stern 博士领衔的独立科学家所组成的委员会评出。年龄不超过 35 岁的科学家可以申请参选。

您可能就是下一位获奖者并获得：

- > 25,000 美元奖金
- > 获奖论文发表在《Science》杂志上
- > 得以全额资助参与美国神经科学协会年会和颁奖仪式
- > 获邀参观 Eppendorf 位于德国汉堡的总部

申请非常容易！

想了解奖项详情及往届获奖者，请登陆：

[www.eppendorf.com/prize](http://www.eppendorf.com/prize)

eppendorf  
Science  
AAAS



2015 Winner  
Shigeki Watanabe, Ph.D.  
Johns Hopkins University  
For research on synaptic  
vesicle endocytosis

## Call for Entries

申込期限  
2016年6月15日

### Eppendorf & Science Prize for Neurobiology

Eppendorf & Science神経生物学賞は、分子生物学や細胞生物学に基づく神経生物学研究において、卓越した貢献をなされた若手研究者に贈呈している国際賞です。最終選考選出者ならびに受賞者は、Science誌編集主任Dr. Peter Sternをはじめとする科学者達の独立委員会によって選出されます。35歳までの研究者が応募できます。

### 次はあなたの番かもしれません

- > 賞金：25,000米ドル
- > Science誌に研究内容を掲載
- > 米神経科学学会年次総会に併せて開催される授賞式への参加を全面サポート
- > ドイツ、ハンブルグのエッペンドルフ本社にご招待

応募は簡単です！

本賞と過去の受賞者について詳しくはこちら：

[www.eppendorf.com/prize](http://www.eppendorf.com/prize)



# 2016

## Canada Gairdner Awards

Recognizing the world's greatest achievements in biomedical research since 1959



**CANADA GAIRDNER INTERNATIONAL AWARDS RECOGNIZE INDIVIDUALS FROM VARIOUS FIELDS FOR SEMINAL DISCOVERIES OR CONTRIBUTIONS TO BIOMEDICAL SCIENCE**

### **Dr. Rodolphe Barrangou**

Associate Professor, Department of Food, Bioprocessing and Nutrition Sciences; Todd R. Klaenhammer Distinguished Scholar in Probiotics Research, North Carolina State University

**CANADA GAIRDNER INTERNATIONAL AWARD**

Awarded for establishing and characterizing CRISPR-CAS bacterial immune defense system



### **Dr. Philippe Horvath**

Senior Scientist, DuPont

**CANADA GAIRDNER INTERNATIONAL AWARD**



### **Dr. Emmanuelle Charpentier**

Scientific member of the Max Planck Society, Director at the Max Planck Institute for Infection Biology; Professor, Umeå University

**CANADA GAIRDNER INTERNATIONAL AWARD**



### **Dr. Jennifer Doudna**

Li Ka Shing Chancellor's Chair in Biomedical and Health Sciences; Professor of Molecular and Cell Biology and Professor of Chemistry at UC Berkeley; Investigator of the Howard Hughes Medical Institute

**CANADA GAIRDNER INTERNATIONAL AWARD**

Awarded for development of CRISPR-CAS as a genome editing tool for eukaryotic cells



### **Dr. Feng Zhang**

Core Member, Broad Institute of MIT and Harvard; Assistant Professor, McGovern Institute for Brain Research, Department of Brain and Cognitive Sciences, Massachusetts Institute of Technology

**CANADA GAIRDNER INTERNATIONAL AWARD**



**THE JOHN DIRKS CANADA GAIRDNER GLOBAL HEALTH AWARD RECOGNIZES SOMEONE WHO IS RESPONSIBLE FOR A SCIENTIFIC ADVANCEMENT THAT HAS MADE A SIGNIFICANT IMPACT ON HEALTH IN THE DEVELOPING WORLD**

### **Dr. Anthony Fauci**

Director, National Institute of Allergy and Infectious Diseases, National Institutes of Health

**JOHN DIRKS CANADA GAIRDNER GLOBAL HEALTH AWARD**

Awarded for his many pioneering contributions to our understanding of HIV infections and his extraordinary leadership in bringing successful treatment to the developing world



**THE CANADA GAIRDNER WIGHTMAN AWARD IS GIVEN TO A CANADIAN WHO HAS DEMONSTRATED OUTSTANDING LEADERSHIP IN MEDICINE AND MEDICAL SCIENCE THROUGHOUT HIS/HER CAREER**

### **Dr. Frank Plummer**

Senior Advisor, Public Health Agency of Canada; Distinguished Professor, University of Manitoba

**CANADA GAIRDNER WIGHTMAN AWARD**

Awarded for his groundbreaking research in Africa in understanding HIV transmission and his leadership at the Canadian National Microbiology Laboratory with pivotal roles in SARS, influenza and Ebola epidemics

Find out more about the work of the Gairdner Foundation and this year's laureates at [www.gairdner.org](http://www.gairdner.org)

# gairdner

LES PRIX CANADA GAIRDNER AWARDS



"I USED THE BIOXP™ SYSTEM  
TO BUILD GENES TO  
CLONE AND EXPRESS 49  
TRANSCRIPTION FACTORS  
FROM A MARINE DIATOM."

*Sarah R. Smith, Ph.D.*  
Scripps Institution of Oceanography  
and J. Craig Venter Institute

# DNA MY WAY™

When you get DNA your way, the limits of traditional molecular biology disappear. The perfect genes, clones, and proteins are suddenly within your reach.

The **BioXp™ 3200 System** can help you develop new molecular biology workflows through automated DNA assembly.

Based on technologies developed at the J. Craig Venter Institute and Synthetic Genomics, the **BioXp™ 3200 System** enables you to build and clone DNA fragments with hands-free automation.



## SGIDNA

A Synthetic Genomics, Inc. Company

Copyright © 2016 SGI-DNA, Inc. All rights reserved. All noted trademarks are the property of Synthetic Genomics, Inc. and/or its affiliates. BXP030716

Visit [sgidna.com/bioxp](http://sgidna.com/bioxp)

#DNAMYWAY



## AAAS *Travels*



### Discover the Delights of Yunnan **The Torch Festival!** July 21–August 6, 2016

See the spectacular Yunnan Torch Festival of the Yi, Naxi, and Bai peoples in southwestern China. This is an extravaganza of flaming torches, bonfires, parades, bull fights, singing, and dancing—all in this most scenic part of China! Also explore cultural highlights from Dian Chi Lake, the Nationalities Museum, Stone Forest, and Chuxiong to Weishan, Dali and Lijiang, including two World Heritage Sites! \$4,595 + air.

**For a detailed brochure, call (800) 252-4910**

All prices are per person twin share + air



BETCHART EXPEDITIONS Inc.  
17050 Montebello Rd, Cupertino, CA 95014  
Email: AAASInfo@betchartexpeditions.com  
www.betchartexpeditions.com

## FOCUS ON CAREERS

POSTDOCS



## Search results: Careers in high tech

High technology permeates every corner of every enterprise, from global computing corporations, to social media and search establishments, to retail giants. Not surprisingly, these industries offer attractive playgrounds for Ph.D.-level scientists and engineers.

**See the full story on page 1481.**

### Upcoming Features

Cancer Research Careers—April 8  
Regional Focus: China—June 24  
Postdoc Careers—August 26

Produced by the Science/AAAS Custom Publishing Office



# HIV Cure Funding Opportunity

Gilead Sciences has spent 25 years working to improve treatments for people living with HIV, with an ultimate goal in mind: finding a cure. To that end, we've set aside funding to support academic institutions, nonprofit organizations and community groups committed to HIV cure activities.

Visit [www.gilead.com/HIV-Cure-FOA](http://www.gilead.com/HIV-Cure-FOA) to learn more and apply for funding.





# AAAS 2016 ANNUAL MEETING

## Student Poster Competition Winners

The 2016 Student Poster Competition took place at the AAAS Annual Meeting in Washington, DC, February 13-14. These student winners' work displayed originality and understanding that set them apart from their peers. Poster submission for the 2017 AAAS Annual Meeting will open in July 2016.

### BRAIN AND BEHAVIOR

**Winner:** Nalini Rao, University of Miami  
*RAI<sub>1</sub> Mutant Mice Exhibit Smith-Magenis Syndrome Phenotypes*

**Honorable Mention:** Samantha You, Tufts University  
*Glial microRNAs Regulate Circadian Behavior in *Drosophila**

### CELLULAR AND MOLECULAR BIOLOGY

**Winner:** John Ramírez, Del Mar College  
*Exploration of Putative Riboswitches Involved in Bacteriophage Temperate Life Cycle*

**Honorable Mention:** Jill Beaver, Florida International University  
*Proliferating Cell Nuclear Antigen Promotes DNA Trinucleotide Repeat Hairpin Removal*

### DEVELOPMENTAL BIOLOGY, PHYSIOLOGY, AND IMMUNOLOGY

**Winner:** Carolina A. Herrera, University of California, Irvine  
*Improving T-Lymphocyte Recognition of Vaccinia Virus Antigens*

**Honorable Mention:** Mohamed Dandan, University of California, Irvine  
*Inhibiting *Staphylococcus aureus* NorA Efflux Pumps to Restore Ciprofloxacin Activity*

**Honorable Mention:** Hui Yi Grace Lim, Duke University  
*Identification and Characterization of Novel Regulators of Cell Invasion in *C. elegans**

### EDUCATION

**Winner:** Remy Dou, Florida International University  
*Beyond Performance Metrics: Examining a Drop in Students' Physics Self-Efficacy*

**Honorable Mention:** Tanya Das, University of California, Santa Barbara  
*Assessment of an Undergraduate Engineering Design Capstone Course*

### ENVIRONMENT AND ECOLOGY

**Winner:** Tiffany Batarseh, University of California, Irvine  
*Nine Plasmids Discovered in a Multidrug Resistance *Escherichia coli* Isolate*

**Honorable Mention:** Justin Lesser, Northeastern University  
*Natural History of Hamlet Communities Reveals Incipient Speciation Due to Color Morphology*

### MEDICINE AND PUBLIC HEALTH

**Winner:** Ruchi Shah, Stony Brook University  
*Keratin 17 Maintains Proliferation by Binding p27KIP1 and Facilitating its Nuclear Export*

**Honorable Mention:** Cynthia Rodríguez, University of California, Irvine  
*Multidrug Resistant *Klebsiella pneumoniae* Sequence Type 258 Producing KPC-2 Carbapenamase*

### PHYSICAL SCIENCES

**Winner:** Zhe Mei, Bard College  
*Body Fluid Study by Surface Enhanced Raman Spectroscopy for Medical / Forensic Application*

**Honorable Mention:** Abigail Regitsky, Massachusetts Institute of Technology  
*Rheological Characterization of Bioinspired Mineralization in Hydrogels*

### SCIENCE AND SOCIETY

**Winner:** Elyse Aurbach, University of Michigan  
*Evaluation of Language Use After RELATE: A Practice-Based Program to Improve Communication*

**Honorable Mention:** Jemima Omonigho Adepehin, Federal University of Technology, Akure, Nigeria  
*Pearl Millet and Finger Millet Sourdough Bread: A New Innovation*

### SOCIAL SCIENCES

**Winner:** Rhian Stotts, Arizona State University  
*The Emotional Geographies of Climate Change in Three U.S. Contexts*

**Honorable Mention:** Melissa Hopkins, Bucknell University  
*The Effect of Priming Intellectual Virtues on Individual Effort and Understanding*

### TECHNOLOGY, ENGINEERING, AND MATH

**Winner:** Sangwon Hyun, Carnegie Mellon University  
*Epidemiological Forecasting with Statistical Models*

**Honorable Mention:** Aniurka Duverge Carreno, Howard University  
*Exploring Different Configurations of Wire Ropes Supporting Slender Equipment to Minimize*





# Internationalizing Japan's academia: Riding the wave of change

Japan's top universities are implementing programs to meet the goals of recent multimillion dollar government projects to internationalize their campuses and compete in the global competition for top class staff and students. **By Adarsh Sandhu**

## Reforming Japan's universities

Surprisingly, in spite of the fact that Japan has produced more Nobel laureates than any other country in Asia, there were only two Japanese universities in the top 100 of the 2014 *Times Higher Education World University Rankings*. By contrast, there were three each from China and South Korea, and two from Singapore. These facts are of concern to educators in Japan, recently prompting the Ministry of Education, Culture, Sports, Science and Technology (MEXT) to launch two 10-year, multimillion dollar projects: the Program for Promoting the Enhancement of Research Universities (hereafter "RU") in 2013 and the Top Global University (TGU) project in 2014. The purpose of these projects is to support Japanese universities with research and education reforms, enabling them to internationalize and better compete globally (1, 2). The RU program aims to improve research infrastructure, while the TGU program targets internationalization of education.

Each university received initial annual funding of US\$2 million to US\$4 million under the RU program and US\$1.4 million to US\$3.5 million under the TGU program. Both have a mid-

term assessment (after five years), with the possibility of cuts or even termination of funding for those institutes that have not achieved their initial targets. Details of the original applications are posted on the MEXT website, to enhance transparency and accountability.

These programs have generated a lot of interest in both Japan and overseas, particularly because the universities and institutes selected were chosen by an unprecedented, top-down approach based on performance metrics—such as quality of publications and patent submissions—and staff-to-student ratios.

The programs were devised to resolve two major problems facing Japanese academia. The first is the dramatic fall in Japan's birth rate, with government figures indicating that within 20 years, Japan's 780 universities will have more places available than domestic students to fill them. Currently, about 600,000 students apply for approximately 580,000 places at Japan's universities. The projected drop in enrollment will lead to mergers or the closure of less competitive institutes.

The second problem is the need to improve Japan's standing in world ranking tables. University rankings are by no means the most effective means of assessing the quality of research and education in academia, but they do highlight the importance of internationally oriented curricula and strategic outreach programs to enhance visibility. Improving global appeal may also attract international students to counteract future enrollment shortfalls.

## Attracting international students and staff

It is estimated that there are currently around 4 million international students in the world, with the United Nations Organization for Education, Science and Culture (UNESCO) predicting that this number may increase to 7 million by 2020. Japan currently has about 184,000 overseas students (approximately 3% of all students in tertiary education) with plans to increase this number to 300,000 over the next decade. By contrast, from 2013 to 2014, universities in the United States enrolled approximately 886,000 international students. Courses taught in English, the availability of scholarships, and genuine career

opportunities upon graduation are just some of the factors that attract the world's best and brightest to these universities.

Why do Japanese universities struggle to attract international students? The main reason is that the Japanese language is a formidable hurdle to overcome. When Joby Joseph, a physicist at the Indian Institute of Technology (IIT) Delhi, first visited a university in Japan, he was surprised to see that all the courses were taught using Japanese language textbooks. "There was not a single word of English in the books," he said.

To overcome language problems, universities selected for the TGU program have changed their curricula to include more English language courses and have hired bilingual support and administration staff to assist international visitors. Importantly, they have also started to send their own students abroad for short-term stays to hone their English language skills and experience different ways of conducting research and education.

### Career opportunities at Japan's top universities

Universities in Japan are now more open and dynamic in their ideas than they have been in the last 50 years, offering real opportunities for tenured positions for staff from overseas. The drive by Japan's top universities to recruit international staff and students is an unprecedented opportunity for career development for young students and faculty members from outside Japan wishing to collaborate with Japanese researchers.

All scientists, from graduate students to established academics, are encouraged to seek research opportunities in Japan. Prospective graduate students can research laboratories at Japan's top universities through their websites to find academics doing research in their area of interest. They can then contact the faculty directly via e-mail to ask about research openings and the possibility of financial support. It is worth noting that graduate school programs start in either April or October, but the precise dates for formal interviews and examinations depend on the institute. For academics, direct networking at conferences and similar events is critical for building relationships that may lead to finding openings at Japanese universities.

For international scientists, the location of an institute can be important. Prospective visitors should decide whether they would prefer a megametropolis such as Tokyo or Osaka, or less crowded cities such as Kanazawa and Beppu. The availability of English language schools for children, and of local communities and support networks for spouses, are also important factors to consider for long-term stays in Japan.

Visitors to Japan are often surprised by the safety of its cities. Personal safety and peace of mind are some of the attractions of studying or working in Japan. Another is cost, with tuition fees at Japan's national universities considerably lower than universities in the United States and certain European countries. This is an important factor when choosing universities, given the increasing number of students needing loans to pay for their university education in the United States and United Kingdom.

Many opportunities exist for short-term scholarly research in Japan, as many visiting academics will testify. For example, a three-to-nine month sabbatical can enable young researchers to form connections for future collaborations. However, there are challenges filling full-time, tenured positions at Japanese universities because of severe gaps in matching the applicants'

expectations with the realities of low salaries, heavy teaching obligations, and insufficient startup funding for setting up research labs. Furthermore, even if such issues are resolved, people with families may find it difficult to balance their careers with their children's education because of the lack of reasonably priced international schools in Japan.

---

**Universities in Japan  
are now more open and dynamic  
in their ideas than they have been  
in the last 50 years, offering real  
opportunities for tenured positions  
for staff from overseas.**

---

### Surviving Japan's educational reforms

Japan's academia is going through changes on par with those of the Meiji Restoration in the late 19th century. The Meiji movement laid the foundations for the current educational system, devised by Japanese scholars for Japanese students. But a Japanese-only study environment and curriculum has produced students who are unable to function effectively in English—the de facto global language of scholarly communication. Mastery of English is particularly important for Japanese industry, which is becoming increasingly internationalized and needs globally minded employees to run its overseas operations.

Importantly, the outcome of these two high-profile MEXT programs will have significant implications for the future of education and research policy in Japan. The next 5 to 10 years will likely see both mergers and closures of universities large and small that are unable to attract enough students and funding as government subsidies are reduced.

Japan's university administrators face unprecedented and multifaceted problems as they struggle to cope with increased international competition for students and research staff. Finding solutions to these issues will require dynamic, diverse, and global approaches. The academic institutes that survive this wave of educational reform in Japan will be those that implement bold initiatives to create borderless, multicultural, multilingual, and globally connected campuses.

*Adarsh Sandhu is a freelance science writer based in Tokyo.*

### References

1. MEXT, "Program for Promoting the Enhancement of Research Universities" (in Japanese); available at [www.mext.go.jp/a\\_menu/kagaku/sokushinhi/index.htm](http://www.mext.go.jp/a_menu/kagaku/sokushinhi/index.htm).
2. MEXT, "Selection for the FY 2014 Top Global University Project"; available at [www.mext.go.jp/b\\_menu/houdou/26/09/\\_icsFiles/safefieldfile/2014/10/07/1352218\\_02.pdf](http://www.mext.go.jp/b_menu/houdou/26/09/_icsFiles/safefieldfile/2014/10/07/1352218_02.pdf).





Shuji Hashimoto

## Waseda University goes global

**W**aseda University is a top, private academic institution in Japan in terms of prestige, scholarly achievements, and financial capability. The university is rapidly implementing innovative programs to create a worldwide academic network for an open, diverse, and dynamic campus.

"We have set two challenging and ambitious goals for the next 10 years under the Waseda Goes Global (W2G) plan," says Vice President **Shuji Hashimoto**. "Training 100,000 students for global leadership through research and education programs with international academic partners, and being ranked among the world's top 100 universities in 18 different areas of research."

Waseda's goals are supported by funding from the government's Top Global University Project. Waseda was one of only 13 universities selected by Japan's Ministry of Education, Culture, Sports, Science and Technology (MEXT) in the highly competitive Type A group when funding was launched in September 2014. The aim of the project is to help selected universities achieve reforms that will enable them to compete globally.

W2G is a ten-year plan, with approximately ¥540 million (US\$4.7 million) allocated for the first full fiscal year, 2015. The university has demonstrated its commitment to achieving dramatic results by dedicating ¥190 million (US\$1.7 million) of its own funds on top of the ¥350 million (US\$3 million) government grant.

The funding is being used to support six education and research units prioritized by Waseda to implement the goals of the W2G plan. The six units are Global Japanese Studies; Empirical Analyses of Political Economy; Health Promotion: The Joy of Sports and Exercise; Frontier of Embodiment Informatics; Information and Communication Technology (ICT) and

Robotics; Energy and Nanomaterials; and Multiscale Analysis, Modeling, and Simulation. Specific goals of the W2G plan include doubling the number of visiting researchers from 810 to 1,600 and increasing the international faculty from 760 to 1,380.

"We are also making major changes to our personnel recruitment policies to achieve the aims of the W2G plan," explains Hashimoto. "We are actively recruiting faculty from overseas, increasing the number of tenure-track positions and joint appointments."

Furthermore, Waseda is introducing an academic calendar based on quarters to synchronize with those of overseas universities. The university is also creating joint appointment chairs and cotutoring for double degree programs, as well as giving full support to visiting scholars and students studying under the Top Global University Project. The aim of these changes is to support students while they are at Waseda, and to ensure they have priority access to accommodation on or close to campus.

Hashimoto is confident that Waseda will succeed in achieving its goals and will act as a model for other universities with similar ambitions. ***"Waseda is truly going global. We welcome highly motivated students and researchers from around the world to join us on this unique journey."***

### Waseda University at a glance



Okuma Auditorium

- Founded in 1882 by Shigenobu Okuma, who twice served as prime minister of Japan, Waseda University is one of the largest and most influential private universities in Japan, with more than 50,000 students and 5,500 academic staff.
- Waseda is Japan's foremost international university with more than 5,000 international students and more than 700 overseas partner institutions in 81 countries.
- International students can choose from all-English degree programs in 6 undergraduate and 12 graduate schools, and learn

over 25 foreign languages; the curriculum for Japanese language training is Japan's most extensive.

- Waseda's main campus is located in central Tokyo, with convenient access to shopping areas, international schools, embassies, and offices of major corporations.
- The university has a global network of approximately 600,000 alumni, including novelist Haruki Murakami, UNIQLO founder and CEO Tadashi Yanai, Olympic gold medalist Shizuka Arakawa, and seven Japanese prime ministers.
- Waseda University was ranked 33rd in the world and 1st in Japan in the Quacquarelli Symonds graduate employability rankings published in November 2015.

### FURTHER INFORMATION

**Waseda University**  
[www.waseda.jp/top/en](http://www.waseda.jp/top/en)

**Top Global University Project**  
[www.waseda.jp/inst/sgu/en](http://www.waseda.jp/inst/sgu/en)



Hiroyuki Nishide

# Energy and nanomaterials

Searching for innovative means to produce, store, and use energy

**T**he Unit for Energy and Nanomaterials is one of the flagship research hubs established by Waseda University as part of the Top Global University (TGU) project funded by Japan's Ministry of Education, Culture, Sports, Science and Technology (MEXT). "We want to contribute to global efforts to mitigate the daunting problems related to the production, storage, and efficient use of energy," explains **Hiroyuki Nishide**, former dean of the Graduate School of Advanced Science and Engineering, and coordinator of the unit. "We have launched several innovative international initiatives to facilitate this goal, including hiring academic staff and researchers from overseas. We welcome researchers and students from overseas to join us."

## Unit for Energy and Nanomaterials

Research and education within the Unit for Energy and Nanomaterials are driven by international collaborations, with Waseda funding joint appointments of overseas staff as well as student exchanges as part of a joint Ph.D. degree program between a group of partner universities. In 2016, Waseda University will hire full professors from universities in the U.S. and Australia. The new staff will have one-to-three-year fixed contracts and their duties will include teaching and research. Published work in peer-reviewed journals will carry the names of both universities. Salaries are competitive and the staff from the partner universities stay at Waseda for a minimum of three months per academic year.

Regular interuniversity exchanges and close supervision of students are important for the program's success. Students are carefully matched with supervisors from the partner universities and are required to take designated course credits at the partner university and to conduct research there for more than three months. Students successfully completing the program will receive a certificate under the name of Waseda and the partner university.

"Compared with students who undertake doctoral courses at only a single institution, these students will benefit by interacting with top researchers at two universities located in different countries," says Nishide.

## Innovative world-class research on batteries

Hiroyuki Nishide is internationally renowned for the development of "radical polymer" batteries that are semitransparent, flexible to the extent of being foldable, and can be charged in less than 30 seconds. "We use so-called p- and n-type redox couples of radical polymers in our flexible batteries," says Nishide. "For example, we tune radical polymers with a wide selection of molecular structures, enabling these materials to exhibit the properties of both cathode and anode materials. Prototypes show very promising properties such as rapid charging and a long shelf life."

Specifically, 0.5-mm-thick radical polymer batteries with areas of 3 cm<sup>2</sup> exhibit a battery capacity of 6 milliamp hours and a power density of 5 kilowatts/liter. These groundbreaking batteries are expected to find applications in consumer products such as smart wrist watches.

## Research institutions collaborating with the Unit for Energy and Nanomaterials



The Research Support Center

### The Smart Energy System Innovation Center

This center for battery innovation develops high capacity secondary batteries including lithium sulfide and metal air types. Other work includes nondestructive monitoring of batteries and the development of silicon anode batteries.

### Energy Management System Shinjuku R & D Center

This center focuses on research into next-generation energy management system responses and the development of next-generation voltage regulation technology in power networks, including power generated by renewable energy.

## FURTHER INFORMATION

**Unit for Energy and Nanomaterials**  
[www.tgu-enm.sci.waseda.ac.jp](http://www.tgu-enm.sci.waseda.ac.jp)

**Graduate Program in Science and Engineering**  
[www.leading-en.sci.waseda.ac.jp/en](http://www.leading-en.sci.waseda.ac.jp/en)

# Frontiers of embodiment informatics:

## Combining communications and engineering for human symbiotic robots

**R**elationships between people are fraught with difficulties. So imagine the challenges researchers face in forming mutually beneficial relationships between humans and robots. **Shigeki Sugano** has spent a lifetime of research doing just that: formulating ways of enabling robots and humans to interact with and understand each other.

"The fundamental question is whether humans and robots can coexist, and work together closely to achieve goals," says Sugano. "The answer is important for the development of robots to support human activities, particularly in aging societies such as in Japan."

Sugano and colleagues have defined safety, dependability, and dexterity as critical factors for humans and robots to be able to coexist. Extensive research based on instilling these traits in robots led to the development of TWENDY-ONE—a highly dexterous and multifunctional human symbiotic robot able to adapt to human movement and manipulate objects, such as putting bread into a toaster.

"The Graduate Program for Embodiment Informatics is funded by Japan's Ministry of Education, Culture, Sports, Science and Technology [MEXT] as one of its Leading Graduate School Programs. It aims to nurture students to meet the formidable challenges for realizing the perfect human symbiotic robot," explains Sugano. "We welcome highly motivated



Shigeki Sugano

students and researchers from overseas to join us for firsthand insights into Japan's *monozukuri* or manufacturing technology."

The MEXT funding for the Graduate Program for Embodiment Informatics reflects the long and distinguished history of robotics research at Waseda University. Sugano is following in the footsteps of his mentors Ichiro Kato and Katsuhiko Shirai, who combined their talents in mechanical and electrical engineering to develop WABOT-1, the world's first humanoid robot,

in 1973. "It would not be an exaggeration to say that we are standing on the foundations laid by Professors Kato and Shirai," says Sugano.

In the program, students take on projects to build human symbiotic robots by integrating research on mechanical technology and information communications technology. The Kobo Workshop—a shared open space where students from different backgrounds meet and interact freely—is one of the unique facilities of the program.

Future research themes include the WAMOEBA Project (Waseda-Amoeba, Waseda Artificial Mind On Emotion BAse), a methodology for instilling emotion and self-preservation instincts into robots.

### FURTHER INFORMATION

#### Shigeki Sugano

Department of Modern Mechanical Engineering, School of Creative Science and Engineering, and coordinator of the Waseda Graduate Program for Embodiment Informatics.

#### Graduate Program for Embodiment Informatics

[www.leading-sn.waseda.ac.jp/en/](http://www.leading-sn.waseda.ac.jp/en/)

# Fusing science and engineering in real-world modeling of fluid dynamics

**A**ircraft, oil tankers, and nuclear power stations are critical elements of modern society. However, the average citizen is probably unaware that the design, manufacture, and implementation of these important technologies require a deep knowledge of fluid mechanics—how mixtures of gases, liquids, and solids move and interact. Furthermore, in spite of recent advances in computing and mathematical modeling, our understanding of the intricacies of fluid mechanics is still incomplete. Against this background, enhancing our knowledge of mathematical fluid mechanics is the main goal of the international doctoral program at the Research Institute of Nonlinear Partial Differential Equations (PDEs) at Waseda University.

"Our international doctoral program on mathematical fluid mechanics is focused on the analysis of real-world fluidics such as bubble formation in the cooling systems of nuclear reactors," says **Yoshihiro Shibata**, Department of Mathematics, Faculty of Science and Engineering and Research Institute of Nonlinear PDEs. "The program is part of Waseda University's Top Global University (TGU) project."

Examples of research in this program are mathematical analysis of multiscale complex phenomena, biofluid mechanics for production of biofuels using *Euglena* microorganisms, solutions to the free boundary problem of Navier-Stokes equations, and modeling of cavitation



Yoshihiro Shibata

phenomena. Notably, the decommissioning of Japan's nuclear reactor in Fukushima has focused attention on multiscale complex phenomena, including how to understand complicated interactions between molten fuels and the other structures of the reactor.

The doctoral program is evolving into a credit-based system, enabling students to transfer credits to partner institutes in Europe

and North America. Students will be supervised by faculty members at both Waseda and their overseas partners.

"Currently we are creating long-term frameworks with Darmstadt University, Germany, the University of Pittsburgh, U.S., and the Universities of Pisa and Bari in Italy," explains Shibata. "We want to nurture young minds of all nationalities capable of accurate mathematical modeling and simulations based on physics, engineering, and numerical analysis. We welcome people from overseas to join us in making physics and mathematics a driving force behind building the infrastructure of our society."

### FURTHER INFORMATION

#### Yoshihiro Shibata

Department of Mathematics, Faculty of Science and Engineering and Research Institute of Nonlinear Partial Differential Equations

#### Yoshihiro Shibata's website

[www.fluid.sci.waseda.ac.jp/shibata/](http://www.fluid.sci.waseda.ac.jp/shibata/)

#### Mathematics and Physics Unit, TGU project, Waseda University

[www.sgu-mathphys.sci.waseda.ac.jp/en/index.html](http://www.sgu-mathphys.sci.waseda.ac.jp/en/index.html)





### SPE Plates

The Strata-X  $\mu$ Elution 96-Well Plates enable solid phase extraction (SPE) from samples as small as 10  $\mu$ L, along with low elution volumes. These cost-effective 96-well plates conserve precious samples and reduce time requirements compared to traditional SPE plates, which require 200- $\mu$ L elution volumes and a dry-down step to produce sufficient concentration. This dry-down step is time-consuming and can reduce analyte recovery of peptides and thermolabile compounds. The new Strata-X  $\mu$ Elution 96-well plates are ideal for work with biological samples in pharmaceutical, clinical research, and forensic laboratories. Strata-X  $\mu$ Elution 96-well plates follow the same procedure as traditional 96-well SPE plates, however elution volumes are as low as 25  $\mu$ L, eliminating the need to perform a dry-down step. Strata-X  $\mu$ Elution 96-well plates can be used with a vacuum manifold or positive-pressure system and can be automated with a robotic liquid handler for further time and labor savings.

#### Phenomenex

For info: 310-212-0555  
www.phenomenex.com

### Confocal Microscope

The HyVolution true confocal super-resolution technology for the Leica TCS SP8 confocal microscope platform allows researchers to resolve structures down to 140 nm with multiple colors, high imaging speed, and high signal-to-noise ratio. HyVolution can be ordered with every new Leica TCS SP8 and is also available as an upgrade to existing Leica TCS SP8 platforms. HyVolution is based on a combination of the unique Leica HyD hybrid detector, a workflow-oriented software wizard; best-in-class Huygens deconvolution software embedded via a direct interface in the Leica Application Suite X (LAS X) control software; and CUDA graphics processing unit-accelerated computing. Researchers benefit from HyVolution by imaging fast dynamic processes and capturing multiple colors simultaneously with the TCS SP8's spectral detection system, and can still achieve 140-nm resolution.

#### Leica Microsystems

For info: 800-248-0123  
www.leica-microsystems.com



### Thermal Cycler

The new qTOWER<sup>3</sup> real-time polymerase chain reaction (PCR) thermal cycler is a patented fiber-optic shuttle system with a unique light source powered by four high-performance light-emitting diodes (LEDs), which guarantees ideal excitation and detection of known fluorescent dyes up to the dark red. In addition, the system's highly sensitive detection module can be equipped with up to six different color modules. Color modules are upgradeable, allowing the system to benefit from future developments. Silver block technology is at the heart of the qTOWER<sup>3</sup>, offering outstanding homogeneity of only  $\pm 0.1^\circ\text{C}$  over the entire 96-well block. Optionally, the linear gradient function is the optimal tool to easily adjust the instrument to different assays. The qTOWER<sup>3</sup> is available either as a stand-alone device with an integrated 10-in. tablet or as a PC-based system. The software comes with a broad spectrum of optimized analysis algorithms, including absolute and relative quantification, melt point analysis, delta-delta cycle threshold (Ct) method, PCR efficiency, allelic discrimination, endpoint, and protein determination.

#### Analytik Jena

For info: +49-(0)-36-41-77-70  
www.analytik-jena.de

### Cancer Stem Cell Identification Kit

The new AldeRed ALDH Detection Kit is designed for identifying and isolating cancer stem cells. The AldeRed reagent is used to label cancer stem cells with a red fluorescent dye, making it possible to distinguish cancer stem cells in live cell populations where specific identification was previously impossible. Aldehyde dehydrogenase (ALDH), a cancer stem cell marker enzyme, causes the AldeRed reagent to fluoresce in the far-red spectrum, allowing the cancer cells to be identified and isolated with concurrent use of green fluorescent cell lines, transgenic animals, and reporter assays. Previous ALDH reporters exhibited green fluorescence, which made it difficult to identify positive cells in an otherwise green fluorescent background.

#### EMD Millipore

For info: 800-645-5476  
www.emdmillipore.com/stemcells

### Automated Materials Analyzer

The ABR Automated Breakthrough Analyzer is designed to meet the needs of researchers wishing to characterize the gas separation performance of novel materials, such as metal-organic frameworks (MOFs), zeolitic imidazolate frameworks (ZIFs), and covalent organic frameworks (COFs), without the time or expense of synthesizing larger quantities of material. Breakthrough curve measurement allows high-throughput screening and testing of adsorbents, for a wide range of separation processes including CO<sub>2</sub> capture and storage, the purification and recovery of noble gases, natural gas and biogas upgrading, toxic gas removal, and air separation. The ABR is a dedicated breakthrough analyzer, fully automated and supplied with an integrated close-coupled quadrupole mass spectrometer. Different configurations are available to suit

research-scale samples, with bed volumes from 2 cc to 20 cc. Up to six gas inlets are available as well as a dedicated purge stream. Flow rates are selected to suit the specific applications, and the ABR includes an ultralow dead-volume switching valve.

#### Hidden Isochema

For info: +44-(0)-1925-244678  
www.hiddenisochema.com

Electronically submit your new product description or product literature information! Go to [www.sciencemag.org/about/new-products-section](http://www.sciencemag.org/about/new-products-section) for more information.

Newly offered instrumentation, apparatus, and laboratory materials of interest to researchers in all disciplines in academic, industrial, and governmental organizations are featured in this space. Emphasis is given to purpose, chief characteristics, and availability of products and materials. Endorsement by *Science* or AAAS of any products or materials mentioned is not implied. Additional information may be obtained from the manufacturer or supplier.

# Don't miss the debut of ***Science Immunology***.

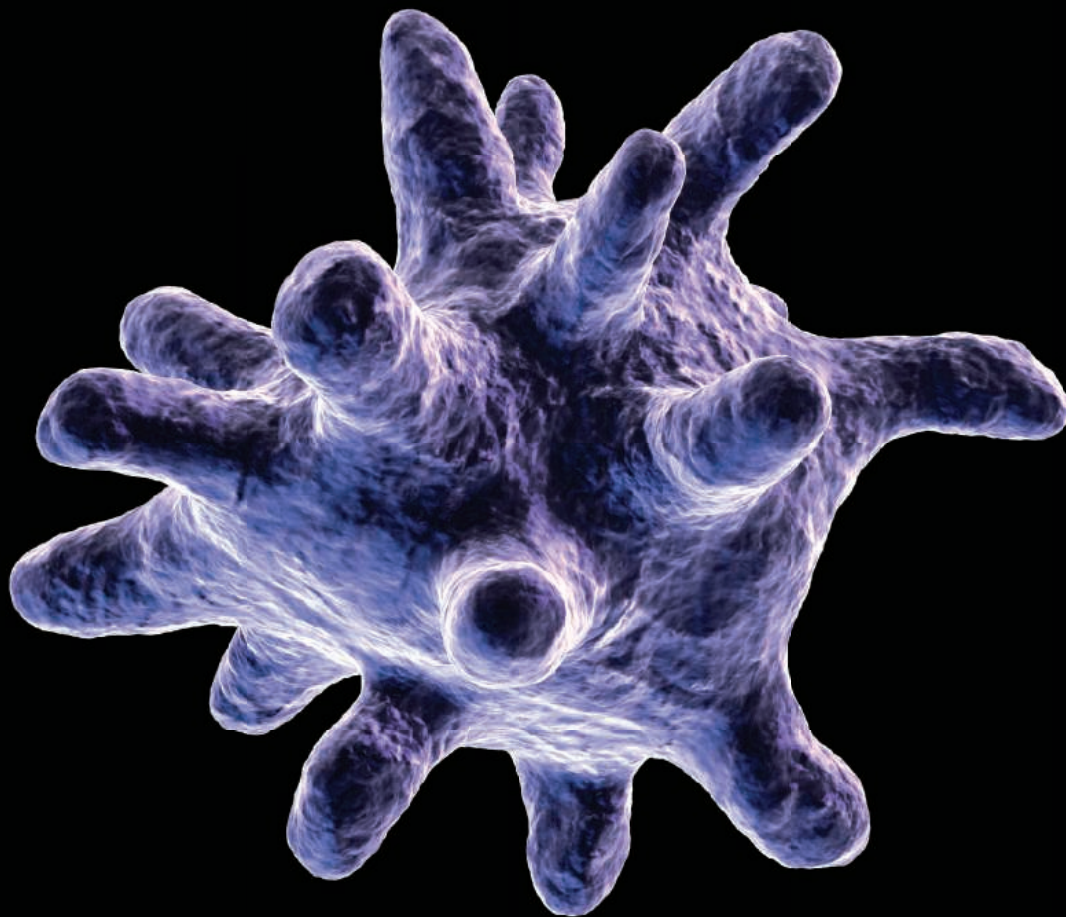


Image: Eraxion / iStockPhoto

---

**NOW ACCEPTING PAPERS**

---

*Science* is expanding its reach into immunology—now offering the newest online-only, weekly journal in the *Science* family of publications. *Science Immunology* will provide original, peer-reviewed research articles that report critical advances in all areas of immunological research, including studies that provide insight into the human immune response in health and disease.

Be a part of the *Science Immunology* debut issue publishing Summer 2016!

Submit your manuscript today at  
**ScienceImmunology.org.**

**ScienceImmunology**

 AAAS

# Time for change.

## Introducing Monarch<sup>™</sup> Nucleic Acid Purification Kits

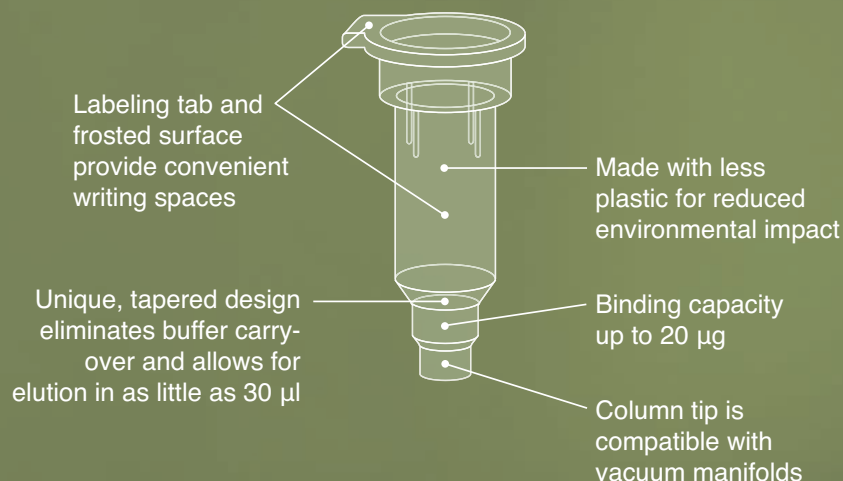
It's time to transform your DNA purification experience. NEB's Monarch Nucleic Acid Purification Kits are optimized for maximum performance and minimal environmental impact. With an innovative column design, buffer retention is prevented, eliminating risk of carryover contamination and enabling elution in smaller volumes. The result – highly pure DNA for your downstream applications.

Make the change and migrate to Monarch today.

---

### Optimized design of Monarch Miniprep Columns

---



---

Request your free sample  
at **NEBMonarch.com**

---





There's only one **Science**

## Science Careers Advertising

For full advertising details, go to ScienceCareers.org and click For Employers, or call one of our representatives.

### Tracy Holmes

Worldwide Associate Director  
Science Careers  
Phone: +44 (0) 1223 326525

### THE AMERICAS

E-mail: [advertise@sciencecareers.org](mailto:advertise@sciencecareers.org)  
Fax: +1 (202) 289 6742

### Tina Burks

Phone: +1 (202) 326 6577

### Nancy Toema

Phone: +1 (202) 326 6578

### Online Job Posting Questions

Phone: +1 (202) 312 6375

### EUROPE / INDIA / AUSTRALIA / NEW ZEALAND / REST OF WORLD

E-mail: [ads@science-int.co.uk](mailto:ads@science-int.co.uk)  
Fax: +44 (0) 1223 326532

### Sarah Lelarge

Phone: +44 (0) 1223 326527

### Kelly Grace

Phone: +44 (0) 1223 326528

### Online Job Posting Questions

Phone: +44 (0) 1223 326528

### JAPAN

### Katsuyoshi Fukamizu (Tokyo)

E-mail: [kfukamizu@aaas.org](mailto:kfukamizu@aaas.org)  
Phone: +81 3 3219 5777

### Hiroyuki Mashiki (Kyoto)

E-mail: [hmashiki@aaas.org](mailto:hmashiki@aaas.org)  
Phone: +81 75 823 1109

### CHINA / KOREA / SINGAPORE / TAIWAN / THAILAND

### Ruolei Wu

E-mail: [rwu@aaas.org](mailto:rwu@aaas.org)  
Phone: +86 186 0082 9345

All ads submitted for publication must comply with applicable U.S. and non-U.S. laws. Science reserves the right to refuse any advertisement at its sole discretion for any reason, including without limitation for offensive language or inappropriate content, and all advertising is subject to publisher approval. Science encourages our readers to alert us to any ads that they feel may be discriminatory or offensive.

**ScienceCareers**

FROM THE JOURNAL SCIENCE

ScienceCareers.org

## POSITIONS OPEN

## MOTE MARINE LABORATORY & AQUARIUM

### 2017-18 POSTDOCTORAL RESEARCH FELLOWSHIP

Mote Marine Laboratory announces a new two-year position beginning January 2017, to support an independent investigator based at Mote's new facility (~ 26,000 square feet of research and science-education infrastructure) in the Florida Keys. Applications are invited from recent (since January 1, 2014) Ph.D. graduates, including those with firm expectation of graduation by December 2016. However, at time of appointment, a doctoral degree must have been awarded. Proposals for any field of marine research will be considered. Competitive applications will focus on research programs that are relevant to conservation and the sustainable uses of marine biodiversity, healthy habitats, and natural resources; will bring or propose new multi-investigator/institutional collaborations to Mote, and will be cognizant of global issues. For complete Fellowship information and application requirements see website: [www.mote.org/about-us/employment-opportunities](http://www.mote.org/about-us/employment-opportunities). The deadline for applications is August 31, 2016 and finalists will be announced in October.

## Yale SCHOOL OF MEDICINE

A position is available to join a multidisciplinary research team studying spinal cord injury and related chronic disorders (see *Tan et al, J Neurosci.*, **28**:13173-13183, 2008; *Tan Prog Mol Biol Transl Sci.*, **131**:385-408, 2015; *Bandaru et al, J Neurophysiol.*, **113**:1598-1615, 2015). Ph.D. and/or M.D. degree, and experience/publications in neurophysiology with animal models of pain or motor dysfunction are essential. Experience with immunohistochemistry and rodent surgical procedures, including models of SCI and *in vivo* electrophysiology, are strongly desired. Superb opportunity to work as part of a rapidly moving, collaborative team, applying state-of-the-art methodology to investigate SCI, glial scarring, neuropathic pain, and spasticity. Send statement of interest, Curriculum Vitae, and three letters of reference to: Stephen G. Waxman, M.D., Ph.D. or Andrew M. Tan, Ph.D., Neuroscience Research Center, Building 34, Veterans Administration Connecticut Medical Center, (127A), 950 Campbell Avenue, West Haven, CT 06516; e-mail: [stephen.waxman@yale.edu](mailto:stephen.waxman@yale.edu); [andrew.tan@yale.edu](mailto:andrew.tan@yale.edu)

### POSTDOCTORAL POSITION MAIZE CHROMOSOMES

A POSTDOCTORAL POSITION is available in the Division of Biological Sciences at the University of Missouri, Columbia to study the epigenetic aspects of centromere function in maize in terms of the molecular parameters that condition activity and inactivity, the sequence analysis of the supernumerary *B chromosome* in general and its centromere in particular, molecular aspects of *B chromosome* evolution, and exploration of the molecular basis of the drive mechanism of the *B chromosome* using sequence information. The *B chromosome* centromere has the advantage for such studies in that a specific repeat is present in and around this centromere that allows it to be distinguished from all others in the karyotype. The project will also be involved with the development and utilization of whole chromosome exonic paints for each maize chromosome. These paints will be used to examine chromosomal structure, behavior and evolution. The University of Missouri-Columbia has a vibrant plant biology group providing an excellent training environment. *The University of Missouri is an Affirmative Action/Equal Opportunity Employer.* Interested applicants should email their curriculum vitae including contact information of three references to James Birchler (e-mail: [BirchlerJ@Missouri.edu](mailto:BirchlerJ@Missouri.edu)).

## POSITIONS OPEN

### MASTER OF BIOMEDICAL INFORMATICS, HARVARD MEDICAL SCHOOL

**Program Description** The program provides the intellectual framework for clinicians and biomedical scientists in the systematic and sound use of quantitative methods to increase agility with such methods in their respective domains. The program includes an intensive, hands-on quantitative boot camp, a range of foundational courses, and courses in emerging areas such as precision medicine, data science, and data visualization. All students are expected to complete a capstone research project and to participate in a longitudinal seminar series.

Who is this Program for? (1) Postdoctoral students who recognize the relevance of informatics to their research

(2) MD's who are interested in qualifying for the subspecialty in clinical informatics (3) Medical students who would like to take a research year during their training to explore the importance of informatics in the practice of medicine

Contact information to learn more about the program, please visit our website and email us with any questions through our 'Contact Us' page: <https://informaticstraining.hms.harvard.edu/>

A POSTDOC RESEARCH ASSOCIATE Position is open at Wright State University (WSU) to study Cell Cycle and Checkpoint Signaling (website: <http://people.wright.edu/yong-jie.xu>). Candidates with experiences in molecular and cell biology, genetics or protein biochemistry are encouraged to apply online at website <http://jobs.wright.edu/postings/10105>.

Wright State University: Affirmative Action/Equal Opportunity Employer/Male/Female/Veteran/Disability.

## Post Your Jobs

1.4 million candidates\*  
235,000 job applications\*



Reach Scientists.  
Fill Positions.

\*Jan-Dec 2015

**ScienceCareers**  
[employers.sciencecareers.org](http://employers.sciencecareers.org)

## SEARCH JOBS ON THE GO!

Download the App

**ScienceCareers**  
[apps.sciencemag.org](http://apps.sciencemag.org)





## Search results: Careers in high tech

High technology permeates every corner of every enterprise, from global computing corporations, to social media and search establishments, to retail giants. Not surprisingly, these industries offer attractive playgrounds for Ph.D.-level scientists and engineers. **By Alaina G. Levine**

**A**lmost every moment of our day is somehow touched by high technology. Whether you are searching for an old friend or buying coffee on the Internet, billions of lines of code, petabytes of data, and a potentially infinite amount of brain power make it possible. And behind every invention are scientists and engineers. As more industries are influenced by big data and computer-based systems, the need for talented Ph.D.-level science, technology, engineering, and mathematics (STEM) professionals to contribute to these arenas has grown considerably.

High tech jobs are exciting and diverse: The problems they address are interesting and intense, involve multifunctional (and in many cases, multinational) teams, and offer the chance to make a difference that is felt by customers the world over. As **Nicholas Clinton**, a developer advocate at Google with a Ph.D. in environmental science, policy, and management, says: "It's great to feel like I'm part of something impactful, with real power to effect global-scale change."

As a member of the developer relations team for Google Earth Engine, a platform for Earth science analysis, Clinton strives to ensure that external developers are able to utilize the instrument effectively. He collaborates with the Earth Engine engineering team to help them identify user needs and to improve the platform. "I conduct a lot of trainings, give a lot of lectures, and create documentation to enable users to do incredible things," he says. "I ensure that

researchers can use Earth Engine to perform high-impact, data-driven science."

**Sun Mi Chung**, a Ph.D. astrophysicist and principal data scientist at AOL, also appreciates how rapidly her work affects the public. In her job, she applies machine learning techniques to optimize real-time bidding for advertisements on the AOL platform. "We have to think deeply about what makes sense in terms of the algorithms we use and whether we can put it into production quickly," she says. **Chandra Narayanan's** doctorate is in oceanography, and as director of data science for Facebook, he has engaged with almost every product in the company. With a background in creating numerical models for Earth systems, he was working for the National Weather Service when he heard that a new group was forming at PayPal that was eventually to become one of the first data science groups in industry. Narayanan came on board at PayPal in 2007, where his responsibilities included risk analytics and fraud identification.

His entry into Facebook in 2010 was facilitated by a former colleague. He initially joined the social network in its risk management practice, but every few months, "I took on a new portfolio," says Narayanan. His accomplishments include building from scratch the teams that focus on Instagram, games, risk, payments, and advertisements. But he is most proud of his ability "to be able to charter a new course for what data science means in industry," he says. "Many companies are using Facebook as their model to form data science teams."

### Investigating the diversity of destinations

Not surprisingly, data science careers are particularly prominent in the high tech space. **David Evans** is a computational linguist with a Ph.D. in computer science from Columbia University. He is also passionate about Japanese language and culture and had studied it since he was an undergraduate. An internship at IBM Japan while in grad school solidified his interest to work in that country and combine his two loves. While pursuing a postdoc at the National Institute of Informatics in Tokyo, Japan, an Amazon recruiter contacted him about an opening related to information retrieval and searching. The company **cont.>**



Sun Mi Chung

### Upcoming Features

**Cancer Research Careers—April 8** ■ **Regional Focus: China—June 24** ■ **Postdoc Careers—August 26**



**“I address grand challenges in Africa and develop solutions that affect people’s lives.”**

— **Temitope A. Ogunyoku**



needed someone who had both data analytic skills and a prowess in Japanese linguistics. “Because Japanese and English are so different, there are very different ways of searching for information in those languages,” says Evans. Given his research in information retrieval and the fact that he was bilingual, “it made sense for me to go to Amazon,” he says, and today he is a senior search engineer working for A9, a wholly owned subsidiary of Amazon Japan.

With data being utilized in increasingly new and creative ways, the diversity of career paths in high tech companies has increased, especially in multinational firms like IBM. **Kristen Beck** and **Temitope A. Ogunyoku** are both IBM employees and scientists who hold a Ph.D.—Beck’s doctorate is in biochemistry, molecular, cellular, and developmental biology, and Ogunyoku’s is in civil and environmental engineering. Their jobs and career paths are very different and are on opposite ends of the planet. And neither of them do what one might expect at Big Blue.

Beck, who is based at IBM Almaden Research Center in Silicon Valley, works on bioinformatics problems in association with the University of California, Davis and Mars, Incorporated. She is examining ways in which analytics can be applied to food safety on various fronts, including pathogen detection, antibiotic resistance, and food fraud or mislabeling. She leverages her biology background to implement solutions based on life science tools, such as next-generation sequencing.

Ogunyoku is a research scientist with IBM Research—Africa in Nairobi, Kenya, one of only 12 global research labs in IBM’s portfolio, where “I address grand challenges in Africa and develop solutions that affect people’s lives,” she says. Her focus is on creatively utilizing analytics to scrutinize complex interconnected datasets and deploy solutions in fields such as public safety and waste management. For example, her team monitored social media in Kenya for data about crime, because people use it as a platform to report public safety concerns. “We used algorithms and natural language processing systems to detect and determine the credibility of these incidences,” she explains, adding that the goal of this research was to develop a product that can be used by security companies to alert their clients of criminal activity.

### Searching for an “in”

At Facebook, there are multiple entry points for Ph.D.-level scientists and engineers interested in joining the company. Your doctorate gives you access to jobs in product management, engineering, design, analytics, user experience

research and even marketing and sales, says Narayanan. The key to employment? “Love the mission, be quantitative, be interested in solving hard problems and building awesome products,” he stresses. As the head of recruitment for analytics, he looks for candidates who display a “ton of curiosity, drive and leadership, have a highly analytic nature, enjoy a fast-paced environment,” and of course have superior coding skills. Interestingly, new employees in Facebook’s analytics department come in through a central pool, and after a five-week boot camp and orientation, can pick which group they want to work with.

Similarly, at Amazon, Ph.D. scientists are recruited for their technical expertise, and “you get to come in and look for a way to apply your work,” says Evans. “Your career is up to you. Amazon matches capabilities to interests and interests to projects.” For his team, he looks for professionals with a background in machine learning, computational linguistics, and information retrieval. But the key to getting a job, especially in software development and analytics, is to clarify “how what you are doing now can be applied to products [and systems] at the company,” he adds. That’s essentially how Clinton landed a position at Google. “The more you can demonstrate how Google can leverage your research and development work to achieve amazing, broadly applicable results, the better [your chances for getting a job],” adds Clinton.

In smaller organizations and startups, the hiring process tends to focus on immediate needs, as dictated by the business plan. When **Kamal Jain**, CEO and founder of Faira, a technology company for real estate, recruits, he



looks for people with skills that match the task to be done. **Radu Rusu**, CEO and cofounder of Fyusion, a startup looking to reinvent the use of 3D imaging for consumer applications, pores over publications to find “research results that match our roadmap,” he says. But he also keeps an eye out for scientists who possess honesty, humility, and flexibility, a marker of their potential to prosper in his organization.

### Navigating a new culture

As you transition into high tech, it is important to recognize the variances in culture among these types of companies, as compared to other sectors. One of the features of Google’s culture that Clinton immediately noticed is its emphasis on teams, which takes a different approach than what is usually found in universities. “The team environment is a big change from academia, where you work in collaborations, but a lot of time is spent on independent study,” he says. At Google, “you need very tight teamwork, timing, communication, and camaraderie to compete successfully.” At FICO, the financial services company, teams are always interdisciplinary, says **Scott Zoldi**, chief analytics officer, who holds a doctorate in physics. “You have to **cont.>**



The National Academies of  
SCIENCES • ENGINEERING • MEDICINE

**Graduate, Postdoctoral, and Senior Research Awards**  
offered for research at  
US federal laboratories and affiliated institutions

**Opportunities for research in all areas of science and engineering**

- Awards for independent research at over 100 participating laboratory locations
- 12-month awards renewable for up to 3 years
- Annual stipend \$45,000 to \$80,000 for recent PhD recipients and higher for additional experience. Graduate entry level stipend is \$30,000 and higher for additional experience
- Relocation, professional travel, and health insurance
- Annual application submission deadlines February 1, May 1, August 1, November 1
- Open to international applicants

Detailed program information, including instructions on how to apply online can be found on the NRC website at:

[www.nationalacademies.org/rap](http://www.nationalacademies.org/rap)

Applicants must contact Adviser(s) at the lab(s) prior to application deadline to discuss research interests and funding opportunities.

Questions should be directed to the:

**NRC Research Associateship Programs**

TEL: 202-334-2760; EMAIL: [rap@nas.edu](mailto:rap@nas.edu)

Qualified applicants will be reviewed without regard to race, religion, color, age, sex or national origin.

The 2017-2018  
Fulbright U.S. Scholar  
Competition is open

*Opportunities in over 125 countries for faculty, administrators, postdocs, professionals, artists, independent scholars and many others.*

► For more information on recent program innovations, including flexible, multi-country opportunities, please visit:

[www.iie.org/cies](http://www.iie.org/cies)

Fulbright  
SCHOLAR PROGRAM



香港大學

THE UNIVERSITY OF HONG KONG

Founded in 1911, the University of Hong Kong is committed to the highest international standards of excellence in teaching and research, and has been at the international forefront of academic scholarship for many years. The University has a comprehensive range of study programmes and research disciplines spread across 10 faculties and over 140 academic departments and institutes/centres. There are 28,000 undergraduate and postgraduate students who are recruited globally, and more than 2,000 members of academic and academic-related staff coming from multi-cultural backgrounds, many of whom are internationally renowned.

**Post-doctoral Fellowships**

Applications are invited for a number of positions as Post-doctoral Fellow (PDF) at the University of Hong Kong. Appointments will be made for a period of 2 to 3 years and the appointees must be in post on or before February 28, 2017.

PDF posts are created specifically to bring new impetus and vigour to the University's research enterprise. Positions are available from time to time to meet the strategic research needs identified by the University. Positions are available in the following Faculties/Departments/Schools/Centres/Units:

- |  |   |
|--|---|
| • Faculty of Architecture                                    | • Medicine  |
| • Real Estate and Construction                               | • Microbiology                                    |
| • Civil Engineering  | • Orthopaedics and Traumatology                   |
| • Computer Science   | • Pathology                                       |
| • Electrical and Electronic Engineering                      | • School of Public Health                         |
| • Mechanical Engineering                                     | • Centre for Reproduction, Development and Growth |
| • School of Biomedical Sciences                              | • Chemistry                                       |
| • Centre for Cancer Research                                 | • Physics   |
| • Research Centre of Heart, Brain, Hormone and Healthy Aging | • Geography                                       |
| • Centre of Influenza Research                               | • Psychology                                      |
|  | • The State Key Laboratory for Liver Research     |

Post-doctoral Fellows

PDFs are expected to devote full-time to research. Applicants should be doctoral degree holders having undertaken original research that has contributed to the body of knowledge. A highly competitive salary commensurate with qualifications and experience will be offered. Annual leave and medical benefits will also be available.

Procedures

Prospective applicants are invited to visit our webpage at <http://jobs.hku.hk/> to view the list of the Faculties/Departments/Schools/Centres/Units and their research areas for which PDF positions are currently available. Before preparing an application, they should contact the Head of the appropriate academic unit, or the contact person as specified, to ascertain that their research expertise matches the research area for which a vacant PDF post is available.

Applicants must submit a completed University application form, which should clearly state **which position they are applying for**, and in which academic discipline. They should also provide further information such as details of their research experience, publications, research proposals, etc.

Application forms (341/1111) can be downloaded at <http://www.hku.hk/apptunit/form-ext.doc> and further particulars can be obtained at <http://jobs.hku.hk/>. **Closes April 17, 2016.** The University thanks applicants for their interest, but advises that only candidates shortlisted for interviews will be notified of the application result.

The University is an equal opportunities employer and is committed to a Non-Smoking Policy

## Featured Participants

**Amazon**  
www.amazon.com

**AOL**  
corp.aol.com

**Data Incubator**  
www.thedataincubator.com

**Facebook**  
www.facebook.com

**Faira**  
www.faira.com

**FICO**  
www.fico.com

**Fyusion**  
www.fyusion.com

**Google**  
www.google.com

**IBM**  
www.ibm.com



Kristen Beck

be a good listener and a good collaborator,” he says. “It’s a rich environment, where different points of view are not just welcome—they’re expected. It’s not going to be one Ph.D. scientist solving the problem, but rather a group of people, from many different fields, working together....[This] yields better results.”

As Narayanan made his way through PayPal and Facebook, he was intrigued by how much his scientific skills easily transferred to the high tech industry. As an oceanographer, he was used to applying models to understand processes associated with natural phenomena. At PayPal and Facebook, he tapped into the same set of abilities. “It was easy to jump in. In fact it was seamless,” he says. “Being able to analyze data, recognize patterns, summarize results, break down problems in the simplest way—these are the kinds of things I learned prior to joining industry.”

Evans notes that the culture of Amazon encourages employees to identify ways to improve the company, whether or not that improvement is related to their job function. “We have the responsibility. We can take a real ownership of a problem,” he says. This translates to an ecosystem where individuals have a large amount of influence and freedom. One of the main projects he’s worked on had little to do with search capabilities. Rather, it was a company-wide effort that he spearheaded on his own, relating to setting the time of product launches according to local time zones as opposed to a central clock working off of the Seattle headquarters. “We had to replumb everything,” he says, referring to programming the systems to make it easier for customers to purchase items. It took years of partnering with teams across the planet, but “it felt surprisingly powerful to make this change worldwide.”

But Evans also clarifies that Amazon’s philosophy is not for everyone. “There is a lot of pressure,” he admits, “and it’s important to know your limits to achieve a work-life balance.” For someone coming straight from academia, adjusting to this fast-paced ecosystem might be challenging.

### Honing skill sets to achieve success

Although there are ample professional opportunities in the high tech sector, it is critical for candidates to differentiate themselves from the competition, and certain skill sets are particularly advantageous to hone. For software

engineering and data science careers, it is vital to understand databases and algorithms and how to apply them to solve real-world problems, says **Michael Li**, whose Ph.D. is in mathematics. He worked for Intel, Google, Foursquare, and JPMorgan Chase before launching the Data Incubator, which trains STEM Ph.D.’s for data science careers. He emphasizes that technical know-how is what hiring managers crave. “No one needs just an ‘ideas’ person. They need someone who can actually get the job done.”

“The people who are the most successful, marketable, and valuable do their job and also understand the broader picture,” says **John Heinlein**, vice president of marketing for ARM, a global designer of semiconductor intellectual property, whose Ph.D. is in electrical engineering. “They don’t stay in silos. You might never change your role, but you’ll do a better job if you understand what’s happening to the right, left, up, and down in the organization.”

### Advancing your career into new realms

One aspect of high tech companies that is especially attractive to Ph.D. scientists and engineers is the flexibility to determine your own career path. The competition for top talent is fierce, and firms want to retain the brightest minds. So they offer their employees wiggle room to design their own career advancement strategy. For example, it is not uncommon to find lateral moves encouraged.

At Amazon, “I could move back to the States and still remain with my current team,” says Evans of his career options in the future. Adds Ogunyoku: “At IBM, you are able to reinvent yourself. I can go work for the design team or a global business unit, [among other choices]. Having a Ph.D. doesn’t limit me to only research and development.”

With this level of latitude across the high tech arena, job prospects and career decisions may seem overly complex. But there is a simple way to determine your next course of action in crafting a career there: Articulate your own values. “If you pick opportunities that align with your passion, that will help you be successful,” says Beck. “You’ll feel like you are part of the larger picture, and it allows you to be an ambassador for the cause of your choosing.”

*Alaina G. Levine is a freelance science writer based in Tucson, AZ.*

DOI: 10.1126/science.opms.r1600162



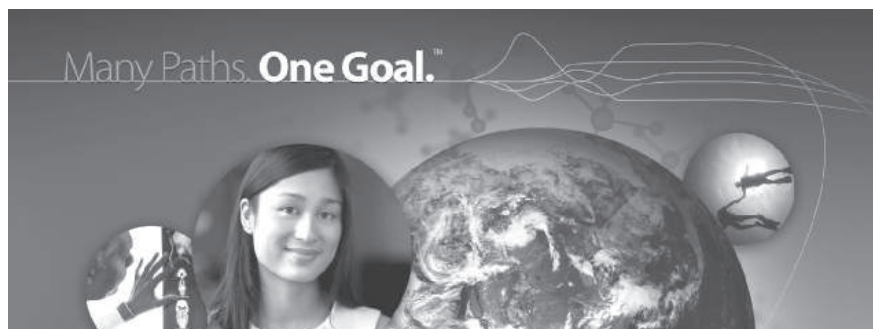
## Postdoctoral Position at the University of Southern California

Postdoctoral position is available immediately in Dr. Yang Chai's laboratory at the Center for Craniofacial Molecular Biology University of Southern California in Los Angeles. We are interested in the regulation of developmental patterning, organogenesis and mesenchymal stem cells. Our studies will seek to define molecular mechanisms governing both normal and abnormal craniofacial development, providing scientific rationales for future therapeutic strategies to prevent and treat craniofacial birth defects.

The candidate must have a PhD and be experienced with molecular and developmental biology. For details, please visit [https://dent-web10.usc.edu/ccmb/faculty\\_detail.asp?RS=1](https://dent-web10.usc.edu/ccmb/faculty_detail.asp?RS=1)

Send application, resume and three letters of recommendation to **Dr. Yang Chai** (c/o [pathomps@usc.edu](mailto:pathomps@usc.edu)).

EOE/AA



## Pfizer Worldwide Research and Development Postdoctoral Program

At Pfizer, postdocs are trained in the art and science of drug discovery, and work side-by-side with scientists who are expert in cutting-edge biology, disease mechanisms, drug delivery and mechanisms of action, and the engineering of novel therapeutic proteins, vaccines, and nucleic acids. Areas of scientific focus include cardiovascular and metabolic diseases, clinical research, comparative medicine, drug safety, biotherapeutics/protein engineering, inflammation and immunology, human exploratory biology, medicinal chemistry, neuroscience and pain, oncology, pharmacology, and vaccines, among several others.

We recruit highly motivated Ph.D. recipients with an outstanding record of scientific productivity and a passion for ground-breaking, fast-paced research that facilitates the development of innovative therapies for human diseases. Our program promotes dissemination of research through publications and participation in scientific meetings, provides opportunities for collaboration with leading academic labs and industry consortia, and offers exceptional professional development training and networking opportunities.

To explore our program and research, visit us online at:  
[www.pfizercareers.com/student-programs/postdoc](http://www.pfizercareers.com/student-programs/postdoc)



Working together for a healthier world®

[www.pfizercareers.com](http://www.pfizercareers.com)



University of California  
San Francisco

## Postdoctoral Positions

The Institute for Neurodegenerative Diseases (IND) is recruiting postdoctoral research fellows to work at the IND with Director Stanley B. Prusiner.

The IND's mission is to investigate and create therapies for neurodegenerative diseases: Alzheimer's, Parkinson's, multiple system atrophy, chronic traumatic encephalopathy, PrP prion diseases. Research opportunities range from the fields of molecular, cell and structural biology and transgenic rodent models to mass spectrometry, synthetic chemistry and computer modeling. A major effort is devoted to an extraordinary drug discovery program.

The IND is housed in the state-of-the-art Sandler Neurosciences Center on the UCSF Mission Bay campus, greatly facilitating interactions with many different scientists possessing diverse expertise.

Applicants should hold or be close to completing an M.D. or Ph.D. degree and possess superior writing skills. Interested candidates should apply online at: <http://ind.ucsf.edu/careers/postdoctoral>

## Immediate Opening for Postdoctoral/Research Associate Level Neurophysiologist

VeroScience is a small but very well developed biotechnology company focusing on neuroendocrine therapies for metabolic and immunological diseases. The company developed and owns Cycloset®, an FDA-approved therapy for the treatment of type 2 diabetes. VeroScience also has a strong pipeline of metabolic disease products and therapies for immunological disorders. The company is a hybrid of academic environment mindset and industrial focus within a small and efficient organization. The company conducts preclinical and clinical research nation-wide, utilizing strong academic and pharmaceutical industry collaborations to advance its development programs.

VeroScience has an immediate opening for a postdoctoral level neurophysiologist-electrophysiologist, **with demonstrated expertise in the use of in vivo electrophysiological techniques to study neuronal activities within the central nervous system, including the use of direct wire micro-electrode recordings.** The successful candidate will have expertise in studies with both in vivo and in vitro models systems to investigate synaptic signal transduction activities between neurons in the central nervous system. A working knowledge of hypothalamic functions in the regulation of metabolism, particularly in insulin resistant states with a working knowledge of fuel sensing mechanisms within the central nervous system and hypothalamus would be a positive attribute for this position, though it is not required. Expertise in diverse molecular and cellular techniques to investigate neuronal signal responses to various fuel and neuro-modulatory exposures would be beneficial. Such activities will be studied in the context of the development and treatment of various metabolic disease states (diabetes, metabolic syndrome) and the impact of novel neuroendocrine therapies upon these disease states. The candidate will be part of an interdisciplinary team of scientists including neuroscientists, molecular biologists, chemists, zoologists, metabolic physiologists, chronobiologists, and endocrinologists in this metabolic disease therapy development program. Also, the group will interact with external collaborators from academia and industry. However, the candidate must be able to work independently and generate reports and publications from such investigations. **Importantly, the successful candidate must have an excellent command of the English language and a demonstrated ability to publish well written articles in peer reviewed journals in this research area.**

VeroScience offers competitive salaries and benefits as well as a very unique and stimulating working environment that allows one's efforts and achievements to be quickly applied to real world health problems. Please send CV, names and contact information of three references, and a 1 page summary of scientific interests to [Anthony\\_Cincotta@VeroScience.com](mailto:Anthony_Cincotta@VeroScience.com).





## 香港中文大學 The Chinese University of Hong Kong

Applications are invited for:-

### Department of Microbiology

The Department has a wide range of research facilities and access to a large comprehensive teaching hospital. The establishment provides a good environment for basic as well as clinical research and facilitates collaboration with other disciplines. Further information about the Department is available at <http://www.cuhk.edu.hk/med/mic/>.

#### (1) Assistant Professor (Non-clinical)

(Ref. 1516/193(665)/2) (Closing date: April 18, 2016)

Applicants should have (i) a PhD or equivalent; (ii) a strong research track record in the field of microbiology; and (iii) commitment to undergraduate teaching and postgraduate student supervision. Experience in gut microbiome, microbiota and faecal transplant research will be an advantage.

The appointee will (a) undertake teaching and related educational activities for undergraduate and postgraduate students; (b) supervise MPhil and PhD students; (c) apply for competitive research grants and related funding; and (d) conduct high-standard research projects independently and in collaboration with other parties.

Appointment will normally be made on contract basis for three years initially commencing as soon as possible, which, subject to mutual agreement, may lead to longer-term appointment or substantiation later.

#### (2) Research Assistant Professor

(Ref. 1516/194(665)/2) (Closing date: April 18, 2016)

Applicants should have (i) a PhD or equivalent; and (ii) a strong research track record in the field of microbiology. Experience in gut microbiome, microbiota and faecal transplant research will be an advantage.

The appointee will (a) apply for competitive research grants and related funding; and (b) conducting high-standard research projects independently and in collaboration with other parties.

Appointment will initially be made on contract basis for three years commencing as soon as possible, renewable subject to mutual agreement.

#### Salary and Fringe Benefits

Salary will be highly competitive, commensurate with qualifications and experience. The University offers a comprehensive fringe benefit package, including medical care, plus a contract-end gratuity for appointments of two years or longer, and housing benefits for eligible appointees. Further information about the University and the general terms of service for appointments is available at <https://www2.per.cuhk.edu.hk/>. The terms mentioned herein are for reference only and are subject to revision by the University.

#### Application Procedure

Application forms are obtainable (a) at <https://www2.per.cuhk.edu.hk/>, or (b) in person/by mail with a stamped, self-addressed envelope from the Personnel Office, The Chinese University of Hong Kong, Shatin, Hong Kong.

Please send the completed application form and/or full curriculum vitae, together with copies of qualification documents, a publication list and/or abstracts of selected published papers, and names, addresses and fax numbers/ e-mail addresses of three referees to whom the applicants' consent has been given for their providing references (unless otherwise specified), to the Personnel Office by post or by fax to (852) 3942 0947 by the closing date.

Please quote the reference number and mark 'Application - Confidential' on cover. The Personal Information Collection Statement is obtainable at <https://www2.per.cuhk.edu.hk/>.

## POSITIONS OPEN



## UNIVERSITY OF SOUTH CAROLINA SCHOOL OF MEDICINE

### UNIVERSITY OF SOUTH CAROLINA TENURE-TRACK ASSISTANT PROFESSOR

The Department of Pathology, Microbiology, and Immunology at the University of South Carolina's School of Medicine invites applications for a tenure-track ASSISTANT PROFESSOR position with expertise in Immunology or Microbiology. Special consideration will be given to candidates with expertise in Microbiome or other Omics research. The successful candidate is expected to develop a strong extramurally funded research program complementing current faculty research interests (<http://pmi.med.sc.edu/>), and participate in teaching. The department is currently ranked in the top 15 among Pathology departments in the nation in NIH funding, and hosts several NIH-funded Research Centers including the Center for Complementary and Alternative Medicine, the Center of Biomedical Research Excellence on Dietary Supplements and Inflammation, and the IDeA Network of Biomedical Research Excellence. The department and Centers provide excellent mentoring opportunity to junior faculty. Candidates must have a PhD or equivalent, and at least 3 years of postdoctoral research experience. Competitive salary and startup funds are available. Please submit curriculum vitae and a statement of research and teaching interests with names of 3 references to **Dr. Mitzi Nagarkatti, Chair, Department of Pathology, Microbiology, and Immunology, University of South Carolina School of Medicine, Columbia, SC 29208** or e-mail: [pmi.immunology@uscmed.sc.edu](mailto:pmi.immunology@uscmed.sc.edu). The search will start immediately and will continue until the position is filled. *University of South Carolina Columbia is an Equal Opportunity Affirmative Action Employer and encourages applications from women and minorities and is responsive to the needs of dual career couples.*



### California State University, Long Beach TENURED PROFESSOR Health, Biomedical, or Behavioral Sciences, or Engineering

California State University, Long Beach (CSULB) invites applicants with record of accomplishments to qualify for appointment at the rank of **Full Professor** with tenure starting August 17, 2016. The successful candidate will serve as a 50% Principal Investigator (PI) with two other PIs on the National Institutes of Health funded CSULB BUILD (Building Infrastructure Leading to Diversity) award (website: <http://www.csulb.edu/build>). 50% time academic year for teaching and service in discipline area. For further information, see the position description at website: [www.csulb.edu/divisions/aa/personnel/jobs/posting/2362/index.html](http://www.csulb.edu/divisions/aa/personnel/jobs/posting/2362/index.html). Screening of applications to begin April 18, 2016. CSULB is an Equal Opportunity Employer.

Advance your career  
with expert advice from  
**Science Careers.**



Download Free Career Advice Booklets!

[ScienceCareers.org/booklets](http://ScienceCareers.org/booklets)

#### Featured Topics:

- Networking
- Industry or Academia
- Job Searching
- Non-Bench Careers
- And More



**Science Careers**

FROM THE JOURNAL SCIENCE **AAAS**

Post your jobs Fast and Easy



**Science Careers**

[employers.sciencecareers.org](http://employers.sciencecareers.org)



## CUNY ADVANCED SCIENCE RESEARCH CENTER

The **CUNY Advanced Science Research Center (ASRC)** seeks a dynamic and innovative scientist with demonstrated leadership and research accomplishments in Photonics to serve as:

### CUNY ASRC Director of Photonics & Professor

The ASRC is a hub of scientific exploration in Upper Manhattan, the centerpiece of an integrated network that brings together researchers from a number of science's most dynamic disciplines — Nanoscience, Photonics, Structural Biology, Neuroscience, and Environmental Sciences — in a highly collaborative research environment. Offering state-of-the-art facilities and instrumentation to CUNY scientists of all levels — faculty, postdoctoral fellows, and graduate and undergraduate students — and other researchers from the New York City scientific community, the center positions the University at the vanguard of scientific research and education.

The successful candidate will be expected to develop a center of excellence in photonics research to complement and be integrated with existing activities within the ASRC, CUNY, and the NYC metro area. The candidate is expected to: lead an internationally leading research program; recruit new faculty; build consortia; contribute to teaching at one of the senior CUNY colleges; oversee the Photonics Initiative; and ensure compliance with federal research guidelines and University policies.

Applicants must be accomplished researchers with international stature in a photonics area with an outstanding record of scholarly activities and possess appropriate credentials for a senior faculty appointment at one of the CUNY colleges. The Director will develop the Photonics Initiative into an integral component of the ASRC's scientific portfolio. Preference will be given to those whose experimental research focus areas include but are not limited to one or more of the following: biophotonics, nanophotonics, terahertz technology, ultrafast spectroscopy, single molecule spectroscopy, or plasmonics.

*For more information about the CUNY ASRC Nanofabrication Facility, please visit [nanofab.asrc.cuny.edu](http://nanofab.asrc.cuny.edu)*

*For general information about the CUNY ASRC, please visit [asrc.cuny.edu](http://asrc.cuny.edu)*



To apply, visit [asrc.cuny.edu/jobs](http://asrc.cuny.edu/jobs)

We are committed to enhancing our diverse academic community by actively encouraging people with disabilities, minorities, veterans, and women to apply. We take pride in our pluralistic community and continue to see excellence through diversity and inclusion. EO/AA Employer.



### AAAS is here – helping scientists achieve career success.

Every month, over 400,000 students and scientists visit ScienceCareers.org in search of the information, advice, and opportunities they need to take the next step in their careers.

A complete career resource, free to the public, *Science Careers* offers hundreds of career development articles, webinars and downloadable booklets filled with practical advice, a community forum providing answers to career questions, and thousands of job listings in academia, government, and industry. As a AAAS member, your dues help AAAS make this service available to the scientific community. If you're not a member, join us. Together we can make a difference.

To learn more, visit [aaas.org/plusyou/sciencecareers](http://aaas.org/plusyou/sciencecareers)



## Universitätsklinikum Würzburg



The **Interdisciplinary Center for Clinical Research (IZKF)** organizes the internal research funding of the Medical Faculty of the University of Würzburg. Its major goal is to strengthen clinical research on the basis of interdisciplinary cooperation between clinical and basic research groups. To carry out its mission, the IZKF supports cooperative research grants, promotes training and advancement of young researchers in medicine and improves the scientific infrastructure.

The IZKF intends to establish a new

### Junior Research Group Tissue Regeneration in Musculoskeletal Diseases

to be affiliated with the **Musculoskeletal Center Würzburg (MCW)**. We are looking for a researcher with outstanding postdoctoral experience and international recognition in the general fields of tissue regeneration. This research group should focus on molecular dissection and reconstitution of early tissue regeneration including stem cell technologies, physical and biochemical cues and materials / scaffolds, in order to support concept strategies to establish e.g. SFB initiatives in these areas of research.

In addition to the **position of the Group Leader** the grant of the IZKF will provide funding for up to 5 years for:

- a postdoctoral scientist
- a PhD student
- a technician
- Consumables and start-up funding

Laboratory space and basic equipment will be provided at the Department of Orthopedics König Ludwig Haus.

Further information on our homepage at <http://www.izkf.ukw.de/>

Interested individuals should send a one-page description of their research interests and future directions, CV and publication list, and the names of three academic referees by 14.04.2016. We may request that short-listed candidates provide a more detailed research proposal at a later date. These candidates also will be invited to present their research in Würzburg.

Preference will be given to people with disabilities in the case of otherwise equal aptitude. The University aims to increase the proportion of female researchers; therefore applications from qualified women are particularly welcome.

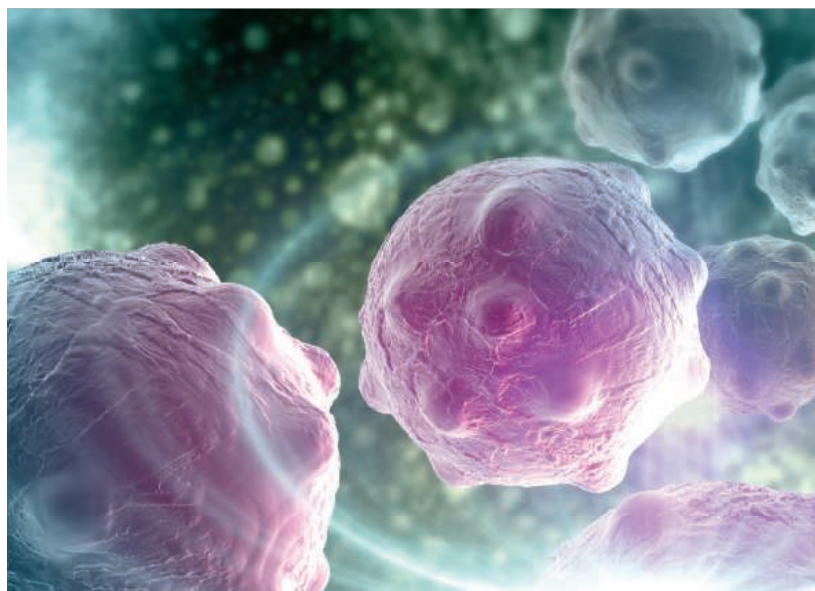
Applications should be sent via email in one pdf-file to the IZKF office to:

[hawks\\_m@ukw.de](mailto:hawks_m@ukw.de)

Informal inquiries can be made to Prof. Heike Walles – [heike.walles@uni-wuerzburg.de](mailto:heike.walles@uni-wuerzburg.de)

APPLICATION DEADLINE: 14.04.2016





Cancer Feature:

# Cancer Research

Issue date: April 8

Ads accepted until April 1 if space allows

For recruitment in science, there's only one *Science*.

**Looking to hire a cancer researcher?** Reach them through the pages of *Science*. Our upcoming cancer feature explores how major institutions are planning to prepare for the challenges involved in precision medicine. This hot research area is sure to draw the readers you need to reach.

## What makes *Science* the best choice for recruiting?

- Read and respected by 400,000 readers around the globe
- Your ad dollars support AAAS and its programs, which strengthens the global scientific community.

## Why choose this feature for your advertisement?

- Relevant ads lead off the career section with a special cancer research banner
- Bonus distributions:

American Association for Cancer Research,  
April 16–20, New Orleans, LA

AACR Career Fair, April 16, New Orleans, LA.

## Expand your exposure by posting your print ad online:

- Link on the job board homepage to a landing page for cancer research positions.

**Deliver your message to a global audience of targeted, qualified scientists.**

**129,574**

subscribers in print every week

**352,966**

monthly unique browsers on ScienceCareers.org

**65 %**

of our weekly readers are Ph.D.s



Produced by the *Science*/AAAS Custom Publishing Office.

SCIENCECAREERS.ORG

# Science Careers

FROM THE JOURNAL SCIENCE  AAAS

To book your ad: [advertise@sciencecareers.org](mailto:advertise@sciencecareers.org)

The Americas  
+202 326 6582  
Japan  
+81 3 3219 5777

Europe/RoW  
+44 (0) 1223 326500  
China/Korea/Singapore/Taiwan  
+86 186 0082 9345





## Chief, Division of Endocrinology

Stony Brook University School of Medicine at the State University of New York invites applications for the position of Division Chief of Endocrinology from experienced Endocrinology faculty.

**Required Qualifications:** Physician candidates with U.S. Board Certification in Internal Medicine and either an MD or combined MD/Ph.D. degrees. High level of clinical competence. Collaborative leadership style. Strong administrative skills. Strong scholarly background and a vision to expand the division's existing clinical, research and training endeavors. Strong interpersonal and communication skills. Experience in budgetary/fiscal/personnel management as well as proven mentorship ability.

**Preferred Qualifications:** Demonstrated publication and/or funding track record in clinical, translational, and/or basic research. Commitment to advancing scientific knowledge of the field of Endocrinology, as well as demonstrate a strong commitment to clinical, educational and academic excellence. Experience with development, management and expansion of a robust clinical program.

**Responsibilities & Requirements:** The Division Chief of Endocrinology is a full time position reporting directly to the Chair of the Department of Medicine. Responsibilities include overseeing the clinical care delivered by faculty within the division, promoting investigator-initiated scholarship and engaging in the training and professional development of junior faculty, fellows, residents and students. Other responsibilities include strengthening collaborative relationships with related departments. A critically important role for the Division Chief will be to engage faculty physicians in delivering high-quality care, improved service, and lower costs for our patients. Under strong leadership, the Division is anticipated to evolve into a major national and regional force in Endocrinology.

To qualify for an appointment as Associate Professor or Professor, the candidate must meet the criteria established by the School of Medicine (School of Medicine's Criteria for Appointment, Promotion and Tenure).

**Anticipated Start Date:** ASAP.

**Salary:** Commensurate with experience.

**Application Procedure:** Those interested in this position should submit a State employment application, cover letter and resume/CV to:

Vincent W. Yang, MD, Ph.D.  
c/o Susan Legrady  
Department of Medicine  
Health Sciences Center, Level 16, Room 020  
Stony Brook University  
Stony Brook, NY 11794-8160  
Fax: (631) 444-3144

For a full position description, or application procedures, visit: [www.stonybrook.edu/jobs](http://www.stonybrook.edu/jobs) (Ref. # F-9618-16-03).

*Equal Opportunity Employer; females, minorities, disabled, veterans*



## FUNDING OPPORTUNITIES — U.S. Department of Defense

### Defense Health Program

### Peer Reviewed Medical Research Program

The Peer Reviewed Medical Research Program (PRMRP) funds exceptional research with the goal to improve the health and well-being of all military Service Members, Veterans, and their beneficiaries. The PRMRP received **\$278.7 million** in fiscal year 2016 (FY16) and seeks grant applications in the following **topic areas**:

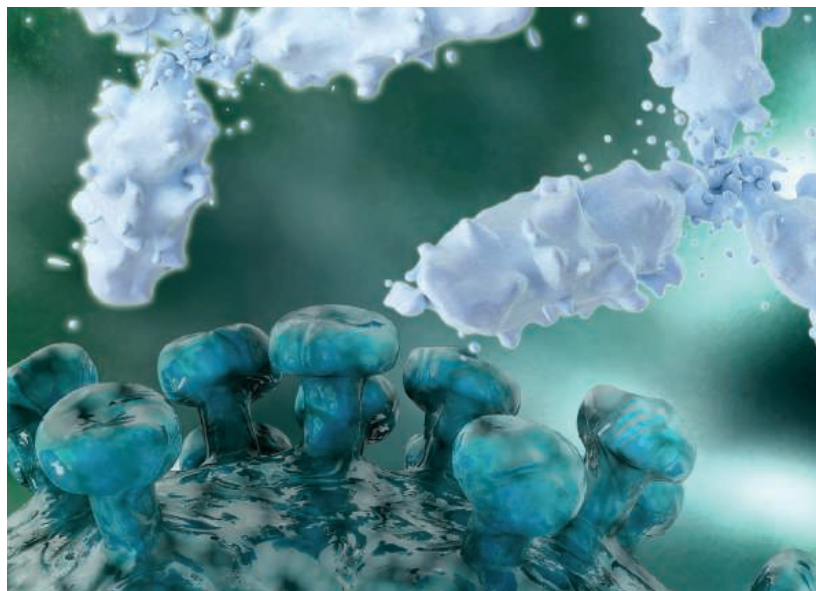
Acute Lung Injury	Fragile X Syndrome	Mitochondrial Disease	Rett Syndrome
Antimicrobial Resistance	Hepatitis B	Nanomaterials for Bone Regeneration	Rheumatoid Arthritis
Chronic Migraine and Post-Traumatic Headache	Hereditary Angioedema	Nonopioid Pain Management	Scleroderma
Congenital Heart Disease	Hydrocephalus	Pancreatitis	Sleep Disorders
Constrictive Bronchiolitis	Inflammatory Bowel Disease	Pathogen-Inactivated Dried Plasma	Tinnitus
Diabetes	Influenza	Polycystic Kidney Disease	Tuberculosis
Dystonia	Integrative Medicine	Post-Traumatic Osteoarthritis	Vaccine Development for Infectious Disease
Emerging Infectious Diseases	Interstitial Cystitis	Psychotropic Medications	Vascular Malformations
Focal Segmental Glomerulosclerosis	Lupus	Pulmonary Fibrosis	Women's Heart Disease
	Malaria	Respiratory Health	
	Metals Toxicology		

Descriptions of the FY16 PRMRP Program Announcements and General Application Instructions are anticipated to be posted on Grants.gov by **mid-March 2016**:

- Clinical Trial Award
- Discovery Award
- Focused Program Award
- Investigator-Initiated Research Award
- Technology/Therapeutic Development Award

*All applications must conform to the Program Announcements and General Application Instructions that will be available for electronic downloading from the Grants.gov website (all viewable under CFDA number 12.420). Execution management support will be provided by the Congressionally Directed Medical Research Programs.*

For more information, please visit: <http://cdmrp.army.mil/funding/prmrp.shtml>  
<http://cdmrp.army.mil>



For recruitment in science, there's only one *Science*.

Special Job Focus:

# Immunology

Issue date: May 6

Book ad by April 19 to  
guarantee space

Ads accepted until April 29  
if space allows

## What makes *Science* the best choice?

- Read and respected by 400,00 readers around the globe
- 75% of readers read *Science* more often than any other journal
- Your ad dollars support AAAS and its programs, which strengthens the global scientific community.

## Why choose this Immunology Focus for your advertisement?

- Relevant ads lead off the career section with special immunology banner
- Bonus distribution to Immunology 2016 (AAI), May 13–17, Seattle, WA.

## Expand your exposure.

### Post your print ad online to benefit from:

- Link on the job board homepage directly to immunology jobs
- Dedicated landing page for jobs in immunology
- Additional marketing driving relevant job seekers to the job board.

Deliver your message to a  
global audience of targeted,  
qualified scientists.

# 129,574

subscribers in print  
every week

# 37,942

unique active job seekers  
searching for **immunology**  
positions in 2015

# 41,047

applications submitted  
for **immunology** positions  
in 2015



Produced by the *Science*/AAAS Custom Publishing Office.

SCIENCECAREERS.ORG

# Science Careers

FROM THE JOURNAL SCIENCE AAAS

To book your ad: [advertise@sciencecareers.org](mailto:advertise@sciencecareers.org)

**The Americas**  
+202 326 6582  
**Japan**  
+81 3 3219 5777

**Europe/RoW**  
+44 (0) 1223 326500  
**China/Korea/Singapore/Taiwan**  
+86 186 0082 9345



暨南大学  
JINAN UNIVERSITY



## Principal investigator (PI) recruitment - Orthopedic research – Guangzhou, the First Affiliated Hospital of Jinan University

### Job description

The Department of Orthopedics of the First Affiliated Hospital at Jinan University invites applications for a full-time Orthopedic research PI position in the area of Orthopedic diseases, including: I) epigenetic regulation mechanisms of knee osteoarthritis and diabetic osteoarthritis; II) the discovery of circulating biomarkers (peptide, protein, DNA, exosome) for the early diagnosis of human osteoarthritis and arthritis-related diseases; III) development of novel approaches for the early detection of osteoarthritis and infection after total knee (hip) arthroplasty. Applicant should have at least a Doctorate degree (M.D. and/or Ph.D.) with senior level research experience in research lab or at least 2-4 years of productive post-doctoral training experiences. Applicants must demonstrate a research focus on the elucidation of the cellular and molecular mechanisms of osteoarthritis, diabetic osteoarthritis and arthritis-related diseases. Candidates will be considered who employ relevant training in cells and molecular biology, molecular pathology, and preferably related to epigenetic regulation, circulating biomarkers discovery and arthritis study. Experience in type-2-diabetes or knee osteoarthritis diseases would be a plus. Applicants should send a curriculum vita, a summary of planned and/or ongoing research, and three letters of reference to: Director of Orthopedic of the First Affiliated Hospital at Jinan University (<http://www.jd120.com/>)

### Salary Range

Refer to Type II recruitment of Jinan University (Thousand Talents Plan, Cheung Kong Scholar, and Distinguished Young Scientists)

### Applicant Special Instructions

Materials needed to send: CV, research plan or summary, and three references to:

Contact Name: Zhen-Gang Zha, M.D. and Ph.D.

Phone: 86-20-38688617 FAX: 86-20-38688000 Email: zhgzg@vip.163.com

Mailing Address: Institute of Orthopedic Diseases and Department of Orthopedics, the First Affiliated Hospital, Jinan University, Guangzhou, 510630, China

**Deadline for Application:** April 30, 2016

## Job Vacancies in China's Universities



### China's Rapid Development — More Opportunities

- ❖ **Nanjing Normal University(Nanjing, China)**  
Distinguished professors wanted all over the world at Jangsu, China for multiple disciplines, and provides competitive conditions.
- ❖ **Southeast University (Nanjing, China)**  
Southeast University invites applications from outstanding scientists for tenure track positions, and positions of chair professors and visiting professors.
- ❖ **Nanjing University of Aeronautics and Astronautics (Nanjing, China)**  
NUAA hunts for talents from home and abroad in Natural Sciences, Humanities, Social Sciences, Management, Aeronautics, Astronautics and Civil Aviation.
- ❖ **Sichuan University ( Chengdu, China)**  
Open Faculty and Postdoc Positions at Industrial Internet Institute offered: physics, mathematics, automation control, computer science, artificial Intelligence, information technology, mechanical engineering.
- ❖ **The Institute for Advanced Study (IAS) of Shenzhen University (Shenzhen, China)**  
Professors Positions Available at Shenzhen University in Risk Management, Statistics, Material Physics, Soft-Matter Physics & Physical Biology, Material Chemistry, Marine Biology, Bio-Medicine.
- ❖ **Wuhan University ( Wuhan, China)**  
Job vacancies in mechanical engineering, information and communication engineering, power systems and automation, environmental science and engineering, new energy materials, transportation engineering and so on.

Looking for more positions , please send your CV to [acabridge@163.com](mailto:acabridge@163.com)  
Hotline: +86-10-62603373 +86 15300215485

广告联系: 赵佳 zhaojia@eol.cn +86-10-62603373



## Faculty Recruitment of Tianjin University & Invitation of PEIYANG Forum for Young Scholars 27th-30th Apr 2016, Tianjin

### Positions

Tianjin University ([www.tju.edu.cn](http://www.tju.edu.cn)) invites outstanding applicants for full-time positions of full professorship, and looks for candidates in the following areas.

### Science or Engineering:

Engineering, natural science, life science, pharmacy, information technology, relevant emerging inter-disciplines, etc.

### Other Academic Fields:

Architecture, economics, business, management, social sciences, relevant emerging inter-disciplines, etc. Applicants with research background of multi-disciplinary and non-traditional approach are highly expected.

### Qualifications

Applicants shall be no more than 40 years old, holding a PhD degree with at least 2 years of working experiences at abroad. Applicants shall be expected to be promising scholars who have obtained outstanding academic performance and international acknowledgements in their academic fields.

### Salary and Benefits

The appointee, who is successfully entitled National Youth "1000-Plan" by applying through TJU, shall be qualified for the benefits as following:

An annual pre-tax salary ranging from 400k to 600k, the relocation allowance of 1.5 million, the academic title of professor, the arrangement of spouse's work and children education.

The salary standards in other academic fields shall be formulated in references with that of science or engineering, and can also be pertinently adjusted according to the identity, credentials, and academic characteristics.

### Work Supports

The work supports concerning with the start-up funds, working space and enrolling quota of postgraduate shall be offered to appointee.

### Forum Arrangements

In order to help applicants getting well known about TJU, the PEIYANG Forum for Young Scholars in Science and Engineering will be held from April 27 to 30, 2016 at TJU. The invitee's travel and accommodation will be covered by TJU. Each applicant's reimbursement is no more than 10,000 RMB. More details can be referred to the website <http://hr.tju.edu.cn/zpxx/js/>.

The arrangements of the PEIYANG Forum for Young Scholars in other fields will be informed later.

### Deadline for Applications

Please submit a complete application package consisting of the following documents to [oplan@tju.edu.cn](mailto:oplan@tju.edu.cn). The application deadline is 15th April 2016.

- (1) A detailed application form which can be downloaded from <http://hr.tju.edu.cn/zpxx/js/>;
- (2) A detailed curriculum vitae;
- (3) Publication list and five full-text representative publications.

### Contacts

**Contact Persons :** Ms. ZHANG Yinlu, Dr. LIU Na  
Human Resource Department,  
Tianjin University, China

**E-mail:** [oplan@tju.edu.cn](mailto:oplan@tju.edu.cn)

**Telephone:** (+) 86-022-27402079

**Fax:** (+) 86-022-27404177

**Address:** B316/Building XINGSUN, 135 YAGUAN Road, JINNAN District, Tianjin, 300350





For recruitment in science, there's only one *Science*.

Special Job Focus:

# Biotechnology

Issue date: May 27

Book ad by May 10 to  
guarantee space

Ads accepted until May 20  
if space allows

## What makes *Science* the best choice?

- Read and respected by 400,00 readers around the globe
- 75% of readers read *Science* more often than any other journal
- Your ad dollars support AAAS and its programs, which strengthens the global scientific community.

## Why choose this Biotechnology Focus for your advertisement?

- Relevant ads lead off the career section with special biotechnology banner
- Bonus distributions:  
BIO, June 6–9, San Francisco, CA  
BIO Career Fair, June 9, San Francisco, CA.

## Expand your exposure.

### Post your print ad online to benefit from:

- Link on the job board homepage directly to biotechnology jobs
- Dedicated landing page for jobs in biotechnology
- Additional marketing driving relevant job seekers to the job board.

Deliver your message to a  
global audience of targeted,  
qualified scientists.

# 129,574

subscribers in print  
every week

# 48,366

unique active job seekers  
searching for **biotechnology**  
positions in 2015

# 27,111

applications submitted for  
**biotechnology** positions  
in 2015



Produced by the *Science*/AAAS Custom Publishing Office.

SCIENCECAREERS.ORG

# ScienceCareers

FROM THE JOURNAL SCIENCE AAAS

To book your ad: [advertise@sciencecareers.org](mailto:advertise@sciencecareers.org)

The Americas  
+202 326 6582

Japan  
+81 3 3219 5777

Europe/RoW

+44 (0) 1223 326500

China/Korea/Singapore/Taiwan  
+86 186 0082 9345

## Laboratory Based Assistant/Associate Professor in Ovarian Cancer Research

The Department of Medical Oncology at the Dana-Farber Cancer Institute, the Gynecologic Oncology Program of the Susan F. Smith Center for Women's Cancers, and the Brigham and Women's Hospital invite applications for a full-time appointment at the Assistant or Associate Professor level. This individual will develop an independent laboratory-based translational research program focused on ovarian cancer. The research program will interface directly with the translational and clinical research efforts within the Gynecologic Oncology program at DFCl as well as other laboratories at DFCl. Candidates with interests in the genomic basis of ovarian cancer, ovarian cancer biology, and/or immunology as well as research engaged in pre-clinical development of new therapeutic approaches are especially encouraged to apply. The candidate must have an MD and/or PhD and a proven track record of outstanding laboratory research.

The candidate will work principally at the Dana-Farber Cancer Institute and the Brigham and Women's Hospital. Appointment as Assistant or Associate Professor at the Harvard Medical School will be commensurate with experience, training and achievements. Salary and benefits will be competitive with other institutions. Dana-Farber Cancer Institute is an NCI-designated Comprehensive Cancer Center and is an equal opportunity employer.

**Interested candidates must submit a curriculum vitae, a research plan and 3 letters of reference to: Ursula Matulonis, M.D., Director, Gynecologic Oncology Program, Dana-Farber Cancer Institute, 450 Brookline Avenue, Boston, MA 02215. Please send submissions via email to: [umatulonis@partners.org](mailto:umatulonis@partners.org)**



HARVARD  
MEDICAL SCHOOL



BRIGHAM AND  
WOMEN'S HOSPITAL

We are an equal opportunity employer and all qualified applicants will receive consideration for employment without regard to race, color, religion, sex, sexual orientation, gender identity, national origin, disability status, protected veteran status, or any other characteristic protected by law.

## Physician-Scientists

The Penn State Milton S. Hershey Medical Center and Penn State College of Medicine in Hershey, PA, are recruiting five tenure-track physician-scientists at all faculty levels in any clinical or research discipline. These positions include 75% protected time (guaranteed during the four-year start-up period) for basic or translational research, while maintaining some clinical activity.

Candidates should possess M.D. or M.D./Ph.D. degrees, be licensed to practice medicine in the US, and have completed residency, fellowship and/or postdoctoral training. Successful candidates will be expected to maintain a robust externally-funded research program and participate in graduate and postdoctoral training.

Penn State College of Medicine is a collaborative research environment in biomedical and health sciences research with several interdisciplinary graduate degree programs and a physician-scientist pipeline that includes a required research component for all medical students and a vigorous M.D./Ph.D. program. The Penn State Milton S. Hershey Medical Center is a 551-bed, tertiary care facility that serves central Pennsylvania. Review of applications will begin upon receipt.

Interested individuals should submit their CV, a letter of interest, and a description of their research program to [physicianscircuit@hmc.psu.edu](mailto:physicianscircuit@hmc.psu.edu) by June 1, 2016.

The Penn State Milton S. Hershey Medical Center is committed to affirmative action, equal opportunity and the diversity of its workforce. Equal Opportunity Employer - Minorities/Women/Protected Veterans Disabled.



**PennState Health**  
Milton S. Hershey  
Medical Center



**PennState**  
College of Medicine

The Medical Faculty of the University of Bern is accepting applications for a faculty position at the level of

## Full Professor (Ordinariat) for Biomedical Research associated with the Directorate of the Department of Biomedical Research

starting January 1, 2017.

The Department of Biomedical Research (DBMR) is an institution affiliated with the Medical Faculty of the University of Bern with the task of coordinating and supporting biomedical research and the operation of core facilities.

Founded in 1994 as the Department of Clinical Research (DCR), the DBMR supports today the entire biomedical research conducted by the medical clinics of the Bern University Hospital (Inselspital). The DBMR provides an umbrella for all research groups with the aim to promote the exchange of important technologies and encourage scientific cooperation in the field of clinical, basic and translational research. Currently, 47 research groups are located within the DBMR that also encompasses a number of operational core facilities including flow cytometry, proteomics, genomics and live cell imaging. The Director DBMR is responsible for a total of 50 employees.

As Director, the applicant should be a highly qualified scientist and be internationally recognized as a pioneer in the biomedical research field. He/she will be responsible for the organization of research infrastructure affecting all clinics of the Bern University Hospital (Inselspital) and direct the development of core facilities within the DBMR. The applicant will work with clinical researchers, provide scientific advice to research groups and promote the continued development of junior scientists. The candidate will support the scientific development of the Medical Faculty by conducting his/her own research. A collaboration with the NCCR RNA and Disease Program is desired and preference will be given to candidates with a corresponding research interest.

We seek applicants with exemplary leadership, management, communication, and networking skills. Candidates must demonstrate the ability to integrate expertise across disciplines and will be called upon to motivate different sectors and professional groups within the DBMR.

A «Habilitation» or equivalent academic track record is required.

The University of Bern is an equal opportunity employer. Women are particularly encouraged to apply in accordance to the DBMR's effort to increase the number of women in leadership positions within the teaching staff of the medical faculty.

Further information can be obtained from the President of the Successor Commission, Prof. Aurel Perren, Director of the Institute of Pathology (E-mail: [aurel.perren@pathology.unibe.ch](mailto:aurel.perren@pathology.unibe.ch)).

Applications must be submitted by April 22, 2016 electronically to the Office of the Dean (E-mail: [bewerbungen@meddek.unibe.ch](mailto:bewerbungen@meddek.unibe.ch)). Information regarding requested documents you find under [http://www.medin.unibe.ch/dienstleistungen/fakultaere\\_rechtssammlung/akademische\\_laufbahn/ausgeschriebene\\_professuren/index\\_ger.html](http://www.medin.unibe.ch/dienstleistungen/fakultaere_rechtssammlung/akademische_laufbahn/ausgeschriebene_professuren/index_ger.html).

Office of the Dean, Medical Faculty, University of Bern,  
Murtenstrasse 11, CH-3008 Bern

By Rosalind A. Segal

# Lessons from a bridge generation

I am part of a bridge generation: the middle of three generations of women working in the sciences. My mother, a cognitive scientist and tenured professor, received her Ph.D. in 1961. I earned my Ph.D. in 1985 and am now a tenured professor of neurobiology. My daughter is currently pursuing a Ph.D. in biology and looks forward to a career in scientific research. Looking across the three generations in my family, I see huge improvements in the experience of women in science, but obstacles still remain for my daughter's generation.

My mother dealt with explicit sexism throughout her career. As an undergraduate, her advisers suggested that she embark on a master's program that would be more flexible for beginning a family, rather than the Ph.D. program she had in mind. When she finished her Ph.D., her advisers assumed it marked the end of her scientific career and that she would stay home to care for her growing family. When she applied for her first grant, she deliberately eliminated all indications of her gender so that the reviewers would assume that her first name, Sydney, was a man's.

In spite of the obstacles, my mother felt her career demonstrated that women could succeed in academic science. Because of her influence, I thought sexism was no longer an impediment to success and so could be ignored, and I was confident that I would not need to choose between children and career. My mentors also provided strong encouragement and support, which strengthened my belief that sexism would not be an obstacle for me.

In retrospect, though, I recognize that my peers and I dealt with attitudes that would now be considered sexist, if not illegal. When a professor propositioned us, we assumed this was acceptable behavior, and all we could do was change classes and alert our friends. When our evaluations and reference letters stated we were "quiet" or we "asked for help frequently," we assumed this indicated our deficiencies. Only later did we realize that such comments are disproportionately used for women, often to the detriment of their careers. These seemingly minor impediments discouraged many of the researchers in my cohort from continuing in science.

As my career progressed, I gradually became aware of the attitudes and policies pervading science that are discouraging to women. When I started as a tenure-track



*"I believe there is reason to be optimistic [for] my daughter's generation."*

assistant professor with two young children, I chose to reduce my salary so that I could concentrate on developing my research program without conflicting administrative duties. Instead, my department chair expected me to do as much administrative work as my male peers, who had negotiated higher salaries and better titles. After being awarded a grant for early-stage investigators, I was dismayed to find that I, the lone woman recipient, was the only one not asked to speak at the foundation meeting. Each episode may be minor, but over time, such incidents accumulate and hinder career advancement.

I believe there is reason to be optimistic that scientists in my daughter's generation are less

likely to encounter such situations. At a recent meeting, two younger women stated that they had never experienced any sexism. I am thrilled to hear this—and I hope it truly reflects an improved environment for women. I worry, however, that it is the same attitude I had early in my career, when gender issues seemed too minor for complaint.

My daughter knows that sexism in science exists and that bias is often unconscious. This awareness prepares her to confront sexist behaviors politely but firmly, confident that the behavior will change and will not impede her success. My hope for her and her generation of scientists is that continued awareness of bias will help push the scientific community to initiate reforms that prevent "minor" problems from accumulating and creating disparities. ■

*Rosalind A. Segal is a neurobiology professor at Harvard Medical School and co-chair of cancer biology at the Dana-Farber Cancer Institute in Boston. Send your story to [SciCareerEditor@aaas.org](mailto:SciCareerEditor@aaas.org).*